

Proceedings of the 2021 session of the 13th *fib* International PhD Symposium in Civil Engineering

held in Paris, France
July 21-22, 2021.

Edited by: Fabrice Gatuingt & Jean-Michel Torrenti

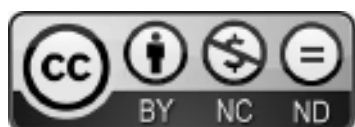
© Fédération Internationale du Béton – International Federation for Structural Concrete

Every effort has been made to ensure that all published information has been reviewed by suitably qualified professionals and that all information submitted is original, has not been published previously and is not being considered for publication elsewhere. Further, the *fib* has made every effort to ensure that any and all permissions to quote from other sources has been obtained. The editor and the publisher are not responsible for the statements or opinions expressed in this publication.

fib Books of Abstracts are not able to, nor intended to, supplant individual training, responsibility or judgement of the user, or the supplier, of the information presented. Although the Scientific Committee did its best to ensure that all the information presented in this publication is accurate, no liability or responsibility of any kind, including liability for negligence, is accepted in this respect by the organization, its members, employees or agents.

All rights reserved. No part of this publication may be reproduced, modified, translated, stored in a retrieval system or transmitted in any form or by any means – electronically, mechanically, through photocopying, recording or otherwise – without prior written permission from the *fib*.

This publication is available on Internet under the following Creative Commons license
Some rights reserved



Published: <http://creativecommons.org/licenses/by-nc-nd/4.0/>

ISSN : 2617-4820

ISBN : 978-2-940643-11-0

Printed in Switzerland.

Symposium Sponsors



École Française du béton
<https://www.efbeton.com>



Association Universitaire de Génie
Civil
<https://augc.asso.fr>



International Union of
Laboratories and Experts in
Construction Materials, Systems
and Structures
<https://www.rilem.net>



Master Builders Solutions
<https://www.master-builders-solutions.com>

***fib* President's message**

Dear PhD candidates,

The *fib* is very happy about the 13th *fib* International PhD-Symposium Session 2 and very pleased with the organization of Chairman Jean-Michel Torrenti and his colleagues.

The PhD Symposia were initiated in 1996 by *fib* Honorary President György Balázs, who saw the value of such events.

Since then, young engineers and researchers have been meeting socially and sharing their experiences in each PhD Symposia. Unfortunately, it is not possible to meet in person this year.

The biggest advantage of the PhD Symposium is to discuss with experienced, long-time *fib* members from different organizations. Therefore, discussion time is much longer compared with other international conferences. This opportunity is valuable not only for young generations but also for long-time members. I hope you seize this benefit from presenting your own work and enjoy the work of others.

Finally, I would congratulate you all on your success. And I would thank the Organizers for their big efforts.

Akio Kasuga

President of the International Federation for Structural Concrete (*fib*)

Preface

A long-standing tradition of the *fib*, the PhD Symposia started in 1996. They were established by Prof. Balázs in Budapest to support young researchers and practitioners. Since then, the *fib* National Groups have already organised twelve symposia. The PhD symposia have become highly-recognised events, boasting the participation of international experts attending the symposia as PhD students' supervisors or keynote speakers. A two-year interval between each symposium allows for a thorough preparation of the event and for a sufficient amount of new information. The spirit of these symposia is to allow for a relaxed and friendly atmosphere, which befits the young generation.

The 13th *fib* Symposium was to be held in Paris in 2020, following the previous symposium in Prague in 2018. Due to the Covid-19 pandemic, we decided to split the symposium into two parts. In 2020 (26 to 28 August), we had an online symposium with the hope to be able to organise an in-person symposium in 2021. Unfortunately, the evolution of the pandemic did not allow us to envisage this. The second session of the 13th *fib* Symposium is therefore also being organised online on 21-22 July 2021.

Two organisations are involved in the preparation of these events: The University Gustave Eiffel and the École normale supérieure Paris-Saclay, with the support of the French association of civil engineering (AFGC - representing the national *fib* group) and the University - Association of Civil Engineering (AUGC) and, of course, of the *fib*.

After a classic review process, the 35 selected papers for 2021 are divided into four themes for the oral presentations with two parallel sessions over two days. Thirty minutes are allowed for each presentation in order to have the opportunity for a long discussion, which is a part of the spirit of these PhD symposia. The best papers will be rewarded by our sponsor (EFB-école française du béton) and by the *fib*. It is a great pleasure for us to express our gratitude to all the sponsors who contributed to the organisation of the symposium.

For 2021, a keynote also enriches the program as in 2020. Magali Anderson (<https://www.holcim.com/magali-anderson>) will present a talk entitled: "Why concrete and cement are key for a net-zero world?" A topic close to the 2020 one and also very important, especially for the researchers of the future.

Finally, let us wish to all participants – especially PhD students – an interesting event. We hope that this Symposium will help them to progress in scientific work and perhaps also in the *fib* activities.

Fabrice Gatuingt, École normale supérieure Paris-Saclay & Jean Michel Torrenti, Université Gustave Eiffel

Scientific committee

Sofiane Amziane - Chair

Maria Aiello, Karim Aït-Mokhtar, Pedro de Oliveira Almeida, György Balázs, José Bastien, Beatrice Belletti, Konrad Bergmeister, Hans-Dieter Beushausen, Francesco Biasioli, Stéphanie Bonnet, Mikael Braestrup, Abraham Corriols, Edoardo Cosenza, Manfred Curbach, Radim Čajka, Avraham Dancygier, Frank Dehn, Wit Derkowski, Vyacheslav Falikman, Michael Fardis, David Fernández-Ordóñez, Stephen Foster, Hans-Rudolf Ganz, Fabrice Gatuingt, Elhem Ghorbel, Petr Hájek, Steinar Helland, Nico Herrmann, Sung Gul Hong, Dick Hordijk, Gintaris Kaklauskas, Milan Kalný, Akio Kasuga, Alena Kohoutková, Lidia La Mendola, Ahmed Loukili, Xilin Lu, Koichi Maekawa, Yann Malecot, Riadh Al-Mahaidi, Giuseppe Mancini, Antonio Marí, Alberto Meda, Aurelio Muttoni, Harald Müller, Takafumi Noguchi, Albert Noumowe, Tor Ole Olsen, Alessandro Palermo, Peter Paulík, Marisa Pecce, Hugo Corres Peiretti, Carlo Pellegrino, Arnaud Perrot, Giovanni Plizzari, Marco di Prisco, Radomír Pukl, Sébastien Remond, Paolo Riva, Anna Saetta, Koji Sakai, Marco Savoia, Johan Silfwerbrand, Alfred Strauss, Fernando Stucchi, Luc Taerwe, Jean-Michel Torrenti, François Toutlemonde, Lucie Vandewalle, Jan Vitek, Sherif Yehia, Yamei Zhang, Bin Zhao

Organizing committee

Jean Michel Torrenti – Chair

Fabrice Gatuingt
Farid Benboudjema
Jean Luc Clément
Olivier Plé
Jean-Philippe Sellin

Participant's Universities

University of Buenos Aires	Argentina
University of Liège	Belgium
Ku Leuven University	Belgium
University of Campinas	Brazil
Universidade Federal Rural do Semi-Árido	Brazil
University of Calgary	Canada
Tsinghua University	China
Shandong university	China
University of Zagreb, Faculty of Civil engineering	Croatia
University of Cyprus	Cyprus
Brno University of Technology, Faculty of Civil Engineering	Czech Republic
Institute of Structural Mechanics	Czech Republic
Czech Technical University in Prague	Czech Republic
Technical University of Denmark	Denmark
University Saadd Dahleb- Blida1	Denmark
Escuela Superior Politécnica del Litoral	Ecuador
Université Paul Sabatier, Toulouse III	France
Université de Lille	France
Université Gustave Eiffel	France
CY Cergy Paris Université	France
Université de Pau et des Pays de l'Adour	France
Université Clermont Auvergne	France
Université de Bretagne Sud	France
Ecole de l'aménagement durable des territoires	France
Ecole Centrale de Nantes	France
ENS Paris-Saclay	France
Université Gustave Eiffel	France
Ecole des ponts ParisTech	France
COMUE Normandie Université - ESITC Caen	France
Polytech Lille	France
ESTP Paris	France
Ruhr-University Bochum	Germany
Technical University of Munich	Germany
University of Stuttgart	Germany
Technische University Dresden	Germany
Leibniz University Hannover	Germany
University of Stuttgart	Germany
Institution of Civil Engineers	Great Britain
National Technical University of Athens	Great Britain
Budapest University of Technology and Economics	Hungary

Indian Institute of Technology Madras	India
Srm Institute of Science and Technology	India
International Institute of Information Technology Hyderabad	India
Mahindra University	India
Shamoon College of Engineering	Israel
University IUAV di Venezia	Italy
University of Padova	Italy
Scuola Superiore Studi Pavia	Italy
Yokohama National University	Japan
Tokyo institute of technology	Japan
Higher institute of earth quake studies and research	Lebanon
University of Malaya	Malaysia
Faculty of sciences and technology of Tangier	Morocco
Delft University of Technology	Netherlands
Eindhoven University of Technology	Netherlands
Nagoya University	Philippines
Bialystok University of Technology	Poland
Lodz University of Technology	Poland
Instituto Superior Técnico	Portugal
NOVA University Lisbon	Portugal
Slovak University of Technology	Slovakia
University of Cape Town	South Africa
Polytechnic University of Catalonia, Barcelona	Spain
Universitat Politècnica de Catalunya	Spain
Universidad Politécnica de Madrid. Escuela de Caminos.	Spain
Chalmers University	Sweden
Ecole Polytechnique Fédérale de Lausanne	Switzerland
Damascus university	Syria
National Cheng Kung University	Taiwan
Ecole nationale d'ingénieurs de Tunis	Tunisia

Table of contents

Disclaimer

Sponsors

fib President Message

Preface

Scientific Committee

Organizing Committee

Participant

Innovation in materials and structures

Behaviour of glass fiber reinforced gypsum panels as walls and slabs : a review, Shaji Aishwarya [et al.] 2

Identification of mechanical fracture parameters of fine-grained brittle matrix composites, Lipowczan Martin [et al.] 10

Plastic hinge relocation on the beams with innovative beam-to-column joints, Ghayeb Haider Hamad [et al.] 18

The experimental verification of concrete elements strengthened using UHPC, Boháček Lukáš	27
The influence of cyclic freezing – thawing on the effectiveness of anchoring FRP reinforcement, Wasilczyk Rafal [et al.]	37

Structural analysis and design

Semi-probabilistic assessment of prestressed concrete bridge, Novak Lukas [et al.]	45
Conceptual peculiarities of composite steel-concrete shallow floors, Couavoux Laurie [et al.]	52
Fastening of a gusset plate to concrete by means of post-installed anchors - Numerical investigation, Stehle Erik Johannes [et al.]	59
Finite element modeling of size effect on punching shear strength of reinforced concrete slabs without shear reinforcement, Sanabria Díaz Rafael Andrés [et al.]	68
Strengthening of Flat Slabs to Increase in Shear Resistance Using Post-Installed Shear Reinforcement, Bolešová Mária [et al.]	76
Analytical evaluation on the influence of deterioration of bond between rebar and concrete on structural performance of RC structures, Kurihara Ryota [et al.] . .	83
Analysis of creep in plain concrete flexural members, P Mary Williams [et al.] . .	91
Influence of geometry and material parameters' variability on the ultimate condition of doubly reinforced concrete beams, Stella Alberto [et al.]	98

Durability and life assessment

Water Vapor Sorption of Hardened Cement Pastes: Impact of Temperature and Carbonation, Wang Zhen [et al.]	107
Internal hydrophobization of cement-based materials, Grabowska Kalina [et al.] .	115
Toward a new assessment method of the durability of stabilized compacted earth blocks, Al Haffar Noha [et al.]	122
Comparison of normative test methods for evaluating concrete resistance to freeze-thaw cycles to real exposure conditions., Al Haj Sleiman Sara [et al.]	130
Lightweight cement slurries for carbon capture and storage, Martín Christian Marcelo [et al.]	137

Numerical Simulation of Asphalt Pavement Countermeasure at High Temperature Against Protrusion of Vertical PC Bars Using Applied Element Method, Bonger Addisu Desalegne [et al.]	144
Case study of carbonation of 100 years old concrete covered by a thin cement render, Gašpárek Jakub [et al.]	152
Experimental study of the concrete creep potential that is already damaged by Alkali Aggregates Reactions (AAR) in a new finite elements approach, Lacombe Clement [et al.]	160

Sustainability and life cycle assessment

Geopolymer concrete structures: mechanical properties and bond with deformed steel bars, Romanazzi Vincenzo [et al.]	169
Bond stress distribution of ripped steel bars in reinforced concrete with short bond length under various loading conditions, Koschemann Marc	176
Homogenized reinforced concrete model for the evaluation of ASR affected structures, Vo Daniela [et al.]	184

Monitoring and structural assessment

Stop Criteria for Proof Load Testing of Reinforced Concrete Structures, Zarate Garnica Gabriela I. [et al.]	195
Wave-based Indicators of Shear Failure in Reinforced Concrete Members without Shear Reinforcement: A Review, Zhang Fengqiao [et al.]	203
Assessment of Existing Masonry Structures (The ARES project), Hafner Ivan [et al.]	211
Seismic assessment of a RC frame building designed for gravity loads including joint deformation capacity model, Zucconi Maria [et al.]	218

Fatigue of concrete structures

Cyclic Shear Response of Reinforced Concrete Dapped-End Beams (RCDEBs) Under Bond Deterioration, Quadri Ajibola Ibrahim [et al.]	227
Influence of silica fume on the deterioration under compressive fatigue loading in high-strength concrete, Scheiden Tim [et al.]	235

Influence of the concrete production and specimen preparation techniques on the compressive strength and fatigue resistance of HPC, Basaldella Marco [et al.] . .	243
Long-term strain development of concrete subjected to creep and cyclic loading, Kern Bianca [et al.]	251
Damage indication by electrical resistivity measurement of carbon short fibre reinforced concrete in fatigue testing, Lauff Philipp [et al.]	258
Influence of temperature increase on fatigue behaviour of concrete during compressive fatigue loading, Markert Martin [et al.]	266
Microcracking of high-performance concrete under cyclic loading and the influence of the aggregate, Schäfer Niklas [et al.]	275
Author Index	283
Previous fib International PhD Symposia	285

Innovation in materials and structures

Behaviour of Glass Fibre Reinforced Gypsum panels as walls and slabs: A Review

Aishwarya Shaji, A. Meher Prasad, Devdas Menon

Department of Civil Engineering,
Indian Institute of Technology Madras,
Chennai (600036), India

Abstract

The current housing shortage problem in the country, especially among the low-income group and the need to address their shelter needs, led to the introduction of GFRG (Glass fibre reinforced gypsum) panels in India. These are light-weight, load-bearing panels which can resist axial, in-plane and out-of-plane loads and various studies conducted worldwide established the suitability of the panel for the construction of walls and slabs. GFRG buildings consist of GFRG walls and slabs alone and can be constructed up to 5-8 storeys in low to moderate seismic zones, and lesser height in higher seismic zones. Studies were carried out in India and other countries to understand various properties of GFRG panels and this paper presents a critical review of the experimental and theoretical investigations on the structural behaviour of GFRG panels.

1 Introduction

The Glass fibre reinforced gypsum (GFRG) panels are light-weight, load-bearing walls used for rapid construction of affordable and eco-friendly houses (individual units to multi-storeyed buildings) and are being used in India for more than a decade. These are prefabricated in controlled-conditions in factories, from gypsum plaster (a by-product from the fertilizer industries) reinforced with glass fibres (chopped) along with certain special additives and are available in a fixed size of 12 m length, 3 m height and 124 mm thickness. The panels are hollow, with cavities of size, 230×94 mm (formed between 20 mm thick ribs and 15 mm thick flanges), aligned along the height [1] as in Fig. 1.

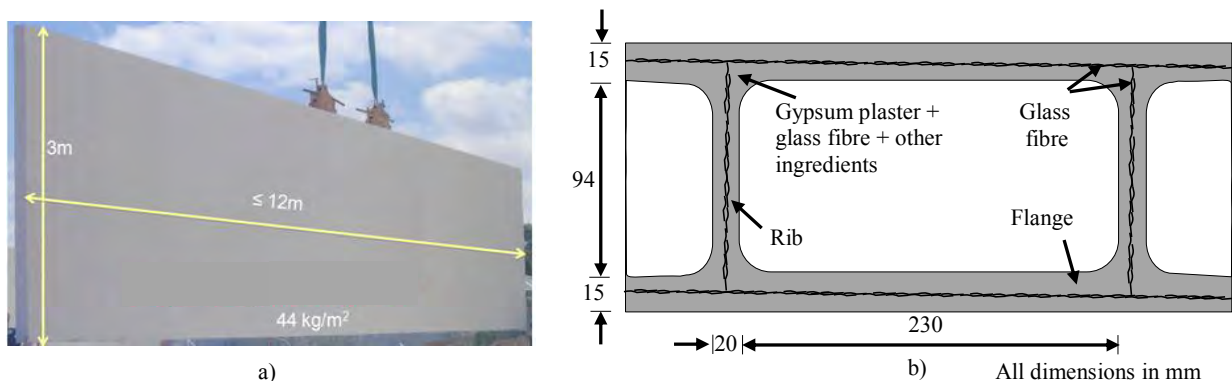


Fig. 1 GFRG panel: a) Elevation, b) Cross-section

These panels were originally developed in Australia in 1990 and later introduced in India, China, Hong Kong and other countries. In a developing country like India, GFRG (with the key advantages of, light-weight construction - advantageous in earthquake-resistant design, sustainable construction – reduced use of steel and concrete, increased carpet area - thin wall panels, improved thermal comfort - saving in operational energy, etc.) is of great significance due to the tremendous need for large-scale affordable housing. These panels can be used for the construction of walls, slabs, staircases and parapet walls.

The structural behaviour of the GFRG walls and the buildings are very much complicated than the conventional system. This is due to the development of a composite action as a result of the interaction between GFRG and the concrete when the cavities of the panel are filled with reinforced concrete [2]. Therefore, the well-established conventional structural theories and design procedure do not apply to

the GFRG buildings. Thus to properly understand the structural behaviour of the GFRG building system and to develop a proper design guideline, comprehensive research works were undertaken, which includes the study to determine the various material and structural properties of the panel. This paper discusses various studies conducted on GFRG wall and slab panels.

2 Material Properties

The physical and mechanical properties of the GFRG panel were obtained based on various tests conducted in Australia and China [2–7]. Compression test on GFRG blocks (520×250×120 mm) and tension test on GFRG flanges (as the tension failure is more likely on flanges) were performed at IIT Madras [8], and thus the stress-strain curve under axial tension and compression were determined. The ultimate shear stress was obtained by performing four-point loading test on a specimen of size 1100×270×120 mm [8] and the results are as in Table 1.

3 Behaviour of GFRG wall panels

The GFRG panels can be used as walls, where the cavities are either left unfilled or filled with plain or reinforced concrete to improve its load-carrying capacity and ductility. GFRG, as a load-bearing structural member is capable of resisting axial load (P), lateral shear (V) and in-plane bending (M_i) and out-of-plane bending (M_o). Various studies conducted on GFRG wall panel are summarised as below:

3.1 Experimental study

3.1.1 Axial and eccentric compressive strength

The axial and eccentric compressive strength of unfilled and concrete-filled (plain or reinforced concrete with one 12 mm bar) GFRG panel (1.02 m wide, 2.85 m high and 120 mm thick) was determined experimentally [7], and it was found that all the unfilled panels failed by local crushing near the supports, and no significant out-of-plane bending occurs when subjected to axial load. All the concrete-filled specimens failed by buckling and flexural tensile breaking. For both ends pinned specimen, failure occurred at the mid-span and for one end pinned and other end fixed specimen, failure was near to the pinned support (Fig. 2). Thus it was observed that the failure load depends on eccentricity and the support conditions, and not on the strength of concrete and reinforcing bar in the cavities [2,7]. Similar observations were also made based on the experimental studies conducted at IIT Madras [8]. A significant increase in the load-carrying capacity was observed when the panels were infilled with concrete and it was also observed that the provision of rebars does not contribute to the strength enhancement.

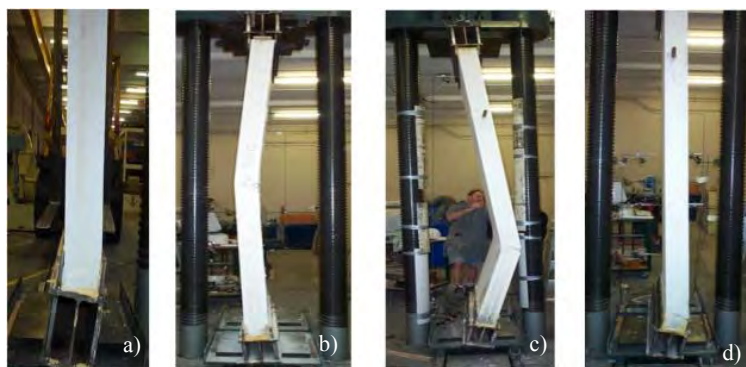


Fig. 2 Failure modes of axially loaded GFRG panel, (a) unfilled panel, (b) both ends pinned concrete-filled panel, (c) and (d) one end pinned and other end fixed concrete-filled panel [9]

3.1.2 Out-of-plane bending strength

The out-of-plane behaviour of the GFRG panel (predominant when it is used as a slab to resist gravity load or wall to resist wind pressure) with the ribs parallel and perpendicular to the span (Fig. 3) was studied experimentally [9]. In the unfilled and concrete-filled panels with the ribs parallel to the span, tension cracking was observed at the panel bottom confirming flexural failure. For the unfilled panels with ribs perpendicular to the span, failure occurred by the crushing of the web (shear deformation).



Fig. 3 Failure modes for out-of-plane bending of the panel: a) Ribs parallel to the span, b) Ribs perpendicular to the span [9]

3.1.3 Shear strength

Unfilled and concrete-filled GFRG panels subjected to lateral load was studied experimentally [2,3,7] to determine the failure modes and factors affecting shear strength. Unfilled panels (1.5 m and 2 m wide) develop diagonal cracks initially (Fig. 3(a)) and failure occurs by compression crushing of plaster in the compression zones (Fig. 3(b)). In concrete-filled panels - 1.5 m wide, with starter bar alone, failure occurs by the tensile breaking of the panel just above the starter bar (due to the discontinuity of the bar) (Fig. 3(c)). For concrete-filled panels - 2 m wide, with starter bars alone and 1.5 m wide, with full-length rebars, 45° shear cracks occur before the peak load and longitudinal shear cracks occur at the peak load (Fig. 3(d)). Thus the panels with this type of configuration develop full shear strength.

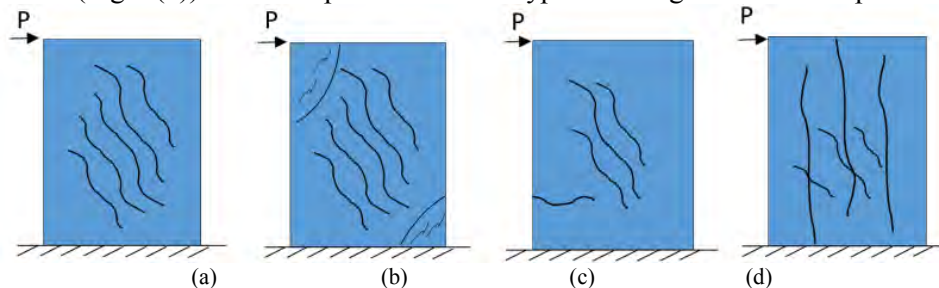


Fig. 4 Various failure modes in a GFRG panel subjected to shear: (a) Diagonal cracking in unfilled panel, (b) End crushing in unfilled panel, (c) Tensile breaking in concrete-filled panels with starter bars, (d) Longitudinal cracking in concrete-filled panels.

The lateral load behaviour of unfilled and concrete-filled GFRG panels (1.02m wide) with one and two rebars was studied [8], and it was observed that panels with one rebar failed in flexure and those with two rebars failed in shear. Cyclic behaviour of RC filled GFRG panels subjected to both in-plane lateral load and constant axial load was studied [10,11], to understand various performance parameters like strength, stiffness, ductility and energy dissipating capacity. 1.02 m wide and 2.02 m wide panels with two rebars in each cavity were studied to investigate the effect of door openings[10], and 3m wide panels were studied to understand the effect of a) two rebars in each cavity and b) provision of tie-beam / tie connection at the wall top [11]. It was observed that the panels exhibited ductile behaviour without any premature failure and thus the RC filled GFRG panels can also be used as shear walls in earthquake-prone areas. The GFRG-OGS building system is a combination of RC beam-column framed structure (with solid RC slab) in the ground storey and GFRG wall-slab system for the above storeys. The performance evaluation of GFRG-OGS building system, with combined gravity and lateral load was carried out experimentally [12], and it was concluded that the gravity loads are transferred from the walls to the columns by the arching mechanism and thus the beams are subjected to only very less force.

3.2 Theoretical study

The ultimate strength of the unfilled, concrete-filled and RC filled GFRG wall panels subjected to axial, eccentric and lateral loads were determined theoretically (using the traditional methods like Euler's theory, Rankine's theory, Reduced modulus theory and Tangent modulus theory for axially loaded specimens, and Secant modulus theory for eccentrically loaded specimens) and from the finite element analysis (FEM) methods [8]. Comparison of the analytical results with the experimental results showed that the traditional methods overestimated the ultimate strength and thus modified methods which incorporate the effect of nonlinearity was proposed and was found to give more accurate results [8,13].

From the lateral load test results, P - M interaction curves were developed, which can be used for the structural design of GFRG shear walls. For laterally loaded panels, an increase in strength was observed due to an increase in reinforcement as well as due to increase in axial load. It was also observed that the lateral load stiffness of the shear wall has two components, in which the flexural component is predominant in narrow walls and shear component is predominant in wide walls [8].

A suitable hysteretic model [14] (as suggested by Ibarra et al. [15]) for the RC filled GFRG panel which considers pinching and cyclic deterioration in the experimental results is identified and calibrated to match the experimental responses up to 80% of the peak load. It was observed that the energy dissipation and pinching parameters obtained for various specimens were the same.

Based on the experimental and theoretical studies on the lateral load behaviour of unfilled and concrete-filled GFRG panels, factors affecting the shear strength of the GFRG wall panels are summarized as below:

- Concrete strength:** Inspection of the exposed concrete core gave an insight that the longitudinal cracks are due to the tearing of the panel skin alone. Thus the shear strength of the GFRG panel depends only on the strength of the panel and not on the grade of concrete and reinforcement. Thus partial filling of cavities (Fig 5(a)) can be adopted and the number of cavities to be filled depends on the strength requirements [2–4,16]
- Reinforcement bar:** Shear strength of GFRG walls is not affected by the longitudinal rebars. Two types of wall to floor connections are used. In the type-one connection, only starter bars are used and in the type-two connection, longitudinal reinforcements are used along with the starter bars, ensuring the continuity of longitudinal bars along the height of the wall. From the study on the effect of the continuity of longitudinal reinforcement at the wall to floor joint [6], it was observed that type-one connection is acceptable for low rise GFRG buildings where the failure is governed by shear strength and not by the flexural strength. For walls with significant flexural deformation, the continuity of the longitudinal rebars is necessary for the tensile resistance of the wall and the overall stability and integrity of the building [2]. It was also observed that the number of rebars (one or two) in each cavity, do not have a significant effect on the shear strength or stiffness. But the provision of two rebars helps to sustain the load in the post-peak region and thus ensures more ductile behaviour [11].
- Axial load:** The shear resistance of an RC wall increases with axial load, but the shear resistance of a GFRG wall depends on the interface property[3]. If the interface is smooth, then the axial load does not affect the shear resistance, whereas, axial load affects the shear resistance in the case of a rough interface. In actual practice, the effect of axial load on shear strength is usually neglected to have a conservative design.
- Internal frame action:** Internal frame action exists when floor beams are provided and are cast monolithically with the internal RC cores (Fig. 5(b)). Then the total shear strength of the GFRG walls includes the shear resistance of the GFRG panel as well as the lateral resistance of the RC frame.

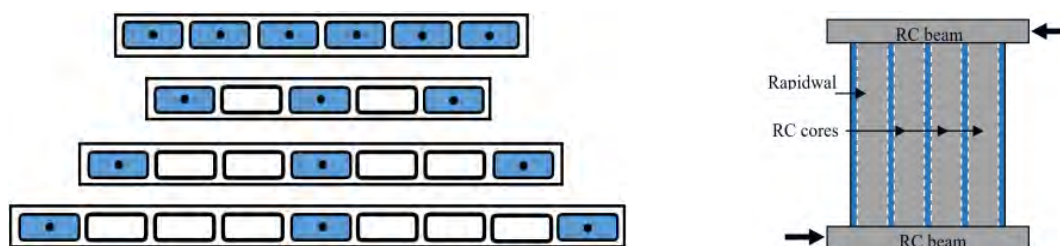


Fig. 5 (a) Various arrangements for filling cavities in a GFRG panel, (b) Concrete-filled GFRG panels with RC beam at top and bottom

4 Behaviour of GFRG-RC composite slab

The applicability of GFRG panel as roof and staircase waist slab was first studied at IIT Madras [17] by conducting experimental and theoretical studies. GFRG panels, with ribs aligned in the direction of bending (out-of-plane), possess sufficient flexural strength [9] and the introduction of reinforced concrete into the cavities of the panel further enhances the flexural strength. GFRG panels with ribs aligned in the direction of bending can be designed as a one-way slab. Concealed RC beams are provided by opening the flanges and filling the cavities at regular intervals (typically every 3rd cavity for roof slab

and all the cavities for staircase waist slabs). A screed concrete of thickness 50 mm and reinforced with welded wire fabric of 10 gauge at 100×100 mm spacing is provided to minimize the thermal and shrinkage cracks (Fig. 6). Thus the entire assembly provides a T beam action.

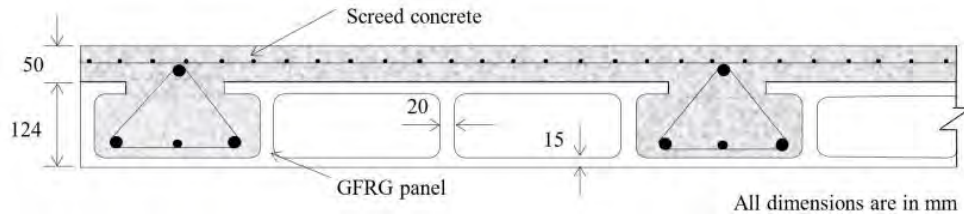


Fig. 6 Cross-section of GFRG-RC slab

Extensive studies were conducted on GFRG-RC slab and ribbed RC slabs (RC-T beam system) to understand the behaviour of GFRG-RC slab system [18]. The specimens tested included unit modular width slabs (2.75 m x 0.77 m) and one-way and two-way prototype slabs (3.02 m x 3.018 m). Four-point bending test was done on unit modular width GFRG-RC slab and ribbed RC slabs and it was observed that the GFRG enhances strength by 10 to 20 % and stiffness by 16 to 36 % (Fig. 7(a)). For GFRG-RC slab, two cases corresponding to the full bond and zero bond at the interface between the GFRG and RC were studied theoretically. The load-deflection curve obtained from the experiment was found to lie in between the full bond and zero bond predictions, thus indicating a partial bond.

The load-deflection behaviour of GFRG one-way prototype slab (simply supported on two opposite sides) subjected to uniformly distributed load (UDL) was determined experimentally and theoretically and comparison of this with ribbed RC slab (Fig. 7(b)), showed a strength enhancement of 17% and stiffness enhancement of 36 %, which is due to the contribution of GFRG. The maximum span of the GFRG-RC slab which can be provided is 5 m in a residential building and 4.5 m in a commercial and industrial building. When the slab is greater than 3 m, 2 pieces of panel need to be joined in such a way that the concealed RC beam can run continuously throughout the GFRG panel between the supports. It was also observed experimentally that the strength and stiffness of the panel with and without a cut was almost the same, indicating that there is no reduction in strength and stiffness due to cut in the panel as long as the continuity of the RC rib across the joint is ensured [17].

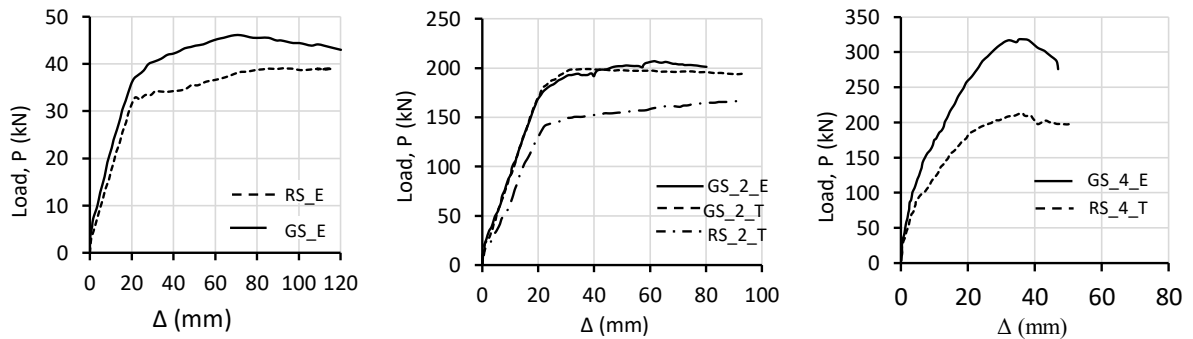


Fig. 7 Load-deflection curve of (a) unit width slab, (b) one-way prototype slab, (c) two way prototype slab [17]

The behaviour of GFRG-RC and ribbed RC two way prototype slabs (simply supported on all the four sides) subjected to UDL were obtained experimentally and the comparison between the two indicates a strength increase of 17% and initial stiffness increase of 36%, due to the contribution of GFRG (Fig. 7(c)). Similarly, the comparison between the one-way and two-way GFRG-RC slab indicates a strength increase of 59 % and 3 fold increase in initial stiffness and this increase is due to the two-way action of GFRG-RC slab. Experimental testing was also carried out to know the effect of various type of loading (UDL, line load and point load) and aspect ratio (1:1 and 1:1.5). It was observed that the GFRG-RC slab showed good performance under the line load and point load, with less load-carrying capacity. Water load test simulating uniformly distributed live load was also performed on a portion of the terrace of the GFRG demonstration building at IIT Madras and it was observed that the serviceability performance of the GFRG-RC slab is good when compared with the solid RC slab [17].

5 Large scale testing

Large-scale shake table tests on full-scale two-storeyed (one storey model plus weight on top) GFRG buildings have been undertaken at Structural Engineering Research Centre (SERC), Chennai with two different plan and three different infill configurations (Fig. 8(a)). Excellent seismic performance and suitability of GFRG buildings up to two storeys in seismic zone V were established from the study [19].

A destructive test was done on a full-scale five-storey GFRG building (Fig. 8(b)) at Shandong Construction University, China [20]. Visible structural cracks were not found when a cyclic lateral load equivalent to a zone 8 earthquake in the Chinese seismic code (100 tons) was applied. At small deformations, flexural type deformation and at large deformations, a combination of flexural and shear type was observed. The evaluation of the performance of the GFRG building system was done by performing an in-plane cyclic lateral load test on a system unit which represents a typical room of an 8 storeyed GFRG building [21]. System unit comprises of a floor slab with in-plane walls on either side (out of plane strength contribution of the walls are neglected) as in (Fig. 8(c)). This test aimed to evaluate the performance of the connections, system ductility and modes of failure.

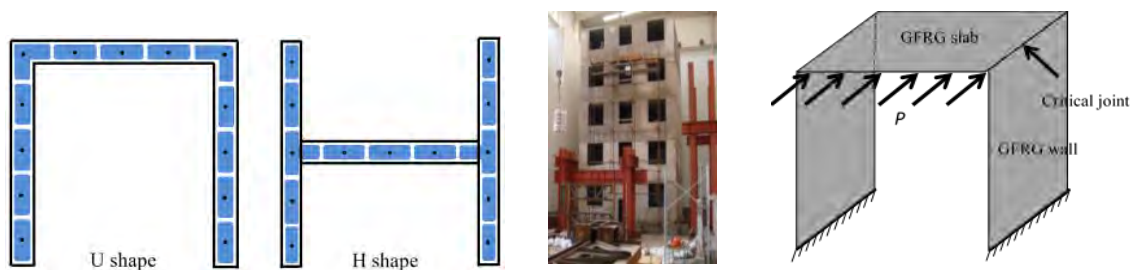


Fig. 8 (a) Shake table test configurations, (b) Five storeyed building under test at China [20], (c) System unit test setup

Some other minor studies were also conducted on these panels. Lintels above the doors and window openings of GFRG walls can be constructed by removing the ribs on the top of openings and filling reinforced concrete into the hollow cavities of the wall. The flexural and shear behaviour of the GFRG composite lintel was studied experimentally [5] and it was found that the conventional flexural design theory for RC beams can be used for GFRG lintels, by considering the concrete cross-section alone and ignoring the GFRG panel.

Durability and sustainability studies [11] – 1) test for the bursting pressure of the panel, 2) exposure of the panel towards marine atmosphere, normal and acid rain, 3) biological study on algae and fungal resistance, 4) joint sealant test for doors and windows and 5) studies on indoor thermal performance, were carried out and the GFRG panel was found to perform well under these extreme exposure conditions. For demonstrating the GFRG technology and the construction of GFRG buildings a two-storey GFRG demonstration building was constructed at IIT Madras [18,22].

6 Conclusions

In Australia, the GFRG panels were used as load-bearing walls to resisting gravity loads and the slabs were made of reinforced concrete. From the studies conducted in India, an earthquake-resistant design procedure for the use of GFRG panels for buildings in different seismic zones of the country was developed. GFRG panels with embedded micro-beams and RC screed can be used as floor/roof slabs and thus the suitability of constructing walls, slabs, staircases, and parapet walls using GFRG is well established. From various studies, the properties obtained are given in table 1.

Based on these studies at IIT Madras, GFRG has been approved as a building material suitable for construction of buildings in India up to 10 storeys by BMTPC (Building Materials Technology Promotion Council), and the following manuals were published for adoption in practice:

1. GFRG / Rapidwall Building Structural Design Manual [1]
2. Manual on waterproofing of GFRG / Rapidwall Buildings [23]
3. Schedule of Items and Rate analysis for GFRG Construction [24]
4. Manual on Construction of GFRG / Rapidwall Buildings [25]
5. A BIS code on the specifications, design and construction of GFRG buildings

These guidelines can be used by architects, structural engineers and construction engineers on the design and construction of GFRG buildings. GFRG panels can also be used advantageously as infills in RC framed buildings without any restriction on the number of storeys and thus ensures faster and economic construction.

Table 1 Mechanical properties of GFRG panel

Property	Nominal value
Unit weight	0.44 kN/m ²
Elastic Modulus	4000 - 7500 MPa
Poisson's ratio	0.15 – 0.23
Uni-axial tensile strength (on flange)	35 kN/m
Uni-axial compressive strength	160 kN/m (unfilled)
	1310 kN/m (filled*)
Ultimate shear strength	21.6 kN/m (unfilled)
	61 kN/m (filled*)
Out of plane bending capacity	2.1 kNm/m (ribs parallel to span)
	0.88 kNm/m (ribs perpendicular to span)
Water absorption	1% in 1 h, 5% in 24 h
	2.3 h rating (unfilled)
Fire resistance	2.3 h rating (unfilled)
	4 h rating (filled*) - withstood 900 –1000 °C
Co-efficient of thermal expansion	12 x 10 ⁻⁶ mm/mm/ °C
Thermal resistance	0.36 m ² K/W (unfilled)
Sound transmission class	28 (unfilled)
	45 (filled*)

* filled with M20 concrete

References

- [1] GFRG/Rapidwall Building Structural Design Manual (2012), Prepared by Structural Engineering division, Department of Civil Engineering, IIT Madras (*Building Materials & Technology Promotion Council, Ministry of Housing & Urban Poverty Alleviation, Government of India*).
- [2] Wu, Y. F. 2009. "The structural behavior and design methodology for a new building system consisting of glass fiber reinforced gypsum panels." *Construction and Building Materials*, 23(8), 2905–2913. doi:10.1016/j.conbuildmat.2009.02.026.
- [3] Liu, K., Wu, Y. F., and Jiang, X. L. 2008. "Shear strength of concrete filled glass fiber reinforced gypsum walls." *Material and Structures*, 41, 649–662. doi:10.1617/s11527-007-9271-8.
- [4] Yue, J., and Bao, P. 2007. "Test on glass fibre reinforced gypsum panels partially filled with RC." *The Indian Concrete Journal*, (81(2)), 7–14.
- [5] Wu, Y. F., and Dare, M. P. 2006. "Flexural and Shear Strength of Composite Lintels in Glass-Fiber-Reinforced Gypsum Wall Constructions." *Journal of Materials in Civil Engineering*, 18(3), 415–423. doi:10.1061/(ASCE)0899-1561(2006)18:3(415).
- [6] Wu, Y. F. 2004. "The effect of longitudinal reinforcement on the cyclic shear behavior of glass fiber reinforced gypsum wall panels: Tests." *Engineering Structures*, 26(11), 1633–1646. doi:10.1016/j.engstruct.2004.06.009.

- [7] Wu, Y. F., and Dare, M. P. 2004. "Axial and Shear Behavior of Glass Fiber Reinforced Gypsum Wall Panels: Tests." *Journal of Composites for Construction*, 8(6), 569–578. doi:10.1061/(ASCE)1090-0268(2004)8:6(569).
- [8] Sreenivasa, R. L. 2010. "Strength and Behaviour of Glass Fibre Reinforced Gypsum Wall Panels." PhD diss., Department of Civil Engineering, IIT Madras, Chennai, India.
- [9] Wu, Y. F. 2002. *Report into the physical testing and the development of design guidelines for the structural application of Rapidwall in building construction*. Dare Sutton Clarke Engineers, Adelaide, Australia., 1–151.
- [10] Janardhana, M. 2010. "Cyclic Behaviour of Glass Fibre Reinforced Gypsum Panels." PhD diss., Department of Civil Engineering, IIT Madras, Chennai, India.
- [11] Cherian, P. 2019. "Performance Evaluation of GFRG Panels and Building Systems." PhD diss., Department of Civil Engineering, IIT Madras, Chennai, India.
- [12] Krishna, S. R. G., David, D., Prasad, A. M., and Menon, D. 2017. "Seismic behaviour of GFRG - OGS building system – A computational study." 16th World Conference on Earthquake, 16WCEE 2017 Santiago Chile, January 9th to 13th.
- [13] Sreenivasa, R. L., Menon, D., and Prasad, A. M. 2008. "Prediction of Axial Compressive Strength of Glass Fiber Reinforced Gypsum Wall Panels." Proceedings of 7th International Conference on Civil and Architecture Engineering ICCAE-7, May 27th to 29th. Military Technical College, Cairo, Egypt, 33.
- [14] Janardhana, M., Robin Davis, P., Ravichandran, S. S., Prasad, A. M., and Menon, D. 2014. "Calibration of a hysteretic model for glass fiber reinforced gypsum wall panels." *Earthquake Engineering and Engineering Vibration*, 13(2), 347–355. doi:10.1007/s11803-014-0236-y.
- [15] Ibarra, L. F., Medina, R. A., and Krawinkler, H. 2005. "Hysteretic models that incorporate strength and stiffness deterioration." *Earthquake Engineering and Structural Dynamics*, 34(12), 1489–1511. doi:10.1002/eqe.495.
- [16] Jiang, X., and Gu, Y. 2007. "Cyclic behaviour of fiber-reinforced plasterboard with core concrete composite shear walls." Ninth Canadian conference on Earthquake Engineering, Ottawa, Ontario, Canada 26-29 June.
- [17] Paul, S. 2018. "Performance Evaluation of GFRG-RC Floor Slabs Systems." PhD diss., Department of Civil Engineering, IIT Madras, Chennai, India.
- [18] Paul, S., Cherian, P., Menon, D., and Prasad, A. M. 2016. "Use of glass fibre reinforced gypsum panels with reinforced concrete infills for construction of walls and slabs." *Indian Concrete Journal*, 90(12), 19–32.
- [19] State of the Art Report. 2015. *State of the Art Report - GFRG*. Chennai, India.
- [20] Kaozhong, Z., Zhang, X., and Wei, T. 2010. "Full-scale Model Test Research on the Performance of a Five-Storey Fiber Plaster Board Building." *Journal of Shandong Jianzhu University*, 1–9.
- [21] Cherian, P., Prasad, A. M., and Menon, D. 2017. "Lateral cyclic load behaviour of GFRG building systems - Experimental studies." 16th World Conference on Earthquake, 16WCEE 2017 Santiago Chile, January 9th to 13th.
- [22] Cherian, P., Paul, S., Krishna, S. R. G., Menon, D., and Prasad, A. M. 2017. "Mass Housing Using GFRG Panels: A Sustainable, Rapid and Affordable Solution." *Journal of The Institution of Engineers (India): Series A*, Springer India, 98(1–2), 95–100.
- [23] Manual on Waterproofing of GFRG/Rapidwall Buildings, 2015, Prepared by Structural Engineering division, Department of Civil Engineering, IIT Madras (*Building Materials & Technology Promotion Council, Ministry of Housing & Urban Poverty Alleviation, Government of India*).
- [24] Schedule of Items & Rate Analysis for GFRG Construction, 2015, Prepared by Structural Engineering division, Department of Civil Engineering, IIT Madras (*Building Materials & Technology Promotion Council, Ministry of Housing & Urban Poverty Alleviation, Government of India*).
- [25] GFRG / Rapidwall Construction Manual, 2018, Prepared by Structural Engineering division, Department of Civil Engineering, IIT Madras (*Building Materials & Technology Promotion Council, Ministry of Housing & Urban Poverty Alleviation, Government of India*).

Identification of mechanical fracture parameters of fine-grained brittle matrix composites

Martin Lipowczan, David Lehký, Hana Šimonová, Barbara Kucharczyková
and Zbyněk Keršner

Brno University of Technology, Faculty of Civil Engineering,
Institute of Structural Mechanics and Institute of Building Testing,
Veveří 331/95, 602 00 Brno, Czech Republic

Abstract

The paper describes a method for the identification of mechanical fracture parameters of fine-grained brittle matrix composites. An identification procedure utilizes the results of fracture tests, artificial intelligence methods, and nonlinear finite element-based analysis. Fracture properties of fine-grained brittle matrix composites are typically evaluated from the response of a notched prismatic specimen with a nominal depth of 40 mm tested in a three-point bending configuration. The aim is to identify parameters for the various composite mixtures and to feed material models for the deterministic and stochastic simulations of the quasi-brittle/ductile response of structures made of studied materials.

1 Introduction

The recent development of new ecologically and economically attractive materials brings requirements for a comprehensive description of their properties. The mechanical fracture parameters of the studied material can be obtained based on laboratory fracture experiments. The measured response of tested notched specimens in the form of a force vs. displacement diagram can be evaluated by direct methods such as the Work-of-Fracture method [1] and the Effective Crack Model [2]. The second possibility is to identify parameters indirectly e.g. by using a combination of fracture test and Artificial Neural Network-based (ANN) inverse analysis [3]. The advantage of this method is its ability to identify also parameters that cannot be obtained by direct methods, such as tensile strength.

The ANN-based inverse analysis method was implemented in FraMePID-3PB software [4], where it is used to determine the parameters of a standard concrete with a wide range of strengths. Prismatic specimen with a central edge notch and nominal depth of 100 mm tested in a three-point bending configuration is used, see Fig. 1 (left). In this case, identification is performed with the help of one robust neural network, which covers the entire space of the identified parameters [4]. Due to the high variability of the responses obtained from the tests of specimens made of fine-grained composites with a nominal depth of 40 mm, see Fig. 1 (right), utilization of a single network didn't provide sufficient accuracy. For that reason, a neural network ensemble was designed for fine-grained composites. It is a robust, accurate, and easily expandable system. By limiting the range of parameters for one network to a certain subspace, more accurate identification results are achieved. Based on the initial analysis of the fracture test data, one or more networks are activated.

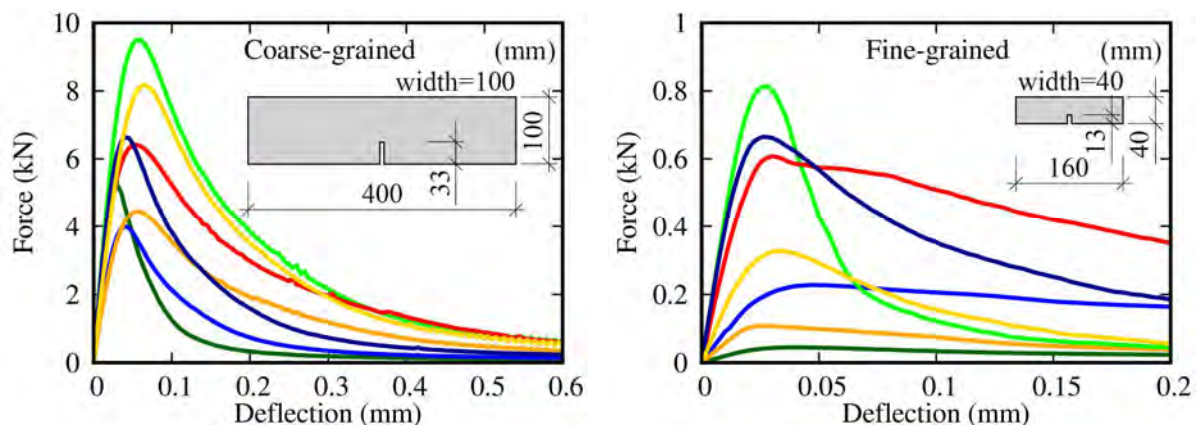


Fig. 1 Example of experimentally obtained load–deflection diagrams of coarse-grained composites (left) and fine-grained composites (right) with a brittle matrix.

The paper aims to present the proposed methodology for the identification of mechanical fracture parameters of fine-grained composites with a brittle matrix. The application part presents the results of testing the functionality of a neural network ensemble on selected sets of fine-grained alkali-activated slag based specimens, which differ in the type of curing condition during their maturation.

2 Methodology for identification of mechanical fracture parameters of fine-grained composites

The identification method of mechanical fracture parameters of fine-grained composites is divided into three phases, see the color branches of the identification flowchart in Fig. 2: (1) fracture tests, (2) creation of a neural network ensemble, and (3) identification of mechanical fracture parameters. In this paper, special attention is paid to the creation of a neural network ensemble and the identification of mechanical fracture parameters of specimens made of fine-grained brittle matrix composites.

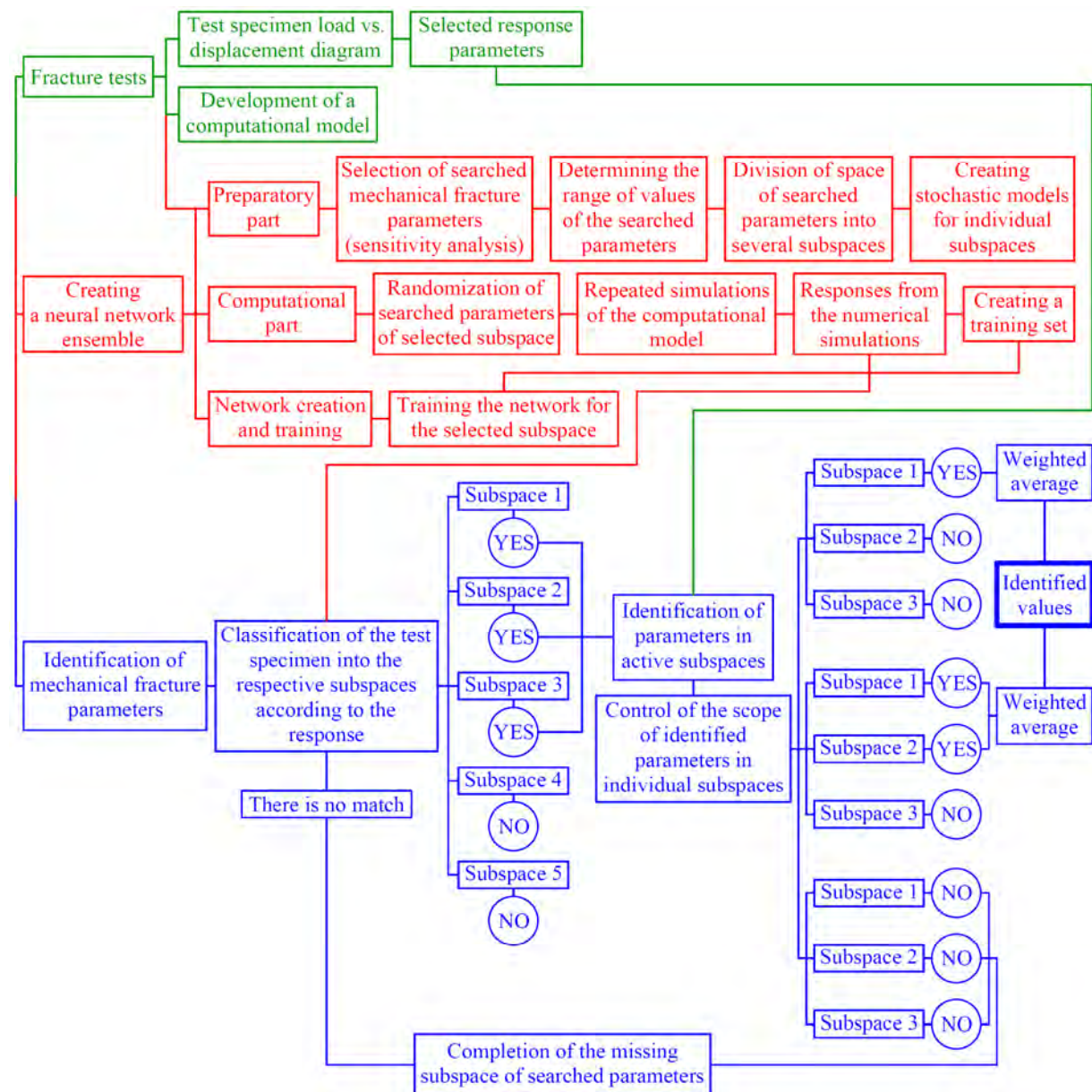


Fig. 2 The identification flowchart of fine-grained composites using neural network ensemble.

2.1 Fracture tests

In the first phase of the method, the fracture test records in the form of force vs. deflection diagrams of the test specimens are evaluated and the appropriate response parameters are selected for subsequent identification, see below. The paper deals with the results of fracture tests of specimens made of fine-grained composites with brittle matrix, which have nominal dimensions of $40 \times 40 \times 160$ mm with

a central notch to a depth of 1/3 of the specimen's height. The specimens were tested in a three-point bending (3PB) test configuration. The distance between the supports was 120 mm. A stable test course was ensured by a sufficiently stiff mechanical testing machine. The loading was performed with a constant displacement increment, which was set at 0.02 mm/min. The result of each test was a force vs. deflection diagram ($F-d$ diagram), which was then used to determine the mechanical fracture parameters.

2.2 Numerical model

At the turn of the first and second phase of the identification method, the finite element method (FEM) model of the tested specimen subjected to 3PB was created. The deterministic computational model was developed in the ATENA 2D software, which uses 3D Non Linear Cementitious 2 material model [5] for quasi-brittle materials. The tensile softening of the material is described using an exponential model according to Hordijk [6]. From a static point of view, the specimen is a simply-supported beam with overhangs, supported by two steel rollers, see Fig. 3. The supports are simplified in the model and are considered as steel plates made of elastic isotropic material. The beam is loaded by its self-weight and with a constant increment of vertical displacement in the middle of the span just above the notch.

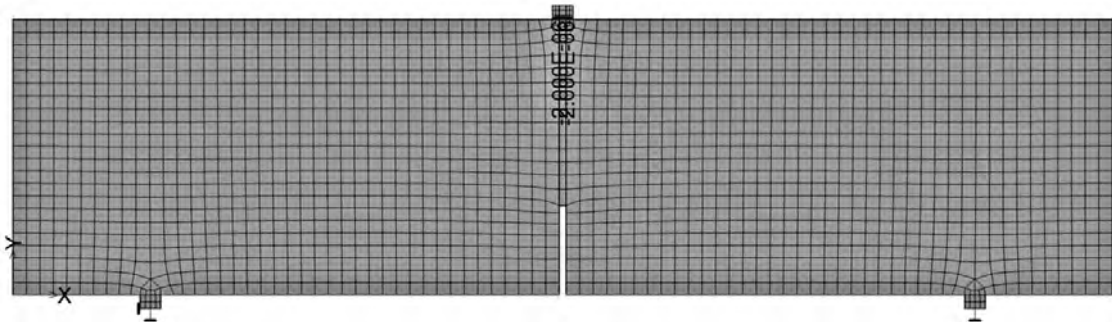


Fig. 3 Computational model for specimens made of fine-grained composites tested in 3PB.

2.3 A neural network ensemble (NNE)

As mentioned above, the developed identification method for fine-grained composites is based on inverse analysis using artificial neural networks [3]–[4]. The second phase deals with the creation of a neural network ensemble and is divided into three parts. First, the set of relevant mechanical fracture parameters is selected utilizing sensitivity analysis. In this case, three parameters, which are modulus of elasticity, tensile strength, and fracture energy, are subject to identification. These parameters form a three-dimensional space, as can be seen in Fig. 4 (right). The range of values of these parameters is systematically divided into smaller subspaces based on the functions below. Based on a sensitivity analysis, these functions have been selected so that the generated samples suitably cover the entire 3D space while maintaining good accuracy across the range of parameters. Emphasis is placed on areas with lower values, where parameter sensitivity is greater than in areas with higher values. The obtained intervals were further extended on both sides by 1/10 of the limit values, thus achieving an overlap of the individual parameter subspaces as shown in Fig. 4 (left).

The first identified parameter is the modulus of elasticity $E_{c,ID}$, which has subspaces arranged according to the function:

$$x_{n+1} = x_n + 2^n, \text{ for } n = 0, 1, 2, \dots, m, \quad (1)$$

where x_0 is equal to 0.3.

The second searched parameter is the fracture energy $G_{F,ID}$, which has subspaces divided by function:

$$y_n = e^{\frac{n \cdot \ln 10}{2}}, \text{ for } n = 1, 2, \dots, m. \quad (2)$$

The last identified parameter is the tensile strength $f_{t,ID}$, which has a division of subspaces defined according to the function:

$$z_{n+1} = z_n + 2^n, \text{ for } n = 0, 1, 2, \dots, m, \quad (3)$$

where z_0 is equal to 0.1.

A stochastic model is created for each parameter subspace. The random variables $E_{c,ID}$ and $f_{t,ID}$ are defined by a rectangular probability distribution, and the parameter $G_{F,ID}$ is described by a left-sided trapezoidal probability distribution, which is composed of rectangular and triangular distributions. The probability of a triangular part is the same as the probability of a rectangular part, see Fig. 5. The trapezoidal distribution is used to concentrate the fracture energy values in regions with lower values and thus increase the accuracy of its identification.

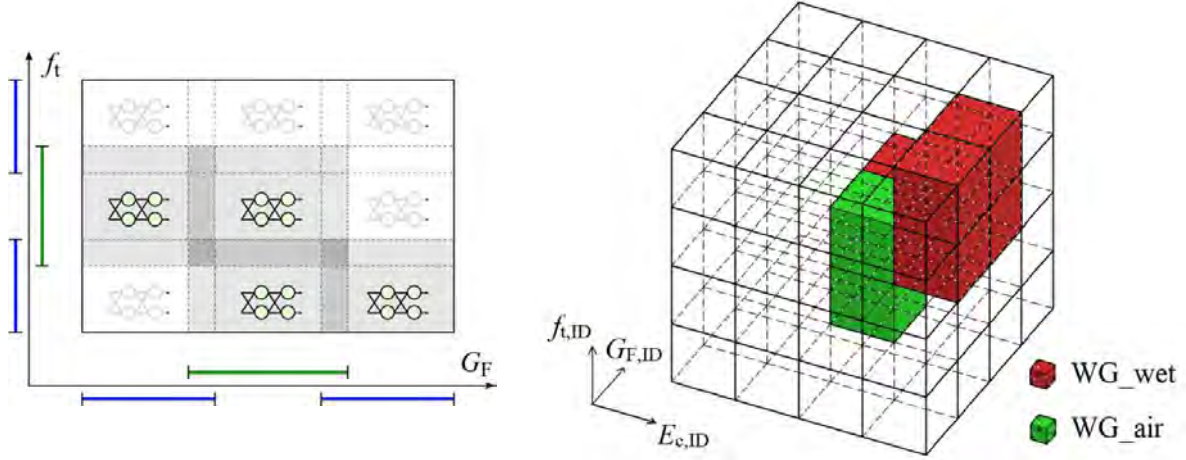


Fig. 4 Example of active subspaces of an identification system based on a neural networks ensemble – a two-dimensional section through space and visible overlapping subspaces (left) and the entire three-dimensional space of the identified parameters (right).

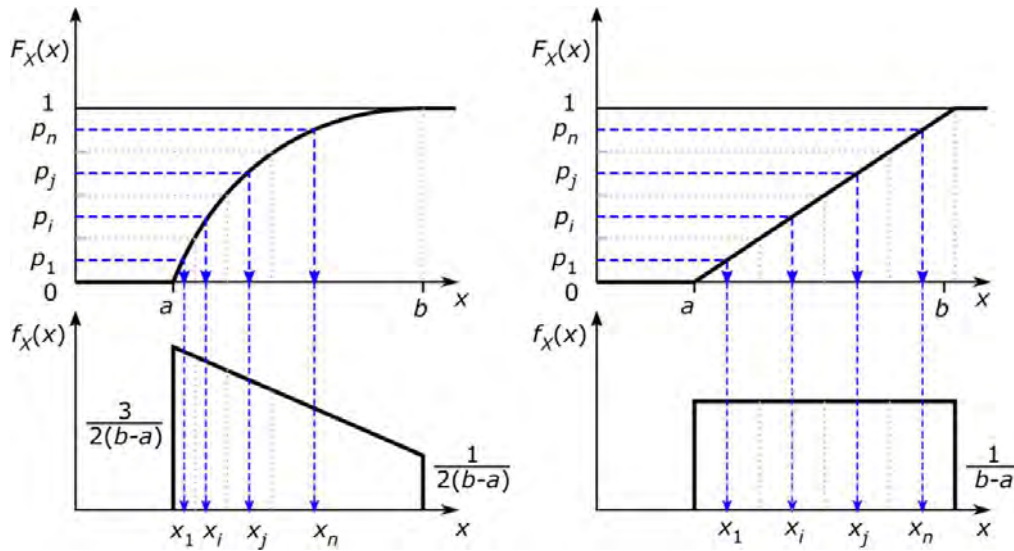


Fig. 5 Generating random samples from the descending trapezoidal probability distribution (left), and the rectangular distribution (right).

The second phase then continues with the computational part. First, random realizations of identified parameters are generated reflecting its probability distributions mentioned above using the LHS simulation method [7]. The number of simulations depends mainly on the required accuracy. Here, 50 or 100 simulations were used. Repeated FEM analysis of the deterministic computational model is carried out with the generated realizations of parameters and a corresponding response is obtained. Arranged pairs formed by random realizations of the identified parameters and their corresponding random response parameters are later used as the training set for neural networks.

The last step of the second phase is focused on the creation and training of neural networks in each subspace of identified parameters. Networks are trained using optimization techniques, such as gradient method, genetic algorithms, etc. The trained neural network, which approximates the inverse function between the response parameters and the material parameters, then serves to identify the material parameters of the respective experiment. Verification of sufficient accuracy of the inverse function approximation is performed using a test set and numerical simulation of the studied specimen.

The structure of all neural networks which form the neural network ensemble is the same and has the following parameters: 3 inputs, 1 hidden layer containing 6 neurons with a nonlinear transfer function (hyperbolic tangent), and 1 output layer with 3 neurons having linear transfer function. The schematic view of the utilized networks is in Fig. 6.

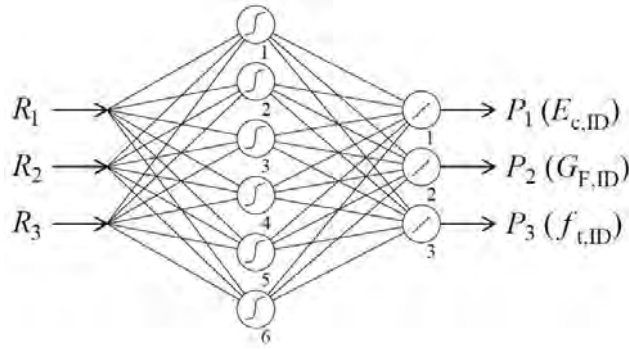


Fig. 6 Structure of forward multilayer network.

2.4 Identification of mechanical fracture parameters of fine-grained composites

The last phase of the proposed method is the identification of mechanical fracture parameters for the selected test specimen. First, the response parameters of the test specimen are classified into the appropriate subspaces causing the activation of their neural networks. The response parameters of the test specimen may fall into one or several adjacent subspaces. If the response parameters do not fit into any of the already prepared subspaces, the new subspace of the material parameters needs to be created and added to the current neural network ensemble.

In the next step, the mechanical fracture parameters in the active subspaces are identified using activated neural networks. The obtained values of material parameters are then verified whether they still correspond to the activated subspaces. When the obtained values fall into several overlapping subspaces the final values of parameters are obtained as a weighted average depending on the distance of the value from the center of its subspace. For more details see [8].

3 Application on selected fine-grained composite with brittle matrix

The application part of the paper presents the results of the identification of a selected fine-grained composite using NNE. The identified values from the NNE are compared with the values obtained by the direct methods.

3.1 Mixture and specimens

The alkali activated blast furnace slag based-mortar (AASM) with slag to sand ratio 1 : 3 (by weight) was prepared. The slag was activated with a waterglass of silicate modulus (SiO_2 to Na_2O molar ratio) equal to 2.34; the waterglass dose was adjusted to 6% Na_2O with respect to the slag weight. The water to slag ratio was adjusted to 0.45 including both water present in waterglass and extra added water before mixing. Lignosulfonate-based plasticizer was added in an amount corresponding to 1% of the slag weight to maintain the appropriate workability of mortar.

The prismatic specimens with nominal dimensions of $40 \times 40 \times 160$ mm made of the above described AASM were manufactured for the experiment. The specimens were stored in the moulds covered with a PE foil for 24 hours. Then, the specimens were demoulded. The first set of specimens (WG_wet) was stored in the closed chamber with $\text{RH} > 95\%$ and the second set (WG_air) was exposed to free drying under laboratory conditions until fracture tests were performed. Prior to the test, a notch was cut with a diamond saw to a depth of 1/3 of the specimen's height. The fracture tests were performed on 3 specimens from each set. The age of specimens was about 40 days.

3.2 Results and discussions

With the data obtained from the laboratory fracture tests, an inverse analysis was performed using NNE, and the following parameters were identified: modulus of elasticity $E_{c,ID}$, tensile strength $f_{t,ID}$ and fracture energy $G_{F,ID}$; from these parameters the characteristic length $l_{ch} = E_{c,ID} \cdot G_{F,ID} / (f_{t,ID})^2$ was also calculated [2]. The values of the identified parameters belong to a total of 7 active subspaces, see Fig.

4 (right), of which WG_wet specimens belong to 5 subspaces and WG_air specimens to 2 subspaces. The following parameters were determined by direct evaluation of F - d diagrams using the Work-of-Fracture method [1] and the Effective Crack Model [2]: specific fracture energy G_F^* , modulus of elasticity E_c , effective fracture toughness K_{Ice} . The results of the parameters obtained by direct methods and from the NNE are shown in Table 1. The mean value accompanied by the coefficient of variation (in %) are shown for all investigated characteristics. This table also lists the relative values of the parameters in the form of two ratios: (1) the $P_{air/wet}$ ratio reflecting differences between two composite types (100 % corresponds to the values of the WG_wet composite), (2) $P_{ID/TEST}$ ratio comparing two methods of parameter's determination (100 % corresponds to the values determined from direct evaluation of fracture tests).

The identified parameters were also used for numerical simulation of the fracture tests, while the criterion of numerical agreement between the curves obtained from experiments and numerical simulation was observed, see Table 1. First, the mean absolute percentage error (MAPE) was calculated between the forces over the entire F - d diagram up to deformation of 0.2 mm:

$$MAPE_{0.2} = \frac{100\%}{n} \sum_{d=1}^n \left| \frac{F_{e,d} - F_{s,d}}{F_{e,d}} \right|, \quad (4)$$

where n is the number of points of the F - d diagram (in this case 100), $F_{e,d}$ is the force at a given deformation obtained experimentally, and $F_{s,d}$ is the force at a given deformation obtained by numerical simulation.

Second, the mean absolute percentage error between the areas under the obtained F - d diagrams which correspond to work of fracture (the work necessary to break a specimen and form two surfaces) was calculated:

$$MAPE_{W0.2} = 100\% \left| \frac{W_e - W_s}{W_e} \right|, \quad (5)$$

where W_e is the area under the experimentally obtained curve and W_s is the area under the curve obtained by the numerical simulation.

Table 1 Mean values (coefficients of variation in %) of the mechanical fracture parameters and relative values $P_{air/wet}$ related to the type of curing conditions and related to the evaluation method $P_{ID/TEST}$ (in %).

Parameter	Unit	WG_wet	WG_air	$P_{air/wet}$	$P_{ID/TEST}$
E_c	GPa	16.0 (11.0)	10.4 (0.1)	65.0	111.9; 107.7
$E_{c,ID}$	GPa	17.9 (11.0)	11.2 (0.3)	62.6	
K_{Ice}	MPa·m ^{1/2}	0.697 (4.6)	0.348 (3.9)	49.9	–
G_F^*	J/m ²	96.9 (5.6)	51.9 (14.5)	53.6	108.0; 107.9
$G_{F,ID}$	J/m ²	104.7 (6.6)	56.0 (24.7)	53.5	
$f_{t,ID}$	MPa	3.06 (11.0)	1.10 (9.6)	35.9	–
l_{ch}	mm	210.8 (40.0)	539.9 (45.4)	256.1	–
$MAPE_{0.2}$	%	2.40	3.10	–	–
$MAPE_{W0.2}$	%	0.78	0.45	–	–

A graphical comparison for all specimens was also performed. The F - d diagrams obtained from the simulations with the identified values of the parameters are compared with the fracture test results in Fig. 7. The figure also shows the course of the absolute percentage error (APE), which is based on equation (4). From both numerical and graphical comparisons, we can conclude that very good agreements were achieved between experimental and numerical responses of all tested specimens.

If compare the results for two sets of specimens, the mean values of specimen parameters of both sets determined by direct methods as well as by NNE reach significantly different values depending on

the type of curing condition during maturation. According to the relative $P_{\text{air/wet}}$ value, the largest difference between the two sets is in tensile strength (approximately 64 %), while the smallest difference is in the modulus of elasticity (approximately 35–37 %). A separate chapter is the characteristic length l_{ch} , for which the difference between the two sets is more than double.

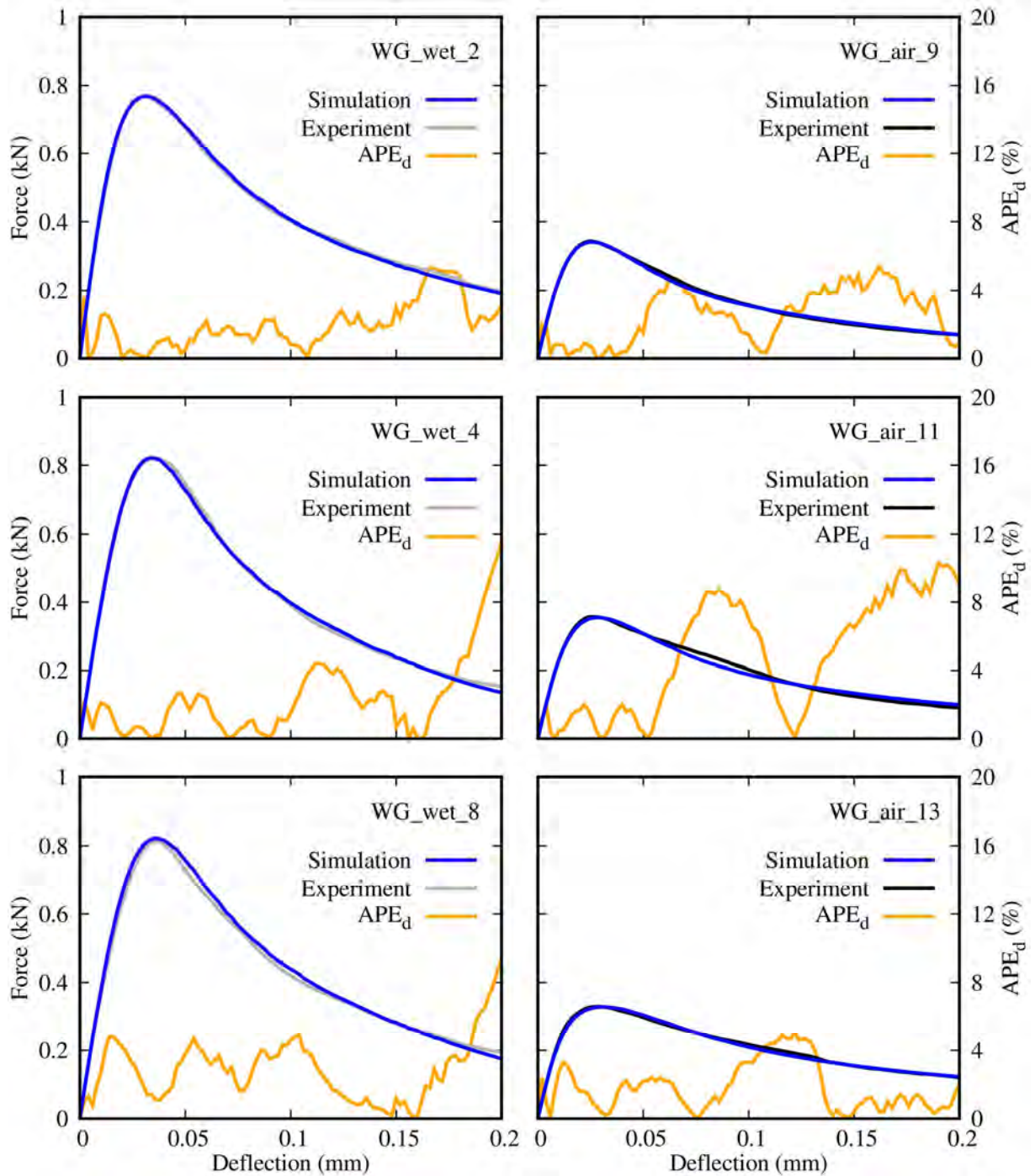


Fig. 7 Comparison of selected F – d diagrams obtained from laboratory tests and numerical model simulations with identified values of parameters of tested specimens – WG_wet (left) and WG_air (right).

4 Conclusions

The paper describes a methodology for the identification of mechanical fracture parameters of fine-grained composites. The NNE identification system was designed to be easily implemented in the existing FraMePID-3PB software tool and also expanded for other types of composites at any time in the future.

In the application part, the NNE system was tested in determining the parameters of two sets of AASM, which differ in curing conditions during its maturation. From a statistical point of view, the values of comparable parameters obtained from identification by NNE were slightly higher compared to the values obtained by direct methods. The difference in modulus of elasticity is about 7.5 to 12 %, while in fracture energy it is about 8 %. From the visual comparison, it can be concluded that the experimentally and numerically obtained F - d diagrams had a good agreement. In the case of AASM, using the Hordijk tensile softening model seems to be a good choice.

Acknowledgements

The authors would like to express their thanks for the support provided from the Czech Science Foundation project MUFRAS No. 19-09491S and the specific university research project No. FAST-J-21-7552 granted by Brno University of Technology. The fracture tests were performed within the mobility project No. 8J20PL073.

References

- [1] RILEM TC-50 FM. 1985. "Determination of the fracture energy of mortar and concrete by means of three-point bend tests on notched beams." *Materials and Structures* 18, 107:287–90.
- [2] Karihaloo, B.L. 1995. *Fracture Mechanics and Structural Concrete*. New York: Longman Scientific & Technical.
- [3] Novák, D., Lehký, D. 2006. "ANN inverse analysis based on stochastic small-sample training set simulation." *Engineering Applications of Artificial Intelligence* 19, 7:731–740.
- [4] Lehký, D., Keršner, Z., Novák, D. 2014. "FraMePID-3PB Software for Material Parameters Identification Using Fracture Test and Inverse Analysis." *Advances in Engineering Software* 72:147–154.
- [5] Červenka, V., Jendele, L., Červenka, J. 2016. *ATENA program documentation – Part 1: theory*. Prague: Cervenka Consulting.
- [6] Hordijk, D.A. 1991. "Local approach to fatigue of concrete." PhD diss., Technische Universiteit Delft.
- [7] Mckay, M. D., Beckman, R. J., Conover, W. J. 1979. "A Comparison of Three Methods for Selecting Values of Input Variables in the Analysis of Output from a Computer Code." *Technometrics* 21, 2:239–245.
- [8] Lehký, D., Lipowczan, M., Šimonová, H., Keršner, Z. 2019. "A neural network ensemble for the identification of mechanical fracture parameters of fine-grained brittle matrix composites." FraMCoS-X conference, Bayonne, France, June 24–26.

Plastic hinge relocation on the beams with innovative beam-to-column joints

Haider Hamad Ghayeb¹, Hashim Abdul Razak¹, N.H. Ramli Sulong^{1,2}, Kim Hung Mo¹

¹*Department of Civil Engineering, Faculty of Engineering,
University of Malaya,
50603 Kuala Lumpur, Malaysia*

²*School of Civil and Environmental Engineering,
Queensland University of Technology,
2 George St, Brisbane, QLD 4000, Australia*

Abstract

The present study utilises the new hybrid precast beam-to-column joints cast with Engineered Cementitious Composite (ECC) for relocating the plastic hinge zone on the beams outside the joint zone. Three samples including a monolithic reinforced concrete (RC) sample were tested under a quasi-static-cyclic loading to assess the seismic behaviour of the joints. The test results exhibited that the use of ECC for casting the hybrid joints and the adjacent beams areas can prevent brittle failure due to the superior mechanical properties of ECC. Moreover, the increase of energy dissipation capacity of the proposed hybrid joints was also observed compared to the RC sample. Therefore, casting the joint using ECC is recommended for enhancing the seismic behaviour.

1 Introduction

Many developing countries have used precast concrete (PC) systems for constructing building structures to reduce waste materials, time consumption, and safety risks during construction. Precast concrete building systems offer a variety of advantages, including fast construction, high-quality control, and cost-effectiveness [1-4]. Moreover, PC structure is a sustainable approach for reducing carbon dioxide (CO₂) emissions [5-8]. However, the precast joints of many PC buildings can be damaged due to earthquakes [8-11]. Past seismic events have demonstrated the poor behaviour of joint system designs [12]. As a result, efforts have been made to improve the design details of PC joint to meet the seismic criteria for structural buildings [13,14]. Precast joints are an important part of the PC structural buildings since they have a critical role in ensuring sufficient seismic performance, particularly failure mode, load-deformation capacity, energy absorption, stiffness, strength, and ductility [3,15]. The existing codes [16-18] stated that the failure should be located outside the joint zone, thus brittle failure is not recommended in the PC buildings [17,19]. However, using advanced construction materials such as Engineered Cementitious Composite (ECC) for casting the PC joints, which is characterised by high ductility, pseudo strain hardening behaviour, high strain capacity, and energy absorption, can be a viable approach to enhance the seismic behaviour of the joints [20,21]. In addition, different strengthening techniques were used to relocate plastic hinge zones away from the joint zone as an alternative approach to improve the seismic efficiency of monolithic reinforced concrete (RC) beam-to-column joints [22-24]. As a result, the resistance of beam-to-column joints against earthquake loads was significantly improved and brittle failure was avoided in these RC joints. These studies have focused on evaluating the use of various strengthening methods only in RC beam-to-column joints. Hence, the studies on the improvement of PC joints in terms of forming the plastic hinge on beam and located outside the joint zone is limited [25,26]. Therefore, this research is aimed to improve the seismic performance of innovative PC beam-to-column joints by casting the joints using ECC. Besides, for developing the failure mode of the joints by preventing the brittle failure and relocating the plastic hinge on the PC beams of the proposed hybrid joints.

2 Experimental methodology

2.1 Materials properties and mixes design

In this research, two mixes were prepared as follows: (i) the control for the normal concrete (NC) and (ii) ECC containing different fibres, namely PVA fibre and hooked-end steel fibre, at 1% volume fraction for PVA fibre and 0.75% for hooked-end steel fibre. The NC mix was designed according to a previous study [27] and used to cast the RC sample and PC members, while ECC was used to cast the PC joints and the adjacent PC beams areas. Table 1 presents the design mixes of NC and ECC of this research. According to Table 1, C refers to the cement, FA refers to the fly ash, SF represents the silica fume, RS is river sand, S1 is silica sand with a maximum size of 200 μ m, S2 is silica sand with size ranging between 200 μ m-1.25mm, CA is coarse aggregate with size ranging between 5mm-12.5mm, W is water, and SP is superplasticiser.

Table 1 Mix proportions for NC and ECC used in this research.

	Kilogram/ cubic meter, (kg/m ³)								
Mix type	C	FA	SF	RS	S1	S2	CA	W	SP
NC	450.0	-	-	670.0	-	-	1014.0	171.0	4.50
ECC	720.0	144.0	69.12	-	717.12	405.08	-	251.94	27.99

2.2 Sample design and details

The seismic efficiency of the exterior hybrid PC joints was evaluated under quasi-static reversed cyclic loading. One control sample of monolithic RC (MRC) joint and two samples of the innovative hybrid PC joints, namely HPCH1 and HPCH2 were used; see Fig. 1.

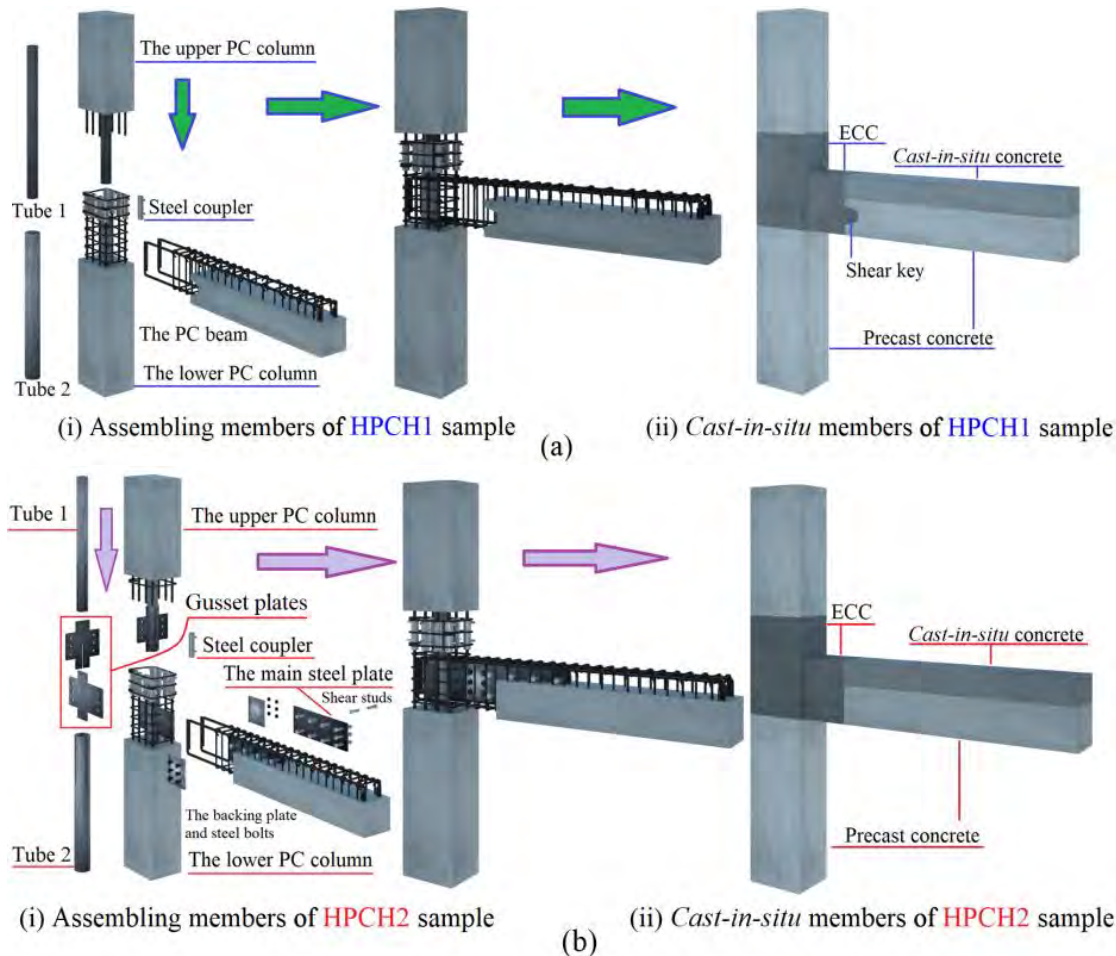


Fig. 1 3D view of innovative hybrid PC joints of the (a) HPCH1 and (b) HPCH2 samples.

The innovative hybrid joints were proposed in this research and used steel tubes (Tube 1 and Tube 2), steel plates (main steel plate and gusset steel plates in the HPCH2 sample only) to connect the PC beams and PC columns. In addition, grouted steel couplers with an embedded length of 8 times the bar diameter (Φ) [28] were used to connect the main longitudinal steel bars of PC columns of the hybrid (HPCH1 and HPCH2) samples (Figs. 1 and 2). The steel tubes (Tube 1 and 2) have the same dimensions and mechanical properties in HPCH1 and HPCH2 samples. The reinforcing details of the MRC, HPCH1, and HPCH2 joint samples are presented in Fig. 2.

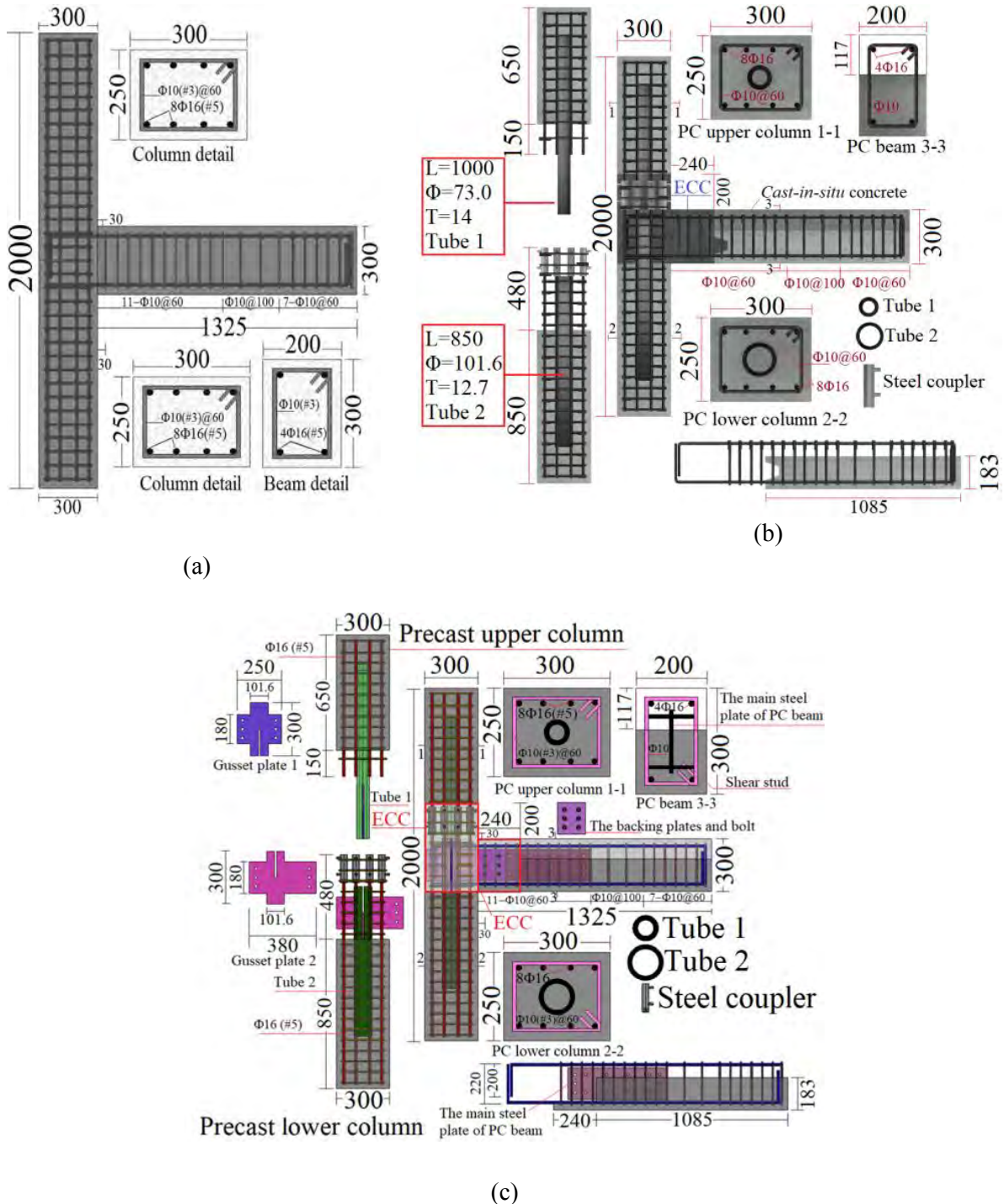


Fig. 2 The reinforcement details of the (a) MRC, (b) HPCH1, and (c) HPCH2 samples (dimensions are in mm).

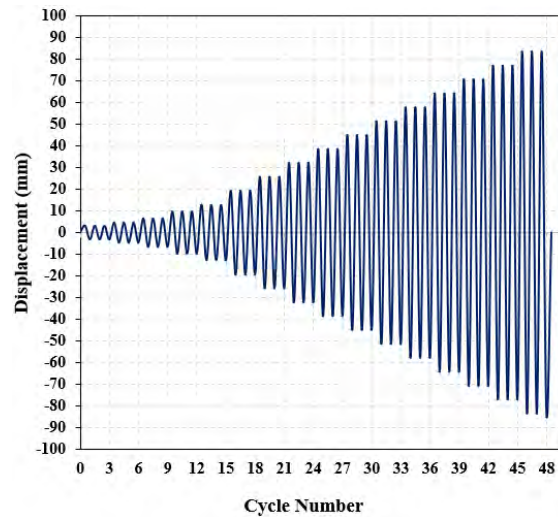
Based on the test results of three specimens for steel materials, the average yield strength (f_y) of the main reinforcing bar ($\Phi 16\text{mm}$), transverse reinforcing bar ($\Phi 10\text{mm}$), steel plate with a thickness (T) of 10mm, Tube 1 ($\Phi 73\text{mm}$ and $T=14\text{mm}$), and Tube 2 ($\Phi 101.6\text{mm}$ and $T=12.7\text{mm}$) is 573 MPa, 505MPa, 367.40MPa, 320MPa, and 315MPa, respectively. The minimum ratio of the (f_u/f_y) was 1.25; here f_u represents the ultimate strength of steel materials. In addition, the compressive strength of *cast-in-situ* using NC is 73.40MPa for the MRC sample, and it is 72.20 MPa for the PC members of HPC1 and HPC2 samples. The compressive strength of *cast-in-situ* ECC is 78.40MPa for the hybrid samples and 74.10MPa for *cast-in-situ* NC for PC beams of the hybrid samples.

2.3 Test setup and protocol

The test setup and instrumentation of samples subjected to the quasi-static cyclic loading are shown in Fig. 3(a). The exterior beam-to-column sub-assemblies were supported by pin support at the bottom of the column.



(a)



(b)

Fig. 3 The view of the (a) schematic test setup of the sample and (b) cyclic loading protocol of the samples.

A constant axial load equivalent to $(0.1 A_g f_c)$ was applied on the column top at the beginning of the test through an actuator capacity of 2000kN. A_g and f_c are the gross section area and the compressive strength, respectively of the column.

The cyclic protocol load presented in Fig. 3(b) was applied at the beam end using displacement control and the load was applied through an actuator with the capacity of $\pm 450\text{kN}$. During the test, vertical, horizontal, and diagonal displacements were measured using load linear variable displacement transducer (LVDTs).

3 Results and discussion

3.1 The failure mode of samples

A beam-to-column joint can fail under different modes as follow: (i) beam flexural failure; (ii) beam shear failure; (iii) column flexural failure; (iii) column shear failure; (iv) joint shear failure; (v) bond failure of the reinforcement; and (vi) a combination of the various modes listed above. Some of these failure modes should be prevented if the beam-to-column joint undergo large plastic deformations (e.g., shear failure of the column or joint and bond failure of reinforcement). The collapse of the whole structure may occur due to the limited deformation capacity of such a brittle plastic mechanism [29,30]. To reach the ductile structure, in particular a ductile joint, each element should be designed for having sufficient displacement capacity. Fig. 4 presents the failure modes of the tested samples. According to the failure modes of the tested samples, the plastic hinge of the MRC sample was

formed at the beam end and extended a little bit to the joint area. The plastic hinge of HPCH1 and HPCH2 samples were formed outside the joint zone and located at a distance of 20mm and 60mm, respectively, measured from the column face. In general, the tensile strengths of the concrete, transverse reinforcing bars, and longitudinal reinforcing bars, and effective joint width can contribute significantly to the shear capacity of the joint. Moreover, the high tensile strength and strain capacity of the ECC compared to the NC [31,32] can significantly improve the shear strength capacity of the joint. Furthermore, the steel section element of the joint greatly enhanced the shear strength of hybrid joints. Therefore, the use of ECC to cast the joint area can relocate the plastic hinge to form at the beam area.



Fig. 4 Failure mode of the (a) MRC sample, (b) HPCH1 sample, and (c) HPCH2 sample.

3.2 Load, displacement, and energy dissipation of the tested samples

The load-displacement curves of the MRC, HPCH1, and HPCH2 samples during the quasi-static reversed cyclic loading test are presented in Fig. 5. In addition, the average displacements and loads curves (envelop curves) of both push (+) and pull (-) directions of the tested samples are illustrated in Fig. 6 (a). The capacity of the drift ratio at the failure stage of the MRC, HPCH1, and HPCH2 samples was 4%, 4.5%, and 6%, respectively (Fig. 6 (a)). There is an improvement in the drift ratio of the HPCH1 and HPCH2 samples by a factor of 1.125 and 1.5, respectively compared to the MRC sample. This is resulted from using ECC that contained hybrid fibres.

The building structural elements and joints should be able to dissipate the energy under lateral loading for enhancing the seismic behaviour of the structures. The sufficient energy dissipation for the joints

subjected to the seismic excitation can decrease the transmitting loads and deformations to other structural elements. The energy dissipation of each sample was calculated using the region enclosed in the hysteretic cycles. The energy dissipation of HPCH1 and HPCH2 samples was increased by a ratio of about 44% and 213%, respectively compared to the MRC sample (Fig. 6(b)). Table 2 presents the results of the tested samples. The improvement of mechanical bridging in the crack region, adequate amount and distribution of PVA and hooked-end steel fibres, and good bonding in the ECC resulted in an increase in the drift ratio and energy dissipation capacities of the HPCH1 and HPCH2 samples compared to the MRC sample.

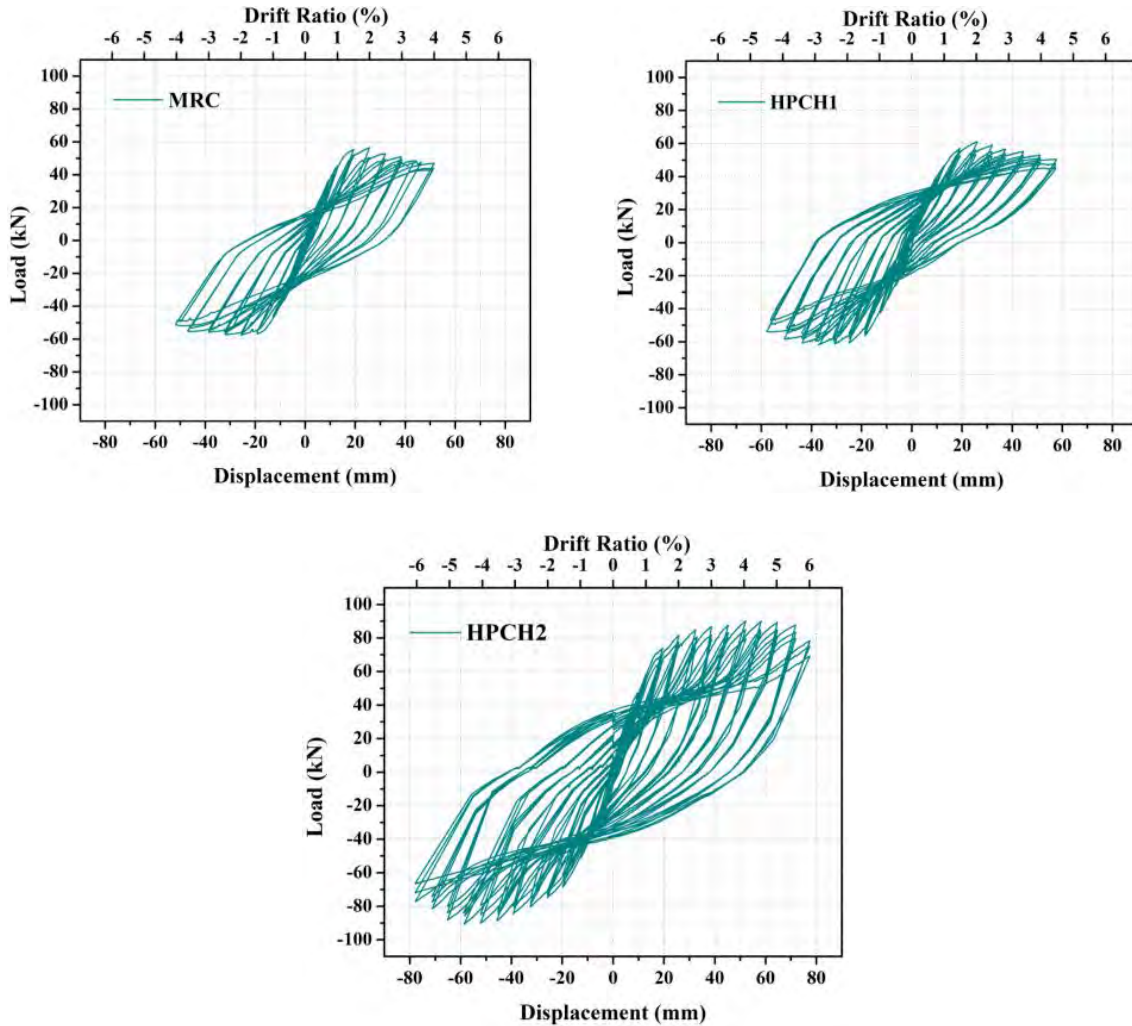


Fig. 5 The load-displacement curve of the MRC, HPCH1, and HPCH2 samples.

Table 2 The results of the tested samples in terms of load, displacement, and energy dissipation.

Sample	Direction	Max. Load	Max. Displacement	Energy dissipation
		kN	mm	kN.mm
MRC	Push	56.55	51.50	19701.10
	Pull	-57.57	-51.60	
HPCH1	Push	61.10	57.70	28347.72
	Pull	-61.74	-57.90	
HPCH2	Push	90.16	77.50	61735.60
	Pull	-90.60	-77.94	

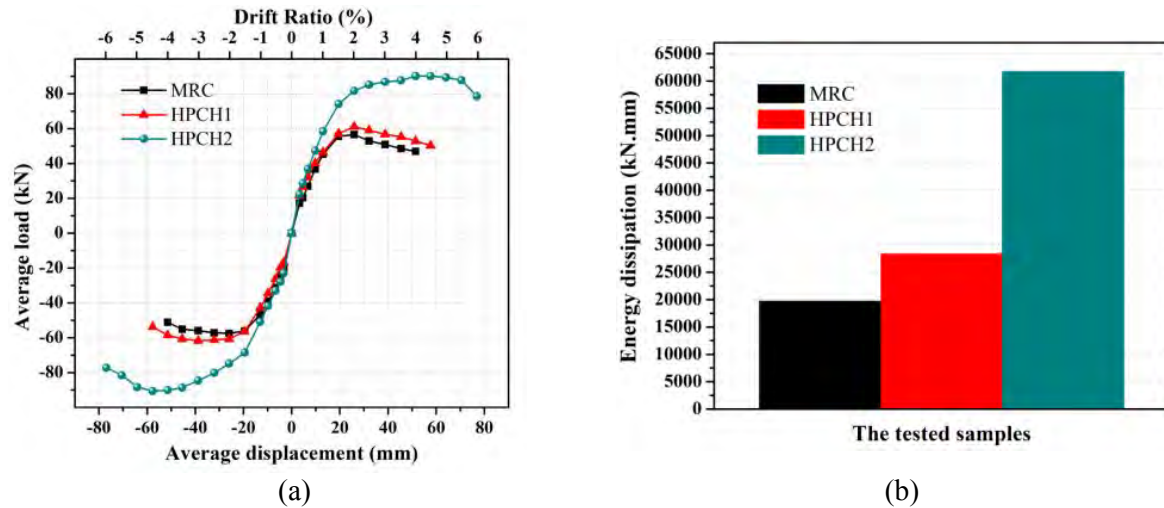


Fig. 6 The result of the (a) envelop curves in both directions (push and pull) of the samples and (b) energy dissipations of the tested samples.

4 Conclusions

In this research, the ECC was used for casting the joints and the adjacent beams areas of the innovative precast beam-to-column joints. The following conclusions can be drawn based on the findings made during the experimental campaign and the results discussed in this article:

1. The plastic hinge relocation on beams of the hybrid PC joints due to using the steel sections to connect the beams and columns. Besides that, casting the joints using ECC can result in the formation of the plastic hinges on beams and outside the joints.
2. The energy dissipations of the hybrid joints were increased by the ratio of about 44% for the HPCH1 sample and 213% for the HPCH2 sample compared with that of the MRC sample.
3. Based on the test results, using ECC for casting joint is highly recommended for enhancing the seismic performance of the PC joints and the PC joints can emulate the performance of the RC joint.

Overall, the hybrid fibres can increase the deformation capacity of the hybrid PC samples. The improvement of mechanical properties such as better bridging in the crack region, adequate amount and distribution of PVA and hooked-end steel fibres, good bonding in the ECC, and increased slip resistance for reinforcing bars enhanced the drift ratio and energy dissipation capacities of the HPCH1 and HPCH2 samples compared to the MRC sample. Therefore, casting the joint and adjacent beam area using ECC can significantly improve the seismic performance of the hybrid PC samples compared to the MRC sample that is used NC for the casting joint.

Acknowledgements

The authors wish to express their gratitude and sincere appreciation to the University of Malaya and the Ministry of Higher Education, Malaysia for the support provided through Postgraduate Research Grants PPP-Project No.PG199-2015B. Also, we like to sincerely thank the Faculty of Engineering, University of Malaya, Malaysia for the support given through research Project No: GPF071A-2018.

References

- [1] Elliott, K.2019. *Precast concrete structures*. CRC Press, Taylor & Francis Group, Boca Raton, FL, USA, 2nd edition: 2019.
- [2] Brecolotti, M.; Gentile, S. Tommasini, M.; Materazzi, A.L.; Bonfigli, M.F.; Pasqualini, B.; Colone, V.; Ganesini, M. 2016. "Beam-column joints in continuous RC frames: Comparison between cast-in-situ and precast solutions". *Engineering Structures*, 127, 129-144, <http://10.1016/j.engstruct.2016.08.018>.
- [3] Ghayeb, H.H.; Razak, H.A.; Sulong, N.R. 2019. "Performance of dowel beam-to-column connections for precast concrete systems under seismic loads: A review. " *Constr Build Mater* 2020, 237, 117582, <http://doi.org/10.1016/j.conbuildmat.2019.117582>.

- [4] Ghayeb, H.H.; Razak, H.A.; Sulong, N.H.R. 2017. "Development and testing of hybrid precast concrete beam-to-column connections under cyclic loading." *Constr Build Mater*, 151, 258-278, <http://doi:10.1016/j.conbuildmat.2017.06.073>.
- [5] Nadoushani, Z.S.M.; Akbarnezhad, A. 2015. "Effects of structural system on the life cycle carbon footprint of buildings." *Energy and Buildings*, 102, 337-346. <http://doi.org/10.1016/j.enbuild.2015.05.044>.
- [6] Oh, B.K.; Park, J.S.; Choi, S.W.; Park, H.S. 2016. "Design model for analysis of relationships among CO₂ emissions, cost, and structural parameters in green building construction with composite columns." *Energy and Buildings*, 118, 301-315, <http://doi.org/10.1016/j.enbuild.2016.03.015>.
- [7] Park, H.S.; Lee, H.; Kim, Y.; Hong, T.; Choi, S.W. 2014. "Evaluation of the influence of design factors on the CO₂ emissions and costs of reinforced concrete columns." *Energy and Buildings*, 82, 378-384. <http://doi.org/10.1016/j.enbuild.2014.07.038>.
- [8] Ghayeb, H.H.; Razak, H.A.; Sulong, N.R. 2019. "Evaluation of the CO₂ emissions of an innovative composite precast concrete structure building frame." *Journal of Cleaner Production*, 118567. <http://doi.org/10.1016/j.jclepro.2019.118567>.
- [9] Toniolo, G.; Colombo, A. 2012. "Precast concrete structures: the lessons learned from the L'Aquila earthquake." *Structural Concrete*, 13, 73-83, doi:10.1002/suco.201100052. https://doi.org/10.1002/suco.201100052.
- [10] Belleri, A.; Brunesi, E.; Nascimbene, R.; Pagani, M.; Riva, P. 2014. "Seismic performance of precast industrial facilities following major earthquakes in the Italian territory." *Journal of Performance of Constructed Facilities*. [http://doi.org/10.1061/\(ASCE\)CF.1943-5509.0000617](http://doi.org/10.1061/(ASCE)CF.1943-5509.0000617).
- [11] Ghayeb, H.H., Abdul Razak, H., Ramli Sulong, N.H. 2019. "A sustainable precast frame of a low-rise building using geopolymers concrete." In *Proceedings of the IAPE '19, Oxford, United Kingdom*. <http://doi:10.17501>.
- [12] Magliulo, G.; Ercolino, M.; Petrone, C.; Coppola, O.; Manfredi, G. 2014. "The Emilia Earthquake: Seismic Performance of Precast Reinforced Concrete Buildings." *Earthquake Spectra*, 30, 891-912, <http://doi:10.1193/091012eqs285m>.
- [13] Alcocer, S.M.; Carranza, R.; Perez-Navarrete, D.; Martinez, R. 2002. "Seismic tests of beam-to-column connections in a precast concrete frame." *PCI Journal*, 47, 70-+, <http://doi:10.15554/pcij.05012002.70.89>.
- [14] Blandon, J.J.; Rodriguez, M.E. 2005. "Behavior of connections and floor diaphragms in seismic-resisting precast concrete buildings." *PCI Journal*, 50, 56-+, <http://doi:10.15554/pcij.03012005.56.75>.
- [15] Ghayeb, H.H.; Razak, H.A.; Sulong, N.R. 2020. "Seismic performance of innovative hybrid precast reinforced concrete beam-to-column connections." *Engineering Structures*, 202, 109886. <http://doi.org/10.1016/j.engstruct.2019.109886>.
- [16] ACI 318. American Concrete Institute, ACI 318. Building Code Requirements for Structural Concrete and Commentary (ACI 318-20): An ACI Standard. American Concrete Institute Farmington Hills, Michigan, USA. 2020.
- [17] NZS. New Zealand Standard (NZS). Standards New Zealand, Appendix B: special provisions for the seismic design of ductile jointed precast concrete structural systems. NZS 3101. *New Zealand* 2005.
- [18] CEN-EC8. European Committee for Standardisation (CEN). Eurocode 8 (EC8): Design of structures for earthquake resistance-Part 1: General rules, seismic actions and rules for buildings. *UK* 2005.
- [19] NZS. New Zealand Standard (NZS). Concrete structures standard: part 1-the design of concrete structures and part 2-commentary, standards New Zealand. Wellington (NZS 3101). *New Zealand* 2006.
- [20] Ismail, M.K.; Abdelaleem, B.H.; Hassan, A.A. 2018. "Effect of fiber type on the behavior of cementitious composite beam-column joints under reversed cyclic loading." *Constr Build Mater*, 186, 969-977. <http://doi.org/10.1016/j.conbuildmat.2018.08.024>.
- [21] Frank, T.E.; Lepech, M.D.; Billington, S.L. 2018. "Experimental testing of reinforced ECC beams subjected to various cyclic deformation histories." *Journal of Structural Engineering*, 144, 04018052. [http://doi.org/10.1061/\(ASCE\)ST.1943-541X.0002034](http://doi.org/10.1061/(ASCE)ST.1943-541X.0002034).

- [22] Dalalbashi, A.; Eslami, A.; Ronagh, H.R.2012. "Plastic hinge relocation in RC joints as an alternative method of retrofitting using FRP." *Composite Structures*, 94, 2433-2439. <http://doi.org/10.1016/j.compstruct.2012.02.016>.
- [23] Pimanmas, A.; Chaimahawan, P.2010. "Shear strength of beam-column joint with enlarged joint area." *Engineering structures*, 32, 2529-2545. <http://doi.org/10.1016/j.engstruct.2010.04.021>.
- [24] Niroomandi, A.; Maheri, A.; Maheri, M.R.; Mahini, S.S.2010. "Seismic performance of ordinary RC frames retrofitted at joints by FRP sheets." *Engineering Structures*, 32, 2326-2336. <http://doi.org/10.1016/j.engstruct.2010.04.008>.
- [25] Eom, T.-S.; Park, H.-G.; Hwang, H.-J.; Kang, S.-M.2016. "Plastic hinge relocation methods for emulative PC beam-column connections." *Journal of Structural Engineering*, 142, 04015111. [http://doi.org/10.1061/\(ASCE\)ST.1943-541X.0001378](http://doi.org/10.1061/(ASCE)ST.1943-541X.0001378).
- [26] Parastesh, H.; Hajirasouliha, I.; Ramezani, R.2014. "A new ductile moment-resisting connection for precast concrete frames in seismic regions: An experimental investigation." *Engineering Structures*, 70, 144-157, <http://doi:10.1016/j.engstruct.2014.04.001>.
- [27] Ghayeb, H.; Razak, H.A.; Sulong, N.; Hanoon, A.; Abutaha, F.; Ibrahim, H.; Gordan, M.; Alnahhal, M.2019. "Predicting the Mechanical Properties of Concrete Using Intelligent Techniques to Reduce CO2 Emissions. " *Materiales de Construcción*, 69, 190. <http://10.3989/mc.2019.07018>.
- [28] Ghayeb, H.H.; Razak, H.A.; Sulong, N.R.; Mo, K.H.; Abutaha, F.; Gordan, M.2020. "Performance of Mechanical Steel Bar Splices using Grouted Couplers under Uniaxial Tension." *Journal of Building Engineering*, 101892. <http://doi.org/10.1016/j.jobbe.2020.101892>.
- [29] Hwang, H.-J.; Park, H.-G.; Choi, W.-S.; Chung, L.; Kim, J.-K.2014. "Cyclic loading test for beam-column connections with 600 MPa (87 ksi) beam flexural reinforcing bars." *ACI Structural Journal*, 111, 913. <http://doi:10.14359/51686920>.
- [30] Ricci, P.; De Risi, M.T.; Verderame, G.M.; Manfredi, G. 2016. "Experimental tests of unreinforced exterior beam-column joints with plain bars." *Engineering Structures*, 118, 178-194. <http://doi.org/10.1016/j.engstruct.2016.03.033>.
- [31] Zhang, R.; Matsumoto, K.; Hirata, T.; Ishizeki, Y.; Niwa, J. 2015. "Application of PP-ECC in beam-column joint connections of rigid-framed railway bridges to reduce transverse reinforcements." *Engineering Structures*, 86, 146-156. <http://doi.org/10.1016/j.engstruct.2015.01.005>.
- [32] Xu, L.; Pan, J.; Chen, J. 2017. "Mechanical behavior of ECC and ECC/RC composite columns under reversed cyclic loading. " *Journal of Materials in Civil Engineering*, 29, 04017097. [http://doi.org/10.1061/\(ASCE\)MT.1943-5533.0001950](http://doi.org/10.1061/(ASCE)MT.1943-5533.0001950).

The experimental verification of concrete elements strengthened using ultra-high-performance concrete

Lukáš Boháček, Jan L. Vitek

*Faculty of Civil Engineering,
Czech Technical University in Prague,
Thákurova 7, Prague 6 (166 29), Czech Republic*

Abstract

UHPC (ultrahigh-performance concrete) is a type concrete that has significantly better properties than commonly used concrete. In addition to the widely known high compression and tensile strengths, greater durability and resistance are also advantages of these types of concrete. These concretes can be used for both new structures and reconstructions. Nowadays, these types of concrete are in minority due to higher price and complex casting.

This paper deals with the properties and behaviour of concrete structures strengthened using UHPC. One of the most important properties is a good bond between old concrete and the layer of UHPC. According to this fact, some types of bond were tested and evaluated. Then, using the most effective type of connection, experiments to determine and to compare values of bending load capacity both specimens strengthened using UHPC and without strengthening were made. Three types of elements were used; elements without strengthening and elements strengthened using 30 mm and 50 mm of UHPC. Besides the load bearing capacity, deformations and cracks were observed. Finally, measured values were compared with results of simplified calculations.

1 General information on experiments

The concept of strengthening of concrete slabs considered in this paper is casting UHPC (ultra-high-performance concrete) layer on top of the old concrete slab. To determine load bearing capacities of elements composed of two layers of concretes (concrete with regular properties and ultra-high-performance concrete), it was crucial to find out the proper bond between these two layers. This bond type must have both good properties and easy realization on site. Due to this fact, experiments to compare bond types were made at the beginning of the research.

After this, experiments to determine load bearing capacities under some types of loading were made. There are usually three important ultimate limits states for concrete elements – bending, shear and punching. All these three ultimate states were verified. These experiments were executed according to the application of mentioned strengthening method (UHPC layer is on top of the old concrete element). This article deals with bending of slab elements.

A bending capacity was tested using UHPC in both compression and tension. There were always three types of specimens for all the experiments – specimens without strengthening, specimens with 30 mm of UHPC without bar reinforcement and specimens with 50 mm of UHPC with bar reinforcement. This variation was designed to determine the significance of strengthening.

Before the experiments, some basic calculations to predict the performance were executed. For the calculations, literature and standards were used, e.g., [1]-[3].

2 Bond experiments

2.1 Specification of the experiments

The sufficient bond between two types of concretes is an elementary condition for improving properties and bearing capacity of slab elements. Choosing the most effective type of bond with respect to its strength and difficulties making on site was the aim of these experiments. According to the second condition and properties of UHPC, only methods of improving bond without mechanical connectors (i.e. steel) were chosen and tested.

2.2 Preparation and execution of the experiments

There were old prefabricated concrete panels with two types of surface – smooth surface shaped by formwork and rough surface without contact with formwork. On these panels, four types of preparation of the surfaces were applied: mechanical water blasting (higher pressure of water), manual water blasting (lower pressure of water), sandblasting and surface without any modification. In fact, six types of surfaces were prepared using these methods:

- Surface without modification shaped by formwork (S1)
- Surface without modification (S2)
- Sandblasted surface shaped by formwork (S3)
- Sandblasted surface (S4)
- Manually water jet blasted surface (S5)
- Mechanically water jet blasted surface (S6)

Water jet blasted surfaces are not divided according to contact with formwork, because these surfaces were became significantly rough and this difference of the original surface quality disappeared.

Later, on one half of the surfaces the adhesive bridge was applied to determine its significance to properties of bond. This was followed by casting the UHPC layer. The whole preparation was finished by core drilling to get specimens for tension tests. The drills had a diameter of 100 mm, were drilled through the whole slab and for every type of bond three specimens were drilled.

2.3 Results of the experiments

Results from these experiments are summarized in Table 1. In this table, the treatment of surface and whether the adhesion bridge was used or not, is shown. In the next columns the average stresses in the moment of failure are shown, the standard deviation of these stresses and where the crack developed.

Table 1 Average failure stress and its standard deviation according to the type of bonding (surface preparation). Explanation: D – failure during drilling, C – crack in old concrete, AB – crack in adhesion bridge.

Modification	Without adhesion bridge			With adhesion bridge		
	Area of failure	Failure average tension stress [MPa]	Standard deviation [MPa]	Area of failure	Failure average tension stress [MPa]	Standard deviation [MPa]
S1	D	-	-	D	-	-
S2	C	2.59	0.17	AB	1.24	0.29
S3	C	3.19	0.18	AB	0.80	0.17
S4	C	2.28	0.33	AB	1.40	0.31
S5	C	2.81	0.28	AB	1.69	0.42
S6	C	2.84	0.20	AB	1.99	0.18

As it is shown in Table 1, adhesion bridge provides lower bond strength for each type of surface treatment. It means UHPC itself had better adhesive properties and adhesion bridge was not used for other experiments. Surfaces without treatment that were in contact with formwork were too smooth, the bond between materials was weak and the layers of concrete delaminated during drilling. For all other cases there was a failure in old concrete, so the bond between concretes was sufficient. For following experiments panels, the type S5 – water jet blasting with lower water pressure was chosen, because this method is quite easy to use and effective.

3 Bending experiments with UHPC in compressive zone

3.1 Specification of the experiments

The experiments were made using about 10 years old concrete panels which were strengthened using UHPC layers – one type of panels with 30 mm UHPC and second type with 50 mm UHPC including reinforcing mesh with bars of 8 mm in diameter in the distance of 100 mm. Because of the weak reinforcement, these old panels were also strengthened using another reinforcement bars to make the reinforcement more similar to ordinary used structures. The average strength of cylinders of the old concrete was 32.3 MPa and the reinforcement was assumed as B500B. The strength of cylinders of UHPC was 140 MPa and the experiments were executed about 30 days after casting.

The experiment was designed as a four-point flexural test due to its advantages. This experiment should approximate the situation when the maximal bending moments are in the middle of the span with low values of shear forces. The span between supports was 2.5 m and the distance between point load locations was 0.8 m (Fig. 1). For the experiment, one hydraulic jack and a steel beam to transport load into two steel tubes were used. The point loads were uniformly distributed in the transversal direction across the panel.

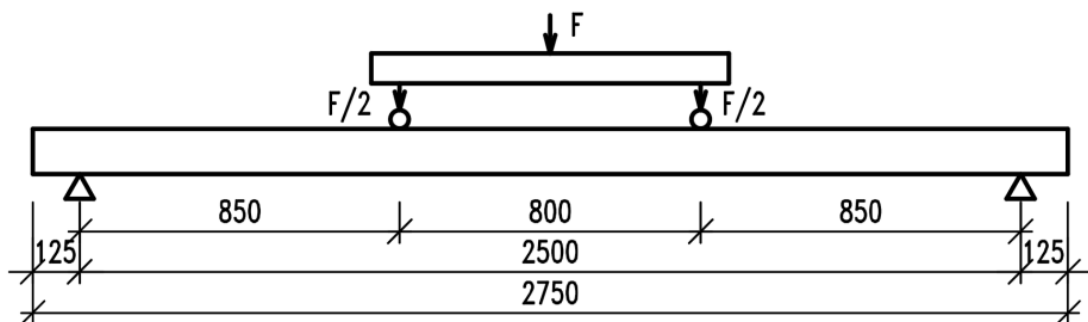


Fig. 1 Longitudinal scheme of the bending test

3.2 Preparation and execution of the experiments

The panels used for experiments were 490 mm wide, 120 mm high and 2750 mm long. The original longitudinal reinforcement ratio was about 0.8% ($4 \times \varnothing 12 \text{ mm}$) and these bars were placed irregularly in the panel (Fig 2). Because of this, panels were strengthened using four bars with diameter 10 mm near the bottom surface. This raised the longitudinal reinforcement ratio to 1.3% and these panels were appropriate to experiments.

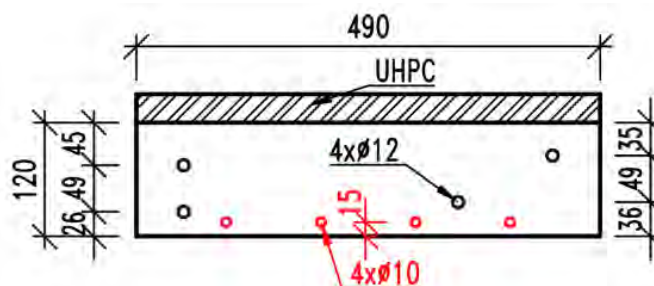


Fig. 2 Cross-sectional dimensions of original concrete panel and reinforcement of this panel.

This process was followed by strengthening using UHPC layer. Nine panels were needed in total to execute the experiments. Three panels were left without modification, three panels were strengthened using 30 mm UHPC layer and last three panels were strengthened using 50 mm UHPC and rebar mesh to reduce shrinkage deformation and load of the whole specimen.

During the experiments, two main values were measured – the deflection in the middle of the span and the force induced by the hydraulic jack.

3.3 Results of the experiments

In Fig. 3, values of bending moments in dependence on the deflection of the specimens are shown. This chart shows, that panels with UHPC had similar stiffness at the beginning. On the other hand,

specimen ref-1 had no visible change of stiffness due to first cracks of concrete. This change of gradient is visible for specimen ref-2, unfortunately most of the values from this record were incorrect due to the failure of the measuring system, so only results to deflection 20 mm are shown. It can be seen, that for all specimens, the deformation of about 20 mm was important. It is clearly visible that reinforcement is reaching its yield point at this deflection and the gradients of the charts are significantly changing. After reaching yield stress of the reinforcement, the curves in the chart were growing very slowly.

Figure 3 also shows that strengthened panels reached greater deflection before failure.

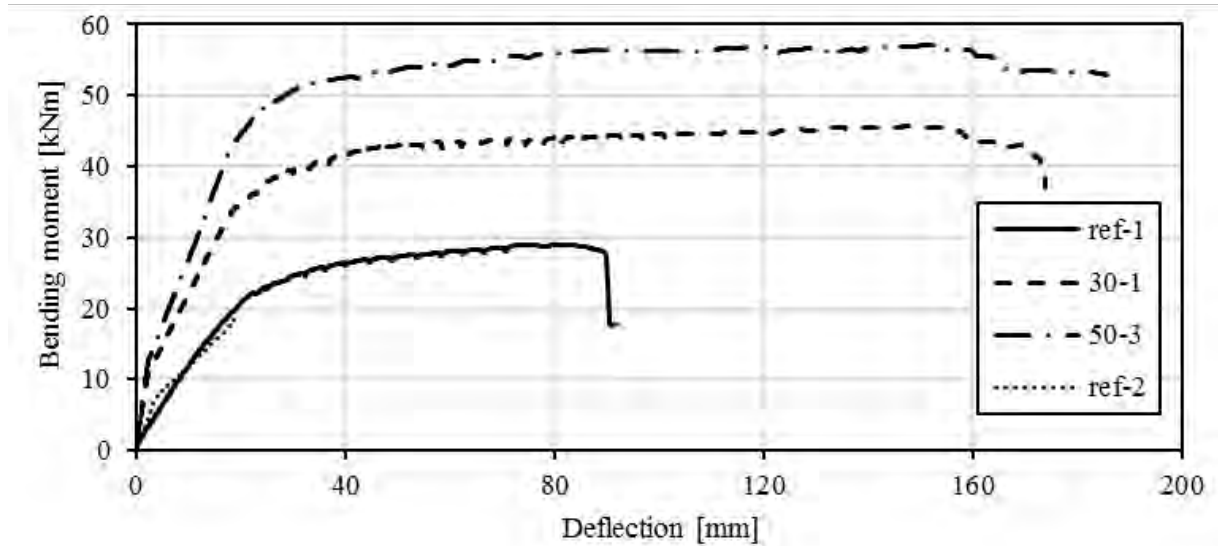


Fig. 3 Bending moment in the middle of the span in dependence on the deflection in the middle of the span.



Fig. 4 Cracks at the bottom surface of the panels after executing experiments. Left figure is reference panel and right figure is panel with 30 mm UHPC.

Figure 4 shows the difference between the performance of reference panels and strengthened panels. It is visible that cracks in specimen with 30 mm of UHPC (on the right) are wider than cracks in reference panel (on the left).

Table 2 summarizes numerical results from the experiments. It can be seen that bending moments of strengthened specimens increased significantly comparing to reference specimens. The bearing capacity of reference panels is about 30 kNm, panels with 30 mm UHPC has average bearing capacity 40.7 kNm (161% of reference panels bearing capacity) and panels with 50 mm UHPC and rebar mesh has average bearing capacity 59.5 kNm (201% of reference panels bearing capacity).

Table 2 Bending moments M_{\max} in the moment of failure in the middle of the span for tested specimens. Averages for used types of panels and comparison with calculated values.

Type of panels	Specimen	M_{\max} [kNm]	Average M_{\max} [kNm]	Standard deviation [kNm]	Coefficient of variation [%]
Reference	ref-1	30.2	29.6	1.1	3.6
	ref-2	28.1			
	ref-3	30.6			
30 mm of UHPC	30-1	47.1	47.0	0.3	0.6
	30-2	47.4			
	30-3	46.7			
50 mm of UHPC	50-1	60.1	59.5	0.6	1.0
	50-2	59.7			
	50-3	58.8			

3.4 Simplified analysis and discussion

Table 2 shows that bearing capacities were increased significantly due to the strengthening. Usually, with the same reinforcement and concrete, the bending bearing capacity increases in the similar ratio to the height of the section. However, for specimens with 30 mm of UHPC, the bending bearing capacity was increased to 159% of bending capacity of reference panels, when the thickness of the specimens was increased to 125%. For specimens with 50 mm of UHPC, the bending bearing capacity was increased to 200% of bending capacity of reference panels, when the thickness of the specimens was increased to 140%. This means, that the lever arm of internal forces was increased more than the depth of the cross-section. Lately, it was confirmed by calculation, because the depth of the compression zone was calculated 28 mm for reference specimens and about 11 mm for strengthened specimens because of the high compression strength of UHPC.

These panels are rather thin, and the increase of the ultimate load in thicker slabs would not be so significant. However, using UHPC could be considered as very efficient also at thicker slabs. No delamination appeared at any of the strengthened specimens, although a significant deformation was achieved. No necessity of mechanical connectors was confirmed.

Better ductility which is important for safety of the structures is another advantage. In figure 3, it is visible that strengthened panels reached higher deflection, which is related to high compressive strength of the UHPC and small compression area in the cross section (confirmed by calculations). Also, wider cracks in strengthened specimen (Fig. 4) indicate larger deformation of the reinforcement.

To analyse results of the experiment, the bearing capacities of specimens were determined by simple calculation. For analysis, calculation of ultimate bending moment of given cross section according to fib Model Code 2010 [1] was used. A parabolic material diagram with maximal stress 140.0 MPa (average strength of the cylinders) was used for UHPC and bilinear material diagram with characteristic values for material B500B was used for rebars. Geometry was used according to Fig. 2.

Calculated bearing capacities were: 27.5 kNm for the cross section without strengthening (93% of experimentally determined bearing capacity), 43.2 kNm for cross section with 30 mm of UHPC (92% of experimentally determined bearing capacity) and 51.6 kNm for cross section with 50 mm of UHPC (87% of experimentally determined bearing capacity). Based on these results, it could be said that the differences between the experiments and calculations are consistent and using simple calculation to determine bearing capacity of strengthened cross-section is satisfactory.

The main part of the difference is probably caused by the insufficient accuracy of reinforcement parameters. Characteristic parameters were used for the reinforcement and it can be assumed that the actual parameters of the reinforcement were higher than characteristic values. Another reason of the difference is that the shrinkage of UHPC and the self-weight of the panels were not considered in the calculation.

4 Bending experiments with UHPC in the tensile zone

4.1 Specification of the experiments

These experiments were executed few months later than previous experiments and different panels were available. These panels (Fig. 5) had a different cross-section (790 mm x 120 mm) and different reinforcement (two rows with six reinforcement bars with diameter of 10 mm). The average compressive strength of cylinders was determined using experiments and the result was 65.8 MPa. It is important to mention, that vertical distances between reinforcement bars and surfaces were very variable and it was not possible to determine the exact position of the reinforcement for all panels. Positions in Fig. 5 are approximately.

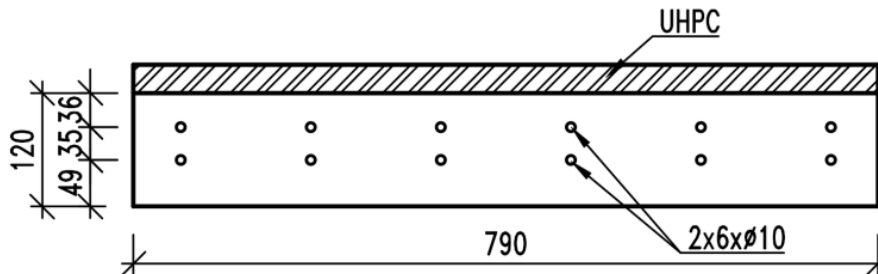


Fig. 5 Cross-section of the specimens. Distances between the rows of bars were variable; average positions are shown.

It was important to specify properties of the UHPC in tension for these experiments. Experimentally determined properties of UHPC; tensile strength was 4.9 MPa and bending strength was 18.6 MPa.

As shown in Fig. 6, the experiment was designed as the overhanging beam loaded at the end of the cantilever. Exactly, the hydraulic jack was placed 0.6 m behind the support and the sensor recording the deflections was 0.75 m behind the support. The span of the supported beam part was 1.6 m. This arrangement corresponds to the real conditions. Bending moments with tensioned upper surface generally reach the maximum values above the supports and these supports are usually local and cause the change of shear force. In fact, these experiments evaluate behaving of the strengthened panels exposed to the bending moments and shear forces.

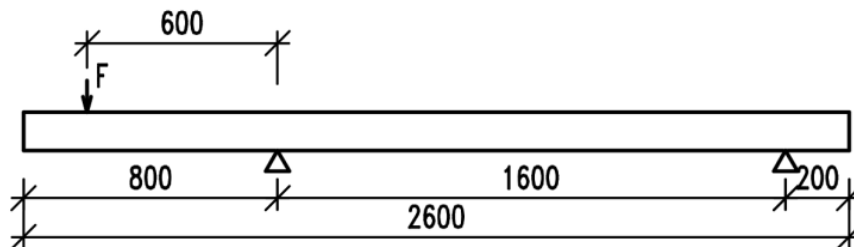


Fig. 6 Diagram of the experiments to test the UHPC in tension area. “F” represents the force caused by hydraulic jack.

4.2 Preparation and execution of the experiments

Figure 6 corresponds with the practical set up of the experiment. The tensioned surface was oriented up to provide better view of the cracks. Similar to previous experiments, six panels were strengthened using UHPC layer – three panels with 30 mm of UHPC and three panels with 50 mm of UHPC and rebar mesh. Last three panels were left without strengthening.

The force from hydraulic jack was distributed into uniform line load using steel transversal beam. Transversal beams were used as supports and the right-hand end of the beam had to be fixed to prevent its lifting.

Experiments were executed in the laboratory within two days and approximately 30 days after casting the UHPC layer, so the experiments were not distinctly influenced by weather conditions and time. The experiments were controlled by displacement of hydraulic jack and the speed of loading was set to 0.1 mm/s.

4.3 Results of the experiments

Firstly, it needs to be said that for any specimen, any failure of the interface between the layers of old concrete and UHPC was not visible. The chart in Fig. 7 shows the record of the deflection and the bending moment above the support for chosen specimens. From every type of specimens, those with the middle value of maximal bending moment were chosen for illustration. The results for all specimens are given in the Table 3.

Bearing capacity of panels without strengthening, as it can be seen in Fig. 7, was very low due to the unsuitable position of reinforcing bars (Fig. 5). In general, the values of bending moments were very similar at increasing deflections which showed a large ductility of the panels without strengthening. The maximal value was reached with deflection of about 40 mm.

Comparing specimens 30-2 and 50-2, it is visible that curves in elastic part of deformation had very stable growth of deflections, which means that the layer of UHPC had good tension properties and had no failures. It is visible, that chart of specimen 30-2 change its gradient about bending moment 15 kNm. Around this value, first cracks in UHPC layer were initiated and it caused reduction of the moment of inertia and the stiffness of the section. These cracks caused activation of fibre reinforcement and the bending moment was still increasing with variable gradient and after reaching its peak (19 kNm), the curve decreased slowly. Before reaching the maximum value, the change of the gradient was caused by initiating and widening of cracks. After the maximum value of bending moment, only widening of initiated cracks was occurring. The fibres were gradually tearing out of the concrete and the section lost its bearing capacity and stiffness. The diagram also shows that after reduction of the UHPC's tensile strength, the bending moment was similar to that of the specimen ref-1.

Chart of specimen 50-2 has a different shape compared to that of the specimen 30-2, because of the rebar mesh. There is a change of gradient when reaching the bending moment about 40 kNm, which is related to initiation of first cracks in UHPC layer. After origin of these cracks, the value of bending moment is still growing due to the rebar mesh and the maximum value is about 55 kNm. After this maximum value, the bending moment was decreasing slowly as the specimen lost its strength due to the failure of the UHPC.

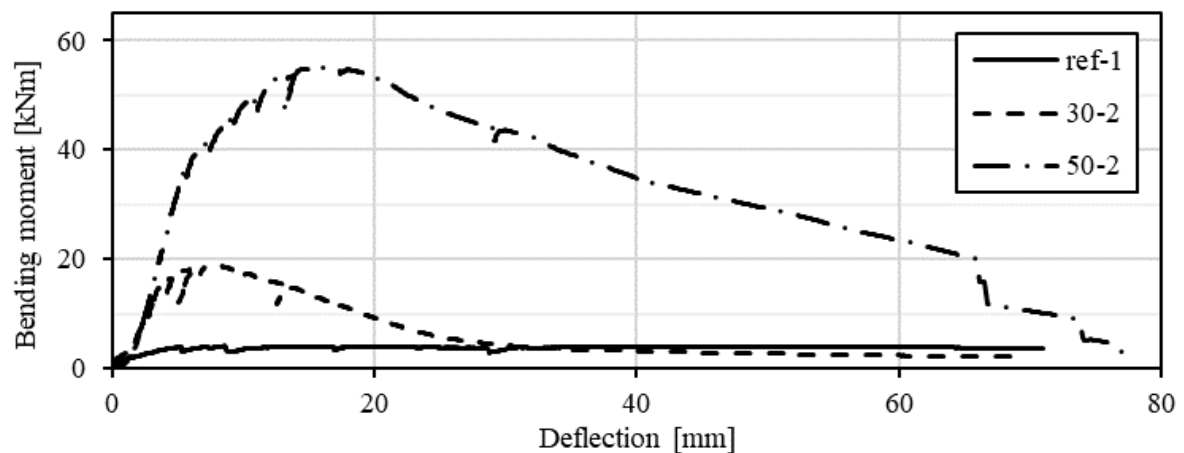


Fig. 7 Bending moment above the support (calculated according to force in hydraulic jack) in dependence on the deflection of the overhanging end of the panel.

The Table 3 shows, that the ultimate bending moments of strengthened specimens increased significantly compared to specimens without strengthening. The bearing capacity of reference panels is about 4.7 kNm, panels with 30 mm UHPC has average bearing capacity 20.1 kNm (428% of bending capacity of reference specimens) and panels with 50 mm UHPC and rebar mesh has average bearing capacity 56.7 kNm (1206% of bearing capacity of reference panels). The bearing capacity of reference panels is low because of their low thickness and inappropriate position of rebars. Therefore, it can be said that strengthening of panels is effective.

Table 3 Maximum bending moments M_{\max} (calculated according to force in hydraulic jack) above the support for tested specimens, height of the UHPC layer, average maximal bending moments of tested types of panels, its standard deviations and coefficients of variation.

Type of panels	Specimen	M_{\max} [kNm]	Thickness of UHPC [mm]	Average M_{\max} [kNm]	Standard deviation [kNm]	Coefficient of variation [%]
Reference	ref-1	4.1	-	4.7	1.3	28
	ref-2	6.6	-			
	ref-3	3.6	-			
30 mm of UHPC	30-1	15.9	31	20.1	4.1	20
	30-2	18.7	33			
	30-3	25.6	43			
50 mm of UHPC	50-1	52.9	58	56.7	3.9	7
	50-2	55.0	58			
	50-3	62.1	58			

According to Table 3, reference panels have high coefficient of variation. It is probably caused by big variation of reinforcement bars positions as mentioned before. In case of panels with 30 mm of UHPC, also high coefficient of variation can be seen, but this fact is related to high bearing capacity of the specimen 30-3, that is caused by thicker layer of UHPC (inaccuracy during casting of UHPC). The coefficient of variation of panels with 50 mm of UHPC is about 7% and it is related to constant thickness of UHPC in these specimens and using the rebar mesh. The thickness of UHPC for all specimens was actually 58 mm (instead of the value 50 mm, which is used to keep the article consistent). These thicknesses were different than the required, but it is important that thicknesses are similar for purposes of this research.



Fig. 8 Cracks at the top surface of the panels after executing experiments. Left figure is reference panel and right figure is detail of the panel with 30 mm UHPC.

Tested panels after the experiment are shown in Fig. 8. In the left figure, it is clearly visible that there is one wide crack above the support and other cracks are marginal. This crack corresponds to the peak of bending moment above the support in this set up of the experiment. In the right figure, there is a detail of the crack in strengthened specimen. In this detail, the wide crack in the UHPC layer is visible. The later stage of performance shows that due to the wide crack, the UHPC layer was not able to contribute to the load carrying capacity of the section at this stage.

4.4 Simplified analysis and discussion

Simple calculations to estimate load bearing capacity of cross sections and stresses in the cross sections were executed. They were compared with the experimental results.

The calculated load bearing capacity of the cross-section of the reference panel according to Fig. 5 (without UHPC) was 22.8 kNm, which does not correspond to the experimental results. The reason may be found in different positions of reinforcing bars. Perhaps, the reinforcement was closer to compressed area (lower layer). Based on this experience, the reinforcements of the original panels were neglected in calculations of strengthened elements.

The elastic calculation was used to analyse behaving of specimens with 30 mm of UHPC. At first, the stress of uncracked ideal cross-section (including different modulus of elasticity) exposed to bending moment of 18.1 kNm (average bending moment when the first crack was initiated) was calculated. The tensile stress in UHPC layer according to this bending moment was 5.87 MPa on the outer edge and 3.72 MPa on the inner edge (in contact with old concrete). The old concrete is of a rather good quality, so it can be assumed that this stress did not cause any cracks in the original panel.

To analyse the behaviour of specimens with 50 mm UHPC, two calculations were executed: 1. Elastic calculation as in case of the specimens with 30 mm of UHPC (the depth of the cross section was 178 mm, according to the measured thickness of the specimens) and 2. Calculation of the behaviour of the cross-section under the assumption of a large crack where reinforcement with the rebar mesh 8/100mm was introduced and the UHPC was neglected (because of a large crack and negligible effect of fibres). The ultimate bending moment in the critical cross-section was 36.0 kNm (the moments of initiation of first cracks were registered during experiments). Stresses calculated according to these assumptions, are 7.9 MPa on the outer edge and 3.1 MPa on the inner edge.

From elastic calculations before initiating of the first cracks for specimens with 30 mm and 50 mm of UHPC, it can be seen, that calculated stresses are slightly higher than tensile strength of the UHPC itself. On the other hand, these values are much smaller than its flexural strength. Stress values close to tensile strength were expected, because the layer of UHPC is completely in tension. This means, that the impact of nonlinear stress distribution in UHPC is rather small and can be neglected. Panels with 50 mm of UHPC reached higher stress values probably because of rebar mesh, that probably helps with the redistribution of the stress.

Comparing calculated of bending moment 36.0 kNm with measured average maximal bending moment 56.7 kNm can be assumed, that the maximum bending capacity is given by combination of UHPC and rebar mesh.

5 Conclusion

The bearing capacities of panels with UHPC in compression were raised to 200% with 50 mm of UHPC and to 159% with 30 mm UHPC comparing to reference specimens. The bearing capacity of panels with UHPC in tension were raised to 1206% with 58 mm of UHPC and to 428% with 30 mm of UHPC comparing to reference specimens. It has to be said, that the increase for specimens with 50 mm UHPC is rather distorted, because of the reinforcement of reference panels. Despite specific conditions (thickness and reinforcement of original panels) strengthening using UHPC is a convenient way to improve properties of old concrete structures. Results of the experiments are also a good background to more detailed analysis of the behaviour of strengthened panels. However, only very thin specimens were used. The increase of load carrying capacities of thicker elements will be lower.

Using UHPC for strengthening of structures is quite simple, because it does not need any special precautions comparing to strengthening using ordinary concrete. Using of UHPC improves the properties even more than ordinary concrete. Low thickness of UHPC is an important advantage. Experiments confirmed, that 30 mm UHPC without any reinforcement is a layer thick enough to achieve significant improvement of properties of the specimens. Comparing to ordinary concrete layer with minimum thickness around 45 mm (without reinforcement) or 70 mm (with reinforcement), thinner layer of UHPC saves the load and depth of the structure.

Acknowledgements

This project runs with the financial support of Ministry of Industry and Trade (Czech Republic), project no. FV20472 – Application of ultra-high-performance composites for reconstruction of concrete buildings. The experiments were executed in laboratories in Klokner Institute (Czech Technical

University in Prague) and samples were made in cooperation with TBG Metrostav a.s. and Metrostav a.s.

References

- [1] fib – fédération internationale du béton. 2013. *fib Model Code for concrete structures 2010*. Berlin: Ernst & Sohn GmbH & CO. KG.
- [2] Bentur, Arnonn and Sidney Mindess. 2007. *Fibre reinforced cementitious composites*. London: Talyor & Francis
- [3] Toutlemonde, Francois and Jacques Resplendino. 2013. *UHPFRC 2013 – Proceedings of the RILEM-fib-AFGC International Symposium on Ultra-High Performance Fibre-Reinforced Concrete*. France. RILEM Publications S.A.R.L

The influence of cyclic freezing – thawing on the effectiveness of anchoring FRP reinforcement

Rafał Wasilczyk^{1*}, Marta Kosior-Kazberuk¹

¹ *Department of Building Structures and Architecture, Faculty of Civil Engineering and Environmental Sciences, Białystok University of Technology, Wiejska St. 45E, PL-15 351 Białystok, Poland * r.wasilczyk@pb.edu.pl*

Abstract

The aim of the research work was to determine the influence of cyclic freezing and thawing on anchoring non-metallic BFRP and HFRP reinforcements in concrete beams. The tests were carried out on HFRP (Carbon-Basalt Fiber Reinforced Polymer) and BFRP (Basalt Fiber Reinforced Polymer) bars with diameters of Ø4 mm, Ø6 mm and Ø8 mm. The scope of the analysis included testing the efficiency of reinforcement anchoring in concrete, testing the longitudinal and transverse thermal expansion

of reinforcing bars, as well as the visual assessment of structure of bars stored at a constant temperature of +20°C in comparison to bars subjected to 150 freezing and thawing cycles in the range of temperature from -20 °C to +20 °C. Determining the standard parameters of the anchoring efficiency required making a reinforced concrete beam connected in the upper part of the span section using a steel joint, and in the lower one with a common FRP bar and testing it in a 4-point bending system. The composite bar slips on both ends of the tested beam were measured. The stand used to determine thermal expansion coefficients was an original technical solution. Measurements of changes in bar length and diameter were made in a climate chamber with a set range of temperature changes.

The analyses allowed confirmation of the analogy of the behavior of innovative HFRP bars in relation to the widely known BFRP bars. The correlations between stresses at the reinforcement-concrete interface, stresses in reinforcing bars and anchor length of bars were determined. Additionally, the degree of degradation of reinforcement anchorage in concrete was determined after subjecting the samples

to 150 cycles of freezing and thawing, thereby simulating the 50-year service life of concrete structure in changing temperature conditions.

1 Introduction

The fibre reinforced polymer (FRP) bars have a higher thermal expansion coefficient than concrete (CTE, $10 \times 10^{-6} \text{ } ^\circ\text{C}$). For composite materials, the values of the coefficient in the transverse direction to the fibers (TCTE), depending mainly on the properties of the polymer matrix, and longitudinal (LCTE), depending mainly on the properties of the fibers should be distinguished. The values of the TCTE coefficients for the AFRP, CFRP and GFRP bars are respectively, 8 times, 3 times and 3 times higher than the value of the above-mentioned coefficient for concrete [6]. Due to the cyclic effect of freezing and thawing, the composite reinforcement inside reinforced concrete members exhibits much greater deformation than the surrounding concrete. This phenomenon in turn creates stresses and microcracks at the interface of both materials. The consequence of the described phenomenon is a decrease in bond between reinforcement and concrete, which leads to premature loss of load bearing capacity of concrete members [2, 5]. Most of the studies describing the issue of thermal expansion

of reinforcement concerned the behavior of GFRP, CFRP or AFRP under the influence of variable temperatures [1, 5], while only a few studies dealt with BFRP [4, 7], which gave rise to the following experiments.

The research program included determination of longitudinal thermal expansion coefficient LCTE and transverse thermal expansion coefficient TCTE as well as testing the efficiency of anchoring of HFRP (Hybrid - Carbon and Basalt Fiber Reinforced Polymer) and BFRP (Basalt Fiber Reinforced Polymer) reinforcements in concrete. Their purpose was to determine the effect of cyclic freezing and thawing on the anchoring efficiency of the basalt and hybrid bars in concrete.

2 Test procedure for determination of thermal expansion coefficient

The procedure for testing the coefficient LCTE (Longitudinal Coefficient of Thermal Expansion) and TCTE (Transverse Coefficient of Thermal Expansion) of composite bars included placing a 250 mm long straight segment of a BFRP or HFRP type bar in a specially designed steel support frame and applying 2 opposing pairs of dial indicators with an accuracy of 0.001 mm and a range of 1.0 mm, as shown in Fig. 1. The samples were simply supported on two supports. Their position was stabilized by the pressure forces of the measuring probe stems. In order to increase the accuracy of measurements and to avoid accidental slipping of the sensor heads from the irregular surface of the bars, steel plates with sizes of 20×20×2 mm were glued in places of planned measurement points.

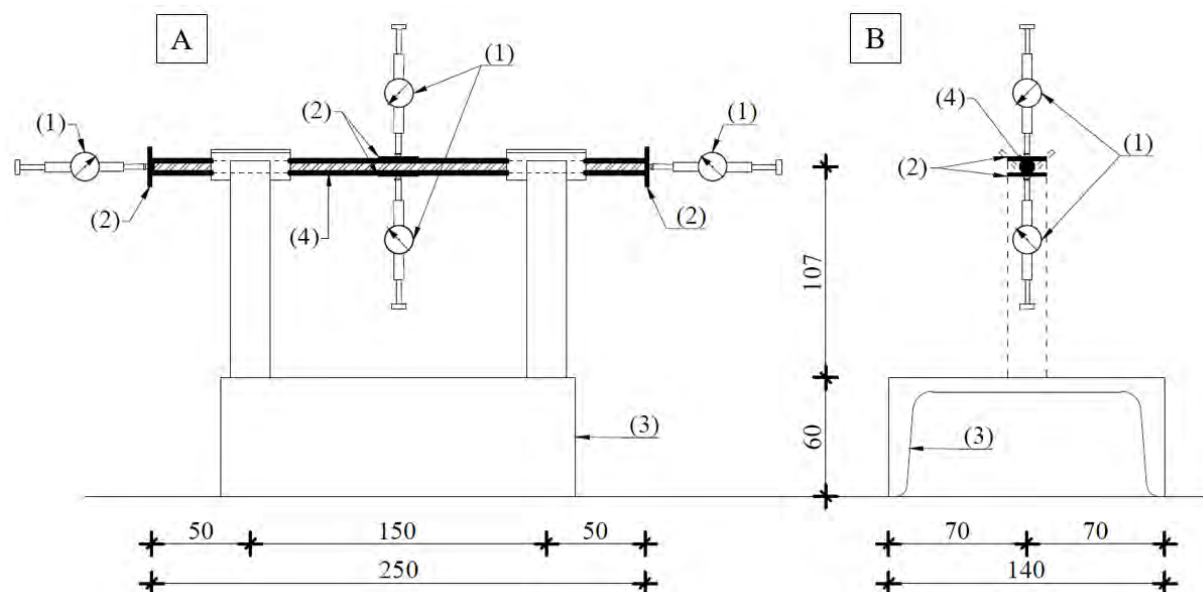


Fig. 1 Schema of a test stand for testing longitudinal and transverse thermal expansion of composite bars; A - side view, B - cross-section; (1) - dial indicators, (2) - steel plates, (3) - support frame, (4) - composite bars 250 mm long. All dimensions are in mm

The subject of the study were BFRP and HFRP bars containing an epoxy resin matrix and basalt or hybrid fibers (75% basalt fibers and 25% carbon fibers). Bars with diameters of Ø4 mm, Ø6 mm and Ø8 mm were used for the experiment. First, the entire system presented was placed in a climate chamber and reference measurements were made using 4 dial indicators at a temperature of +20 °C. Then

the test started, setting a total of 3 freezing and thawing cycles in the temperature range from -20 °C to +20 °C for 8 hours each one. The measurements of elongation at temperature -20 °C and +20 °C were made in 5 points of each of the reinforcing bars. The results were presented in the form of thermal expansion coefficients LCTE and TCTE [$10^{-6} \times ^\circ\text{C}$] referring to the length of the samples.

3 Procedure for efficiency of anchoring test

The members for testing the anchoring efficiency consisted of two concrete beams connected by a steel joint using a common reinforcing bar, as shown in Fig. 2. The dimensions of the beams made corresponded to type A samples for reinforcing bars with diameter up to 16 mm according to [10].

A simply supported beam loaded with two symmetrical forces was tested. The anchor length in the concrete was 10 times greater than its diameter. The remaining sections of the bar were placed in metal sleeves, protecting against contact with concrete, enabling its free movement along its axis. Sensors

for measuring reinforcement slips with an accuracy of 0.001 mm and a range of 30 mm were mounted at the ends of bars protruding beyond the beams. It was required to prepare special molds enabling centric laying of reinforcing bars and steel structural reinforcement, preventing concrete splitting, as shown in Fig. 3. For the tests, concrete class C30 / 37 was used, meeting the requirements for concrete structures operated in exposure class XF3 according to [9].

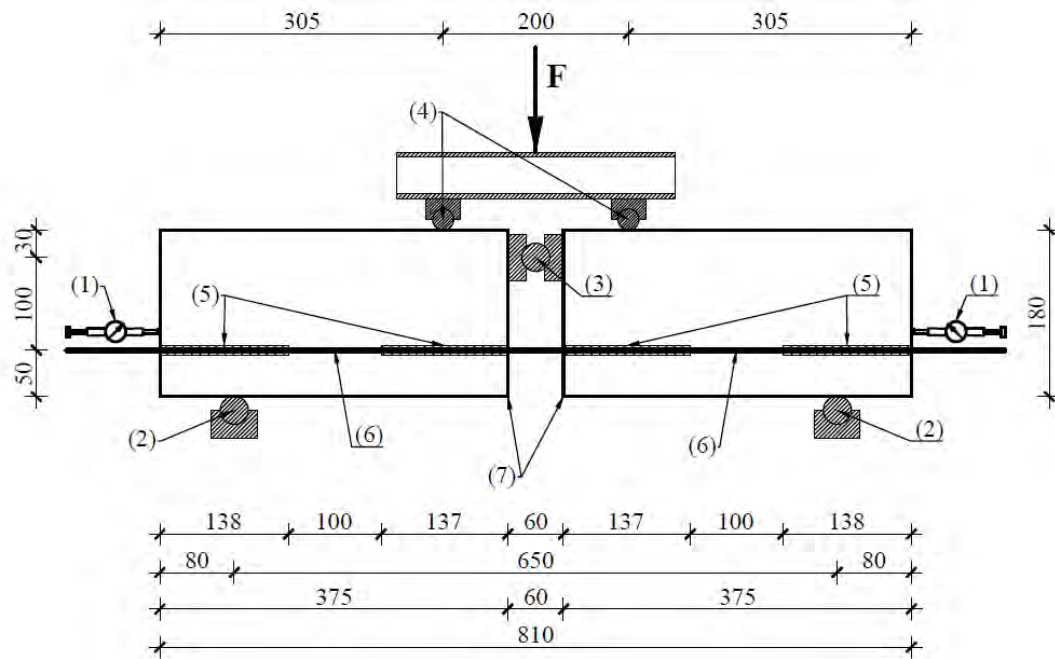


Fig. 2 Scheme of sample for testing the efficiency of bar anchoring; (1) - dial indicators, (2) - supports, (3) - steel joint, (4) - load rollers, (5) - aluminum shielded tubes, (6) - anchoring zone of FRP bars (length of $10 \times \varnothing$) with diameter 4 or 6 or 8 mm, (7) - concrete beams. All dimensions are in mm



Fig. 3 Sample reinforcement during assembly in the mold

The beams (12 series) were made using BFRP and HFRP bars with diameters of $\varnothing 4$ mm, $\varnothing 6$ mm and $\varnothing 8$ mm. The test members were stored in various temperature conditions. Firstly, all samples were

stored for 28 days in water at a constant temperature of +20 °C. Then 6 series of samples were placed in a freezing chamber with controlled temperature, and subjected to 150 freezing and thawing cycles in the temperature range from -20 °C to +20 °C at 100% air humidity, reflecting the 50-year service life of the members in the zone of fluctuation of water levels or subjected deicing agents according to [8]. The remaining 6 series of samples were placed in an air-conditioned room with a constant temperature of +20 °C and 40% RH. Prior to destructive testing, all samples were stored for 24 hours at temperature +20 °C.

The spacing of supports in the testing machine was 650 mm. The loads were applied with two steel rollers at a distance of 200 mm from each other (Fig. 2). The loading was carried out in stages, stopping the growth and stabilizing their level after reaching the set stress values in the bars, every 80 MPa.

The load was increased steadily until the tested specimen failed. Each of the given load steps was achieved within 30 seconds. The duration with a constant force for a given step lasted no more than 120 seconds. The measurements of bar slips were made after stabilization of both dial gauges' indications.

During the test, the values of load for reinforcing bar slips equal to 0.01 mm, 0.1 mm, 1 mm, as well as the value of maximum force were recorded. The test was completed after complete loss of adhesion of tested bars to concrete in both beam halves or after breaking of the composite reinforcing bar. If a slip of more than 3.0 mm was recorded at one end of the beam, the anchor of the bar was strengthened to block further displacement and the test was continued until the bond in the rest of the test specimen was broken.

4 Coefficients of thermal expansion

The obtained values of coefficients of thermal expansion of BFRP and HFRP bars corresponded to the typical range of coefficient values that are characteristic for bars with carbon or glass fibers. The test results are presented in Table 1.

Table 1 Average values of longitudinal (LCTE) and transverse (TCTE) thermal expansion coefficients and standard deviation (σ) values for BFRP and HFRP reinforcement

Rod type	Diameter [mm]	LCTE (σ) [$10^{-6}/^{\circ}\text{C}$]		TCTE (σ) [$10^{-6}/^{\circ}\text{C}$]	
BFRP	4,0	1,4 ($\pm 0,2$)	1,5 ($\pm 0,2$)	38,8 ($\pm 2,3$)	37,8 ($\pm 2,1$)
	6,0	1,7 ($\pm 0,2$)		36,5 ($\pm 2,5$)	
	8,0	1,5 ($\pm 0,3$)		38,2 ($\pm 1,4$)	
HFRP	4,0	1,3 ($\pm 0,2$)	1,4 ($\pm 0,2$)	32,6 ($\pm 2,5$)	33,5 ($\pm 2,0$)
	6,0	1,5 ($\pm 0,2$)		34,2 ($\pm 2,9$)	
	8,0	1,5 ($\pm 0,2$)		33,7 ($\pm 0,4$)	

The test results have shown that HFRP bars are characterised by TCTE value 11.4% lower and a LCTE value 6.7% lower than BFRP bars. It was the effect of 25% carbon content in HFRP bars. According to the data presented in [6], specimens based on carbon fibers (CFRP) showed lower values of the coefficient of thermal expansion compared to specimens based on basalt fibers (BFRP) obtained in test presented.

5 Effectiveness of anchoring FRP reinforcement

During the experiment, 12 series of BFRP and HFRP reinforcement beams with diameters of Ø4 mm, Ø6 mm and Ø8 mm were examined. Members which were subjected to cyclic freezing and thawing were marked as FT, while the reference members stored at constant temperature as REF. The values of bar slips depending on the applied load were shown in Fig. 4.

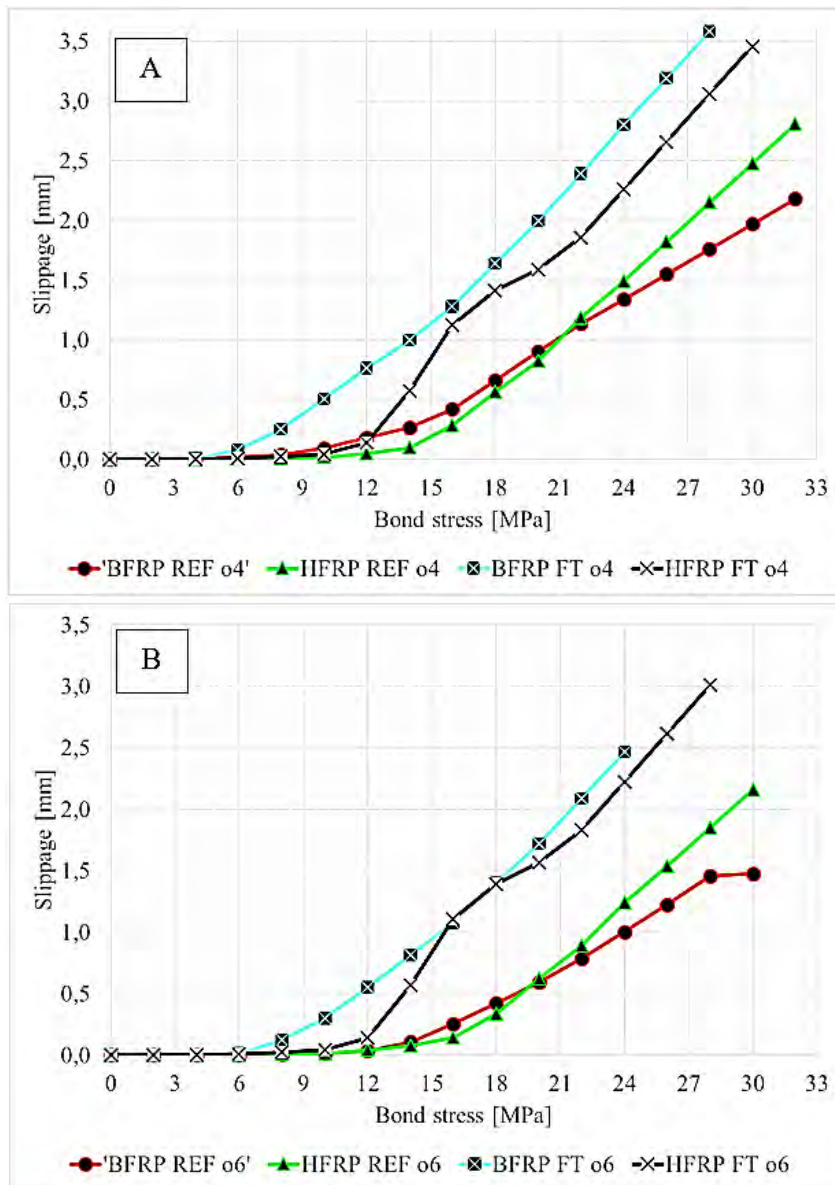
The destructive influence of cyclic freezing and thawing on the durability of the concrete-composite bar interfacial zone could be observed by comparing the values of FRP bar slips at indivi-

dual

levels

of beam loading. The BFRP REF series was characterized by 51% lower bar slip values than the BFRP FT series. Similarly, the HFRP REF series showed 48% lower bar slip values than the HFRP FT series.

The ultimate criterion for the destruction of all tested elements was the breaking of composite bars which confirms very good bond in concrete. For none of the test members, the complete reinforcement slipping from concrete beams was achieved. The maximum achieved stress levels in the bars were approximately consistent with the predicted tensile strength values. Beams of the FT series were destroyed on average at 10% lower load value than those of the REF series.



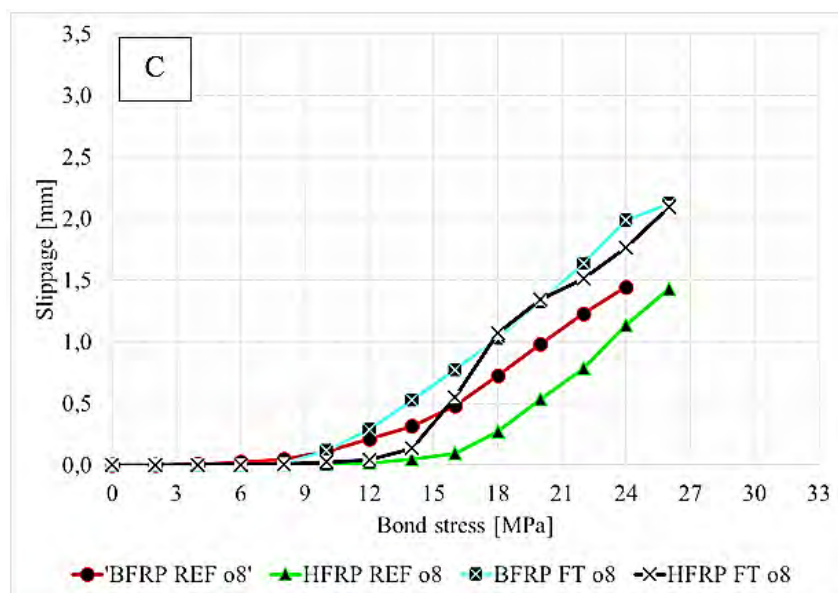


Fig. 4 Average values of bar slips [mm] depending on the value of adhesion stress [MPa] for bars with diameters of Ø4 mm (diagram A), Ø6 mm (diagram B), Ø8 mm (diagram C).

The above observation confirms the fact that the degradation of concrete-composite bond has the important effect on the decrease in durability of concrete members reinforced with composite bars. In addition, research confirmed that beams made using BFRP and HFRP bars were characterized by similar slip values of reinforcing bars in concrete. The external appearance of both types of bars was almost identical, which makes them difficult to distinguish with the unaided eye. Even subjecting specimens to cyclic freezing and thawing did not cause differences in their surfaces.

6 Conclusions

During the experiment, the physical properties of composite bars made of basalt fibers (BFRP) as well as basalt and carbon fibers HFRP were determined, under variable temperature conditions ranging from -20 °C to +20 °C. The HFRP bars showed a 11.4% lower transverse coefficient of thermal expansion TCTE than BFRP bars, which is insignificant difference.

An evaluation and comparison of the effectiveness of anchoring BFRP and HFRP bars in concrete subjected to cyclic freezing and thawing as well as for concrete members stored at constant temperature +20 °C were carried out. Exposure to variable temperatures was aimed at accelerating the aging of the tested elements, simulating the 50-year service life of structures in the zone of water level fluctuations or subjected to deicing agents.

The degradation of concrete-composite interfacial zone has a significant influence on the decrease in durability of concrete members reinforced with composite bars. The values of slip for beams stored in the climate chamber were an average of 50% greater than the values of slip recorded for those kept at constant temperature +20 °C. Thus, the decrease in the anchoring efficiency for members subjected for a long time in cyclically variable temperatures. Therefore, an increase of 50% in the required anchor length for components exposed to the XF3 environment should be considered compared to structural members protected from adverse temperature conditions. However, this issue requires further testing and verification. In terms of anchoring efficiency, durability, appearance or the degree of visible degradation of the bar surface, no significant differences were found between the BFRP and HFRP reinforcement.

References

- [1] Aydin F. 2018. „Experimental investigation of thermal expansion and concrete strength effects on FRP bars behavior embedded in concrete“. Construction and Building Materials, Vol. 163, 1-8
- [2] Belarbi A., Wang H. 2002. „Bond durability of FRP bars embedded in fiber-reinforced concrete), J. Compos. Constr. 16 (4), 371–380.

- [3] CAN/CSA-S806-12. 2012. „Design and construction of building structures with fibre reinforced polymers“. Ontario, Canada: Canadian Standard Association.
- [4] Elgabbas F., Ahmed E., Benmokrane B. 2014. „Development and characterization of basalt FRP reinforcing bars for concrete structures“, The 7th International Conference on FRP Composites in Civil Engineering International Institute for FRP in Construction, Vancouver, Canada, August 20-22.
- [5] Masmoudi R., Zaidi A., Gérard P. 2005. „Transverse thermal expansion of FRP bars embedded in concrete“, J. Compos. Constr. 9 (5), 377–387.
- [6] Mossakowski P. 2006. „Reinforcing bars of polymer composites used in concrete engineering structures“ Roads and Bridges - Drogi i Mosty, 1/2006: 35–52
- [7] Pavalan V., Sivagamasundari R. 2019, „Thermal Expansion Coefficient Of Basalt Fibre Reinforced Polymer Bars“, International Journal for Research in Engineering Application & Management (IJREAM), Vol-05, Issue-01, April 2019, 414-418.
- [8] PN-B-06265:2018-10, 2018. „Concrete -- Specification, performance, production and conformity -- National Annex to PN-EN 206+A1:2016-12“. Warsaw: PKN
- [9] PN-EN 206+A1:2016-12, 2016. „Concrete - Part 1: Specification, performance, production and conformity“. Warsaw: PKN
- [10] RILEM Recommendation RC5. 1982. „Bond test for reinforcement steel. 1. Beam test“, 2 edition. RILEM.

Structural analysis and design

Semi-probabilistic Assessment of Prestressed Concrete Bridge

Lukas Novak, Drahomir Novak

*Institute of Structural Mechanics, Faculty of Civil Engineering
Brno University of Technology
Veveri 331/95, Brno 60200, Czech Republic*

Abstract

The paper is focused on the assessment of existing prestressed concrete bridge by advanced semi-probabilistic methods. The bridge is represented by a non-linear finite element computational model and thus it is necessary to employ efficient methods for estimation of a coefficient of variation (ECoV). There are two practical cases studied presented in this paper: Semi-probabilistic analysis of single bridge girder and application of ECoV methods to bridge structure. It is shown how to determine design value of ultimate load capacity by semi-probabilistic approach in case of single bridge girder and obtained results are compared. Moreover, ECoV methods are applied in the second case study with a limited stochastic model and three analyzed limit states. Employed ECoV methods are compared to the reference value determined by Latin Hypercube Sampling technique.

1 Introduction

The non-linear finite element analysis (NLFEA) represents a powerful tool for accurate assessment of existing structures and thus it is employed more often also for practical applications in recent years. Nonetheless, it is also necessary to assume uncertainty in input variables for proper modeling of real structures. Therefore, it is necessary to perform complex stochastic analysis instead of deterministic computation of NLFEA. On the other hand, it is still highly time-consuming to perform a fully probabilistic analysis of large non-linear models with many stochastic input variables. The solution can be represented by semi probabilistic approach focused on the determination of the design value of resistance under prescribed simplifications, which can greatly reduce the number of needed calculations.

The key ingredient in a semi-probabilistic design and assessment of structures is an estimation of a coefficient of variation (ECoV) of resistance. In recent years, the development of ECoV methods is an area of interest for many researchers and engineers, and there are several known approaches in the scientific literature [1]–[3]. Selected ECoV methods are employed in this paper for the assessment of the existing prestressed concrete bridge failing in bending. This bridge was selected in the framework of the European Project Safebridge (interreg project Austria-Czech Republic) focused on advanced numerical analysis of existing bridges. Specifically, the paper presents the first study focused on the semi-probabilistic assessment of one typical bridge girder KA-61 (frequently used in the Czech Republic) and the application of ECoV methods to an existing bridge with the limited stochastic model.

2 Semi-probabilistic Methods

According to the semi-probabilistic approach, the resistance of a structure R is separated, and the design value R_d satisfying given safety requirements is evaluated instead of calculating the failure probability. Such an approach directly leads to the design value of resistance which can be easily used for a design and an assessment of structures in the industry, similarly to the Partial Safety Factor method (PSF). It is assumed that R is lognormally distributed; thus, the design value of resistance R_d is defined as

$$R_d = \mu_R \exp(-\alpha_R \beta v_R) \quad (1)$$

where v_R is the coefficient of variation (CoV) of resistance, and α_R represents the sensitivity factor associated with R derived from the First Order Reliability Method (FORM). For industrial applications, FORM is simplified by fixed value $\alpha_R = 0.8$. Target reliability index β can be found in codes for specific types of structures and class of consequences. As can be seen, in order to accurately deter-

mine the design value of resistance by a semi-probabilistic approach, it is crucial to correctly estimate the mean value and variance of structural resistance, which can be seen as a function of a random vector $\mathbf{r}(\mathbf{X})$. This task might be challenging due to a fact that input random variables can generally be non-Gaussian and correlated. The only general approach to estimate statistical moments is pseudo-random sampling by a Monte Carlo type algorithm such as Crude Monte Carlo or Latin Hypercube Sampling [4] employed in case studies as a reference solution. However, it is necessary to perform a high number of simulations of the original mathematical model, which usually can not be employed in industrial applications due to the enormous computational burden. On the other hand, it is possible to assume several simplifications and use simplified methods, presented in the following paragraphs.

Note that, one should assume model uncertainty and geometrical uncertainty in order to estimate the design value of resistance in compliance with Eurocode [5]. In this case, one should calculate CoV of R as:

$$v_R = \sqrt{v_g^2 + v_m^2 + v_f^2} \quad (2)$$

where v_f is part of CoV caused by the uncertainty of input random variables, v_m represents the coefficient of variation associated with model uncertainty [6] and v_g represents CoV caused by geometrical uncertainty. For the sake of generality, this paper is further focused only on v_f .

ECoV methods are focused on the estimation of statistical moments of resistance and estimation of the design value of resistance under the assumption of the lognormal distribution. CoV of resistance R according to Červenka [1] can be estimated as follows:

$$v_f = \frac{1}{1.65} \ln \left(\frac{R_m}{R_k} \right) \quad (3)$$

Note that, just 2 simulations of NLFEA are needed in this approach: R_m with mean values of input random variables and R_k using characteristic values (5% quantile). The global resistance safety factor is then calculated assuming Lognormal distribution as:

$$\gamma_R = \exp(\alpha_R \beta v_f) \quad (4)$$

The described concept was adopted in the fib Model Code 2010 [7] and design value R_d was later decreased by $\gamma_{Rd} = 1.06$ in order to take model uncertainties into account:

$$R_d = \frac{R_m}{\gamma_R \gamma_{Rd}} \quad (5)$$

Improved ECoV method based on Taylor Series Expansion was proposed by Schlune et al. [2]. The coefficient of variation v_f , if material parameters are not correlated, can be calculated as:

$$v_f \approx \frac{1}{R_m} \sqrt{\sum_i^N \left(\frac{R_m - R_{\Delta X_i}}{\Delta X_i} \sigma_{X_i} \right)^2} \quad (6)$$

where the response of construction $R_{\Delta X_i}$ is determined by NLFEA using reduced mean values of material variables by ΔX_i and σ_{X_i} is the standard deviation of the i -th variable. If the lognormal distribution of material variables is assumed, the reduced values of X_i can be calculated as:

$$X_{\Delta i} = X_{mi} \exp(-c \cdot v_{X_i}) \quad (7)$$

where X_{mi} is the mean value of i -th material characteristic and step size parameter $c = (\alpha_R \beta) / \sqrt{2}$.

Besides ECoV methods, there are two general methods for the design of structures in Eurocodes using NLFEA. Commonly known general partial safety factors according to EN 1990 [5] and the global safety factor method for NLFEA of concrete structures according to EN 1992-2 [8]. These methods are based on the very strict assumption that a numerical simulation with input variables set to a generally desired quantile leads to a result corresponding to the identical desired quantile of response distribution R . Of course, this might be a severe problem in case of NLFEA, where a simulation with extreme values of input variable may lead to the unrealistic behavior of the computational

model, which is usually verified within a specific range of input variables (working conditions). However, such an approach can be acceptable for simple structural members with a single almost linear failure mode and low v_R , e.g. the bending of a simply supported beam.

According to EN 1990 numerical simulation is computed with design values of input random variables (such as design value of yield strength of reinforcement f_{yd} or compressive strength of concrete f_{cd}) and obtained result of simulation corresponds to design value of resistance R_d . Design values of material characteristics can be obtained from laboratory experiments or directly from EN. Typical approach for the determination of design values of input variables is the usage of normative coefficients, which contains model uncertainty, thus no additional reduction by safety factor is needed (further denoted as PSF tabular). On the other hand, the design values can be estimated from laboratory experiments as a following percentile of statistically processed values:

$$X_d = \mu_X \exp(-\alpha_R \beta v_X) \quad (8)$$

where v_X is CoV of a random variable (material characteristic). The results of NLFEA leads to design value \widetilde{R}_d , however partial safety factors in EN include reduction due to model uncertainty, thus additional reduction of the design value of resistance by the safety factor $\gamma_{Rd} = 1.06$ should be applied:

$$R_d = \frac{\widetilde{R}_d}{\gamma_{Rd}} = \frac{R(f_{yd}, f_{cd}, \dots)}{1.06} \quad (9)$$

In the global safety factor concept according to EN 1992-2, the design value resistance is estimated as:

$$R_d = \frac{R(f_{ym}, f_{cEN2}, \dots)}{\gamma_R} \quad (10)$$

where the global safety factor for resistance is set as $\gamma_R = 1.27$ including model uncertainties, $f_{ym} = 1.1 f_{yk}$ is the mean value of yield strength of reinforcement, f_{yk} represents its characteristic value (5% quantile), and f_{cEN2} is the reduced mean value of concrete obtained as $f_{cEN2} = 0.85 f_{ck}$. This reduction reflects higher variability of concrete material parameters in comparison to reinforcement. The global safety factor method can be recommended in combination with NLFEA for concrete structures with lower v_R , since $\gamma_R = 1.27$ was not derived for special structures with a high variance of resistance such as shear failure.

3 Single Bridge Girder KA-61

The very first case study is focused on a comparison of ultimate limit state design values of resistance determined by normative methods and semi-probabilistic approach. In the first step of the study, the structure is represented by one girder: simply supported prefabricated prestressed bridge girder KA-61 failing in bending and loaded by half of special six-axle truck according to Eurocode national annex. The KA-61 girder is 19.98 m long; a rectangular cross-section (see Fig. 1 left) is 0.85 m high and 0.98 m wide. The girder is prestressed by 15 tendons (4 parabolic and 11 straight). Material of reinforcement is 10 400B and concrete class is C35/45 according to the bridge documentation.

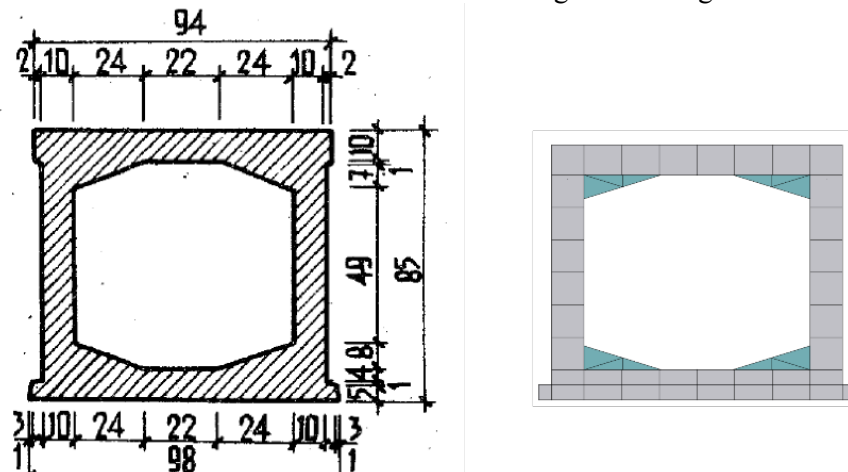


Fig. 1 Original geometry of cross-section (left) and simplified geometry for NLFEA (right).

The non-linear finite element model was created in software ATENA 3D and it consists of 13,000 elements of hexahedra type in the major part of the volume and triangular 'PRISM' elements in the blue-colored parts of cross-section (see Fig. 1 right). Brick elements were preferred due to general numerical stability and mesh compatibility between two volumes connected by fixed contact, i.e. nodes of elements share the same position in both connected volumes. Moreover, brick elements allow easy definition of structured mesh significantly reducing the number of finite elements in comparison to unstructured mesh consisting of tetrahedra elements. Concrete is described by a non-linear mathematical model according to [9] based on the theory of fracture mechanics. Reinforcement and tendons are represented by discrete 1D elements with geometry according to original documentation. The ultimate limit state is represented by the load applied in the last step of the analysis representing structural failure (peak of load-deflection diagram). Bending failure mode and locations of cracks in the last step of analysis (ULS) can be seen in Fig. 2.

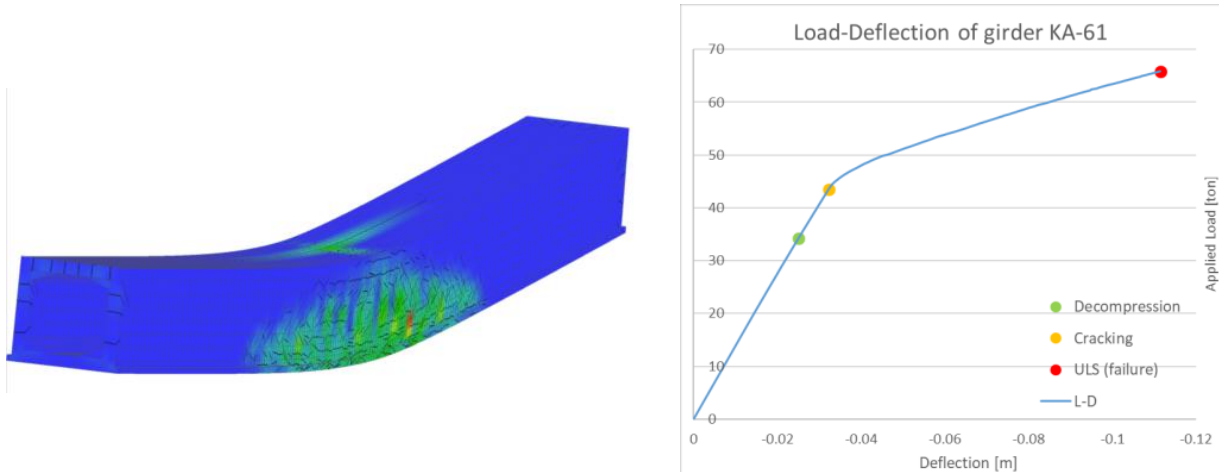


Fig. 2 Prestressed concrete girder KA-61: bending failure mode and locations of cracks during ULS (right), corresponding load-deflection diagram of KA-61(right).

Variability of concrete material characteristics are summarized in Table 1 and it is assumed according to recommendations of JCSS [10] - Young's modulus E ; laboratory experiments of material obtained from original documentation of the bridge - compressive strength of concrete f_c ; and experiences from the large testing campaign [11] - tensile strength of concrete f_t and fracture energy G_f . Mean values of E , f_t , G_f were determined according to formulas implemented in the *fib* Model Code 2010.

Table 1 Stochastic model of single prestressed bridge girder KA-61.

Parameter	Mean	CoV [%]	Probability distribution	Units
f_c	59	9	Lognormal	[MPa]
f_t	4.6	16	Lognormal	[MPa]
E	38.8	15	Lognormal	[GPa]
G_f	152	22	Lognormal	[Jm ²]

Determined results are depicted in Fig. 3. Reference statistical moments of resistance R were obtained by LHS method with 30 simulations: the mean value is $\mu_{LHS} = 692.7 \text{ kN}$ and the standard deviation is $\sigma_{LHS} = 40.2 \text{ kN}$. The ultimate limit state design values were determined for reliability index $\beta = 3.8$ and under the assumption of Lognormal distribution of resistance. Although the design value estimated by the ECoV method is very close to the result of LHS, it significantly underestimates both the standard deviation $\sigma_{ECov} = 21.5 \text{ kN}$ and the mean value $\mu_{ECov} = 652.8 \text{ kN}$. On the other hand, ECoV by Schlune slightly overestimates the standard deviation $\sigma_{Schlune} = 44.8 \text{ kN}$, which in combination with the mean value identical to μ_{ECov} leads to a lower design value of resistance. Nevertheless, the problem is in the estimation of mean value by a single simulation with

mean values of material characteristics and the assumption that $R_m(\mu_X) \approx \mu_R$ which is standard in ECoV methods, but it does not lead to correct estimation in this case. Interesting results are obtained by normative methods: partial safety factors (PSF tabular) method highly overestimates the design value of resistance (even after calibration of safety factors by experiments in PSF experiment). On the other hand, EN 1992-2 method leads to very accurate result close to the reference value obtained by LHS. Note that all performed non-linear simulations assuming given probability distribution of input variables lead to identical flexural failure mode in bending and thus all design values compared in Fig. 3 are directly comparable.

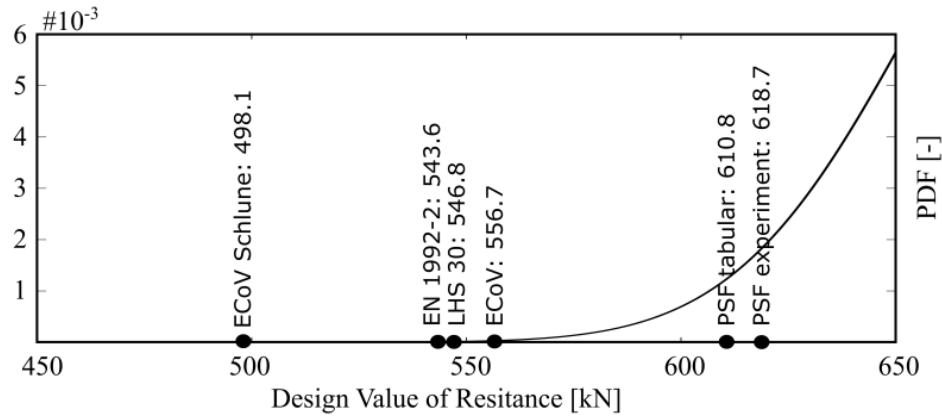


Fig. 3 Comparison of design values of resistance determined by various techniques.

4 Prestressed Concrete Bridge

It was decided to create a mathematical model of the middle span of the bridge with a length of superstructure 19.98m and total width 16.60m, which represents the crucial span of the whole bridge. The geometry of single bridge girders KA-61 is assumed according to original documentation including reinforcement and tendons. The shape of the cross-section is simplified to regular shapes (triangular and rectangular) in order to obtain regular mesh, see Fig. 1 (geometry is measured in centimeters). The girder is assumed as a simply supported beam and supports are assumed as elastic blocks with boundary conditions corresponding to simply supported beam. The geometry of supporting elastic blocks and elastic blocks representing loading plates is assumed according to bridge documentation and national annex of Eurocode for load-bearing capacity of road bridges by exclusive loading by six-axial truck.

Due to the fact, that single girders are not transversally prestressed and thus there is different influence of girders to stiffness of bridge in dependence on their distance to the loading position, it was necessary to create the numerical model of the whole bridge span, see Fig. 4. It consists of 16 bridge girders KA-61 in a transverse direction, each girder is 19.98m long. The girders are connected by reinforcement according to original documentation together with a concrete mixture between single girders, which leads to realistic behavior of the numerical model.

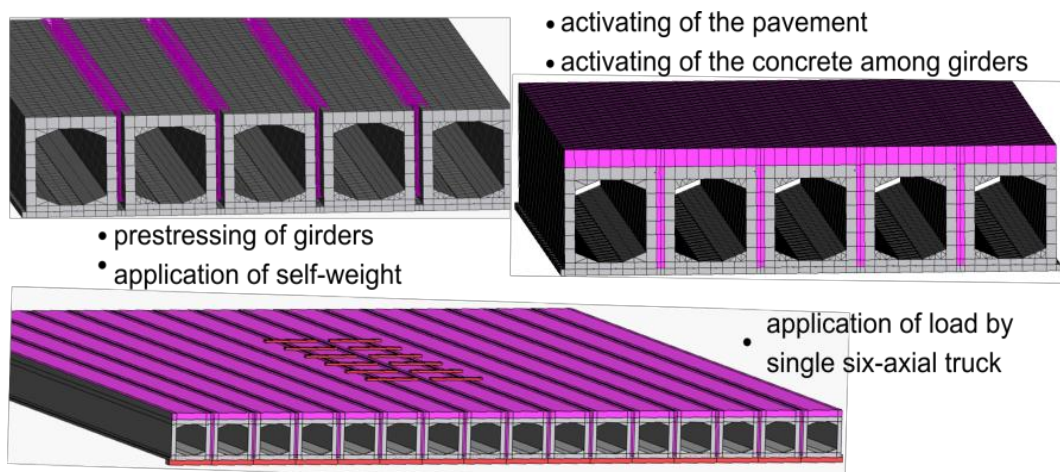


Fig. 4 Construction process (3 steps) of the bridge consisting of 16 girders KA-61

During prestressing of structure, especially during prestressing of the superstructure, neglecting the construction process might lead to unrealistic behavior of the whole structure. Therefore, it is often necessary to respect the real construction process in order to obtain the same boundary conditions of mathematical model and real structure. In the case of this bridge, it was decided to model all important construction steps:

1. Prestressing of girders and application of self-weight.
2. Activating the concrete mixture between girders and the pavement.
3. Application of the exclusive load by single six-axial truck.

In this first study, the stochastic model is limited only to two random variables: compressive strength of concrete $F_c \sim \text{Lognormal}$ (CoV 9%) and prestressing force (after losses) $P \sim \text{Gaussian}$ (CoV 6%). Mean value and CoV of f_c is obtained from material experiments; mean value of P is obtained from original deterministic calculation and CoV is determined according to JCSS. Note that additional material characteristics of concrete are calculated according to fib Model Code 2010 based on the specific realization of F_c . The quantity of interest R represents the weight of a single six-axle truck in tons corresponding to specific limit state. Using software ATENA based on theory of fracture mechanics, the following three limit states were analyzed: a) limit state of decompression, b) limit state of cracking (beginning of cracking) and c) ultimate limit state (load during failure of the bridge). Selected ECoV methods are compared with Latin Hypercube Sampling using 30 simulations in Tab.2.

Table 2 Obtained results of ECoV methods employed for semi-probabilistic analysis of the bridge.

Limit state	Červenka (μ_R [ton] / v_f [-])	Schlune (μ_R [ton] / v_f [-])	LHS (μ_R [ton] / v_f [-])
a)	295 / 0.062	295 / 0.039	295 / 0.062
b)	728 / 0.094	728 / 0.062	717 / 0.045
c)	800 / 0.079	800 / 0.071	792 / 0.059

As can be seen from summarized results in Tab. 2, both ECoV methods lead to accurate estimation of mean values in all three limit states. However, there is a significant deviation in estimated CoV for limit state of cracking by both methods. Overestimated CoV leads to conservative design values of resistance and thus such deviation might be still acceptable, but significant overestimation might also lead to unnecessary intervention and thus significant economic impact. Moreover, ECoV by Schlune based on Taylor Series Expansion underestimated the CoV of limit state of decompression. This might be caused by fixed step-size parameter c for all limit states in order to reduce computational demands of this method, though it can be adapted according to $c = (\alpha_R \beta) / \sqrt{2}$ for each limit state separately.

5 Conclusion

The paper presents the results of an initial study focused on the semi-probabilistic assessment of existing concrete bridges using a combination of non-linear finite element method and advanced ECoV methods in order to estimate the design value of resistance. The two practical case studies were presented: Typical single bridge girder and a whole bridge structure. The ultimate limit state of the single bridge girder was analyzed by various safety formats and ECoV methods. Obtained results were compared in terms of estimated design values of resistance. The whole bridge structure was analyzed with respect to three typical limit states. Selected ECoV methods and LHS were employed for the estimation of coefficient of variation of all three limit states. It can be seen, that simplified ECoV methods lead to significantly overestimated CoV of limit state of cracking. Further work will be focused on advanced analysis of the whole bridge structure, i.e. application of presented safety formats (including PSF and EN 1992-2) for estimation of the design value of resistance and since the limited stochastic model might lead to inaccurate results, an extended stochastic model used for single girder will be used in case of the whole bridge structure and obtained results will be compared.

Acknowledgments

The development of the theoretical part of this contribution has been progressed under the project of Czech Science Foundation Project No. 20-01781S. Practical application was part of the research project No. TH04010138 funded by the Technology Agency of the Czech Republic.

References

1. Červenka, V. 2013. "Reliability-based non-linear analysis according to fib model code 2010." *Structural Concrete* 14(1):19–28.
2. Schlune, H., K. Gylltoft, and M. Plos. 2012. "Safety formats for non-linear analysis of concrete structures." *Magazine of Concrete Research* 64(7):563–574 .
3. Castaldo, P., D. Gino, and G. Mancini. 2019. "Safety formats for non-linear finite element analysis of reinforced concrete structures: discussion, comparison and proposals." *Engineering Structures* 193:136 -153.
4. McKay, M. D. 1992. "Latin hypercube sampling as a tool in uncertainty analysis of computer models." In: *Proceedings of the 24th Conference on Winter Simulation, WSC '92*, pp. 557-564. New York, NY, USA.
5. CEN. 2002. *EN 1990 - Eurocode: basis of structural design*. Brussels: European Comitee for Standardization, Brussels.
6. Holicky, M., J. V. Retief, and M. Sykora. 2016. "Assessment of model uncertainties for structural resistance." *Probabilistic Engineering Mechanics* 45:188 – 197.
7. fib federation internationale du beton. 2013. *fib Model Code for Concrete Structures 2010*. ISBN: 9783433030615.
8. CEN. 2004. *EN 1992 – Eurocode 2: Design of concrete structures*. Brussels: European Comitee for Standardization, Brussels.
9. Červenka, J., and V. K. Papanikolaou. 2008. "Three dimensional combined fracture plastic material model for concrete." *International Journal of Plasticity* 24(12): 2192–2220.
10. JCSS. 2001. *JCSS Probabilistic Model Code*. Joint Committee on Structural Safety. ISBN 978-3-909386-79-6.
11. Novák, D., L. Řoutil, L. Novák, O. Slowik, A. Strauss, and B. Krug. 2015. "Database of fracture-mechanical concrete parameters and its implementation into reliability software FReET." In: *Proc. of the 13th International Probabilistic Workshop (IPW 2015)*. ISBN 978-981-09-7963-8.

Conceptual peculiarities of composite steel-concrete shallow floors

Laurie Couavoux^{1,3}, Jan Bujnak², Abdelhamid Bouchaïr³

¹ Peikko France SAS, 5 Rue Gallice, Grenoble (38100), France

² Peikko Group, P.O Box 104 Voimakatu, Lahti (15101), Finland

³ Université Clermont Auvergne, CNRS, SIGMA Clermont, Institut Pascal, Clermont- Ferrand (63000), France

Abstract

Shallow floors made of precast hollow-core slabs supported on steel-concrete composite beams offer numerous advantages to different stakeholders involved in the construction process. Among others, the combination of steel and precast concrete allows to create functional and architecturally valuable open space buildings. While the resistance of steel parts of the composite floor can be assessed using state of the art design methods, the different stiffness of the steel and concrete part of the composite floor might affect the structural performance of the concrete slabs. The paper will summarize research-based design and detailing rules used to assess the effect of the beam stiffness on the performance of concrete slabs. Methods currently used by practitioners in different European countries will be compared against test results available from literature.

1 Introduction

Flat slabs locally supported on columns without down stand beams are a structural system allowing to create buildings with open spaces offering a high functional and aesthetic value. Traditionally (since 1950's), this kind of structures has been executed as cast in situ concrete slabs. Such slabs must be reinforced to carry bending moments in two orthogonal directions in the span and column area. Vertical shear reinforcement is typically installed adjacent to the column to provide resistance against punching shear failure. More recently (since 1990's), the development of so-called shallow floors allowed to introduce a high degree of prefabrication into the construction process of flat slabs. Shallow floors typically consist of precast or semi precast slabs bearing on transverse steel beams integrated in the depth of the slab and supported on vertical columns as Fig 1. The bending resistance and stiffness of the transverse beams might be optimized by creating a bond between steel and concrete using mechanical shear connectors. From general point of view, the shallow floor is nowadays a very competitive construction method as it allows to combine the functional benefits of flat slabs with the advantages offered by prefabrication (speed and ease of design and construction).

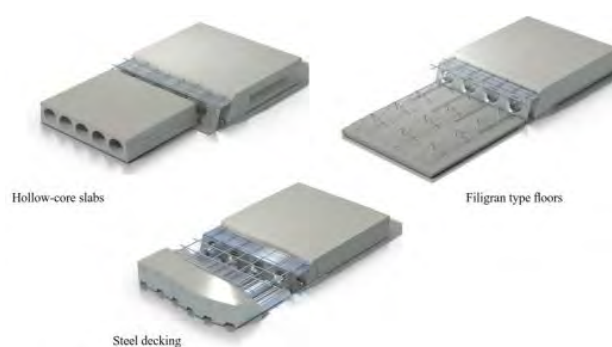


Fig. 1 Examples of floor types with shallow beam [1]

The structural performance of shallow floors is typically assessed by demonstrating the conformity of their components (steel or composite beams and precast slabs) with harmonized European standards or technical approvals of proprietary building products. The joints between slab and beams are further reinforced with a system of reinforcement bars and hooks that help to secure a proper transfer of forces between the two structural elements and are typically designed to fulfill best practice requirements that are in place on the particular markets. While such assessment might seem a priori enough

to secure a reliable design of a shallow floor, some specific behavior patterns resulting from the fact that the shallow floor associate structural members with different bending stiffness might negatively influence the structural performance of the hollow core floor. Despite having been identified by research, these specific behavior patterns are yet only partly normalized and thus little known by practitioners. The aim of the present paper is to summarize some current practice about the structural behavior of precast slabs supported on steel or composite beams and provide practical recommendations for the design.

2 Structural behaviour of shallow floor

2.1 Hollow core slabs

The hollow core units are traditional elements for prefabricated floors, produced in factories using the basic technologies of production (extrusion and slip-forming). This type of slab is composed of prestressed concrete with longitudinal voids (in the order of 30 to 50 % empty space) as Fig. 2, longitudinal strands and without transverse reinforcement. These longitudinal strands ensure the bending capacity and increase the shear capacity of non-reinforced webs. The characteristics and properties of hollow core units allow to obtain much lighter slabs, larger spans (up to 18 m), smaller thicknesses (between 12 and 40 cm), with high mechanical performance. Initially, the hollow core units were developed and designed for rigid supports, such as walls. However, with the emergence of column-beam structures, and especially with shallow floors in the 1990's, the hollow core slabs began to be used on supports qualified as flexible, such as beam (concrete or steel shallow beam, composite shallow beam, etc.).

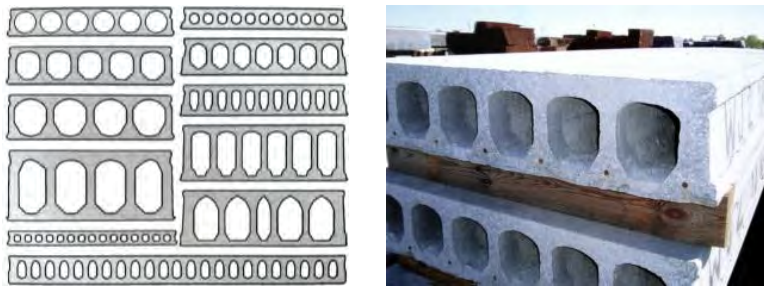


Fig. 2 Hollow core slabs [2]

2.2 Steel shallow beam

The steel shallow beams are integrated into the depth of the hollow core units, where these prefabricated slabs are supported on the edge of the bottom flange of these profiles as Fig. 3 (right). In this way, it is possible to obtain floors with low thickness without down stand beams. This type of profile is therefore designed to fully support the loads of the floor through its bottom flange, both in the erection stage (without joint concrete) and in the final stage (with joint concrete). Shallow steel beams usually have significant flanges and webs thicknesses to ensure the correct functioning of the floor.

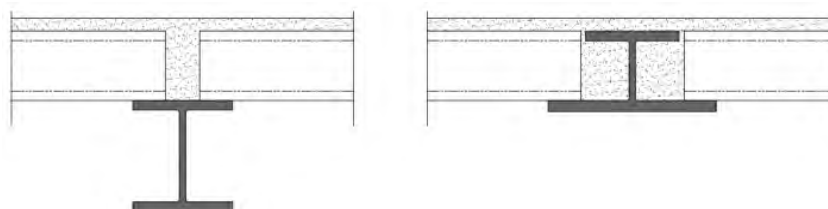


Fig. 3 Steel beam with hollow core slabs

2.3 Composite shallow beam

Composite shallow beam, such as integrated steel beam, allow to obtain floors without down stand beam by integrating in their depth the hollow cores units, but with lower profiles. This is enabled through the composite interaction between the slabs and the beam through the joint concrete, allowing the advantages of steel and concrete to be used in the floor design. In other words, the good compressive strength of the concrete and the good tensile strength of the steel.

An example of composite beam is the DELTABEAM[®] as Fig. 4. This beam is a box-shaped profile, composed of a bottom flange wider than the top flange and has openings in these two inclined webs, in order to develop a composite interaction between the beam and the floor (thanks to the joint concrete crossing the DELTABEAM[®]). This composite section can be reinforced with transversal reinforcement to the slabs (transverse to the beam section as Fig 1.).

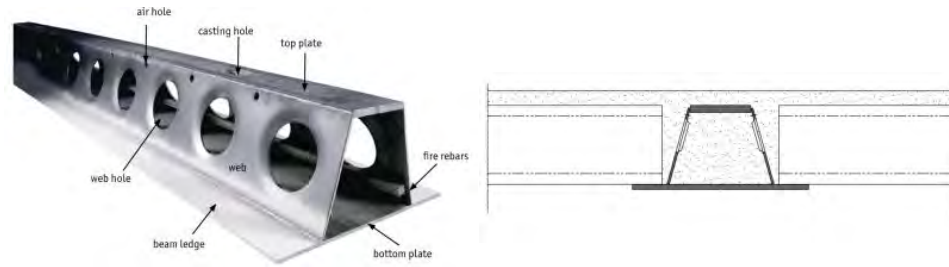


Fig. 4 Composite beam DELTABEAM[®]

2.4 Particularity of shallow beam with hollow core slabs

Hollow core units on flexible supports, compared to rigid bearings, are subjected to a double curvature induced by the deformation of the beams, when the floor is subject to a uniformly distributed load as Fig. 5 (left). Moreover, as the loading increases, the slip of the hollow core units in relation to the beam increases as shown in Fig.5 (right b). In practice, the chemical and mechanical bond, the friction between the slabs ends and the joint concrete tend to prevent this displacement. In that case, a horizontal shear flow is formed in the transversal direction of the hollow core slabs. Specifically, this flow is created at the level of the webs (the link between the top member and the bottom member of the hollow core slabs), where a compressive force in the top part is opposed an adhesion in the bottom part of the hollow core slab [2]. This flow can cause shear-tension cracks in the hollow core slabs on flexible supports (mainly in the edge slabs), until a shear-tension failure (also called web-shear failure) of the prefabricated slabs occurs prematurely, compared to rigid bearings. Consequently, the design of the hollow core units on flexible supports has been the subject of many researches and studies (the most significant are discussed in the following section).

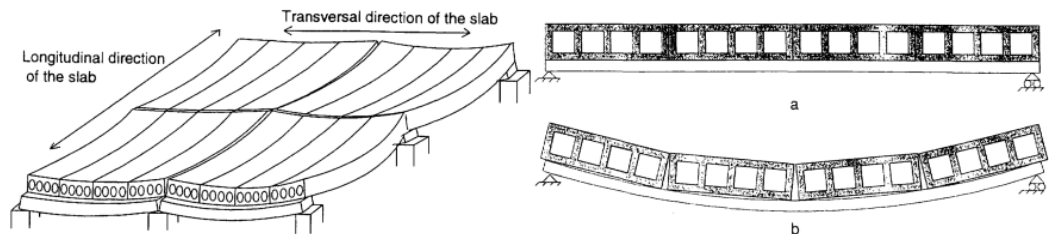


Fig. 5 Deformation of hollow core slabs on flexible supports [2]

3 Tests of hollow core slabs supported on steel/composite beam

The first research on the behavior of hollow core units on flexible supports began in 1990 in the Finnish Technical Research Center VTT, with three large-scale tests, where the objective was to analyze the possibility of a reduction in the load capacity of prefabricated slabs due to the formation of longitudinal cracks (cracks along the beam) [3]. However, during these first experiments, a shear-tension failure of the slabs webs has always been decisive, and the resulting failure load was only 40 to 70 % of the respective load on rigid supports. Consequently, further large-scale tests were conducted with different type of hollow core units and supporting beams (concrete, steel, composite), as well as analytical and numerical studies. Pajari collected and published 20 of these experiments in the Technical Paper n°148 of the VTT [3]. For all these investigations, Pajari observed that the origin of the breach on the floors was an unexpected failure of the web in the slab edges by shear-tension, with a reduction of up to 60 % in the shear capacity. Nevertheless, according to Pajari, the decrease in the load capacity of prefabricated slabs on flexible supports is not only due to the deflection of the beam, but also to other important parameters, such as the bond properties between the floor elements (beams and slabs) and the cross section of the prefabricated slabs. Indeed, for some beams type, even slight deflection of the beams led to a significant reduction in the load-bearing capacity of the hollow core slabs.

In Sweden, Ferreira and Bajic conducted 8 tests on individual hollow core units, simulating flexible supports with plates of different thicknesses under the prefabricated slabs tested, in order to recreate the deflection of the beam [4]. According to Roggendorf's researches [5], the Swedish experiments also showed a reduction in the load capacity of the hollow core units on flexible supports, in order of 15 to 24 %, due to the transverse bending on the slabs.

More recently in Germany, in 2000's, Roggendorf [5] tested 8 large-scale experiences on the behavior of hollow core units on flexible bearings. The shallow mixed floors were composed of two type of IFB steel beams (two different bending stiffness) integrated into the depth of hollow core slabs (265 or 250 mm thick with different cross-section shapes). During these experimental results, Roggendorf observed in all cases a shear-tension failure of one or more edge webs. Moreover, he found that the load capacity of the prefabricated slabs on the various flexible bearings tested was only 52 to 78 % compared to the references on rigid supports. However, despite several beam stiffnesses and the different deflection associated, the load capacities obtained for the floors tested were relatively the same. Roggendorf, as Pajari, explains that the deformation of the beam is not the only decisive parameter responsible for the reduction in the load capacity on flexible supports. Consequently, no effect of the beam stiffness on the shear strength of the slabs could be determined.

In France, the researches are more restricted, only Polania's experiments [6] were found on the behavior of hollow core slabs on beams, where the objective of his experiments were to show the effects of the beam's flexibility on the hollow core units. He tested two floors, each composed of 8 hollow core slabs of the same dimensions and characteristics, but with two different central beams, one test with prestressed concrete beam and the other with an I-shape steel beam. During these experiments, Polania observed a shear-tension failure of the web at the edge units, as well as a 33% reduction in the slab strength between these two beams. In the results, according to this scientist, this decrease was in accordance with the ratio of bending stiffness between the two beams tested. However, Polania explains that the effect of other factor responsible for a reduction in the load capacity of the hollow core slabs could not be measured or studied, such as the composite action.

4 Design recommendations for hollow core slabs on flexible supports

The European standards [7] and [8] include no information on the effects of flexible supports about the behavior of hollow core slabs, or specific formulae for the design of the shear resistance of slab webs. The specific standard of hollow core slabs [7] only indicates that it is necessary to reduce the shear resistance of the hollow core slabs in the case of flexible supports, in order to consider transverse stresses (acc. section 4.3.3.2.2.1 (3) [7]). Consequently, some countries have implemented their own recommendations. This paper focuses on the Finnish method developed and the German recommendations for hollow cores slabs on flexible bearings.

In Finland, the Concrete Association of Finland developed the Code Card N°18 for the design of hollow core units supported on beams [9]. It is based on the design model developed in the Finnish researches and the experimentations (all references are given in the document [9]).

In the Code Card N°18, the phenomenon of transverse shear flow inducing premature failure of the webs is considered in the design of hollow core slabs, as in (1). This formula uses the principal tensile stress, noted σ_I and limited to the tensile strength of the concrete at the critical point of the cross-section. This principal tensile stress, established from the Mohr circle, is calculated according to the normal stress (σ_{cp} and σ_{cm}), the vertical stress (τ_{hc} and τ_{cp}) and the transversal stress (τ_{vl}). That is:

$$\sigma_I = \frac{\sigma_{cp} + \sigma_{cm}}{2} + \sqrt{\frac{(\sigma_{cp} + \sigma_{cm})^2}{4} + (\tau_{hc} + \tau_{cp})^2 + \beta_r \tau_{vl}^2} \leq f_{ctd,hc} \quad (1)$$

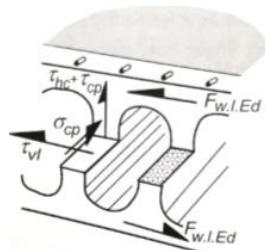


Fig. 6 Representation of the principal stresses of the hollow core slabs supported on beams [10]

This principal tensile stress condition, as in (1), can be expressed in an easier form to determine the failure of hollow core slabs webs on beams. In this way, this failure condition, noted F_{fail} , is given to the equation (2) by the Code Card n°18. If this equation is fulfilled, the strength verification of hollow core slabs on beams is satisfied.

$$F_{fail} = \left(\frac{\tau_{hc} + \tau_{cp}}{f_{ctd,hc}} \right)^2 + \left(\frac{\tau_{vl}}{f_{ctd,hc}} \right)^2 - \frac{|\sigma_{cp}| - \sigma_{cM}}{f_{ctd,hc}} \leq 1 \quad (2)$$

The first and the last component in the failure function appear in any slabs and the one in the middle appears only in the slabs supported on flexible supports. With:

- σ_{cp} : is the compressive normal stress in the slabs due to prestressing, appearing in the critical section for the stresses of the webs in the hollow core units. It is determined on the assumption of a linear distribution of stresses in this section and according to St Venant (analogously with the formula for prestressed concrete beam). The Code Card 18 gives these values according to a certain number of hollow core slab types (Table 2/B [9]).
- σ_{cM} : is the normal stress component due to bending moments of the hollow core slabs in the critical section for the stresses of the webs (≥ 0).
- τ_{cp} : is the shear stress due to development of the prestressing force within the transmission length, appearing in the critical section. The Code Card 18 gives these values according to a certain number of hollow core slab types (Table 2/B [9]).
- τ_{hc} : is the shear stress in the webs in the direction of the slab, due to the vertical shear flow of the slab, appearing in the critical section, and determined according to the theory of beams (section 3.3.1 of the Code card 18 [9]).
- $f_{ctd,hc}$: is the design tensile strength of the slab webs.
- τ_{vl} : is the transversal horizontal shear stress in the slab webs, due to the longitudinal shear flow, appearing in the critical section, as Fig 6, given through:

$$\tau_{vl} = \frac{3}{2} \frac{F_{w.l.Ed}}{A_{we.1}} \beta_f = \frac{3}{2} \frac{v_{lw} b_{sl}}{(h_{hc} - h_{ct}) \sum b_{w.i}} \beta_f \quad (3)$$

Where:

- $F_{w.l.Ed}$: is the design horizontal transversal shear force on a single web, based on the shear flow v_{lw} and the nominal width of the slab unit b_{sl} . The shear flow v_{lw} should be assessed considering all the effects of the charges after the beginning of the mixed action.
- $A_{we.1}$: is the effective shearing area of the single web, according to the depth of the slab h_{hc} , the depth of the plated section in the slab webs h_{ct} , the sum of the width of the slab webs $b_{w.i}$ and the reduction facteur β_f (for the cases when the effective length of the core infill exceeds 50 mm). As Fig 7.

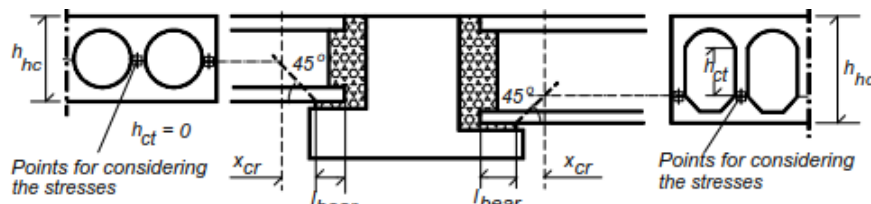


Fig. 7 Definition of the critical section according to the shape of the slabs in the Code Card 18 [9]

In Germany, the technical approval of DIBt Z-15.10-279 [11] is used for the design of hollow core slabs on flexible supports. In this approval, no formula is given to verify and estimate the transverse shear strength of the webs. However, based on researches, it gives four specifications to be considered in the design of the hollow core units on beams:

- (1) A 50 % shear capacity reduction on flexible supports (shear strength calculated in accordance with Part 3.9 of the DIBt and based on European standards). Let $V_{ed} \leq 0,5 V_{Rd}$.
- (2) A permissible deflection of $L/300$ for the beam.
- (3) A mandatory installation of hollow core units on an elastomer strip. This strip must be checked according to the bearing force and must not be less than 35 mm wide and 10 mm thick.

- (4) A concrete filling of the exterior cells of the hollow core units over a length at least 80 cm with reinforcements (stirrups) or concrete filling of all the cells on a depth at least 25 cm.

5 Comparaison between code results and results in flexible support tests

The results provided by the Finnish and German codes are compared with the test results, shown in the table below. The comparison includes the experimental tests carried out in Finland [3], Germany [5] and France [6] with hollow core slabs on flexible supports (with integrated steel beam or composite beam), where shear failure of the webs occurred (section 3).

For the Finnish code, the formula of σ_I , as in (1), is compared with the main tensile strength of the hollow core slabs concrete, f_{ctm} . Regarding f_{ctm} , it is derived from the cubic resistance measured in the real tests [5], using the following formulas.

$$f_{ctm} = 0.3 f_{ck}^{2/3} = 0.3 (f_c - 4)^{2/3} [MPa] \text{ with } f_c = 0.824 f_{c.cube} \quad (4)$$

On the Germany regulation side, the 4 recommendations given are compared with the schemes of the tests.

Table 1 Summary of experimental research for hollow core slabs on flexible supports.

N	Tests	Center of research	Beam type	Authors	Years	Code[9] σ_I / f_{ctm}	Dibt[11] 4 conditions fulfilled
1	DELTA 265	VTT	CR	Koukkari	1990	1,23	no ⁽¹⁻³⁻⁴⁾
2	WQ 265	VTT	S	Koukkari	1990	1,30	no ⁽²⁻³⁻⁴⁾
3	WQ 400	VTT	S	Pajari	1992	1,42	no ⁽³⁻⁴⁾
4	MEK 265	VTT	CR	Iso-Mustajärvi & Pertti	1994	1,40	no ⁽³⁻⁴⁾
5	LBL 320	VTT	CP	Pajari	1998	1,64	no ⁽²⁻³⁻⁴⁾
6	DELTA 400	VTT	CR	Pajari	1999	1,41	no ⁽²⁻³⁻⁴⁾
7	SUPER 320	VTT	CR	Pajari	2002	1,10	no ⁽²⁻³⁻⁴⁾
8	LB 320	TUT	CP	Suonio & Taskinen	2002	1,48	no ⁽¹⁻²⁻³⁻⁴⁾
9	WQ 500	VTT	S	Pajari	2005	1,36	no ⁽¹⁻³⁻⁴⁾
10	DELTA 500	VTT	CR	Pajari	2005	1,59	no ⁽²⁻³⁻⁴⁾
11	A BEAM 320	VTT	CR	Pajari	2006	1,25	no ⁽²⁻³⁻⁴⁾
12	IFB 265 (1)	IMB	S	Roggendorf	2010	1,42	no ⁽²⁾
13	IFB 265 B (3)	IMB	S	Roggendorf	2010	1,29	no ⁽²⁾
14	IFB 265 M (6)	IMB	S	Roggendorf	2010	1,19	no ⁽²⁾
15	IFB 265 RD (7)	IMB	S	Roggendorf	2010	1,14	no ⁽²⁾
16	IFB 250 (2)	IMB	S	Roggendorf	2010	-	no ⁽²⁾
17	IFB 250 B (4)	IMB	S	Roggendorf	2010	-	no ⁽²⁾
18	IFB 250 M (5)	IMB	S	Roggendorf	2010	-	no ⁽²⁾
19	IFB 250 RD (8)	IMB	S	Roggendorf	2010	-	no ⁽²⁾
20	I Profile	INSA	S	Polania	2006	1.81	no ⁽³⁻⁴⁾
Average value						1,38	-
Coefficient of variation						0.14	-
Characteristic value						1.01	-

VTT and TUT: Finland	S: Steel beam
IMB: Germany	A-beam, Delta, MEK, LB, LBL et Super: Patented composite beams
INSA: France	WQ: Top-hat steel beam
CP: Composite, prestressed beam	no ^(x) : x condition number(s) no fullfided
CR: Composite reinforced beam	

The calculation model developed in the Code Card 18 presents homogeneous and coherent values in relation to the available test results. The mean value of the test to calculated value is 1.38 with a COV of 0.14. The model consistently predicts the correct failure mode. The evaluation shows that the model original developed for slabs produced in Northern Europe can provide a realistic and reliable estimate of the effect of the support flexibility also for slabs produced in France and Germany.

The detailing of most of the tests was different from the requirement of the DIBT approval, therefore the applicability of the empirical design method for these tests can not be verified.

6 Conclusions

Thanks to numerous practical advantages they offer, shallow floors are an increasingly popular method to construct flat slabs. The fact that the structure associate structural members with different stiffness offers possibilities to optimize the design of the slab. On the other hand, it requires a proper and sensitive assessment of the interaction between the different structural components. The paper does summarize some practical recommendations for the design of precast hollow core slabs supported on flexible beams.

References

- [1] Peikko Group, 2014. *Deltabeam Composite Beam*, Technical Manuel.
- [2] FIB, January 2000. *Special design considerations for precast prestressed hollow core floors, Guide to good practice*. Bulletin 6.
- [3] Pajari, 2010. *Prestressed hollow core slabs supported on beams - Finnish shear tests on floors in 1990-2006*, VTT working papers 148. Finlande.
- [4] Ferraira and Bajic, 2002. *Hollow core slab units with different support conditions*. Department of concrete structure Royal Institute of Technology.
- [5] Roggendorf, 2010. *Zum Traverhalten von Spannbeton-Fertigdecken bei biegeweicher Lagerung, Rheinisch-Westfälischen Technischen Hochschule Aachen*. Allemagne.
- [6] Polania, 2006. *Contribution à l'étude du comportement des planchers composites poutres - Dalles alvéolées préfabriquées en béton*. France.
- [7] EN 1168: 2005 + A3 :2009, *Precast concrete products: Hollow core slabs*.
- [8] EN 1992-1-1, Eurocode 2, 2003. *Design of concrete structure: Part 1.1 General rules and rules for buildings*.
- [9] Code Card No18, 2017. *Design of hollow core slabs supported in beams*. English Edition for Peikko Group Oy with updates 25.11.2012-2.8.2017.
- [10] Peikko Group Corporation, 2017. *PG 0917 Behavior and design of steel-concrete composite structure*. First edition.
- [11] DIBt Z-15,10-279, 2014. *Verwendung von Spannbeton-Holplatten nach DIN EN 1168:2011-12 und DIN EN 1992-2-2:2011-01 System BRESPA*.

Fastening of a gusset plate to concrete by means of post-installed anchors - Numerical investigation

Erik Johannes Stehle and Akanshu Sharma

*Institute of Construction Materials,
University of Stuttgart,
Pfaffenwaldring 4G, 70569 Stuttgart, Germany*

Abstract

In this paper, numerical simulations are performed to investigate the performance of post-installed anchors used to connect a gusset plate in corner configuration. Thereby, the complete connection is both fully and partly fastened to the concrete specimen to determine the effect of the concrete corner. It is found that the stiffness and ultimate load of the fully fastened connection is twice compared to the partly fastened connection. Furthermore, an analytical approach is applied to design such a configuration using the methods provided by current standards and the obtained capacities are compared to the numerical results. The comparison shows that the applied analytical approach yields conservative results compared to the numerical results.

1 Introduction

Before the introduction of modern seismic codes, the design of RC structures was, if at all, not sufficiently considering the high demands and the adverse effects of earthquake loading. This is especially the case for RC frame structures as they are particularly prone to lateral loads. As a result, RC structures suffered severe damage or even collapse during strong earthquakes in past decades [1]-[3]. One main reason for the poor performance during an earthquake is the reinforcement detailing of these structures as they were mostly designed for gravity loads. Consequences thereof are unfavourable failure modes such as beam column joint failure, column shear failure or soft-story mechanisms [4]-[6]. The essential challenge is to develop retrofit solutions, which on the one hand ensure adequate safety and improved performance during future earthquakes and on the other hand offer a practical and economical solution with low invasion and interference with the existing structure. Steel bracing is a popular solution as it results in a substantial increase in lateral capacity and because of its beneficial impact on the global ductile behaviour as shown in [7], [8]. Furthermore, when directly connected to the existing RC frame structure, it provides a practical, low-invasive solution which is highly adaptable to the architectural preconditions. Several direct connection methods have been investigated such as steel-jackets, bolted-through connections, external rods, or precast headed studs. These methods have been applied in experimental studies ([9]-[12]) where it was shown that the direct approach offers an efficient way to connect the bracing system. However, the above-mentioned methods have certain shortcomings when it comes to retrofitting of existing structures. It becomes apparent that precast headed studs are not suitable for retrofitting, but also other methods require, for example, the accessibility of two sides of the columns and beams in which the connections are installed. In some cases, however, the required access cannot be provided, or the accessibility is associated with elaborate construction work. In these cases, the beneficial effects such as practicability and low invasiveness are significantly reduced. Forming a connection using post-installed anchors offers an alternative approach that can be installed also with one-sided access. In addition, the use of post-installed anchors can further reduce the invasiveness and allows for easy and fast installation. Connections using post-installed anchors have been applied in experimental studies such as [13], [14] where it was shown that the behaviour and performance of such a connection is sufficient to guarantee the effectiveness of the steel bracing in enhancing the global structural behaviour.

1.1 Problem statement

In case of diagonal bracing, the steel braces are connected to the corner joint of the frame structure as illustrated in Fig. 1 (a). The connection element generally comprises a gusset plate which is welded to an anchor bracket. The bracket is in turn fixed to the RC members using post-installed anchors. One problem that arises particularly when using post-installed anchors is that for such an anchor configu-

ration no design recommendations are provided by current guidelines and standards. A simple and convenient design solution based on engineering judgement could be to treat the complete connection as two separate anchor groups. In the example shown in Fig. 1 (b), the connection would be treated as two 2x2 anchor groups, which are located perpendicular to each other. The total capacity of the connection could then be calculated by adding up the individual capacities of the two groups.

When designing anchor groups, concrete related failure modes such as concrete cone failure are often governing the design. Thereby, a cone like breakout body forms, where at the bottom of the breakout body, cracks propagate from the embedded ends of the anchors towards the concrete surface. The evaluation of a large number of experimental data has shown that the angle of the resulting cone is approximately 35° ([15]). For the case at hand this means that if the embedment depth of the anchors is large enough compared to the distance from the back anchors to the corner, the breakout bodies of the two perpendicular anchor groups would overlap as indicated in Fig. 1 (a). It becomes apparent that in this case, the two anchor groups might have a mutual influence. However, the type and extent of the influence is not clear. On one hand, the compressive struts of the two groups may stabilize each other but on the other hand, they might interfere and have a negative impact on the overall performance.

In [13] the potential negative influence is discussed, and two approaches are distinguished. The rather conservative approach considers a free edge at the beam or column face ignoring the joint panel whereas the second approach simply neglects any potential influence. Thereby, the experimental results suggest that the second approach reflects the capacity of the connection more realistically.

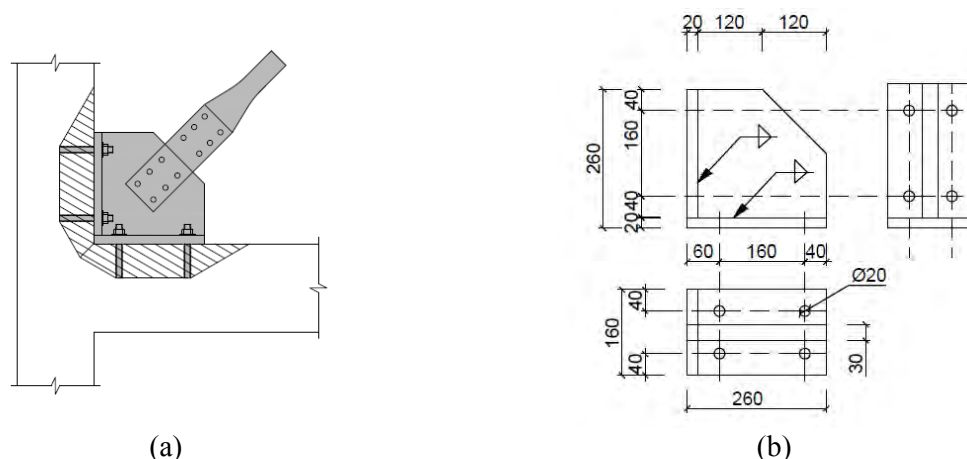


Fig. 1 (a) Connection between steel bracing and RC members using post-installed anchors and (b) Dimensions of the connection element comprising a gusset plate and an anchor bracket. (Note: All dimensions are in mm).

1.2 Scope and methodology

The aim of the present work is to investigate the concrete breakout behaviour of the corner connection as described above. To this end, a numerical parametric study is conducted where the effect of varying embedment depth is investigated. In the numerical simulation bonded anchors are used to fasten the connection element to the concrete specimen. Besides the variation of the embedment depth, simulations are performed in which only one of the two anchor groups is fixed to the concrete specimen keeping other conditions, such as the direction of loading or the dimensions of the specimen, the same. By comparing the capacities of the fully fastened connection with the partly fastened connection, a conclusion can be drawn as to how great the mutual influence of the neighbouring anchor groups is. Besides the general behaviour of the connection, the capacities obtained from the numerical simulations are compared to the capacities obtained from an analytical approach using the design methods given in EN 1992-4 [16] for the design of fastenings.

In order to focus on geometrical influences on the breakout behaviour of this type of anchor configuration, it is necessary to exclude some of the effects which would make a basic evaluation of the connection difficult. This includes for example bending of the RC members or the frame action effect on the gusset plate [17], which is expected to affect the behaviour of the connection but is not considered in this study for simplification. In this regard the concrete specimen used in this study is not

modelled as a beam-column joint per se, but in such a way that the focus on the corner connection is possible. Furthermore, it should be noted that this study considers the design case where the post-installed anchors are only loaded when the steel bracing is in tension. Whereas, when the steel bracing is loaded in compression, the respective loads are directly transferred to the RC members by the anchor bracket. This essentially means that this study concentrates on the behaviour of the connection when it is statically loaded in tension. Reversed or cyclic loading is not considered.

2 Numerical investigation

2.1 Description of the concrete specimen and the connection element

The connection element to be investigated, together with its dimensions is shown in Fig. 1 (b). It comprises a gusset plate, an anchor bracket and eight bonded anchors. The bonded anchor system which is used to fasten the connection element to the concrete specimen comprises a high strength threaded rod and an epoxy mortar. The anchors have a diameter of $d = 16$ mm and are embedded in the concrete with different effective embedment depths ($h_{ef,1} = 80$ mm, $h_{ef,2} = 110$ mm and $h_{ef,3} = 150$ mm). The anchor bracket which connects the anchors has a thickness of 20 mm and is made of steel. This anchor bracket can be thought of in simplified terms as two perpendicular anchor groups (two 2x2 anchor groups). For each of these groups, the spacing between the anchors is $s_1 = 160$ mm and $s_2 = 80$ mm. The load is applied on the upper face of the gusset plate as indicated in Fig. 2, from where it is transferred to the anchor bracket and to the anchors. An unreinforced concrete specimen is used in the numerical simulation. The exact dimensions are provided in Fig. 2. The anchors are placed close to two parallel edges, with an edge distance of $c_2 = 80$ mm. The distance from the back anchors (the two anchors which are closest to the corner in each of the two groups) to the corner is 60 mm. In addition to the simulations where the connection is fully fastened to the concrete specimen using eight bonded anchors, additional simulations are performed where the connection is only partly fastened to the concrete specimen by means of four bonded anchors (See Figure 2).

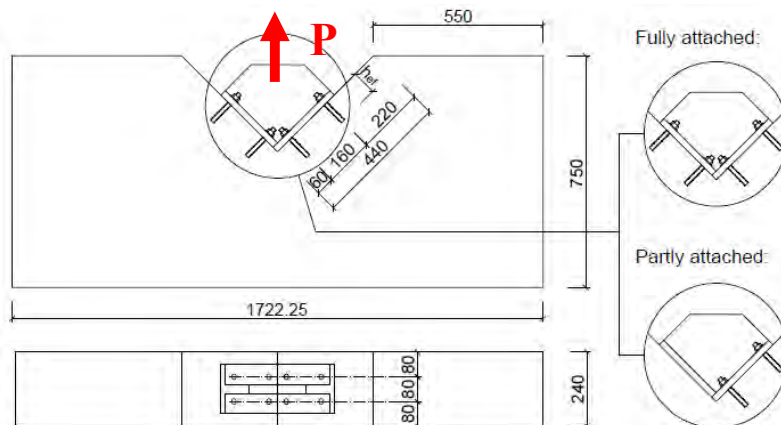


Fig. 2 Dimensions of the concrete specimen. (Note: All dimensions are in mm).

2.2 Numerical modelling approach

To perform the numerical analysis in this work, the 3D finite element software MASA (Macroscopic Space Analysis) is used, which was developed at the Institute of Construction Materials at the University of Stuttgart. MASA uses the microplane model with relaxed kinematic constraint proposed by [18] as the constitutive law for concrete. Smeared crack approach is applied to simulate the damage and fracture phenomena. The basis of the model are planes of various orientation. These planes can be interpreted as damage planes on a microstructural level, like for example the contact layer between aggregates in case of concrete. In MASA the static constraint is replaced by kinematic constraint by calculating the strain components on the microplanes as the projection of the macroscopic strain tensor. By doing so, the uniqueness of the solution for a quasi-brittle material such as concrete can be guaranteed. Furthermore, for realistic modelling of concrete material behaviour under dominant compressive load, it is required to decompose the normal strain component into a volumetric and deviatoric part. However, this leads to an unrealistic model response in case of dominant tensile loading which is expressed by lateral expansion in case of uniaxial tension load. Therefore, the microplane

strain components need modification to relax the kinematic constraint to prevent such pathological behaviour [18]. To ensure mesh-independent results, a so-called localization limiter is required. Therefore, in MASA, the crack band method is used [19].

The finite element model is created using the software FEMAP (Siemens) which is also used for post-processing the results. The discretization of the concrete specimen and the connection element is shown in Fig. 3 (a). The concrete specimen is modelled using 4-node tetrahedral elements. Steel elements, such as the gusset plate, the anchor bracket and the anchor rods are modelled using 8-node hexahedral elements. The gusset plate and the anchor bracket, which are welded together, are considered as one component in the numerical model. To simulate the bond between the anchor rods and the concrete, 2-node bar elements are utilized. The 2-node bar elements are able to transfer compression and shear (bond) forces. The corresponding discretization of the bond stress-slip behaviour is illustrated in Fig. 3 (b). It should be noted that besides the simulation of bonded anchors, this approach is capable to simulate the interaction between concrete and reinforcement steel. The contact between the anchor bracket and the concrete is modelled using compression-only 2-node bar elements. The applied modelling approach has been successfully employed in previous studies ([20]-[22]) to simulate the behaviour of bonded anchors embedded in concrete and has been validated against experimental results.

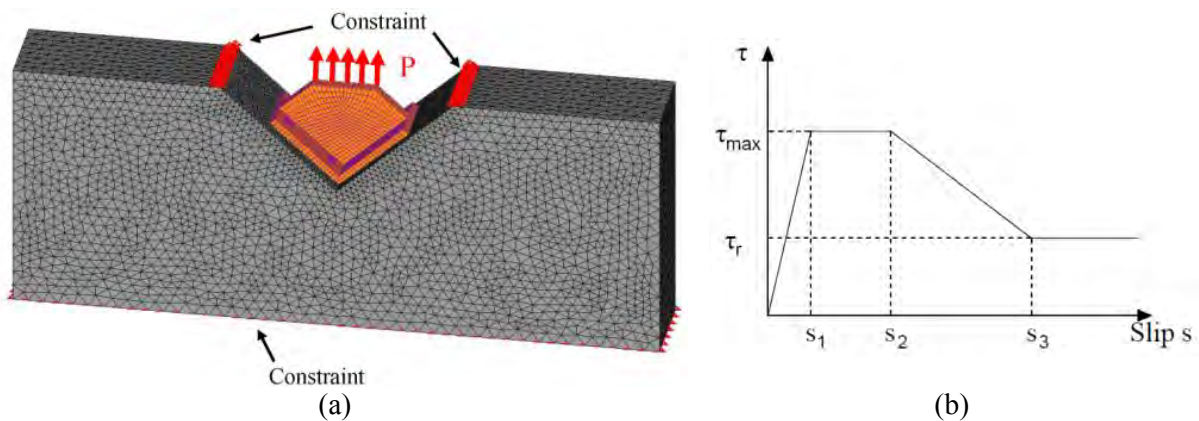


Fig. 3 (a) FE discretization of the complete specimen and (b) Idealization of bond stress-slip relation.

The connection element is loaded in displacement control by directly applying the load to the nodes of the upper face of the gusset plate as indicated in Fig. 3. The displacements are stepwise increased in increments of $\sqrt{2} \cdot 10^{-2}$ mm (0.01 mm per step applied to each anchor group). In this way, it generally takes 50-80 steps to reach the ultimate load of the connection. The total force acting on the connection is calculated from the sum of forces on the loaded nodes in the direction of loading. Similarly, the constraints are directly applied onto the nodes. On the upper side of the concrete specimen, constraints are applied to the nodes located directly on the edge of the triangular recess. On the bottom side of the specimen all nodes are constraint to prevent sliding and bending of the concrete specimen.

In the numerical study the mean cylinder compressive strength of concrete is considered as $f_c = 20$ N/mm², the tensile strength of concrete is taken as $f_t = 2.2$ N/mm². Further material properties for concrete that need to be specified are the modulus of elasticity of concrete $E_c = 30000$ N/mm², Poisson's ratio $\mu_c = 0.18$, and the fracture energy $G_f = 0.06$ Nmm/mm². For the problem at hand, the investigation is focused on the breakout behaviour of concrete. Therefore, the size of the anchor rods, the embedment depths and the concrete strength was chosen in a way to ensure concrete failure before yielding of the steel elements. In this regard, the steel elements are modelled assuming linear-elastic material behaviour with Young's Modulus $E_s = 200000$ N/mm² and Poisson's ratio $\mu_s = 0.33$. In the simulations where the connection is only partly fastened to the concrete specimen, however, the nonlinear behaviour of the anchor rods is considered using von Mises plasticity criteria. The yield stress is assumed as $f_y = 640$ N/mm² and the ultimate strength as $f_u = 800$ N/mm².

2.3 Numerical results and evaluation

The numerical program and the results of the numerical parametric study in terms of ultimate loads and displacements at ultimate load are summarized in Table 1. In Fig. 4 (a) the load-displacement curves of the respective simulations are shown. The solid curves map the results of the simulations with fully fastened connection and the dashed curves map the numerical results of the case where only one of the two anchor groups was fastened to the concrete specimen (partially fastened connection). Fig. 4 (b) shows the typical failure mode and the corresponding crack pattern in case of the fully (top) and partially (bottom) fastened connection for an embedment depth of 150 mm. Note that the cracks are displayed in terms of principal tensile strain, where red elements represent cracks with a crack width of 0.1 mm or larger.

Table 1 Numerical program and summary of the numerical results.

ID	Effective embedment depth, h_{ef} (mm)	Value	Ultimate load, $P_{u,num}$ (kN)	Displacement at ultimate load, s_u (mm)
BC-80-FA	80	Fully fastened	240.91	1.089
BC-110-FA	110	Fully fastened	291.29	0.877
BC-150-FA	150	Fully fastened	381.77	0.820
BC-80-PA	80	Partly fastened	126.59	1.117
BC-110-PA	110	Partly fastened	145.67	0.735
BC-150-PA	150	Partly fastened	187.30	0.933

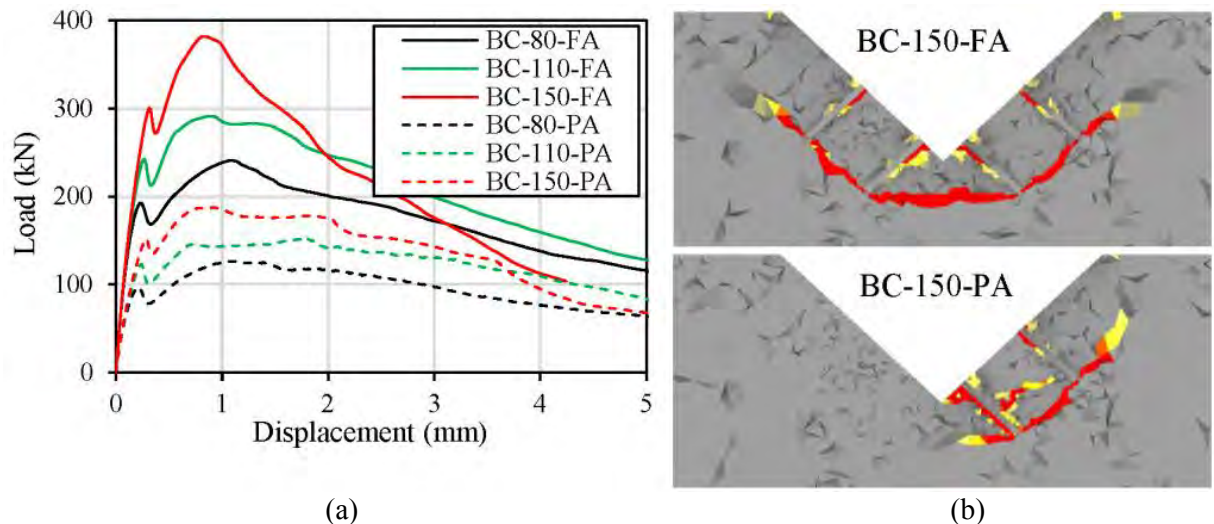


Fig. 4 (a) Load-displacement curves obtained from the numerical analysis and (b) Crack pattern obtained for $h_{ef} = 150$ mm in case of a fully (FA) and partially (PA) fastened connection.

2.3.1 Behaviour of the fully fastened connection

As can be seen in Fig. 4 (a), the initial behaviour of the connection is similar for different embedment depths. The curves show a relatively linear behaviour until reaching the first peak. At first peak initial circumferential cracking occurs at the tips of the embedded ends of the anchor rods. After the first peak has been reached, the load slightly reduces while cracks start to propagate from the tips of the anchors closest to the corner towards each other. As the cracks between the anchors merge, the short phase of load reduction ends, and the crack growth stabilizes again. Upon further increase of the load the initial microcracks that occurred at the tips of the front anchors (the anchors farthest away from the corner in each of the two groups) become wider and propagate towards the concrete surface while

the cracks between the anchors at the bottom of the breakout body become wider. Until the ultimate load is reached the crack growths remains relatively stable.

After the first peak and the short phase of load reduction, the load-displacement behaviour varies for different embedment depths. It can be seen, that with increasing embedment depth the behaviour of the connection in the second loading phase is markedly stiffer. This is also reflected by the secant stiffness value at ultimate load which increases with increasing embedment depth. It was also observed in the numerical study that with increasing embedment depth, the post-peak behaviour becomes more brittle.

2.3.2 Comparison of fully and partly fastened connection

As could be expected the ultimate load reduces significantly when only one group is fastened to the concrete specimen. Compared to the fully fastened connections, around 50% of the previously achieved ultimate load is obtained. It was further observed that when the ultimate load is reached in the simulations with the partly fastened connection, a load plateau occurs before the connection fails. Like the ultimate load, the initial stiffness reduces markedly when only one of the two groups is fastened to the concrete specimen as can be seen in Fig. 4 (a). To compare the initial stiffness of the partly and the fully fastened connections the secant stiffness values at first peak are determined. It is found that when only one group is fastened to the concrete specimen the stiffness reduces by around 45% on average as compared to the fully fastened connection. This also applies to the secant stiffness at ultimate load where the stiffness of the partly fastened connections is on average 52% of the stiffness obtained from the fully fastened connections. These findings suggest that, assuming two stand-alone anchor groups, the stiffness and ultimate load of the complete connection is simply composed of the individual values of the two groups. The load-displacement behaviour of the connection can therefore be determined from the behaviour of the individual anchor groups. However, the validity of this assumption is limited to the ascending branch of the load-displacement curve until the ultimate load is reached. Thereafter the potential beneficial geometrical effect of the corner that led to the load plateau in case of the partly fastened connection is neutralized by the mutual effect of the two anchor groups.

3 Analytical design approach

Current standards for the design of fastenings, such as EN 1992-4 [16], are limiting the use of post-installed anchors to rectangular anchor configurations with maximum three anchors in a row. An anchor configuration as shown in Fig. 1 is out of the scope of current standards and guidelines and hence no design solution is available for such a configuration. In the numerical parametric study, it was shown that the ultimate capacity of the complete connection is basically twice the capacity of the connection when only one of the two perpendicular groups is fastened to the concrete. Accordingly, the simplest design solution for the complete connection is to determine the capacity of one anchor group by using the methods provided by EN 1992-4 [16] and calculate the capacity of the complete connection as twice the capacity of one group.

When calculating the ultimate capacity of one group, it is assumed that the load is acting on the anchor group at an angle of 45°. Thus, the anchor group is simultaneously loaded in shear and tension. In EN 1992-4 [16] an interaction between tension and shear is considered using the following equation:

$$\left(\frac{N}{N_R}\right)^k + \left(\frac{V}{V_R}\right)^k \leq 1 \quad (1)$$

In Equation 1, N and V are the tension and shear loads acting on the anchor groups, respectively, N_R and V_R are the minimum capacities for tension and shear calculated for the relevant failure modes, respectively, and k is the exponent which defines the interaction between tension and shear loads.

According to EN 1992-4 [16] relevant failure modes in tension include steel failure, concrete cone failure, splitting failure and combined concrete cone and pull-out failure for bonded anchors. In shear, steel failure and pry-out failure are considered. Often the concrete related failure modes are governing the design as they yield the lowest capacity. This is also the case with the problem at hand where concrete cone failure governs the design for the tension related failure modes and pry-out failure governs the design for the shear related failure modes. It should be noted that mean values were used to calculate the capacities of the concrete related failure modes. For the interaction between tension

and shear, an exponent $k = 1.5$ is considered as proposed by EN 1992-4 [16] for failure modes other than steel failure. It is assumed that due to the gusset plate the loads are evenly distributed to the individual anchors of the group and thus centric loading is considered. Furthermore, two close parallel edges have to be considered with an edge distance of 80 mm. The ultimate capacity of one group is then calculated assuming 100% utilization of Equation 1. The capacities thus obtained are summarized in Table 2.

Table 2 Calculated values for the ultimate capacity of one group and the complete connection and comparison with numerical results.

Effective embedment depth, h_{ef} (mm)	One anchor group		Complete connection (two groups)	
	Calculated capacity, $P_{EN1992-4,PA}$ (kN)	$\frac{P_{EN1992-4,PA}}{P_{u,num,PA}}$	Calculated capacity, $P_{EN1992-4,FA}$ (kN)	$\frac{P_{EN1992-4,FA}}{P_{u,num,FA}}$
$h_{ef} = 80$ mm	81.2	0.64	162.4	0.67
$h_{ef} = 110$ mm	79.6	0.55	159.2	0.55
$h_{ef} = 150$ mm	81.0	0.43	162.0	0.42

As can be seen, the capacities calculated for different embedment depths are essentially the same. Compared to the numerically obtained results, this results in a significant underestimation of the capacity of the connection, especially for larger embedment depths. There are several possible explanations for this. First, the fact that EN 1992-4 [16] does not recognize a corner configuration means that no possible beneficial effect of the same can be considered. A favourable behaviour of the complete connection until the ultimate load is reached, would partly explain the significant difference between the numerical and the analytically obtained results. Second, prying action between the anchor bracket and the concrete specimen might result in an increased capacity of the connection. Third, the capacities for concrete related failure modes when more than one edge needs to be considered yields already conservative results.

4 Summary and conclusion

In this work, the geometrical effect of a corner configuration was investigated numerically. Therefore, an anchor bracket-to-gusset plate connection was simulated where bonded anchors were used to fasten the connection to the concrete specimen. Two cases were distinguished. In the first case the complete connection was fastened to the concrete specimen and in the second case only one of the two perpendicular groups was fastened to the concrete specimen. In both cases three different embedment depths were simulated. Furthermore, the numerical results were compared to an analytical approach using the methods provided by EN 1992-4 [16]. The main conclusions of the investigation are:

1. With increasing embedment depth, the behaviour of the fully fastened connection becomes stiffer in the ascending branch of the load-displacement curve, while the post-peak behaviour becomes more brittle.
2. When the connection is fully fastened, the ultimate capacity is around double the capacity of the partly fastened connection. Thereby, the stiffness of the fully fastened connection is also doubled compared to the partly fastened connection.
3. The applied analytical approach using the methods provided by EN 1992-4 [16] resulted in capacities which were well below the numerically obtained capacities of the connection. With increasing embedment depth, the difference between the analytically and numerically obtained capacities became even greater.

Acknowledgements

The researchers wish to thank fischerwerke GmbH & Co. KG for their financial support. Opinions, conclusions, and recommendations expressed in this paper are those of the authors and do not necessarily reflect those of the sponsoring organization.

References

- [1] Watanabe, Fumio. 1997. "Behavior of Reinforced Concrete Buildings during the Hyougoken-Nanbu Earthquake." *Cement and Concrete Composites* 19(3):492–502.
- [2] Kam, Wenig Y., Pampanin, Stefano, and Ken Elwood. 2011. "Seismic Performance of Reinforced Concrete Buildings in the 22 February Christchurch (Lyttelton) Earthquake." *Bulletin of the New Zealand Society for Earthquake Engineering* 44(4):239–78.
- [3] Ricci, Paolo, De Luca, Flavia, and Gerardo M. Verderame. 2011. "6th April 2009 L'Aquila earthquake, Italy: reinforced concrete building performance." *Bulletin of Earthquake Engineering* 9(1):203–211.
- [4] Sharma, Akanshu. 2013. "Seismic Behavior and Retrofitting of RC Frame Structures with Emphasis on Beam-Column Joints – Experiments and Numerical Modeling." PhD diss., University of Stuttgart.
- [5] Sadjadi, Reza, Kianoush, M.R., and S. Talebi. 2007. "Seismic performance of reinforced concrete moment resisting frames." *Engineering Structures* 29(9):2365–2380.
- [6] Liel, Abbie B., Haselton, Curt B., and Gregory G. Deierlein. 2011. "Seismic Collapse Safety of Reinforced Concrete Buildings. II: Comparative Assessment of Nonductile and Ductile Moment Frames." *Journal of Structural Engineering* 137(4):492–502.
- [7] Abou-Elfath, Hamdy, and Ahmed Ghobarah. 2000. "Behaviour of reinforced concrete frames rehabilitated with concentric steel bracing." *Canadian Journal of Civil Engineering* 27(3):433–444.
- [8] Badoux, Marc, and James O. Jirsa. 1990. "Steel bracing of RC frames for seismic retrofitting." *Journal of Structural Engineering* 116(1):55–74.
- [9] Maheri, Mahmoud R., and Akbar Hadjipour. 2003. "Experimental investigation and design of steel brace connection to RC frame." *Engineering Structures* 25(13):1707–1714.
- [10] Massumi, Ali, and Abbas A. Tasnimi. 2008. "Strengthening of low ductile reinforced concrete frames using steel X-bracings with different details." Paper presented at the 14th World Conference on Earthquake Engineering, Beijing, China, October 12–17.
- [11] TahamouliRoudsari, Mehrzad, Entezari, Alireza, Hadidi MohammadHessam, and Omid Gandomian. 2017. "Experimental assessment of retrofitted RC frames with different steel braces." *Structures* 11:206–17.
- [12] Maheri, Mahmoud R., and Hosein Ghaffarzadeh. 2006. "Internal steel bracing for seismic design of RC buildings." Paper presented at the 8th International Conference on Steel & Space Structures, Kuala Lumpur, Malaysia, May 15–17.
- [13] Mahrenholtz, Christoph, Lin, Pao-Chun, Wu, An-Chien, Tsai, Keh-Chyuan, Hwang, Shyh-Jiann, Lin, Ruei-Yan, and Muhammad Y. Bhayusukma. 2015. "Retrofit of reinforced concrete frames with buckling-restrained braces." *Earthquake Engineering & Structural Dynamics* 44(1):59–78.
- [14] Yooprasertchai, Ekkachai, and Pennung Warnitchai. 2008. "Seismic retrofitting of low-rise nonductile reinforced concrete buildings by buckling-restrained braces." Paper presented at the 14th World Conference on Earthquake Engineering, Beijing, China, October 12–17.
- [15] Eligehausen, Rolf, Mallée, Rainer, and John F. Silva. 2006. *Anchorage in Concrete Construction*. Berlin: Ernst & Sohn.
- [16] European committee for standardization. 2018. *EN1992-4:2018 (E) - Eurocode 2 Design of concrete structures – Part 4. Design of fastenings for use in concrete*. Brussels, Belgium: European committee for standardization.
- [17] Lee, Cheol-He. 2002. "Seismic Design of Rib-Reinforced Steel Moment Connections based on Equivlaent Strut Model." *Journal of Structural Engineering* 128(9):1121–1129.
- [18] Ožbolt, Joško, Li, Yijun, and Ivica Kožar. 2001. "Microplane model for concrete with relaxed kinematic constraint." *International Journal of Solids and Structures* 38(16):2683–2711.
- [19] Ožbolt, Joško. "MASA: Finite element program for 3D nonlinear analysis of concrete and reinforced concrete structures." Manual, Institute of Construction Materials, University of Stuttgart, Germany.

- [20] Grosser, Philipp R. 2012. "Load-bearing behavior and design of anchorages subjected to shear and torsion loading in uncracked concrete." PhD diss., University of Stuttgart.
- [21] Stehle, Erik J., and Akanshu Sharma. 2019. "Numerical Investigation of Anchor Groups Under Seismic Tension Actions." *Otto Graf Journal* 18:313–324.
- [22] Stehle, Erik J., and Akanshu Sharma. 2020. "Seismic Behavior of Anchor Groups – Experimental and Numerical Study." Paper presented at the 17th World Conference on Earthquake Engineering, Sendai, Japan, September 13–18.

Finite element modeling of size effect on punching shear strength concrete slabs without shear reinforcement

Rafael Sanabria Díaz, Leandro Mouta Trautwein and Luiz Carlos de Almeida

*LABMEM, Structural Modeling and Monitoring Laboratory,
Universidade Estadual de Campinas,
Av. Albert Einstein, 951, 13083-852, Campinas, Brazil*

Abstract

The size effect is an important factor in the shear strength of reinforced concrete elements (e.g., beams and flat slabs). In this paper, nonlinear numerical analyses are carried out to study the influence of the size effect in the punching shear resistance of reinforced concrete slabs without shear reinforcement. Experimental tests of isolated flat slab specimens were simulated to validate the adopted material constitutive laws and modeling strategies. In general, the numerical models provided a reasonable estimation of the failure load and reproduced the size effect observed in the experimental tests. The numerical and experimental results were analyzed and compared with analytical approaches. Furthermore, the results were compared with design code equations, including the recent ACI-318-19, the *fib* Model Code 2010 and Eurocode 2.

1 Introduction

The size effect refers to the reduction of the nominal strength with the increase of the structural size. In the case of cementitious materials, both the nominal strength and material brittleness decrease with increasing element size under tension. Different experimental works have recognized that this phenomenon plays an important role in the shear strength of reinforced concrete elements (e.g., beams and flat slabs) without shear reinforcement. Despite the intensive research in the last decades, there is still no consensus on the mechanics governing the size effect and how to implement it within a physical approach.

Pioneering works related to size effect in quasi-brittle materials, such as concrete, were carried out by Bažant (1984) [1]. Based on fracture mechanics, he proposed an energy-based size effect law (SEL) in which the phenomenon is associated with the energy rate released in the cracking process and the fracture process zone (FPZ). The SEL accounts for the transition between strength criterion (limit state) for small structures and linear fracture mechanics for very large structures. This law has been widely used to study the shear failure of RC members, especially beams. For the case of punching shear, Bažant and Cao (1987) [2] proposed a semi-empirical equation based on the proposed structural size effect law and databank evaluations. However, the databank did not contradict the proposed equation, but it either validated. As an alternative, several authors proposed empirical coefficients to consider the size effect as a function of the effective slab depth based on experimental punching shear tests. [3]-[6].

A different approach to consider the size effect in concrete structures has been proposed in the Modified Compression Field Theory (MCFT) [7] and the Critical Shear Crack Theory (CSCT) [8]. According to these models formulation, the size effect can be directly accounted through the crack width and the aggregate interlock mechanism in the shear cracks, without including additional coefficients. Although this approach seems to be more appropriate, recently, some critics were raised about the assumption and hypothesis of the MCFT and CSCT and their divergence with the SEL [9],[10]. Furthermore, the criticism was refuted in [11], [12].

Due to this controversy, this work aims to investigate the size effect by simulating experimental tests of slab-column connections. In the simulations, the smeared fixed crack approach is used to represent concrete nonlinear behavior. After the validation of the numerical strategies, the experimental test data was extended with additional models, and it was compared with the provisions of CSCT and the punching shear equation proposed by Dönmez and Bažant (2017) [9]. Finally, the results are compared with code provisions, including the recent ACI 318-19 [13], the current Eurocode 2 [14], and the *fib* Model Code 2010 [15].

2 Application of NLFEA to investigate slab punching

Finite elements (FE) simulations have been used in the last decades to study the behavior of reinforced concrete structures. The first works applied rotational symmetric continuum elements to simulate the punching shear failures (e.g., [16]). With the development of computer capacities, the numerical investigations focused on the application of spatial (3D) continuum elements using, in most cases, the smeared crack approach (e.g., [17], [18], [19] among others). In this paper, the software DIANA FEA (version 10.3) is used to simulate the punching shear failure. The following section explains the constitutive model implemented to represent the nonlinear behavior of reinforced concrete.

2.1 Material constitutive models

The concrete behavior was modeled using the total strain fixed smeared crack approach implemented in DIANA FEA, which is based on the formulations of the MCFT (Vecchio and Collins, 1993 [7]) and its 3D extension by Selby and Vecchio (1997) [20]. Before cracking, the concrete is represented as a linear elastic isotropic material. As soon as the principal stress violates the tensile strength in an integration point, the isotropic formulation is switched into an orthotropic formulation defined at a local coordinate system along the crack planes. The cracked concrete is treated as a continuum material, and the quase-brittle behavior is simulated with the reduction of the material strength as a function of the loading history. In this model, both the tensile and the compressive behavior of concrete can be captured within uniaxial stress-strain for tension and compression.

The adopted stress-strain tension softening curve is considered according to Hordijk (1991) [21] as a function of the fracture energy (G_F) and tensile strength (f_t). The concrete compressive behavior is described with the parabolic curve proposed by Feenstra (1993) [22], in which the softening of the concrete is governed by the compressive fracture energy (G_c) and the characteristic element length (h). The failure criterion for compression considers lateral confinement, according to Hsieh et al. (1982) [23]. A variable shear retention factor is used for the reduction of the shear stiffness in the cracked state. The cracked shear modulus is calculated assuming that the secant shear stiffness degrades at the same rate as the normal stiffness due to cracking and considering the reduction of the Poisson's ratio as a function of crack strain values. The reinforcing bars adopted a linear elastic-ideally plastic behavior. Additionally, interface elements are used to model the bond stress and slip between the steel bar and concrete.

3 Benchmark

The described reinforced concrete constitutive model was validated through the numerical simulation of experimental tests performed by Guandalini et al. (2009) [24]. The selected slab tests were focused on studying the size effect and reinforcement ratio in punching shear failure. The specimens corresponded to squared isolated slab and represented the negative moment region of an internal column (Figure 1). In total, seven isolated slab specimens were considered for the numerical investigation (Table 1). These specimens were divided into three categories half-size, full-size, and double-size. The amount of flexural reinforcement (ρ) ranged between 0.28% and 1.5% with yielding stress (f_y) about 550 MPa. The slabs were cast with a 30 MPa concrete strength (f_c) and a maximum aggregate size of 16 mm.

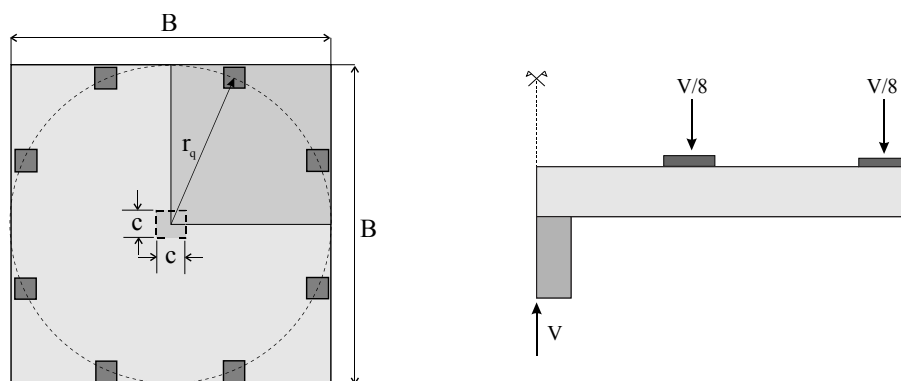


Fig. 1 Geometry of slabs tested by Guandalini et al. (2009) [24]: plan view (left) and lateral view (right).

Table 1 Main parameters of the series tested by Guandalini et al. (2009) [24].

Slab	Dimensions				Material properties		
	B [m]	r_q [m]	c [m]	d [m]	f_c [MPa]	ρ [%]	f_y [MPa]
PG-8	1.5	0.752	0.130	0.117	34.7	0.28	525
PG-10	3.0	1.50	0.260	0.210	28.5	0.33	577
PG-3	6.0	2.85	0.520	0.456	32.4	0.33	520
PG-7	1.5	0.752	0.130	0.100	34.7	0.75	550
PG-11	3.0	1.50	0.260	0.210	31.5	0.75	570
PG-6	1.5	0.752	0.130	0.096	34.7	1.5	526
PG-1	3.0	1.50	0.260	0.210	27.6	1.5	573

3.1 Modeling strategies

The slab and steel plates were represented by a structural mesh consisting of hexahedral elements with 20 nodes and quadratic interpolation. Interface elements, with zero tensile stiffness, were placed between the concrete and plate elements. Reinforced bars were represented by embedded beam elements, that included bond-slip with concrete elements. As shown in Figure 2, only one-quarter of the slabs was simulated in order to reduce computational cost. Lateral constraints were imposed at the symmetry axis, and vertical displacement was restricted at support plates. The test loading was simulated with an incremental displacement at the center node of the loading plate.

All the FE models were discretized with eight element layers through the slab thickness; this means that, in general, the number of degrees of freedom was the same for all the simulations. This approach covers the possibility of mesh bias, which may occur using smeared crack models [25]. As shown in Figure 2, a more refined mesh was used close to the loaded area, where was expected to occur the punching shear failure. For the simulations, the material properties were modelled according to the data reported from the tests and the constitute models presented in the previous sections. The crack band, h , was considered as the cubic root of element volume. For the incremental iterative solution analysis, the quasi-Newton (secant) method was adopted. The convergence criteria were based on energy and force balance criteria.

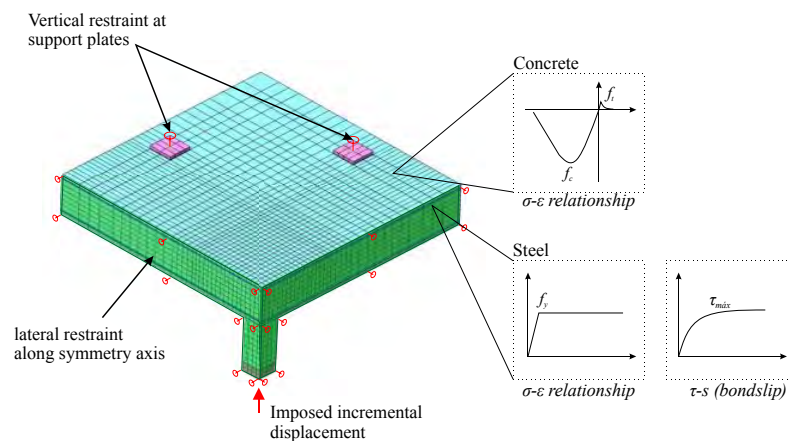


Fig. 2 Typical mesh and boundary conditions adopted for the simulations.

3.2 Comparison between numerical and experimental results

The ultimate punching capacity, the load-rotation (ψ) response and crack pattern between the numerical and experimental results are compared in this section. As can be seen in Figure 3(a), the punching shear was accurately estimated by the numerical simulations. This comparison reveals that the size effect observed experimentally was reproduced numerically with a good agreement. This result is also verified in Figure 3(b), in which the load-rotation response of slabs PG-10 (normal-size) and PG-3 (double-size)

are compared. The shape of the curves confirms that the failure in the double-size slab is caused mainly by a brittle cracking failure at an ultimate load lower than the slab's flexural capacity. On the other hand, the slab PG-10 exhibits a long horizontal plateau, indicating ductile behavior. These results represent a confirmation of the size effect law. The numerical simulations carried out in this study were capable of representing this behavior.

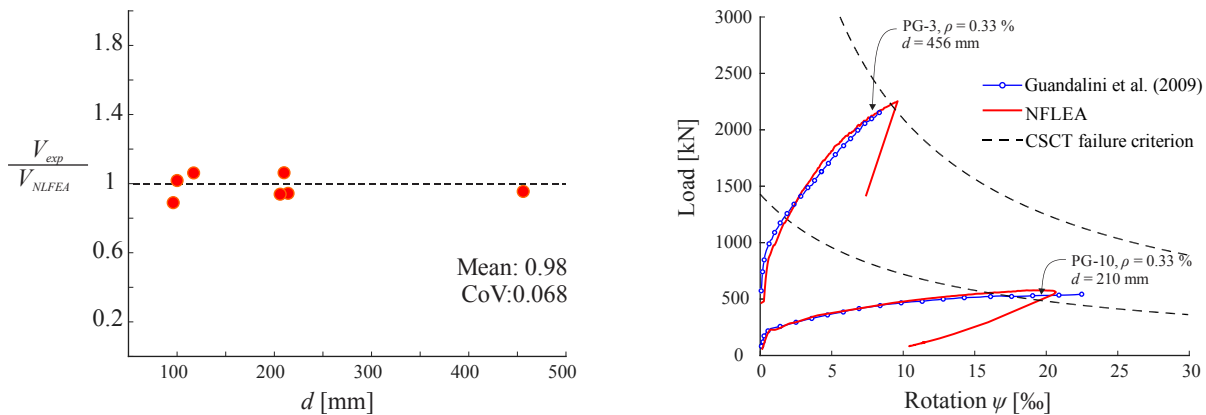


Fig. 3 Punching shear capacity (left). Load-rotation curves of PG-10 and PG-3 slabs (right).

The numerical cracking pattern was obtained multiplying the maximum principal strain by the characteristic element length (h). The Figure 6 presents the comparison of the crack patterns of slab PG-3 and PG-10 at the peak load. In the numerical contour plot, the color legend corresponds to the status crack, and it is linked to the Hordijk (1991) [21] softening curve. Based on the location and the shape of the critical shear cracks, the simulations show a good agreement with the experimental failure cracks. Furthermore, numerical models were able to capture the localized punching shear crack at the peak load.

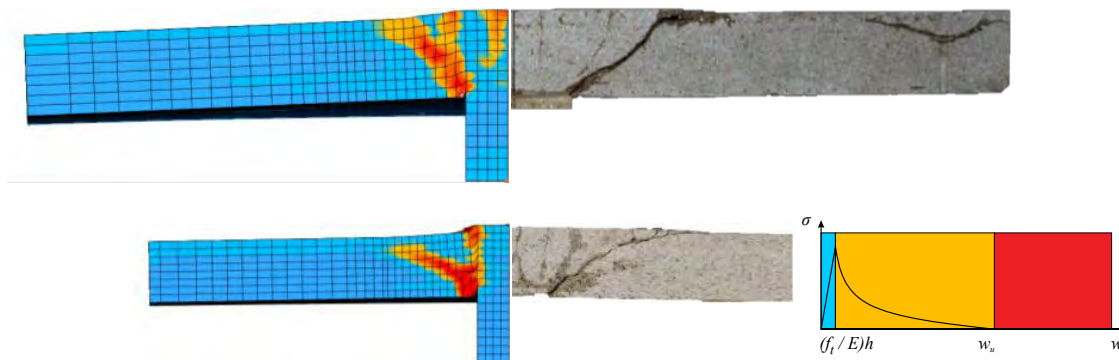


Fig. 4 Comparison between the numerical and experimental crack patterns at peak load for slabs PG-3 (top) and PG-10 (bottom). The color legend indicated the status crack: elastic, no crack (blue), opening (orange), and full opening (red).

4 Comparison of predicted the size effect according to the CSCT and Fracture Mechanics

To investigate the size effect on punching shear failure and extend the experimental data obtained by Guandalini et al. (2009) [24], three additional models were simulated in this study. Using the constitutive models and modelling strategies, validated in previous section, the following slabs were simulated: (i) half-size with $\rho = 0.33\%$; (ii) double-size with $\rho = 0.75\%$, and (iii) double-size with $\rho = 1.5\%$. The load obtained from the numerical models was compared to the ones calculated according to the CSCT and the equation proposed by Dönmez and Bažant (2017) [9].

Dönmez and Bažant (2017) [9] proposed the Equations 1-3 for the punching shear strength in two ways slabs based on least-square optimization of the fit of the ACI 445 database, using fracture mechanics principles:

$$v_c = v_0 \theta \quad (1)$$

$$v_0 = \lambda \sqrt{f_c} (100\rho)^{0.3} \left(\frac{d}{b}\right)^{0.2} \left(\frac{c}{b}\right)^{0.4} \quad (2)$$

$$\theta = \frac{1}{\sqrt{1 + d/d_0}} \quad (3)$$

where v_0 is the nominal punching shear strength, θ is the size effect factor; d_0 and λ are empirical constants corresponding to 60 mm and $2.0 \text{ MPa}^{1/2}$, respectively, and b is the perimeter of the loaded area.

In the mechanical model proposed by Muttoni (2008) [8], the punching shear capacity is calculating as a function of the aggregate size (d_g) and the opening of a critical shear crack. The punching load is estimated by applying the following failure criterion :

$$\frac{V}{b_0 d \sqrt{f_c}} = \frac{3/4}{1 + 15 \frac{\psi d}{d_{g,0} + d_g}} \quad (4)$$

where b_0 is the perimeter measured at distance $d/2$ from column face and $d_{g,0}$ is the reference aggregate size (16 mm). Despite the theoretical background and experimental validation of the CSCT, some discussion has been raised about how the size effect is accounted for in this approach. According to the energetic size effect law (SEL), the steepest possible slope for $d \rightarrow \infty$ is $-1/2$ (in double-log scale), corresponding to the energy dissipation by a point-wise crack tip. However, the CSCT predicts an asymptotic slope for size effect in punching failure milder than $-1/2$. In fact, the load-rotation curve (based on quadrilinear moment-curvature) and the failure criterion yields to an influence of the size effect on punching strength governed by a slope closer to $-1/3$. This trend is justified by the redistribution of internal forces in redundant structures such as flat slabs [26].

The previous approaches were compared with the numerical results obtained from the simulations. Figure 5 compares the load-rotation response of the additional simulations with the quadrilinear load-rotation relationship. Furthermore, the punching load obtained based on the CSCT failure criterion and the equation proposed by Dönmez and Bažant (2017) are also compared. It can be observed that in general, both approaches gave similar estimation.

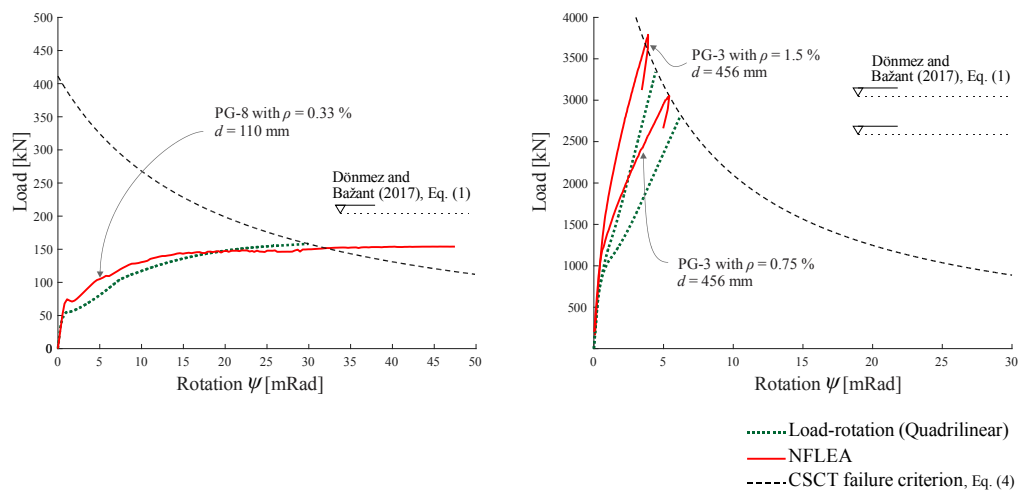


Fig. 5 Additional numerical models: PG-8 (half-size) with $\rho = 0.33\%$ (left); PG-3 (double-size) with $\rho = 0.75\%$, and PG-3 with $\rho = 1.5\%$ (right). Comparison of load predicted by the CSCT, the equation proposed by Dönmez and Bažant (2017) [9], and numerical simulation.

Figure 6 shows the nominal punching shear strength, v_c , as a function of d in a double-log scale plot for the three different reinforcement ratios. The SEL curve was adjusted to the NLFEA results using the Levenberg-Marquardt nonlinear regression algorithm. In the three plots is observed a reduction of v_c by increasing the value of d . The estimations by Dönmez and Bažant (2017) [9] equation tend to be steeper than the ones predicted by the numerical simulations and the CSCT. However, the difference is small, at least for values of d used in slabs for practice design (100-500 mm).

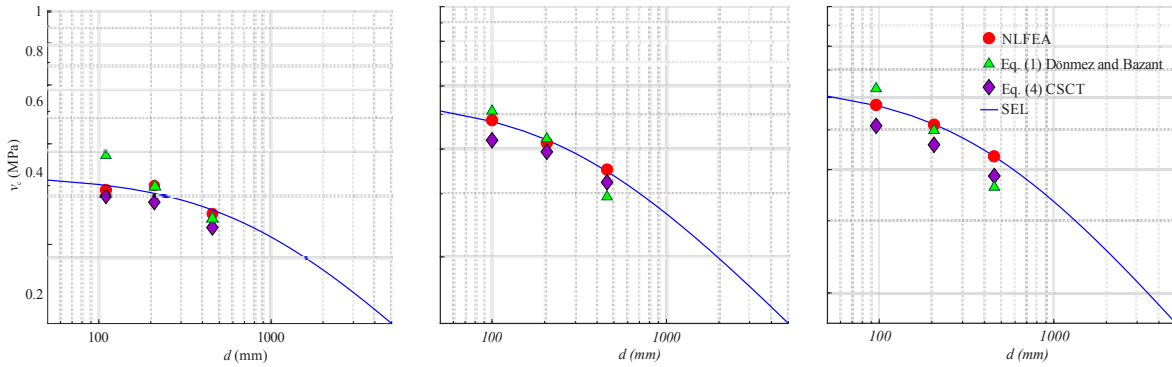


Fig. 6 Comparison of the nominal punching shear resistance determined by CSCT and the equation proposed Dönmez and Bažant (2017) [9] and the SEL fitted according the numerical results for $\rho = 0.33\%$ (left), $\rho = 0.75\%$ (center), and $\rho = 1.5\%$ (right).

4.1 Comparison with design code equations

In general, punching shear design code provisions rely on the verification of the shear stress on a critical perimeter defined at a certain distance of the column. According to the ACI 318-19, for square columns, the punching shear strength is calculated as : (in SI units; MPa, mm):

$$V_{ACI} = \frac{1}{3} b_{ACI} d \lambda_s \lambda \sqrt{f_c}; \quad \lambda_s = \sqrt{\frac{2}{1 + 0.004 \cdot d}} \leq 1 \quad (5)$$

where b_{ACI} is the control perimeter, with straight corners, located at a distance $d/2$ away from the column face, d is the effective depth, λ is the modification factor for lightweight concrete, taken as one for normal-weight concrete, and λ_s is a factor for accounting for size effect.

For the punching shear capacity, the current Eurocode 2 (2004) specifies:

$$V_{EC2} = 0.18 b_{EC2} d \xi (100 \rho f_c)^{1/3}; \quad \xi = 1 + \sqrt{\frac{200 \text{ mm}}{d}} < 2 \text{ mm} \quad (6)$$

where b_{EC2} is the control perimeter, with rounded corners, located at a distance $2d$ away from the column face, ρ is the flexural reinforcement ratio and ξ is the size effect factor.

The *fib* Model Code 2010 formulation is based on the CSCT. For design purposes, the punching shear capacity can be estimated using the Equation 5 and a simplified load-rotation relationship (Equation 6), in which the rotation, ψ , is function of the distance of zero radial moment (r_s), the shear force (V), the nominal moment capacity (m_R), and the yield strength and elastic modulus of flexural reinforcement (f_y and E_s , respectively):

$$\psi = 1.5 \frac{r_s}{d} \frac{f_y}{E_s} \left(\frac{V}{8m_R} \right)^{3/2} \quad (7)$$

Figure 7 summarizes the comparison of the shear punching strength estimated according to current design codes. Only the experimental tests with punching failure were considered for this comparison (specimens PG-8 and PG-10 were excluded). For the double-size, the additional numerical models were included with the punching load obtained from the nonlinear analysis. It is to say that the comparison of code provisions with experimental results is not completely fair because the code are may use different partial safety factors. Nevertheless, this type of comparison is important to get an idea of the safety margins and identified unconservative results.

For the slabs analyzed in this paper, the predictions of the EC2 are closer to the experimental values; however, for the PG-3 (double-size) slab with $\rho = 0.33\%$, the predicted value is slightly higher than the experimental one. The ACI 318-19 shows a good safety margin, except for the PG-3 slab, in which the strength is overestimated by 32%. The fib MC (LoA II) presented the safety estimation for all the sizes and reinforced ratios, with the smallest coefficient variation (0.064).

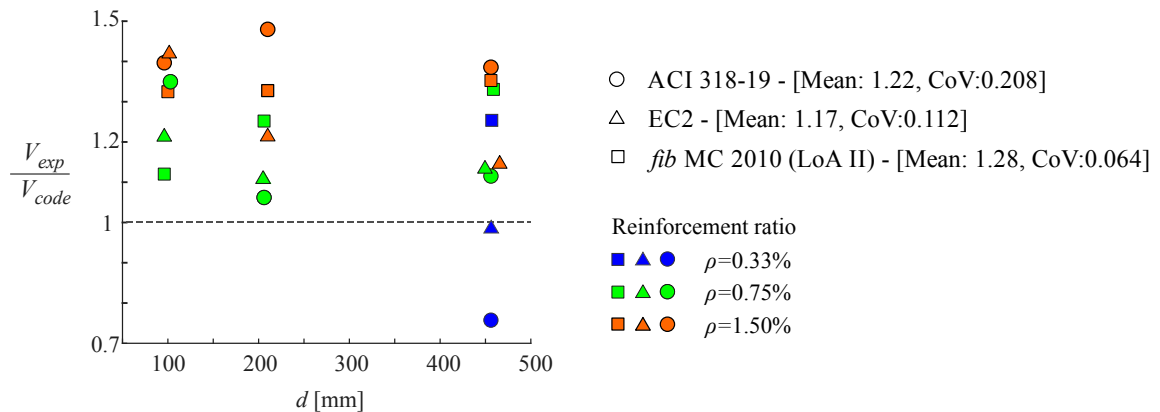


Fig. 7 Comparison of the nominal punching shear resistance predicted by different design codes and the experimental results obtained by Guandalini et al. (2009) [24]. For the full-size slabs, the comparison was extended using the numerical results obtained in this study.

5 Conclusions and Outlook

In this paper, nonlinear simulations were carried out to study the size effect in punching shear failure of reinforced concrete flat slabs. Experimental tests were used as a benchmark to validate the material parameters adopted and the modeling strategies. In general, the numerical simulations provide a reasonable estimation of the failure load and the rupture mode. The size effect observed in the tests was well represented in the analyses. As the slab thickness increased, the punching shear strength decreased and a more brittle failure was observed in the simulations. Furthermore, the numerical models were able to capture the localized punching shear crack at the peak load. The comparison between the CSCT and the punching shear equation proposed by Dönmez and Bažant (2017) showed that both approaches gave similar estimation for the ranges of d considered in this study. Thus, both approaches are suitable for account the size effect for punching shear design. Finally, the comparison with the code equations showed that the fib MC (LoA II) presents a safety margin for all the sizes and reinforced ratios with the smallest coefficient variation in the analyzed sample.

Future studies will focus on the analysis of the influence of shear reinforcement on the size effect as well as the influence of slab continuity.

Acknowledgments

The authors would like to acknowledge the support given by the Brazilian Coordination for the Improvement of Higher Education Personnel (CAPES) - Grant No. 88882.435128.

References

- [1] Bažant, Z. P. (1984). "Size effect in blunt fracture: concrete, rock, metal." *Journal of engineering mechanics*, 110(4), 518-535.
- [2] Bažant, Z. P., and Cao, Z. (1987). "Size effect in punching shear failure of slabs. " *ACI Structural Journal*, 84(1), 44-53.
- [3] Regan, P. E. e M. W. Braestrup (1985). "Punching Shear in Reinforced Concrete: A State of Art Report". *Bulletin d'Information*, No. 168. Lausanne, International Federation for Structural Concrete (fib): 232.
- [4] Broms, C. E. (1990). "Punching of Flat Plates - A Question of Concrete Properties in Biaxial Compression and Size Effect." *ACI Structural Journal*, Vol. 87, No. 3: 292-304.
- [5] Shehata, I. A. E. M. (1990). "Rational Method for Designing RC Slabs to Resist Punching." *Journal of Structural Engineering*, Vol. 116, No. 7(ASCE): 2055-2060.

- [6] Sherif, A. G. e W. H. Dilger (1996). "Critical review of the CSA A23.3-94 punching shear strength provisions for interior columns." *Canadian Journal of Civil Engineering*, Vol. 23, No. 5(NRC): 998-1011.
- [7] Vecchio, F. J., and Collins, M. P. "The modified compression-field theory for reinforced concrete elements subjected to shear." *ACI Structural Journal*. Vol. 83, No. 2, p. 219–231, 1986.
- [8] Muttoni, A. (2008). "Punching Shear Strength of Reinforced Concrete Slabs without Transverse Reinforcement." *ACI Structural Journal*, Vol. 105, No. 4: 440-450.
- [9] Dönmez, A., and Bažant, Z. P. (2017). "Size effect on punching strength of reinforced concrete slabs with and without shear reinforcement." *ACI Structural Journal*, 114(4), 875.
- [10] Dönmez, A., and Bažant, Z. P. (2019). "Critique of critical shear crack theory for fib Model Code articles on shear strength and size effect of reinforced concrete beams." *Structural Concrete*, 20(4), 1451-1463.
- [11] Muttoni, A., & Fernández Ruiz, M. (2019). "From experimental evidence to mechanical modeling and design expressions: The Critical Shear Crack Theory for shear design." *Structural Concrete*, 20(4), 1464-1480.
- [12] Bentz, E. C., & Foster, S. J. (2019). "On shear in members without stirrups and the application of energy-based methods in light of 30 years of test observations." *Structural Concrete*, 20(4), 1481-1489.
- [13] ACI Committee 318 (2019). *Building code requirements for structural concrete (ACI 318-19)*. ACI, 403 Farmington Hills, MI.
- [14] CEN (European Committee for Standardization) (2004). *Eurocode 2: Design of Concrete Structures. Part 1-1: General rules and rules for buildings*. Thomas Telford, Brussels, Belgium.
- [15] fib (Fédération Internationale du Béton) (2013). *fib model code for concrete structures 2010 (MC-2010)*. Ernst and Sohn.
- [16] Menétrey, P. (1994). "Numerical analysis of punching failure in reinforced concrete structures." Ph.D. thesis, École polytechnique fédérale de Lausanne, Lausanne, Switzerland.
- [17] Mamede, N. F. S., Ramos, A. P., and Faria, D. M. (2013). "Experimental and parametric 3d nonlinear finite element analysis on punching of flat slabs with orthogonal reinforcement." *Engineering Structures*, 48, 442–457.
- [18] Genikomsou, A. S. and Polak, M. A. (2016). "Finite-element analysis of reinforced concrete slabs with punching shear reinforcement." *Journal of Structural Engineering*, 142(12), 04016129.
- [19] Goh, C. Y. M. and Hrynyk, T. D. (2018). "Numerical investigation of the punching resistance of reinforced concrete flat plates." *Journal of Structural Engineering*, 144(10), 04018166.
- [20] Selby, R. and Vecchio, F. (1997). "A constitutive model for analysis of reinforced concrete solids." *Canadian Journal of Civil Engineering*, 24(3), 460–470.
- [21] Hordijk, D. (1991). "Local approach to fracture of concrete." Ph.D. thesis, Delft University of Technology, Delft, The Netherlands.
- [22] Feenstra, P. H. (1993). "Computational aspects of biaxial stress in plain and reinforced concrete." Ph.D. thesis, Delft University of Technology, Delft, The Netherlands.
- [23] Hsieh, S., Ting, E., and Chen, W. (1982). "A plastic-fracture model for concrete." *International Journal of Solids and Structures*, 18(3), 181–197.
- [24] Guandalini, S., Burdet, O., and Muttoni, A. (2009). "Punching tests of slabs with low reinforcement ratios." *ACI Structural Journal*, Vol. 106, No. 1.
- [25] Cervenka, V., Cervenka, J., & Kadlec, L. (2018). "Model uncertainties in numerical simulations of reinforced concrete structures." *Structural Concrete*, 19(6), 2004-2016.
- [26] Fernández Ruiz, M., & Muttoni, A. (2018). "Size effect in shear and punching shear failures of concrete members without transverse reinforcement: Differences between statically determinate members and redundant structures." *Structural Concrete*, 19(1), 65-75.

Strengthening of Flat Slabs to Increase in Shear Resistance Using Post-Installed Shear Reinforcement

Mária Bolešová, Katarína Gajdošová

*Faculty of Civil Engineering STU in Bratislava,
Slovak University of Technology in Bratislava,
Radlinskeho 11, 810 05 Bratislava, Slovakia*

Abstract

A lot of existing flat slabs requires strengthening to increase in punching shear resistance because of the increase in applied loads (change of use of the building, replacement of floors, ceilings, and non-bearing structure), defects during design or construction, or even for the reason of meeting more strict code requirements. Shear stresses have the most significant effects near the support (column, wall), which can result in a very sudden collapse of the structure. The paper is focused on strengthening reinforced concrete flat slabs with the post-installed shear reinforcement (bolts and screw anchors). Numerical verification was performed on experimentally tested fragments of flat slabs. According to the observed results, the new experimental study was determined. This work presents the results of numerical models for setting up the following experimental study.

1 Introduction

Locally supported flat slabs without shear reinforcement are the frequently used structure. The high concentration of the shear stresses around the support may lead to the brittle failure of the slab. Therefore, attention should be paid to designing and strengthening these structures. The flat slab with low shear resistance is a common situation for structural engineers to deal with when renovating an existing building. One of the strengthening techniques uses post-installed shear reinforcement, for which the research is being prepared at the Slovak University of Technology in Bratislava. In engineering practice, a model developed for new constructions is used, although there are some differences in the behavior of strengthened and new flat slabs.

The experimental program aims to verify the shear resistance of the flat slabs that have been preloaded before strengthening. To prepare the experimental study, it was first necessary to perform a numerical analysis, which was based on experimental studies performed at our university before. At the Slovak University of Technology in Bratislava, a large part of the experimental work focuses on flat slabs, their maximum shear capacity, the effect of openings near the support, and also on the installation of shear reinforcement.

All investigated specimens have a square floor plan with a length of 2.5 m and a width of 2.5 m. The material and geometric properties of the experimental specimens are given in Table 1.

Maximum shear capacity was verified by Majtanova (2017) [1]. The experimental testing was performed on the specimens of 250 mm thick flat slabs, with compressive strength of concrete of 28 MPa, longitudinal reinforcement ratio of 1.57 %, and with or without shear reinforcement. As a shear reinforcement, 10 radii with 16 studs of the diameter of 10 mm on each radius were used. The slab was supported by a column with a circular cross-section with a diameter of 180 mm. The specimen without shear reinforcement resulted in brittle punching at a shear force of 690 kN. The specimen with shear reinforcement failed by crushing concrete struts at a shear force of 1250 kN.

The effect of post-installed shear reinforcement was verified by Keseli (2018) [2] on the specimens with a thickness of 250 mm, with longitudinal reinforcement ratio ρ_l of 1.7%, the compressive strength of concrete of 74,3 MPa and 29,5 MPa, supported by the column with the circular cross-section with the diameter of 250 mm. Two types of shear reinforcement were used: post-installed shear bolts and bonded post-installed shear anchors, both of them were bonded with chemical adhesive. The failure of the strengthened specimen by using anchors was within the shear-reinforced region. The strengthened specimen by using bolts failed in flexure.

The results of experimental measurements were compared with theoretical predictions according to three numerical approaches - Eurocode 2 [3], Model Code 2010 [4] [5], and the latest version of the new generation of Eurocode 2 [6], see Table 1.

The results of the numerical calculation according to Model Code 2010 are in very good compliance with the experimental results of Majtanova (2017) [1]. The failure of the first specimen without shear reinforcement is determined by the shear strength of the concrete and the longitudinal reinforcement ($V_{R,c}$). In the second specimen, the shear reinforcement (double-headed studs) increases the shear resistance and the failure is determined by the maximum punching shear resistance in the face of the column ($V_{R,max}$). When calculated according to Eurocode 2 the value of $C_{R,c}$ is considered to be 0.18 MPa.

The other two specimens are the part of the experimental research provided by Keseli (2018) [2]. The first specimen is strengthened by using a post-installed shear reinforcement (bonded bolts) with a very high value of concrete compressive strength, which caused a higher capacity in shear which caused the bending failure. The second specimen with post-installed bonded anchors failed at the front of the column due to a lack of maximum shear resistance ($V_{R,max}$).

Table 1 Comparison of experimental results of different specimens with numerical approaches

Specimen	f_{cm}	ρ_l	Shear reinforcement	Maximum experimental resistance	Type of failure	Eurocode 2 $\min(V_{R,max}; V_{R,cs})$ or $\min(V_{R,max}; V_{R,c})$	Model Code 2010 $\min(V_{R,max}; V_{R,cs})$ or $\min(V_{R,max}; V_{R,c})$	Eurocode 2, 2021-01 $\min(V_{R,max}; V_{R,cs})$ or $\min(V_{R,max}; V_{R,c})$	Bending resistance	Nonlinear analysis calculated in program AETNA
	MPa	%	-	kN	-	kN	kN	kN	kN	kN
Majtanova WSR ¹	28.1	1.57	none	690	punching - $V_{R,c}$	785	690	625	1780	700
Majtanova SR ² – studs	28.3	1.57	16 ϕ 10 mm	1250	max. shear - $V_{R,max}$	850	1265	1135	1780	1200
Keseli SR – bolts	74.3	1.70	12 ϕ M20 mm	1890	flexure	2280	2180	2160	1985	1950
Keseli – SR bonded anchors	29.5	1.74	8 ϕ M20 mm	1170	max. shear - $V_{R,max}$	1110	1370	1070	1750	1120

¹ specimen without shear reinforcement, ² specimen with shear reinforcement, f_{cm} – mean compressive strength of concrete (MPa), ρ_l – reinforcement ratio of bonded longitudinal reinforcement (%), ϕ – diameter of a reinforcing bar (mm), $V_{R,max}$ – maximum punching shear resistance of the slab (kN), $V_{R,c}$ – shear resistance of the slab without shear reinforcement (kN), $V_{R,cs}$ – shear resistance of the slab with shear reinforcement (kN)

The following experimental study will focus on reinforced flat slabs with a loading history.

2 Strengthening of flat slabs

2.1 Behavior of pre-damaged flat slabs

Due to the planned experimental verification of the effectiveness of the reconstruction, it is important to look at the behavior of the locally supported flat slab during its existence.

As the shear force V increases, the rotation of the slab ψ also increases (ψ refers to an angle between the horizontal axis and the deformed slab) until the flexural strength V_{flex} of the slab is reached. If the punching shear strength V_{Rl} of the flat slab is reduced and the rotation of the slab increases by unloading and reloading, the flat slab will fail (according to the failure criterion presented by Muttoni) [9]. The first crack opens around support (column) at the load value of V_{cr} that is approximately one-third of the

ultimate load and the service load V_{serv} is around 70% of V_{R1} [8]. The strengthened flat slab goes through several phases during its existence as it is shown in Fig 1. After the service load is applied to a new structure it has corresponding rotation (due to crack opening) represented by point A. During the flat slab strengthening, unloading, and installation of temporary supports under the pre-damaged slab, some open cracks close but the residual rotation $\psi_{residual}$ remains. The residual rotation and partial plasticizing of the reinforcing steel bars will reduce the shear strength from V_{R1} to V_{R2} (Fig.1). For this reason, a shear strength reduction should be considered when designing the strengthening of the flat slab, resulting in a previously damaged structure.

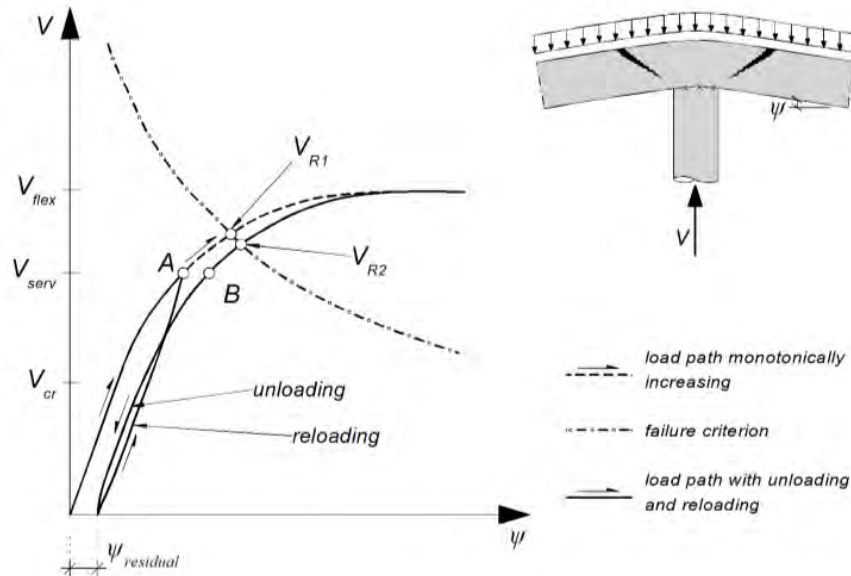


Fig. 1 Relationship between shear force and rotation of flat slab during loading, unloading, and reloading [8]. The failure criterion according to [7].

2.2 Methods for strengthening existing concrete flat slabs

The punching shear resistance depends on the effective depth of the slab, flexural reinforcement ratio, column size, concrete strength, yield strength of the reinforcing steel, maximum aggregate size, and the span to depth ratio of the slab. Not each numerical model takes all these factors into account.

In practice, the most used strengthening techniques are the enlargement of supporting area, strengthening with additional flexural reinforcement (by casting an additional concrete layer or near-surface mounted FRP reinforcement), or using a post-installed shear reinforcement.

The strengthening of a flat slab by casting a new additional concrete layer is an effective way to reliably increase in shear capacity (resistance without shear reinforcement $V_{R,c}$ and the maximum shear capacity $V_{R,max}$) but also the flexural resistance. The disadvantage of this strengthening technique is the demanding construction process in which it is necessary to remove the floor layers, roughen up the upper surface of the load-bearing structure to ensure the interaction of the existing slab with the new layer of concrete. In addition, this method affects the size of the door openings and the weight of the slab as a whole.

Another way to strengthen the flat slab is to increase the dimensions of the column, which does not increase the weight of the slab, does not have a significant effect on the floor layers, and also increases the load-bearing capacity of the column. The most problematic part during this reconstruction is to ensure interaction between the new concrete and the existing surface of the column.

The use of post-installed shear reinforcement for increasing the punching shear resistance of the flat slab does not affect the weight of the slab and the structure as a whole and the ceiling or the floor layers are only affected locally around the support. When adding bonded post-installed shear reinforcement in the form of glued anchors, it is not necessary to remove the floor layers, only the ceiling. It is not necessary to locate the bending reinforcement, because this type of reinforcement does not drill across the entire slab.

As an alternative to bonded anchors, the bolts without or even with the adhesive can be used. The position of the bending reinforcement should be known before installing the bolts, as the holes will be drilled through the whole slab thickness. The use of shear reinforcement can reliably ensure the transfer

of shear forces, but the maximum shear resistance of the slab on the face of the column ($V_{R,max}$) is not increased by this type of strengthening. This often becomes the limiting factor in increasing the shear resistance of the flat slab.

2.3 Behavior of strengthened flat slabs with post-installed shear reinforcement

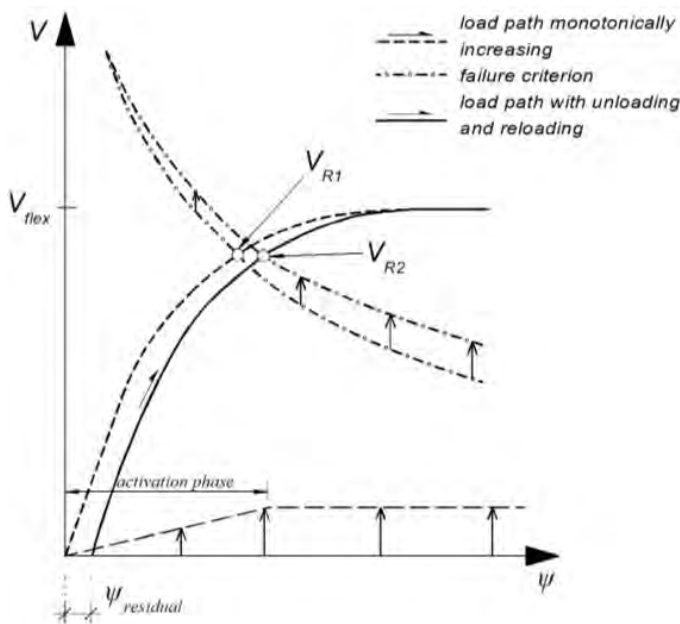


Fig. 2 The behavior of strengthened slab with post-installed shear reinforcement (according to [8]).

After the shear reinforcement is installed, the failure criterion line shifts vertically, as shown in Fig. 2. The strengthened flat slab has higher shear resistance and higher ductility. If the shear reinforcement is not prestressed, the reinforcement is activated only by the rotation of the slab (activation phase), therefore it is only able to transfer additional loads. It follows that a slab with a low rotational capacity can lead to a low level of utilization, and thus to low efficiency of this strengthening method because the slab fails before the shear reinforcement is fully activated.

3 Experimental study

3.1 Experimental specimens

The behavior of a previously loaded flat slab should be considered. The prepared experimental study is focused on the influence of a previously loaded and then strengthened flat slab to increase its shear resistance by non-bonded shear bolts.

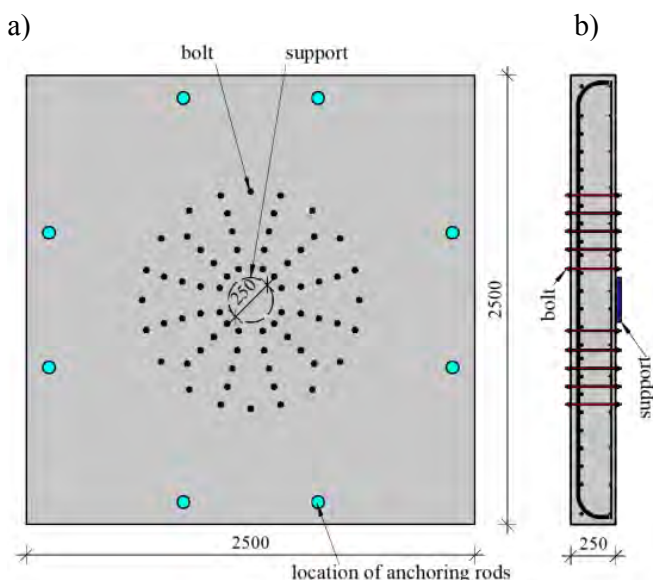


Fig. 3 The specimen with shear reinforcement a) top view and b) section.

The specimens (Fig. 3a,b) are squared in shape with dimensions of 2500 x 2500 mm and a thickness of 250 mm. The support of each specimen has a diameter of 250 mm and is represented by a steel plate. Each specimen has a mean compressive strength in the concrete of 30 MPa, yield strength of steel of 500 MPa, and a longitudinal reinforcement ratio of 1.57 %. Shear bolts are symmetrically distributed around the support and have a diameter of 12 mm or 10 mm with steel class 8.8 and 4.8, respectively. The bolts are made of threaded rods, larger and smaller washers, and nuts at both ends (Table 2). For better performance of shear reinforcement, bigger washers was used. According to a study by *Inacio et al.* [9], the washer or steel plate increases the contribution of the shear reinforcement to the shear resistance of the flat slab.

Table 2 Material mechanical and physical properties of the post-installed shear reinforcement

Shear reinforcement	Grade of steel	External diameter, d	Core diameter	Tensile strength, R_m	Stress at 0,2 % nonproportional elongation $R_{p0.2}$	Stress at 0,0048 d non-pro- portional elongation for full-size fasteners, R_{pf}	Percentage elon- gation after frac- ture for machined test pieces, A	Percentage elon- gation after frac- ture for full-size fasteners, A_f
		mm	mm	MPa	MPa	MPa	%	%
M10	4.8	9.968	8.128	500	-	400		22
M12	8.8	11.966	9.602	800	640	-	12	

Five specimens are prepared, one without and four with shear reinforcements. Two specimens are strengthened before loading. The other two specimens are loaded up to 50% and 75% of their shear resistance without shear reinforcement, then unloaded, strengthened with bolts (12 bolts with 10 mm in diameter), and reloaded again until failure. A numerical calculation was performed before the experimental verification.

3.2 Numerical analysis

Before the experimental verification, the numerical investigation was performed. Specimens with and without shear reinforcement are analyzed by using numerical models of Eurocode 2 [3], Model Code 2 [4], [5], and the latest version of new the generation of Eurocode 2 [6], and also by non-linear analysis in Atena 3D software.

Table 3 Comparison of different numerical approaches on an experimental specimen

Specimen	f_{cm}	ρ_l	Shear reinforcement	Theoretical type of failure	Eurocode 2 $\min(V_{R,max}; V_{R,cs})$ or $\min(\bar{V}_{R,max}; \bar{V}_{R,c})$	Model Code 2010 $\min(V_{R,max}; V_{R,cs})$ or $\min(\bar{V}_{R,max}; \bar{V}_{R,c})$	Eurocode 2, 2021-01 $\min(V_{R,max}; V_{R,cs})$ or $\min(\bar{V}_{R,max}; \bar{V}_{R,c})$	Bending resistance	Non-linear analysis calculated in AETNA software
	MPa	%			kN	kN	kN	kN	kN
FS-01 WSR ¹	30	1.57	none	punching - $V_{R,c}$	855	775	770	1910	800
FS-02 SR ²	30	1.57	12 ϕ M12 mm	Max. shear - $\bar{V}_{R,max}$	1490	1370 $V_{R,cs}$	1535	1910	1150
FS-03 SR ²	30	1.57	12 ϕ M10 mm	shear - $V_{R,cs}$	1490 $V_{R,max}$	1065	1230	1910	1040

¹ specimen without shear reinforcement, ² specimen with shear reinforcement, f_{cm} – mean compressive strength of concrete (MPa), ρ_l – reinforcement ratio of bonded longitudinal reinforcement, ϕ – diameter of a reinforcing bar (mm), $V_{R,max}$ – maximum punching shear resistance of the slab (kN), $V_{R,c}$ – shear resistance of the slab without shear reinforcement (kN), $V_{R,cs}$ – shear resistance of the slab with shear reinforcement (kN)

Due to the experimental program by Majtanova [1], the value of the maximum shear resistance $V_{R,max}$ in chapter 6.4.5 according to the Eurocode 2 was changed from 0.4 to 0.6.

The results according to the numerical models differ in the type of failure (Table 3), except for the specimen without shear reinforcement (FS-01), which fails by crushing a concrete strut. The specimen with shear reinforcement (FS-02, FS-03) fails in shear but results differ in the type of shear failure. The results from numerical models provide an idea of the future failure of experimental specimens.

The non-linear calculation in Atena 3D shows a smaller value of shear resistance with shear reinforcement than the results according to numerical models. The specimen without shear reinforcement has shown a good agreement between the results of the nonlinear and numerical calculation.

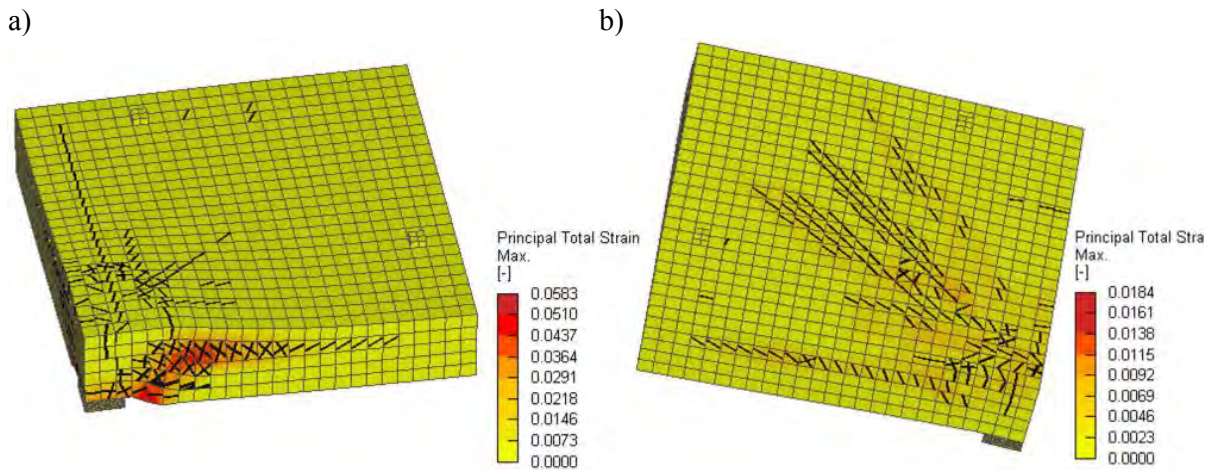


Fig. 4 Results from non-linear analysis of a) fragment from FS-01, b) fragment from FS-02.

3.3 Test setup

The configuration of the experimental program with post-installed shear reinforcement in a flat slab was performed by numerical models and nonlinear numerical analysis in the ATENA software (Fig. 4). Based on a good agreement between the numerical model and previously experimentally measured results, an experimental study was prepared. The test setup of the prepared experimental study is shown in Fig. 5.

The test setup is designed to simulate a flat slab with an inner column, which is performed by a hydraulic jack pushing a force on the sample and stabilizing rods.

Until the publication of the article, 3 samples were tested using post-installed shear reinforcement. Their resistance was higher than the calculation of shear resistance (in Table 2) according to the previously mentioned calculation models.

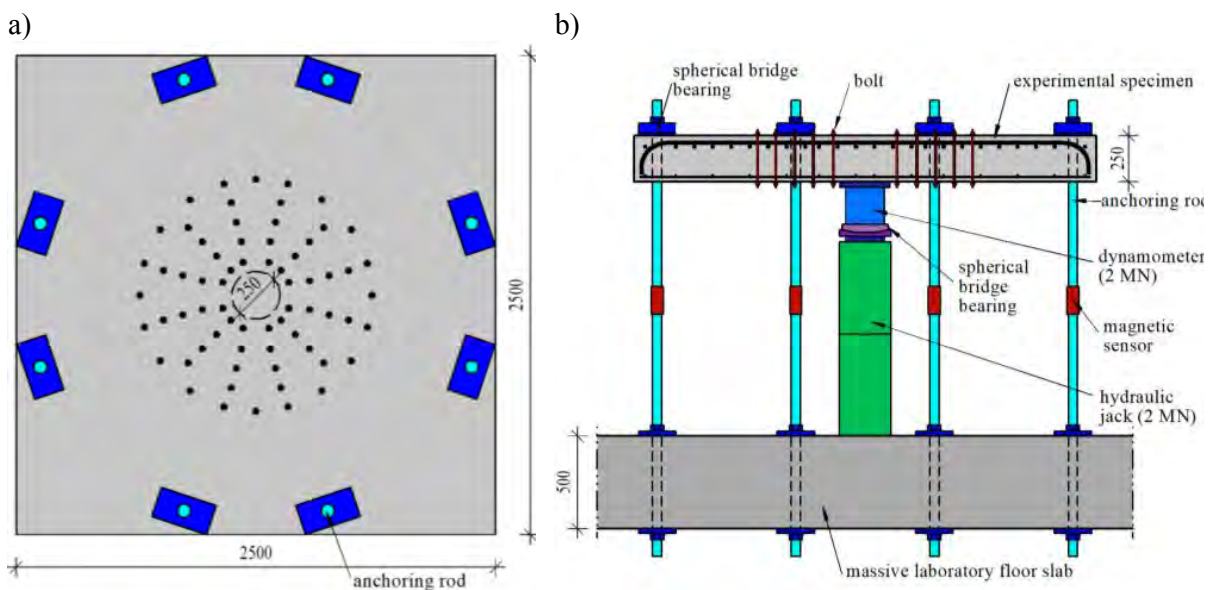


Fig. 5 Test setup (dimensions in mm) a) top view, b) section.

4 Conclusions

The paper presents previous experimental studies, numerical calculations, and its nonlinear numerical verifications. Most numerical procedures are based on models that have been derived for new structures and do not have a loading history. The existing flat slab has a certain rotation (deformation) which should be considered. This experimental study is supposed to verify the influence of the loading history on the final resistance of a flat slab reinforced with post-installed shear reinforcement.

Acknowledgements

This work was supported by the Scientific Grant Agency VEGA under the contract No. VEGA 1/0522/20.

References

- [1] Majtánová L. 2017. "Maximum punching resistance of locally supported slabs with shear reinforcement." PhD-diss., Slovak University of Technology in Bratislava, Faculty of Civil Engineering.
- [2] Keseli O. 2018. "Strengthening of locally supported slabs for the effect of punching by additionally mounted shear reinforcement." PhD-diss., Slovak University of Technology in Bratislava, Faculty of Civil Engineering.
- [3] Eurocode 2, Design of Concrete Structures - Part 1-1: General Rules and Rules for Buildings, CEN, EN 1992-1-1, Brussels, Belgium, 2004, p.225.
- [4] Fédération internationale du béton. 2012. "fib Model Code 2010 - Final draft, Vol. 1." *Bulletin* 65, Lausanne, Switzerland.
- [5] Fédération internationale du béton. 2012. "fib Model Code 2010 - Final draft, Vol. 2." *Bulletin* 66, Lausanne, Switzerland.
- [6] Latest draft prEN 1992-1-1 ver. 2021-01. Work document N 1874 of CEN/TC 250/SC 2.
- [7] Muttoni, A. 2008. "Punching shear strength of reinforced concrete slabs without transverse reinforcement." *ACI Struct J* 2008;105(4):440-50.
- [8] Koppitz, R., Kenel, A. and Keller, T. 2013. "Punching shear of RC flat slabs – Review of analytical models for new and strengthening of existing slabs." *Engineering Structures* 52:123-130.
- [9] M. M. Inácio, A. P. Ramos, D. M. V. Faria, Strengthening of flat slabs with transverse reinforcement by introduction of steel bolts using different anchorage approaches, *Engineering Structures*, no. 44, 2012, pp. 63-77.

Analytical evaluation on the influence of deterioration of bond between rebar and concrete on structural performance of RC structures

Ryota KURIHARA, Youhei ITO, Nobuhiro CHIJIWA

*Department of Civil and Environmental Engineering, School of Environment and Society,
Tokyo Institute of Technology,
2-12-1 Ookayama, Meguro-Ku, Tokyo 152-8550, Japan*

Abstract

Structural behavior of reinforced concrete (RC) structures is greatly influenced by bond loss between rebar and concrete due to rebar corrosion. It is important to understand the influence of bond deterioration more deeply for improvement of performance assessment for deteriorated structures. This research aims to numerically investigate the impact of bond deterioration on the structural performance of RC beam, especially due to loss of interlocking by lug on the deformed bar. With the parameters used in reproduction analysis on the previous experiment, we tried to analyze the effect of bond loss under more realistic states such as a part of lug loss on rebar surface or height reduction of lug. It is shown that bond performance reduction is slight in the case that lug remains on rebars even if its height is reduced, although smooth surface by complete loss of lug has significant influence.

1 Introduction

Corrosion of reinforcement bar is one of the significant issues on RC structures. Rebar corrosion causes section loss of rebar, cracks around rebars by expansion force generated by corrosion product, and bond loss between rebar and concrete. These phenomena have influence on load capacity, rigidity, and load-carrying mechanism. Assessment of corrosion affected RC structure is essential [1]-[3].

The bond between rebar and concrete is one of the dominant factors for the load carrying mechanism of RC member. Bond is defined as the union mechanism between rebar and concrete. Bond includes three mechanisms; interlocking by mechanical contact, resistance by friction, and chemical adhesion. When deformed bars are embedded as reinforcement, lug on the reinforcement bar surface is mechanically interlocked with surrounding concrete, and the predominant bond can overcome the bond by friction or chemical adhesion. It is one of the reasons that deformed bar is widely used around the world. Therefore the loss of rebar lugs by corrosion causes bond loss and have a significant impact on structural performance. It is crucial to understand the effect of bond deterioration deeply to improve the assessment accuracy of the remaining structural performance of RC structures with rebar corrosion.

This research focused on the change of structural performance by bond deterioration especially from interlocking loss with nonuniformity. Previous studies have reported the effects on structural performance by bond loss, such as flexure rigidity reduction, ductility change, or shear capacity increase due to tied arch formation [4]-[6]. On the other hand, researches focusing on bond performance with ununiform lug loss are not so many. Many factors due to rebar corrosion are interlinked on bond performance. For example, crack induced by corrosion along with the rebar also deteriorate the stress transfer around the crack, and sometimes it can be regarded as the apparent bond loss. To understand the influence of corrosion on the structural performance more deeply, it is important to purely extract the deterioration of interlocking in the corroded RC member. In this study, the influence of interlocking loss due to corrosion on lugs is investigated by 3D finite element analysis.

2 Overview of the experiment

The authors have conducted the static loading test on RC beam specimens with different bond conditions. [7] This study tries to reproduce this experiment by 3D finite element analysis, and more cases

that were closer to the practical state were computed and evaluated to understand the mechanism of interlocking by lug on rebar surface.

2.1 Experimental setup

Three RC beam specimens with different bond conditions, 100%, 50%, and 0% of the proportion of interlocking area were tested as shown in Table 1. The specimen with 100% interlocking was a sound RC beam using normal deformed bars as the main reinforcement. The specimen with 50% interlocking was an RC beam whose cover concrete along the main rebars was physically removed. It means that the bottom half sides of the rebars were exposed. The specimen with 0% interlocking was the beam using round bars. This beam had no interlocking effect.

All beams were designed to fail in shear. The rebar arrangement and beam dimension are shown in Fig. 1, and Table 2 shows the material property of concrete and rebars. Ready-mixed concrete was used for casting, and its mix proportion is shown in Table 3. Beams were cured under sealed condition to prevent the drying shrinkage of concrete. Static loading test was conducted in 12 days age.

Table 1 3 bond conditions of beam specimen

Case	Main rebar	Overview diagram
100 % interlocking (sound beam)	Deformed bar	
50 % interlocking (Bottom half side of rebar are exposed)	Deformed bar	
0 % interlocking (No interlocking)	Round bar	

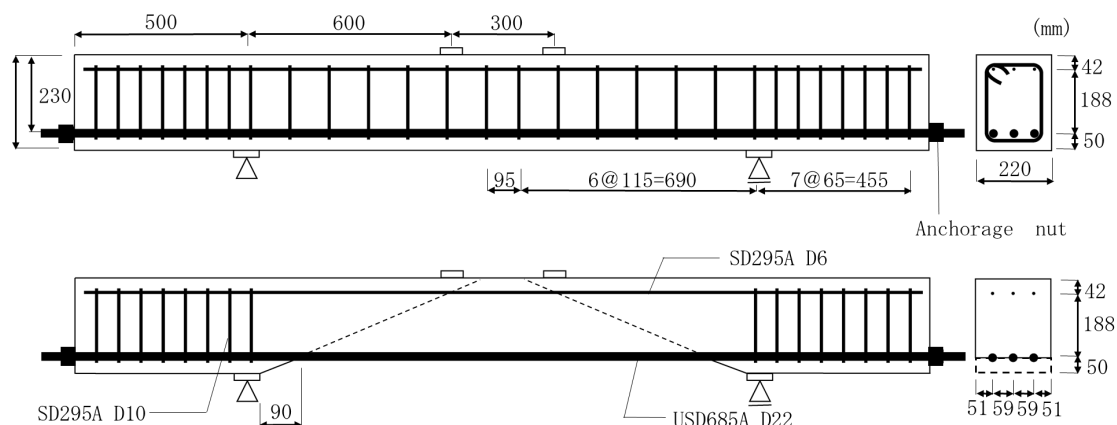


Fig. 1 The dimension of specimens (Top: 100% interlocking, Bottom: 0% interlocking)

Table 2. Material properties of concrete and rebar

Concrete property		Yield strength of Rebar (MPa)		
Compressive Strength (MPa)	Young's modulus (GPa)	Stirrup SD295A D10	Deformed bar USD685A D22	Round bar PC rod Class B
39.7	26.5	304	710	1018

Table 3. Mix proportion of concrete

W/C (%)	Maximum size of gravel (mm)	Unit quantity (kg/m ²)			
		Water	Cement(OPC)	Gravel	Sand
42.5	20	173	408	1033	697

2.2 Experimental results

In the static loading test, the deflection of beam and applied load were measured by displacement transducer and load cell. The Load-deflection curve and crack patterns in each specimen are shown in Fig 2.

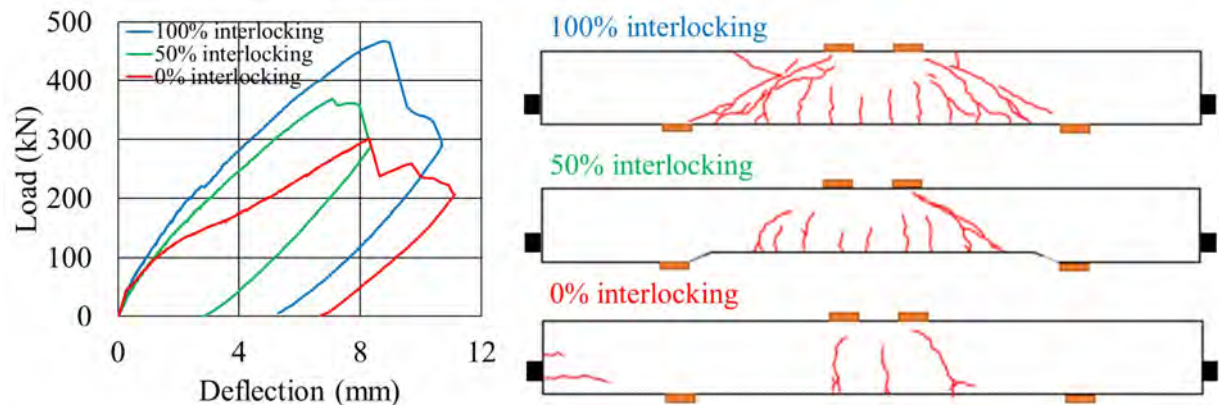


Fig. 2 Load-deflection curve (left) and crack distribution (right)

In the case of the specimen with 0% interlocking, the flexural rigidity declined significantly from 120kN, the middle stage of loading. It was found that the flexure cracks were concentrated in the center of the span. The specimens with 0% interlocking failed by anchorage failure. Because of the bond loss on the rebars, a tied arch was formed in the beam; tensile stress was distributed uniformly on the rebars as the tie, and the compression strut was formed between the loading point and the anchorage nuts. Finally, anchorage failure occurred when the compressive stress exceeded the compressive strength of concrete.

The rigidity of specimens with 50% interlocking also declined after the middle stage of loading, but the rigidity reduction degree was smaller than the case of 0% interlocking. The whole behavior against load was similar to that of 100 % interlocking case. It is known that the shear capacity can be improved due to the formation of the tied arch when the bond is lost on the rebars. In the 50% interlocking case, improvement of the shear capacity was not observed, and its failure mode was the same as that of 100 % interlocking specimen. It meant that the bond loss was not so significant.

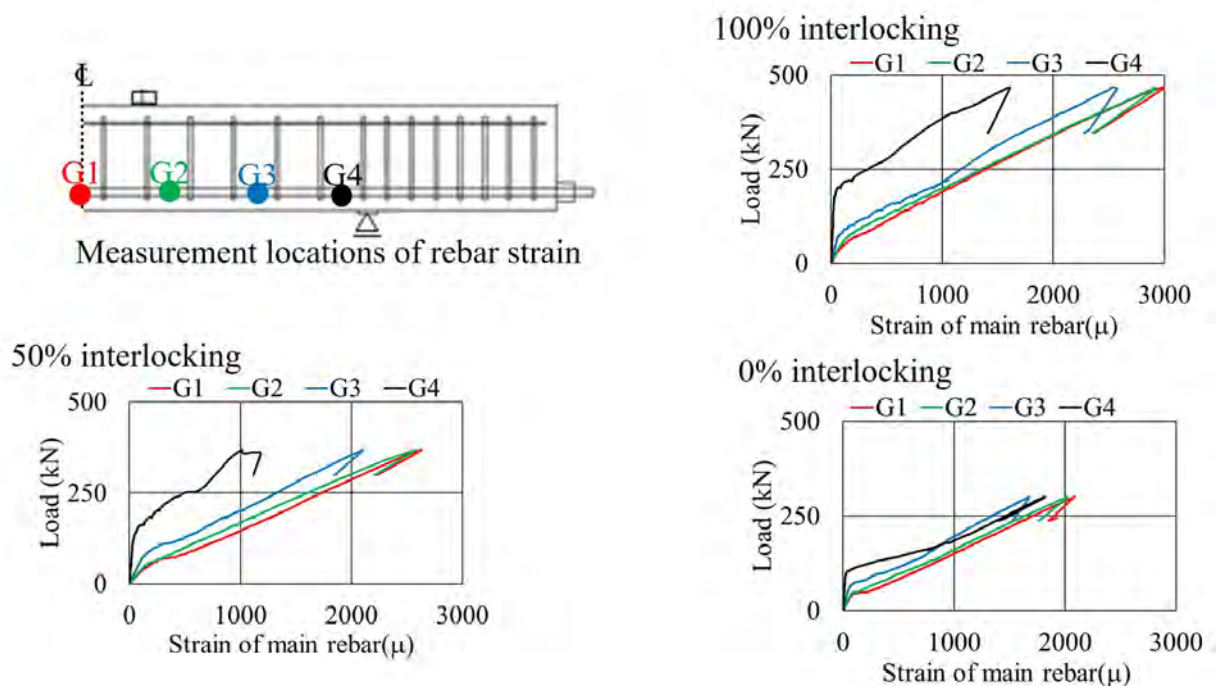


Fig. 3 Load-Strain curves of main rebar on each case

The bond condition can be also estimated from the strain distribution on the main rebars. Fig. 3 shows the location of strain gauges for rebars and the relationship of load and strain of the main rebar. As long as the bond is sound, the strain distribution of the main rebars is the same trend as that of the bending moment. In this experiment, strain should be the largest at the center of the span and decrease as getting closer to the supports. In the 50% and 100% interlocking cases, this trend was observed under loading as shown in Fig. 3. However, the strain distribution of 0% interlocking beam was different from the other cases. In the initial stage of loading, strains at each location had the same trend. However, after the middle period of loading, each strain value was getting close. It meant that the strain on main rebars became uniform. This phenomenon started from about 150kN, and it is the same timing as rigidity declination in the load-deflection curve. Tapping sound had been heard from this stage many times. It seems to be caused by the rebar slipping when the chemical bond was lost locally.

2.3 Outcomes from the experiment

From the crack pattern in Fig.2, the sound bond can clearly diversified flexural cracks, and it prevented crack localization. Crack dispersion has an important role on the viewpoint of the durability and load-carrying mechanism. In the 50% interlocking case, the interlocking effect by lug was reduced, but the cracking behavior was not significantly changed from that of the 100 % interlocking case.

There was a clear difference in the load-deflection curve among three specimens. The bond performance influenced the rigidity after flexural cracks are formed. When the concrete-rebar bond does not work, cracked concrete does not resist tensile stress. When the concrete and rebar are well integrated by bond, the concrete between the flexural cracks can carry some tensile stress. Therefore the rigidity dropped sharply when the flexural cracks were formed in the specimens with 0% interlocking. In the case of 50% interlocking, the bond is deteriorated slightly and it can cause the reduction of rigidity. The shear cracks of 50% interlocking case were more localized than that of 100% bond case. It is thought that interlocking resistance by aggregates at crack surface became weaker by the opening of concentrated shear cracks, and shear capacity reduced. However, a significant difference in structural performance between 100% and 50% interlocking was not observed. It is considered that bond performance can be preserved even when the interlocking becomes half.

3 Reproduction analysis

3.1 3D nonlinear finite element model

For investigating the influence on the structural performance by bond deterioration, numerical analysis was conducted. 3D nonlinear finite element analytical system “COM3” is used for reproducing our experiment and for the case study of interlocking loss.[8] This system is based on the smeared cracking model, and multi-directional non-orthogonal cracks can be considered in the computation to simulate the behavior of the concrete structure under various external actions. In recent years, the system is enhanced to reproduce the deteriorated RC structural system [9] [10]. In this study, the shape of rebars embedded in the concrete was modelled precisely, and the bond between steel and concrete was modelled by 2-dimensional interface elements for the stress transfer on the interface. COM3 can also simulate the structure which has multiple materials and interface between them, such as composite structure or underground structure [11] [12].

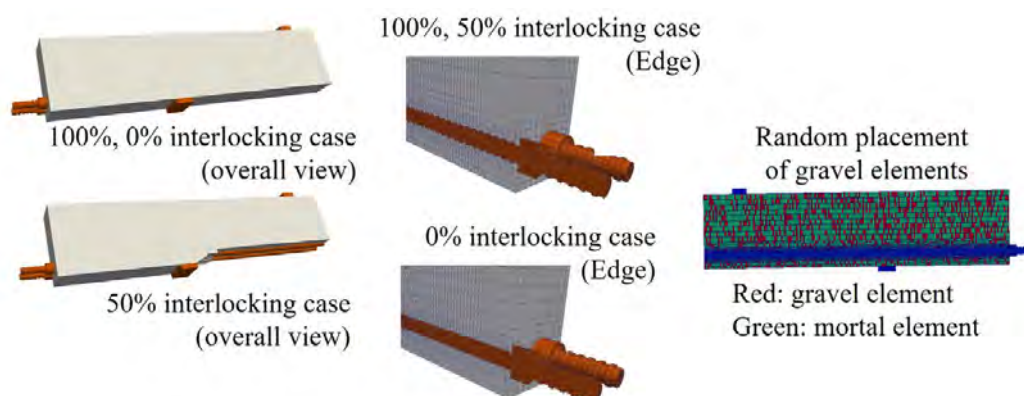


Fig 4. Geometry of analysis model (left and center) and random gravel placement (right)

Fig 4. shows the quarter-cut FE beam model with 60,000 cube solid elements and 8,000 interface elements between main rebar and concrete. Main rebar shape, including lugs, was modelled precisely and embedded in concrete for focusing on the interlocking effect. Reproduced lugs had 2mm height and 60-degree angle from the bar axis. These values were based on the Japanese Industrial Standard (JIS). Stirrups and compression rebars were modelled by providing smeared reinforcement ratio.

The mesh size of the model was fine (minimum 2mm) to reproduce the geometry of the lug. In the original concrete model in this system, concrete components, such as cement matrix and aggregate, are averaged as a concrete element. However, this original model is not appropriate in this case because the mesh size is much finer than the model assumption. Therefore, the concrete part was divided into two types of elements, as mortar elements and gravel elements, and proper material properties were set for them. The volume proportion of gravel elements was 36%, which was decided from the mix proportion in the experiment. Gravel elements were modelled as RC element with 140 MPa of compressive strength, 10 MPa of tensile strength, and 54 GPa of young's modulus. These properties were decided based on the general material property of limestone produced in the same area as the gravel that is used in the experiments [13]. It is noted that the basic material property of limestone has a small scatter.

3.2 Reproduction analysis on experiment

As shown in Fig. 5, the numerical analysis could reproduce the load-deflection curves on each case in the reduce of load capacity and rigidity after cracking. In the case of 0% interlocking, the stress concentration in the anchorage zone and crack localization under loading points were observed. Slipping between rebar and concrete happened in 120 kN and rigidity decreased significantly after that. In contrast, local rebar slipping in the experiment occurred intermittently with load increment, not in whole area of rebar in a certain load. In the 50% interlocking case, rigidity and the number of flexural crack of analytical result were smaller than experiment. This difference was caused by the modelling of the stirrups. In the experiment, stirrups keep rebar and upper concrete contacted, and the interlocking effect was preserved. However, such kind of effect was not explicitly modelled in the analysis, and main rebar could peel off from upper concrete as the displacement got larger. It caused interlocking loss. Even though there are some minor differences, the numerical analysis successfully reproduced the influence of lug loss on structural behavior.

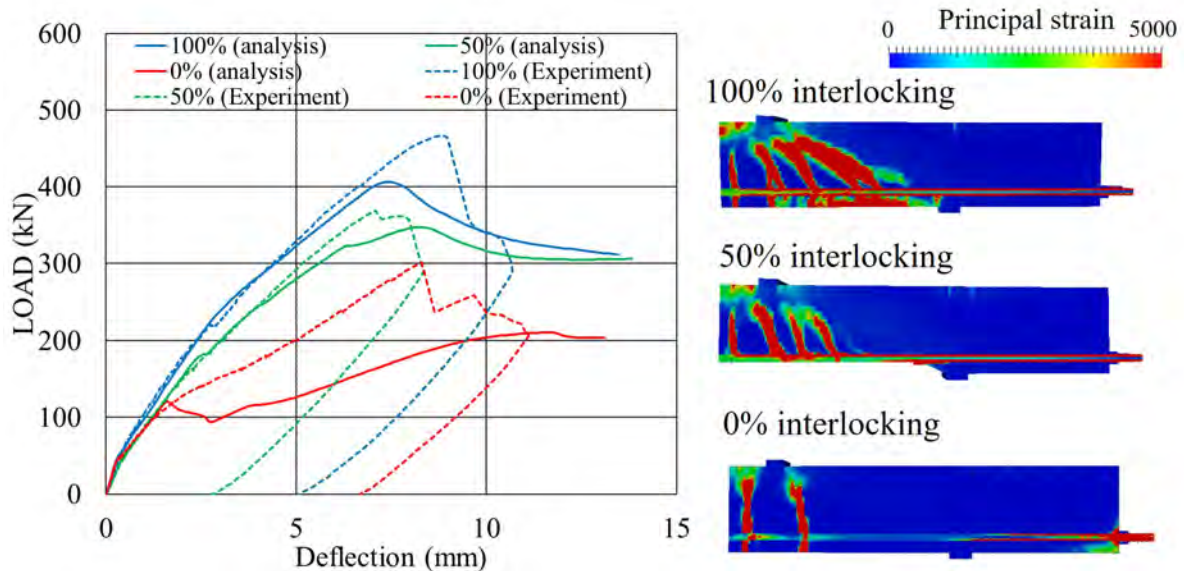


Fig. 5 Comparison analytical and experimental results on Load-displacement curve (left) and strain distribution at failure (right)

4 Case study on structural performance due to bond reduction by lug loss

The validity of the analysis model with embedded rebar was confirmed in Chapter 3. With the parameters used to reproduce the experiment, more cases that were closer to the practical condition were computed and evaluated for understanding the role of interlocking more deeply. This study tried to







analyze focusing on two viewpoints to simulate the effect of bond loss under a more realistic state, height decreasing of the lugs due to corrosion and ununiform distribution of corrosion.

4.1 Analytical cases

In general, the rebar corrosion process is as follows; penetration of deterioration factor such as chloride ion, starting corrosion of rebar, cracking around rebar by expansive stress due to corrosion product, and spalling of cover concrete. In the initial stage of corrosion, rebar corrosion is considered to occur in the rebar area closer to the concrete surface. It causes lug loss in a partial area of rebar surfaces such as only the bottom area or side area. This study set 3 conditions on the lug loss area; half surface lug loss on the bottom (Bottom-0%), in outside surface (Outer-0%), and on all surface of the outer two rebars in three ones (Side-0%). In order to grasp the difference clearly, an ultimate situation that lugs were completely lost in damaged area and sound in other area were reproduced.

In the corrosion stage after cracking, lugs in all surface of rebar are considered to be deteriorated. However under this process, rebar shape becomes not like round bars, but the roughness of rebar surfaces will be maintained. For reproducing this condition, the 3 cases with reduced lug height (75%, 50% and 25% of height) were analyzed. Table 5 shows the lug condition of 6 cases which was evaluated in this study.

Table 5 Analytical cases (parts lug loss of rebar surface)

Parameter	Area of lug loss			Loss of lug height		
Name	Bottom-0%	Side-0%	Outer-0%	LugH-75%	LugH-50%	LugH-25%
Lug condition						
Ratio of Sound lug	50% (50% loss)	33% (67% loss)	33% (67% loss)	75% (25% loss)	50% (50% loss)	25% (75% loss)

4.2 Analysis results and discussions

4.2.1 Effects of lug loss location

Fig. 6 shows the analysis results on beams with different locations of complete lug loss area. The bottom-0% case has almost the same behavior as that of 50 % interlocking case without cover concrete in the former chapter from the point of rigidity, capacity declination, and crack pattern. On the other hand, in Side-0% and Outer-0% cases, bond loss was observed as the crack localization. Side-0% beam showed load reduction by rebar slipping at about 160kN.

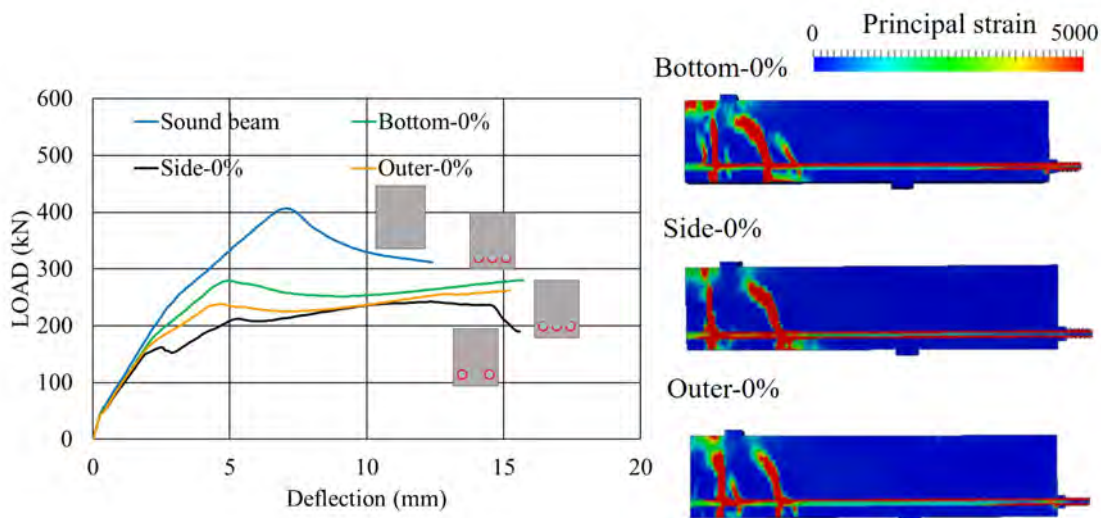


Fig. 6 Load-displacement curve (left) and strain distribution at failure (right)

When a half or more of the section of rebar lugs are lost, bond deterioration was observed in terms of crack concentration and rigidity declination. Rebar slipping was observed only in Side-0% case, although Side-0% and Outer-0% had the same lug loss ratio. The surface of two outside rebars were smooth in Side-0%. It can be said that the uniform distribution of interlocking by lug had a significant effect to prevent brittle behavior by rebar slipping even though lugs became small.

4.2.2 The effects of loss of lug height

Analytical results with the different lug height are shown in Fig. 7. In the case of 75% and 50% lug height, almost the same load-deflection curves were observed, and the rigidity and load capacity of LugH-25% becomes low. From the principal strain distribution map, the beams with 100% and 50% of lug height show similar flexure and shear crack patterns. On the other hand, in the case of LugH-25%, the number of flexural cracks is decreased, and shear crack formation was suppressed due to the tied arch effect by bond deterioration.

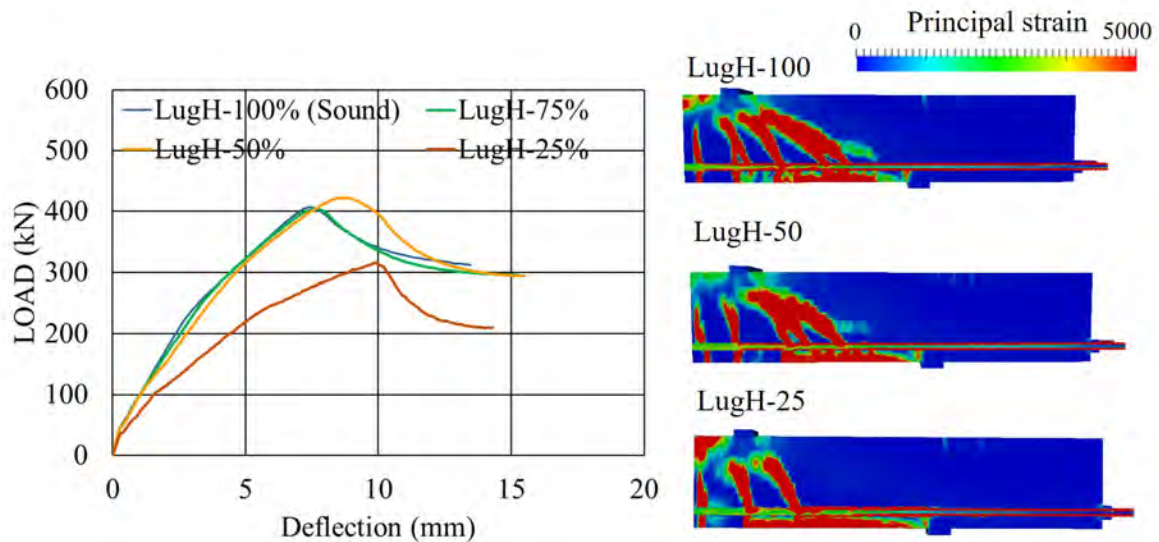


Fig. 7 Load-displacement curve (left) and strain distribution at failure (right) of each beam with different lug height

The influence of lug height reduction on the structural performance was smaller than that of local complete lug loss. The chemical bond between rebar and concrete is small, and it is why the rebars can not resist large pull-out force when the bar does not have lugs. After the bar slips, the bond consists of just friction. When the surface of the rebars is rough, the bond can be maintained at the same level as the sound condition even though the roughness is small. The relationship between roughness of rebar surface and bond condition is not linear, and bond performance is considered to decrease rapidly after a certain deteriorated condition. In the real structure, the roughness of the rebar surface can be preserved even after lug height is reduced by corrosion. It means that stress can be transferred between rebar and concrete unless contact between rebar and concrete lost by spoiling of concrete.

To assess the residual structural performance of corroded RC structure, the reduction of cross-section area of rebar and bond loss are requested to be modelled precisely. This study presented the possibility that surface roughness can preserve the bond between concrete and rebars even when section loss occurs due to corrosion. It needs to investigate the relationship between bond decline ratio and corrosion state deeply for the assessment of real deteriorated RC structures, including the influence of other factors such as cracking along rebar or corrosion product.

5 Conclusions

The static loading behavior of the beam specimens with various interlocking conditions were investigated from the experiment and analysis investigation, and the followings are showed.

1. When the bond is deteriorated, cracks will be localized, and the rigidity and capacity of RC member will be decreased. Significant bond loss induces to form the tied arch in the beam, and it improves the shear capacity.

2. Bond deterioration is slight in case that roughness on rebar surface by lug is maintained. This is because the interlocking between concrete and lug works even after the rebar is corroded. Assumption of complete bond loss between rebar and concrete with rebar corrosion can overestimate the magnitude of bond deterioration.
3. Stirrup can prevent peeling off of main rebar from concrete and keep them contacted. It can prevent bond deterioration even if the bottom surface of rebar lugs are lost.

Acknowledgements

This study was supported by JSPS KAKENHI Grant Number JP19J22658 as Grant-in-Aid for JSPS Research Fellow.

References

- [1] J.G. Cabrela. Deterioration of Concrete Due to Reinforcement Steel Corrosion. *Cement and Concrete Composites*. 18: 47-59
- [2] Rodriguez, J., Ortega, L. M., Casal, J. Load Carrying Capacity of Concrete Structures with Corroded Reinforcement. *Construction and Building Materials*. 11(4): 239-248
- [3] Lim, S., Akiyama, M., Frangopol, Dan M. Assessment of the structural performance of corrosion-affected RC members based on experimental study and probabilistic modelling. *Engineering Structures*. 127 189-205
- [4] Coronelli, D., Corrosion Cracking and Bond Strength Modeling for Corroded Bars in Reinforced Concrete. *ACI structural journal*,99(3): 267-276
- [5] Ikeda, S., Uji K. Studies of Bond on The Shear Behavior of Reinforced concrete Beams. *Journal of Japan Society of Civil Engineers*. 283: 101-109
- [6] Sæther, I. Bond deterioration of corroded steel bars in concrete. *Structure and Infrastructure Engineering*. 7(6): 415-429.
- [7] Ito, Y., Kurihara, R., Chijiwa, N. 2019. The influence of the deterioration of concrete-rebar bond due to corrosion on the structural performance of RC structures. Paper at 16th East Asia-Pacific Conference on Structural Engineering & Construction (EASEC16). P147. December 3-6
- [8] Maekawa, K., Okamura, H. & Pimanmas A. 2003. *Nonlinear mechanics of Reinforced Concrete*. London: Spon Press.
- [9] Toongonthong, K., Maekawa, K. Multi-Mechanical to Structural Performance Assessment of Corroded RC members in Shear. *Journal of Advanced Concrete Technology*, 3(1): 107-122.
- [10] Kurihara, R., Chijiwa, N., Maekawa, K., Thermo-Hygral Analysis on Long-Term Natural Frequency of RC Buildings with Different Dimensions. *Journal of Advanced Concrete Technology*, 15(8): 381-396
- [11] Ito, Y., Chijiwa, N., 2018. The influence of corrugated steel web PC bridge. Paper presented at 8th Regional Symposium on Infrastructure Development in Civil Engineering (RSID8), 2A-5, October. 25–26.
- [12] Maekawa, K., Zhu, X., Chijiwa, N., Tanabe, S., Mechanism of Long-Term Excessive Deformation and Delayed Shear Failure of Underground RC Box Culverts. *Journal of Advanced Concrete Technology*. 14(6). 183-204
- [13] Limestone Association of Japan. 2005. *Limestone aggregate and concrete*. Limestone Association of Japan

ANALYSIS OF CREEP IN PLAIN CONCRETE FLEXURAL MEMBERS

Mary Williams, Devdas Menon and Anumolu Meher Prasad

*Indian Institute of Technology Madras,
Chennai (600036),
Tamil Nadu, India*

Abstract

The most widely accepted methods for estimation of long-term deflections in flexural members are mostly based on axial creep studies in cylinders. The application of these models to flexural creep is questionable because of the stress gradient and the effect of tension (if present). A few flexural creep tests in plain concrete beams reported in the literature are analysed in the present study. In all the tests, the applied load is kept constant throughout the test duration. From the measured strains, using static equilibrium, the stresses can be generated at any time, and the flexural creep behaviour has been studied. The study observes that the compressive stresses decrease with time, whereas tensile stresses increase. Therefore, it is not appropriate to predict the creep strains based on constant stress, rather the varying stresses need to be accounted for in the prediction.

1 Introduction

The study of long-term behaviour is very significant in concrete flexural members because it results in an increase in deflection which in turn affects the serviceability of the structure. This is detrimental especially in lifeline structures like bridges which are mostly creep sensitive. The long-term behaviour of concrete structures is mainly governed by creep, shrinkage and relaxation of steel (in prestressed members). This study mainly focuses on the creep behaviour of concrete. The effect of creep in concrete depends on various [material, environmental and loading] factors, mainly the mix design, temperature, humidity, the stress to strength ratio and the age of loading.

Creep in concrete consists of basic creep and combined creep. While the basic creep depends only on the loading and the member characteristics, combined creep is also affected by environmental conditions. So, to detach the influence of local environmental conditions and to generalise the creep behaviour, most creep tests include a basic creep specimen and a combined creep specimen. A large number of creep tests have been reported on plain concrete cylinders subject to axial compressions for years [1]-[10], and based on these tests, various creep models have been developed, some of which separates basic creep and combined creep [11]-[12]. In practice, these models are being used for all kinds of members (columns, beams, etc.) irrespective of their loading conditions as long as the stress is within the linear range, which is widely accepted to be $0.4 f_c$ (f_c is the cylinder compressive strength).

The creep in members subjected to bending is referred to as flexural creep and the main difference in flexural creep is the stress gradient across the section. In addition to this, if there is tension in the member, the creep mechanism itself may be different. Contradicting results on the difference between tension creep and compression creep have been presented by various researchers over time [1]-[7]. Brooks and Neville (1977) stated that the creep in tension and compression are considerably different and depends on many factors, age of concrete and drying being the most important ones [1]. Some researchers conducted basic creep tests and proved that compressive creep is higher than tensile creep [2]-[4] whereas the opposite is stated by Kristiawan (2006) and Forth (2015) [5],[6]. In literature, few studies showing that the creep in tension and compression are similar [7]. Because of the contradictory results, it is not possible to arrive at a conclusion on the difference in the rates and magnitudes of creep in tension and compression.

Since concrete is rarely subjected to direct tension (uniform tension throughout the cross-section), emphasis should be given to flexural tension which is nearly unavoidable in concrete beams. Since flexural creep has a complex mechanism due to the interaction between tension creep and compression creep, a detailed analysis of the beam response is required to study the effect of tension and the stress gradient on the creep behaviour.

In the current study, few basic creep tests on plain concrete beams subject to constant loading, reported in literature have been analysed and strains are compared with the prediction using existing models. The study is limited to tests where the concrete is not loaded beyond cracking stress. Of the many models available for the prediction of creep and shrinkage, three models (B3, B4 and GL 2000) have been considered that separate basic creep and drying creep.

1.1 Creep models

1.1.1 GL 2000

Gardner and Lockman (2001) proposed the GL2000 model which is given by the following equation.

$$J(t, t_0) = \frac{1}{E_{cm t_0}} + \frac{\Phi_{28}}{E_{cm 28}} \quad (1)$$

$$\Phi_{28} = \Phi(t_s) \left[2 \left(\frac{(t-t_0)^{0.3}}{(t-t_0)^{0.3} + 14} \right) + \left(\frac{7}{t_0} \right)^{0.5} \left(\frac{t-t_0}{t-t_0+7} \right)^{0.5} + 2.5(1-1.086h^2) \left(\frac{t-t_0}{t-t_0+0.15(V/S)^2} \right)^{0.5} \right] \quad (2)$$

$$\Phi(t_s) = \left[1 - \left(\frac{t_0 - t_c}{t_0 - t_c + 0.15(V/S)^2} \right)^{0.5} \right]^{0.5} \quad (3)$$

where t_0 is the age of loading, t_c is the age when drying starts and t is the age of concrete.

1.1.2 B3 model

This model can be used to predict the material parameters of ordinary Portland cement concrete having a 28 day standard cylinder compressive strength between 17MPa and 70MPa. The compliance function using this model is as in (3).

$$J(t, t_0) = q_1 + C_0(t, t_0) + C_d(t, t_0, t_s) \quad (4)$$

$$q_1 = 0.6 \times 10^6 / E_{28} \quad (5)$$

$$C_0(t, t_0) = q_2 Q(t, t_0) + q_3 \ln[1 + (t - t_0)^n] + q_4 \ln \left[\frac{t}{t_0} \right] \quad (6)$$

$$C_d(t, t_0, t_s) = q_5 \left[\exp\{-8H(t)\} - \exp\{-H(t_s^0)\} \right]^{1/2} \quad (7)$$

where $J(t, t_0)$ is the compliance function at time t , the start time of loading is represented by t_0 , q_1 represents the instantaneous strain, C_0 represents the basic creep function and C_d represents the drying creep function.

1.1.3 B4 model

This model is an improved version of the B3 model. It allows for enhanced multi-decade response prediction, distinguishes between the drying and autogenous shrinkage, and introduces new equations to capture the effects of various admixtures and aggregate types. This model accounts for the temperature effect on the curing and ageing process by accelerating the time based on the activation energies.

$$J(\hat{t}, \hat{t}') = q_1 + R_T C_0(\hat{t}, \hat{t}') + C_d(\hat{t}, \hat{t}', \hat{t}_0) \quad (8)$$

where R_T is a scaling factor and the age of concrete, age of loading and drying, are corrected for temperature.

1.2 Review of studies in flexural creep

Rossi *et al.* (2013) conducted experiments on basic creep in tension, compression and flexure and attempted to predict the flexural creep using the strain data from direct tension and compression creep tests. Due to the scale effect related to tensile and compression creep, the prediction was not successful [7]. Similar behaviour between basic creep in tension and compression was observed by Wei *et al.* (2018), and flexural creep was found to be 65 per cent higher when the water-cement ratio increased from 0.3 to 0.4 which implies that flexural creep is sensitive to water-cement ratio [4]. The specific

creep of direct compression is much higher than flexural compression when the stress to strength ratio is the same [8]. The tensile creep shows large variability under different stress levels and flexural creep has minimal non-linearity effects due to higher load level [9].

2 Experimental Data

Few basic creep tests from literature are considered and detailed analysis of the stresses and strains obtained from the experiment has been carried out.

Rainovomanana *et al.* (2013) conducted creep tests on high-performance plain concrete specimens under direct compression, direct tension and flexure tests [8]. Compressive creep tests were carried out on cylinders and, tensile and flexural creep tests on rectangular prisms of size 100x100x500mm. The loading was done at an age of 28 days and the stress to strength ratio is 0.5. The loading was such that, the extreme fibre stress was 0.5 times the direct tensile strength of concrete. The test duration was 70 days (for flexural specimen) and strains have been monitored at the top, bottom and the neutral axis level along the mid-span cross-section. The compressive strength of the concrete used for the tests is 69.7MPa.

Fig. 1(a) shows the measured strains across the cross-section with time and it is observed that the compressive strains keep increasing significantly with time whereas the tensile strains remain almost same.

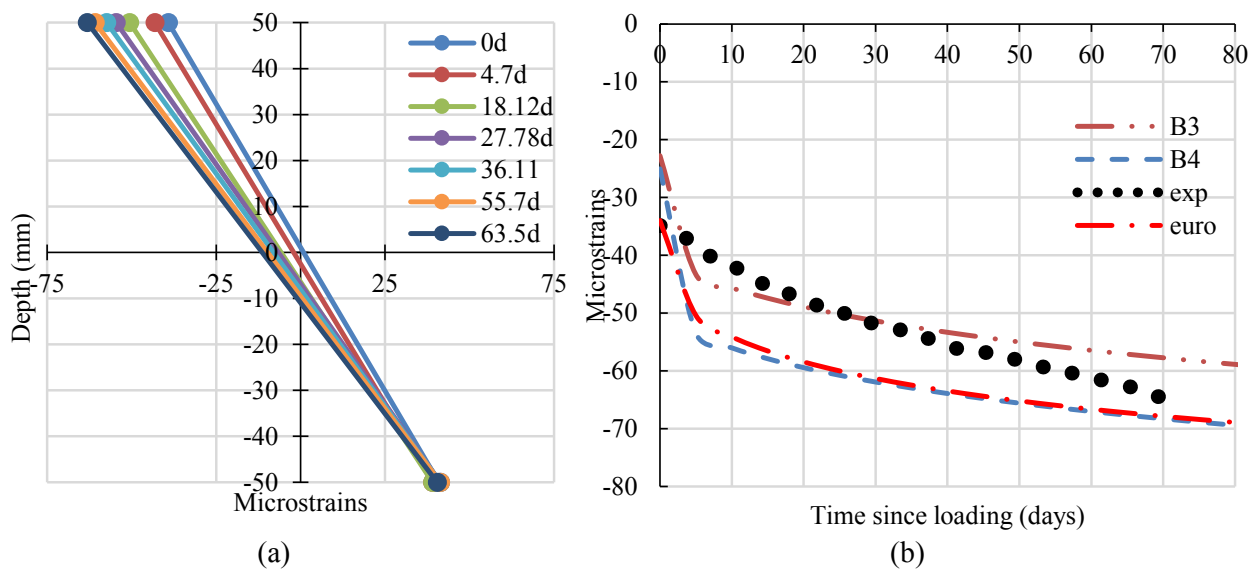


Fig. 1 (a) Measured strains with depth and (b) Measured v/s predicted total strains in the extreme compression fibre.

In order to predict the extreme compression fibre creep strains in flexure, the existing models are used and the results are as shown in Fig. 1(b). It is seen that the magnitude of strains predicted by B3 model are closer to the observed experimental strains while B4 and GL 2000 overestimate the creep strains. Also, the rate of creep observed in the experiment is higher than the predicted rate of creep. All the models give a similar trend in the rate of creep except that the magnitudes are different. The initial rate of creep is overestimated by all the models whereas, at higher ages, the rate of creep is underestimated by the considered models.

It is also seen from Fig. 1(a) that the rate of creep in compression is much higher than that in tension. This causes the neutral axis to shift downward and additional tensile stresses to be developed in the bottom part of the beam. The shift in neutral axis results in the relaxation of stresses in compression. The difference between the predicted and observed creep rates can be attributed to this differential creep mechanism in the beam cross-section. To validate this, an analysis has been carried out using the observed strains.

From the measured strains, the depth of the neutral axis is found and the variation with time is plotted in Fig. 3(a). Since the section is uncracked and the magnitude of stresses are considerably low, a triangular stress profile is considered. Lever arm is calculated from the strain diagram obtained from the experiment. Since the applied moment remains constant, using equilibrium, the top and bottom stresses can be computed at different time intervals using the equations (9) to (12).

$$C = 0.5 \times b \times y_{top} \times \sigma_c \quad (9)$$

$$T = 0.5 \times b \times y_{bottom} \times \sigma_t \quad (10)$$

$$M = C \times \text{Lever arm} \quad (11)$$

$$C = T \quad (12)$$

where C is the resultant compressive force, T is resultant tensile force, M is the applied moment, b is the breadth of specimen, σ_c is the extreme fibre compressive stress, σ_t is the extreme fibre tensile stress, y_{top} and y_{bottom} are the distances of extreme fibres from the neutral axis.

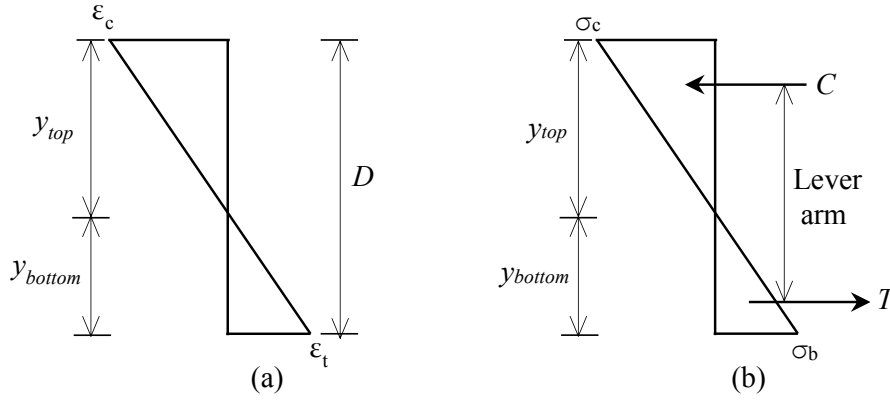


Fig. 2 (a) Representative strain diagram and (b) Representative stress diagram

Due to the shift in neutral axis, it is seen that the stresses keep varying with time to satisfy equilibrium as shown in Fig. 3(b). From the calculated stresses and measured strains, the modulus of elasticity in tension and compression is also computed and the variation is plotted with time as in Fig. 3(c).

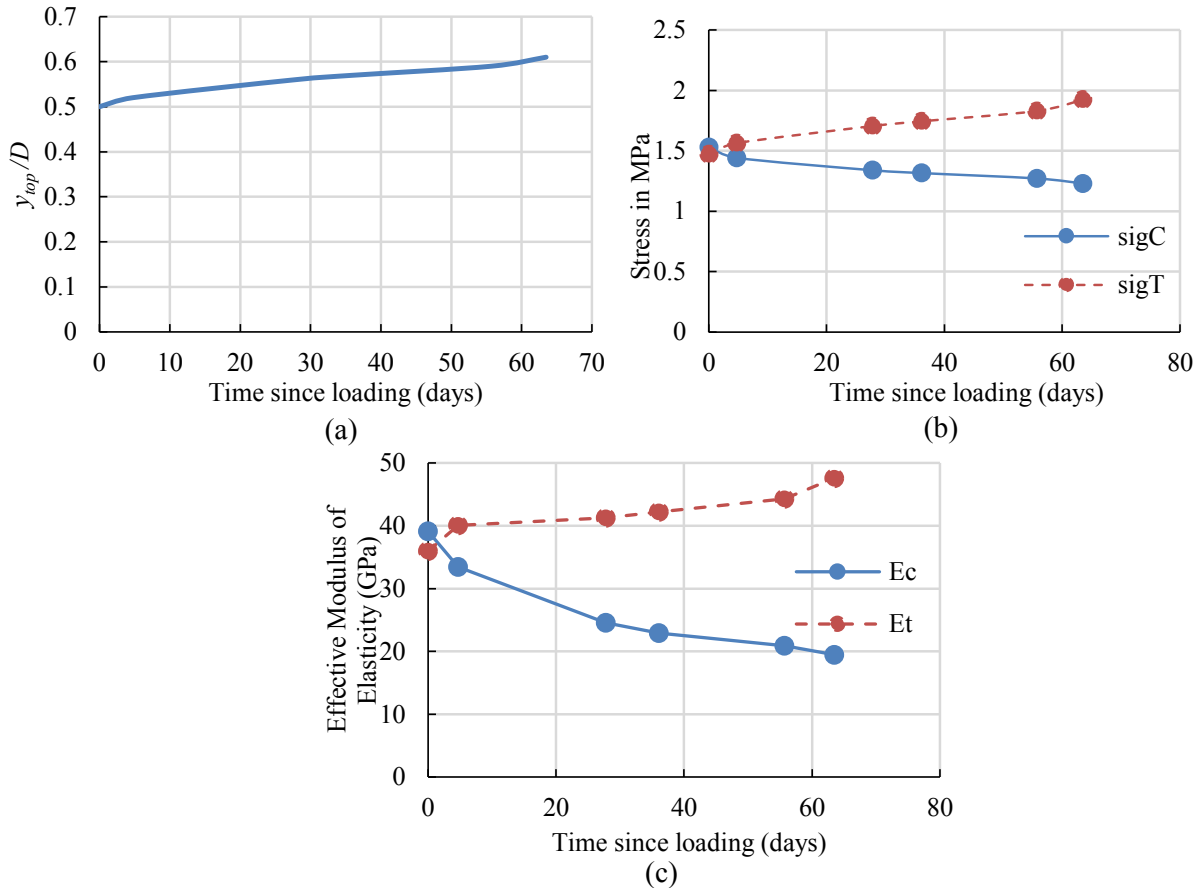


Fig. 3 (a) Ratio of neutral axis depth to beam depth with time, (b) Variation in stress with time and (c) Variation of effective modulus of elasticity in tension and compression with time.

From the analysis, it is seen that the stresses in compression reduce with time (Fig. 3(b)) whereas the stresses in tension increases with time. The lever arm is observed to remain constant.

The modulus of elasticity is different in tension and compression and the effective modulus in tension increases by about 35 per cent whereas the effective modulus in compression reduces by about 50 per cent in 60 days. Hence it is not appropriate to assume constant stress with time in the member even if the beam is subjected to a constant load. To study this, the varying stress profile is considered in the B3 model prediction using the principle of superposition as in (13).

$$\varepsilon(t) = \sum_{i=0}^n J(t, \tau_i) \Delta \sigma_c(\tau_i) \quad (13)$$

where $J(t, \tau_i)$ is the compliance function and $\Delta \sigma_c$ is the stress increment or decrement at time τ .

It is observed that when the stress reduction in compression is considered, the prediction underestimates the actual strains and the rate of creep decreases further, whereas when the increase in tensile stress is considered in the computation, the predicted strains match quite well with the actual strains as shown in Fig. 4. This implies that the interaction of tension and compression creep influences the rate of flexural creep.

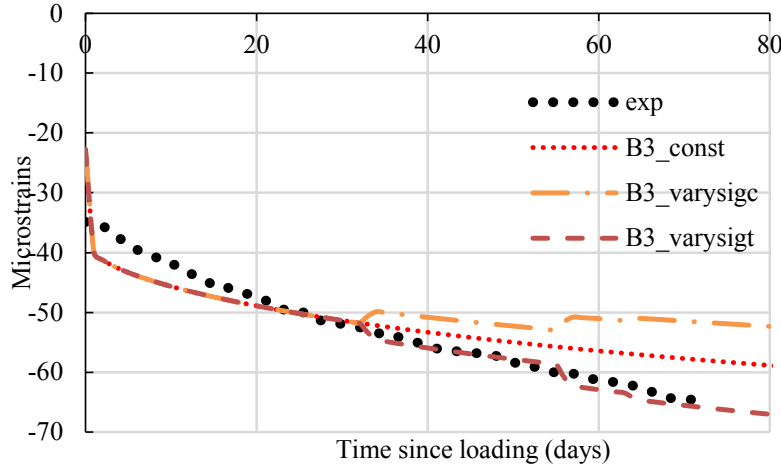


Fig. 4 Predicted top fibre strains at mid-span using B3 model with (a) constant stress assumption (b) varying stress and (c) experimentally observed stains.

To validate these observations, more tests from the literature have been studied.

Hilaire *et al.* [10] studied flexural creep tests done by Reviron (2009) and proposed a three dimensional model for predicting creep. The specimens were loaded at an age of 90 days from casting. The strain variation with depth at different time intervals has been plotted in Fig. 5(a). The study was conducted for only 5 days due to which the variation is small and irregular. The neutral axis position keeps shifting due to the differential strains in tension and compression and is shifting downwards with time. The variation in stress with time has been computed and is observed (Fig. 5(b)) to follow the same pattern.

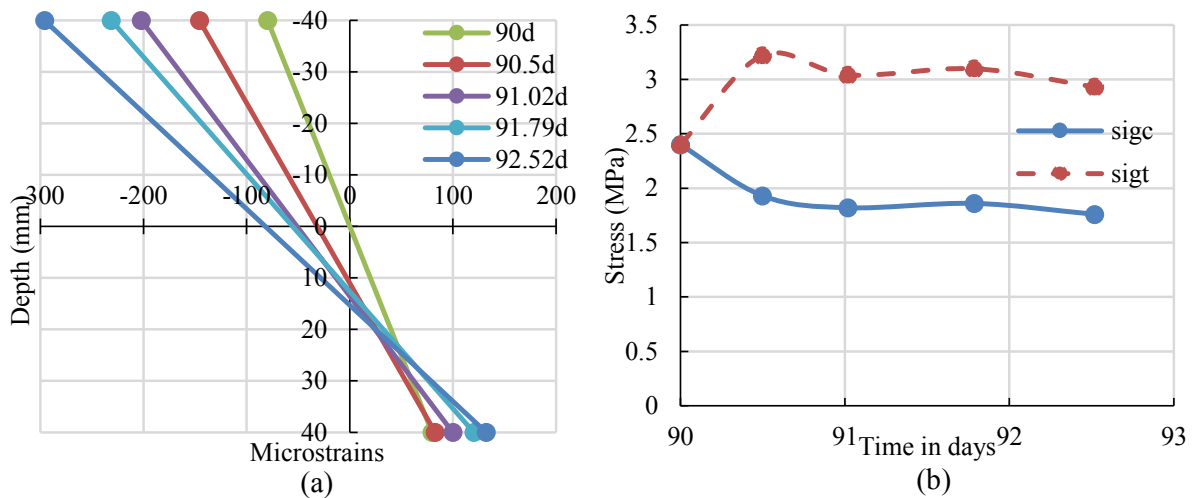


Fig. 5 (a) Measured strains with depth. (b) Variation in stress with time.

Rossi *et al.* (2013), studied creep of concrete in tension and compression by loading one at 50 per cent and one at 70 per cent of the average compressive and tensile strength of concrete measured at 64 days [7]. The flexure creep tests were done on 150x200x700mm plain concrete specimens of 28-day compressive strength 39.9MPa. They were loaded at 70 per cent of the flexural strength (4.8MPa at 64 days) at an age of 64 days.

The mid-span deflections were monitored for a period of 60 days. The deflections obtained in the test are plotted in Fig. 6(a) and using the available creep models (B3, B4 and GL 2000), the long-term deflection has been predicted based on instantaneous deflection. It is seen that the model predictions show variability, some over-predicting and some under-predicting. The rate of creep predicted is also significantly less than the rate observed in the test.

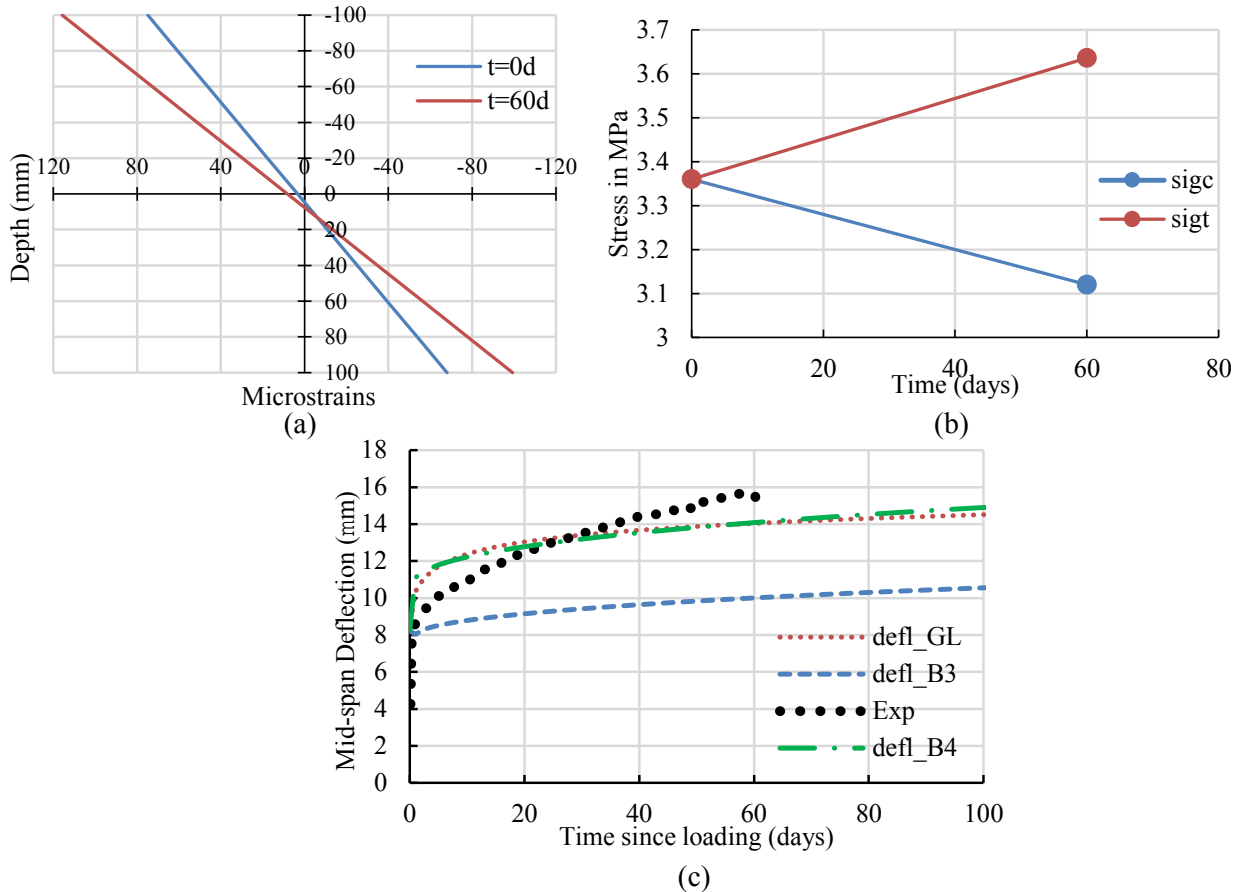


Fig. 6 (a) Measured strains along depth with time, (b) Variation of stress with time and (c) Measured and predicted mid-span deflection with time

Using the measured strains, the stresses are computed and the variation with time is as shown in Fig. 6(c). It follows the same pattern as that of the previous cases. The prediction of creep deflections using models will have more error than using strains because, deflection is controlled by both compressive and tensile strains, whereas while predicting strains, only the extreme compression fibre strains are considered which will give a more realistic value than deflections. With the computed stress profile, the modified strains are computed as shown in Table 1, and it is seen that when the reduced stress is considered, the error in prediction reduces by 8.2%.

Table 1 Predicted and observed strains

T (days)	Exp (mm)	σ_c (MPa)	σ_t (MPa)	B3_const σ (mm)	Error (%)	B3_vary σ (mm)	Error (%)
0	74.86	3.36	3.36	106.93	42.84	106.93	42.84
60	115.74	3.12	3.64	132.78	14.72	123.29	6.5

In all the tests reported in this study, it is observed that, with time, the strain distribution over the beam depth remains linear, but the neutral axis keeps shifting. Due to this, the application of constant stress assumption to predict the creep strains will give an inaccurate result. In order to estimate the actual strains, the varying stress needs to be accounted for and the rate of flexural creep depends on the creep in tension and compression.

To investigate this, an experimental program is being planned as a part of future studies, consisting of prestressed concrete beams, where the effect of tension is eliminated by considering Type I prestress. By doing this, the effect of stress gradient alone on the creep behaviour can be investigated.

3 Observations and Conclusions

It is observed that the rate of flexural creep is different from that of tensile and compressive creep. The models considered in the study (B3,B4 and GL2000) shows some variability in the prediction when compared to the experimental values. Even though the actual values lie within the band of predicted values, the rate of increase in strains or deflections is not captured in the prediction.

In all the tests considered, the compressive strains keep increasing with time whereas the tensile creep shows variability. This implies that the tensile creep may be more sensitive to the material parameters and the flexural creep cannot be accurately predicted without accounting for the tensile creep.

In a basic creep test in plain concrete beams, at any particular cross-section, the stresses in each fibre change with time even if it is ensured that the applied moment remains constant. The analysis shows that the extreme fibre compressive stresses reduce with time whereas the extreme fibre tensile stresses increase with time in order to maintain equilibrium. Therefore the creep in tension and compression are indeed different. This may be the reason for the higher rate of creep in flexure. The prediction improves when this varying stress is accounted for in the analysis. For an accurate prediction, an analytical framework has to be developed based on an iterative procedure and needs to be validated with experiments.

References

- [1] Brooks, J. J. and Neville, A.M. 1977. "A comparison of creep, elasticity and strength of concrete in tension and in compression". *Magazine of Concrete Research*, Vol. 29, No. 100.
- [2] Atrushi, D. S. (2003). "Tensile and Compressive Creep of Early Age Concrete: Testing and Modelling", Doctoral Thesis, The Norwegian University of Science and Technology.
- [3] Rossi, P., Tailhan, C. and Maou, F. L. (2013). "Comparison of concrete creep in tension and in compression: Influence of concrete age at loading and drying conditions", *Cement and Concrete Research*, 51, 78-84.
- [4] Wei, Y., Wu, Z., Huang, J. and Liang, S. (2018). "Comparison of Compressive, Tensile, and Flexural Creep of Early-Age Concretes under Sealed and Drying Conditions", *Journal of Materials in Civil Engineering*, 30(11).
- [5] Kristiawan, S.A. (2006). "Strength, Shrinkage and Creep of Concrete in Tension and Compression", *Civil Engineering Dimension*, Vol. 8, No. 2, 73-80
- [6] Forth, J. P. (2015). "Predicting the tensile creep of concrete", *Cement and Concrete Composites*, 55, 70-80.
- [7] Rossi, P., Tailhan, J., Boulay, C., Maou, F. L. and Martin, E. (2013). "Compressive, tensile and bending basic creep behaviours related to the same concrete", *Structural Concrete 14*, No. 2.
- [8] Ranaivomanana, N. Multon, S. and Turatsinze, A. (2013). "Basic creep of concrete under compression, tension and bending", *Construction and Building Materials*, 38,173-180.
- [9] Ranaivomanana, N. Multon, S. and Turatsinze, A. (2013). "Tensile, compressive and flexural basic creep of concrete at different stress levels", *Cement and Concrete Research*, 52, 1-10.
- [10] Hilaire, A., F. Benboudjema, A. Darquennes, Y. Berthaud, and G. Nahas. (2013). "Analysis of concrete creep in compression, tension and bending: Numerical modelling", Paper presented at Ninth International Conference on Creep, Shrinkage, and Durability Mechanics (CONCREEP-9), Cambridge, Massachusetts, United States, September 22-25.
- [11] ACI Committee 209. (2008). ACI Report 209.2R-08: Guide for Modelling and Calculating Shrinkage and Creep in Hardened Concrete: American Concrete Institute.
- [12] EN 1992-1-1. (2004). Eurocode 2: Design of concrete structures. Part 1-1: General - common rules for buildings and civil engineering structures. London: British Standards Institution.

Influence of geometry and material parameters variability on the ultimate condition of doubly reinforced concrete beams

Alberto Stella, Gianluca Aldrighetti, Luisa Berto, Diego Talledo, Anna Saetta

*Dipartimento di Culture del Progetto,
Università IUAV di Venezia,
Santa Croce dei Tolentini 191, Venezia 35123, Italy*

Abstract

Analytical formulations for the study of ultimate curvature capacity of reinforced concrete members are useful in design practice, especially for preliminary definitions of member characteristics in order to achieve a ductile behavior. This work, part of a broader research, analyzes the influence of various parameters on failure mode of doubly reinforced concrete beams. Differently from classical approaches, in this work all possible ultimate configurations are considered. An approach for identification of ultimate condition based on failure mode domains are developed analytically. It is shown that variations of reinforcing steel amount and ultimate deformation capacity can strongly affect the failure mode of the section and, consequently, its deformation capacity and ductility.

1 Introduction

Most classical analytical formulations for the evaluation of ultimate curvature capacity of reinforced concrete beams (e.g. [1], [2]) consider only concrete failure. Some technical standards propose rules for the construction details of beams derived from these assumptions (e.g. EN1998-1 [3]). Actually, considering the variability of the mechanical parameters and the geometric characteristics of the sections, the beams may develop failure modes different from those considered by the classical formulations. Furthermore, considering cyclic loading conditions [4], [5] or variations in the characteristics of the materials due to degradation phenomena [6], the failure modes may differ significantly from those considered in the design phase. This work aims to study the influence of several parameters on the flexural ultimate condition of the sections of doubly reinforced beams. In particular, the following set of geometrical and material non-dimensional parameters has been considered: the ratio between cover and section height c/H , the geometrical ratio of tensile (bottom) reinforcement ρ , the ratio between compressive (top) and tensile (bottom) reinforcement geometrical ratios ρ'/ρ , the ratio between concrete strength and steel yielding strength f_c/f_y , the ultimate compression strain of concrete ε_{cu} and the ultimate tensile strain of reinforcing steel ε_{su} . An analytical approach is adopted in order to define limit curves aimed to identify domains representing different failure modes. The configurations of the domains are analyzed varying the aforementioned parameters. Special attention is given to the steel properties and in particular to steel ultimate tensile strain. Indeed, alternate cyclic loading, and/or corrosion of rebars can reflect in low values of the steel failure strain [7], [8]. Some considerations on how these aspects can influence the analytical formulations for ultimate curvature capacity and ductility evaluation of reinforced concrete beam sections are proposed. Some improvements and future developments for the proposed study are finally discussed.

2 Basic issues about the ultimate conditions for doubly reinforced concrete beam sections

In this section a brief summary of the main assumptions of the doubly reinforced beam section ultimate conditions for the formulation of failure mode domains is proposed. Figure 1(a) shows a schematization of a generic beam section with the nomenclature adopted in the present study. In Figure 2 the adopted constitutive laws for reinforcing steel and concrete are illustrated.

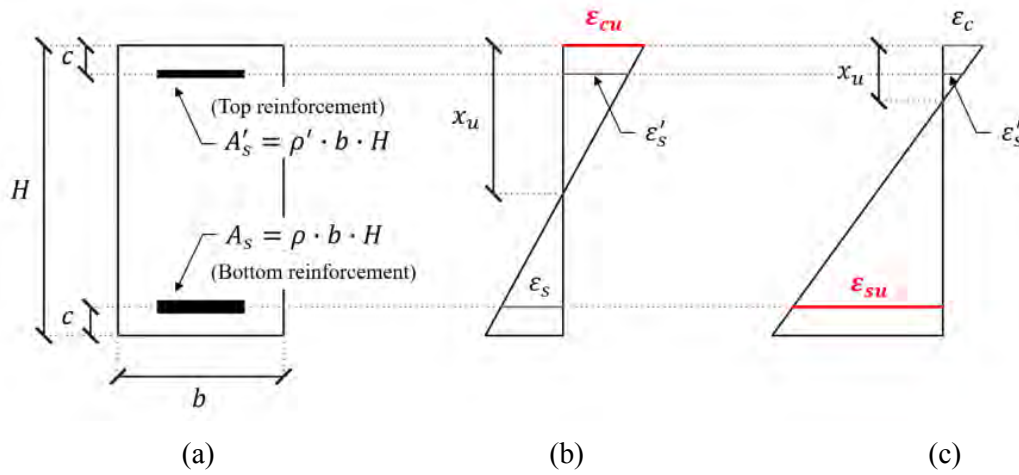


Fig. 1 Description of the beam section and definition of strain profiles at ultimate condition. (a) Section geometry; (b) Strain profile at concrete failure; (c) Strain profile at bottom steel failure

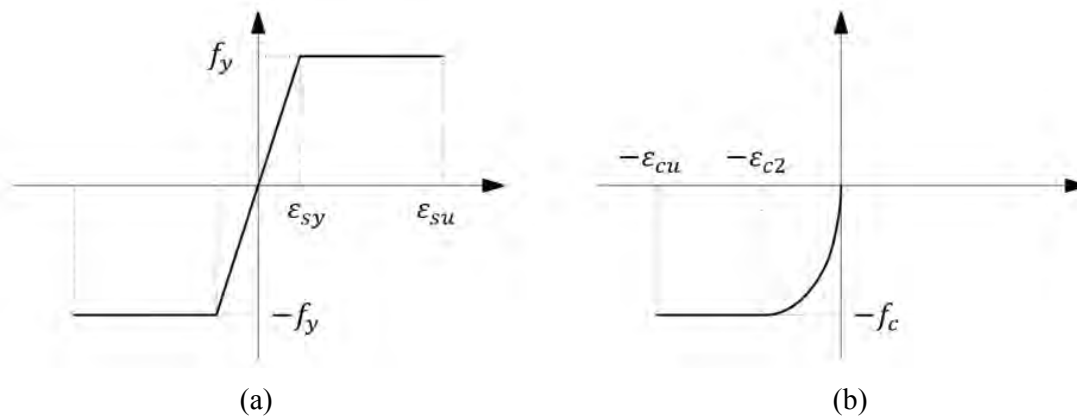


Fig. 2 Constitutive laws used for analytical calculation of section equilibrium (a) Reinforcing steel: Elastic – perfectly plastic law; (b) Unconfined concrete: parabola – rectangle law

An elastic – perfectly plastic stress-strain relationship is used for steel, while the Model Code 2010 [7] parabola – rectangle law is employed for concrete. In this work, any possible effects of concrete confinement are conservatively neglected. Concrete strength in tension is also ignored in the analysis.

In the adopted approach, failure is considered to be achieved either when extreme section fibers reach concrete ultimate compressive strain or when the bottom reinforcement reaches its ultimate tensile strain. Generic deformation profile along section height associated to the two failure types are shown in Figure 1(b) and 1(c), respectively. In order to identify all possible different ultimate conditions, deformation profile is varied in order to consider all possible combination of strain limits at extreme concrete fibers, bottom reinforcement and top reinforcement. Table 1 summarizes all the possible ultimate conditions obtained varying the deformation profile. It is worth noting that not all the listed ultimate conditions can occur for beams of limited height, normal strength concrete and steel with sound mechanical properties.

In order to recognize the failure modes which can actually occur for a given section, specific graphs are developed, where a set of curves divide the plotted area into domains, each representing the occurrence of a specific failure mode. The procedure for the calculation of boundary curves which define failure mode domains is presented in the next section, together with some examples of domains graphs.

Table 1 Possible ultimate conditions for doubly reinforced concrete beam sections: Failure modes labeled from A to J; failure type (C = Concrete, S = Steel); corresponding strain values for extreme concrete fiber, bottom steel and top steel

Failure mode	Failure type	Concrete	Bottom steel	Top Steel
A	C	$\varepsilon_c = -\varepsilon_{cu}$	$\varepsilon_s \leq \varepsilon_{sy}$	$-\varepsilon_{sy} \leq \varepsilon'_s \leq \varepsilon_{sy}$
B	C	$\varepsilon_c = -\varepsilon_{cu}$	$\varepsilon_s \leq \varepsilon_{sy}$	$\varepsilon'_s \leq -\varepsilon_{sy}$
C	C	$\varepsilon_c = -\varepsilon_{cu}$	$\varepsilon_{sy} \leq \varepsilon_s \leq \varepsilon_{su}$	$\varepsilon'_s \geq \varepsilon_{sy}$
D	C	$\varepsilon_c = -\varepsilon_{cu}$	$\varepsilon_{sy} \leq \varepsilon_s \leq \varepsilon_{su}$	$-\varepsilon_{sy} \leq \varepsilon'_s \leq \varepsilon_{sy}$
E	C	$\varepsilon_c = -\varepsilon_{cu}$	$\varepsilon_{sy} \leq \varepsilon_s \leq \varepsilon_{su}$	$\varepsilon'_s \leq -\varepsilon_{sy}$
F	S	$-\varepsilon_{c2} \geq \varepsilon_c > 0$	$\varepsilon_s = \varepsilon_{su}$	$\varepsilon'_s \geq \varepsilon_{sy}$
G	S	$-\varepsilon_{c2} \geq \varepsilon_c > 0$	$\varepsilon_s = \varepsilon_{su}$	$-\varepsilon_{sy} \leq \varepsilon'_s \leq \varepsilon_{sy}$
H	S	$-\varepsilon_{cu} \geq \varepsilon_c \geq -\varepsilon_{c2}$	$\varepsilon_s = \varepsilon_{su}$	$\varepsilon'_s \geq \varepsilon_{sy}$
I	S	$-\varepsilon_{cu} \geq \varepsilon_c \geq -\varepsilon_{c2}$	$\varepsilon_s = \varepsilon_{su}$	$-\varepsilon_{sy} \leq \varepsilon'_s \leq \varepsilon_{sy}$
J	S	$-\varepsilon_{cu} \geq \varepsilon_c \geq -\varepsilon_{c2}$	$\varepsilon_s = \varepsilon_{su}$	$\varepsilon'_s \leq -\varepsilon_{sy}$

3 Domains for identification of failure mode

The axial force equilibrium of the section along the beam axis at failure can be expressed in non-dimensional form by the following equation, considering a null value of the axial load:

$$k - k' \cdot \frac{\rho'}{\rho} - \alpha \cdot \frac{1}{\rho} \cdot \frac{f_c}{f_y} \cdot \frac{x_u}{H} = 0 \quad (1)$$

where k , k' and α are expressed by the following relations:

$$k = \frac{\varepsilon_s}{\varepsilon_{sy}} \leq 1 \quad (2)$$

$$k' = -1 \leq -\frac{\varepsilon'_s}{\varepsilon_{sy}} \leq 1 \quad (3)$$

$$\alpha = -\frac{\int_0^{x_u} \sigma_c dx}{f_c \cdot x_u} \quad (4)$$

The mean stress factor α [1], [2] is determined using Eq. (4) considering the effective value of neutral axis depth x_u when the section reaches ultimate condition, either it is characterized by steel or concrete failure. In Eq. (4), the term σ_c is the concrete stress corresponding to the strain ε , according to the concrete constitutive law illustrated in Figure 2(b). The choice to express Eq. (1) in non-dimensional form using H has been here adopted since it allows to consider independently the influence of parameters c/H , ρ and ρ'/ρ . Writing Eq. (1) for each of the limit conditions which represents a transition between failure modes reported in Table 1 allows to define a set of equations which identify the boundaries of the corresponding failure mode domains. In this work it was chosen to represent the domains for different values of parameters ρ , f_c/f_y , ε_{su} in a Cartesian plane with the ratio ρ'/ρ in the horizontal axis and the cover-to-height ratio c/H in the vertical axis. An example of the obtained graphs is shown in Figure 3(a). By assuming a constant value of the concrete cover c , it is possible to show on the vertical axis the corresponding values of the heights H obtained varying the cover-to-height ratio, as shown in Figure 3(b). Graphs illustrated in Figure 3 are obtained using $\rho=2.5\%$, $f_c=25$ MPa, $f_y=450$ MPa, $\varepsilon_{cu}=3.5\%$ and $\varepsilon_{su}=75\%$.

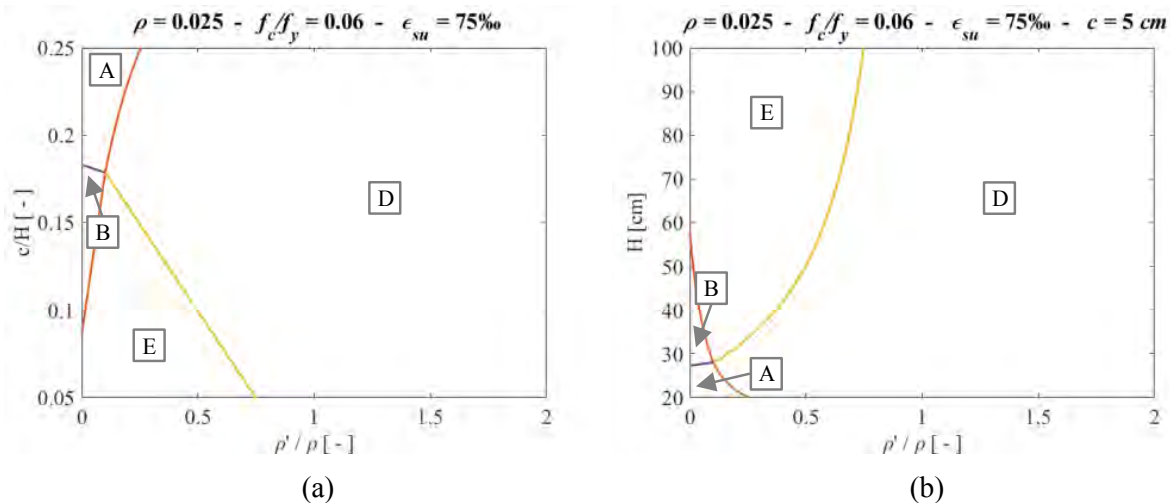


Fig. 3 Example of domains for identification of the ultimate condition for doubly reinforced concrete beam sections (a) as a function of non-dimensional parameters; (b) as a function of section height H , given a constant value of concrete cover $c = 5$ cm

This representation of the domains evidences the dependence of the failure mode on geometrical ratios c/H and ρ'/ρ . The parameter c/H varies between 0.05 and 0.25 (its physical limit is 0.5, but it is unreasonable to assume too high values, as they are not representative of real beam sections). The ratio ρ'/ρ varies between 0 and 2. It can be seen that, despite the range considered for values of parameters c/H and ρ'/ρ , only few of the possible failure modes actually occur.

Varying the other non-dimensional parameters which influence the ultimate condition of the beam section, it is possible to investigate how they affects the shape and location of failure mode domains. Figure 4 shows three domains configurations obtained by varying the reinforcement ratio ρ , between 0.5‰ and 2.5‰, all other parameters being constant. This range is chosen in order not to represent sections for which premature failures could occur just after concrete cracks [3], while assuring section have sufficient ductility by limiting the maximum value of ρ [2]. Mechanical material properties are the same as previously adopted for graphs in Figure 3. It can be seen that, as the reinforcement ratio ρ increases, the top steel is more prone to yield in compression (occurrence of failure mode E). It is worth noting that European Standard EN1998-1 [3] provides a detail rule for ductility of beam sections assuming the occurrence of failure mode E only [4].

The next section deals with the combined influence of geometrical and material parameters on the configuration of failure mode domains.

4 Combined influence of non-dimensional geometrical and material parameters on failure mode domains configuration

By significantly varying the mechanical material parameters, the corresponding domains notably change, showing significantly different failure modes. The effect of the f_c/f_y parameter on the domain shape is examined by varying concrete strength f_c between 30 MPa and 50 MPa while assuming a constant value for steel yielding strength f_y , equal to 450 MPa. According to the Model Code 2010 parabola – rectangle law [7], the ultimate compression strain of concrete ϵ_{cu} can be assumed as a constant equal to 3.5‰ for different concrete strength classes, up to the C50/60 class. In order to analyze the effect of the ultimate tensile strain of reinforcing steel ϵ_{su} on the domains shape, some preliminary considerations about the values of this parameter at the ultimate condition of the beam section are proposed in the following. Due to cyclic loading, buckling of longitudinal rebars can develop. In such a case, premature failure of the longitudinal reinforcement in tension may occur [4]. The Model Code 2010 [7] proposes for ultimate curvature calculation a reduced value of ultimate steel strain under cyclic loading equal to $3/8 \cdot \epsilon_{su,k}$, being $\epsilon_{su,k}$ the characteristic value of ultimate strain. In order to avoid the occurrence of buckling, longitudinal rebars need to be adequately constrained by the presence of stirrups or other retaining devices. To ensure this, limitations on longitudinal rebars diameter and/or limitations on spacing and diameter of the stirrups need to be assumed.

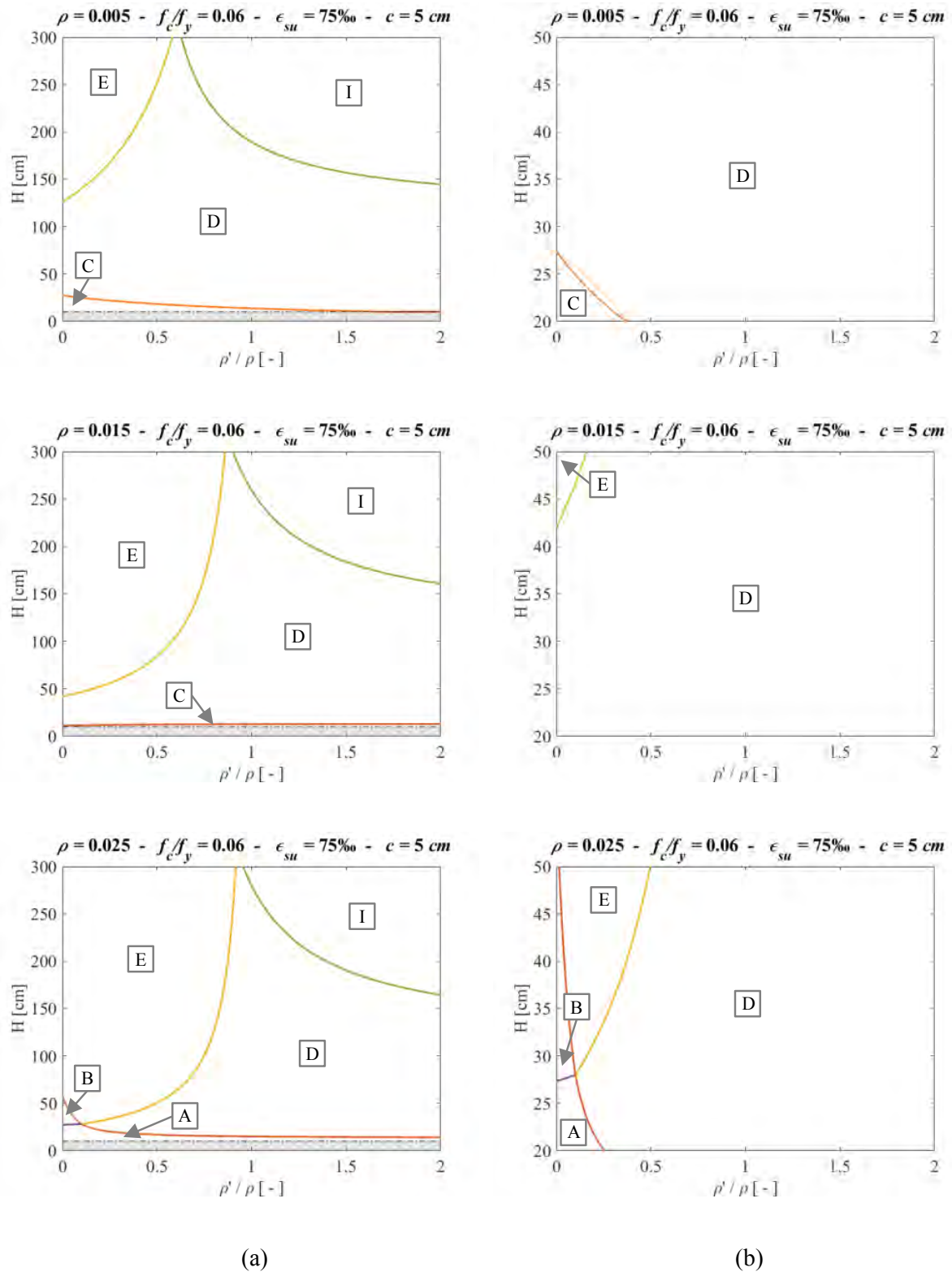


Fig. 4 Influence of the bottom reinforcement geometrical ratio ρ on the shapes of failure mode domains for a section with $f_c=25\text{MPa}$, $f_y=450\text{MPa}$, $\epsilon_{cu}=3.5\text{‰}$ (a) Complete height range; (b) Usual height range for doubly reinforced concrete beams

Some indications about such limitations are reported in the work of Priestley et al. [5], which provides a maximum value of stirrups spacing. A similar criterion is proposed by the New Zealand Standard NZS3101 [9], which explicitly defines limits to be respected in the construction details of the stirrups of ductile beams in order to prevent buckling of the longitudinal reinforcement. Priestley et al. [5] underlined that the ultimate tensile strain of reinforcing steel of a beam section under alternate cyclic loading should be assumed lower than the value assumed for monotonic load condition, even if buckling phenomena in longitudinal rebars are prevented. The authors propose to use in calculations a value for ultimate steel tensile strain equal to $0.6 \cdot \varepsilon_{su,n}$, assuming $\varepsilon_{su,n}$ to be the nominal ultimate tensile strain, which can be conservatively assumed equal to the characteristic value. If, in addition, possible situations in which the reinforcement is affected by corrosion are considered, then, as is well known, the ultimate tensile strain of the corroded reinforcement will be lower than that of the sound rebars [8], [9]. Therefore, a steel failure of the section for which the reinforcement develops an ultimate tensile strain ε_{su} almost equal to the characteristic value $\varepsilon_{su,k}$ appears to be possible only if construction details which prevent buckling of the compressed reinforcement are present, the loading condition is monotonic and the materials are not affected by degradation phenomena. It can be seen that, due to the causes listed above, the value of the ultimate steel strain ε_{su} to be used in the calculation of the failure condition can vary significantly.

Considering the variability of the parameters analyzed above, three possible configurations of failure mode domains are identified, indicated as *Type 1*, *Type 2* and *Type 3*, as depicted in Figure 5. The domains configuration changes from *Type 1* to *Type 2* and up to *Type 3*, when either ultimate steel strain ε_{su} and/or reinforcement ratio ρ decrease and when the ratio between concrete strength and steel yielding strength f_c/f_y increases. Accordingly, the non-dimensional parameters ε_{su} , ρ and f_c/f_y have been varied in order to obtain the three different configuration types represented in Figure 5. In particular, Figure 5(a, b) represent *Type 1* configuration, which is the same illustrated in Figure 3 and Figure 4. For this configuration steel failures almost never occur, considering reasonable values of c/H . For *Type 2* configuration, Figure 5(c, d), steel failures may be achieved for beams with low values of parameters ρ'/ρ and c/H . In *Type 3* configuration, Figure 5(e, f), domains related to steel failures overwhelm the other ones. Since *Type 2* and *Type 3* configurations are characterized by low values of ultimate steel strain, the deformation capacity of the section associated with steel failures for those cases will be very low. This fact must be taken into account during the design phase.

Analyzing the variation of the boundaries of the failure mode domains with the non-dimensional parameters, it is possible to determine analytical conditions which define the domains configuration type which takes place. In particular, the *Type 1* configuration occurs when the following inequality applies:

$$\varepsilon_{su} - \varepsilon_{cu} \cdot \left(\alpha \cdot \frac{1}{\rho} \cdot \frac{f_c}{f_y} - 2 \right) > 0 \quad (5)$$

The *Type 3* configuration occurs instead when:

$$\varepsilon_{su} - \varepsilon_{c2} \cdot \left(\alpha \cdot \frac{1}{\rho} \cdot \frac{f_c}{f_y} - 2 \right) < 0 \quad (6)$$

In cases when nor Eq. (5) neither Eq. (6) are satisfied, the *Type 2* configuration is achieved.

5 Conclusions

This work is part of a broader research dealing with behaviour of new and existing reinforced concrete elements also accounting for degradation phenomena, with a particular focus on flexural behaviour and ductility. The presented study proposed failure mode domains which can be useful to analyze the ultimate conditions of beam sections during the design phase, studying the influence of different non-dimensional parameters, allowing as a consequence a more conscious design. The influence of phenomena such as cyclic loading related to seismic actions and the presence of corrosion in the reinforcement can also be considered, though in a simplified way, through a modification of the reinforcing steel properties.

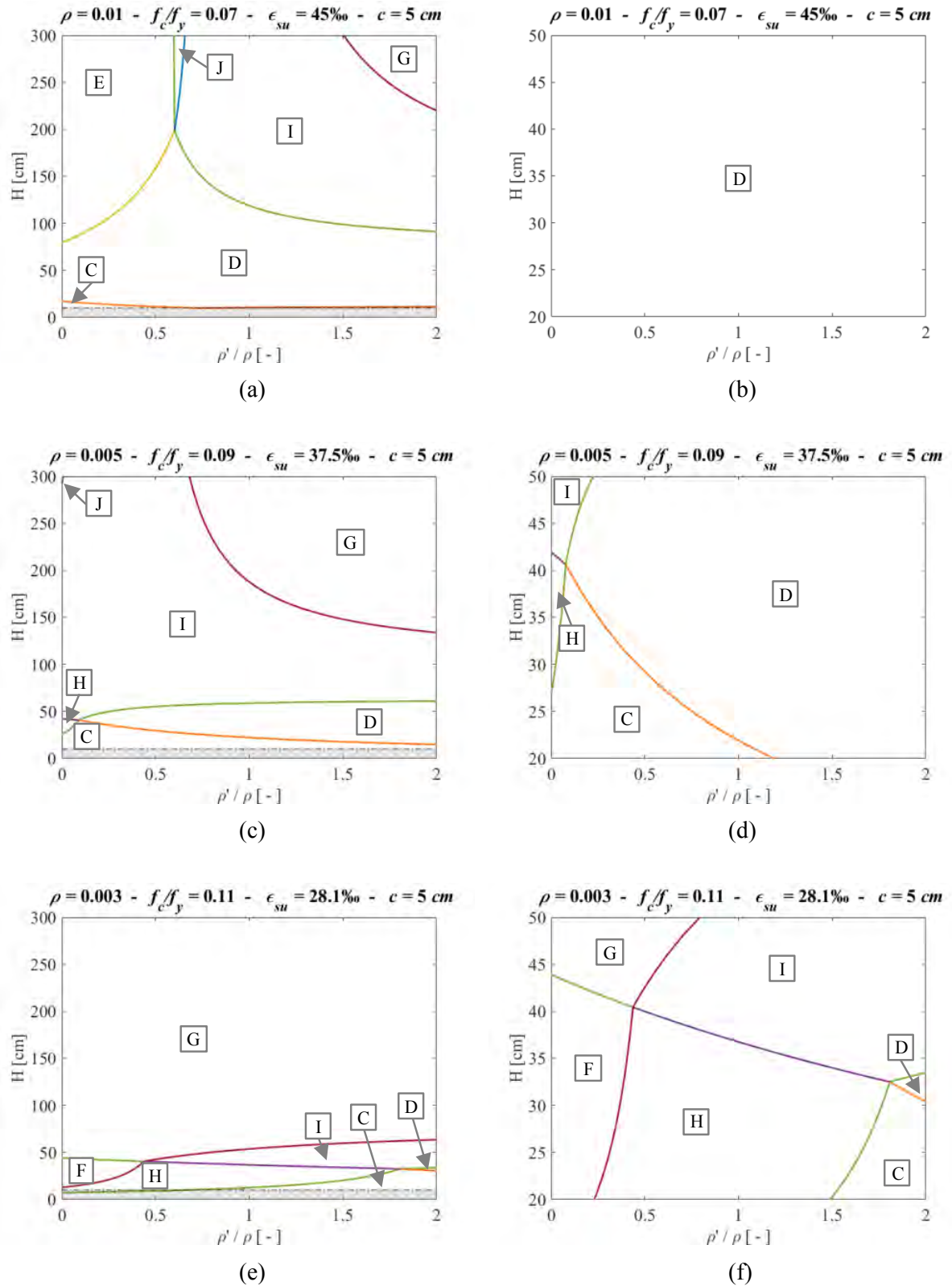


Fig. 5 Example of domains for identification of the ultimate condition for doubly reinforced concrete beams, given a constant value of concrete cover $c = 5$ cm. (a), (b) *Type 1* configuration, $f_c = 30$ MPa, $f_y = 450$ MPa; (c), (d) *Type 2* configuration, $f_c = 40$ MPa, $f_y = 450$ MPa; (e), (f) *Type 3* configuration, $f_c = 50$ MPa, $f_y = 450$ MPa.

The presented analytical formulation is based on some simplifications, as an example, in terms of the the adopted constitutive laws for steel and concrete. A further development of the presented work concerns the adoption of concrete constitutive models with post-peak strength degradation and the accounting of cover spalling at the ultimate condition.

The proposed approach is particularly effective for the formulation of curvature capacity models for new and existing doubly reinforced concrete beams.

Acknowledgements

The research activity was partially funded by the project DPC-ReLUIs 2019-21 - WP11 Contribution and review of technical standards for constructions – Concrete structures. Authors wish to acknowledge encouragement and useful suggestions from Eng. Alessandro Gasparini.

References

- [1] Park R, Paulay T. 1975. Reinforced Concrete Structures. Wiley.
- [2] Park R, Ruitong D. 1988. Ductility of Doubly Reinforced Concrete Beam Sections. *ACI Struct J* 85:217–225.
- [3] CEB. 2004. EN1998 *Eurocode 8: Design of structures for earthquake resistance*.
- [4] Fardis MN. 2009. *Seismic design, assessment and retrofitting of concrete buildings: based on EN-Eurocode 8*. Springer Science & Business Media.
- [5] Priestley MJ., Calvi GM, Kowalsky M. 2007. *Displacement-Based Seismic Design of Structures*. Pavia, Italy: IUSS Press.
- [6] Du Y, Clark LA, Chan AHC. 2007. Impact of reinforcement corrosion on ductile behavior of reinforced concrete beams. *ACI Struct J* 104:285–93.
- [7] The International Federation for Structural Concrete (*fib*). 2011. Model Code 2010. *Fib Model Code for Concrete Structures 2010*.
- [8] Cairns J, Plizzari GA, Du Y, Law DW, Franzoni C. 2005. Mechanical Properties of Corrosion-Damaged Reinforcement. *ACI Struct J* 102:256–64.
- [9] Finozzi I, Satta A, Budelmann H. 2018. Structural response of reinforcing bars affected by pitting corrosion: experimental evaluation. *Constr Build Mater* 192:478–88.

Durability and life assessment

Water Vapor Sorption of Hardened Cement Pastes: Impact of Temperature and Carbonation

Zhen Wang, Kefei Li

*Civil Engineering Department,
Tsinghua University,
100084 Beijing, P.R. China*

Abstract

Water vapor sorption is the key tool for characterizing the moisture properties of cement-based materials, temperature and carbonation have significant impact on it. The water vapor sorption isotherms and kinetics were measured with a dynamic vapor sorption instrument, for noncarbonated and carbonated cement pastes under three temperatures. The isotherms were analyzed and the GAB (Guggenheim-Andersen-de Boer) [1] model was used to fit the isotherms. The sorption kinetics were interpreted through the pseudo-first and -second order models. The results show that carbonation reduces moisture content and specific surface area, turns the kinetics to lower order law while higher temperatures have opposite impacts, but both inhibit hysteresis and strengthen the surface attraction to water.

1 Introduction

Moisture is closely related to various processes of cement-based material deterioration. The long-term durability of cement-based materials is significantly impacted by the interaction between moisture and porous matrix, therefore, an accurate knowledge of moisture properties is indispensable for realistic assessment of cement-based materials in engineering service states. Water vapor sorption is the key tool for characterizing the moisture properties of cement-based materials, including equilibrium properties and kinetics. Water vapor sorption isotherm (WVSI) describes the relationship between the moisture content retained at equilibrium and the ambient relative humidity (RH), providing basic inputs for the multi-phase transport model. Meanwhile, water molecules can probe the smallest C-S-H interlayer spaces [2], allowing WVSI to provide abundant information on pore structures, surface properties, and insights into the underlying mechanisms of water-matrix interaction. Sorption kinetics is related to different mechanisms involved in overall sorption process. Proper kinetic models are of crucial importance for predicting sorption rate and revealing underlying mechanism. Furthermore, the responses of water vapor sorption to ambient temperature change and carbonation are of particular interests for engineering application, for concrete structures which are exposed to different temperatures and carbonation by atmospheric CO₂.

Considerable works have been done to investigate the water vapor sorption characteristics of cement-based materials. Saturated salt solution method and dynamic vapor sorption (DVS) method have been adopted to measure WVSI and sorption kinetics, a series of models has been applied to analyze them. Hysteresis, especially low-RH hysteresis was found in WVSI of cement-based materials. Pore structures, surface properties, transport properties can be deduced from water vapor sorption characteristics. Some studies focused on the thermal impact on water vapor sorption [3]-[6], but the conclusions were inconsistent with each other. Some results are also available for carbonation impact on WVSI [7]-[9], but further research is needed for a better knowledge of the impact.

In this study, a systematic measurement on the water vapor sorption behaviors of hardened cement paste was conducted using automatic DVS devices, under different temperatures (25, 40, and 60°C) and with or without carbonation. The sample compositions were determined with thermogravimetric methods. Measured WVSI and kinetics were analyzed along with the temperature and carbonation impacts. The GAB (Guggenheim-Andersen-de Boer) model [1] was adopted to fit the WVSI, and the regressed parameters were discussed. The kinetics was interpreted through pseudo-first order and pseudo-second order models.

2 Materials and experiments

Hardened cement pastes were prepared with water-to-cement ratio of 0.5. The cement used was of type ordinary Portland cement PO 42.5, the mineral composition provided by the manufacturer is given in Table 1. The pastes were cast into molds of 4 cm × 4 cm × 16 cm, demolded at 1d and cured in saturated lime water under ambient temperature controlled to (20±3)°C. Prisms were divided into two groups, the non-carbonation group and carbonation group. The carbonation group were taken out of water at the age of 28 days, 60°C-oven dried for 2d, sliced with saw, and then placed in a test chamber in which the CO₂ concentration was kept at (3±0.2)%, the temperature at (20±2)°C, and relative humidity at (70±5)% RH until total carbonation, which was checked by phenolphthalein indicator and thermogravimetric (TGA) results. The non-carbonation group was taken out of water at the age of 720 days, sliced with saw, vacuum-dried at 40°C for 48 hours, then oven-dried at 60°C for 48 hours. After this treatment, the samples were stored in a slight vacuum to prevent carbonation. The non-carbonated sample was noted as PN, and the carbonated samples was note as PC.

Table 1 The mineral composition (wt.%) of cement in this study.

CaO	SiO ₂	Al ₂ O ₃	Fe ₂ O ₃	SO ₃	MgO	Na ₂ O	Cl	Ignition loss
62.99	22.02	4.00	3.48	2.72	2.58	0.53	0.01	1.67

Dynamic water vapor sorption experiments were conducted with a DVS-Adventure analyzer manufactured by Surface Measurement Systems, UK. This device continuously records the mass change of the sample in a gas flow with precisely controlled flow rate, RH and temperature. High purity nitrogen was used as carrier gas to prevent possible carbonation during sorption experiments. Samples for DVS sorption experiments were crushed, ground and sieved between 200µm and 500µm, and each water vapor sorption experiment used approximately 30mg of dry particles. The target temperature of incubator was set to be 25, 40, and 60°C, respectively, for different PN and PC samples. The RH control program includes a zero-humidity drying stage, and a full adsorption – desorption cycle between 0% and 95% RH, with a 10% RH step. The criterion of equilibrium in a single RH step was $|dm/dt| \leq 0.002$ wt.%/min continuously in a 10 minutes period. Extrapolations with the kinetic models in Section 3.2 predict differences less than 0.002 g/g and 0.005 g/g below and above 80% RH between asymptotic sorption values and measured data, which are insignificant compared to the total sorption. The maximum stage time was set to be 10 hours, which is enough for all the steps. The whole program took about 50 hours for PN samples and 24 hours for PC samples. At the end of each experiment, the recorded sample mass was determined as the reference mass m_0 (mg) for calculating evaporable moisture mass. It is noteworthy that samples equilibrated at zero humidity under different temperatures correspond to different hygral state. In order to provide a common reference for comparing data measured under different temperatures, samples were dried at zero humidity under 25, 40, and 60°C consecutively in DVS IsoActivity mode, with the same equilibrium criterion in sorption experiments. The evaporable moisture content W (g/g) was calculated with

$$W = \frac{m - m_0}{m_{\text{ref}}} \quad (1)$$

where m is the sample mass (mg), m_{ref} is the reference mass (mg) which corresponds to isothermally-dried state at zero humidity under 60°C.

Thermogravimetric analysis (TGA) was performed on powdered PN and PC samples. TGA was conducted using a TA Q5000IR analyzer, the temperature range was room temperature to 900°C, and the heating rate was 10°C/min. Portlandite content was calculated with the peak between 400-500°C in the derivative of TGA curve (DTG) using tangential method [10], and the mass loss between 520-950°C was converted to the amount of calcium carbonate. In addition, to measure the mass increase due to carbonation and provide a common reference for analyzing compositions, samples were oven-dried at 105°C for 24 hours to achieve constant weight, then heated to 1050°C in muffle furnace and calcined for 3 hours. Under the assumption that PN and PC have the same compositions at 1050°C, the ratios between mass at 105 and 1050°C were used to normalize sample compositions.

3 Analysis of water vapor sorption

3.1 Sorption isotherms and hysteresis

The WVSIs depict the moisture content retained at equilibrium in terms of ambient RH. In adsorption isotherms (WVAIs), ambient RH increases monotonically from 0% RH. The WVAIs of most building materials, including cement-based materials, are inverse S-shaped type II isotherms [11]. Desorption isotherms (WVDIs) measures moisture content as ambient RH decreases to zero humidity. Measured WVSIs of PN and PC under 25°C are illustrated in Fig. 1 (left). WVAIs are inverse S-shaped, but the WVDI of PN sample has different shape, and a sudden drop in 40-30% RH can be observed. The hysteresis between WVAI and WVDI of PN sample is notable, even in low-RH region. Carbonation significantly reduced moisture content and hysteresis extent in the whole RH range, however, it is noteworthy that PC sample adsorbed slightly more water in the first 0-10% RH range.

We define a moisture storage coefficient $k = \Delta W / \Delta RH$ of each sorption step for a better description and interpretation of WVSIs. The coefficient k for PN and PC samples under 25, 40 and 60°C is plotted in Fig. 1 (right), with the x-coordinates of data representing the target RH of each step. All adsorption k -curves are U-shaped, representing ranges of monolayer adsorption, multilayer adsorption and capillary condensation. High values of k at 10% RH, followed by a sharp drop at 20% RH, indicate a strong monolayer adsorption in 0-10% RH and a conversion to multilayer adsorption in 10-20% RH. Minor variation of k was found between 20 and 60% RH, corresponding to the predominating multilayer adsorption in this range. Above 60% RH, k starts to increase and reaches quite high value in 90-95% RH, implying significant capillary condensation in this range. For PN sample, increased temperatures lead to higher k in 0-10% RH, but this tendency is reversed immediately above 20% RH, and much lower k under 40 and 60°C was measured in capillary condensation region. For PC sample, k -curves share similar shape with that of PN sample, but much less water was adsorbed above 20% RH, and only limited temperature impact was observed.

In desorption branches, the shape of k -curves of PN sample is more complicated. A sudden drop of moisture content can be distinguished in the range of 50-30% RH, which is believed to be induced by the spontaneous cavitation of water confined in cavities of ink-bottle pores [12]. In 10%-0% RH, more water is desorbed than adsorbed in corresponding RH range. For PC samples, the cavitation extent was much smaller, and the k -curves are much closer to that in adsorption branches.

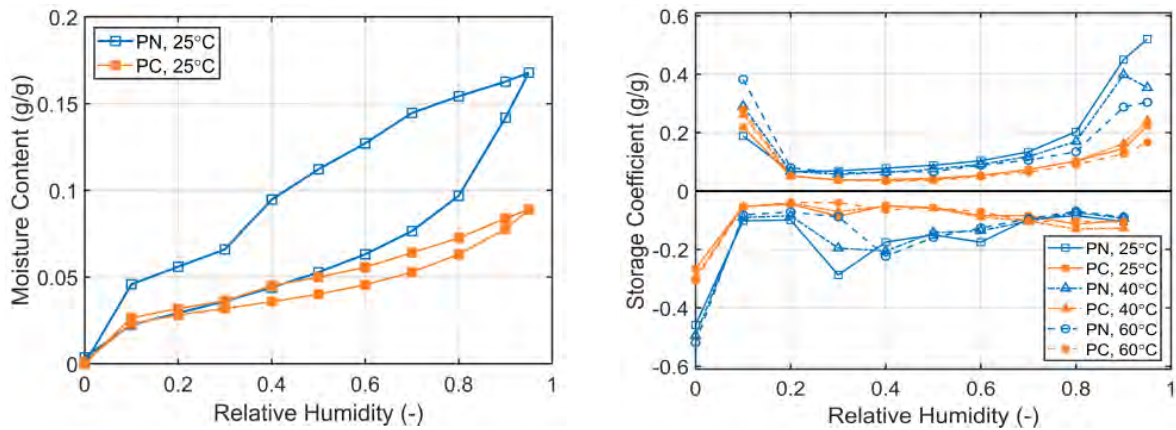


Fig. 1 WVSIs of PN and PC samples under 25°C (left). Water vapor storage coefficients of PN and PC samples under 25, 40 and 60°C (right).

The hysteresis curves are plotted in Fig. 2. For PN samples, a peak at 70% RH is available for all curves. In high RH ranges, hysteresis may arise from ink-bottle / pore blocking effects [13]. The cavitation-induced drop in desorption branches leads to the reduction of hysteresis by removing liquid water constricted in ink-bottle pores. Hysteresis in low-RH range remains obvious, which is different from nitrogen sorption results [2]. For cement-based materials, the snap-through instability [14], hindered molecular condensation during nanopore filling [15], and C-S-H interlayer space collapse and recover [16] may explain the low-RH hysteresis. The inhibition effect of increased temperatures on hysteresis can be observed clearly. The dissipation of “metastable” ink-bottle effect may be accelerated by increased temperatures [2], and similar mechanism may apply for low-RH hysteresis, for

water molecules with higher energy can penetrate interlayer spaces more easily. For PC samples, the hysteresis is sharply reduced in the whole RH range under 25°C, and it further decreases with temperature. Special attention should be given to the low-RH hysteresis of PC samples, which may be related to the properties of decalcified C-S-H.

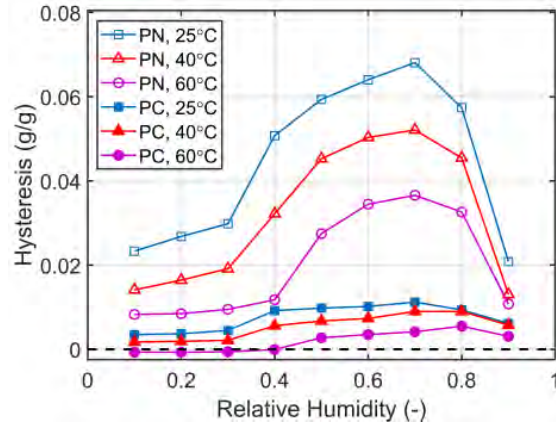


Fig. 2 Water vapor sorption hysteresis curves of PN and PC samples at 25, 40 and 60°C.

The GAB (Guggenheim-Andersen-de Boer) model [1], which is a refinement to the classical BET (Brunauer-Emmett-Teller) [17] model for multilayer physisorption, is adopted in this study to fit the WVSIs in the range of 0-80% RH. The three-parameter GAB equation reads

$$W = W_m \frac{CK \cdot RH}{(1 - K \cdot RH)[1 + (C-1)K \cdot RH]} \quad (2)$$

where W_m is the monolayer capacity (g/g), C and K are energy-related constants which can be expressed as [18]

$$C = \exp \left\{ \frac{\mu'_{\text{multilayer}} - \mu'_{\text{monolayer}}}{RT} \right\} > 1 \quad (3)$$

$$K = \exp \left\{ \frac{\mu'_{\text{liquid}} - \mu'_{\text{multilayer}}}{RT} \right\} < 1 \quad (4)$$

where $\mu'_{\text{monolayer}}$, $\mu'_{\text{multilayer}}$ and μ'_{liquid} are the standard values of chemical potentials (kJ/mol) of water molecules in the monolayer, multilayer and liquid state, respectively. R is the ideal gas constant ($8.314 \text{ J} \cdot \text{K}^{-1} \cdot \text{mol}^{-1}$), and T is the absolute temperature (K). The product CK and constant K reflect the interaction strength of molecules in monolayer and multilayer with respect to molecules in bulk water. The specific surface area S (SSA, m^2/g) can be calculated with W_m as

$$S = \frac{W_m N_A}{M_w} A_m \quad (5)$$

where N_A is the Avogadro constant ($6.022 \times 10^{23} \text{ mol}^{-1}$), M_w is the molar mass of water (18.02 g/mol), and A_m is the area occupied by a single water molecule in the adsorbed monolayer (10.5 \AA^2). It is noteworthy that regressed SSA values are apparent values because the filling of nanoscale interlayer spaces might be different from physisorption.

The GAB-fitted curves are shown in Fig. 3. In the range of 0-80% RH, the GAB model can well fit the WVAIs of PN and PC samples and the WVDIs of PC samples with $R^2 > 0.99$, but fails to capture the cavitation phenomenon in WVDIs of PN samples. All regressed parameters from WVAIs are showed in Table 2 and Table 3. The ambient RH h_m corresponds to monolayer coverage is calculated by letting $W = W_m$ in Eq. (1), and the SSA is calculated from W_m with Eq. (5). Data in Table 2 correspond to full monolayer coverage, and data in Table 3 provide energy-related information. Higher temperatures lead to remarkable increase of W_m and SSA. The value of h_m is reduced with temperature, suggesting that water molecules adsorbed in monolayer region may have stronger interaction with matrix at increased temperatures, which is also suggested by the increased value of CK with

temperature in Table 3. After carbonation, the SSAs decreased by about 10-30% for PC samples, indicating that the majority of monolayer sorption sites are still available in PC samples. The notable increase of CK and decrease of h_m suggest a stronger attraction of matrix surface to water molecules after carbonation. The decrease of k under increased temperatures and carbonation implies that water molecules in multilayer become less stable in these states.

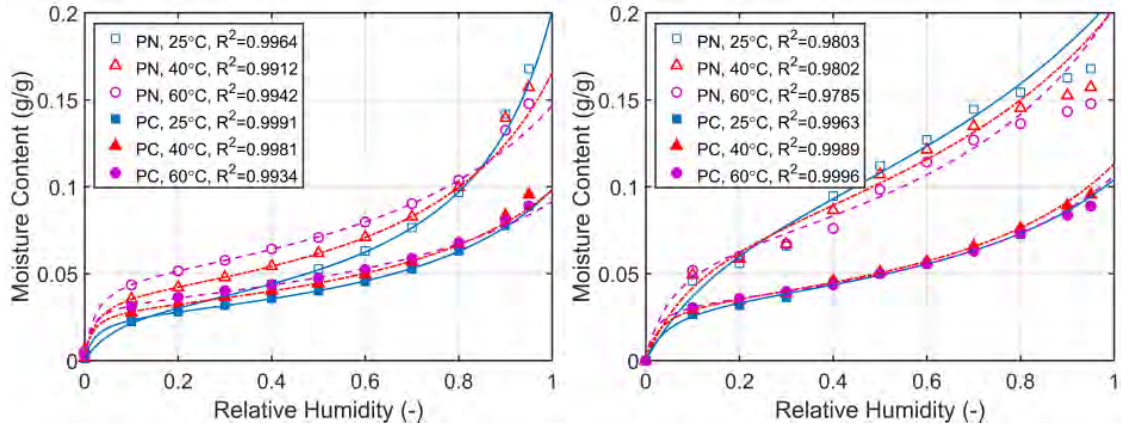


Fig. 3 GAB-fitted curves for WVAIs (left) and WVDIs (right).

Table 2 Regressed GAB monolayer capacity W_m , specific surface area (SSA), and corresponding ambient RH h_m calculated from WVAIs measured at 25°C, (40°C), and [60°C].

Samples	W_m (% g/g)	SSA (m ² /g)	h_m (%)
PN	3.30 (3.91) [4.86]	116 (137) [171]	23.9 (14.9) [15.8]
PC	2.61 (2.96) [3.31]	91.8 (104) [116]	15.6 (13.1) [12.8]

Table 3 Regressed GAB energy-related constants calculated from WVAIs (0-80% RH) at 25°C, (40°C), and [60°C].

Samples	C	K	CK
PN	16.0 (60.5) [71.5]	0.839 (0.766) [0.671]	13.4 (46.3) [48.0]
PC	59.1 (98.2) [126.2]	0.737 (0.699) [0.640]	43.5 (68.7) [80.7]

3.2 Sorption kinetics

Non-Fickian sorption kinetics has been observed for cement-based materials [19]. In this study, the pseudo-first and pseudo-second order (PFO and PSO) models are used to fit the kinetic curves of PN and PC samples. The sorption rates are respectively proportional to the first and second power of the difference between sorption mass $q(t)$ (mg) and equilibrium sorption mass q_e (mg). With the initial condition $q(t=0) = 0$, the sorption mass $q(t)$ is expressed in the PFO and PSO model as

$$q(t) = q_e [1 - \exp(-K_1 t)] \quad (6)$$

$$q(t) = \frac{K_2 q_e^2 t}{1 + K_2 q_e t} \quad (7)$$

where K_1 (min⁻¹) and K_2 ((g/g·min)⁻¹) are respectively the PFO and PSO rate constants. It was suggested in [20] that the PFO model fits kinetic curves better when transport process of adsorbate limits the overall sorption rate, while the PSO model dominates as the sorption between adsorbate molecules and substrate surface is rate-controlling. Some fitting results for adsorption and desorption kinetic curves are plotted in Fig. 4 and Fig. 5.

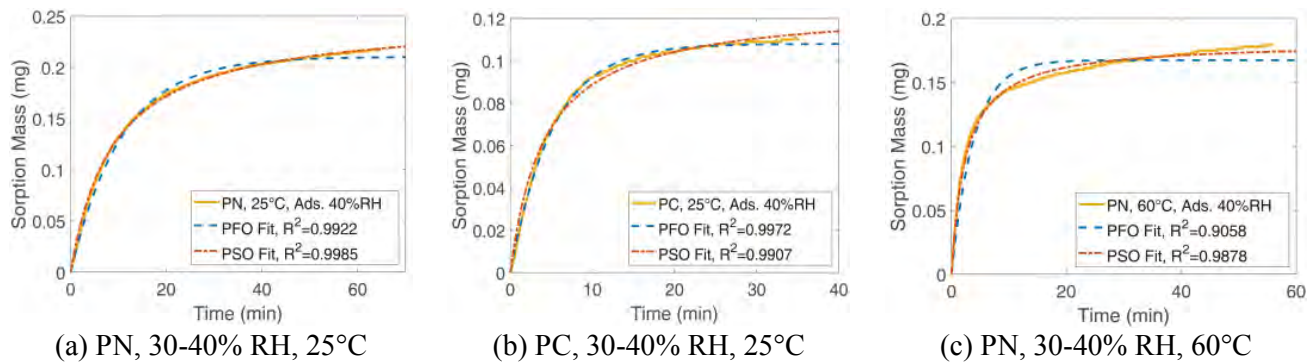


Fig. 4 Typical PFO- and PSO-fitted adsorption kinetic curves of PN and PC samples.

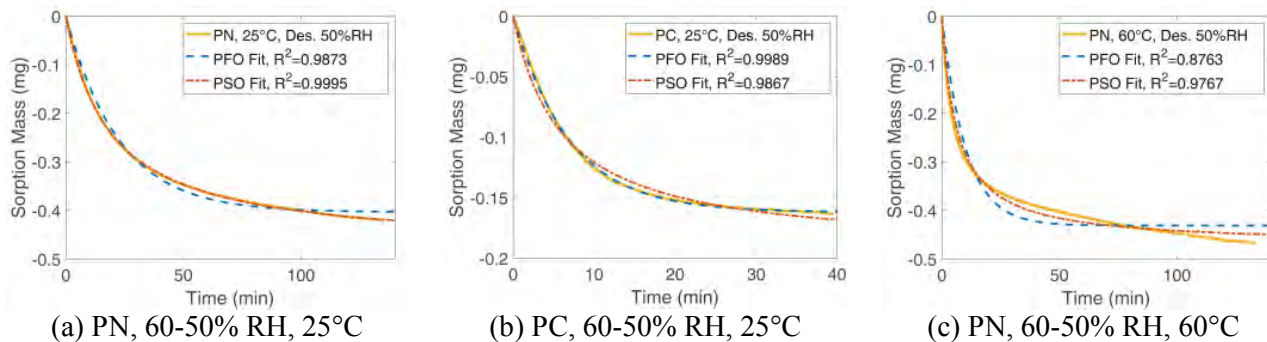


Fig. 5 Typical PFO- and PSO-fitted desorption kinetic curves of PN and PC samples.

For PN samples, the PFO model is suitable for describing monolayer adsorption kinetic curves in 0-10% RH, while the PSO model can better depict most kinetic curves of other RH steps. In 0-10% RH, the bare substrate surface has strong attraction towards the water molecules, and the sorption sites are fully available, therefore, the transport of water molecules may be rate-controlling. After the completion of monolayer coverage, kinetics is more related to weaker interaction between water molecules in vapor state and in adsorbed multilayer film, resulting in slower adsorption rates. In 80-90% RH, both models fail to depict the kinetics, suggesting that other mechanisms during pore condensation may intervene. Globally, the PSO model can better describe desorption kinetics in most RH steps, except for the cavitation and pore evaporation region. After carbonation, the PFO model globally fits better than the PSO model for both adsorption and desorption steps, cf. Fig. 4(b) and 5(b), even in capillary condensation/evaporation regions. Under increased temperatures, higher-order kinetic law may be necessary to describe the kinetic curves in multilayer region, cf. Fig 4(c) and 5(c).

4 Further discussion

4.1 Temperature impact on water vapor sorption

Theoretically, physisorption is an exothermic process, which should be depressed under increased temperatures, leading to the “thermal desorption” described in [3]. However, in this study, increased temperatures lead to significantly higher evaporable moisture content retained below 80% RH in adsorption and above 30% RH in desorption, cf. Fig. 3. It is believed that much higher amount of water adsorbed in 0-10% RH, cf. Fig. 1 (right), is the main reason for the elevation of moisture content. We believe that this phenomenon derives from different hygral state at zero humidity under different temperatures. At zero humidity, increased temperature further mobilizes and removes water from interlayer spaces, where water molecules have stronger interactions with C-S-H sheets. The re-entry of this part of water, which may act differently from physisorption, will lead to elevation of isotherms with temperature and increased value of regressed SSAs and CK. The value of k decreases with temperature above 20% RH, cf. Fig. 1 (right), which suggests that the “thermal desorption” mechanism is still valid.

4.2 Carbonation impact on water vapor sorption

After carbonation, moisture content above 20% RH decreased significantly, while the monolayer sorption in 0-10% RH increased slightly under 25°C. The GAB regression gives much higher monolayer adsorption energy CK after carbonation, while the calculated SSAs decrease only by 10-30%. Hysteresis and cavitation are notably depressed, the low-RH hysteresis is almost eliminated. The TGA results in Table 4 show that the C-S-H of PN samples was also carbonated significantly.

During carbonation, the precipitation of carbonates microcrystals in mesopores will lead to the reduction of capillary porosity and ink-bottle effect, which can explain the reduction of moisture content and hysteresis in intermediate and high RH ranges. However, variations in low RH range should be related to decalcified C-S-H properties. Groves et al. [21] suggested that the overall morphology of the C-S-H gel is preserved after carbonation, which may account for the largely remained SSAs observed in PC samples. Meanwhile, the enhanced monolayer adsorption after carbonation indicated by the increased value of CK might be explained by the reduction of alkaline ions concentration in pore solution and their shield effect on surface. In addition, the decalcified C-S-H have a more deformable structure, which may account for the reduction of low-RH hysteresis.

Table 4 Portlandite (CH) and carbonate (CC) contents calculated with TGA results (wt. % corresponding to NC samples).

Samples	CH content	CC content	CC from CH carbonation	CC from C-S-H carbonation
PN	11.35	6.10	--	--
PC	--	61.90	15.34	40.46

5 Conclusions

The water vapor sorption of hardened cement pastes was investigated along with the impact of temperature and carbonation. The WVSIs, hysteresis and sorption kinetics were described in detail, the GAB model was applied to fit the WVSIs, and the pseudo-first and -second order models were used to analyze the kinetic curves. The results show that carbonation reduces moisture content and specific surface area, turns the kinetics to lower order law while higher temperatures have opposite impacts, but both of them inhibit hysteresis and strengthen the surface attraction to water. The elevation of WVSIs under increased temperatures were attributed to the re-entry of interlayer water molecules motivated and removed by higher temperatures at zero humidity. The carbonation impact on water vapor sorption was explained with changes in pore structure, C-S-H morphology, concentration of alkali ions in pore solution, and the possible inter-layer deformability of C-S-H.

Acknowledgements

The research is supported by National Key R&D Program of China No. 2017YFB0309904, and NSFC project No. 51778332.

References

- [1] Anderson, Robert. B. 1946. "Modifications of the Brunauer, Emmett and Teller Equation." *Journal of the American Chemical Society* 68.4: 686-691.
- [2] Baroghel-Bouny, Véronique. 2007. "Water Vapour Sorption Experiments on Hardened Cementitious Materials. Part I: Essential Tool for Analysis of Hygral Behaviour and Its Relation to Pore Structure." *Cement and Concrete Research* 37.3: 414-37.
- [3] Poyet, Stéphane, and Sébastien Charles. 2009. "Temperature Dependence of the Sorption Isotherms of Cement-Based Materials: Heat of Sorption and Clausius–Clapeyron Formula." *Cement and Concrete Research* 39.11: 1060-67.
- [4] de Burgh, James M., and Stephen J. Foster. 2017. "Influence of Temperature on Water Vapour Sorption Isotherms and Kinetics of Hardened Cement Paste and Concrete." *Cement and Concrete Research* 92: 37-55.

- [5] Maruyama, Ippei., et al. 2019. "Dynamic Microstructural Evolution of Hardened Cement Paste During First Drying Monitored by 1-H NMR Relaxometry." *Cement and Concrete Research* 122: 107-17.
- [6] Wu, Min, Björn Johannesson, and Mette Geiker. 2014. "A Study of the Water Vapor Sorption Isotherms of Hardened Cement Pastes: Possible Pore Structure Changes at Low Relative Humidity and the Impact of Temperature on Isotherms." *Cement and Concrete Research* 56: 97-105.
- [7] Johannesson, Björn., and P. Utgenannt. 2001. "Microstructural Changes Caused by Carbonation of Cement Mortar." *Cement and Concrete Research* 31.6: 925-31.
- [8] Snoeck, D., et al. 2014. "The Influence of Different Drying Techniques on the Water Sorption Properties of Cement-Based Materials." *Cement and Concrete Research* 64: 54-62.
- [9] Auroy, Martin, et al. 2015. "Impact of Carbonation on Unsaturated Water Transport Properties of Cement-Based Materials." *Cement and Concrete Research* 74: 44-58.
- [10] Scrivener, Karen, Ruben Snellings, and Barbara Lothenbach. 2016. *A Practical Guide to Microstructural Analysis of Cementitious Materials*. Boca Raton: CRC Press.
- [11] Pavlík, Zbyšek, et al. 2011. "Water Vapor Adsorption in Porous Building Materials: Experimental Measurement and Theoretical Analysis." *Transport in Porous Media* 91.3: 939-54.
- [12] Maruyama, Ippei, et al. 2018. "Cavitation of Water in Hardened Cement Paste under Short-Term Desorption Measurements." *Materials and Structures* 51.6: 159.
- [13] Nguyen, Phuong T. M., D. D. Do, and D. Nicholson. 2011. "On the Cavitation and Pore Blocking in Cylindrical Pores with Simple Connectivity." *The Journal of Physical Chemistry B* 115.42: 12160-72.
- [14] Bažant, Zdeněk P., and Martin Z. Bazant. 2012. "Theory of Sorption Hysteresis in Nanoporous Solids: Part I Snap-through Instabilities." *Journal of the Mechanics and Physics of Solids* 60.9: 1644-59.
- [15] Bazant, Martin Z., and Zdeněk P. Bažant. 2012. "Theory of Sorption Hysteresis in Nanoporous Solids: Part II Molecular Condensation." *Journal of the Mechanics and Physics of Solids* 60.9: 1660-75.
- [16] Jennings, Hamlin M. 2008. "Refinements to Colloid Model of C-S-H in Cement: Cm-II." *Cement and Concrete Research* 38.3: 275-89.
- [17] Brunauer, S., P.H. Emmett, and E. Teller. 1938. "Adsorption of Gases in Multimolecular Layers." *Journal of the American Chemical Society* 60.2: 309-319.
- [18] Timmermann, Ernesto O. 2003. "Multilayer Sorption Parameters: BET or GAB Values?" *Colloids and Surfaces A: Physicochemical and Engineering Aspects* 220.1-3: 235-60.
- [19] Saeidpour, Mahsa, and Lars Wadsö. 2015. "Evidence for Anomalous Water Vapor Sorption Kinetics in Cement Based Materials." *Cement and Concrete Research* 70: 60-66.
- [20] Plazinski, W., W. Rudzinski, and A. Plazinska. 2009. "Theoretical Models of Sorption Kinetics Including a Surface Reaction Mechanism: A Review." *Adv Colloid Interface Sci* 152.1-2: 2-13.
- [21] Groves, G. W., D. I. Rodway, and I. G. Richardson. 1990. "The Carbonation of Hardened Cement Pastes." *Advances in Cement Research* 3.11: 117-25.

Internal hydrophobization of cement-based materials

Kalina Grabowska, Marcin Koniorczyk

*Department of Building Materials Physics and Sustainable Design,
Lodz University of Technology,
Al. Politechniki 6, 90-924 Lodz, Poland*

Abstract

The aim of the research was to assess the possibility of the use of various organosilicon compounds as admixtures for internal hydrophobization of porous building materials such as cement mortar. The study examined the effectiveness of three type of organosilicon compounds for internal hydrophobization. The following tests were performed: compressive strength, capillary water absorption and contact angle. The results have shown that two types of silicon-based compounds: poly(dimethylsiloxane) and triethoxyoctylsilane might provide an effective, but with some limitations, volume hydrophobization.

1 Introduction

Water has a crucial influence on the durability of building materials which are mostly porous. Penetrating water into the pore system of the material might cause its accelerated and irreversible destruction. The freezing water by increasing its volume might induce cracks. In addition, salt crystallization, growth of mold and fungi and general deterioration of hydrothermal conditions might occur. In case of cementitious materials appropriate implementation, selection of the components, relevant water to cement ratio, as well as further care of the material can partially contribute to the increase in the durability of the material. However, the use of appropriate additives and chemical admixtures may be important to increase the durability of the material, and thus the construction. One of the ways for protection of porous cement-based materials is internal hydrophobization by means of organosilicon compounds. The “*hydrophobization*” comes from Greek and means fear of water. A hydrophobic material is not or hardly wettable by water. A water-repellent agent used as admixture interact with cement phases during hydration and provides hydrophobicity of the internal pore structure of the material. The key function of the hydrophobic admixture is to prevent penetration of moisture or water into the pore structure of the porous material and thus increase its durability.

The organosilicon compounds (e.g., silicone resins, silanes and siloxanes) consist of chains and networks of silicon, oxygen and carbon atoms. The primary structure of organosilicon compounds is a polysiloxane chain (—O—Si—O—Si—O—) (Fig. 1A). The non-polar alkyl groups are attached as sidechains to the main siloxane chain. These organic substituents provide the water-repelling properties to organosilicon compound. The longer alkyl chain provides better hydrophobic effects. Due to this the organosilicon compounds are called amphiphilic ones which means they have both hydrophilic and hydrophobic parts in their structures. It allows for a gas and water vapor permeability, the ability to bind of organosilicon compound to the hydrophilic cement phases and at the same time the internal hydrophobization [1-4].

In this study three different commercial admixture based on three different organosilicon compounds were used. One of them is based on the poly(dimethylsiloxane) (PDMS) of which the schematic structure is shown at Figure 1B. PDMS is a complex, macromolecular, polymeric compound with a repeating group (unit) of the general formula: $\text{—[R}_2\text{Si—O]—}$ with methyl groups (—CH_3) as substituents attached to silicon atoms. Poly(dimethylsiloxane) is distinguished by flexible siloxane chain (Fig. 1A) arranged in helix with the methyl groups directed outwards. During interaction with hydrophilic substrate the siloxane chain of the PDMS will interact with the substrate and the non-polar groups will be located as far from the hydrophilic matrix as possible. Considering that poly(dimethylsiloxane) is already a polymer compound we assume that the only way for chemical reaction between cement phases and PDMS is by detaching one of the methyl groups from silicon atoms [1-4]. The other admixture is a water solution of potassium methylsiliconate (Fig. 2A). It is an alkaline ($\text{pH}=14$) solution of siloxane resin (Fig. 2B) in potassium hydroxide. Methylsiliconate under the influence of moisture (H_2O) and carbon dioxide (CO_2) present in the air, undergoes some chemical reactions which result in the separation of potassium carbonate and polycondensation of

methylsilicates into larger, spatially expanded particles [1,2,5-7]. Heretofore the siliconates were used as surface protection and preservation of monuments against water [8,9]. The main component of the third admixture is monomeric organosilicon compound: triethoxyoctylsilane (OTES) (Fig. 3). OTES is an emulsion of alkyltrialkoxysilane. Three ethoxy groups ($-\text{OEt}$) and one octyl group ($-\text{C}_8\text{H}_{17}$) are attached to one silicon atom. During hydrolysis reactions the silanol groups are formed. The hydroxyl groups can bond covalently to hydrophilic surface of cement-based materials and at the same time the polycondensation reactions take place between silanols molecules. Polycondensation of silanols leads to cross-linking and the formation of siloxane chains, resulting into a hydrophobic properties of the material. The alkyl substituent "R" is an organic, non-polar group which provide the hydrophobic properties to the cement matrix [3,6,7,10,11].

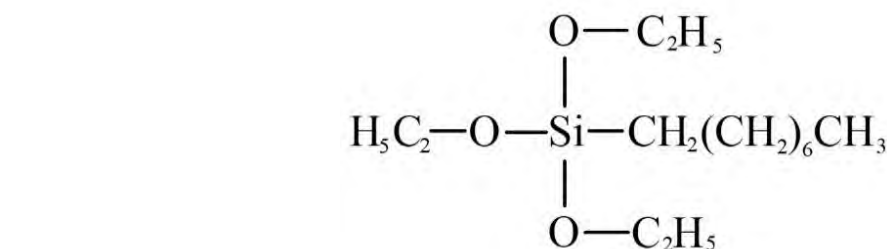
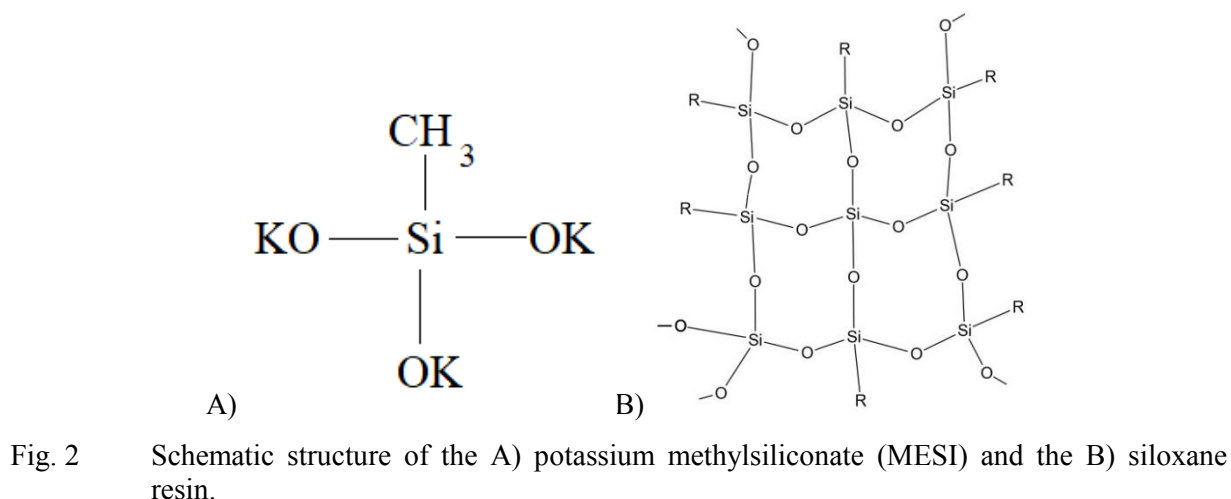
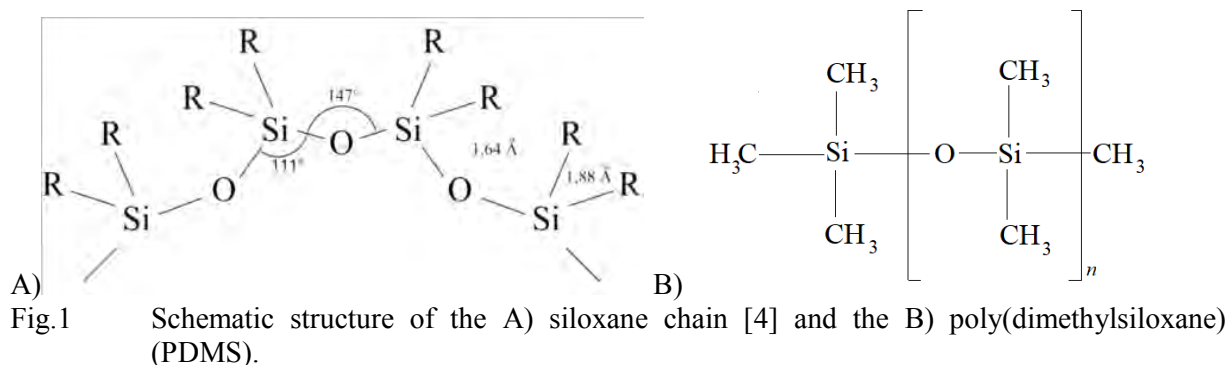


Fig. 3 Schematic structure of the triethoxyoctylsilane (OTES).

The purpose of our study is to determine the possibilities, advantages and limitations of using different organosilicon compounds for internal hydrophobization of cementitious building materials. In our research we used three commercial admixtures based on siliconate (MESI), polysiloxane (PDMS) and silane (OTES) compounds and we investigated their influence on the basic properties of cement mortar.

2 Materials and methods

Preliminary research was carried out for cement mortar and cement paste. The objective of our study was to determine the influence of commercial organosilicon admixtures on the basic properties of cement mortar. Both, mortar and paste, were prepared by using the Ordinary Portland Cement 42.5 R. The composition of cement mortar per one batch is given in Table 1. The water to cement ratio was equal to 0.5 for both mortar and paste. Mortar was prepared according to EN 196-1 standard [12]. Prismatic bars of hardened cement mortar, with dimensions 160x40x40 mm, were prepared for following tests: mechanical and capillary water absorption tests. Cement paste was prepared to wetting angle test. In this paper the impact of three different organosilicon admixtures (based on three different organosilicon compounds) on the effectiveness and reasonableness of internal hydrophobization of cement mortar is shown. The first admixture is based on an aqueous emulsion of triethoxyoctylsilane (OTES). The second admixture is also an aqueous emulsion, but the main ingredient is a poly(dimethylsiloxane) (PDMS). The third one is based on potassium methylsiliconate (MESI). It is a water solution of silicone resin in potassium hydroxide. The following amounts of hydrophobic admixtures were used: 0% (as a reference), 1%, 2% or 3% referring to cement mass. Water-repellents were added to batch water. All used admixtures are recommended for volume hydrophobization by manufactures. In case of MESI admixture the manufacturer requires a reduction in the amount of used mixing water. We decided that the sum of used water and MESI admixture should be 225g per one batch of cement mortar (Table 1). None of the other admixture manufactures (OTES or PDMS based one) do not recommend reducing of amount of mixing water. The authors are aware that the water to cement ratio might be not constant. The authors do not have knowledge about the composition of the commercial admixtures, especially about the amount of the water in it, so it is not possible to calculate the appropriate amount of water which should be subtracted from the amount of mixing water.

The mechanical properties of cement mortar were examined according to EN 1015-11 standard [13], and it was determined after 28 days of curing. The compressive strength was verified on six mortar samples with dimensions 40x40x80 mm. Capillary water absorption test was carried out after 28 days of curing according to EN 1015-18 standard [14]. The capillary water absorption test was carried out on six, prismatic mortar specimens with dimensions 40x40x80 mm. First mortar samples were dried and next the sides walls of the samples were sealed and left for dry for the next 24 hours. Subsequently, the mortar bars were placed vertically in water to a depth of 1 cm. The mass of each sample was examined after 10 min, 30 min, 60 min, 90 min, 2h, 3h, 4h and 24h. As confirmation of internal hydrophobicity of cement paste the wetting angle test was carried out. For this purpose, a goniometer OCA15EC DataPhysics equipped with a Braun DS-D 1000 SF camera was used.

Table 1 Cement mortar composition.

	ORGANOSILICON COMPOUND					
	OTES/PDMS			MESI		
Admixture [%]	1%	2%	3%	1%	2%	3%
W/C	0.5					
Cement [g]	450.0					
Sand [g]	1350.0					
Water [g]	225.0			220.5	216.0	211.5
Admixture [g]	4.5	9.0	13.5	4.5	9.0	13.5

3 Results and discussion

3.1 Capillary water absorption test

The main aim of the internal hydrophobization is decrease of the water absorption ability of the material. The results of capillary water absorption test, shown in Table 2, indicate that two of three used admixtures significantly decrease in the water absorption of cement mortar caused by capillary suc-

tion. It can be assumed that regardless of the amount used poly(dimethylsiloxane) (PDMS) based admixture the capillary water absorption coefficient is approximately half of the reference sample one. The lowest coefficient was obtained for addition of 3% of OTES based admixture, and it was 90% lower than the reference sample. The difference in capillary water absorption coefficient between 2% and 3% dosage of OTES based admixture seems to be irrelevant. Although the absolute change of the coefficient is only 0.03, the relative change is 13%, which is significant. The test clearly indicate that silane admixture provides better internal hydrophobization. The polycondensation of triethoxyoctylsilane during cement hydration and presence of octyl groups ensure better protection against water absorption of cement mortar. The MESI admixture did not provide internal hydrophobization of the cement mortar and did not decrease capillary water absorption, on the contrary it rose it up (in regard to reference sample). A higher dosage than 3% of the admixture based on PDMS or OTES is not used due to the adverse effect of admixtures on the strength of the hardened cement mortar, which is presented in section 3.3 Compressive strength.

Table 2 Capillary water absorption coefficient of cement mortar.

Silicon-based agent	Amount of admixture	Capillary water absorption coefficient, $\frac{\text{m}^2 \cdot \text{min}^{0.5}}$
Reference	0%	0.206
OTES	1%	0.042
	2%	0.023
	3%	0.020
PDMS	1%	0.115
	2%	0.106
	3%	0.098
MESI	1%	0.248
	2%	0.259
	3%	0.260

3.2 Wetting angle

The wetting angle test is a measure of the hydrophobicity and hydrophilicity of a material. The shape of a drop of the measuring liquid placed on the tested surface and the value of the wetting angle indicate the nature (hydrophilic or hydrophobic) of tested material. The results of wetting angle test are shown in Table 3. Wetting angle of reference sample of cement paste is 14.59° for water (Fig. 4 (left)). It means that the surface of reference sample is easily wettable by water. The addition of any water-repellent admixture caused increase in contact angle. A slight increase in the wetting angle is observed with methylsiliconate based admixture. Much higher contact angles are provided by the admixture based on poly(dimethylsiloxane) and the largest by triethoxyoctylsilane. It is noteworthy that the wetting angle is almost the same for 3% of PDMS (Fig. 5 (left)) admixture and 3% of OTES one (Fig. 4 (right)). The highest wetting angle was obtained for addition of 3% admixture based on triethoxyoctylsilane (106.91°) (Fig. 4 (right)). Wetting angle test confirmed results obtained during capillary water absorption test. The potassium methylsiliconate does not provide internal hydrophobization of cementitious materials (Fig. 5 (right)) while poly(dimethylsiloxane) and triethoxyoctylsilane led to visible effect of volume hydrophobization. Differences in obtained results are due to organic, non-polar substituents attached to silicon atoms: octyl and methyl groups. Clearly the longer octyl group provides better hydrophobic effects due to its lower polarity of the octyl sidechain (greater ability to repel water molecules).

Table 3 Wetting angle of cement paste for water.

Water repellent agent	Amount of admixture	Wetting angle for water
-----------------------	---------------------	-------------------------

Reference	0%	14.59°
OTES	1%	65.93°
	2%	86.36°
	3%	106.91°
PDMS	1%	53.68°
	2%	43.64°
	3%	64.04°
MESI	1%	26.75°
	2%	20.00°
	3%	21.13°

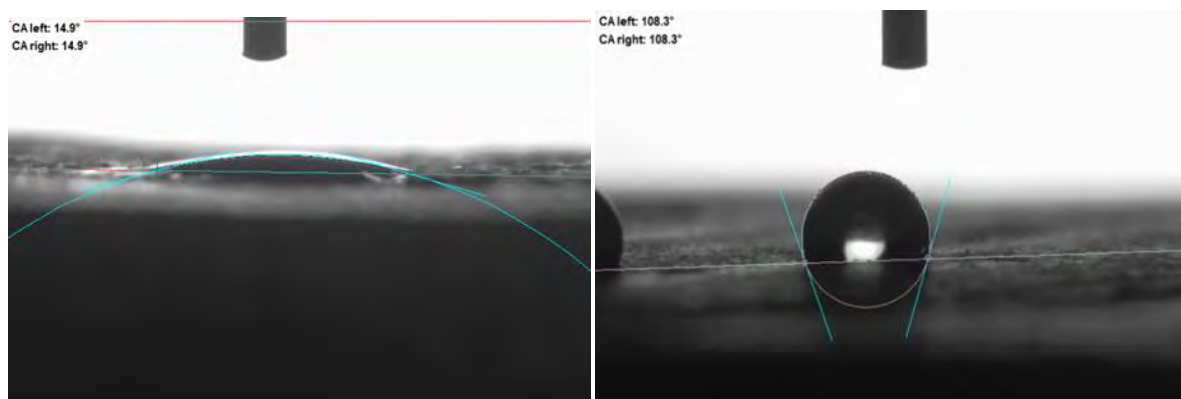


Fig. 4 Wetting angle of reference cement paste (left) and cement paste with 3% of OTES admixture (right).

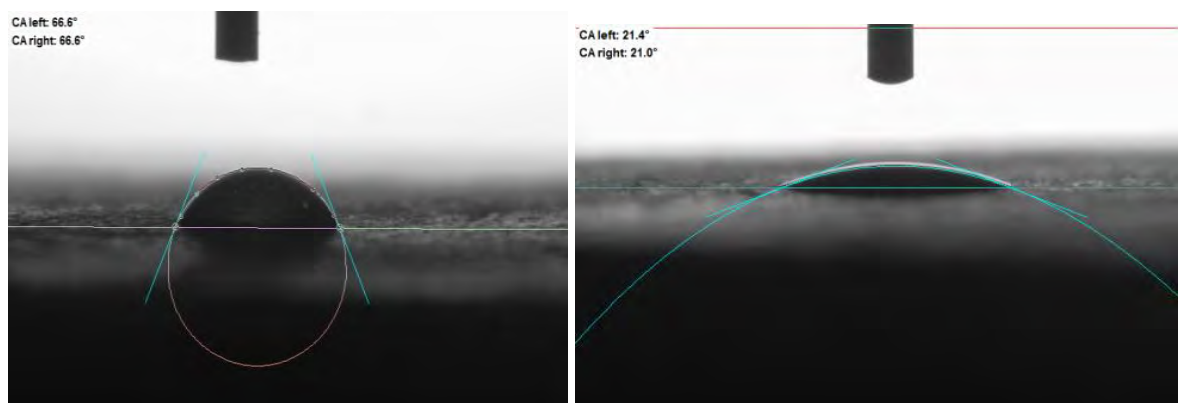


Fig. 5 Wetting angle of cement paste with 3% of PDMS admixture (left) and cement paste with 3% of MESI admixture (right).

3.3 Compressive strength

Results of compressive strength of cement mortar carried out after 28 days of curing are shown in Table 4. Both, poly(dimethylsiloxane) and triethoxyoctylsilane based admixture caused significant decrease in mechanical properties. In case of addition 3% of PDMS admixture the compressive strength dropped by 51% to the reference sample. A strength decrease is a bit lower in case of OTES admixture. The highest decrease in compressive strength is observed for 3% of OTES admixture and it is 20%. It might be assumed that decrease in mechanical properties of cement mortar is caused by prevented cement hydration by the presence of silane and siloxane compounds. The presence of organosilicon compounds with organic, non-polar substituents in their structure, might hinder the cement hydration or even partially inhibit it. This is particularly noticeable in the case of poly(dimethylsiloxane) when the huge polymeric structure interacts with cement phases. In case of

silane-based admixture the hinder effect of cement hydration is a bit smaller. It is probably also associated with the chemical structure of silane itself. As it was mentioned before, triethoxyoctylsilane is a monomer, which is a much smaller molecule than polymer such PDMS, thus the impact of silane on cement hydration is slighter.

Table 4 Compressive strength of cement mortar after 28 days of curing.

Water repellent agent	Amount of admixture	Compressive strength, MPa
Reference	0%	45.25
OTES	1%	38.35
	2%	38.19
	3%	36.36
	3%	36.36
PDMS	1%	25.84
	2%	23.53
	3%	22.16
	3%	22.16
MESI	1%	49.94
	2%	46.83
	3%	42.96
	3%	42.96

4 Conclusions

In view of the presented results the following conclusions can be drawn:

- Two of three of the used admixtures provide visible internal hydrophobization of cement mortar by means of decrease in capillary water absorption and increase in contact angle.
- Potassium methylsiliconate is not appropriate organosilicon compound to volume hydrophobization. The effectiveness of MESI based admixture for internal treatment is not pronounced.
- The best hydrophobic effects are observed for triethoxyoctylsilane based admixture. The highest contact angle (106.9°) and the lowest capillary water absorption coefficient ($0. \frac{m^2 \cdot \min^{0.5}}{m^2 \cdot \min^{0.5}}$) was obtained for addition of 3% of the OTES admixture. Importantly, the silane-based admixture does not decrease the compressive strength as much as PDMS one.
- The results presented in this paper clearly indicate that the type of used organosilicon compound and type of organic, alkyl group has significant impact on the process and effect of internal hydrophobization. The reactions of silane polycondensation which run parallel to cement hydration probably allow the silane to bond to cement phases which provide better internal hydrophobization effect. Also, the longer non-polar octyl groups definitely ensure improved hydrophobic effect than short methyl groups.

References

- [1] Barnat-Hunek D., "Surface free energy as a factor affecting hydrophobisation effectiveness in protection of building construction" (in Polish). Publishing House Lublin University of Technology, Lublin, Poland, 2016.
- [2] Grabowska K., and Koniorczyk M., "The effect of hydrophobic treatment by organosilicon admixtures of cement mortar," *Cement Lime Concrete*, 4, 2019, pp. 320–329.
- [3] Roos M., König F., Stadtmüller S., and Weyershausen B., "Evolution of Silicone Based Water Repellents for Modern Building Protection," 5th International Conference on Water Repellent Treatment of Building Materials, Aedificatio Publishers, 2008, pp. 3-16.
- [4] Cypryk, M., Delczyk, B., Pospiech, P., and Strzelec, K., „Modifications of siloxane polymers,” (in Polish), *Polymers*, 52, 2007, pp. 496-502.

- [5] Fic S., and Barnat-Hunek D., "The Effectiveness of Hydrophobisation of Porous Building Materials by Using the Polymers and Nanopolymers Solutions," *International Journal of Materials Science and Engineering*, 2, 2014, pp. 93-98.
- [6] Rościszewski P., and Zielecka M., "Silicones – properties and applications" (in Polish), Scientific and Technical Publishers, Warsaw, 2002.
- [7] Ciabach J., "Properties of synthetic resins used in monument conservation" (in Polish), Nicolaus Copernicus University Publishing House, 2001.
- [8] Barnat-Hunek D., Smarzewski P., and Suchora Z., "Effect of hydrophobisation on durability related properties of ceramic brick," *Construction and Building Materials*, 111, 2016, pp. 275–285.
- [9] Barnat-Hunek D., and Smarzewski P., "Influence of hydrophobisation on surface free energy of hybrid fiber reinforced ultra-high-performance concrete," *Construction and Building Materials*, 102, 2016, pp. 367–377.
- [10] Spaeth V., Delplancke-Ogletree M. P., and Lecomte J.P., "Hydration Process and Microstructure Development of Integral Water Repellent Cement Based Materials," 5th International Conference on Water Repellent Treatment of Building Materials, Aedificatio Publishers, 2008, pp. 245-254.
- [11] Feng H., Le H. T. N., Wanga S., and Zhang M-H., "Effects of silanes and silane derivatives on cement hydration and mechanical properties of mortars," *Construction and Building Materials*, 129, 2016, pp. 48-60.
- [12] European Committee for Standardization. EN 196-1:2005 Methods of testing cement – Part 1: Determination of strength. CEN: Brussels, Belgium, 2005.
- [13] European Committee for Standardization. EN 1015-11:1999 Methods of test for mortar for masonry – Part 11: Determination of flexural and compressive strength of hardened mortar CEN: Brussels, Belgium, 1999.
- [14] European Committee for Standardization. EN 1015-18:2002 Methods of test for mortar for masonry – Part 18: Determination of water absorption coefficient due to capillary action of hardened mortar. CEN: Brussels, Belgium, 2002.

Toward a new assessment method of the durability of stabilized compacted earth blocks

Noha Al Haffar, Antonin Fabbri, Fionn McGregor

*LTDS/ENTPE UMR CNRS 5513,
Lyon University,
2 rue Maurice Audin, 69120 Vaulx-en-Velin, France*

Abstract

The aim of this work is to assess the durability of stabilized and unstabilized compacted earth toward water. To do so, three common laboratory testing methods were selected to evaluate their effectiveness in delivering consistent information on the durability of the earthen product. They consist of the “wet to dry strength test”, the “accelerated erosion test” and the “stability in static water test”. Results show that the performance of samples depends on earth characteristics rather than cement composition. Moreover, the tested methods tend to overestimate the performance of stabilized products.

1 Introduction

Increasing water content in earth walls remain one of the main deterioration factors affecting the durability of earthen materials [1]–[3]. However, there is still no consensus on how this durability issue should be assessed in the laboratory. The main problem is that no clear correlation has been made between the laboratory tests and the real performance of the material [4], [5]. In this context, a recent review of past literature discussing earthen material durability assessment was made in [6]. The interested reader is referred to the latter paper and references therein for more details about the subject. This work focusses only on the durability assessment of compacted earth block (CEB) at the material scale. To the best of our knowledge, existing testing laboratory methods designed to estimate the durability of CEB toward water could be classified in three main categories.

The first one aims at assessing the resistance to water erosion like the so-called spray erosion test and drip erosion test. The spray test mimics the effects of wind driven rain erosion by spraying water on one surface of the block with a constant pressure for a certain amount of time. The durability of the block is evaluated from the rate of erosion calculated from the maximum depth of erosion measured with a 10mm flat ended rod. Different international standards propose this method of assessment like the Australian earth building handbook (HB-195) [5], the Indian Standard (IS 1725) [7] and the New Zealand Standards (NZS 4297) [8]. The main differences between these Standards concern the exposed area of the sample, the spraying time, the spray application distance, and the water pressure. As for the drip erosion test, it consists of evaluating the damage caused by submitting earth block inclined at 27° from the horizontal to a continuous stream of water suspended at a fixed level above the sample's upper surface. The erosion resistance is evaluated based on the average pitting depth measured with a 3mm probe. In the Australian earth building handbook (HB-195) there is two examples of this test, namely the Geelong drip test and the Swinburne Accelerated Erosion test (SAET). They differ mainly in the level from which the water fall, the way in which water droplets are generated and the dropping duration.

The second category of tests looks at the durability against an abnormal, and potentially cyclic, excess supply of water. In the Australian earth building handbook (HB 195), this problem is assessed though the wet-dry appraisal test. It consists in placing the specimen in 10mm of water for 30s and then dry it at ambient temperature until no color changes, then repeating this cycle six times. After the final cycle, the durability is evaluated based on the surface cracking patterns, the local swelling, the pitting, the loss of soil layers, the penetration of water by more than 70% of specimen, the loss of fragments greater than 50mm and the surface salt deposits. In the German Standard (DIN 18945) [9] this durability issue is assessed through other methods like the contact test and the suction test. The first one aims to reproduce the contact between an earth block and a 15mm thick mortar layer. It consists of putting a wet cellulose cloth, containing an amount of water of 0.5g/cm², onto the surface of earth block. The specimen is then stored for 1 day in an ambience at 100% of relative humidity before being exposed to natural atmospheric conditions for 2 days. The durability assessment is made from the analysis of cracks

and/or irreversible swelling deformations. The second one was designed to represent the impact of capillary rises, and/or exterior timber frame walls during driving rains [10]. It consists of placing the sample on a conventional fired brick with an absorbent cloth on its top. This assemblage is placed inside a pan filled with water up to 1–5 mm below the upper edge of the fired brick. The durability assessment is made through visual detection of cracks and permanent deformations after 30min, 3h and 24h. On the other hand, the Bureau of Indian Standards (IS 1725 [7] and IS 3495248 [11]) propose a simpler method which is the immersion test. In this latter, sample is fully immersed in room temperature water over a definite period or until reaching a constant value. The performance of the sample is evaluated based on the absorbed water content and the mass loss of the sample.

The last category concerns the assessment of risk of wetting collapse, which is commonly checked through saturated uniaxial compressive strength. The most common method that belong to this category is the saturated to dry strength testing. According to the specifications of this test, a minimum saturated and dry plus a minimum saturated to dry strength ratio are required to consider that the material is sufficiently durable, and they vary from author to another.

In this study, one method of each category was selected to evaluate its effectiveness in delivering consistent information on the durability of compacted earth. From the first category, the spray erosion test was chosen because it was too easy for all stabilized materials to pass the drip test without any noticeable damage or change. From the second category the immersion test was chosen for its simplicity. And the wet to dry strength testing was chosen from the last category. Two different natural earths suitable for construction coming from the “Auvergne Rhône-Alpes” region in southeastern France were used for the experimental campaign. Both stabilized and unstabilized earthen material were studied. Indeed, stabilizing earth with moderate dosages of hydraulic binders is one of the most employed methods to enhance strength and durability towards water [12]–[15]. When cement is chosen as a hydraulic binder, cements with high clinker content are generally used, i.e., ordinary Portland cement (OPC). In this study, different types of cement were selected for stabilizing the chosen earths. The main differences between the chosen cements are their clinker content and strength class. This choice was made to optimize stabilization with regard to the relation between durability of stabilized compacted earth and clinker content of cement employed for stabilization. It's worth mentioning that this work is a preparative stage to the development of a new laboratory testing method concerned by the assessment of the durability of cement stabilized compacted earth blocks.

2 Tested materials

Compacted earth samples were made of two local earths coming from the “Auvergne Rhône-Alpes” region in southeastern France, referenced as DAG and STA. The first one was collected from centenarian rammed earth construction located at the city of “Dagneux”. The second one was extracted from subsoil at the village of “Saint Antoine l'Abbaye”. The collected earths were crushed and sieved at 5mm to eliminate coarse grains. Their geotechnical properties are summarized in (Table 1). Four types of cements were employed for stabilization and their main properties are presented in (Table 2). Stabilized formulations were treated with 8% of cement by dry mass of earth. The manufacturing properties (i.e., optimum water content OWC and maximum dry density MDD) of stabilized and unstabilized formulations were determined in previous work [16] following the procedure detailed in [17] and they are summarized in (Table 3). The tested samples were prepared by double compaction with an equivalent compaction stress of 4MPa using a hydraulic press. Directly after compaction, all samples were cured for 7 days at 21°C/100%RH then dried in laboratory-controlled conditions at 21°C±2°C/50%RH±5%RH until reaching a constant mass.

Table 1 Earths properties

Properties	DAG	STA
Sand and fine gravel (5-0.06mm)	27%	45%
Silt (60-2µm)	55%	28%
Clay (<2µm)	18%	27%
Methylene Blue value (V _B)	1.8	1.5
Plastic Limit (W _P)	17.9	21.9

Liquid Limit (W_L)	31.2	40.3
Plasticity Index (I_P)	13.3	18.4

Table 2 Cements characteristics

Cement type		CEM II/A-LL – 42.5R	CEM II/B-LL – 32.5R	CEM V/A (S-V) – 42.5N	MC 12.5
Designation		CA	CB	CV	CM
Composition [%]	Clinker	86	77	58	57
	Limestone	13	22	-	42
	Siliceous fly ash	-	-	21	-
	Blast furnace slag	-	-	20	-
	Minor additional constituents	1	1	1	1
Average compressive strength of cement pastes at 28 days [MPa]		54	40	54	20

Table 3 Formulations properties

Formulation	Cement type	OWC [%]	MDD [g/cm^3]
DUS	-	14.0	1.85
DA	CA	14.7	1.77
DB	CB		
DV	CV		
DM	CM		
SUS	-	19.0	1.73
SA	CA	21.5	1.66
SB	CB		
SV	CV		
SM	CM		

3 Testing procedures

3.1 Wet to dry strength testing

Uniaxial compressive strength was performed on cylindrical samples of 35mm in diameter and 70mm in height by applying a continuous loading at a steady rate of 0.02mm/s up to failure. Compressive strength of each sample was determined from its failure load and averaged cross-sectional area. Compressive strength measured at 28 days on dried samples at 21°C/50%RH is termed as dry compressive strength. In order to avoid disintegrating samples due to soaking samples in water, the wet compressive strength was measured on wet samples conserved 28 days at 100%RH and 21°C \pm 2°C. In these conditions, the monitored mass of the samples was relatively constant and the water content of all samples at the 28th day was equal to the optimum water content.

3.2 Accelerated Erosion Test (AET)

The method consists in submitting sample's surface to a horizontal water spray at 50kPa for 60 minutes. The area of application is of 70mm in diameter from a distance of 470mm. This test was applied on

cylindrical samples having 40mm in thickness and 100mm in diameter. The depth of erosion is measured at the end of the test with 10mm flat ended rod. The performance of the sample is judged on the basis of the erosion rate calculated as follow:

$$\text{Erosion rate [mm/min]} = \frac{d}{t} \quad (1)$$

Where:

d [mm] is the maximum eroded depth.

t [min] is the spraying duration.

3.3 Immersion test

The procedure consists in immersing samples under 10cm of water for 10 minutes in room temperature at $23^{\circ}\text{C} \pm 2^{\circ}\text{C}$. The performance of samples is evaluated in function of the mass loss calculated as follow:

$$\text{Mass loss [g/min]} = \frac{M_{di} - M_{df}}{t} \times 100 \quad (2)$$

Where:

M_{di} [kg] is the dry mass of the sample before immersion.

M_{df} [kg] is the dry mass of the sample after immersion.

t [min]: immersion duration.

4 Results

4.1 Wet/Dry strength ratio

Results of the dry and wet strength and wet to dry strength ratio of the tested formulations are presented in Fig. 1. It shows that, for the same earth, there is hardly any difference in the dry compressive strength of samples stabilized with CB, CV and CM. Another remarkable feature in these results is that cement stabilization increased the wet resistance of the two earth with a better impact on DAG earth. For example, CA increased the wet compressive strength of DAG by an average factor of 7 while this increment factor is about 2.5 in case of STA.

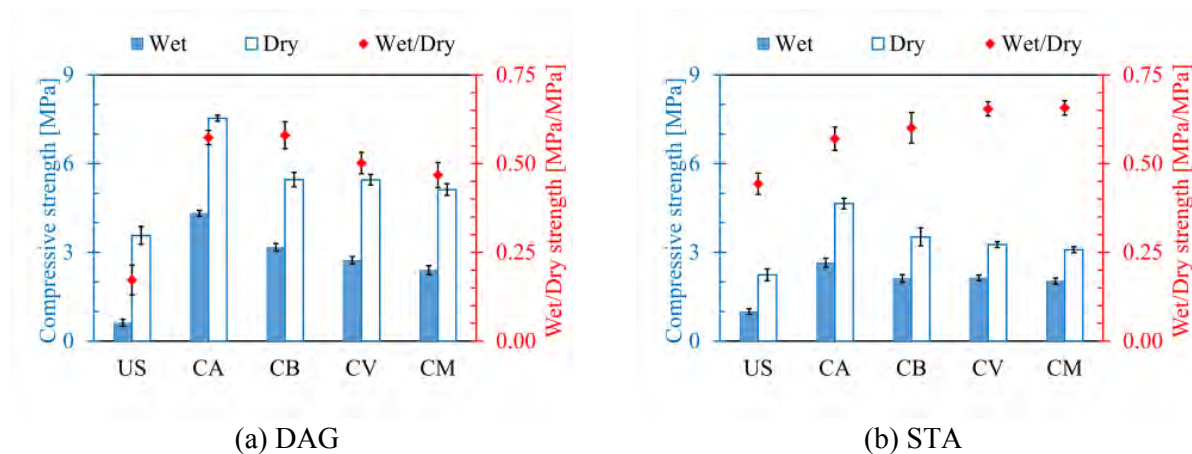


Fig. 1 Dry and wet compressive strength and wet/dry strength ratio of all formulations

The calculated wet to dry strength ratios lies between 0.4 and 0.7, except for DUS formulation, which recorded an average ratio lower than 0.2 due to its negligible wet strength. In this context, a minimum wet to dry strength ratio of 0.33 was recommended by Heathcote [18] as a performance indicator to pass the AET. While CRATERre organization recommend a minimum ratio of 0.5 as reported in [18] and [19]. Here let mention that these recommendations correspond to a wet strength measured on samples soaked for 24-48 hours in water. Let recall that in this study, “wet strength” corresponds to the strength measured on samples having a water content equal to their OWC. This condition was adopted because

it was not possible for unstabilized samples to survive total immersion for 24 hours. It could be assumed that the obtained wet to dry strength ratios are slightly higher than what they are supposed to be if wet strength was measured on 24-hours-soaked samples. But anyhow, to pass this test there is other requirements like a minimum dry and wet strengths that should be greater than the maximum stress supported by the material. However, since there's no consensus on strength's determination of compacted earth blocks [20], [21], it will be unrealistic to propose unified criteria to pass this test. In this study, it's rather a tool to evaluate the effectiveness of cement stabilization rather than long term durability of the product.

4.2 Resistance to spray erosion

Table 4 shows examples of the state of the samples's surface subjected to the water spray erosion test. Important improvement in the sample's resistance after stabilization could be seen clearly. Average erosion's rates of the formulations are summarized in Table 5. Let mention that the erosion rate of SUS formulation was determined at the time at which water penetrates the opposite face of the sample, since it happened before the end of the test. The erosion rate of unstabilized formulations indicate that SUS is prone to more erosion than DUS. Results show important decrease in the erosion rate with the 4 types of the cements used without significant difference between them, except for CA that seems to be more effective than the remaining tested cements. Knowing that CA is the cement having the highest clincker content and strength class between the stabilizers of the study. After all, all formulations passed this test except SUS because in this latter erosion progressed at a rate higher than 1mm/min. It's worth mentioning that the conditions of this test are more severe than actual climatic conditions [22], [23] and the performance of unstabilized materials against this test cannot be used as an indicator of their durability. Here the test was performed on unstabilized samples to put in context the effectiveness of cement stabilization.

Table 4 Resistance to water erosion













		Unstabilized		Stabilized			
				CA	CB	CV	CM
DAG							
STA							
	t = 0	t = 60 min	t = 0	t = 60 min			

Table 5 Rate of erosion

Formulation	DAG	STA
US	0.4 mm/min	1.6 mm/min
CA	0 mm/min	0.016 mm/min
CB	0 mm/min	0.05 mm/min
CV	0 mm/min	0.05 mm/min
CM	0 mm/min	0.08 mm/min

4.3 Resistance to water immersion

The average total mass losses of the tested samples are shown in Fig. 2. After stabilization with CA, the mass loss of DAG and STA earths was reduced by 98% and 90% respectively. While a treatment with CM, which is the cement of the lowest strength class and clincker content between the tested

cements, have reduced the mass loss of DAG and STA by 82% and 52% respectively. It appears from the obtained results that the higher is the strength class of the cement, the lower is the mass loss of sample at the end of the test. Moreover, this assessment tool proves again that cement stabilization is more effective with DAG than STA.

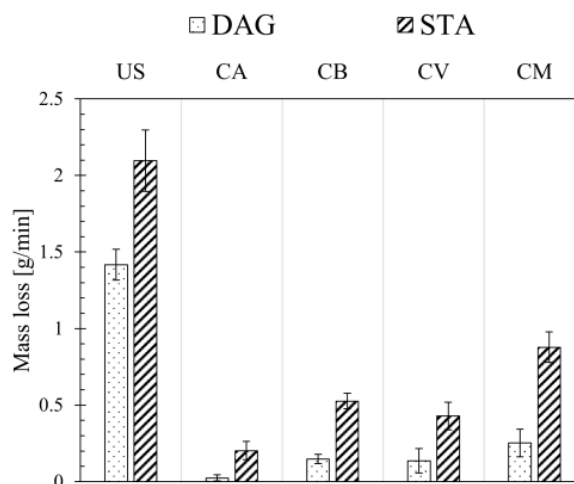


Fig. 2 Results of the immersion test

5 Discussion

It appears that a coherent relation between results of different categories of durability tests cannot be generalized since it may depend on the characteristics of the earth used. Let's begin with the unstabilized formulations. DUS reported a wet to dry strength ratio two times lower than SUS but it shows at the same time a much better resistance to AET and water immersion test. The same issue happened with stabilized formulations made with STA earth. SM has a wet to dry strength ratio higher than SA but its degradation against AET and immersion test was more important than it. The same issue could be said about SV. Thus, results from one method cannot be used to predict those of another. Nonetheless, the common point between the three assessment methods is that they tend to provide information about the short-term effectiveness of cement stabilization rather than the durability of the product.

Another problematic issue is that tests like AET and immersion tests and other tests prescribed in the introductory section could not be considered as realistic tools to evaluate the durability of unstabilized materials since those materials are not supposed to be subjected to severe environmental conditions. Indeed, unstabilized materials should be protected from risks of water deterioration through a correct design. Moreover, the unfair comparison between the performance of unstabilized and stabilized materials in the laboratory lead to conclude that stabilized products have exceptional resistance and can withstand the normal operating conditions of the building without problem, which is not necessarily true. The first key durability factor that should be the subject of interest in future assessment methods is the way or the rate in which the stabilized material loses its characteristics. This issue cannot be investigated in the absence of the cyclic effect of water action on the stabilized material, because in such conditions the durability will be misestimated, usually overestimated. For instance, it's not because samples resisted to harsh conditions like water sprayed at 50kPa during 60min that it will resist to non-severe prolonged wind-driven rainfall. The latter situation could be more harmful for the same amount of water because in this case water will have more time to penetrate the material and, thus, to reduce its resistance [18].

The second factor that should be taken into account is the way in which the stabilized material is humidified during the test. To explain this point let's consider the wire brush test which is the only known method that consists of wetting/drying cycles to evaluate the durability of earthen materials. It consists of immersing sample 5 hours in water then drying it at 72°C for 42 hours. Thereafter sample's surface is brushed with a wire brush and the sequence is repeated 12 times [24], [25]. The performance of the sample is connected to its total mass loss at the end. The duration of wetting and drying and maximum mass loss to pass the test varies with normative documents and standards. Although the cyclic effect of water, the test lacks of correlation with realistic wetting/drying conditions and could be classified as a stabilizer efficacy test. To that end, this work will be followed by developing a laboratory test that

aims at simulating the effect of wind-driven rainfall that stabilized earth construction may undergo during its lifetime.

6 Conclusion

This paper presented results of preliminary study on the durability assessment of unstabilized and stabilized compacted earth blocks. 10 formulations were tested through three common laboratory methods. The obtained results demonstrated that these methods give information on the stabilizer efficacy rather than the material durability. Otherwise, the unfair comparison between stabilized and unstabilized formulations underestimates the performance of unstabilized material that is not supposed to be exposed to severe humidification's conditions, and overestimates the performance of stabilized material, which was initially treated with cement in the aim of extending its service life in humid environment. Therefore, it's essential to develop laboratory methods more convenient to evaluate the durability of stabilized earth blocks. This issue will be the main subject of the following publication that belong to a project aiming at optimizing cement stabilization for building construction applications.

Acknowledgements

The authors would like to acknowledge technical staff in the ENTPE Stephane Cointet for his assistance in performing experimental work. This study benefits from the financial support of the ATILH (Association Technique de l'Industrie des Liants Hydrauliques), via the CIFRE convention n° 2017/1512 of the ANRT project number 2017/1512. The authors would like to thank Laurent Izoret for following this work, as well as the experts from the cement companies for the fruitful discussions around the results.

References

- [1] Q. B. Bui, J. C. Morel, S. Hans, and P. Walker, "Effect of moisture content on the mechanical characteristics of rammed earth," *Constr. Build. Mater.*, vol. 54, no. March, pp. 163–169, 2014, doi: 10.1016/j.conbuildmat.2013.12.067.
- [2] A. Fabbri and J. C. Morel, "Earthen materials and constructions," in *Nonconventional and Vernacular Construction Materials*, 2016, pp. 273–299.
- [3] P. Gerard, M. Mahdad, A. Robert McCormack, and B. François, "A unified failure criterion for unstabilized rammed earth materials upon varying relative humidity conditions," *Constr. Build. Mater.*, vol. 95, pp. 437–447, 2015, doi: 10.1016/j.conbuildmat.2015.07.100.
- [4] J. Cid-Falceto, F. R. Mazarrón, and I. Cañas, "Assessment of compressed earth blocks made in Spain: International durability tests," *Constr. Build. Mater.*, vol. 37, pp. 738–745, 2012, doi: 10.1016/j.conbuildmat.2012.08.019.
- [5] P. J. Walker and Standards Australia, "HB 195: The Australian Earth Building Handbook," 2002.
- [6] C. T. S. Beckett, P. A. Jaquin, and J. C. Morel, "Weathering the storm: A framework to assess the resistance of earthen structures to water damage," *Constr. Build. Mater.*, vol. 242, no. January, 2020, doi: 10.1016/j.conbuildmat.2020.118098.
- [7] BIS, "Specification for soil based blocks used in general building construction. IS 1725 Indian Bureau of Indian Standards," 1982.
- [8] H. Morris *et al.*, "Engineering design of earth buildings - NZS 4297:1998," *Stand. New Zeal.*, vol. 4297, p. 63, 1998.
- [9] DIN 18945:2013-08, "Lehmsteine - Begriffe, Anforderungen, Prüfverfahren," 2013.
- [10] H. Schroeder, *Sustainable Building with Earth*, Springer. .
- [11] BIS, "IS 3495 Parts 1-4 : Methods of Tests of Burnt Clay building brick," *IS 3495 1992 - Parts 1 to 4 - METHODS TESTS Burn. CLAY Build. BRICKS*, pp. 1–7, 1992.

- [12] M. Lunt, “Stabilized soil blocks for buildings,” *Overseas Build. Note*, pp. 184:1–15, 1980.
- [13] B. V. Venkatarama Reddy and P. Prasanna Kumar, “Cement stabilised rammed earth. Part A: Compaction characteristics and physical properties of compacted cement stabilised soils,” *Mater. Struct. Constr.*, vol. 44, no. 3, pp. 681–693, 2011, doi: 10.1617/s11527-010-9658-9.
- [14] R. Fitzmaurice, *Manual on stabilised soil constructions for housing*. New York: Technical Assistance Program, United Nations, 1958.
- [15] K. Heathcote, “Compressive strength of cement stabilized pressed earth blocks,” *Build. Res. Inf.*, vol. 19, no. 2, pp. 101–105, Mar. 1991, doi: 10.1080/09613219108727106.
- [16] N. Al Haffar, A. Fabbri, and F. McGregor, “Curing conditions impact on compressive strength development in cement stabilized compacted earth,” *Mater. Struct.*, vol. 54, no. 3, p. 103, 2021, doi: 10.1617/s11527-021-01702-0.
- [17] F. Champire, “Étude expérimentale du comportement hydro-mécanique de la terre crue compactée pour la construction,” Ecole Nationale des Travaux Publics de l’Etat, 2017.
- [18] K. A. Heathcote, “Durability of earthwall buildings,” *Constr. Build. Mater.*, vol. 9, no. 3, pp. 185–189, 1995, doi: 10.1016/0950-0618(95)00035-E.
- [19] J. C. Morel, Q. B. Bui, and E. Hamard, “Weathering and durability of earthen material and structures,” in *Modern Earth Buildings: Materials, Engineering, Constructions and Applications*, Woodhead Publishing, 2012, pp. 282–303.
- [20] J. C. Morel, A. Pkila, and P. Walker, “Compressive strength testing of compressed earth blocks,” *Constr. Build. Mater.*, vol. 21, no. 2, pp. 303–309, 2007, doi: 10.1016/j.conbuildmat.2005.08.021.
- [21] A. Fabbri, J.-C. Morel, and D. Gallipoli, “Assessing the performance of earth building materials: a review of recent developments,” *RILEM Tech. Lett.*, vol. 3, no. December, pp. 46–58, 2018, doi: 10.21809/rilemtechlett.2018.71.
- [22] P. Walker, R. Keable, J. Martin, and V. Maniatidis, *Rammed Earth : Design and Construction Guidelines*. BRE Bookshop, 2005.
- [23] K. A. Heathcote, “An investigation into the erodibility of earth wall units,” University of Sydney, 2002.
- [24] ASTM, “ASTM D559-96. Standard test methods for wetting and drying compacted soil-cement mixtures.,” 1996.
- [25] BIS, “IS 1725: Stabilized Soil Blocks Used in General Building Construction - Specifications,” 2013.

Comparison of normative test methods for evaluating concrete resistance to freeze-thaw cycles to real exposure conditions

Sara AL HAJ SLEIMAN^{1,2}, Laurent Izoret², Frédéric GRONDIN¹, Syed Yasir ALAM¹, Ahmed LOUKILI¹

¹ *Institut de Recherche en Génie Civil et Mécanique (GeM), UMR 6183, Centrale Nantes – Université de Nantes – CNRS,*

1 Rue de la Noë, 44300 Nantes, France

² *Association Technique de l'Industrie des Liants Hydrauliques (ATILH), 7, place de la Défense 92974 Paris-la-Défense Cedex, France*

Abstract

The durability of concrete structures in winter has always been one of the most important topics in civil engineering research, including the normative approach, obviously because maintenance and repairing costs are not negligible. National standards authorities such as AFNOR (F), DIN (D) or SNV(CH), as well as European and International Standards organizations (CEN, ISO), have developed test methods in the form of normative documents to assess the frost resistance of concrete. This is done by measuring several factors associated with the durability of concrete in cold weather such as: scaled masses, relative Young's modulus, relative elongation, etc. The procedure in each test method consists in keeping the concrete for a specific curing period to each test, then exposing the material to freeze-thaw cycles inside a climate chamber by applying conventional thermal cycles with variable amplitude influencing cooling and thawing rates, specific to each test method, which can reach up to 10°C/h. Finally, the evaluation of the frost resistance of concrete is done by comparing the measured factors with limit values that also vary from one standard operating procedure to another. It is obvious that the experimental conditions imposed in each test are variable and significant differences exist not only between the various test methods but also with the real environmental conditions to which concrete is exposed, even in regions with a harsh winter environment. Furthermore, we show that there is an important dispersion in the temperature evolutions inside the climatic chamber at different positions during the test. Moreover, many questions arise as to the representativeness of these tests and their correlations to real exposure conditions. Therefore, the following campaign was proposed: temperature measurements of concrete placed in winter environment were carried out at Mont Aigoual, a French mountainous region located in an area classified as a "severe frost zone" (according to the exposure classes of the NF EN 206-1 and Koppen-Geiger classification). This paper is reporting the conditions of measurements and an analysis of the obtained results. We show that the natural conditions are very far from the laboratory conditions in terms of full amplitude, freezing rates and frequency of freezing-thawing cycles. Other observations of the air mass temperature profiles in different countries with severe climates confirm our Mont Aigoual study.

Keywords: concrete, freeze and thaw, damage, durability, performance tests.

1 Introduction

Freeze and thaw attack is among the most severe factors affecting the durability of concrete structures. Two main types of deterioration may appear in the concrete material: internal damage and superficial scaling. Internal damage is the result of developed internal pressures induced by the phase change of water and the corresponding volume expansion. Hydraulic[1], osmotic (in presence of de-icing salts) [2] and cristallisation [3] pressures are the main causes of internal damage. It results a loss

in strength and cohesion of the material as well as an increase in porosity and permeability to aggressive agents. As for scaling, only few theories and models exist to explain the mechanisms behind this type of deterioration. “The glue-spalling” [4] is one of the most known scaling model so far. The superficial deterioration is assumed to be related to the thermal mismatch between the ice layer and the concrete surface. But, the effect of entrained air is not explained in this theory. However, despite these tentatives, there is currently no satisfactory model able to predict the concrete behaviour with a reliable confidence, especially to scaling

Many standardized methods exist to test the resistance of concrete to scaling. In Europe, they are described in CEN/TS12390-9 with one reference method (Cube test and CDF test). These methods consist in exposing concrete specimens to a series of freeze and thaw cycles of 40°C amplitude (ranging from +20/-20°C) with cooling rates ranging from 2 to 10°C/h (Slab test and CDF Test respectively). However, as a matter of technical fact, the temperature cycles to which concrete specimens, placed at different locations, inside a climatic chamber, are subjected are highly scattered during the same test. Moreover, the correlation of the applied conventional thermal cycle to real exposure conditions can be questioned. It appeared that the assessment of the representativeness of a durability test method on freeze-thaw should start by the measurement of the concrete response to its natural environment with regards to temperature. Therefore an experimental campaign was held in Mont Aigoual, a mountainous region in France. This campaign is presented in the following parts. The thermal behaviour of concrete exposed to real meteorological conditions is modelled, in order to understand the multiple phenomena involved in the exposure conditions, this was published in [5]. We show that many phenomena are included in the overall thermal behaviour of exposed concrete such as solar radiation during diurnal periods, and nocturnal radiation under certain meteorological conditions [6] that makes the concrete surface colder than the surrounding air and induce the formation of white frost.

2 Laboratory freeze-thaw temperature cycles

As a standard procedure at GeM laboratory of Ecole Centrale de Nantes (France), we undertook a calibration step of a brand new climatic chamber BINDER MKF 240. For this purpose, 8 concrete specimens were cast from a unique batch of the same mix design and prepared according to the slab test of the CEN/TS 12390-9 [7]. These specimens were placed at different positions inside the climatic chamber with 8 thermocouples placed at the interface [saline solution (3%) / concrete sample], according to the test procedure. The temperature evolutions were monitored during several days. Figure 1 shows the evolution of the freeze-thaw cycles for the 8 specimens. The main characteristic is that each individual curve falls inside the range of temperature authorized by the CEN/TS 12390-9, allowing to qualify the position, the thermocouple and the monitoring device. However, it is also interesting to note that the full authorized range of temperature is swept by the 8 curves. In quantitative terms, this means that for a given time during the freezing regime (e.g. 8h) two samples can show a temperature difference up to 10°C. The minimum temperature reached varies between -18 and -22°C, as for the maximum temperature, it reaches 10 °C for a specimen and 19°C for another specimen during the same test. Therefore, the freezing and thawing rates are different as well, depending on the position of the specimen in the climatic chamber. Moreover, considering the freezing point due to latent heat of solidification of water, a detailed analysis of each curve shows large variations in temperature and duration of the plateau. This is certainly a reason behind the large scattering of the scaling results and has an effect on the reliability of this test.

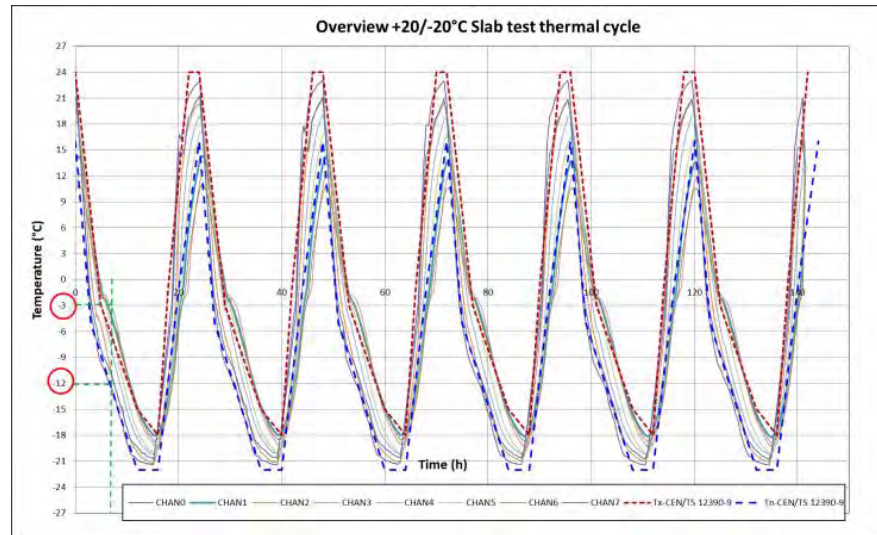


Figure 1: 6 Freeze/thaw cycles registered in the saline solution of 8 specimens during a scaling test according to the slab test of the CEN/TS 12390-9

3 Mont Aigoual experimental campaign

The meteorological station of Mount Aigoual (44° 07' 15'' N / 3° 34' 53'' E), located at the southern boundary of the Cevennes mountain in the southern part of France is chosen for the experimental program for several reasons. First, it is a full meteorological station dedicated to observations, measurements and experiments. Second, it is an official Météo-France test centre ensuring certified measurements data with a human presence of technicians who can do the maintenance of the concrete blocks e.g. de-icing as well as sensors maintenance. Finally, this station is located in a severe freezing environment area at 1,567 m of altitude, which was a pre-requisite for our experiments. The meteorological test centre is equipped with a test platform and different sensors types that allow the measurements of the air mass temperature (sheltered temperature), the visibility, the wind speed, the relative humidity as well as the global solar radiation. Therefore, a full meteorological characterization is possible.

3.1 Concrete samples installation

The two concrete blocks were cast in marine plywood formworks of dimensions: Length $L = 60$ cm, height $h = 46$ cm and thickness $e = 17$ cm. Each block was equipped with thermocouples near the surface, Figure 3. The blocks are configured according to the slab test of the CEN/TS 12390-9.



Fig. 2 Mont Aigoual meteo station.

Measurements were done on large period during 2013 to 2015 at different months over these years. A new experimental campaign is running for 2019-2020.



Fig. 3 Concrete blocks in Mont Aigoual field (left). Concrete blocks covered with snow (right).

4 Temperature evolutions in Mont Aigoual and countries with severe climates

A section of the measurements is presented in Figure 3 that corresponds to a period from 7th to 16th of March 2013. As we can see, temperature cycles ranging between +20°C/-20°C never occurred during this period. An important difference can be recognized between real cycles that concrete undergoes in field exposure and temperature cycles applied in normative test methods that correspond to freeze-thaw cycles ranging from +20°C to -20°C. Another section of the Mont Aigoual meteorological study during the winter period 2019-2020 is presented in Figure 4. The same observation was also found regarding the real thermal amplitude of freeze and thaw cycles.

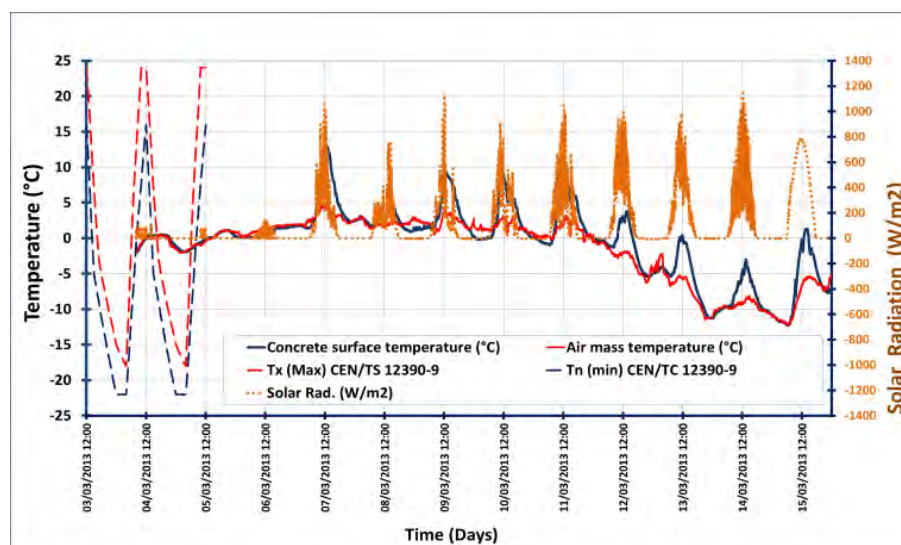


Fig. 3 Time series concrete surface temperature, air mass (sheltered) temperature (Y axis) and global radiance (Y' axis) with reference to CEN/TS 12390-9 thermal cycle (left) from 7th to 16th of March 2013.

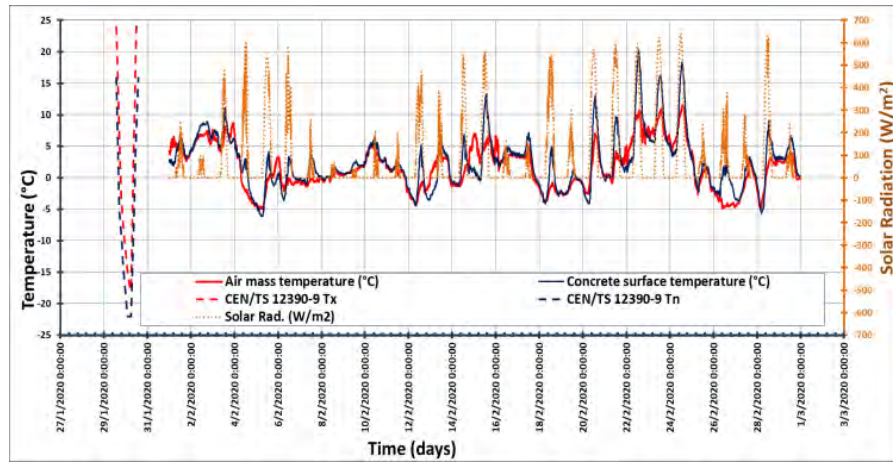


Fig. 4 Time series concrete surface temperature, air mass (sheltered) temperature (Y axis) and global radiance (Y' axis) with reference to CEN/TS 12390-9 thermal cycle (left) from 1st to 29th of February 2020.

From Mont Aigoual study, we noticed that the minimum values of the air mass temperature (which is known as sheltered temperature) corresponds most of the time to concrete surface minimum temperature. However, there is a difference in maximum values of sheltered and concrete surface temperature because of the effect of solar radiation during diurnal periods. This solar radiation will make the concrete surface hotter than the air mass temperature (measured with a thermocouple in a double sheltered cabinet, protected from solar radiation, wind and relative humidity effects). The difference in maximum temperature values is less than 10°C.

Based on this observation, a study of the air mass temperature evolutions of different countries with severe climates is done, using data available on national meteorological sites. Figures 5 and 6 show the thermal evolutions in Winnipeg (Canada) and Ulaan Baator (Mongolia) for the month of March 2020. The studies of the thermal conditions of these regions and more show that first, the freeze and thaw cycles appear in the beginning and the end of the winter period. In the middle of the winter, the temperature does not go above than zero degrees Celsius. Frost cycles only occur during the winter and temperature can reach rarely -30°C. Second of all, the full amplitude designated by FA in Figures 5 and 6 does not exceed 20°C even in the middle of the winter. A full amplitude of 10 to 15°C is frequently met during winter and is expressed in terms of freeze/thaw cycles in the beginning and the end of the winter season, and freezing cycles only during the winter.

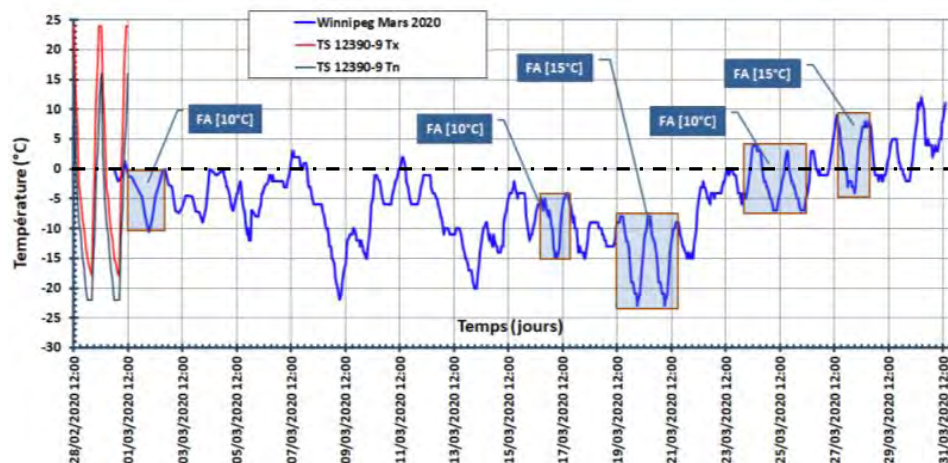


Fig. 5 Time series air mass temperature with reference to CEN/TS 12390-9 thermal cycle in Winnipeg in Canada from 1st to 31st of March 2020.

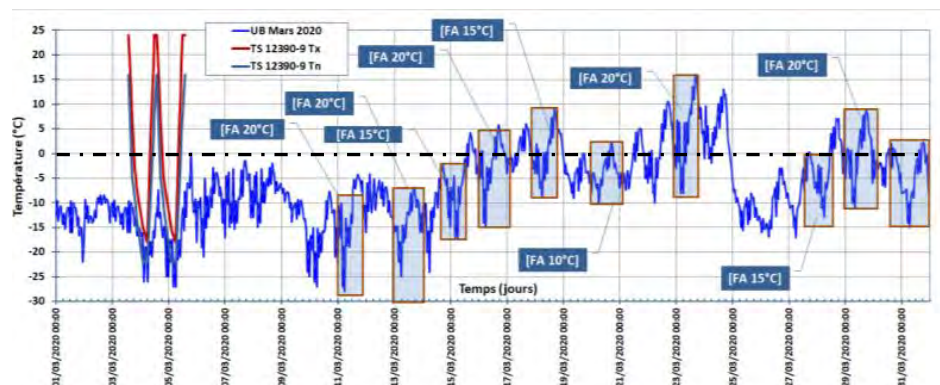


Fig. 6 Time series air mass temperature with reference to CEN/TS 12390-9 thermal cycle in Ulaan Baator in Mongolia from 1st to 31st of March 2020.

This study of the thermal conditions of countries with reputed severe climates show confirms again that the full amplitude of 40°C never occurs during winter. An amplitude of 15°C is more frequent. In terms of freeze and thaw cycles, this amplitude can be expressed in terms of a +5/-15°C with more moderate cooling and thawing rates.

5 Conclusion

Temperatures are widely dispersed in the climatic chamber by imposing the current normative freeze-thaw cycle of +20/-20°C. This dispersion highly affects the reliability of the test method. Moreover, our studies of concrete surface temperature and air mass temperature profiles in Mont Aigoual in France and other countries with severe climates show that:

- The thermal profile measured on concrete block under real exposure conditions is strongly asymmetric and not correlated to the normative freeze/thaw cycle.
- The full amplitude of the thermal cycle has never been found equal to [+20/-20°C] but rather [+5/-15°C] range which seem to be also representative of Nordic countries. The corresponding freezing rates are ranging between 0.6 to 1.5°C/h which is close to the German Cube test.

Therefore, many questions arise as to the representativeness of these tests and their correlations to real exposure conditions.

Experimental scaling test are actually running with the thermal freeze/thaw cycle of +5/-15°C on different concrete formulations. The first results are promising and show that the temperature dispersion inside the climatic chamber is reduced. The assessment of the repetability and reproductibility of the test using the proposed freeze/thaw cycle is undergoing. This will be the subject of a forthcoming paper.

Acknowledgments

The financial support of this work by ATILH (Technical Association of French Cement Industry) and the grant by ANRT by mean of CIFRE convention n°2017/891 for Sara AL HAJ SLEIMAN are great fully acknowledged.

The authors address sincere thanks to Sigma Béton laboratory of VICAT for providing technical support in producing concrete blocks and the technical maintenance of the recording system. The authors thank as well Meteo-France team in Mount Aigoual (Chantal Vimperc and Christian Pialot) for their technical assistance and on-site maintenance.

References

- [1] T. C. POWERS, “The air requirement of frost-resistant concrete,” in *Proceedings of the Highway Research Board*, 1949, vol. 29, pp. 184–211.
- [2] R. A. Powers, T. C., and Helmuth, “Theory of volume changes in hardened Portland cement paste during freezing,” in *Highway Research Board Proceedings* 32, 1953, vol. 32, pp. 285–297.
- [3] G. W. Scherer, “Stress from crystallization of salt,” *Cem. Concr. Res.*, vol. 34, no. 9, pp. 1613–1624, 2004, doi: 10.1016/j.cemconres.2003.12.034.
- [4] J. J. Valenza and G. W. Scherer, “Mechanism for salt scaling of a cementitious surface,” *Mater. Struct. Constr.*, vol. 40, no. 3, pp. 259–268, 2007, doi: 10.1617/s11527-006-9104-1.
- [5] L. Izoret, S. Al Haj Sleiman, N. Matoiri-Chaibati, and F. Grondin, “Concrete in a severe freezing environment: a meteorological characterization,” *Mater. Struct.*, vol. 54, no. 1, p. 36, 2021, doi: 10.1617/s11527-020-01603-8.
- [6] B. Bokor, L. Kajtár, and D. Eryener, “Nocturnal Radiation: New Opportunity in Building Cooling,” *Energy Procedia*, vol. 112, no. October 2016, pp. 118–125, 2017, doi: 10.1016/j.egypro.2017.03.1072.
- [7] CEN/TC51 “Cement and building limes”, “FprCEN/TS 12390-9:2015-Testing hardened concrete — Part 9 : Freeze-thaw resistance - Scaling - Complementary element,” 2015.

Chemical interaction of Hollow Glass Microspheres with oilwell cement slurries

Christian M. Martín^{1,2}, Nadia B. Scarponi³, Yury A. Villagrán^{3,4}, Diego Manzanal⁵ and Teresa M. Piqué²

1 Instituto de Tecnología en Polímeros y Nanotecnología (ITPN UBA- CONICET) Av. Las Heras 2214, 1426, Buenos Aires, Argentina

2 Universidad de Buenos Aires (UBA), Facultad de Ingeniería, LAME, Av. Las Heras 2214, 1426, Buenos Aires, Argentina

3 LEMIT, CONICET, 52 entre 121 y 122 s/n, 1900, La Plata, Argentina

4 Magnel-Vandenpitte Laboratory for Structural Engineering and Building Materials, Ghent University, "Tech Lane Ghent Science Park, Campus A", Technologiepark-Zwijnaarde 60, B-9052, Ghent, Belgium

5 Universidad Politécnica de Madrid, ETS de Ingenieros de Caminos, Canales y Puertos, España

Abstract

Usually, for oil field applications, when a light-weight cement slurry is needed, a density reduction is obtained by increasing the water to cement ratio (w/c), which also implies a compressive strength reduction. To avoid the compressive strength decrease, hollow glass microspheres (HGMS) have been widely used in this industry. Many researchers have been done focusing mainly on the mechanical properties of cement slurries with HGMS. In this study an analysis of the chemical interaction between HGMS and cement slurries is presented and, since HGMS are mainly composed of amorphous SiO₂, its pozzolanic activity is assessed.

1 Introduction

Cement slurries in fresh conditions are pumped through the extraction well to their final location, occupying the annular space comprehended between the rock mass and the casing. During this procedure, a hydrostatic type pressure is generated over the rock mass which can overcome its fracture gradient. This is defined as the required pressure to generate fractures in a rock mass at a given depth. This pressure is controlled by adjusting the cement slurry's density. Given the mechanical limitations of traditional lightweight cement slurries with high (w/c), the exceptionally low density of HGMS make them appropriate for their use in cement slurries designed for extraction wells with low fracture gradient [1]. These HGMS are characterized by their high crushing strength, low density and SiO₂ composition [2].

In the research developed by Martín et al. [3] many results obtained by various authors of the use of HGMS in oil well cement slurries were presented. The use of HGMS signified a reduction between 200 kg/m³ and 700 kg/m³ on cement slurries' densities.

As presented in Figure 1, a relation between cement slurries' uniaxial compressive strength (UCS) and their density is verified. Slurries' density is related to HGMS density and to the amount of cement replacement by HGMS. Despite the lower crushing strength of lower density HGMS (Figure 2), the use of lower density HGMS implies a reduction on the amount of cement replacement and, therefore, an increase in slurry's UCS (Figure 3). Besides, it is also noteworthy that there is no clear relation between HGMS's crushing strength and slurries' UCS as shown in Figure 4.

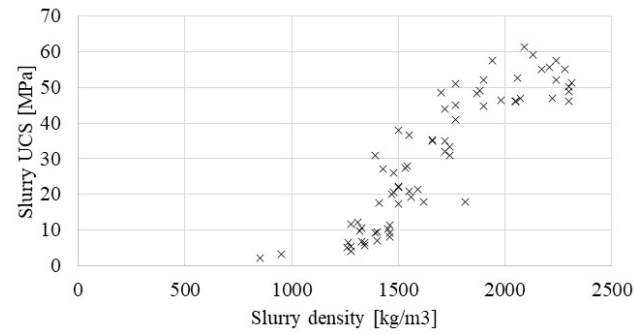


Fig. 1 Cement slurry density vs. cement slurry uniaxial compressive strength. After [3].

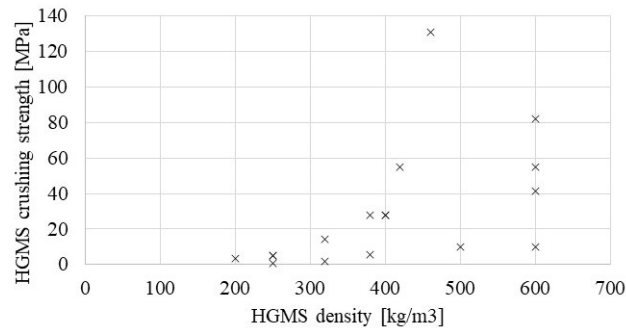


Fig. 2 HGMS density vs. HGMS crushing strength. After [3].

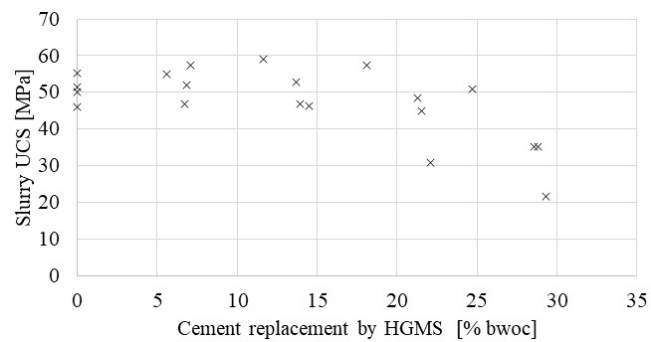


Fig. 3 Cement replacement by HGMS vs. cement slurry uniaxial compressive strength. After [3].

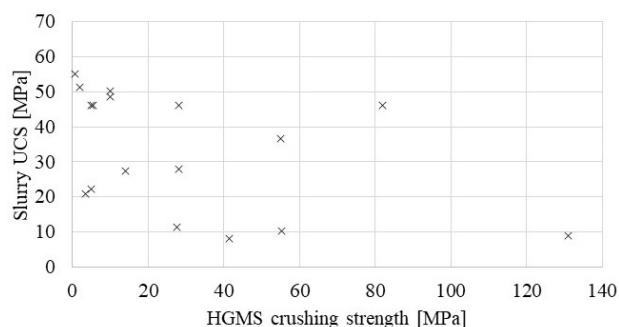


Fig. 4 HGMS crushing strength vs. cement slurry uniaxial compressive strength. After [3].

Some authors have studied or mentioned the pozzolanic activity of HGMS or materials similar in composition, size and shape [4], [5]. They concluded that those materials present some pozzolanic activity. Pozzolanic materials are characterized by their interaction with cement hydration products, particularly calcium hydroxide (CH), whereupon they generate calcium silicate hydrates (CSH), which is known for improving the mechanical properties and the durability of cement pastes.

In this work the chemical interaction between HGMS and cement in oil well cement slurries is studied, especially considering the possible pozzolanic reaction of HGMS since it is mainly composed of amorphous SiO_2 . To assess and quantify it, chemical and physical properties are evaluated through the modified Chapelle test, the determination of the strength activity index (SAI) and scanning electron microscopy (SEM) images, including elemental mapping through energy-dispersive spectroscopy (EDS).

2 Materials and experimental methods

In order to design cement slurries suitable for cementing oilwells through low fracture formations, class G Portland Cement and HGMS as 10% by weight of cement (bwoc) cement replacement were used. The dosage of three slurries were prepared in accordance with API Standard 10A [6]. Class G cement is made up of the same compounds as ordinary cements (mainly C_3S , C_2S , C_3A and C_4AF). However, the proportions of these vary to obtain a cement suitable for oilwell cementing purpose, with specified thickening time (related to the ability to be pumped) and compressive strength to 8 hours in different determined curing conditions. The used HGMS are small borosilicate glass spheres [3], whose size are 30 and 40 micrometers for HGMS27 and HGMS41 respectively. They are characterized by their chemical and thermal stability, their high crushing resistance and their low density (0.28 and 0.46 gr/cm^3 for HGMS27 and HGMS41 respectively). The water/binder ratio (w/b) used was 0.44. In the case of the slurries with w/b of 0.44 and the addition of HGMS, a super plasticizer was used to facilitate mixing as indicated in Table 1. The slurries were poured into molds and kept at 20°C and atmospheric pressure for 7, 28 and 100 days.

Table 1 Cement slurries mixture proportions and classifications.

	Cement [kg/m^3]	HGMS27 [kg/m^3]	HGMS41 [kg/m^3]	Water [kg/m^3]	Superplasticizer [kg/m^3]
CS00	1320.2	-	-	580.9	-
CS27	829.0	92.1	-	405.3	2.8
CS41	952.5	-	105.8	465.6	2.1

Quantification of the CH consumption developed by both classes of HGMS was determined through the modified Chapelle test. This test was performed following the specifications of NF P18 - 513 [7]. The HGMS were exposed to a 2 g CaO - 250 ml water solution for 16 hours at 90°C. Given the

conditions within this test, it could be interpreted that through this test the maximum pozzolanic activity of the addition being evaluated is measured. Direct quantification of the CH consumption by HGMS is obtained from Equation (1). The modified Chapelle test results correspond to the average obtained from two samples of each HGMS, HGMS27 and HGMS41.

$$CH = 2 \cdot \frac{V_1 - V_2}{V_1} \cdot \frac{74}{56} \cdot 1000 \quad (1)$$

Where, CH: mg of CH consumed per gram of HGMS, V_1 : volume of HCl (0.1 N) required to titrate 25.0 ± 2 ml of the filtrate solution of the blanc experiment, and V_2 : the volume of HCl (0.1 N) required to titrate 25.0 ± 2 ml of the filtrate solution of the HGMS experiment.

The SAI is measured following the specifications of ASTM C311 [8]. This index is obtained by measuring UCS of the cement mortars with specific dosages at 7 and 28 days of curing time. This standard was adapted for well cement slurries, using the proportions mentioned in Table 2. The results reported correspond to the average of six samples for each slurry at both curing times. The UCS was done in an INSTRON 5900 series universal machine provided with a spherical head at a 0.7 mm/min rate. Equation (2) specifies the method to obtain the SAI through the UCS results at both curing times.

$$SAI [\%] = \frac{RC_{a,i}}{RC_{p,i}} \cdot 100 \quad (2)$$

Where $RC_{a,i}$ is the UCS [MPa] of cement slurry with 10% bwoc of HGMS at curing time i (7 or 28 days) and $RC_{p,i}$ is the UCS [MPa] of plain class G cement slurry at curing time i (7 or 28 days).

Finally, a FEI QUANTA 250 FEG microscope at 30 kV was used to obtain the SEM images and the EDS elemental mapping. The samples were covered with a thin layer of gold coating. These images were acquired for cement slurries CS27 and CS41 at 28 and 100 days of curing time. In addition, EDS elemental mapping images were obtained to qualitatively measure the presence of Ca and Si near HGMS.

3 Results and discussion

The chemical interaction of HGMS with oilwell cement slurries was characterized by analyzing their pozzolanic activity through CH consumption and comparing with reference tests. Through the modified Chapelle test, CH consumptions per gram of addition of 1365 CHmg/g and 1107 CHmg/g were obtained for HGMS 27 and HGMS 41, respectively. Both HGMS showed a CH consumption higher than the standard limit of 700 CHmg/g to consider an addition as pozzolan [7].

Through this test, several authors studied the degree of pozzolanic activity of various sorts of traditional supplementary cementitious materials (SCMs). The silica fume studied by Vejmelkova et al. [9] yielded 1600 CHmg/g; the numerous commercial metakaolins tested by Ferraz et al. [10] showed a consumption between 900 and 1600 CHmg/g; and Ali et al. [11] found that fly ashes achieved an average consumption of 450 CHmg/g consumption.

In addition, in the research developed by Ferraz et al. [10], a relationship between the results obtained through the modified Chapelle test and the mean particle size was proposed. For a given SCM, the greater the mean particle size, the lower the consumption of CHmg/g obtained. This proposed tendency is verified throughout all the SCM studied in the previous research works.

From comparing HGMS27 and HGMS41 with reference results it is shown that both classes of HGMS present a pozzolanic activity comparable to that of the commercial metakaolins tested in the research of Ferraz et al. [10]. Additionally, the relationship between the mean particle size (D_{50}) and CHmg/g consumption is also verified for these HGMS. HGMS41's D_{50} is greater than that of HGMS27 and the CH consumption of HGMS27 is greater than that of HGMS41.

It is worth mentioning that, though both classes of HGMS present a similar CH consumption to that of commercial metakaolins, their D_{50} is considerably larger. This behavior could be attributed to the higher reactivity of HGMS or to their higher specific surface given their low density.

The SAI was measured in agreement with ASTM C-311 [8] and the results obtained at 7 and 28 days of curing time are presented in Table 2. A considerable increment in the UCS for samples with 28 days of curing time is expected in samples with pozzolanic additions [12], [13].

Table 2 UCS and SAI results obtained for the studied slurries.

	UCS [MPa]		SAI [%]	
	7 days	28 days	7 days	28 days
CS00	31.0	44.6	-	-
CS27	27.5	30.2	88.8	67.7
CS41	29.5	39.0	95.2	87.5

In ASTM C-618 standard [14], SAI lower limit of 75% is established considering a cement replacement by the addition being evaluated of 20% bwoc in a mortar with a w/c of 0.5. Given the inadequate workability obtained in cement slurries with that cement replacement with HGMS, a 10% bwoc replacement was chosen. Besides, following the American Petroleum Institute [15], the w/b adopted was 0.44. Despite these differences, the SAI lower limit of 75% could be considered as a reference value to study the pozzolanic activity of HGMS. Both slurries presented at 7 days of curing time a SAI higher than 80%, while at 28 days of curing time this index is higher than the limit of 75% only for CS41 slurry.

The influence of hollow additions on cement slurry UCS is not only determined by their pozzolanic activity. Instead, in accordance to Brooks et al. [16] the results obtained through this test are affected by physical and mechanical properties of the addition such as its mean particle size and its crushing strength (which is related to its shell thickness). Larger particle size and lower crushing strength yield lower UCS of the slurry. Thus, evaluating the pozzolanic activity of this kind of addition solely through mechanical tests should be avoided.

Also, it is important to notice that the higher the amount of HGMS added to the slurries the higher the unconnected porosity. This could be why the lower strengths obtained of SAI for CS27 than those of CS41. Given the lower density of HGMS27 than HGMS41, 10% bwoc cement replacement of HGMS27 represents a greater unconnected porosity than HGMS41.

Finally, in Figures 5 and 6 the SEM images obtained for CS27 and CS41 at 28 and 100 days of curing time are presented. Given the magnification used to obtain these SEM images allows studying the interfacial transition zone (ITZ). In accordance with Ismail et al. [13], it is worth studying the quality of the ITZ to understand the mechanical behavior of the paste.

At 28 days the contact between HGMS27 and the cement paste is not continuous on CS27, while CS41 presents a full contact between HGMS41 and cement paste. Though hydration products cannot be completely defined with these SEM magnifications, it is clear that the cement paste surrounding the HGMS is dense in both cases.

Through the SEM images obtained at 100 days of curing time, though the already mentioned microcracks on CS27 at 28 days of curing time are still present, a more significant interaction between HGMS and cement is appreciated. Because of their pozzolanic activity, some HGMS appear to have been partially consumed by cement hydration products.

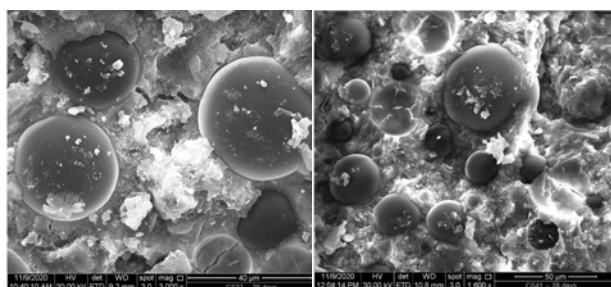


Fig. 5 SEM images of cement slurries CS27 (left) and CS41 (right) at 28 days of curing time.

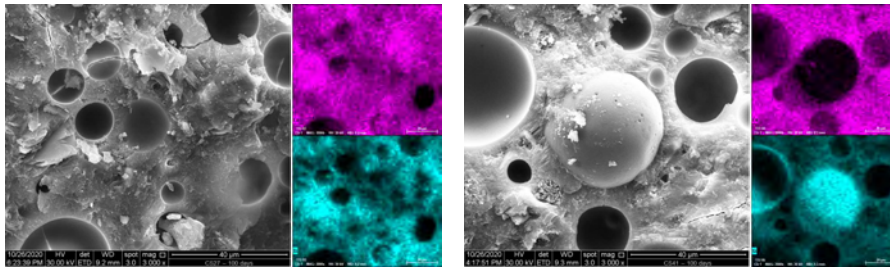


Fig. 6 SEM images and Ca (pink) and Si (light blue) elemental mapping of cement slurries CS27 (left) and CS41 (right) at 100 days of curing time.

By deeply analyzing Figure 6, it is possible to distinguish that, on the broken HGMS, the transitions between HGMS and cement paste seem smooth, which could be an indicator of the pozzolanic activity advancement. As suggested by Aslani and Wang [17], this assumption is confirmed by the presence of Ca (pink) on the shell of those broken HGMS shown on the elemental mapping. The Si elemental mapping (light blue) of CS27 does not present a significant concentration of this element as it occurs over unreacted HGMS41 in CS41. This indicates that, as suggested in the modified Chapelle test section, HGMS27 (corresponding to cement slurry CS27) seem to have a more significant interaction with CH than HGMS41 (corresponding to cement slurry CS41).

4 Conclusions

In this research, the chemical interaction of two classes of HGMS was assessed by studying the pozzolanic activity through two reference tests and then confirmed via SEM and elemental mapping images. HGMS's pozzolanic activity was initially confirmed and quantified through the modified Chapelle test, indicating that both HGMS present CH consumptions higher than the standard limit. Furthermore, the values obtained are comparable to that of commercial metakaolin, even though HGMS present a higher D50. Regarding the SAI, the shell properties of these hollow additions and the unconnected porosity that they generate are more important than their pozzolanic activity. Thus, this test proved to be inappropriate for quantifying the pozzolanic activity of this type of addition. SEM images at 28 days of curing time showed the compatibility between HGMS and cement's hydration products. Moreover, SEM images and elemental mapping obtained at 100 days of curing time confirmed the results presented through the modified Chapelle test.

Acknowledgements

The authors acknowledge Consejo Nacional de Investigaciones Científicas y Técnicas (CONICET), the financial support of Universidad de Buenos Aires (Project UBACYT 20020160100055BA/20020190200005BA) and to the Agency of Scientific and Technological Promotion (Agencia Nacional de Promoción Científica y Tecnológica) from Ministry of Science and Technology of the Argentine Republic (Projects PICT 2016-4543 and PICT 2017-0091). The authors would also like to acknowledge the European Commission's financial support-H2020 MSCA-RISE 2020 Project DISCO2-STORE, Grant Agreement No101007851 and the Universidad Nacional de la Patagonia San Juan Bosco-Project UNPSJB PI1614 80020190200006 IP, Res. R/9N°207-2020 CRD1365FI004/17. As a Postdoctoral Researcher Marie Skłodowska-Curie Actions - Seal of Excellence, Y.A. Villagrán would like to thank the Research Foundation-Flanders (FWO-Vlaanderen) for the financial support.

References

- [1] Pique, Teresa M., Giurich, Federico, Martín, Christian M., Spinazzola, Florencia, and Manzanal, Diego G. 2020. "Lightweight cement-based materials." in *New Materials in Civil Engineering*. Oxford: Butterworth-Heinemann.
- [2] Li, Fang, Zhang, Zhanwen, Li, Jing, Pan, Dawei, Feng, Jianhong, and Shi, Ruiting. 2017. "Study on the strength of titanium doped hollow glass microspheres." *Journal of Non-Crystalline Solids* 459:18–25. doi:10.1016/j.jnoncrysol.2016.12.029.

- [3] Martín, Christian M., Scarponi, Nadia B., Villagrán, Yury A., Manzanal, Diego G., and Piqué, Teresa M. 2021. "Pozzolanic activity quantification of hollow glass microspheres." *Cement and Concrete Composites* 118. doi: 10.1016/j.cemconcomp.2021.103981.
- [4] Lanzón Torres, Marcos and García-Ruiz, P.A. 2009. "Lightweight pozzolanic materials used in mortars: Evaluation of their influence on density, mechanical strength and water absorption." *Cement and Concrete Composites* 31:114–119. doi: 10.1016/j.cemconcomp.2008.11.003.
- [5] Perfilov, V. A., Oreshkin, D. V., and Semenov, V. S. 2016. "Environmentally Safe Mortar and Grouting Solutions with Hollow Glass Microspheres." *Procedia Engineering* 150:1479–1484. doi: 10.1016/j.proeng.2016.07.086.
- [6] American Petroleum Institute. 2019. "API 10A: Cements and Materials for Well Cementing - Twenty-fifth Edition."
- [7] Association Française De Normalisation. 2012. "Modified Chapelle Test."
- [8] American Society for Testing and Materials. 2018. "ASTM C311/C311M - 18. Standard Test Methods for Sampling and Testing Fly Ash or Natural Pozzolans for Use in Portland-Cement Concrete." doi:10.1520/C0311_C0311M-18.
- [9] Vejmelková, Eva, Koňáková, Dana, Doleželová, Magdalena, Scheinherrová, Lenka, Svora, Petr, Keppert, Martin, Reiterman, Pavel, and Černý, Robert. 2018. "Effect of calcined Czech claystone on the properties of high performance concrete: Microstructure, strength and durability." *Construction and Building Materials* 168:966–974. doi:10.1016/j.conbuildmat.2018.02.204.
- [10] Ferraz, Eduardo, Andrejkovičová, Slávka, Hajjaji, Walid, Velosa, Ana Luísa, Silva, António Santos, and Rocha, Fernando. 2015. "Pozzolanic activity of metakaolins by the French standard of the modified Chapelle test: A direct methodology." *Acta Geodynamica et Geomaterialia* 12:289–298. doi:10.13168/AGG.2015.0026.
- [11] Ali, Hafiz Asad, Xuan, Dongxing, and Poon, Chi Sun. 2020. "Assessment of long-term reactivity of initially lowly-reactive solid wastes as supplementary cementitious materials (SCMs)." *Construction and Building Materials* 232. doi:10.1016/j.conbuildmat.2019.117192.
- [12] Matos, Ana Mafalda, and Sousa-Coutinho, Joana. 2012. "Durability of mortar using waste glass powder as cement replacement." *Construction and Building Materials* 36:205–215. doi: 10.1016/j.conbuildmat.2012.04.027.
- [13] Ismail, Amalina H., Kusbiantoro, Andri, Chin, Siew Choo, Muthusamy, Khairunisa, Islam, Mukhlis, and Tee, Kong Fah. 2020. "Pozzolanic reactivity and strength activity index of mortar containing palm oil clinker pretreated with hydrochloric acid." *Journal of Cleaner Production* 242. doi:10.1016/j.jclepro.2019.118565.
- [14] American Society for Testing and Materials. 2012. "ASTM C-618 - 2012. Standard Specification for Coal Fly Ash and Raw or Calcined Natural Pozzolan for Use in Concrete." doi:10.1520/C0618.
- [15] American Petroleum Institute. 2013. "API 10B-2: Recommended Practice for Testing Well Cements, Second Edition."
- [16] Brooks, Adam L., Zhou, Hongyu, and Hanna, Dominic. 2017. "Comparative study of the mechanical and thermal properties of lightweight cementitious composites." *Construction and Building Materials* 159:316–328. doi:10.1016/j.conbuildmat.2017.10.102.
- [17] Aslani, Farhad, and Wang, Lining. 2019. "Development of strain-hardening lightweight engineered cementitious composites using hollow glass microspheres." *Structural Concrete* 21:673–688. doi:10.1002/suco.201900096.

Numerical Simulation of Asphalt Pavement Countermeasure at High Temperature Against Protrusion of Vertical PC Bars Using Applied Element Method

Addisu Desalegne Bonger^{1*}, Akira Hosoda², Hamed Salem³, Takahisa Fukaya⁴

^{1&2} Graduate School of Urban Innovation, Yokohama National University, 79-5 Tokiwadai, Hodogaya-ku, Yokohama 240-8501 JAPAN

³ Structural Engineering Department, Cairo University, Jamaa Street, Giza 12316, EGYPT

⁴ Metropolitan Expressway Co., Ltd., Maintenance Technology Division, 1-4-1 Kasumigaseki Chiyoda-ku, Tokyo 100-8930, JAPAN

Abstract

Corrosion due to insufficient grout filling can result in a sudden fracture of PC steel tendons. When a vertically tightened PC tendon in PC girders ruptured, they protrude from the anchorage section and damage the asphalt pavement, which is likely to cause a severe accident. In this research, different kind of asphalt pavements at 40°C were used as a countermeasure to prevent protrusion of vertically tightened PC bar tendon with different impact energy. Numerical simulations were carried out using Applied Element Method (AEM). Many influential parameters such as, bending properties of asphalt pavement at different temperature, strain rate and material properties, were numerically investigated. The results of the study showed that 80mm asphalt pavement system at 40°C with appropriate material and thickness could prevent 1,959J and 2,939J impact energy of the PC bar.

1 Introduction

Most problems associated with bonded post-tensioned construction occur as a result of inadequate grout injection or poor-quality grout [1]–[3]. Corrosion-related deterioration of poorly grouted and inadequately protected tendons in structures has also been well documented [4]–[7]. When a vertically tightened PC bar tendon is ruptured, all the strain energy in the PC bar is suddenly released, which can damage cover concrete and asphalt pavement [8]–[9]. The brittle fracture of prestressing tendon sometimes results in the protrusion of a torn portion from the bridge, causing a serious public safety hazard due to ejecting bars and falling concrete because such fractures can occur with no warning in advance [10]–[12]. Protection measures against eruption of PC bar tendon are necessary, so that damage to third party is avoided [13]. The objective of the present study is to numerically investigate the effects of asphalt pavement system at 40°C on preventing the protrusion of PC bars and concrete spalling.



Fig. 1 Rupture and protrusion of PC bar tendon [9], [10], [14]

2 Experimental program

2.1 Specimen details

The details of the specimen with 80mm thick asphalt pavement simulating the top of a bridge girder is shown in Fig. 2. Two layered asphalt pavement was provided in this specimen. The concrete part consisted of two independent parts that were connected using two additional side PC bars. A coupler was used to connect the main PC bar tendons due to the restrictions caused by the conditions for constructing

the pavement. PC bar rupture length was 4.5m. The diameter of the PC bar tendon was $\phi 32\text{mm}$ and that for the sheath was $\phi 45\text{mm}$. The sheath was not grouted. Cover concrete was 0mm simulating the worst condition in reality. The asphalt pavement countermeasure had a total thickness of 80mm with 2m x 2m area. The base layer among the two layers had a thickness of 50mm, and the cover layer had a thickness of 30mm.

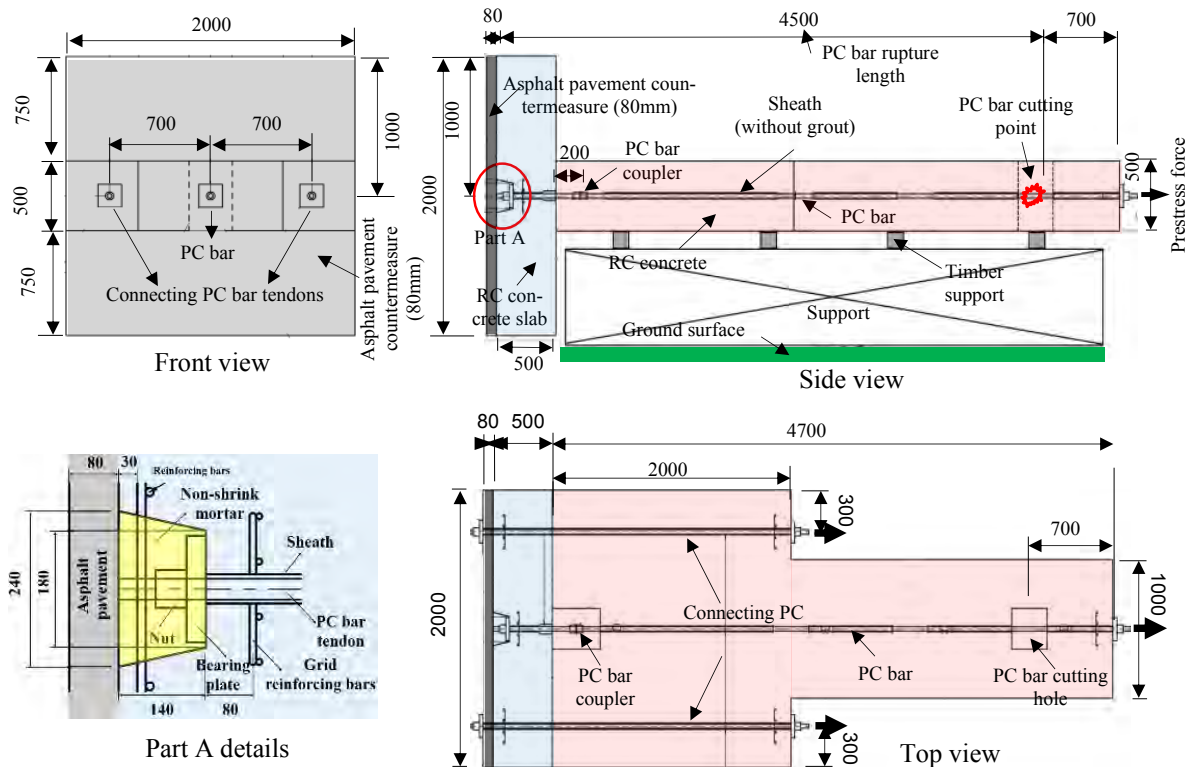


Fig. 2 Specimen details

2.2 Materials

The concrete had a compressive strength of 40MPa, 80mm slump and 4.5% air volume. The PC bar tendon was standard steel bar: SBPR930/1180 (class B2 in JIS, tensile strength $\geq 1180\text{MPa}$). The applied prestress force, after the prestress loss due to relaxation, creep and shrinkage, was 591 kN (0.6Pu). Strain energy of the PC bar was 4,408J. The two asphalt pavement layers (cover layer and base layer) had different material properties. Bending test for asphalt materials was conducted in this study. Non-shrinking mortar was used in the anchor zone, whose compressive strength was 60MPa.

3 The Applied Element Method (AEM)

Applied Element Method is based on division of the structural members into virtual elements connected through springs. Each spring entirely represents the stresses, strains, deformations, and failure of a certain portion of the structure. AEM allows to perform static and dynamic analysis [15]–[17]. In this study, a non-linear structural analysis software 'Extreme Loading for Structure (ELS)' based on Applied Element Method (AEM) was used as a nonlinear structural analysis tool to study the rupture and protrusion of PC steel bar [18].

4 Asphalt pavement bending test at different temperature

AEM numerical simulation was carried out for the base layer asphalt material and the cover layer asphalt material to calibrate tensile stress-strain relationships for the two asphalt materials. The asphalt specimens had a dimension of 300mm x 100mm x 50mm (Fig. 3(a)). In this study, the constitutive model of the asphalt pavement until ultimate strength was implemented through a bilinear material in AEM simulation. Fig. 3(b) and Fig. 3(c) show the tensile stress-strain relationships for the cover layer asphalt pavement and for the base layer asphalt pavement used in this research at a temperature of 0°C, 20°C and 40°C. In AEM simulation, the asphalt pavement was modeled with elements of 5mm

x 5mm x 5mm size. The experiment was carried out at a temperature of 0°C, 20°C and 40°C. In this study, the effect of temperature on the asphalt pavement was investigated whether the pavement can prevent the protrusion of PC bar during summer hot season.

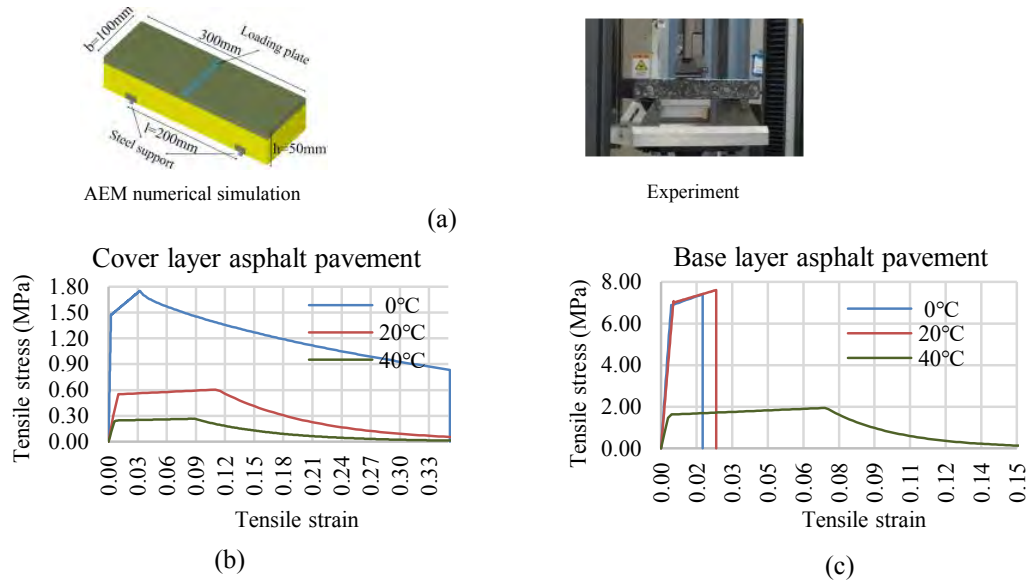


Fig. 3 Asphalt pavement bending test and modeling in AEM

The relationships between load-displacement are shown in Fig. 4. In AEM simulation for the cover layer asphalt pavement at 0°C, the observed maximum load was 3,389N at a displacement of 2.59mm. However, the observed maximum load at 20°C was 1,059N at a displacement of 6.95mm, and it was 505N at 40°C at a displacement of 7.00mm. As shown in Fig. 4(a), the bending strength of the cover layer decreased with the increase of temperature, despite the ductility enhancement. In the cover layer at 20°C, the first crack on the bottom surface of the specimen at the mid span was observed at a load of 697N and at a displacement of 11.40mm. After that, the crack gradually propagated upward until the complete collapse of the specimen. Similarly at 0°C and 40°C, a crack originated on the bottom surface of the specimen at the mid span gradually propagated upward until the complete collapse of the specimen.

On the other hand, in the base layer asphalt pavement, the observed maximum load was 10,973N at a displacement of 2.05mm and 11,138N at a displacement of 2.50mm at 0°C and 20°C respectively (Fig. 4(b)). At 0°C and 20°C, the first crack was observed at maximum load on the bottom surface at the mid span of the specimen. After that, the load suddenly dropped to zero without showing additional deformation. They showed brittle failure. At 40°C, the observed maximum load was 3,992N at a displacement of 3.98mm. At 40°C, a crack originated from the bottom surface of the specimen at the mid span gradually propagated upward until the complete collapse of the specimen. High temperature of 40 °C significantly decreased the load capacity of the base layer, however increased the ductility as shown in Fig. 4(b).

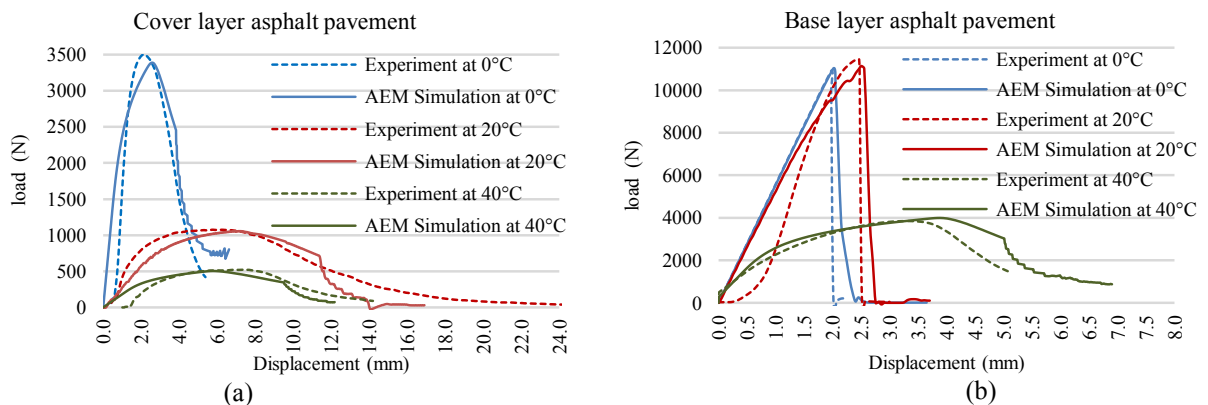


Fig. 4 Relationship between load-displacement for cover layer asphalt and base layer asphalt

The interface material which binds the concrete slab and the base layer asphalt pavement is also dependent on temperature. A pull-off test was carried out on the pavement at different temperature to investigate the bond performance of the interface material. As shown in Fig. 5, the bond performance was decreased with the increase of temperature.

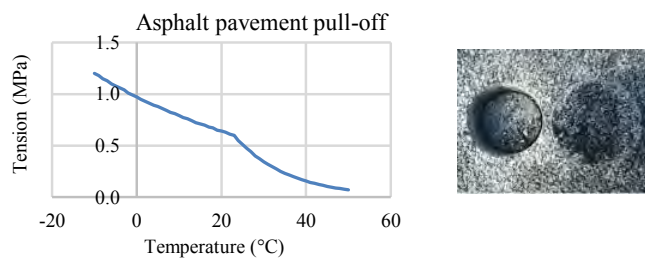


Fig. 5 Temperature effect on the bond between the concrete slab and the base layer

5 AEM numerical simulation with asphalt pavement at 20°C

AEM numerical simulation was made for the experiment explained in section 2. Reference [19] shows the details of the modeling about AEM numerical simulation with asphalt pavement at 20°C. It was found in this study that, the asphalt pavement system at a temperature of 20°C was effective in preventing PC bar protrusion of 4,408J (4.5m PC bar rupture length) impact energy of the PC bar. The maximum PC bar protrusion was 46 mm. The numerical simulation was verified based on the experimental result. The AEM numerical simulation showed good agreement with the experimental result as shown in Fig 6.

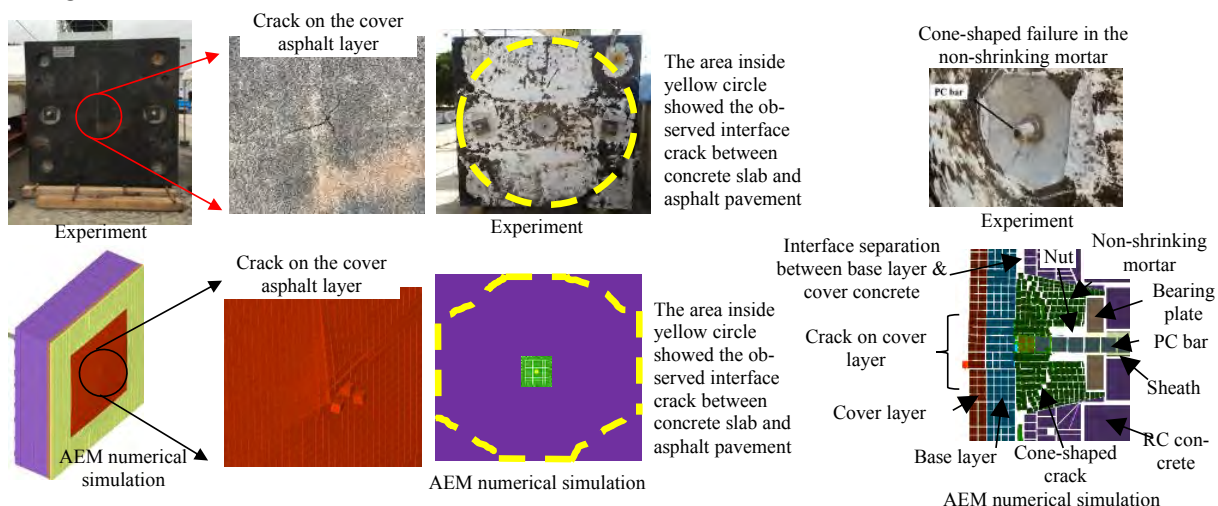


Fig. 6 AEM numerical simulation with asphalt pavement at 20°C (4,408J impact energy)

6 AEM numerical simulation with asphalt pavement at 40°C

AEM numerical simulation was made for the experiment explained in section 2. Reference [20] shows the details of the modeling about the PC bar tendon, the bearing plate, the nut and the sheath. The interface material between (sheath and bearing plate) and PC bar was modelled as a “bearing material” which could carry only compressive force. On the other hand, the interface material between (PC bar, nut and bearing plate) and non-shrink mortar was modelled as mortar (60MPa compressive strength). The interface material between concrete block and base layer asphalt pavement was modeled as a bi-linear material (0.97MPa yield stress).

Temperature and strain rate of asphalt pavement have significant effect on failure mode, mechanical characteristic and stress-strain curve [21], [22]. When the PC bar protruded, the asphalt pavement was fractured under a high loading rate. It was necessary to consider the effect of strain rate in the numerical simulation [19]. For the asphalt pavement under high loading rate, the yield stress and the elastic modulus was increased by the respective Dynamic Increase Factors (*DIF*), the ratio of the dynamic strength

to quasi static strength. The *DIF* was considered for the base layer and for the cover layer inside the red region of 1600mm x1600mm as shown in Fig. 8. Material properties of the cover layer and the base layer after considering strain rate effect are shown in Fig. 7. Reference [22] shows the details of the *DIF*.

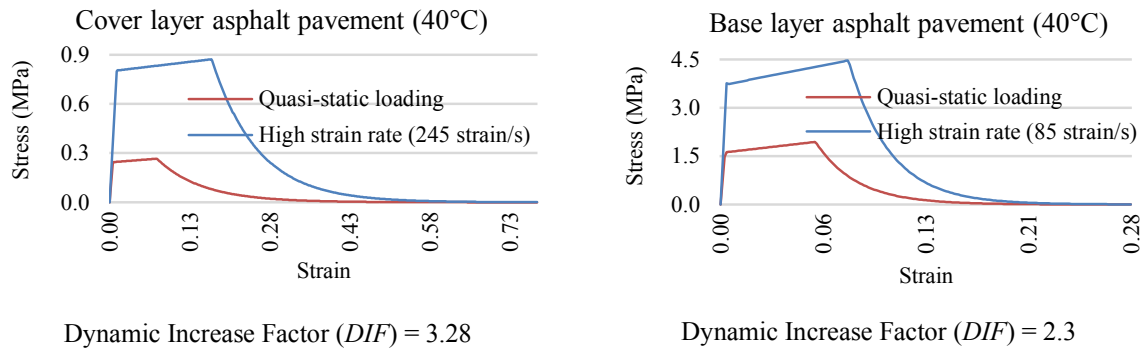


Fig. 7 Strain rate effect on the cover layer asphalt pavement and the base layer asphalt pavement

In the simulation, three stages of loading were applied. The first one was static to account for pre-stressing stage, while the second and the third ones were dynamic to simulate the rupture of the PC bar and its impact to concrete and asphalt pavement. The 1st dynamic stage had a duration of 0.7 second with a time interval of 5×10^{-6} second and the 2nd dynamic stage had a duration of 0.4 second with a time interval of 10^{-3} second. In the dynamic stages, the rupture of the PC bar was simulated by sudden removing one element of the PC bar at the cut point.

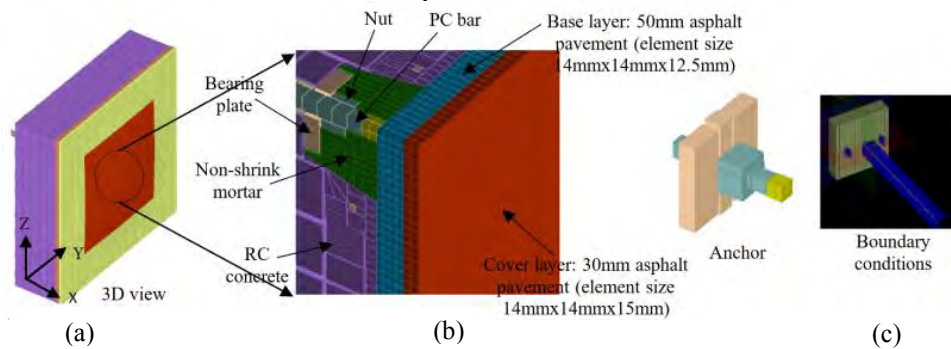


Fig. 8 Modeling for AEM numerical simulation

7 Result and discussion

Immediately after the rupture of the PC bar tendon, stress in the non-shrinking mortar and in the base layer asphalt pavement was generated from the head of the nut and also from the head of the PC bar respectively and propagated diagonally (Fig. 9). This stress distribution resulted in cone shaped crack in the mortar and in the asphalt pavement. Asphalt pavement destruction and spalling was observed near the center of the PC bar (Fig. 9(a)). As the PC bar tendon pushed the mortar forward, both the base layer and the cover layer asphalt pavement deformed together. At the same time, separation was observed at the interface between the concrete slab and the base layer as shown in Fig. 10(b). Asphalt pavement crack was observed around the corner of the concrete specimen and resulted the whole pavement system to fall down as shown in Fig. 10(a).

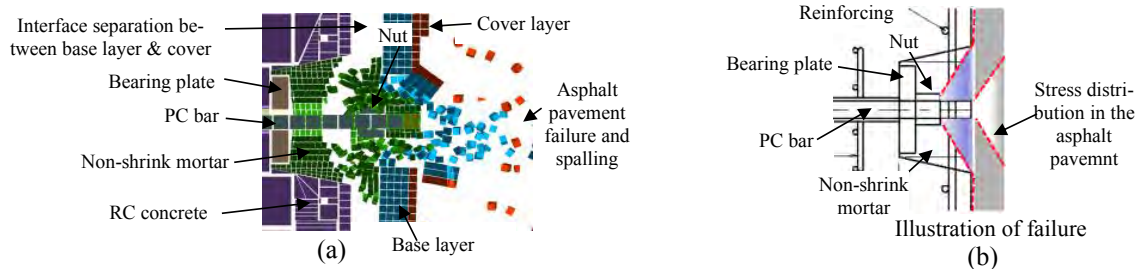


Fig. 9 Failure mechanism after rupture of the PC bar

The displacement of the PC bar in the numerical simulation was observed in Fig. 10(c). Between 0.001 and 0.0025 second, the average speed of the PC bar was 13.14m/sec and the average momentum was 372.8kg-m/sec towards the asphalt pavement. During the next time interval of 0.0026 – 0.0075 second, the average speed of the PC bar reduced to 5.30 m/sec as most of the strain energy of the PC bar was dissipated by damaging the asphalt pavement. The maximum PC bar protrusion was 125 mm at 0.052 second. After that, the PC bar stopped moving.

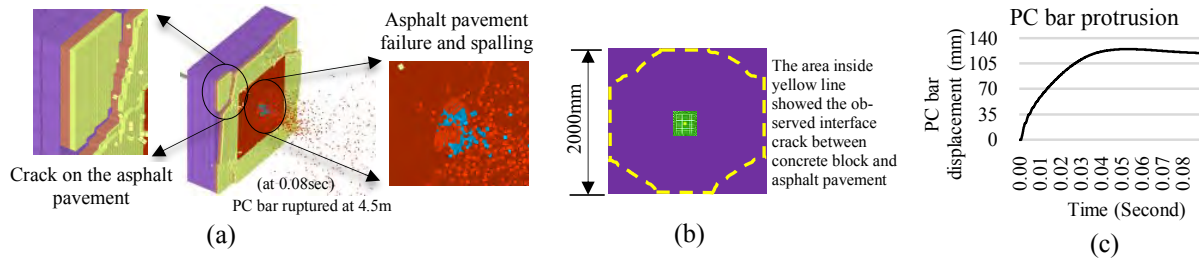


Fig. 10 Asphalt pavement failure, interface separation and PC bar protrusion (4,408J impact energy)

From this investigation, it was revealed that the asphalt pavement system at a temperature of 40°C was not effective in preventing PC bar protrusion and asphalt pavement spalling. The effectiveness of the asphalt pavement system depends on energy of ruptured PC bars. In this study, the PC bar tendon used had 5.0m in length and the PC bar rupture length was 4.5m measured from the PC bar head. Strain energy of the PC bar was 4,408J. However, according to our investigation in 2018, there were 19,657 vertical PC bars in Metropolitan Expressway (MEX) in Japan, and about 93% of the vertical PC bars had a length shorter than 3m. A similar AEM numerical simulation was carried out by reducing the PC bar impact energy from 4,408J (4.5m PC bar rupture length) to 1,959J (2.0m PC bar rupture length) and 2,939J (3.0m PC bar rupture length).

When the PC bar rupture length was 2m, all the 1,959J strain energy of the PC bar was dissipated by the asphalt pavement deformation, interface bond delamination between the concrete slab and the base layer and cracks in the non-shrinking mortar as shown in Fig. 11. The interface bond delamination between the concrete slab and the base layer was around 55% of the total area of the concrete slab (4m²). One surface element layer (15mm thickness) of the cover layer asphalt pavement near the PC bar was spalled off due to the shock force from the PC bar. No crack was observed in the asphalt pavement. The maximum PC bar protrusion was 13mm at 0.004 second as shown in Fig. 11(d). After that, the PC bar stopped moving.

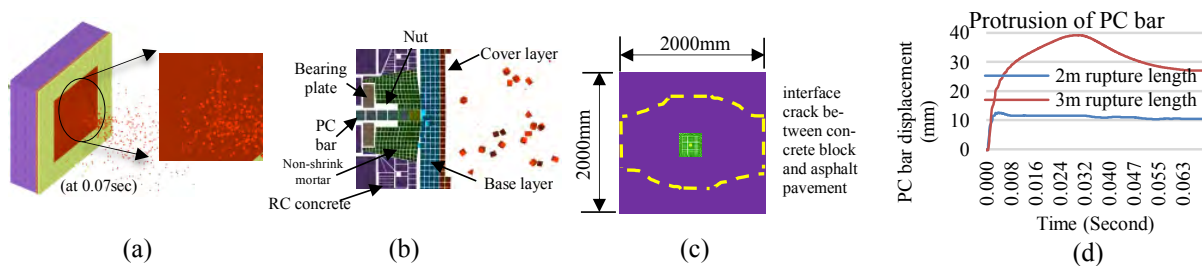


Fig. 11 AEM simulation with 2m PC bar rupture length (1,959J impact energy)

When the PC bar rupture length was 3m, all the 2,939J strain energy of the PC bar was dissipated by the asphalt pavement deformation, asphalt pavement cracks, interface bond delamination between the concrete slab and the base layer and cracks in the non-shrinking mortar as shown in Fig. 12. The interface bond delamination between the concrete slab and the base layer was around 93% of the the total area (4m²). The surface element layer (15mm thickness) of the cover layer asphalt pavement near the PC bar was spalled off due to the shock force from the PC bar. No crack was observed in the spahlat pavement around the PC bar. The asphalt pavement system did not fall down, though there was a crack at two corners (Fig. 12(a)). The maximum PC bar protrusion was 39mm at 0.03 second as shown in Fig. 11(d)). After that, the PC bar moved into the reversed direction. Finally, the PC bar stopped moving at a protrusion of 27mm after 0.062 second.

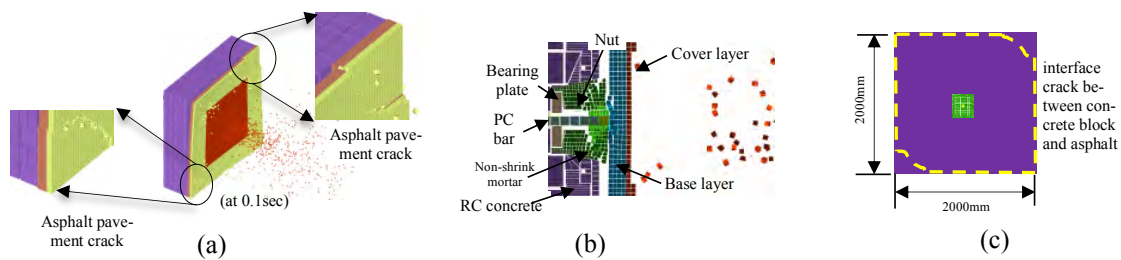


Fig. 12 AEM simulation with 3m PC bar rupture length (2,939J impact energy)

The same kind of numerical simulation was carried out without considering asphalt pavement countermeasure with 4,408J impact energy (4.5m PC bar rupture length) of the PC bar to understand the effects of the asphalt pavement countermeasure in preventing PC bar protrusion. The numerical simulation result indicated that the maximum PC bar protrusion was 2,780mm (Fig. 13).

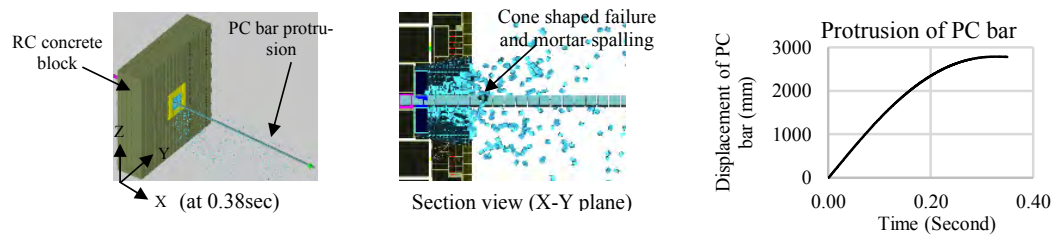


Fig. 13 Numerical simulation without asphalt pavement countermeasure

The effectiveness of the asphalt pavement system depends on so many factors, such as temperature, impact energy of ruptured PC bar, material properties of asphalt pavements including strain rate, interface material property between the concrete slab and the base layer asphalt pavement, etc. The numerical simulation tool developed in this study can be utilized for detailed investigation of the protrusion behavior and for evaluating the effectiveness of countermeasures at high temperature.

8 Conclusion

Based on numerical simulation investigations using the Applied Element Method for rupture and protrusion of vertically tightened PC bars in PC girders and for the effect of asphalt pavement, the following conclusions were obtained:

- Appropriate numerical simulation with the AEM can be conducted with appropriate modeling for asphalt pavement layers, interface material properties between the concrete slab and the asphalt pavement, and by considering strain rate effect in the asphalt pavement.
- The performance of the base layer asphalt pavement and the cover layer asphalt pavement were reduced with the increase of temperature. On the other hand, with the increase of temperature, the failure mode of asphalt specimens was shifted to ductile failure.
- Asphalt pavement system at a temperature of 40°C couldn't prevent 4,408J (4.5m PC bar rupture length) impact energy of the PC bar. However, the asphalt pavement system at a temperature of 40°C could prevent 2,939J (3.0m PC bar rupture length) impact energy of the PC bar.
- The strain energy of the PC bar was dissipated by a simultaneous action of asphalt pavement deformation, asphalt pavement crack, crack in the mortar and interface delamination between the concrete slab and the asphalt pavement.

References

- [1] ACI. 2001. *Corrosion of Prestressing Steels*. Reported by ACI Committee 222, ACI 222.2R, 01-38.
- [2] Podolny, W. 1992. "Corrosion of Prestressing Steels and Its Mitigation." *Journal of the Prestressed Concrete Institute*, V. 27, Issue. 5, 34-55.
- [3] Freyermuth, C. L. 2001. "Status of the durability of post-tensioning tendons in the United States." *Durability of Post-tensioning tendons*. fib-IABSE Technical Report, Bulletin 15. Workshop 15-16 November 2001, Ghent (Belgium), 43-50.

- [4] Fallis, G., Ball, J.C. and Moad, A. 2007. "Innovative Corrosion Evaluation System for Unbonded Post-Tensioned Cables." *Concrete Repair Bulletin*, 7-8.
- [5] Isuru, W., Hiroshi, M. and Toshihiro, Y. 2018. "Effects of Tendon Rupture and Re-Grouting on the Flexural Behavior of Prestressed Concrete Beams." 10th International Conference on Short and Medium Span Bridges Quebec City, Quebec, Canada, 154, 1-10.
- [6] Godart, B. 2001. "Status of durability of post tension tendons in France," *Durability of Post-tensioning tendons. fib-IABSE Technical Report, Bulletin 15. Workshop 15-16 November 2001, Ghent (Belgium)*, 25-42.
- [7] Mutsuyoshi, H. 2001. "Present situation of durability of post-tensioned PC bridges in Japan." *Durability of Post-tensioning tendons. fib-IABSE Technical Report, Bulletin 15. Workshop 15-16 November 2001, Ghent (Belgium)*, 75-88.
- [8] Proverbio, E. and Bonaccorsi, L.M. 2002. "Failure of Prestressing Steel Induced by Crevice Corrosion in Prestressed Concrete Structures." University of Messina Italy, 9DBMC-2002 Paper 026, 1-7.
- [9] Kamada, T. 2013. "The Latest Non-destructive Inspection Technologies for Evaluation of Grouting Condition of Tendon Ducts in Prestressed Concrete Beams." Third International Conference on Sustainable Construction Materials and Technologies, ISSN 2515-3056.
- [10] Nagata, Y., Shiratori, A., Ito, T. and Ueki, H. 2014. "Diagnosis for Grouted Condition of Transverse Prestressing Tendon in PC Bridges In-Service using Impact Elastic Wave Methods." *Concrete Research and Technology*, Vol. 25, 57-64.
- [11] Nishi, H., Otsuka, T., Kamei, K. and Onishi, H. 2018. "Risk Assessment About the Maintenance of the PC Bridge in Tozai Line." *Journal of the Society of Material Science, Japan*, V.67, No.2, 163-169.
- [12] Naso, T.R. 2017. "A Stitch in Time Saves Nine: A Post Tensioning Repair Case Study." *Journal of Post Tensioning Institute*, V. 13, No. 2, 53-60.
- [13] Harder, J. and Webster, N.R. 2001. "Durability of post-tensioning tendons: Canadian experience." *Durability of Post-tensioning tendons. fib-IABSE Technical Report, Bulletin Workshop 15-16 November 2001, Ghent (Belgium)*, 51-73.
- [14] Bangladesh Ministry of Road Transport and Bridges, Roads and Highways Department. 2018. *Bangladesh Bridge Inspection and Evaluation Manual*. pp. 152.
- [15] Meguro K. and Hatem Tagel-Din, 1999. "Applied Element Simulation for Collapse Analysis of Structures." *Bulletin of Earthquake Resistance Structures*, No. 32, pp. 113-123.
- [16] Meguro K. and Hatem Tagel-Din. 2000. "Applied Element Method for dynamic large deformation analysis of structures." *Structural Eng. / Earthquake Eng., JSCE*, vol. 17, no. 2, pp. 215-224.
- [17] Meguro K. and Hatem Tagel-Din. 2002. "Applied Element Method Used for Large Displacement Structural Analysis." *Journal of Natural Disaster Science*, vol. 24, No. 1, pp. 25
- [18] Applied Science International. 2017. [http://www.Extreme Loading for Structures \(ELS\)](http://www.Extreme Loading for Structures (ELS)).
- [19] Addisu Desalegne Bonger, Akira Hosoda, Hamed Salem, Takahisa Fukaya. 2021. "Numerical Simulation of Rupture and Protrusion of Vertically Tightened PC Bars in PC Girders with Asphalt Pavement Using Applied Element Method." *Journal of Advanced Concrete Technology* (under review).
- [20] Addisu Desalegne Bonger, Akira Hosoda, Hamed Salem, Kazuya Kaba. 2019. "Numerical Simulation of Rupture Protrusion of Vertically Tightened PC Steel Bars Using Applied Element Method." *Internet Journal of Society for Social Management Systems* Vol.12 Issue 1 sms19-3671, ISSN: 2432-552X, pp 110.
- [21] Rui Tang, Zhenpeng Yu, Guoqing Liu, Furong Li and Wenbin Tang. 2020. "Uniaxial Dynamic Compressive Behaviors of Hydraulic Asphalt Concrete under the Coupling Effect between Temperature and Strain Rate." *MDPI Journals, Materials* 2020, 13, 5348; doi:10.3390/ma13235348.
- [22] Wei Si, Ning Li, Biao Ma, Yu-xiang Tian and Xue-yan Zhou. 2015. "Temperature Response to Tensile Characteristics of the Hot Asphalt Mixtures." *KSCE Journal of Civil Engineering* (2016) 20(4): DOI 10.1007/s12205-015-0688-2, 1336-1346.

Case study of carbonation of 100 years old concrete covered by a thin cement render.

Jakub Gašpárek, Lukáš Húlek, Peter Paulík

*Department of Concrete Structures and Bridges,
Slovak University of Technology, Faculty of Civil Engineering
Radlinského 11, 81005 Bratislava, Slovakia*

Abstract

The research study performed on 100-years-old concrete bridges shows, that a thin layer of cement-based protective render coat (PRC), typically a few millimetres thick (2-4) mm, could significantly reduce the rate of carbonation of underlying concrete. During previous research, carried out on reinforced concrete bridges near the towns Sládkovičovo and Krásno nad Kysucou in Slovakia, very low values of carbonation depths were measured. The measured carbonation depths, using the phenolphthalein indicator, were very small after 100 years of service life in XC3 exposure class (according to EN 206). Last year, another 100-years old railway bridge was discovered near the town Rimavská Sobota which concrete showed very low carbonation depths. As in the previous case, this was caused by the PRCs applied to a concrete surface around 100 years ago. Measured values from in-situ and laboratory research are presented in the article, as well as the possible explanation of this phenomenon. The article aims at the effort to apply the knowledge gained by the research to increase the service life of existing concrete bridges with small reinforcement cover.

1 Introduction

The chemical reaction of cementitious constituents in concrete, primarily calcium hydroxide also known as portlandite $\text{Ca}(\text{OH})_2$, and atmospheric carbon dioxide CO_2 , causes chemical changes in the concrete, resulting in a pH reduction. This process is known as carbonation. Atmospheric carbon dioxide diffusing into the concrete is dissolved in the porous water to form aqueous HCO_3^- and CO_3^{2-} , which reacts with dissolved Ca^{2+} to precipitate mainly calcite CaCO_3 . Sufficient moisture is therefore required for this process. The dissolution of CO_2 in porous water and precipitation of CaCO_3 is determined by the temperature and relative humidity and the partial pressure of carbon dioxide on the concrete surface or the liquid in the pores of the concrete, respectively [1]. This is largely controlled by the diffusion rate of carbon dioxide through the microstructure of concrete [2]. Chemical changes in concrete by carbonation results in the reduced porosity because the arisen CaCO_3 has a larger molar volume (mainly calcite $36,93 \text{ cm}^3/\text{mol}$) than the primary reactant $\text{Ca}(\text{OH})_2$ ($32,29 \text{ cm}^3/\text{mol}$) [3], which reduces permeability and increases the microhardness of the cementitious matrix. The reaction reduces the alkalinity of the concrete below pH 9, which is no longer able to protect the steel reinforcement against corrosion. It should be noted that the carbonation process is very slow and dependent also on the carbon dioxide concentration in the atmosphere. It could be also stated that better concrete quality results in a lower carbonation rate due to decreased permeability [4].

2 Measurement methods

In-situ measurements were performed according to the following procedures:

- After visual inspection, exploratory boreholes (ϕ 16 mm) were performed using a drilling device to determine the preliminary depth of carbonation.
- Permeability testing was performed after exploratory boreholes. The surface was cleaned and permeability measurements with the Torrent method were performed [5].
- After the permeability test, core drilling was performed directly at the place, where permeability was measured in the previous step.
- The drilling core specimens were properly cleaned with water pouring in the direction from the outer surface of the cylinder to avoid contamination of the carbonated layer by noncarbonated concrete dust particles. After cleaning the sample was wiped and a 1% solution of

phenolphthalein was applied to its surface, again in the direction from the outer surface of the cylinder.

- By this procedure, the carbonation depth was measured in-situ at all drilled core specimens, which were then taken to the laboratory for further chemical analyses, mainly by thermal and chemical methods.

3 Results

During the diagnostics of the railway bridge, cylindrical samples were drilled from its abutment. As reported in Table 2 the average cylindrical compressive strength is 18,4 MPa. This value takes into account the fact, that it was measured on drilled core specimens according to STN EN 13791 [6]. The characteristic cylindrical compressive strength is then 11,4 MPa and the classification of the concrete is C10/12. As reported in Table 1, according to the determined concrete strength class and taking into account 100 years of the service life of the structure in XC3 exposure class, a much greater depth of carbonation was expected.

Table 1 Results of in-situ measurement of carbonation depth at the bridge near Rimavská Sobota performed in June 2019.

Sample		Permeability by Torrent method	Average carbonation depth
Denotation	Surface	kT ($\times 10^{-16} \text{ m}^2$)	(mm)
2.2a	PRC	Not measured	< 2
2.2b		Not measured	< 5
2.2c		Not measured	< 2

Table 2 Results of laboratory tests on drilled core samples at the bridge near Rimavská Sobota performed in June 2019.

Sample	Average diameter	Average height	Mass	Density	Young's modulus of elasticity	Sample cylindrical compressive strength
Denotation	(mm)	(mm)	(g)	(kg/m^3)	(GPa)	(MPa)
2.2a	104.2	92.0	1722	2195	-	24.9
2.2b	104.3	209.5	3777	2115	17.5	12.9
2.2c	104.1	200.0	3709	2175	20.0	16.3

As it was found out in the previous study [7] these low carbonation depths originate in the protection of the concrete surface by PRC, as shown in Fig. 1. This PRC has been probably applied 100 years ago to the concrete surface only for aesthetic reasons. Since 100 years ago vibrating equipment was not available to compact the concrete and instead of smooth formwork only plain wooden planks were used, there was probably a reason to apply PRCs. In Slovakia, it was common practice to additionally modify the concrete of bridge piers and abutments, whether by tiling or plastering [8]. On Fig. 1 (left), there is the specimen after cleaning with water. The PRC layer is visible on the specimen surface. On Fig. 1 (right), there is the specimen after application of the phenolphthalein indicator. Also, the figures show a crack under the PRC where the layer was not perfectly bonded to the underlying concrete. The cracks in the PRC and its imperfect connection to the concrete beneath caused its bit higher carbonation depth as shown in the figure on the right. However, this carbonation depth is only less than 10mm under the PRC despite 100 years of service life.

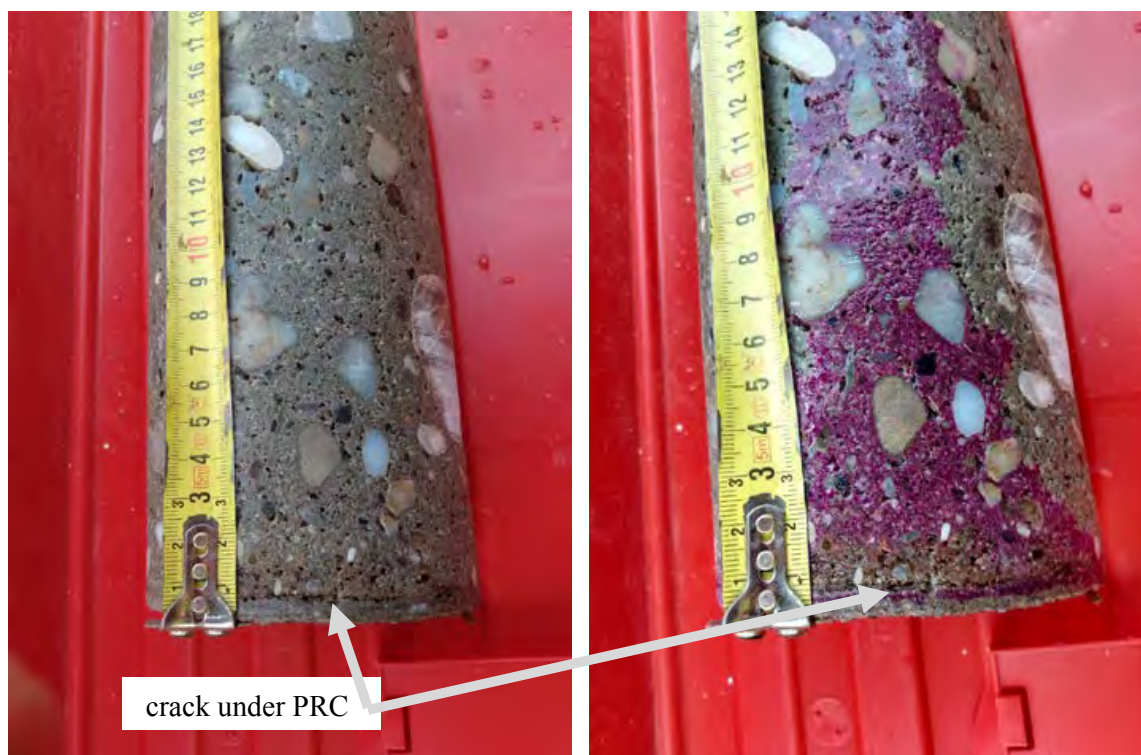


Fig. 1 The specimen 2.2b taken from the bridge abutment (June 2019).

To prove the functioning of this additional surface treatment to significantly slow down carbonation of underlying concrete, another series of more detailed tests were performed, which is evaluated in the following Table 3.

In Fig. 2, there is the location where the specimens were taken from the bridge abutment in November 2019, which are subsequently evaluated in Table 3. The PRC layer on the surface of the concrete is locally cracked in some places, resulting in increased permeability as shown in specimen RS2-A.

Table 3 Results of in-situ measurement of carbonation depth at the Bridge near Rimavská Sobota performed in November 2019^a.

Specimen		Permeability by Torrent method	Carbonation depth	Notes
Denotation	Surface	kT ($\times 10^{-16} \text{ m}^2$)	(mm)	
RS2-A	PRC	7.163	15	Small cracks of the width less than 0,05mm in the render
RS2-C		0.001	< 2	High-quality cement - based
RS2-D		0.001	< 2	
RS2-B	Uncovered concrete	> 10 ^b	50	Spalled or missing render
RS2-E		> 10 ^b	50	

^athe results are also evaluated in Table 4

^bthe value is greater than the measurable limit of the instrument

The results show a clear relationship between the depth of carbonation of the underlying concrete and the low-permeability of the thin layer of protective render coat which shows Table 3. With the optimal interplay of all factors: high-quality PRC, absence of concrete defects under a PRC (e. g. caverns or direct contact of aggregates to a PRC), and thus a firm, compact PRC interface and concrete, the depth of carbonation of 100-year concrete is extremely low. This proves that PRC can function as a

simple, easy-to-make surface finish, which represents synchronously a highly effective anti-carbonization barrier.



Fig. 2 The place where the specimens RS2-D, RS2-A, RS2-C were taken from the bridge abutment – a location with PRC (November 2019).

3.1 TG-DTA analysis, degree and stages of carbonation

To proof the in-situ results of carbonation depth, TG-DTA analysis was performed on the chosen samples. The degree of carbonation (CD) as the $\text{CaO}_{\text{Carb}}/\text{CaO}_{\text{Total}} \times 100$ (% wt.), was calculated from TG-DTA results and chemical analysis. CaO_{Carb} means the CaO content bound in CaCO_3 originated from carbonation reaction and $\text{CaO}_{\text{Total}}$ concerns CaO bound in CaCO_3 , $\text{Ca}(\text{OH})_2$, gel-like hydration products (C-S-H, C-A-H) and $\text{CaSO}_4 \times 2\text{H}_2\text{O}$. The extent of carbonation attack is also specified by the degree of modification changes (DMC) given by the $\text{CaCO}_3, \text{coarse-grained} / \text{CaCO}_3, \text{fine-grained}$ ratio. The fine-grained CaCO_3 is detected by TG-DTA between 575-700 °C and coarse-grained CaCO_3 between 700-1100 °C. The total content of CaO is estimated from the chemical analysis according to STN EN 196-2 [9]. The extent of CO_2 attack is characterized by four stages of carbonation (I < 55 %; II: 55-65 %; III: 66-80 %; IV: > 80 %) [7].

TG-DTA analysis was performed for the concrete samples as well as for the PRC (“surface” means (0-20) mm and “internal” means approximately (280-300) mm distance from the surface of the drilled core specimen). For TG-DTA analysis the PRC samples were separated into three parts according to Fig. 3.

Fig. 4 shows results for the cover layer of PRC. This thin layer probably served only as a colour treatment and is composed of silica sand and lime, as can be seen from Fig. 3 (colour difference). Locally in some places on the surface of the PRC, it is very thin less than 1 mm, or completely missing (Fig. 1). DTA curve is specified by a couple of partial mass losses, from which the only one clear is that attributed to CaCO_3 decomposition at peak maximum 798,6 °C originating from the carbonation of lime.

Fig. 5 shows results for the outside part of PRC according to Fig. 3. The DTA plot shows negligible signs of the endothermic peak between 100-300 °C and at about 500 °C. By contrast, the TG curve is specified by a couple of partial mass losses, from which the only one clear is that attributed to

CaCO_3 decomposition at peak maximum 813,5 °C. This is due to a large amount of CaCO_3 content in this layer. There is no significant change of mass in the 100-300 °C range, as the structure fully carbonate - the gel-like products are lacking in this region, the structure is closed by the products of the carbonation reaction as shown by the permeability test.

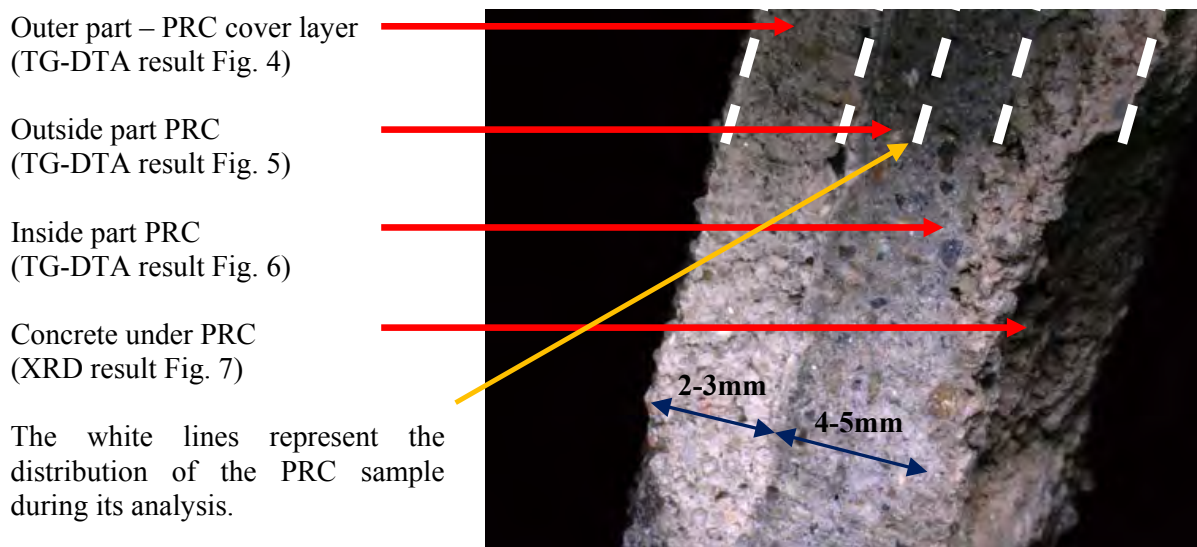


Fig. 3 Optical microscope image – view of the edge of PRC quarry (wider PRC sample).

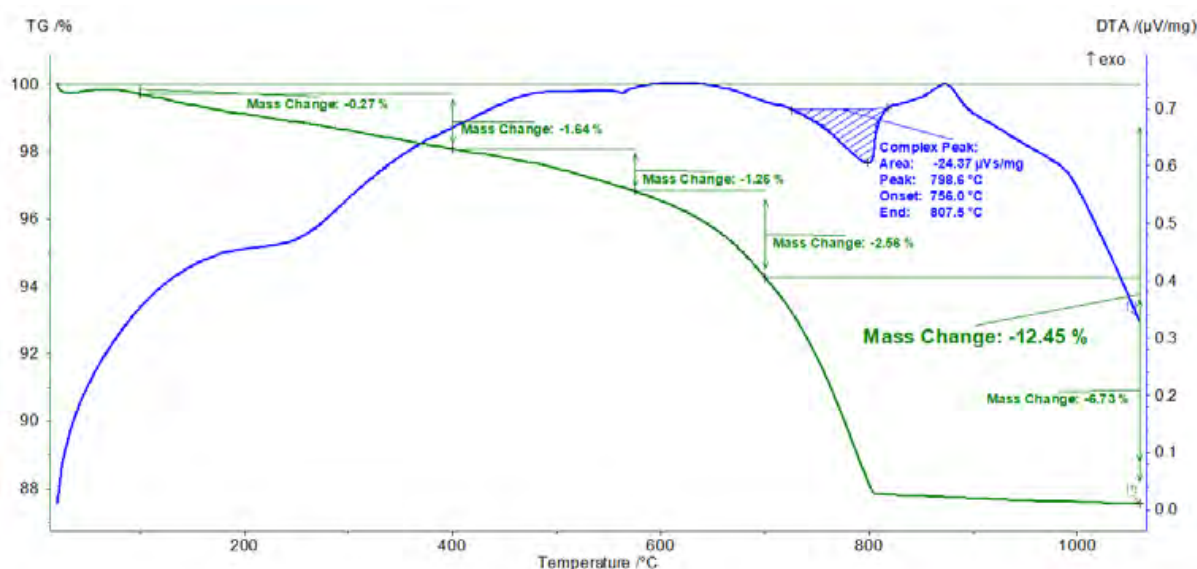


Fig. 4 TG-DTA plot for the PRC cover layer (outer part of the sample according to Fig. 3).

Fig. 6 shows the results for the internal sample of PRC at the concrete interface. The presence of gel-like hydration products and $\text{Ca}(\text{OH})_2$ are confirmed, the DTA plot shows very strong signs of the endothermic peak between 100 and 300 °C and at about 500 °C. A smaller mass change at 600-800 °C is attributed to CaCO_3 decomposition at a peak maximum of 770,3 °C. This is due to the low content of CaCO_3 in this layer at the internal PRC-concrete interface and the great amount of gel-like hydration products and the contrary negligible occurrence of portlandite $\text{Ca}(\text{OH})_2$ in the studied PRC sample.

The mineral composition of the concrete under PRC is shown in Fig. 7. Concrete shows a small amount of calcite, which is considered to be a carbonation product and a small amount of portlandite. This result is in good agreement with thermal and chemical analysis in Table 4, which summarizes the carbonation characteristics of uncovered concrete, PRC-protected concrete, and the PRC from the bridge near Rimavská Sobota. This barrier formed by the carbonated PRC significantly slowed down the carbonation process of the underlying concrete and will be the subject of further research.

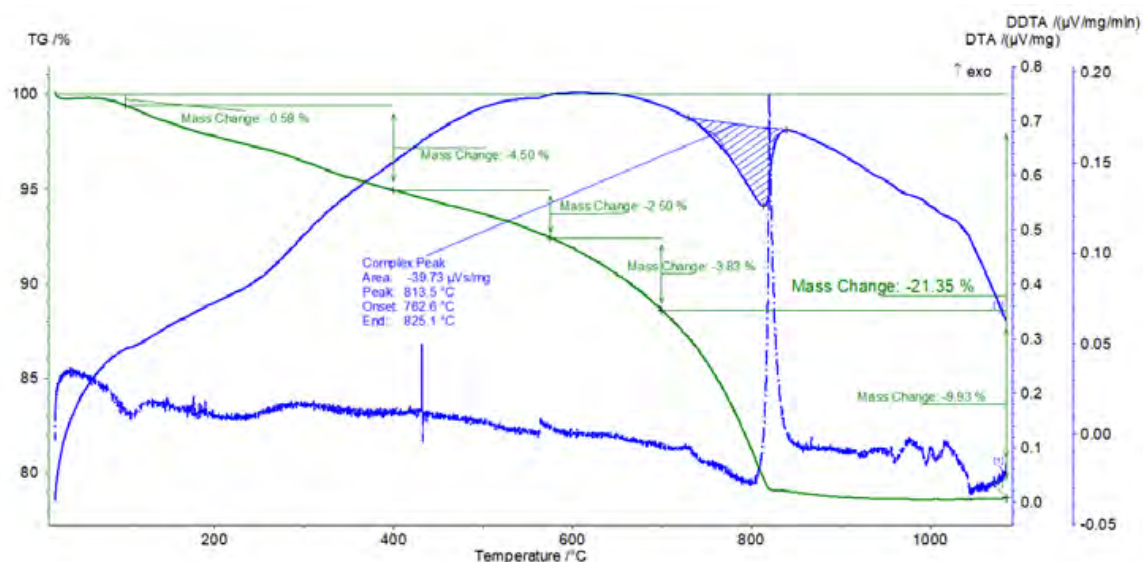


Fig. 5 TG-DTA plot for the PRC (outside part of the sample according to Fig. 3).

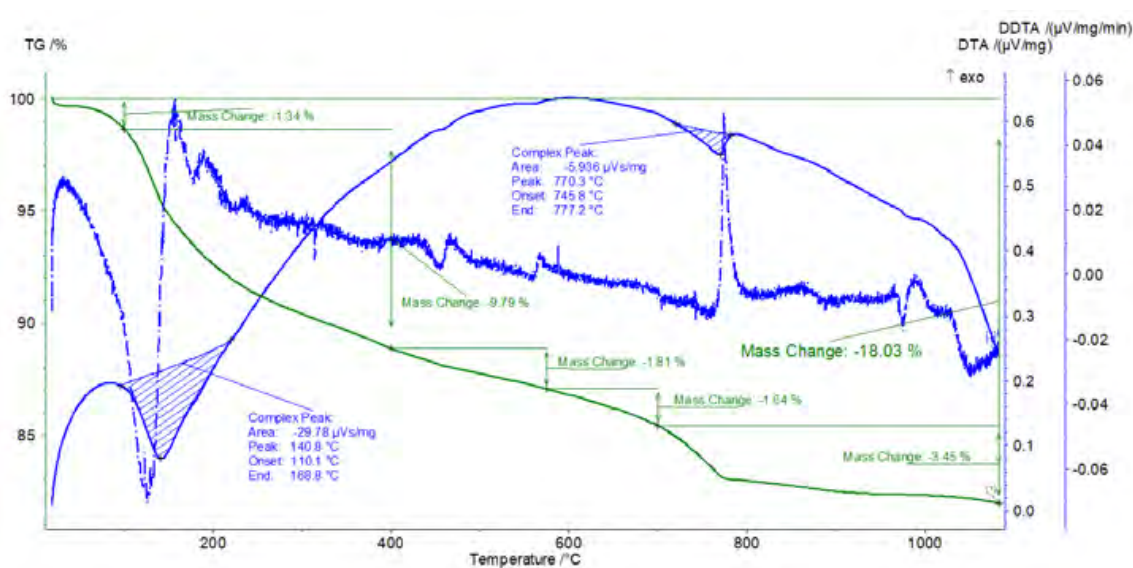


Fig. 6 TG-DTA plot for the PRC (inside part of the sample according to Fig. 3).

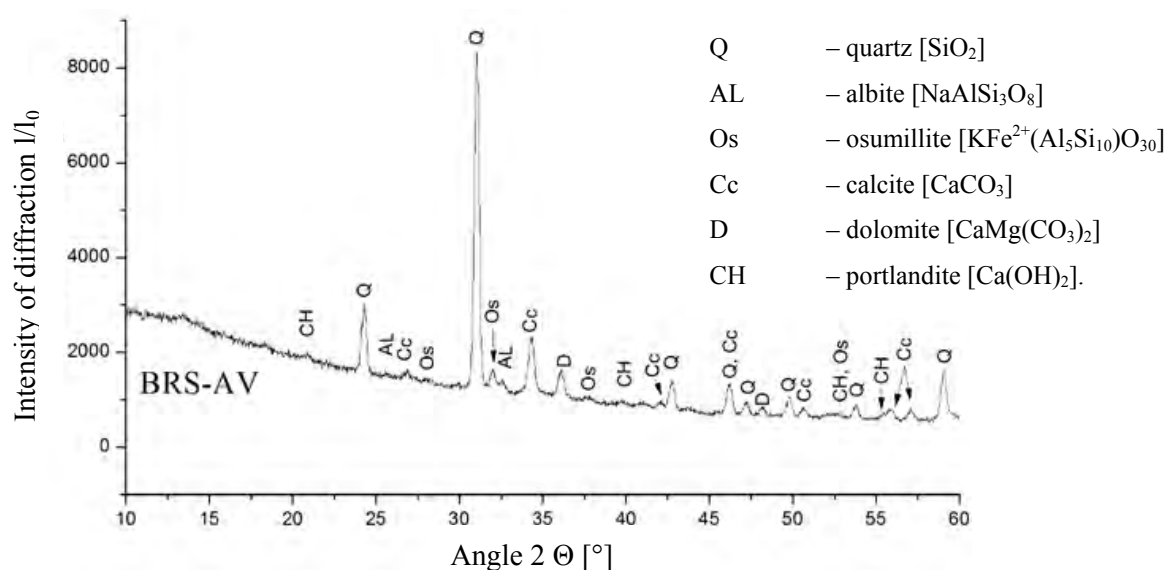


Fig. 7 Mineral composition of concrete under PRC according to Fig. 3.

Table 4 The assessment of carbonation attack by the results of chemical and thermal analysis.

Sample as marked in Table 3	CaO _{total} (% wt.)	CaO _{carb} (% wt.) occurring in			Assessment of carbonation		
		fine-grained CaCO ₃	coarse-grained CaCO ₃	total CaCO ₃	CD (%)	DMC (-)	Carbonation stage (-)
RS2-B – surface ¹	15.66	4.91	9.55	14.46	92	1.9	IV
RS2-B – internal ¹	19.41	1.75	9.48	11.23	58	5.4	II
RS2-C – surface ²	20.68	2.10	10.79	12.89	62	5.1	II
RS2-C – internal ²	19.42	1.63	8.41	10.04	52	5.2	I
RS2-D – surface ²	19.90	1.80	8.78	10.58	53	4.9	I
RS2-D – internal ²	16.07	1.67	7.36	9.03	56	4.4	II
PRC over RS2-A ³	20.25	4.32	12.14	16.46	81	2.8	IV
PRC over RS2-C ³	19.23	4.29	10.89	15.18	79	2.5	III
PRC over RS2-D ³	20.15	4.42	13.40	17.82	88	3.0	IV

¹ uncovered concrete sample² concrete samples covered with PRC³ PRC sample in its entire thickness

A similar conclusion can be drawn from previous research [7] on the bridges near the towns Sládkovičovo and Krásno nad Kysucou in Slovakia. The exposed concrete surface layer without PRC (RS2-B - surface) is characterized by an extremely high degree of carbonation, the highest degree of modification changes, and therefore the carbonation stage IV that is specified by an extensive carbonation attack. In contrast, the internal sample (RS2-B - internal) indicates stage II of carbonation, characterized by an insignificant effect on the concrete properties and durability. In the case of samples RS2-C and RS2-D, many similarities can be observed. The carbonation of the surface (0-20) mm and internal (280-300) mm concrete layer is almost the same. These similarities are due to the PRC application, which protects the underlying concrete. Very small differences between the samples RS2-C and RS2-D, specifically between the internal and surface samples, may be due to the ability of the PRC to mitigate CO₂ diffusion into the underlying concrete situated below a PRC. These facts cause the carbonation stage to vary only negligibly between the internal and surface portions. The high degree of carbonation of the PRCs confirms the accumulation of carbonation products in the thin layer of PRC. The carbonation products formed in the PRCs tight their pore space by this way that they become an effective anti-carbonation barrier.

The samples of PRC (PRC over RS2-A, PRC over RS2-C, PRC over RS2-D) indicates the degree of carbonation stage IV or stage III in the case of the sample PRC over RS2-C. The samples also characterize the largest amount of total CaCO₃ and a higher degree of carbonation (CD) in contrast to concrete below the PRC.

4 Further research

The mix-design of PRC is developed in Building Testing and Research Institute in Bratislava (TSÚS) since Jul 2020 based on chemical analysis of existing PRC. After consistency tests, the newly developed PRC was applied to a concrete wall and permeability testing was performed. Based on the permeability tests the newly developed PRC mix was applied to cylindrical concrete specimens with a diameter of 300 mm (Fig. 8 left). Specimens were sealed on other sides with a special impermeable sealant to prevent carbon dioxide penetration (Fig. 8 right). The low strength of underlying concrete (C8/10) was chosen in order to make the concrete carbonation immediately visible in the case of the applied render is not protecting it properly and to simulate the strength of concrete from 100 years ago. Then the specimens were placed in a carbonation chamber according to TSÚS methodology.



Fig. 8 Newly developed PRC; on the left: its application on the C8/10 underlying concrete, on the right: special impermeable sealant applied on other sides.

5 Conclusions

Based on the results of the performed tests, the following conclusions could be drawn:

- The in-situ measurements of carbonation depth show that high quality, (2-4) mm thin, cement-based protective render coat can effectively protect the underlying concrete against carbonation within the 100-year service life of a bridge.
- Carbonation depth of the concrete depends upon the low permeability of the PRC applied to its surface. A close mutual correlation between the depth and extent of carbonation (measured by phenolphthalein test, and TG-DTA analysis) and the coefficient of surface permeability (measured by the Torrent method) was observed.
- The very low permeability of the PRC is probably caused by the accumulated carbonates in a narrow spatial volume of the PRC, thus creating an impermeable barrier for CO₂.

Acknowledgements

This work was supported by the Slovak Research and Development Agency under contract No. APVV-17-0204 and the University Science Park (USP) of the Slovak University of Technology in Bratislava (ITMS: 26240220084).

References

1. Glasser, F.P., Marchand, J., and Samson, E. 2008. "Durability of concrete — Degradation phenomena involving detrimental chemical reactions". *Cement and Concrete Research* 38:226–246. Accessed February 19, 2021. doi:10.1016/j.cemconres.2007.09.015.
2. Ngala, V.T. and Page, C.L. 1997. "EFFECTS OF CARBONATION ON PORE STRUCTURE AND DIFFUSIONAL PROPERTIES OF HYDRATED CEMENT PASTES". *Cement and Concrete Research* 27:995–1007. Accessed February 19, 2021. doi:10.1016/S0008-8846(97)00102-6.
3. Silva, C.A.R. da., Reis, R.J.P., Lameiras, F.S., and Vasconcelos, W.L. 2002. "Carbonation-Related Microstructural Changes in Long-Term Durability Concrete". *Materials Research* 5:287–293. Accessed February 19, 2021. doi:10.1590/S1516-14392002000300012.
4. Matthews, S. 2014. "Design of durable concrete structures". Glasgow: IHS BRE Press. 312 p.
5. Torrent, R. and Frenzer, G. 1995. "Study on methods to determine and judge characteristic values of the coverconcrete on site Report No. 516":105.
6. STN EN 13791. "Assessment of in-situ compressive strength in structures and precast concrete components".
7. Janotka, I., Bačuvčík, M., and Paulík, P. 2018. "Low carbonation of concrete found on 100-year-old bridges". *Case Studies in Construction Materials* 8:97–115. Accessed February 19, 2021. doi:10.1016/j.cscm.2017.12.006.
8. Kubáček, J. 1999. "Dejiny železníc na území Slovenska". Bratislava: Železnice Slovenskej republiky. 461 p.
9. STN EN 196-2. "Methods of testing cement. Part 2: Chemical analysis of cement".

Creep potential of concrete damaged by Alkali Aggregate Reaction

Clément Lacombe, Alain Sellier, Thierry Vidal, Christine Noret*, Patrice Anthiniac*

*LMDC (Laboratoire Matériaux et Durabilité des Constructions),
Université Toulouse III Paul Sabatier,
135 Avenue de Rangueil, 31077 Toulouse Cedex 4, France*

** Tractebel ENGIE France
5 Rue du 19 Mars 1962, Gennevilliers, France*

Abstract

The durability of concrete structures, especially when concrete is affected by Alkali Aggregates Reaction (AAR), is a major concern. Indeed, the AAR swelling can induce changes in the stresses distribution within the structure which could affect its functionality. Previous studies have demonstrated the swelling mitigation in compressive stress directions, and the low effect of AAR on creep rate in this configuration. However, very few studies have investigated the creep behaviour of a concrete already damaged by AAR. Nevertheless, in real structures, compressive stresses may develop with AAR and become significant only after a certain level of swelling. That is the reason why it is necessary to characterize the creep rate of a concrete already damaged by AAR before loading.

The present study consists of an original experimental programme of creep tests carried out on concrete previously damaged by AAR in free swelling condition. Two concrete mixes were designed differing only by their aggregates. The first concrete incorporated reactive aggregates and the second non-reactive aggregates. Both mixes are similar regarding the proportions of cement, water, alkali content, sand and aggregates.

Under stress, a reduction of the swelling is observed which is the consequence of two phenomena. The first one is the effect of the AAR on the instantaneous elastic strain of the reactive concrete and the second one, is due by a higher creep rate of the affected concrete during the first 15 days after loading.

1 Introduction

Numerous studies have investigated the chemistry of the Alkali Aggregates Reaction (AAR) and its three main causes [1], namely alkali-sensitive aggregates, high relative humidity and alkali content in the cement. Other studies dealt with the structural effects of AAR, studying the mechanical properties and long-term strains of affected concretes.

The free swelling “S” curve induced by the reaction was proposed by Larive in 1997 [2], but these strains can be reduced or cancelled in the stress direction if the specimens are loaded before the reaction initiation [3]. In 1994, Charlwood had already observed these phenomena on real size structures and proposed an empirical law between the swelling rate and the compressive stress with an 8 MPa vanishing limit [4]. This first model and numerous others which followed were reviewed in 2017 [5].

In these models, AAR is modeled at different levels, from the smallest scale, i.e. the reaction products to the largest structure scale. One of these models considers swelling reduction directly using a rheological model coupled with a micro-mechanics cracking criterion that permits large structure analysis once incorporated into finite element softwares [6]. Others tried to explain these phenomena using numerical meso scale approaches with concrete matrix considered as a viscoelastic material that can absorb swelling. Depending on creep model used for the matrix, the creep velocity rate immediately around the aggregates could be able to absorb a part of the gel overpressure [7]. In order to take into consideration this phenomenon in future models, a first step consists of quantifying it experimentally.

In 2019, the time-dependent strains of concretes incorporating different types of reactive aggregates were quantified by Reinhardt et al [8]. In this study, the reaction was stopped when the samples were loaded. The experimental programme presented here is intended to clarify the interactions between creep behaviour and the ongoing AAR.

2 Experimental test programme

2.1 General

The investigation of two concretes, one reactive and the other not, is required to observe the effects of AAR on creep behaviour. Both concrete mixes were designed to reach similar mechanical strength and stiffness. In terms of storage and loading, the conditions were the same for both concretes. In parallel, the strains of free-swelling unloaded specimens were also recorded.

2.2 Choice of aggregates

The properties of both concrete mixes have to be similar before the development of the reaction. Consequently, the type of aggregates is important: for the non-reactive mix, crushed limestone aggregates were chosen. Crushed calcareous-siliceous aggregates (classified as potentially reactive according to the LCPC classification [9]) were used for the reactive ones. To justify this choice, the potentially reactive aggregates were characterized in accordance with standards and recommendations [10]–[11] and compared with the non-reactive crushed limestone in table 1.

Table 1 Mechanical properties of aggregates

Reactivity of the rock	Non-reactive [12]	Reactive
Uniaxial compressive strength	224 ± 25 MPa	178 ± 47 MPa
Young's modulus	80 ± 2 GPa	78.6 ± 0.2 GPa
Poisson's ratio	0.31 ± 0.01	0.31 ± 0.02

2.3 Concrete compositions

Both concrete compositions were designed with the same proportions of materials (presented in table 2). The grading curves were close with a maximum size of the largest grains of 12.5 mm.

The Na₂O equivalent content of both mixes was increased from 0.28% of cement content to 1.25% to ensure the AAR development.

Table 2 Concrete mixes

Components (for 1 m ³)	Non-reactive mix	Reactive mix
Non-reactive sand [0-2 mm]	680 kg/m ³	
Reactive sand [0-4mm]	/	672 kg/m ³
Non-reactive aggregates [4-12.5 mm]	1041 kg/m ³	/
Reactive aggregates [4-6 mm]	/	190 kg/m ³
Reactive aggregates [4-12.5 mm]	/	843 kg/m ³
Cement	410 kg/m ³	
Effective water/Cement ratio	0.46	

2.4 Exposure and loading conditions

The exposure conditions were the same for both concrete samples. These thermo-hydric conditions changed with time as follows: from the day after mixing, they were stored at 20°C in autogenous conditions for 28 days. After this curing, the specimens were immersed in a 1M hydroxide solution kept in barrels to avoid the leaching of alkalis. This was in accordance with previous experiments [13], and stored at 38°C to accelerate the reaction. Once a swelling of about 0.04% was reached for the reactive concrete mix, all the specimens were taken out of the solution and immediately sealed by aluminum foils to avoid desiccation and stored at 20°C. Once protected of desiccation, half of the samples remained free to swell while the others were uniaxially loaded at 30% of the lowest compressive strength of both mixes assessed after immersion.

2.5 Specimens and measurements

For each mix, strains were assessed on 3 unloaded specimens and on 2 loaded specimens. In parallel, 6 samples were used to characterize the mechanical properties. At each date of exposure condition change, the compressive strength and the Young's modulus were measured. All samples were cylinders with 113mm diameter and 220mm high. Longitudinal free strains of the unloaded specimens were measured using an indicator and plugs for the contact points (complied with the norm [14]) during the immersion time and after sealing. The creep tests samples were equipped with an inner LVDT sensor located in a niche centered in each specimen. This sensor allows to record the evolution of longitudinal strain during the curing period and under sustained loading.

3 Results and discussion

3.1 Designations and curve conventions

All the figures are presented with positive swelling strains while shrinkage and compressive creep strains are negative. NR is used for the non-reactive samples that are presented in blue, when R and the red curves are used for the reactive ones. The measurements system used is indicated with IS for the inner sensor and with P for the indicator and plugs system, and represented by continuous lines and dashed lines, respectively.

3.2 Autogenous shrinkage during curing

The strains due to autogenous shrinkage measured on two samples for each concrete using the inner sensors are presented in figure 1. After 28 days, a shrinkage strain of $178 \pm 3 \mu\text{m/m}$ was observed for the non-reactive concrete and $206 \pm 28 \mu\text{m/m}$ for the reactive one. This shrinkage measured at the end of the curing with the external sensor (corresponding to the mean value of three measurements) was $124 \pm 13 \mu\text{m/m}$ for the non-reactive concrete and $137 \pm 5 \mu\text{m/m}$ for the reactive one. The autogenous shrinkage is relatively high for both concretes and may be the consequence of the high alkali content [15].

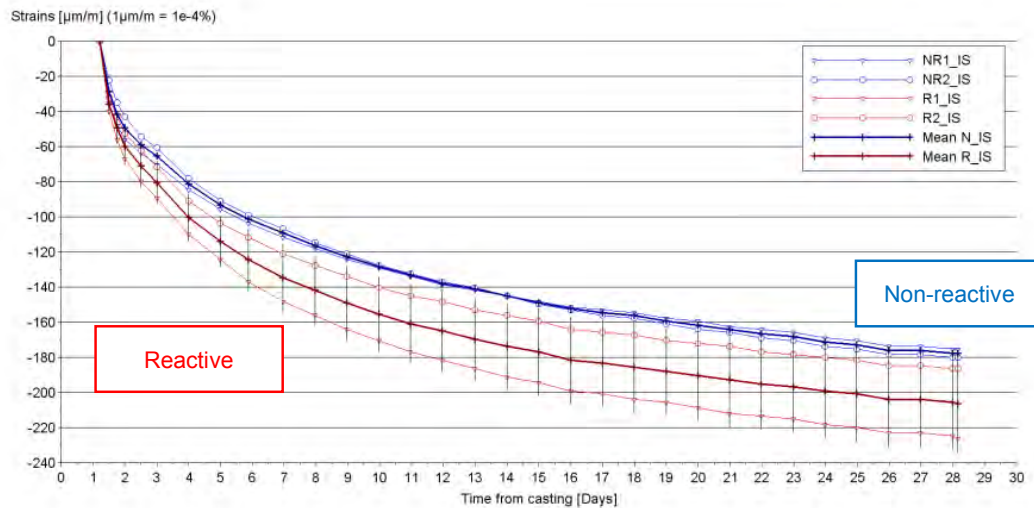


Fig 1 Autogenous shrinkage strains for reactive and non-reactive specimens during the 20°C autogenous curing (measurement by inner sensor)

3.3 Free strains and AAR expansions

The strains measured after the curing period are presented in figure 2, while figure 3 gives the strains evolution measured after samples sealing.

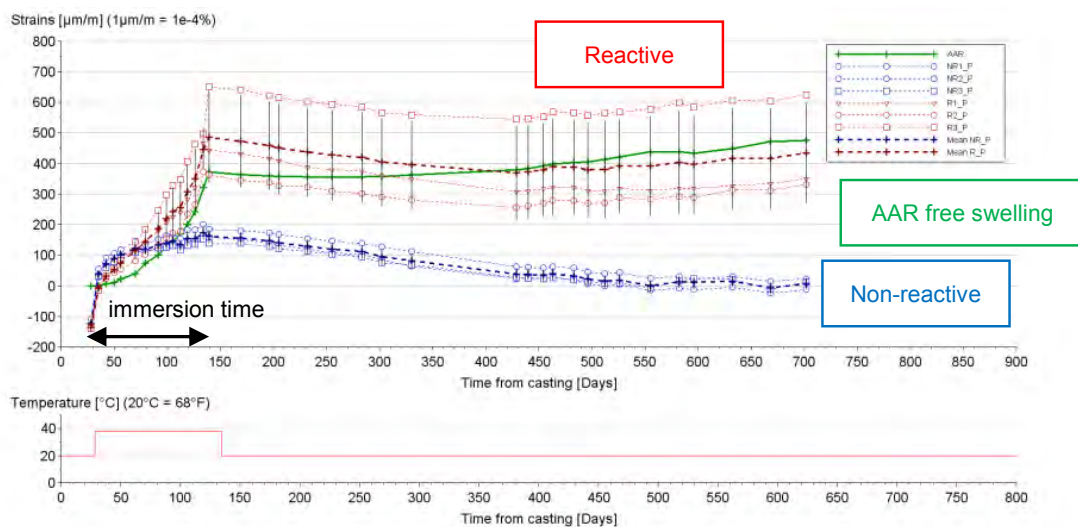


Fig 2 Evolution of the free strains of the reactive (red) and non-reactive (blue) specimens from 28 days to 700 days. (The AAR free swelling corresponding to the difference between the reactive and non-reactive concrete strain evolutions is represented by a green line)

3.3.1 Evolution in NaOH solution at 38°C

The AAR strain evolution (the green line in figure 2) corresponds to the difference between the strains of both types of concrete. This AAR strains curve begins one week after immersion to erase the strain due to the initial water absorption. At the end of the immersed period, the AAR swelling reaches a value of 0.032%. The strains directly measured on specimens were $446 \pm 64 \mu\text{m/m}$ and $173 \pm 24 \mu\text{m/m}$ for the reactive concrete and non-reactive one, respectively.

3.3.2 Free strains in autogenous conditions

At the beginning of the sealed condition period at 20°C, AAR is strongly slowed down and is maintained at a value of 0.038%. But after 420 days after casting, i.e. 300 days in autogenous condition, the kinetic increases again and reaches 0.048% at 700 days. Along with this slow AAR swelling rate, a shrinkage strain evolution was observed for both concrete types (figure 3).

The reduction in swelling rate can be attributed to the temperature decrease (from 38°C to 20°C) as previously observed in [2] - [16]. The change of moisture conditions also contributes to reduce the swelling rate. Nevertheless, the observed AAR swelling evolution with the increase of kinetic after 300 days in autogenous condition at 20°C confirms that this thermo-hydric condition is sufficient to allow the reaction development [17].

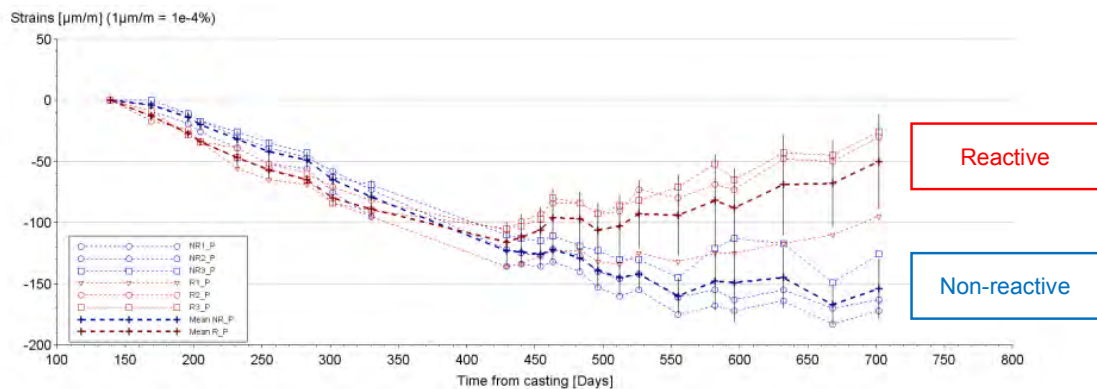


Fig 3 Evolution of free strains from the beginning of the autogenous stage

3.4 Evolution of mechanical properties

At each thermo-hydric condition change, the mechanical properties of both concretes were measured. The results before and after immersion at 35 days and 136 days, respectively, are presented in table 3.

Table 3 Mechanical properties before and after immersion time

Concrete Mix	Non-reactive	Reactive	Relative difference
Compressive Strength			
35 days	$45.3 \pm 1.2 \text{ MPa}$	$51.1 \pm 0.6 \text{ MPa}$	12.8 %
136 days	$56.2 \pm 1.0 \text{ MPa}$	$59.2 \pm 0.9 \text{ MPa}$	4.70 %
Evolution	+ 19.9 %	+13.7 %	/
Young's modulus			
35 days	$39.2 \pm 0.6 \text{ GPa}$	$37.3 \pm 0.4 \text{ GPa}$	4.79 %
136 days	$41.7 \pm 0.2 \text{ GPa}$	$36.1 \pm 0.4 \text{ GPa}$	13.4 %
Evolution	+ 6.01 %	- 3.36 %	/

The aim of the measurements at 35 days in autogenous condition at 20°C after casting was to compare the mechanical performance of both concretes before the beginning of the swelling. The compressive strength of the reactive concrete is slightly higher than the non-reactive one (difference of 12.8%), whereas it is the opposite for the Young's modulus results (difference of 4.79%).

At the end of the immersion period, i.e. 136 days, the AAR swelling reached 0.032%. The compressive strength of both concretes continues to grow but the increase is stronger for the non-reactive concrete (20% compared to 14% so a difference of 4.70%) showing that AAR certainly also affects this mechanical characteristic. The difference between the Young's modulus of both concretes reaches 13.4%. The Young's modulus of the non-reactive concrete increases due to cement hydration while the one of the concrete affected by AAR decreased by 3.36%. This reduction of mechanical properties during AAR agrees with previous observations [2]–[8] and is generally explained by micro-crackings in the cement paste and in the reactive aggregates.

3.5 Time-dependent strains under a uniaxial compressive load

The strains measured during the creep tests are presented in figure 6. These strains, assessed by inner sensors, are plotted with the free strains curves already analyzed in figure 4, and provide an overview of both tests conditions.

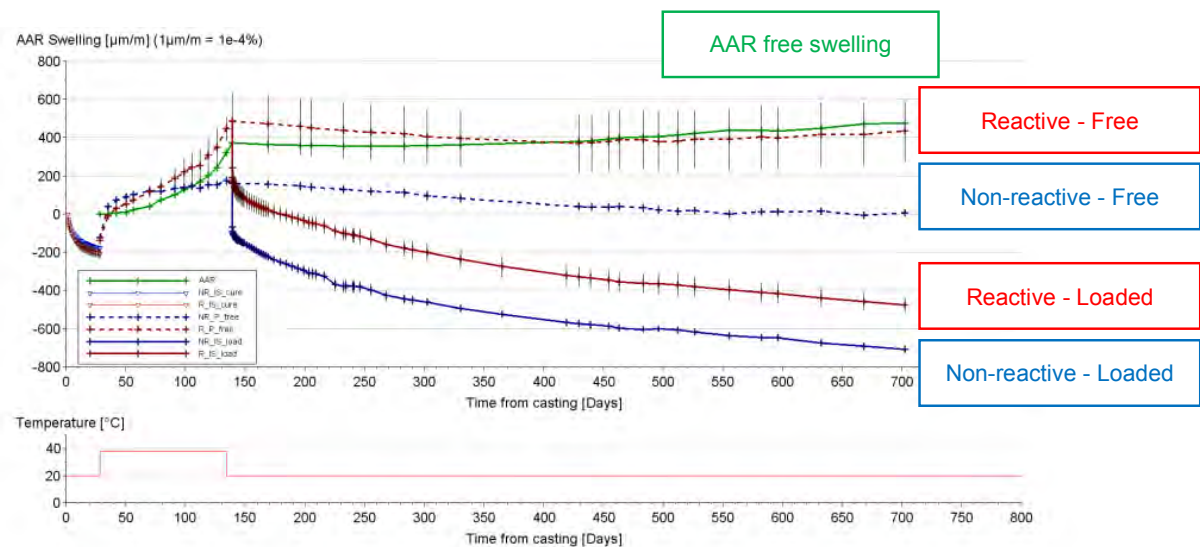


Fig 4 Total axial strains for both test conditions

3.5.1 Loading and elastic strains

A uniaxial compressive stress of 17 MPa was applied to all specimens. This value corresponds to 30% of the lowest compressive strength assessed the day of the loading (i.e. 56.2 MPa measured on the non-reactive concrete at 135 days (table 3)).

The elastic strains were 243 $\mu\text{m/m}$ and 228 $\mu\text{m/m}$ for the reactive and non-reactive concretes, respectively.

3.5.2 Strains under loading

As shown in figure 4, even after 570 days of creep, the total strain under loading of the reactive concrete, loaded after a free swelling period, was still 232 $\mu\text{m/m}$ higher than the non-reactive one. Before loading, this difference was equal to 320 $\mu\text{m/m}$. Thus, the compressive loading reduced the AAR free swelling by 25%.

This reduction is the consequence of two phenomena. Firstly, the instantaneous elastic strain of the reactive concrete is higher than the non-reactive one, due to the damage induced by the previous free swelling. Secondly, during the first 15 days after loading, the creep rate was superior in the reactive concrete.

Afterwards, both creep evolutions were quite similar, even when the AAR kinetic increased as observed on free strains samples, at the date corresponding to 300 days from loading.

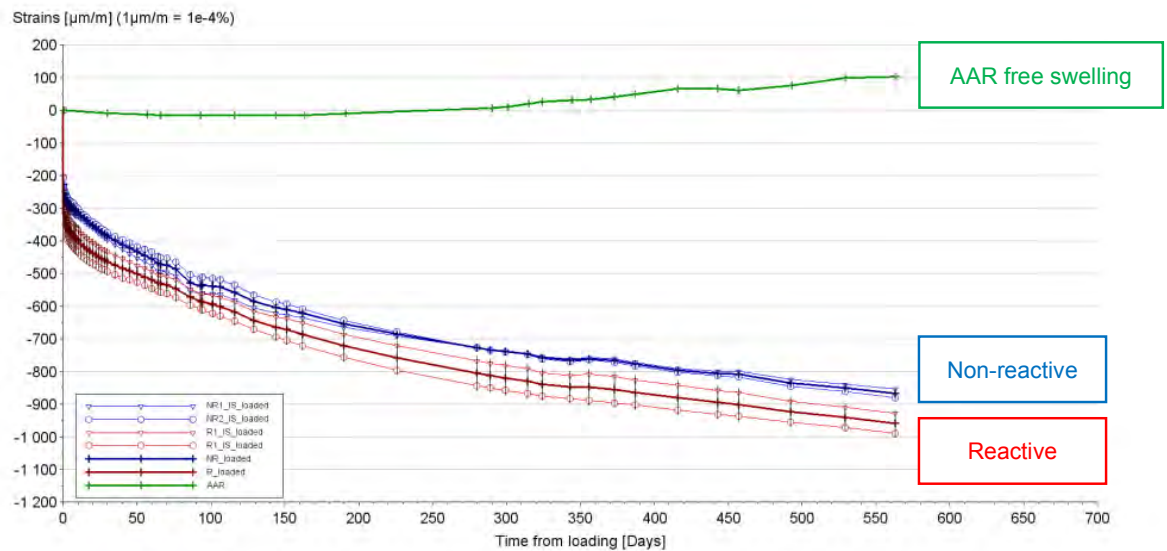


Fig 5 Strains under loading and AAR free swelling during the same period

The same observations were reported by Reinhardt et al [8] on concretes with different free swellings. After two weeks under stress and despite the reaction was already stopped in these tests, the creep velocities were similar whatever the AAR amplitude.

For the tests results detailed in the present paper, a compressive stress corresponding to 30% of the compressive strength provokes a swelling reduction of 25%. This reduction occurs during loading and in the first two weeks after loading. Beyond this period, the creep rate reaches a same level than for the non-reactive concrete, despite the AAR restarts.

4 Conclusions and modelling prospects

The quantification of the interactions between creep and AAR swelling has been done thanks to an experimental comparative study of a reactive concrete and a non-reactive one with similar initial mechanical performances.

This research work shows clearly that a compressive stress corresponding to 30% of the concrete compressive strength can reduce by 25% the free swelling occurred before the loading. A third of this absorption is the result of a high creep rate during the first two weeks of loading. The other part is due to the elastic behaviour of the damaged concrete. Even if the reaction continues, the creep rate remains the same for the concrete affected by AAR than for the non-reactive one.

These results will be considered to set up a structural model under development at LMDC Toulouse. The collaboration with Tractebel-Engie company aims to consider the local behaviour of cement paste around reactive aggregates in this model. This will be done via a micromechanics-based formulation that will consider cement paste creep and partial reclosing of AAR micro-cracks.

Acknowledgment

This work was carried out at LMDC Toulouse in collaboration with and with support from Tractebel-Engie company.

References

- [1] S. Diamond. 1975. "A review of alkali-silica reaction and expansion mechanisms." *Cement and Concrete Research* 5:329-346.
- [2] Larive C. 1997. "Apports combinés de l'expérimentation et de la modélisation à la compréhension de l'alcali-réaction et de ses effets mécaniques." PhD, Ecole Nationale des Ponts et Chaussées.
- [3] Multon S. 2003. "Evaluation expérimentale et théorique des effets mécaniques de l'alcali-réaction sur des structures modèles." PhD, Ecole Nationale des Ponts et Chaussées.
- [4] Charlwood R. G. 1994. "A review of alkali aggregate reaction in hydro plants and dams." *Hydropower and Dams* 1:73-80.
- [5] Esposito R. and Hendriks M. A. N. 2019. "Literature review of modelling approaches for ASR in concrete: a new perspective." *European Journal of Environmental and Civil Engineering* 23:1311-1331.
- [6] Grimal E., Sellier A., Le Pape Y. and Bourdarot E. 2008. "Creep, Shrinkage, and Anisotropic Damage in Alkali-Aggregate Reaction Swelling Mechanism—Part I: A Constitutive Model." *ACI Materials Journal* 105:227-235.
- [7] Dunant C. F. and Scrivener K. L. 2010. "Micro-mechanical modelling of alkali-silica-reaction-induced degradation using the AMIE framework." *Cement and Concrete Research* 51:525-40.
- [8] Reinhardt H. W., Özkan H. and Mielich O. 2019. "Creep of concrete as influenced by the rate of expansion due to alkali-silica reaction," *Structural Concrete* 20:1781-1791-.
- [9] LCPC. 1994. *Recommandations pour la prévention des désordres dus à l'alcali-réaction*.
- [10] NF P18-412. 1981. *Bétons - Caractéristiques particulières des machines hydrauliques pour essais de compression (presses pour matériaux durs)*. AFNOR.
- [11] RILEM. *Recommandations RILEM CPC8. Modulus of elasticity of concrete in compression, Materials and Structures*.
- [12] Makani A. 2011. "Influence de la nature minéralogique des granulats sur le comportement mécanique différé des bétons." PhD, INSA de Toulouse.
- [13] Rivard P., Bérubé M. A., Ollivier J. P. and Balliby G. 2007. "Decrease of pore solution alkalinity in concrete tested for alkali-silica reaction." *Materials and Structures* 40:909-921.
- [14] NF P18-594. 1978. *Granulats - Méthodes d'essai de réactivité aux alcalis*. AFNOR.
- [15] Jawed I. and Skalny J. 1978. "Effects of Alkalies on Hydration and Performance of Portland Cement." *Cement and Concrete Research* 37:52-8.
- [16] Diamond S., Barneyback Jr R. S., and Struble L. J. 1981. "On the physics and chemistry of alkali-silica reactions." Conference on Alkali-Aggregate Reactions in Concrete, Cape Town, South Africa.
- [17] Poyet S. 2003. "Etude de la dégradation des ouvrages en béton atteints par la réaction alcali-silice." PhD, Université de Marne-La-Vallée.

Sustainability and life cycle assessment

Geopolymer concrete structures: mechanical properties and bond with steel and GFRP bars

V. Romanazzi, M. Leone

*Department of Innovations Engineering,
University of Salento,
Via per Monteroni, Lecce (73100), Italy*

Abstract

The high mechanical performances showed by geopolymer concrete led several researchers to investigate about possibilities of using this material in reinforced structural elements. Since geopolymer binder has a different microstructure from ordinary Portland Cement (OPC) it is necessary to investigate on its bonding behavior with steel bar that as well-known influences the service and ultimate conditions. For this reason, in the last decades both direct pull-out and beam-end tests were carried out with this material. Generally, it has been observed that geopolymer concrete (GPC) has higher bond strength than OPC due to the higher compression strength and the dense and compact microstructure of GPC. This means that the existing design equation for bond strength prediction of ordinary concrete can be conservatively used also for GPC. In this paper the mechanical properties of GPC will be analyzed in terms of compressive strength and constitutive behavior. Moreover, the bond-slip behavior of GPC with deformed steel and GFRP bar has been studied. The results showed that GPC is more brittle than OPC concrete despite its high compressive strength. On the other hand, as in case of OPC concrete, also GPC bonding behavior is better with steel bars than GFRP bars.

1 Introduction

The high quantity of CO₂ released during Portland cement production process led to the search for alternative materials to be used as binder in concrete. In this context, geopolymers proved to have good potential. In fact, numerous studies demonstrated the good bonding properties of these material, combined with the possibilities to reach high mechanical properties [1]–[4]. Moreover, several authors observed that bond strength of geopolymer concrete (GPC) with deformed steel bar is higher than ordinary Portland cement (OPC) concrete [5]–[8]. On the other hand, GPC showed a similar behavior to OPC concrete in bond with glass fiber reinforced polymer (GFRP) bar [9].

In this paper compressive strength, constitutive behavior and the bond slip of GPC with both steel and sand-coated GFRP reinforcing bar are investigated. The concrete mix used in this work is cement-free and it is composed by only industrial by-products as ground granulated blast furnace slag (GGBFS) and silica fume. The results of compressive tests showed a significant increase in compressive strength also beyond 28 days of curing and a brittle nature of the material. Finally, from pull-out tests on GPC it has been observed the better bonding behavior with deformed steel bar in respect to the straight GFRP bars.

2 Materials

2.1 Mix design

The experimental campaign shown in this work is part of a larger project that has the objective to develop alternative construction materials by replacing Portland cement with industry by-product in concrete and mortar production. The GPC mix used in this work is summarized in Table 1. The aggregates were natural calcium carbonate type in two different sizes. The binder developed consists of an optimized combination of: GGBFS (by-product of iron and steel making industry); silica fume (by-product of silicon and ferrosilicon alloy industry) and filler powder composed by limestone and gypsum.

Table 1 Geopolymer concrete mix

Components	Quantity (kg/m ³)
GGBFS	224
Filler (limestone and gypsum)	128
Silica Fume	48
Activator Solution	170
Water	140
Additive (Plasticizer)	8
Sand (0-4 mm)	1092
Gravel (8-16 mm)	471

2.2 Tests setup

2.2.1 Compressive tests

Uniaxial compressive tests were performed at different age of curing on a total of 36 cubic specimens with 150 mm size, according to the european standard UNI EN 12390-3 [10] as showed in Fig. 1 (left). All cubic GPC specimens to be tested under compressive load has been cured at ambient temperature 20°C. Moreover, five cylindrical specimens (150 mm diameter and 300 mm height) were subjected to compressive test under displacement control by imposing a constant velocity to the stroke equal to 0.03 mm/min. This tests allowed to evaluate the complete constitutive behavior of the GPC mix. The axial displacements of the cylindrical specimen were measured by means of two LVDTs (Linear Variable Displacement Transducers) positioned on opposite points of the cylinder lateral face as shown in Fig. 1 (right).

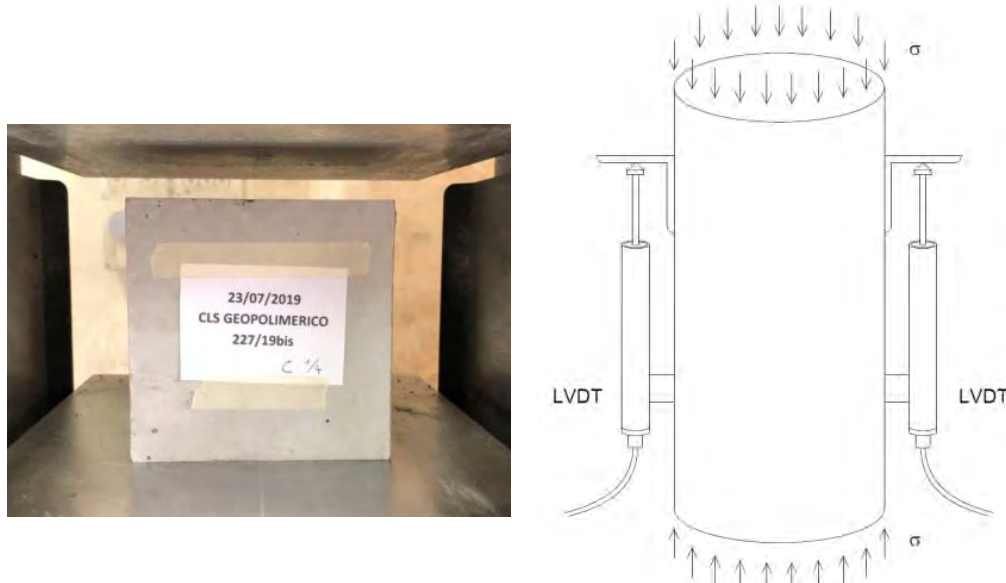


Fig. 1 Cubic specimen for compressive strength test (left) and constitutive law test setup (right)

2.2.2 Pull-out test

Direct pull-out tests with steel and GFRP bars were performed according to the RILEM Recommendations [11]. A total of 24 pull-out samples were casted and tested, of which 4 with steel bar and 5 with GFRP bar (Fig. 2). Both steel and GFRP bars had a total length of 500 mm and diameter equal to 12 mm and, only for steel bar, 16mm. The steel bars were made of a grade B450C steel, meanwhile sand coated GFRP bars were made of chemically resistant glass fiber and polyester thermosetting resin with a declared nominal strength equal to 800MPa.

The pull-out specimens were composed by a GPC matrix cube with dimension 10ϕ and a centered embedded bar such that the concrete cover resulted 4.5ϕ . The bonded zone, L_b , was imposed equal to 5ϕ and 2.5ϕ by applying a plastic sheet on the bar.

The relative slip between the bar and GPC cubic matrix was measured by means of a LVDT positioned on the unloaded side of the bar and can be seen from Fig. 2. The other two LVDTs, positioned on the loaded side, were used to measure the same slip but with the addition of bar deformation.



Fig. 2 Pull-out test setup of specimens with a) deformed steel bar; b) GFRP bar

3 Results

3.1 Compression strength

The compressive strength results are resumed in Table 2. From the obtained results, it can be seen that the GPC mix developed high early compressive strength, reached an average value equal to 52.6 MPa after 28 days of curing and increased up to 82.8 MPa at 106 days of curing. The increase of compressive strength after 28 days of curing turns out to be significant as also observed by [12]. In particular, they explain this phenomenon as the effect of GGBFS presence.

In Fig. 3 it is reported the graph of compressive strength vs. time of curing of GPC and the theoretical model suggested by Eurocode 2 [13] regarding a OPC concrete with the same compressive strength at 28 days of curing. The two curves overlap in the first phase, until 28 days of curing, then the compressive strength of GPC increases faster than that one predicted by Eurocode 2 for OPC concretes.

Table 2 Compressive strength results of GPC at different age of curing

t [days]	R_c [MPa]	CoV
2	29.0	5.7%
7	52.7	5.0%
14	53.1	5.5%
28	52.6	17.0%
58	68.7*	-
106	82.8*	-

*average of two compressive test results

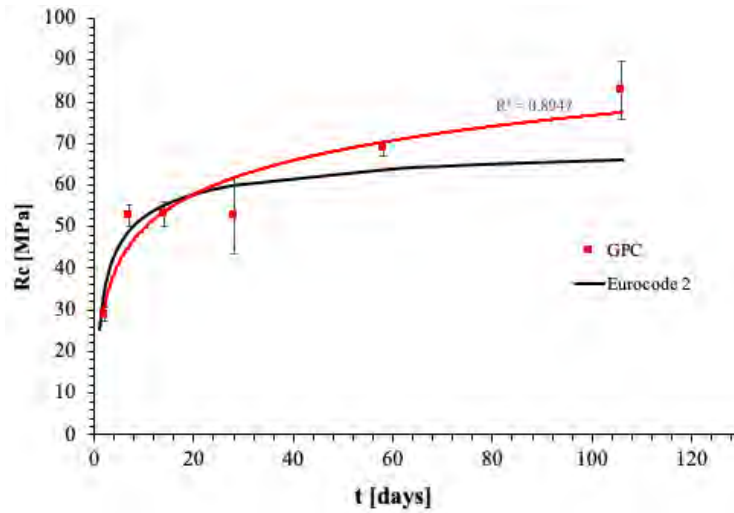


Fig. 3 Evolution of GPC compressive strength

3.2 Stress-strain analysis

Constitutive behaviour parameters have been reported in Table 3. In particular, the cylindrical compressive strength and the ultimate strain values, assumed as the strain corresponding to a 10% stress decay from f_c , are listed. The average value of compressive strength resulted to be 28.5 MPa with a coefficient of variation 7%, while the average ultimate strain was equal to 1.9‰.

As well known, the design value of ultimate strain of OPC concrete is equal to 3.5‰ [14], that is 46% higher than the experimental value obtained with GPC in this work. This confirms the brittle nature of this material, as also observed in the failure stage of these tests (Fig. 4) [15].

Table 3 Constitutive behaviour parameters

Specimen	f_c [MPa]	$f_{c,av}$ [MPa]	ε_u [-]	$\varepsilon_{u,av}$ [-]
GPC_CL_1	28.5	28.5 (7%)	-	0.0019
GPC_CL_2	29.3		0.0018	
GPC_CL_3	27.5		0.0019	
GPC_CL_4	31.5		-	
GPC_CL_5	25.8		0.0029*	

*not considered since largely different in respect to other results

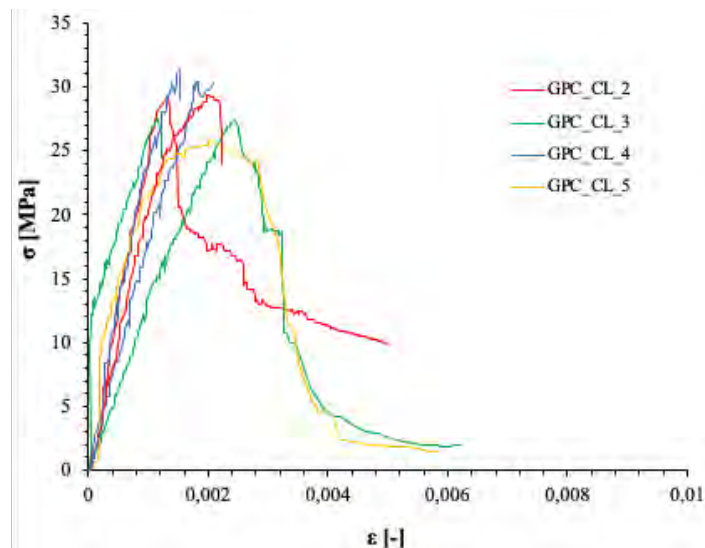


Fig. 4 Cylindrical specimen after failure after compressive strength tests (left) and stress-strain curves of GPC (right)

3.3 Bond-slip behavior of GPC with steel and GFRP bar

Pull-out test results of GPC with both steel and GFRP bars with bond length 5ϕ are shown in Table 4 and Fig. 5 (left). In case of deformed steel bars, apart from specimen GPC_P_12_2, the common mode of failure was concrete splitting. On the other hand, only pull-out failure occurred between GPC and GFRP bars.

Since the three groups of samples (12mm and 16mm steel and GFRP) were tested at different age of curing, bond strength values has been adjusted according to [16] aims to avoid the compressive concrete strength influence.

From $\tau_{b,max,adj,av}$ values in Table 4 and graph Fig. 5 it comes out that the bond strength of GPC with $\phi 12\text{mm}$ steel bar is slightly higher than in case of $\phi 16\text{mm}$ bar. Moreover, it can be seen that deformed steel bar showed significantly higher bond capacity in respect of GFRP bar. This large difference may be attributed to the fact that deformed steel bars surface was characterized with ribs that improve bond with concrete, meanwhile GFRP bars were straight with sand-coating. For this reason, in the first case bond strength benefited from the mechanical interlocking phenomenon. Same observation has been reported in Aiello et al [17].

Table 4 Pull-out test results with bond length equal to 5ϕ

Specimen	Sample	Failure mode	$\tau_{b,max,adj}$ [MPa]	$\tau_{b,max,adj,av}$ [MPa]
Steel $\phi 12\text{mm}$	GPC_P_12_1	-	-	25.5 (3%)
	GPC_P_12_2	P	26.2	
	GPC_P_12_3	S	24.9	
	GPC_P_12_4	S	25.4	
Steel $\phi 16\text{mm}$	GPC_P_12_1	-	-	22.0 (3%)
	GPC_P_12_2	S	21.0	
	GPC_P_12_3	S	22.5	
	GPC_P_12_4	S	22.0	
	GPC_P_12_5	S	22.7	
GFRP $\phi 12\text{mm}$	GPC_GP_12_1	P	10.6	9.7 (14%)
	GPC_GP_12_2	P	7.7	
	GPC_GP_12_3	P	9.5	
	GPC_GP_12_4	P	9.4	
	GPC_GP_12_5	P	11.4	

P = bar pull-out failure

S = concrete splitting failure

On the other hand, pull-out tests results in case of bond length equal to 2.5ϕ are reported in Table 5 and Fig. 5 (right). Differently from the tests previously shown, only specimen GPC_S2.5_4 exhibited concrete splitting failure.

As can be seen in Fig. 5 (right) the shorter bond length allowed to obtain the descending branch and the following plateau of the bond-slip curves of GPC with steel bar. The bond strength of GPC with deformed steel bar was higher than with GFRP bar.

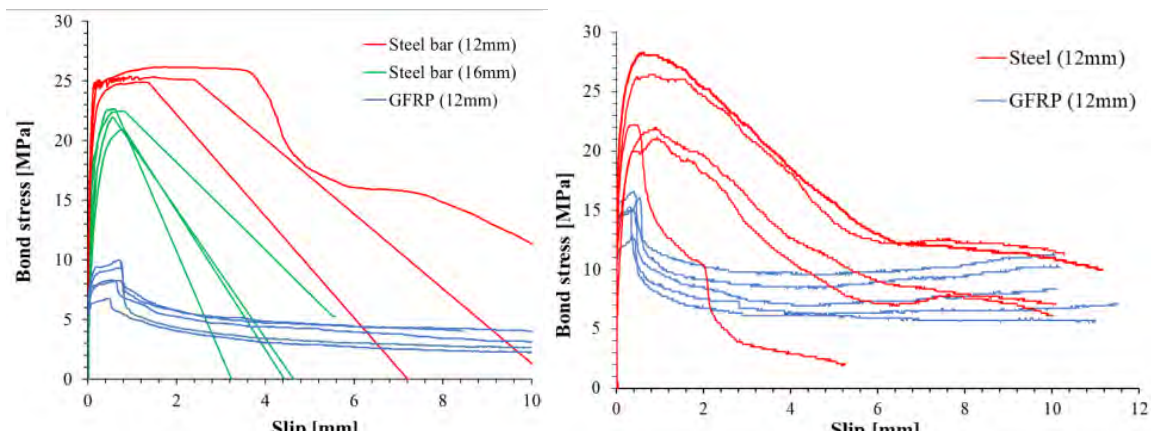
In respect to the pull-out tests results with 5ϕ bond length, $\tau_{b,max,adj,av}$ of GPC with steel bar are slightly lower, whereas in case of GFRP bar $\tau_{b,max,adj,av}$ is higher when the bond length is halved.

Table 5 Pull-out test results with bond length equal to 2.5ϕ

Specimen	Sample	Failure mode	$\tau_{b,max,adj}$ [MPa]	$\tau_{b,max,adj,av}$ [MPa]
Steel $\phi 12\text{mm}$	GPC_S2.5_1	P	23.9	24.5 (11%)
	GPC_S2.5_2	P	28.3	
	GPC_S2.5_3	P	21.9	
	GPC_S2.5_4	S	22.2	
	GPC_S2.5_5	P	26.4	
GFRP $\phi 12\text{mm}$	GPC_G2.5_1	P	15.1	15.1 (10%)
	GPC_G2.5_2	P	16.6	
	GPC_G2.5_3	P	16.1	
	GPC_G2.5_4	P	15.3	
	GPC_G2.5_5	P	12.6	

P = bar pull-out failure

S = concrete splitting failure

Fig. 5 Bond-behavior curves of GPC with deformed steel and GFRP bars with bond length equal to 5ϕ (left) and 2.5ϕ (right)

4 Conclusion

The experimental activity illustrated in this work deals with some properties of GPC. In particular, compressive strength, constitutive law and bond behavior with steel and GFRP bars have been reported as a part of a wider study that includes tests on both material and structural elements.

Based on the results, the GPC mix shown herein encourages to deepen the analysis regarding both the compressive strength and the bond behavior. In fact, the mixture was able to reach high compressive strength combined with the outstanding capacity to increase until 100 days of curing, at least. It will be interesting to perform a specific analysis about this aspect in order to define a new compressive strength evolution model prevision for GPC in function of GGBFS quantity. Moreover, results of pull-out tests with deformed steel and GFRP bars underlined a comparable behavior to OPC concrete.

These results promoting the idea to use this cement-free concrete for structural applications. For this reason, are actually in progress tests on reinforced GPC beam elements designed to exhibit bending or shear failure. The obtained data will be involved in a numerical analysis that provides a rapid and economic tool to study the incidence of the most relevant variables on GPC structural behaviour. Moreover, durability should be investigated in terms for example of water permability and resistance to sulfate attack.

Acknowledgements

This research was carried out in the framework of the Regional Project CIRCE “seCondary raw materials foR a circular Economy in buildings” funded by INNONETWORK 2017 | Sostegno alle attività

di R&S per lo sviluppo di nuove tecnologie sostenibili, di nuovi prodotti e servizi of Puglia Region (Codice Prog S0GS1T3).

References

- [1] B. Singh, G. Ishwarya, M. Gupta, and S. K. Bhattacharyya, "Geopolymer concrete: A review of some recent developments," *Constr. Build. Mater.*, vol. 85, pp. 78–90, 2015, doi: 10.1016/j.conbuildmat.2015.03.036.
- [2] K. H. Mo, U. J. Alengaram, and M. Z. Jumaat, "Structural performance of reinforced geopolymer concrete members: A review," *Constr. Build. Mater.*, vol. 120, pp. 251–264, 2016, doi: 10.1016/j.conbuildmat.2016.05.088.
- [3] Y. Ding, J. G. Dai, and C. J. Shi, "Mechanical properties of alkali-activated concrete: A state-of-the-art review," *Constr. Build. Mater.*, vol. 127, pp. 68–79, 2016, doi: 10.1016/j.conbuildmat.2016.09.121.
- [4] C. K. Ma, A. Z. Awang, and W. Omar, "Structural and material performance of geopolymer concrete: A review," *Constr. Build. Mater.*, vol. 186, pp. 90–102, 2018, doi: 10.1016/j.conbuildmat.2018.07.111.
- [5] P. Sarker, "Bond Strengths of Geopolymer and Cement Concretes," *Adv. Sci. Technol.*, vol. 69, pp. 143–151, 2010, doi: 10.4028/www.scientific.net/ast.69.143.
- [6] A. Fernández-Jiménez and A. Palomo, "Engineering Properties of Compacted Fly Ash," *Aci Mater. J.*, no. March 2006, 2006.
- [7] A. Castel and S. J. Foster, "Bond strength between blended slag and Class F fly ash geopolymer concrete with steel reinforcement," *Cem. Concr. Res.*, vol. 72, pp. 48–53, 2015, doi: 10.1016/j.cemconres.2015.02.016.
- [8] M. Al-Azzawi, T. Yu, and M. N. S. Hadi, "Factors Affecting the Bond Strength Between the Fly Ash-based Geopolymer Concrete and Steel Reinforcement," *Structures*, vol. 14, no. January, pp. 262–272, 2018, doi: 10.1016/j.istruc.2018.03.010.
- [9] B. H. Tekle, Y. Cui, and A. Khennane, "Bond properties of steel and sand-coated GFRP bars in Alkali activated cement concrete," *Struct. Eng. Mech.*, vol. 75, no. 1, pp. 123–131, 2020, doi: 10.12989/sem.2020.75.1.123.
- [10] UNI EN 12390-3, "Testing hardened concrete - Part 3: Compressive strength of test specimens." pp. 4–10, 2001.
- [11] RILEM TC, *RC 6 Bond test for reinforcement steel. 2. Pull-out test.* 1983.
- [12] P. S. Deb, P. Nath, and P. K. Sarker, "The effects of ground granulated blast-furnace slag blending with fly ash and activator content on the workability and strength properties of geopolymer concrete cured at ambient temperature," *Mater. Des.*, 2014, doi: 10.1016/j.matdes.2014.05.001.
- [13] EN 1992-1-1, "Eurocode 2: Design of concrete structures - Part 1-1 : General rules and rules for buildings," 2004.
- [14] CEB-FIP, *Fib Model Code for Concrete Structures.* 2010.
- [15] A. Attanasio *et al.*, "Secondary Raw Materials for a Circular Economy in Concretes [submitted]," *Ital. Concr. Days - Napoli*, 2021.
- [16] V. Romanazzi, M. Leone, M. A. Aiello, G. Maddaloni, and M. Pecce, "Bond strength of geopolymer concrete with steel and GFRP bars [submitted]," *Ital. Concr. Days - Napoli*, 2021.
- [17] M. A. Aiello, M. Leone, and M. Pecce, "Bond Performances of FRP Rebars-Reinforced Concrete," *J. Mater. Civ. Eng.*, vol. 19, pp. 205–213, 2007, doi: 10.1061/(ASCE)0899-1561(2007)19.

Bond stress distribution of ribbed steel bars in reinforced concrete with short bond length under various loading conditions

Marc Koschemann, Manfred Curbach

*Institute of Concrete Structures,
Technische Universität Dresden,
August-Bebel-Straße 30/30a, 01219 Dresden, Germany*

Abstract

In the course of bond research of reinforced concrete for the past decades, the pull-out test with a bond length l_b of 5 times the bar diameter d_s established as the standard to investigate the local bond behaviour. Despite the known disadvantages of this test setup, results of pull-out tests build the basis for bond stress-slip relationships like the approach of *fib* Model Code 2010 [1]. Current investigation at the Technische Universität Dresden focus on the bond behaviour and the bond stress distribution for ribbed bars with short and very short bond lengths under various loading conditions. The investigations include different types of specimens and the targeted use of fibre-optic measuring technology.

1 Introduction

The success story of reinforced concrete is based on the targeted exploitation of the material properties of concrete under compression and of reinforcing steel under tensile stress. The interaction between concrete and steel reinforcement, known as bond, is essential for reinforced concrete. In separation and bending cracks, the reinforcement transmits tensile forces by itself, but to both sides of the crack these forces are reintroduced into the concrete due to the bond action. Thus crack widths and crack spacings are decisively dependent on the bond behaviour. In addition, the bond action influences the constructions stiffness at the cracked state and the resulting load-deformation behavior of a reinforced concrete (RC) element.

In the course of bond research on reinforced concrete over the past 100 years, it can be assumed that more than 30 parameters influence the bond behaviour [2]. Besides the material properties of the individual components and the loading conditions, the configuration of the test setup and especially the bond length in the specimen have a significant influence on experimental results. In this article the experimental and instrumental setup, test results and the procedure of evaluation are shown. Furthermore, the questions of a suitable bond test and what local bond behaviour means are discussed.

2 Bond behaviour in experimental tests

2.1 Bond tests and bond stress distribution

The suitability of test setups for investigating bond behaviour has been the subject of controversial discussion since the beginning of the 20th century [3]. The most used test to evaluate the bond behaviour of steel reinforcement is the pull-out test (PO) according to RILEM [4]. It is known for the comparatively simple setup and easy way of specimen production.

However, the main weaknesses of the RILEM pull-out test are the large concrete cover and the arch effect of the reacting forces (Fig 1). This effect causes a transverse pressure in the bond zone, what increases the bond resistance and subsequently leads to an overestimation of the bearing capacity. However, the load capacity increase can not be quantified by a study so far. Due to the minimum edge length of the test specimen of at least 200 mm or 10.0 times the bar diameter d_s , the minimum concrete cover is at least 90 mm, respectively $\geq 4.5 d_s$. The large concrete cover represents a high level of confinement, which is necessary to achieve the highest possible bond resistance, the so called pull-out failure.

For real structural elements, the concrete cover is usually in the range between 20 and 55 mm. Depending on the bar diameter, this normally corresponds to 1.0 to 4.0 d_s . According to Vandewalle [5], a concrete cover of 2.5 to 3.5 d_s is required to achieve a failure by bar pull-out. Therefore, the

concrete cover of most of the structural elements does not comply this criterion and the reinforcement has an insufficient level of confinement to reach the maximal bond resistance, which can be achieved by pull-out tests.

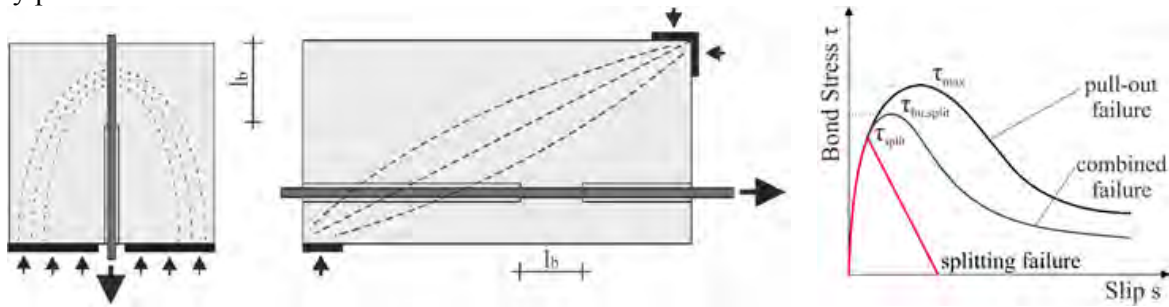


Fig. 1 Left: scheme of pull-out test; middle: scheme of beam-end test; right: modes of bond failure

The lower concrete cover leads to a change of the failure mode towards a more or less sudden splitting failure. Depending on the transverse reinforcement, both failure modes appear in combination (Fig. 1 right), which may be defined as “splitting-induced pull-out failure”. Anyway, an insufficient level of confinement leads to a premature failure and a reduction of the bond resistance. Hence, the pull-out test does not accurately represent stress states and the boundary conditions of bond zones of real RC elements. However, the pull-out test is suitable for testing the influence of individual material parameters such as concrete strength and rib geometry. In contrast, test configurations such as the beam test and the beam-end test (BE) represent the bond conditions of real RC components in a better way (Fig. 1 middle). The force flow within the specimen does not cause any transverse stresses in the bond zone and the concrete cover is adjustable. However, the associated guidelines and standards specify a bond length of $10 d_s$ instead of $5 d_s$ in the pull-out test [4], [6]. The comparison of results of bond tests with differently specified specimen types therefore includes the influence of different bond lengths [7].

$$\tau = \frac{F}{A_b} = \frac{\sigma_s \cdot d_s}{4 \cdot l_b} \quad (1)$$

As early as 1905, Bach [8] determined the decrease in the length-related bond resistance τ (1) with increasing bond length on the basis of tests with plain steel bars. Bach saw the cause of this behaviour in the elasticity of the pull-out bar. As the tensile force decreases, the strain along the embedded bar also decreases. The assumption of a uniform distribution of the bond stress along the bond length is therefore not applicable for longer bond lengths. Mörsch [9] found a plausible explanation for this phenomenon. Fig.2 left shows the tension stress σ_s of the bar and the bond stress distribution along the bond length for different load stages. The local bond stress maximum shifts from the loaded to the unloaded end of the bond length as further the load reaches the bond resistance of the embedded bar. Close to the load limit (Stage III), the load is mainly transmitted by the rear part of the bond length. Areas closer to the loaded end are already damaged, but can still transfer minor load due to friction between the bar and concrete. Depending on the local slip, each point within the bond length is at a different bond stress state. Consequently, the mean value calculated under the assumption of a uniform distribution is smaller than the local maximum. Therefore the average bond stress decreases with increasing bond length.

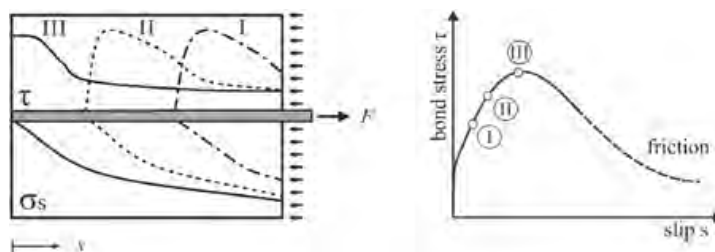


Fig. 2 Left: bond stress distributions at different loading stages according [9], taken from [2]; right: typical bond stress to slip curve

These findings were confirmed by the investigations of Mains for ribbed bars [10]. By means of strain gauges distributed along the pull-out bar of long test specimens, Mains could reveal the non-uniform distribution of bond stresses for different load levels.

2.2 What means local bond behaviour?

To describe local failure criterias of bond between reinforcement and concrete, bond tests with short bond lengths are usually carried out. According to Model Code 2010[1] it is possible to consider an average local bond to local slip relationship for short bond lengths. For the definition of a short bond length l_b the magnitude of $l_b \leq 5 d_s$ has been established in scientific practice, which is in accordance with the standard for the pull-out test by RILEM [4].

Nevertheless, the experimental results of [11] and [12], for example, indicate that the length-related bond stress continues to increase even for shorter bond lengths. Therefore, for a bond length of $5 d_s$, the bond stress is not uniformly distributed along the bar and the bond behaviour cannot be considered local. An accurate description of the local bond-slip relationship allows to derive generally valid statements about the bond behaviour of ribbed reinforcing steel in concrete for any bond length by means of theoretical approaches such as the differential equation of the sliding bond [13] eq 2. In addition to the closed solution by using special approach functions for $\tau(x)$, equation (2) can also be solved by stepwise integration. Martin [13] suggests a step size of one rib spacing for that, which corresponds to roughly $0.6 d_s$ for common rebars. On the other hand, the step size should be equal to the bond length in the experiments on which the associated local bond law is based.

$$\frac{d^2 s(x)}{dx^2} = \frac{\tau(x) \cdot u_s}{E_s \cdot A_s} - \frac{\tau(x) \cdot u_s}{E_c \cdot A_c} \quad (2) \quad \tau(x) = \tau(s(x)) \quad (3)$$

Reference [1] provides a mean bond-stress to slip relationship, where the maximum bond strength τ_{max} is defined in dependence to the square root of the mean concrete's compressive strength f_{cm} , see eq. 3. This is valid for pull-out failure under well confined concrete (concrete cover $\geq 5 d_s$).

$$\tau_{max} = 2.5 \cdot \sqrt{f_{cm}} \quad (3) \quad \tau_{max} = 0.45 \cdot f_{cm} \quad (4)$$

In contrast to this, the investigations of Huang et al. [14] revealed much higher bond stresses than expected by the bond model of MC2010[1]. Based on their results of 28 pull-out tests with a bond length of $2.5 d_s$, they introduced a linear approach to describe the maximal bond stress in case of pull-out failure for normal and high strength concrete, see eq. 4.

Local bond to slip relationships are often used to calculate crack width for different loading situations. Rohling [15], for example, calculated the increase in crack width under permanent load using the bond-oriented crack theory by Krips [16]. The input parameters for these calculations were the results of pull-out tests with a bond length of $5 d_s$. However, Rohling points out, that the quality of these calculations depends on how accurately the local bond law represents the actual conditions in the structural element. This applies in the same way for numerical investigations of bond behaviour like [17].

For few years now, fibre-optic sensing technology is offering the possibility of quasi-continuous measurement of strain values at intervals of less than one millimeter. Distributed optical fibre sensors (DOFS) have already been successfully applied in reinforced concrete for crack detection and strain measurements in concrete, [18] and [19]. Applied in bond tests, this method allows to record local and time-related changes within the bond zone. This makes it possible to record local failure criteria and define local bond stress-slip relationships.

2.3 Specifics of tests with short bond length

When carrying out tests with short bond lengths, some effects have to be taken into account, which are usually not relevant for bond lengths of $5 d_s$ and even more. In general, for short bond lengths, different arrangements and imperfections in the bond zone have a bigger impact on the results, which is mostly reflected in a larger scatter.

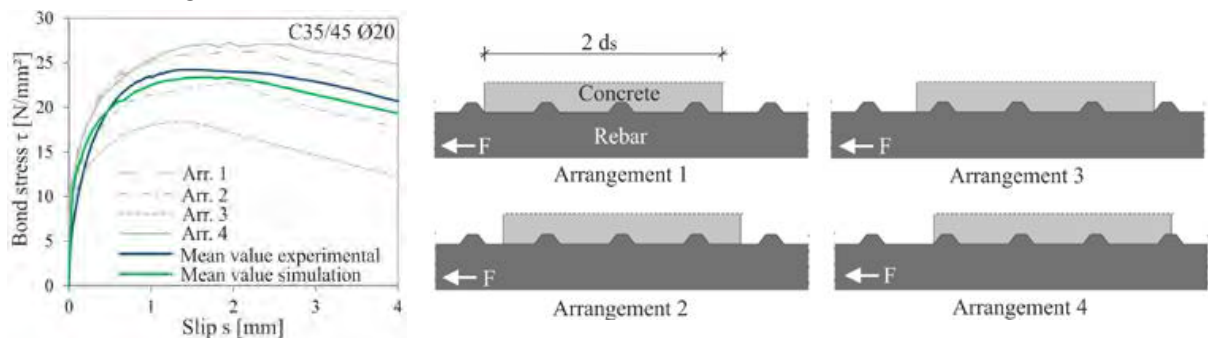


Fig. 3 Left: bond stress-slip curves for different rib arrangements [17]; right: rib arrangements

By means of numerical simulations, Zobel [17] shows that the exact position of the ribs within the bond zone have considerable influence on the results of tests with short bond lengths. Depending on the arrangement, two or three ribs are involved in the force transmission for a bond length of $2 d_s$. Therefore, the ultimate bond stress can vary up to 25% from the average (fig. 3), which covers the scatter of the experimental results from [20] well.

Another influencing factor is the diameter of the bond breaker. Usually plastic sleeves are used to define the bond length within the specimen and to ensure a free pre-length of at least $5 d_s$. However, the plastic sleeve is also an interference for the load transfer, which leads to an early cone-typed failure of the first concrete key. Zobel [17] investigated the influence of the ratio of diameters between bond breaker and bar d_b/d_s with the result, that an increase of this ratio causes a decrease in bond strength (fig. 4). As bigger the diameter of the bond breaker is, as further in reaches the failure cone and pre-damages the bonded zone. This affects the test results with very short bond lengths more than for longer bond lengths.

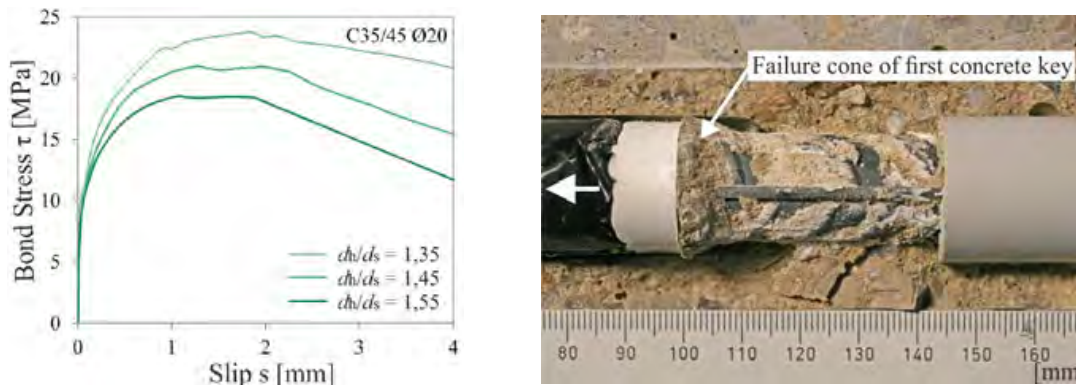


Fig. 4 Left: bond stress-slip curves for different ratios d_b/d_s [17]; right: bond zone after pull-out failure

3 Experimental methods

3.1 General

Current investigations at the Technische Universität Dresden focus on the bond behaviour and the bond stress distribution of ribbed steel bars under various loading conditions, including monotonic, cyclic and long-term loading. The investigations comprise approx. 250 individual tests, 130 carried out so far, on three specimen types and different concrete grades reaching from normal to high strength concrete.

3.2 Material properties and test program

Different kinds of concrete are used, reaching from a mean uniaxial strength of $f_{cm} = 30$ MPa up to $f_{cm} = 120$ MPa. In the test carried out so far, one normal strength concrete named C40 and two high strength concretes named C80 and C120 were used. These two are self-compacting concretes, whereas the C40 must be compacted. All kinds of concrete have a maximum grain size of 16 mm. The compressive strength and splitting tensile strength were determined on 10 cm cubes. The cylinder compressive strength was calculated with a conversion factor, which was determined in advance for each concrete using 6 standard cylinders ($d=15$ cm). Table 1 shows the properties of the concretes after a minimum test age of 56 days.

Table 1 Concrete properties

Type	$f_{c,cube100}$ [MPa]	cal. $f_{c,cyl}$ [MPa]	$f_{ct,sp,cube100}$ [MPa]	E-Modul [MPa]
C40	55.6	48.6	3.9	34000
C80	110.5	96.1	5.6	40800
C120	141.5	123.0	6.6	51900

The nominal bar diameter d_s is 16 mm in all tests and the pull-out bar is made of B500 B (yield strength $f_{yk} = 500$ MPa). The bars are provided with a pressed-on sleeve to apply the loading. The bond breakers

are plastic tubes with a diameter of $d_h = 25$ mm, what means a ratio of $d_h/d_s = 1.56$. The experimental programme includes systematic investigations of the influence of the bond length on the ultimate bond stress using pull-out tests and beam-end tests as well. The pull-out tests were configured according to [4] with a cover of 92 mm ($c = 5.75 d_s$), but with a lead length of 120 mm. The beam-end test allows different configurations of concrete cover, transverse reinforcement and supplies a more realistic stress state inside the specimen. Fig. 5 shows the configuration for a bond length of $2 d_s$ and a cover of $2 d_s$.

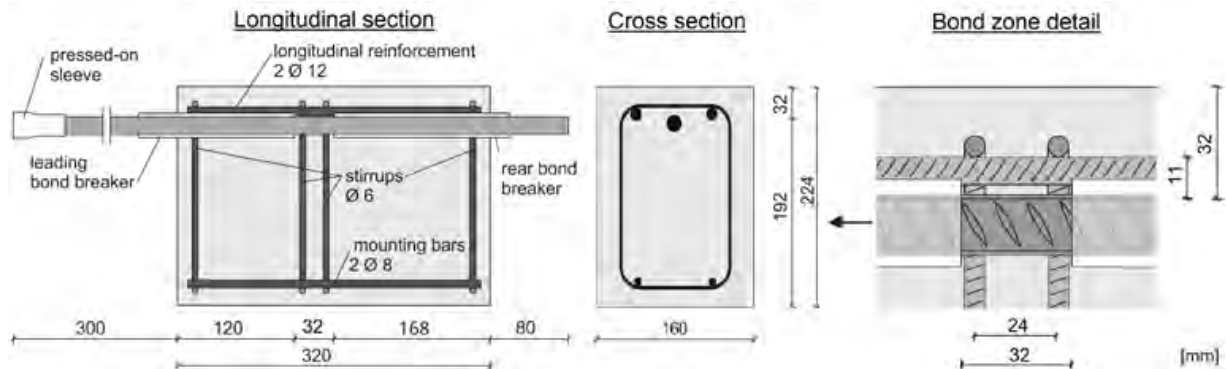


Fig. 5 Configuration of beam-end specimen

The number of ribs and their location, individually for each embedment length, as well as the number of two stirrups $\text{Ø}6$ within the bond zone were kept the same in all of the tests (Fig. 5 right). Table 2 gives an overview about the monotonic loaded tests carried out so far.

Table 2 Test programme

Concrete	Test	$c = 2.0 \text{ (BE)}/5.75 \text{ (PO)}; l_b =$					$l_b = 2.0 d_s; c =$		rotated		no stirr.	shifted	Σ
		1.0	2.0	2.5	3.0	4.0	3.0	4.0	90°	180°			
C40	BE	4	8	-	3	4	-	-	-	-	-	-	19
C80	BE	4	20	-	3	3	3	3	3	3	3	3	48
	PO	4	6	-	3	3	-	-	-	-	-	-	16
C120	BE	3	13	2	3	3	3	3	3	3	3	3	42
	PO	4	6	-	3	-	-	-	-	-	-	-	13

The different configurations are used to investigate the influence of the bond length (col. 3-7), for beam-end tests the influence of concrete cover (col. 8 and 9), a rotation of the bar around the longitudinal axis (col. 10 and 11), the removal of transverse reinforcement (col. 12), and a shift of the rib spacing (col. 13).

The specimens are made in series of 3 or 4 samples out of the same batch. The bar is placed in horizontal position during casting and the beam-end specimens are concreted upside-down to ensure good bonding conditions. After demolding the samples are covered with moist cloths for 6 days and then stored indoor until testing. The monotonic tests are executed path-controlled and are also used as reference for tests with cyclic and long-term loading. For the cyclic experiments, the specimens are exposed to a tensile loading with a lower stress level of $0.4 \tau_{ult}$ and an upper stress level of 0.7 to $0.8 \tau_{ult}$ depending on the static bond strength τ_{ult} of each series. Further information about the cyclic tests can be found in [21]. The continuation of the test programme includes further monotonic tests on normal-strength concretes as well as long-term tests. In addition, tensile tests under long-time loading are planned, the results of which will be used to validate calculated crack widths.

3.3 Instrumentation and fibre-optic sensing

By default, the slip at the unloaded end of the bar is measured by contact-free displacement transducers (LVDT). For beam-end tests another LVDT is attached at the loaded end and two more LVDTs are placed right above the bond zone, one longitudinal and one in transverse direction, to record the growth

of cracks on the upper surface. The measurement distance is 100 mm for both of them. The force is measured with a load cell, which is connected with the hydraulic cylinder. All signals were sampled with a rate of 5 Hz.

In addition, DOFS has already been used in some tests and will be used more in upcoming series. The hair-thin sensors with a polyimide coating are applied directly to the pull-out bars with cyanoacrylate adhesive and enable the quasi-continuous recording of strains along the bar with a resolution of 0.65 mm per measured value. In tests carried out so far, a sensor fibre was redirected several times outside the bond zone so that it was applied along both sides of the two longitudinal ribs. Therefore the sensor passes through the bond zone four times. Within the bond zone, the sensor is covered with a thin layer of silicone to prevent bonding with the concrete. Protective tubes are arranged outside the bond zone (fig. 6).



Fig. 6 Applied sensor fibre and protective tube; left: at the longitudinal rib; middle: in groove through the inclined ribs; right: with support frame in helix form.

In preliminary tests, the sensors are applied at different positions on the bar with the help of grooves in order to identify strain differences within the reinforcement's cross-section. By means of support frames, the sensor fibres are also placed in the surrounding concrete of the bond zone for some samples and can detect strains in the circumferential direction.

4 Results and discussion

Looking at the experimental results for monotonic loading and a bond length of $l_b = 2 d_s$ (fig. 7 left), it can first be seen that an increase of concrete compressive strength results in higher bond strength. All test results are above the approach according to MC 2010, eq. (3). On the other hand, there is good agreement with the linear approach according to [14], eq. (4), although this applies especially to the PO setup and lower bond strengths were determined in the BE tests.

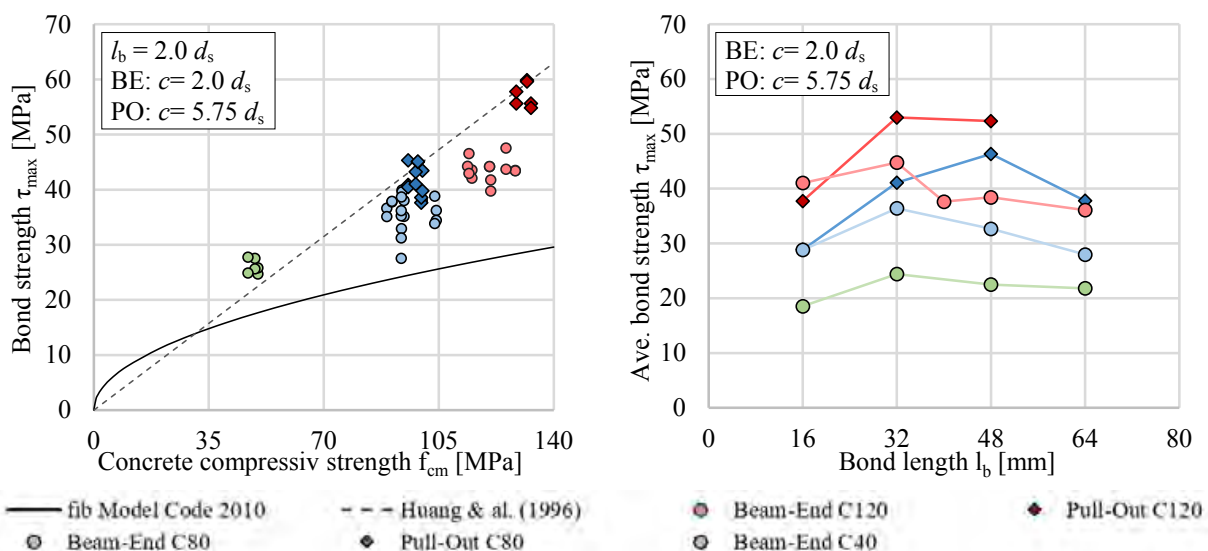


Fig. 7 Left: relationship of bond strength and concrete compressive strength; right: relationship of average bond strength and bond length (with mean concrete strength for each concrete type)

This phenomenon is even more noticeable for bond lengths longer than $2 d_s$ (fig. 7 right). The reason for this is the lower concrete cover in the BE setup, which reduces the confinement effect. For bond

lengths of $2 d_s$ or more, the big ring tensile forces cause splitting cracks, which lead to premature failure and reduced bond strength. The crack propagation of these cracks was recorded during the tests (see 3.3) and the crack patterns were subsequently documented.

However, no cracks were found on the concrete surface in BE tests with $l_b = 1 d_s$. According to this, the same failure mode occurred as in the PO tests, which also explains the almost identical test results for this bond length. The test results also confirm the influence of bond length even for short bond lengths $l_b < 5 d_s$. In BE tests, a doubling of the bond length from 2 to 4 d_s was observed to reduce the bond strength by approx. 30%. With the PO setup, this effect is less significant. The reason for this are probably the higher absolute pull-out forces at longer bond lengths, which increase the splitting effect and lead to larger crack widths in BE specimens. After the splitting is occurred, only the two stirrups ensure a certain level of confinement, which depends on the ring tensile forces. Anyway, for both specimen types and all three concretes, a decrease in bond strength is observed for a bond length of $l_b = 1 d_s$. The cause of this can be found in fig. 4 right. As the first concrete key cannot support itself due to the bond breaker, a breakout cone forms early on. The depth of this cone does not participate in the further load transfer or only by friction and depends on the diameters of the bar and the bond breaker. Under the selected conditions, the depth of the breakout cone is approx. 7 mm, which shortens the effective bond length accordingly. For the bond length of $l_b = 16$ mm, this means a shortening of the transmission length by almost half, for $l_b = 64$ mm only by roughly 10%.

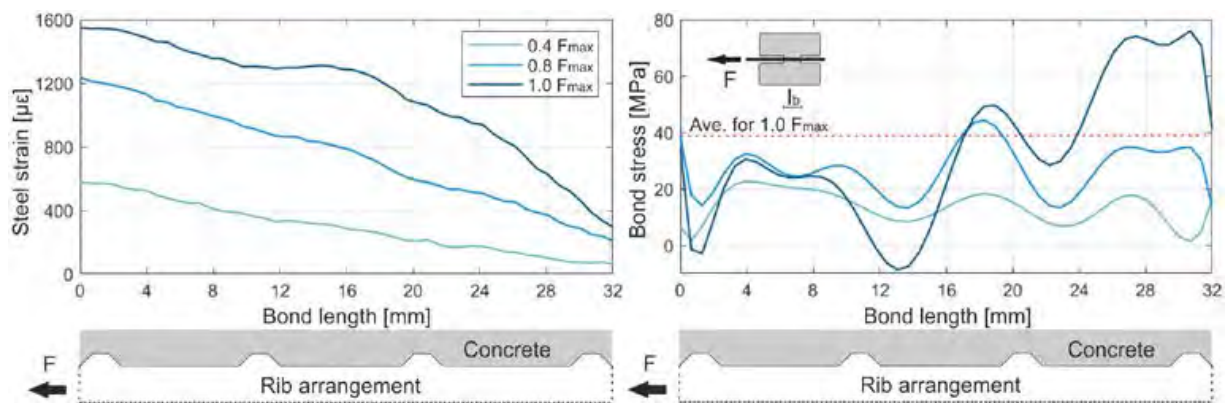


Fig. 8 Left: steel strain curves for different load levels; right bond stress distribution along the bond length

To detect those effects, differences and changes in load transfer within the bond zone during experimental tests, DOFS are used. Fig. 8 left shows steel strain curves along the pull-out bar within the bond zone for different load levels. It is noticeable that the strain curve for a low load level takes on a slightly concave shape. By increasing the load, the shape changes to a convex course, which indicates a redistribution of the load transfer. Through local derivation of the strain curves, it is possible to obtain the bond stress distribution along the bar (Fig. 8 right). If the stress distribution at $0.4 F_{\max}$ can still be declared as quasi uniform, a doubling of the load causes a redistribution towards the middle of the bond length. At the time of failure, the force is mainly transmitted through the last concrete key, resulting in a local bond stress of almost twice the mean value. Hence, it can be stated that there is a redistribution of stress from load close to load far areas during the progress of damage, which confirms Mörsch's theorie [9].

5 Conclusion and Outlook

In this paper, recent investigations on local bond behaviour at short bond lengths were presented. Based on a literature review and the results of over 130 individual tests under monotonic load, it is shown that the bond stress distribution cannot be assumed to be uniform even for short bond lengths. By means of DOFS, it was determined that a redistribution of the load transfer within the bond zone occurs during the damage progress. In addition, local bond stresses could be detected, from which local failure criteria can be derived.

Further investigations will address the effects of different loading situations such as fatigue and creep on the internal load transfer in the bond zone. Subsequently, local bond stress to slip relationships are described, which serve as a basis for determining crack widths.

Acknowledgements

The presented studies are funded by the German Federal Ministry of Economic Affairs and Energy (BMWi, project No. 0324016B and project No. 1501601). In addition, a thank goes to the Otto-Mohr-Laboratory, Technische Universität Dresden, for carrying out the test and the good cooperation.

References

- [1] fib Bulletin 65. 2012. *Model Code 2010 – Final draft, Volume 1*. Federation internationale du béton (fib), Lausanne, Switzerland
- [2] Lindorf, Alexander. 2006. “Ermüdung des Verbundes von Stahlbeton unter Querkzug.” Diss., Technische Universität Dresden.
- [3] Cairns, John and Giovanni A. Plizzari. 2003. “Towards a harmonized European bond test.” *Materials and Structures* 36 (262):498–506.
- [4] RILEM. 1970. “Essais portant sur l’adhérence des armatures du béton.” *Matériaux et Constructions* 3: 169–178.
- [5] Vandevallé, Lucie. 1992. “Theoretical prediction of the ultimate bond strength between a reinforcement bar and concrete.” Paper presented at the International conference bond in concrete from research to practice, Riga, Latvia, October 15–17.
- [6] ASTM international. 2015. „ASTM A944-10 - Standard test method for comparing bond strength of steel reinforcing bars to concrete using beam-end specimens.” West Conshohocken
- [7] Wildermuth, Anke. 2013. „Untersuchung zum Verbundverhalten von Bewehrungsstäben mittels vereinfachter Versuchskörper.“ *Deutscher Ausschuss für Stahlbeton* 609
- [8] Bach, Carl. 1905. „Versuche über den Gleitwiderstand einbetonierten Eisens.“ *Mitteilungen über Forschungsarbeiten* 22:1–41.
- [9] Mörsch, Emil. 1920. *Der Eisenbetonbau*. Stuttgart: Konrad Wittwer
- [10] Mains, R. M. 1951. „Measurement of the distribution of tensile and bond stresses along reinforcing bars.” *Journal of the American Concrete Institute* 23:225–252.
- [11] Müller, Fritz Peter und Werner Eisenbiegler. 1981. „Ermittlung der Verbundspannungen an gedrückten einbetonierten Betonstählen.“ *Deutscher Ausschuss für Stahlbeton* 319
- [12] Rostasy, Ferdinand S. and Jochen Scheuermann. 1987. „Verbundverhalten einbetonierten Betonrippenstahls bei extrem tiefer Temperatur.“ *Deutscher Ausschuss für Stahlbeton* 380: 43–105
- [13] Martin, Horst. 1973. „Zusammenhang zwischen Oberflächenbeschaffenheit, Verbund und Sprengwirkung von Bewehrungsstählen unter Kurzzeitbelastung.“ *Deutscher Ausschuss für Stahlbeton* 228
- [14] Huang, Z., Björn Engström and Jonas Magnusson. 1996. “Experimental and analytical studies of the bond behaviour of deformed bars in high strength concrete.” Paper presented at the 4th International Symposium on Utilization of High-strength/High-performance concrete, Paris, May 29–31
- [15] Rohling, Annette. 1987. „Zum Einfluss des Verbundkriechens auf die Rissbreitenentwicklung sowie auf die Mitwirkung des Betons auf Zug zwischen den Rissen.“ Diss., Technische Universität Braunschweig
- [16] Krips, Martin. 1985. „Rißbreitenbeschränkung im Stahlbeton und Spannbeton.“ Diss., Technische Hochschule Darmstadt.
- [17] Zobel, Robert. 2018. „Verbundmodellierung von Beton- und Spannstahl unter Querkzug.“ Diss., Technische Universität Dresden.
- [18] Berrocal, Carlos G., Ignasi Fernandez and Rasmus Rempling. 2020. „Crack monitoring in reinforced concrete beams by distributed optical fiber sensors.“ *Structure and Infrastructure Engineering*. Accessed February 26, 2020. doi:10.1080/15732479.2020.1731558
- [19] Speck, Kerstin, Fritz Vogdt, Manfred Curbach and Yuri Petryna. 2019. „Faseroptische Sensoren zur kontinuierlichen Dehnungsmessung im Beton.“ *Beton- und Stahlbetonbau* 114: 160–167
- [20] Ritter, Laura. 2014. „Der Einfluss von Querkzug auf den Verbund zwischen Beton und Betonstahl.“ Diss., Technische Universität Dresden.
- [21] Koschemann, Marc and Tino Kühn, Kerstin Speck, Manfred Curbach. 2018. „Bond behaviour of reinforced concrete under high cycle fatigue pull-out loading.” Paper presented at the 5th international fib Congress, Melbourne, November 7–11.

Homogenized reinforced concrete model for the evaluation of Alkali-Silica-Reaction affected structures

Daniela Vo¹, Pierre Morenon¹, Stéphane Multon¹, Alain Sellier¹, Etienne Grimal², Benoit Masson³, Anass Cherki El Idrissi⁴, Philippe Kolmayer²

¹*LMDC, Université de Toulouse III – Paul Sabatier,*

135 avenue de Rangueil, F-31077 Toulouse Cedex 04, France

²*EDF-CIH Technolac, 73373 Le Bourget du Lac, Cedex, France*

³*EDF-DIPNN, 69007 Lyon, France*

⁴*EDF-R&D Lab Paris Saclay, 91120 Palaiseau, France*

Abstract

Alkali-Silica Reaction is a harmful pathology which can alter mechanical properties of a structure. Ensuring security of such affected structures by predicting its behaviour constitutes an important need and challenge, which can be answered by numerical modelling. In this study, affected structures are modelled through a homogenization approach where the homogenized material is directly reinforced concrete. The aim of this paper is the evaluation of the numerical model response in an ASR context. Reinforced concrete beams loaded until failure drawn from the literature are modelled. After a description of the main features of the model, a parametric study on mesh size impact is performed to highlight the model stability.

1 Introduction

Alkali-Silica Reaction (ASR) is an endogenous concrete reaction which can cause important degradation in concrete and could lead to the decrease of structure performances. It is due to the chemical-reactions between alkali present in the pore solution and the amorphous or low crystallised phases contained in siliceous aggregates. This attack leads to the production of new phases and to concrete expansion and cracking. Although this reaction has been studied since a long time [1] [2], works are still necessary to be able to predict future expansion and to evaluate its impact on real structures. Evolutions of swelling and induced cracks are mostly driven by ASR chemical advancement. In spite of that, stress state, induced by external loads or restraints, can cause preferential cracking directions [3] [4] [5]. Hence, the evaluation and the prediction of the structural behaviour of reinforced concrete structures affected by ASR represent more than a challenge, but a real need to ensure their safety. Rehabilitation project and their optimisation constitute also an actual requirement for construction supervisors. Numerical modelling is a suitable solution to help managers, notably in its non-destructive and limited cost nature. Nevertheless, most of the ASR-affected structures are generally large-scale works which are reinforced with a very big and dense reinforcement network. More than a longer computational time, the mesh can lead to important numerical complexities. It can lead to real numerical limits because of physical boundary, especially in the interface zone between steel and concrete. In ASR context, concrete swelling is restrained by the steel bars. It can lead to important stress concentrations, and so, to a localised overestimation of damage. As this area is responsible for the bond ability, its degradation can lead to a too important loss of rigidity and so to an unrealistic structural response. In order to avoid such limits, homogenized model have been developed [6] [7]. This approach is based on the consideration of a unique material called homogenized reinforced concrete. Steel bar does not need to be meshed anymore. Its contribution is evaluated by a specific behaviour law and combined with the concrete law according to their distribution and their direction, to constitute the whole material response. The aim of this study was to validate the prediction ability of this model. In order to evaluate the model stability, a parametric study about mesh size impact is realised in an ASR context. The comparison between numerical response and experimentation is based on the experimental test realized by Ohno and al [8], where ASR affected beams were studied and compared to non-reactive beams. After an aging period, where these structures have been submitted to natural weather, they were loaded under a four-points bending test until their failure. Due to ASR swelling, chemical prestress phenomenon occurs and impacts the structural response (aging and

failure phases). After the model presentation, the behaviours of the beams are modelled, and the responses obtained with different modelling meshes are presented. Fine-meshed, medium-meshed and coarse-meshed are used and results on strain evolution, chemical prestress, load-deflection curves, cracks patterns and stress-profile are analysed.

2 Formulation

2.1 Rheological model

In this work, the modelling of reinforced concrete is made by a homogenized approach. There is no need to mesh the reinforcement network, because the specific material model can consider the whole material as reinforced concrete. The behaviour law is defined by the combination between steel and concrete contributions according to their distribution. Fig. 1 shows the rheological scheme of this model.

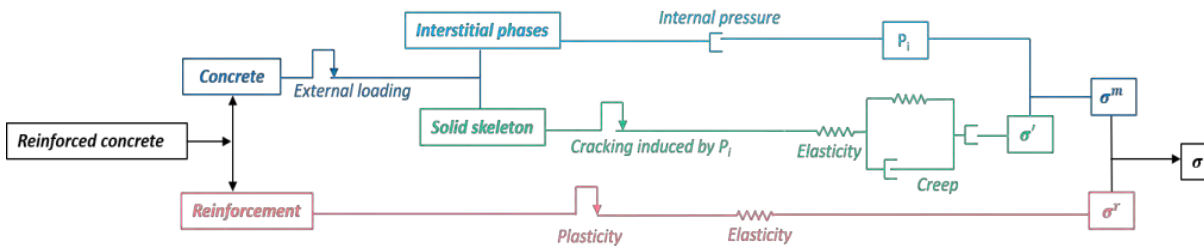


Fig. 1 Rheological scheme

In order to consider the phenomenon of chemical expansion, the concrete behaviour is defined in the poromechanical framework [9]. The total stress is composed by the external stress applied on the solid skeleton and by the internal stress due to ASR, weighted by a Biot coefficient evaluated according to its nature. Cracks induced by localized phenomenon (for example due to structural effect) are differentiated from diffuse cracking induced by internal pore pressure, (for example induced by ASR gels, DEF products, water...). To obtain this distinction, different criteria are used: a Rankine associated criterion for tensile strength at structural scale (localized cracks), a Rankine criterion for tensile strength at micro-scale (diffuse cracking due to internal pressure) and an isotropic Drucker-Prager criterion for compression and shear external loadings. Regarding to the micro-scale, the criterion is written in terms of effective stress within the meaning of poromechanics. In any events, in the both scales, cracks induce specific reduction of mechanical characteristics. To quantify the mechanical evolutions, the model is also based on damage theory [10]. In order to characterize the level of mechanical damage, damage variables are defined according to the phenomenon considered (tension, compression, internal pressures). Shear damage is isotropic while damage induced by tension and pressure are anisotropic. The opening of the cracks induced by external loading can be evaluated from plastic deformations as described in [11]. As this study mainly concerns the ASR evaluation of a reinforced concrete structure, only these parts of the model are developed in the present paper. All the other parts of the model are detailed in [7].

2.2 ASR modelling

First, the ASR-modelling evaluates the chemical advancement of the reaction before computed the induced internal pressure. Chemical advancement leads then to the determination of the gel volume Φ_{ASR}^{eff} . Temperature and moisture impacts on kinetics and amplitude of swelling are considered in the modelling (through Arrhenius law for temperature [12] [13] and Poyet's law [14] modified by Morenon [15] for water effect). This paper focuses on the structural consequences of ASR and its modelling and the laws for the chemical advancement are not totally described. More detailed description of the chemical part of the model can be found in [7]. The ASR pressure (1) is generated by the ASR-gel volume according to the connected porosity Φ_{ASR}^v (volume of the connected porosity becomes higher with the induced internal pressure rise), to the modification of porosity spaces induced by the elastic and delayed strains, ϵ^{el} and ϵ^{cr} respectively and lastly by the volume induced by cracking $\epsilon^{pl,ASR}$.

$$P_{ASR} = M_{ASR} \langle \phi_{ASR}^{eff} - \langle \phi_{ASR}^v \left(\frac{P_{ASR}}{R_0} \right) + b_{ASR} \cdot \text{tr}(\varepsilon^{el} + \varepsilon^{cr}) + (1 - b_{ASR}) \cdot \text{tr}(\varepsilon^{pl,ASR}) \rangle^+ \rangle^+ \quad (1)$$

Finally, the cracking induced by such phenomenon is evaluated through a Rankine associated criterion (2). This cracking is considered as diffuse in concrete. The present model does not propose to evaluate the corresponding crack opening which depends on the reactive silica content and on the aggregate size and distribution in concrete. Induced by the development of internal and swelling pressure, the criterion used to manage is writing in a poromechanical sense. Cracking starts when the effective stress, $\tilde{\sigma}^{eq}$, induced by ASR exceeds the local tensile strength:

$$f_i^{ASR} = \mathcal{S}_i^{eq} - R_i^t \quad (2)$$

$$\text{With } \mathcal{S}_i^{eq} = P_{ASR} + \min(\mathcal{S}_i^0, 0)$$

Note that the evaluation of internal pressure and induced plasticity is also usable for the delayed ettringite formation (DEF) [16]. If the chemical equations are different, the mechanical consequences are close.

The impact of external stress on ASR expansion is well-known: if one direction is reinforced or restrained [3], [4], [5], a chemical prestress phenomenon occurs. Restrained expansions are the cause of compression stress in concrete. This confinement effect leads to decrease the criteria (2), to reproduce the cracking orientation along reinforcement. If the criterion is reached, plastic strain can be evaluated to reproduce ASR diffuse cracking. The damage induced by ASR-expansion is then evaluated according to the plastic strain to reduce the mechanical characteristics in the structure. The impact of expansion is not the same on tensile (3) and compressive diffuse damage (4). The tensile damage is directly evaluated through the plastic strain and a characteristic strain $\varepsilon^{k,ASR}$ [17].

$$D_I^{t,ASR} = \frac{\varepsilon_I^{pl,ASR}}{\varepsilon_I^{pl,ASR} + \varepsilon^{k,ASR}} \quad (3)$$

The compressive damage due to ASR is evaluated by a combination of tensile damage in the two perpendicular directions:

$$D_I^{c,ASR} = 1 - ((1 - D_{II}^{t,ASR})(1 - D_{III}^{t,ASR}))^{\alpha^{ASR}} \quad \text{with} \quad \alpha^{ASR} = 15 \quad (4)$$

This mechanical part has been validated on reactive beams, in cases of ASR and DEF swelling, and two dams by Morenon in [15].

2.3 Reinforcement consideration

After the description of the concrete behaviour, the reinforcement contribution is calculated through a homogenized law [18]. Each reinforcement is defined according to its direction, its quantity, defined by a cross-section ratio ρ^r , and its mechanical strength (yielding, hardening...). Until three directions of reinforcement can be defined by finite element. With Nr the total number of reinforcements, the homogenized behaviour law can be written as:

$$\sigma_{ij} = (1 - \sum_{n=1}^{Nr} \rho^n) \sigma_{ij}^m + \sum_{n=1}^{Nr} \rho^n \sigma_{ij}^{r,n} \quad (5)$$

Each reinforcement acts only along its axial direction. The ‘steel / concrete’ ratio is an input data and can be defined along three different directions (the directions of the reinforcements, defined by vectors, are also an input data of the model). The steel contribution σ^r is evaluated through an elastoplastic law in each considered direction, and its plasticity is driven by a uniaxial plastic hardening criterion:

$$f^r = |E^r (\varepsilon^r - \varepsilon^{r,pl}) - H^r \varepsilon^{r,pl}| - f_y^r \quad (6)$$

In a previous study, Chhun [19] validated this part of the model, on a strongly reinforced beam under a three-points bending test and then on a nuclear power plant containment wall during its operational phase and during a scenario of loss of coolant accident without ASR consideration.

3 Modelling

3.1 Parameters

This numerical study is based on experimentations performed by Ohno et al [8] about the ASR impact on the mechanical behaviour of reinforced concrete beams. In order to evaluate the deterioration due to this pathology, two non-reactive beams and two reactive ones were realized. First, an aging period of the beams was monitored, where they were submitted to natural weather. After this phase, they were submitted to a four-points bending test until their failures. The reinforcement network was composed by four 25 mm diameter steel bars for the longitudinal reinforcement, and by 10 mm diameter for transversal reinforcement. Yield strengths were given by the authors, respectively 420 MPa and 399 MPa. Elastic and hardening modulus were not specified, so it has been decided to consider them as usual values, respectively 200 GPa and 1000 MPa. For the concrete, the initial mechanical strengths were almost the same. The elastic modulus and compressive strength have been evaluated by the authors, and the tensile strength has been extrapolated from the NF_EN_1992 formulas for the numerical analysis. These values are respectively 37 GPa, 27.5 MPa and 2.2 MPa. To access a realistic flexural behaviour and to obtain specific information during the failure phase, it is important to position the reinforcements zones on specific part of the mesh representative of the real reinforcements. Here, longitudinal reinforcements were concentrated in the upper and lower fibers (Fig. 2). For transversal reinforcements, it was chosen to distribute their transversal part in the same way and to homogenize their vertical part overall the beam due to the limited effect on this direction. This distribution is shown on Fig 2.

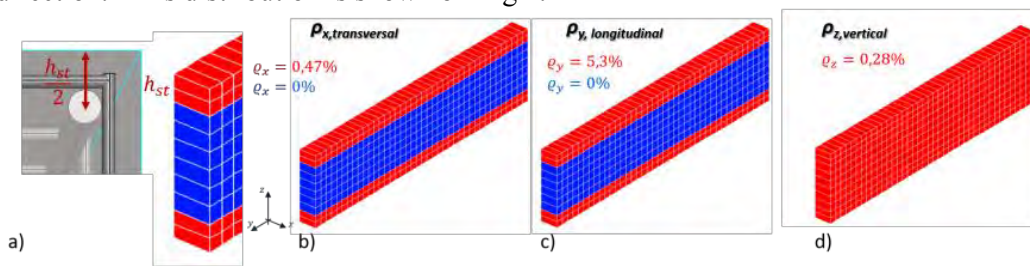


Fig. 2 Beam reinforcements, a) Mesh strategy b) Transversal reinforcement, c) Longitudinal reinforcement, d) Transversal reinforcement

The symmetrical geometries of these beams allow to model their quarter only. To consider these conditions, displacement along transversal and longitudinal direction are blocked on two faces. The other “external” faces are stress-free during the aging period. To represent the simple support of the beams, and the loading, a support line and a loading line are defined on the mesh. Vertical displacements on the support line are vertically blocked. After the aging phases, vertical displacements are imposed on the loading line to simulate the flexural test.

3.2 Aging phase

The first aim of this study is to evaluate the mesh size impact on the structural response of this model. Three meshes are defined, M0 is finely meshed whereas M2 is coarsely meshed, the mesh of M1 is between the two first ones (Fig 3). In this part, the strain during the aging phase and the evaluation of the chemical prestress are the benchmarks for this parametrical study.

3.2.1 Strain

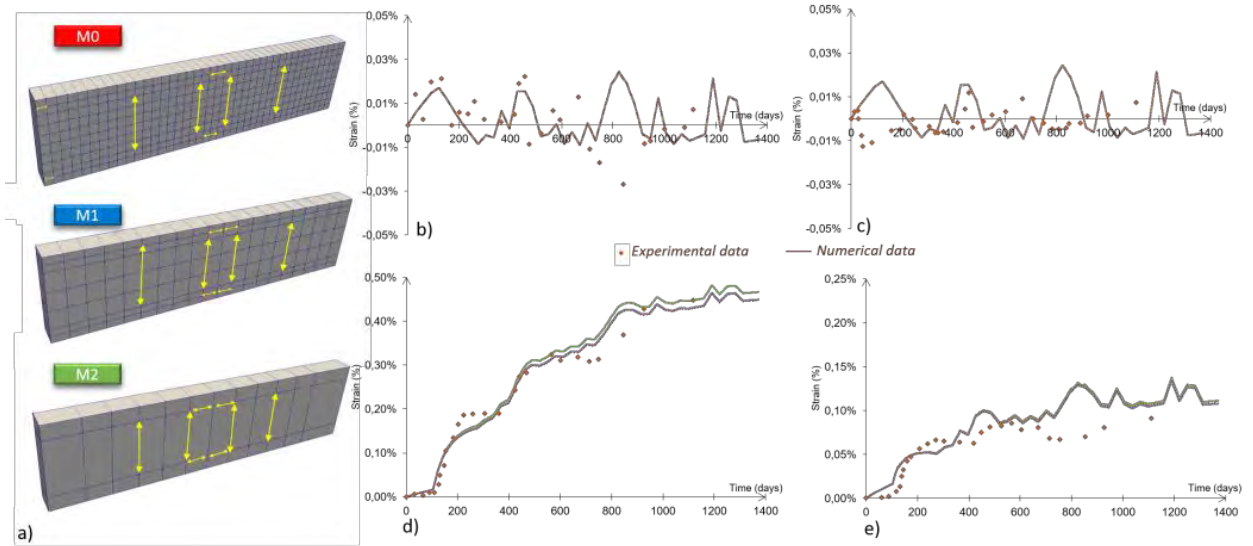


Fig. 3 a) Mesh size and monitoring points b) Nonreactive vertical strain, c) Nonreactive longitudinal strain, d) Reactive vertical strain, e) Reactive longitudinal strain

In order to evaluate the flexural performance after different ASR advancements, two aging-periods were tested experimentally and numerically, one of 17 months and one of 45 months. The differences of numerical results obtained for the strains of non-reactive beams with the differences meshes are very small, with absolute differences of less than 10^{-5} . Due to the numerous and additional calculus, and hence approximations in those calculus, induced by the ASR modelling, a more important variation can be observed for strains of reactive beams than the nonreactive ones. For the vertical strains, the absolute difference is about 10^{-4} . Therefore, mesh size has a negligible impact on evaluated strains for both reactive and non-reactive beams.

The impact of the mesh differences on computational times is considerable. The calculations performed during the aging periods for the reactive beam are 135 times faster for the coarsest mesh than for the finest one. This impact is much less important in non-reactive case, around 10 times less for the aging period.

3.2.2 Chemical prestress

As previously explained, concrete expansion restrained by the reinforcement bars leads to chemical prestress. It induces a confinement effect mainly in the longitudinal direction of concrete. In order to highlight this effect, stress profiles are drawn at the end of the aging phase in Fig. 4. In order to estimate the mesh-size impact, results are presented according to the mesh used to obtain the stress profile. Stress are presented on the Gauss points of the axis of symmetry, then, the evolution is obtained by linear extrapolation on height of the mesh-elements.

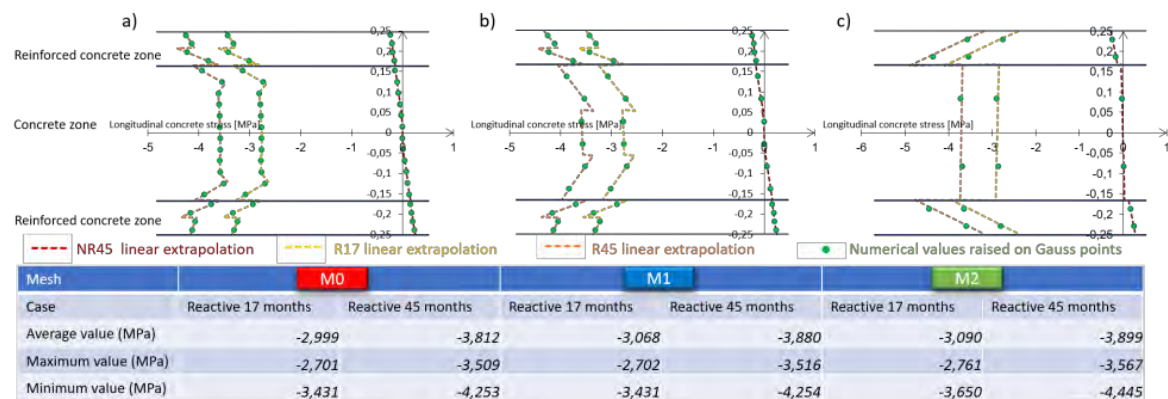


Fig. 4 Longitudinal stress profiles at the end of aging phase a) M0-mesh b) M1-mesh c) M1-mesh

Although the evolution of stress is less continuous with the coarsest mesh, there is not significant differences between these profiles for the three meshes: the cross-section of the beams remains compressed around 4 MPa. For the reactive beams, there are some variations at the upper and the lower fibres where longitudinal reinforcements are concentrated. The variation between the three meshes is about 0.1 MPa around an average value of 3 MPa for the 17 months compressive stress. For the 45 months reactive case, the compressive stress is about 3.8 MPa. The increase in compression is due to the difference in reaction advancement for the longest aging period (45 months).

3.3 Failure phase

3.3.1 Load displacements curves

The modelling has been made in two stages. After the aging phase, load is applied as a displacement on a loading line. Then, vertical displacement and nodal forces are raised to establish the load-deflection curves (Fig 5).

In order to compare the results for the three meshes more easily, the non-reactive curves at 17 months and 45 months have been separated (Fig 5. a) and b)). In all cases (reactive and non-reactive), the structural behaviour during the loading test is well-reproduced. In the non-reactive cases, the finest mesh (M0) presents a slightly stiffer evolution than the coarser ones (M1 and M2) after concrete cracking. But the difference is quite small. For the non-reactive beams tested at 17 months, the load at first concrete crack is around 64 kN, 59 kN and 56 kN for M0, M1 and M2 respectively. For the 45 months case, values are quite the same with a difference of less than 1 kN.

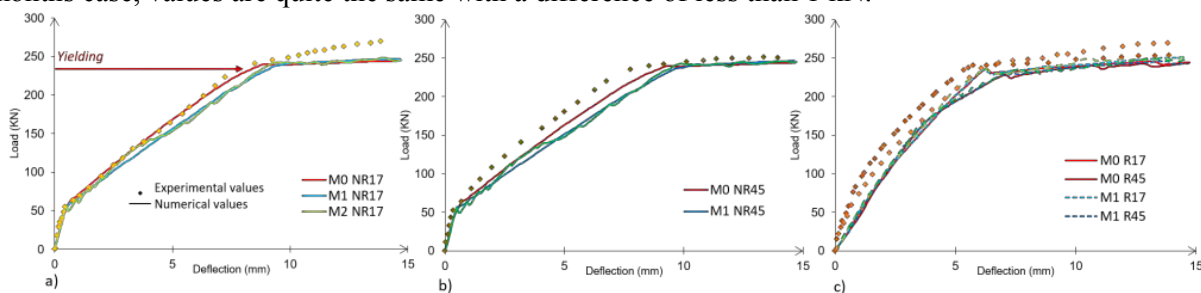


Fig. 5 Load-displacement curves a) Non-reactive cases 17 months, b) Non-reactive cases 45 months, c) Reactive cases 17 and 45 months

For the reactive beams, the dependence of the numerical results to mesh size is smaller than for the non-reactive beams. All cases corresponding to the same aging period show a very similar evolution. Moreover, the gap between the beam tested at 17 months and at 45 months at the yielding phase is well remained. In the same way as the nonreactive case, this difference is induced by the longest aging-period. For the reactive beams, the difference is due to the increase of ASR damage for the longest period of aging. Besides that, and whatever the mesh size, all the reactive beam shows an initial underestimation of their flexural behaviour. This underestimation is induced by the gel rheology consideration. In this model, the gel is considered as a fluid with a high-tension surface and negative angle contact, moving to the porosity in case of impossible cracking (case of reinforced structures). If the intrusion pressure of the gel decreases due to a change in loading (loss of confinement generally), the filled-porosity part of gel decreases too (Equation (1)). The part of gel coming back to its initial reactive site induces a slow pressure decrease, often slower than the decrease of unloading causing it, so, the residual pressure, even if lesser than previously, is yet in an unconfined matrix, what can provoke diffuse cracking of the concrete matrix. Due to this new damage, the subsequent rigidity of the matrix is too much reduced.

In this case, the bending generates a pressure in the bottom of the beam, what acts as a deconfinement of the matrix as explain above, and then damage concrete and over-reduces the stiffness of the beam comparatively to the experimental data. Although this consideration may be unrealistic, further development have to be proposed to limit this “unloading-damage”, which is the aim of our future work.

Note that there is a gain time of about 30 times between the coarsest and the finest meshes during the loading calculations.

3.3.2 Cracks patterns

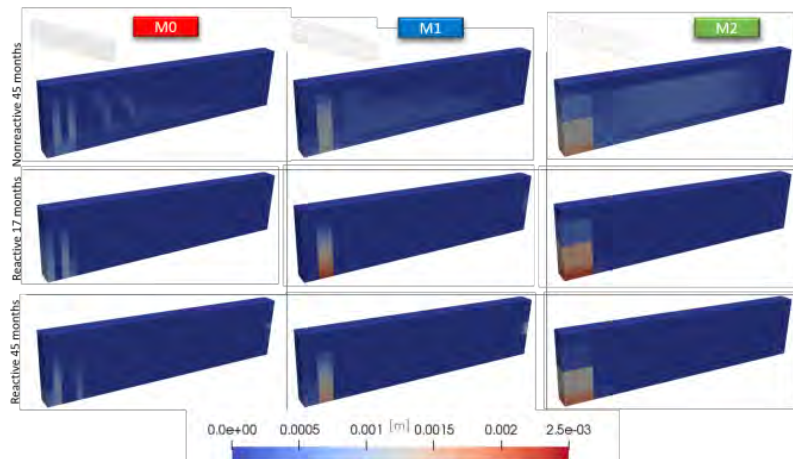


Fig. 6 Structural crack opening at the end of the load for all the meshes (for coarse mesh the element can include two cracks and the plotted crack opening is the cumulated opening in each finite element)

The evolution of cracks opening is an important data for structures evaluations. The location of the cracks is well-reproduced whatever the mesh size (Fig. 6), but the location of cracks and their opening appears less accurate for coarser meshes. Regarding to the maximal and final values, cumulated cracks opening is almost twice larger between the finest and the coarser meshes, M0 and M2. Nevertheless, M0 mesh shows two distinct cracks while there was only one damaged finite element for M2. In M0, there is a single crack by element while for M1 and M2 two cracks can coexist in a single finite element, this is due to the fact that the crack number in a finite element depends also on bond strength and on the finite element length in the tensile direction[7]. The model adapts automatically the fracture energy to the expected crack number.

Finally, at the end of the test, flexural cracks were presents for all the cases and all the mesh, and their values are quite close. The difference in cracks distribution is induced by the presence of chemical prestress in various advancement.

The other kinds of cracks induced by such loading are shear cracks. There were correctly highlighted on the nonreactive case. Those are less obvious for M1 and M2 but have been well reproduced. Because of chemical prestress phenomenon, these shears cracks seem to disappear in reactive cases. Indeed, the confinement effect of stirrups on reactive concrete compensates the shear effect. The absence of shear cracks for the reactive beams are confirmed experimentally in [8].

3.3.3 Stress state before yielding

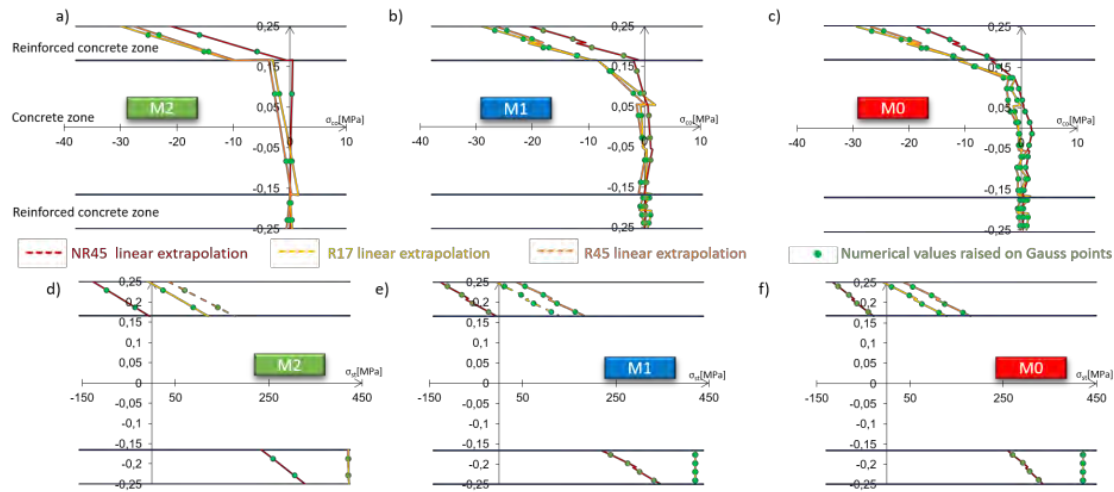


Fig. 7 Stress profile for the nonreactive 45 months aging phase (NR45) and for reactive cases (R17, R45) a) In concrete with M2, b) In concrete with M1, c) In concrete with M0, d) In reinforcement with M2, e) In reinforcement with M1, f) In reinforcement with M0

In the same way as the chemical prestress, stress profiles during the loading tests are established. In Fig. 7, they are represented for concrete (a, b and c) and for reinforcement (d, e and f) just before the yielding phase of the beams (see Fig. 5).

Within concrete, the upper fibre of the beam is compressed because of the flexural test. This effect is even more marked in reactive beams, due to chemical prestress. In the non-reactive case, the rest of the beam seems to be slight tensioned compared to reactive ones. Once more, this difference is induced by the chemical prestress effect. Regarding to mesh size impact, the differences of stress in concrete vary around 1 MPa for reactive beams and a little more for the non-reactive ones. The differences in steel stress of the non-reactive beams can reach a difference up to 20MPa between the different meshes, unlike reactive ones which vary from 2 MPa only.

4 Conclusion

The aim of this study was to evaluate the stability of the model response in front of an important variation of the mesh size. Concerning aging stage, strains evolutions and chemical prestresses are relatively independent of the mesh size. For the loading phase, evolutions of load-deflection curves are also quite similar, even if nonreactive beams present a slight loss of rigidity after concrete cracking with the increase of the mesh size. Cracks pattern is more impacted by the mesh size because several cracks can be embedded in a single finite element in case of coarse mesh. The location of cracks is then less accurate, but the cumulative crack opening in the cracking zone stays stable whatever the mesh. In all cases, the model was able to explain the difference of behaviour observed experimentally during the post swelling. Thanks to the well anchorage conditions of the reinforcements, this experiment is not impacted by concrete-reinforcement sliding. Hence it allows the proposed model to simulate realistically experimental data. Besides that, the model is able to discriminate diffuse cracks due to AAR and localized structural cracks, these last benefits of an energetic regularization method which ensures the model objectivity according to the mesh density.

Finally, the ASR modelling is a complex phenomenon, notably due to the impact of external and internal stress state on concrete expansion. Reinforcement participation and induced chemical prestress phenomena must be considered with attention to access to a realistic structural response. The used of homogenized reinforced finite elements allow to save time computing without loss of accuracy in terms of structural behaviour. Hence, the method can be used to assess the behaviour of larger reinforced structures affected by swelling reactions.

Acknowledgements

Dr S. Ohno and Dr Y. Kawabata are thanked for important precisions on test conditions. Acknowledgement are addressed to Electricité de France (EDF) for its financial support on the EXIGENCE project which is the framework of the present study. The modelling was made with the finite

element software developed by EDF R&D, Code_Aster (V14.2, <https://www.code-aster.org>) and the post-processing with Salome_Meca.

References

- [1] Glasser LSD, Kataoka N. The chemistry of ‘alkali-aggregate’ reaction. *Cement and Concrete Research* 1981;11. [https://doi.org/10.1016/0008-8846\(81\)90003-X](https://doi.org/10.1016/0008-8846(81)90003-X).
- [2] Poole AB. Alkali-silica reactivity mechanisms of gel formation and expansion. *Proceedings of the 9th International Conference on Alkali-Aggregate Reaction*, London (England), vol. 104, Concrete Society Publications CS; 1992, p. 782–9.
- [3] Multon S. Évaluation expérimentale et théorique des effets mécaniques de l’alcali-réaction sur des structures modèles. PhD Thesis. Université de Marne-la-Vallée, 2003.
- [4] Morenon P, Multon S, Sellier A, Grimal E, Hamon F, Bourdarot E. Impact of stresses and restraints on ASR expansion. *Construction and Building Materials* 2017;140:58–74. <https://doi.org/10.1016/j.conbuildmat.2017.02.067>.
- [5] E. K. Jones A, A. Clark L. The effects of restraint on ASR expansion of reinforced concrete. *Magazine of Concrete Research - MAG CONCR RES* 1996;48:1–13. <https://doi.org/10.1680/mac.1996.48.174.1>.
- [6] Pietruszczak S, Winnicki A. Constitutive Model for Concrete with Embedded Sets of Reinforcement. *Journal of Engineering Mechanics-ASCE* 2003;129. [https://doi.org/10.1061/\(ASCE\)0733-9399\(2003\)129:7\(725\)](https://doi.org/10.1061/(ASCE)0733-9399(2003)129:7(725)).
- [7] Sellier A. Anisotropic Damage and Visco-Elasto-Plasticity Applied to Multiphasic Materials. LMDC - Laboratoire Matériaux et Durabilité des Constructions de Toulouse ; Université de Toulouse III - Paul Sabatier ; INSA de Toulouse; 2018.
- [8] Ohno S, Yoshioka Y, Shinozaki Y, Morikawa T. The mechanical behaviour of reinforced beams coated after Alkali-Silica Reaction damage. 8th international conference on Alkali-aggregate reaction. Kyoto, Japan, 1989, p. 697–702.
- [9] Biot MA. General theory of three-dimensional consolidation. *Journal of Applied Physics* 1941;12.
- [10] KACHANOV LM. Time of the rupture process under creep conditions, *Izy Akad. Nank SSR Otd Tech Nauk* 1958;8.
- [11] Sellier A, Casaux-Ginestet G, Buffo-Lacarrière L, Bourbon X. Orthotropic damage coupled with localized crack reclosure processing. Part I: Constitutive laws. *Engineering Fracture Mechanics* 2013;97:148–67. <https://doi.org/10.1016/j.engfracmech.2012.10.012>.
- [12] Larive C. Apports combinés de l’expérimentation et de la modélisation à la compréhension de l’alcali-réaction et de ses effets mécaniques. PhD Thesis. École nationale des ponts et chaussées (France), 1998.
- [13] Grimal E. Caractérisation des effets du gonflement provoqué par la réaction alcali-silice sur le comportement mécanique d’une structure en béton. PhD Thesis. Université de Toulouse, Université Toulouse III-Paul Sabatier, 2007.
- [14] Poyet S. Étude de la dégradation des ouvrages en béton atteints par la réaction alcali-silice : approche expérimentale et modélisation numérique multi-échelles des dégradations dans un environnement hydro-chemo-mécanique variable. PhD Thesis. Université de Marne-la-Vallée, 2003.
- [15] Morenon P. Modélisation des réactions de gonflement interne des bétons avec prise en compte des couplages poro-mécaniques et chimiques. PhD Thesis. Université Toulouse III-Paul Sabatier, 2017.
- [16] Sellier A, Multon S. Chemical modelling of Delayed Ettringite Formation for assessment of affected concrete structures. *Cement and Concrete Research* 2018;108:72–86. <https://doi.org/10.1016/j.cemconres.2018.03.006>.
- [17] Capra B, Sellier A. Orthotropic modelling of alkali-aggregate reaction in concrete structures: numerical simulations. *Mechanics of Materials* 2003;35:817–30. [https://doi.org/10.1016/S0167-6636\(02\)00209-0](https://doi.org/10.1016/S0167-6636(02)00209-0).
- [18] Sellier A, Millard A. A homogenized formulation to account for sliding of non-meshed reinforcements during the cracking of brittle matrix composites: Application to reinforced concrete. *Engineering Fracture Mechanics* 2019;213:182–96. <https://doi.org/10.1016/j.engfracmech.2019.04.008>.

- [19] Chhun P. Modélisation du comportement thermo-hydro-chemo-mécanique des enceintes de confinement nucléaire en béton armé-précontraint. PhD Thesis. Université de Toulouse, Université Toulouse III-Paul Sabatier, 2017.

Monitoring and structural assessment

Stop Criteria for Proof Load Testing of Reinforced Concrete Structures

Gabriela I. Zarate Garnica, Eva O. L. Lantsoght

*Concrete Structures,
Delft University of Technology,
Stevinweg 1, 2628 CN, Delft, The Netherlands*

Abstract

Existing bridges with large uncertainties can be assessed with proof load tests. In such tests, a load representative of the factored live load is applied to the structure. If the bridge can carry the load without any signs of distress or nonlinearity, the test is considered successful. Since large loads are applied in proof load tests, the monitored structural responses are used to define stop criteria. This paper presents stop criteria for shear and flexural failure based on existing codes and guidelines and theoretical considerations. The proposal is verified with the available information from previous tests on reinforced concrete beams, the pilot proof load tests and a collapse test carried out in the Netherlands. The results are that the stop criteria are not exceeded and therefore, the proposed stop criteria can be used for proof load tests. However, further experimental validation is needed, especially for shear failure.

1 Introduction

The assessment of existing bridges is an important aspect for the safety of society. In the Netherlands, many existing bridges, in particular reinforced concrete slab bridges, were built in the 1960s and 1970s which means that they are not designed for the actual traffic loads and they could present material deterioration. Additionally, in comparison with the old codes, the recent codes describe larger live loads, a closer distance between axles and lower shear capacity. Therefore, upon assessment with the new codes, a large number of these bridges rate insufficiently for shear or bending moment. Most of the existing bridges can be assessed with the increasing levels of approximation proposed in [1]. The first levels of approximation include spreadsheet calculations, linear and nonlinear finite element analysis and/or probabilistic approaches [2]. However, if analytical methods prove to be insufficient, proof load testing can be used to demonstrate that a bridge still fulfils the code requirements.

In a proof load test, a load representative of the factored live load is applied to the bridge. If the bridge can carry the loads without any signs of nonlinearity or distress, the proof load test is considered successful. Since the applied loads are large, the structural response of the bridge needs to be monitored during the test. The measurements of parameters such as strains, crack widths and deflections have been used to define limits or stop criteria. If a stop criterion is exceeded, the proof load test must be terminated and further loading is not permitted [3]. Stop criteria define the onset of irreversible damage or even the collapse of the structure.

This paper reviews the stop criteria found in the German guideline [4] and in the literature. This paper focuses on stop criteria for flexural and shear failure based on theoretical considerations. The stop criteria are verified with the available results from previous tests on reinforced concrete beams, the pilot proof load tests and a collapse test that were carried out in the Netherlands. The tests in which failure occurred are used to evaluate the margin of safety provided by the stop criteria and the proof load tests are used to check if the stop criteria are exceeded. This paper provides an update to the previous proposal [2], as it includes a limiting strain in the concrete based on a mechanical model for shear failure.

The results show that the proposed stop criteria were not exceeded during the proof load tests and therefore, they could be used during a proof load test as they are not overly conservative. However, further experiments are still needed to gather more information about the margin of safety, especially for shear failures on slabs. In the coming years, an experimental program will be conducted at Delft University of Technology on slabs under cyclic loads to confirm the validity of the proposed stop criteria.

2 Existing stop criteria

2.1 Codes and guidelines

The German Guideline [4] and ACI 437.2M-13 [5] prescribe stop and acceptance criteria for flexural failure. The stop criteria from the German guideline [4] are based on concrete strain, steel strain, maximum and residual crack width for new and existing cracks (see Table 1), and the residual deflection. The recent update [6] includes a stop criterion for the development of cracks with an inclination of $< 60^\circ$ in the shear span. The stop criterion for the concrete strains is:

$$\varepsilon_c < \varepsilon_{c,lim} - \varepsilon_{c0} \quad (1)$$

with ε_c is the measured strain, $\varepsilon_{c,lim}=800\mu\epsilon$ for concrete with a compressive strength larger than 25 MPa, and ε_{c0} is the strain due to permanent loads.

Table 1 Requirements for new and existing cracks[4]

	During proof loading	After proof loading
New cracks	$w \leq 0.5 \text{ mm}$	$\leq 0.3 \text{ mm}$
Existing cracks	$\Delta w \leq 0.3 \text{ mm}$	$\leq 0.2 \Delta w$

The ACI 437.2M-13 [5] defines acceptance criteria for a prescribed cyclic loading protocol. The acceptance criteria are the repeatability index, permanency ratio, deviation from linearity, and a maximum and residual deflection.

2.2 Theoretical stop criteria

Table 2 presents a summary of the existing theoretical formulations for stop criteria in flexural and shear failure found in the literature.

A theoretical derivation of a limiting strain in the concrete at the bottom of a cross-section (ε_{stop}) was developed in [7]. For this criterion, the stress in the tension steel is limited to 65% of the mean yield strength f_{ym} . This limit is used to calculate the strain at the bottom of the cross-section with Eq.(2), where h is the height of the member, c is the height of the compression zone, d is the effective depth of the member, and E_s is Young's modulus of the steel.

Two proposals for a maximum crack width can be found in the literature. The first limiting crack width (w_{stop}) was proposed in [7] and it is based on the crack width model [8] of large reinforced concrete members subjected to bending. The stress in the reinforcement is limited to $0.65f_{ym}$ and w_{stop} is found using Eq. (4), where d_c is the concrete cover in mm, s is the reinforcement spacing, f_{perm} is the stress caused by the permanent loads and $\beta_{fr}=1+3.15 \times 10^{-3}d_c$ is the strain gradient term. The second proposal for a limiting maximum (w_{vos}) and residual crack ($w_{res,vos}$) width was proposed in [9]. The proposal is based on the experimental work [10] carried out on specimens reinforced with plain bars. This research was chosen since many existing structures in the Netherlands are reinforced with plain bars. The maximum crack width is computed with Eq. (6) and the residual crack width with Eq. (7), with β as the ratio between the permanent load or cyclic load and the total load, $\sigma_{s,l}$ the steel stress in the crack in MPa and s_a is the crack spacing in mm with ϕ the rebar diameter in mm and n the number of rebars.

A deflection stop criterion was proposed in [9] and it is based on the moment-curvature diagram developed by [11], which represents the decreasing of stiffness under first-time loading and unloading. The relation between the deflection and the curvature is the bending stiffness. The bending stiffness of the unloading branch after yielding has occurred, $(EI)_{te}$, is used to calculate the limit deflection (Δ_{vos}). It considers a 10% margin of safety and it is equal to Eq. (8), where ρ_0 is the tensile reinforcement ration in percentage and b is the width of the member.

Stop criteria for shear were based on the Critical Shear Displacement Theory(CSDT) [12]. This theory considers that the opening of the critical inclined crack starts with the opening of a dowel crack, which develops along the tensile reinforcement. The opening is triggered when the shear displacement of a flexural crack reaches a critical value (Δ_{cr}). In the CSDT, the shear capacity is equal to the sum of the shear transfer in the compression zone (V_c) determined with Mörsch's approach [13], the dowel action (V_d) calculated with the expression proposed by Baumann and Rüschi [14], and the

shear transfer by aggregate interlock (V_{ai}) using a simplified formulation based on Walraven's work [15].

A stop criterion for a limiting strain was proposed in [16]. It is based on the consideration that a flexural failure occurs after the development of flexural cracks and before the yielding of the reinforcement. First, the shear capacity is calculated according to the CSDT and then, the corresponding bending moment at the critical cross-section. The value of the curvature (ϕ_{CSDT}) is found by linear interpolation considering the cracking moment and the yielding moment. The strain at the bottom of the cross-section can be found with Eq.(3).

A stop criterion for a limiting crack width was proposed in [17]. The crack width (w_{ai}) is based on the simplified aggregate interlock formulation of the CSDT and it can be calculated with Eq. (5) with Δ_{cr} as the critical shear displacement, s_{cr} as the height of a fully developed crack, R_{ai} as a correction factor for high strength concrete ($f_c > 65$ MPa) and v_{RBK} as the shear capacity taken as the one prescribed in the Dutch Guideline for Assessment of Bridges RBK [18]. The proposal considers the value of 0.4 w_{ai} for elements not cracked in bending and 0.75 w_{ai} for elements cracked in bending.

Table 2 Existing theoretical stop criteria

Flexure	Shear
$\varepsilon_{stop} = \left[\frac{h-c}{d-c} \times \frac{0.65 f_{ym}}{E_s} \right] - \varepsilon_{c0} \quad (2)$	$\varepsilon_{CSDT} = 0.65 \left[\frac{h-c}{d-c} [\phi_{CSDT}(d-c)] \right] - \varepsilon_{c0} \quad (3)$
$w_{stop} = 2 \left[\frac{0.65 f_{ym} - f_{perm}}{E_s} \right] \beta_{fr} \sqrt{d_c^2 + \left(\frac{s}{2} \right)^2} \quad (4)$	$w_{ai} = \frac{0.03 f_c^{0.56} \frac{s_{cr}}{d} (-978 \Delta_{cr}^2 + 85 \Delta_{cr} - 0.27) + R_{ai}}{v_{RBK} + 0.01 mm}$ $s_{cr} = \left[1 + \rho_0 n_e - \sqrt{2 \rho_0 n_e + (\rho_0 n_e)^2} \right] d$ $\Delta_{cr} = \frac{25d}{30610 \phi} + 0.0022 \leq 0.025 mm$ $R_{ai} = 0.85 \sqrt{\left(\frac{7.2}{f_c - 40} + 1 \right)^2 - 1} + 0.34 \quad (5)$
$w_{Vos} = 0.9 [6.12 \beta f_{ym} s_a 10^{-6}]$ $s_a = \left(d_c + \frac{1}{2} \phi + 0.3 n \cdot \phi \right) \left(1 + \sqrt{\frac{1}{\rho_0 n}} \right) \quad (6)$ $w_{res, Vos} = 6.12 \beta \sigma_{s,1} s_a 10^{-6} \quad (7)$	
$(EI)_{te} = \left(\frac{-4.91 \cdot \rho_o^2 + 17.66 \cdot \rho_o + 117.72}{7.274 \cdot 10^{-4} \cdot f_{ym}^2 + \rho_o + 4} \right) b d^3 \cdot 10^2 \quad (8)$ $\Delta_{Vos} = 0.9 \iint \kappa dx = 0.9 \left[\iint \frac{M(x)}{(EI)_{te}} dx \right]$	

3 Experimental results

3.1 Laboratory beam tests

Two series of beam experiments served for the verification of the stop criteria. The beams were simply supported and subjected to a concentrated load. The first series, RSB, consisted of five tests on three beams sawn from the Ruytenschildt bridge [19]. One test resulted in shear failure and the other tests in flexural failure. The second series of tests, P, encompassed six tests on three beams cast in the laboratory reinforced with plain bars [20]. Two tests resulted in shear failure. In general, the beams were instrumented with LVDTs to record crack openings and strains, and laser distance sensors for the measurement of deflections. Fig. 1 shows photographs of the beam experiments.



Fig. 1 Left: Beam RSB03A after shear failure. Right: Beam P804A1 after flexural failure.

3.2 Proof load tests

Since 2007, a series of proof load tests have been carried out in the Netherlands [21]. Four bridges and viaducts were proof loaded: the viaduct Vlijmen Oost [22] (see Fig. 2), the Halvemaans bridge [23] (see Fig. 2), the viaduct Zijlweg [24] and the Viaduct De Beek [25]. Vlijmen Oost was tested in flexure, shear, and at the joint with a BELFA truck, because it presented material damage due to ASR. The maximum load was of 900 kN, however, the final assessment was carried out with finite element models since the applied load showed to be lower than the Eurocode serviceability limit state level. The Halvemaans bridge was tested for flexure using a steel spreader beam and hydraulic jacks. The maximum load was 900 kN, which directly proved that the bridge fulfills the requirements of the Renovation load level of RBK [18]. The ASR-affected viaduct Zijlweg was tested in flexure and shear using a system of a steel beam spreader, jacks, and counterweight. The maximum loads were 1368 kN and 1377 kN, respectively. The result of the tests was that the bridge fulfills the requirements of RBK Design levels. Viaduct De Beek was tested in the flexure with a load of 1751 kN and in shear with 1560 kN in the first span. However, the critical second span was not tested for safety reasons.

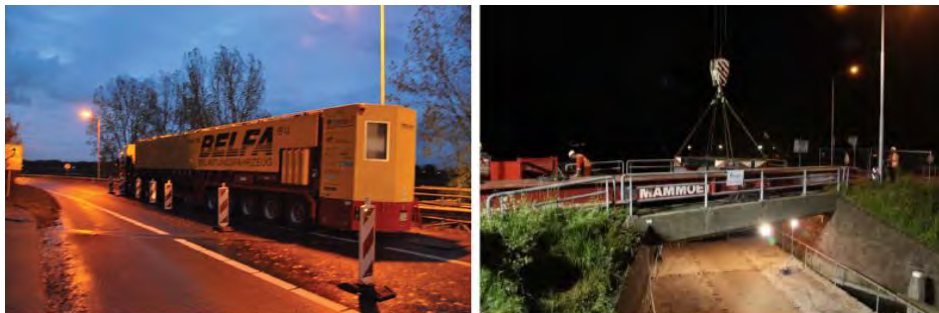


Fig. 2 Left: Viaduct Vlijmen Oost. Right: Halvemaans bridge[21]

3.3 Collapse test

A collapse test was performed on the Ruytenschildt bridge [19],[26]. Two spans were tested at a shear-critical position. In the first span, the maximum load of 3049 kN was limited by the available counterweight and only flexural distress was observed. In the second span, the maximum load was 3991 kN which caused a failure mode that was a combination of the settlement of the support and yielding of the reinforcement with large flexural cracking.

4 Verification of stop criteria

4.1 Comparison with failure tests

The tests in which failure was reached were used to study the margin of safety provided by the stop criteria for flexure and shear. This analysis was carried out for the results of the beam experiments (see Table 2 and Table 3) and the collapse test (see Table 4). The verified stop criteria included the strain limits, maximum and residual crack width and the deflection limit reviewed in the previous section. In addition to the limit of the 25% reduction of stiffness calculated from the load-deflection diagram (S), and the deformation profiles with for the longitudinal deflection (LD), the transversal deflection (TD), the horizontal deformation (HD) and the vertical deformation (VD).

From the results in Table 3, it can be observed that the governing criterion for most of the beams (highlighted in gray and bold) is the maximum crack width w_{stop} . The results from $w_{res, Vos}$ were neglected since the limit values were smaller than 0.05 mm, which resulted in the stop criterion being exceeded in the first load cycle. Regarding the deflection criterion Δ_{Vos} , it was not able to reflect accurately the effect of existing cracks on the stiffness of the beam. The stop criteria were exceeded between 42-70% of P_{max} .

Table 4 shows the results for the shear stop criteria. For the beam previously cracked in bending the governing criterion is the limiting strain $\varepsilon_{lim, CSDT}$ at 50% of the maximum load, for the uncracked beam three stop criteria (S, HD, and VD) were exceeded at 56% of F_{max} and for the beam from the RSB series, S and the HD were reached at 57% of the ultimate load. While the number of experiments is small, the results are promising: the range of percentages for which the first stop criterion is exceeded is between 50% - 57%.

Table 3 Overview of the margin of safety (% of F_{max} when the stop criterion is reached) for flexural

	ε_{DAfstB} [%]	ε_{stop} [%]	$w_{max, DAfstB}$ [%]	$w_{max, Vos}$ [%]	w_{stop} [%]	$w_{res, DAfstB}$ [%]	$w_{res, Vos}$ [%]	Δ_{Vos} [%]	S [%]	DH [%]	DV [%]
P502A1	64	71	96	70	70	-	-	96	-	-	-
P502A2*	62	81	100	56	52	-	-	99	100	84	84
P502B	63	67	93	51	50	67	42	78	67	-	-
P804A1	44	52	87	58	56	68	36	68	58	58	77
RSB01F†	54	53	99	72	53	54	45	91	28-99	54	54
RSB02A	53	62	-	69	64	-	15	69	-	42	42
RSB02B†	53	71	100	62	53	61	47	70	47-100	61	61
RSB03F	54	62	100	80	64	100	49	80	100	58	58

*previously cracked in bending

† two lasers measured the deflection under load (one on each side of the beam). The deflection measurements were unequal because the beam was not sawn completely straight.

Table 4 Overview of the margin of safety (% of F_{max} when the stop criterion is reached) for shear

	ε_{DAfstB} [%]	$\varepsilon_{lim, CSDT}$ [%]	$w_{max, DAfstB}$ [%]	$w_{ai, CSDT}$ [%]	S [%]	DH [%]	DV [%]
P804A2*	47	50	69	65	-	86	-
P804B	57	57	-	88	56	56	56
RSB03A	85	82	-	81	57	-	57

*previously cracked in bending

Table 5 provides an overview of the loads at which the stop criteria is exceeded for the collapse test on the Ruytenschildt bridge. For both spans, the stop criterion that was exceeded first was the deformation profiles. The criterion was exceeded at 62% of F_{max} for span 1 and 65% of F_{max} for span 2 in the longitudinal and transverse direction.

Table 5 Overview of the margin of safety (% of F_{max} when the stop criterion is reached) for flexural on Ruytenschildt bridge

	P_{estop} [kN]	P_{estop}/P_{max}	P_{wstop} [kN]	P_{wstop}/P_{max}	P_S [kN]	P_S/P_{max}	P_{LD} [kN]	P_{LD}/P_{max}	P_{TD} [kN]	P_{TDP}/P_{max}
--	---------------------	---------------------	---------------------	---------------------	---------------	---------------	------------------	------------------	------------------	-------------------

		[%]		[%]		[%]		[%]		[%]
Span1	$>P_{max}$	-	$>P_{max}$	-	1923	63	1900	62	1900	62
Span2	3377	85	3072	93	3159	79	2600	65	2600	65

4.2 Comparison with proof load tests

Table 6 and Table 7 show an overview of the results of the comparison of the measurements obtained during the tests and the proposed stop criteria. The crack widths smaller than 0.05 mm are neglected and taken equal to 0 mm. Therefore, the results from residual crack widths are not considered in the tables since most of them were negligible. The stop criteria that are verified are ϵ_{stop} , w_{stop} , S, LD and TD profiles. The stiffness of the Halvemaans bridge for the flexural test slightly increased during the loading protocol. For Vlijmen Oost no measurements were available of the deflection in the transverse direction. The results show that none of the stop criteria was exceeded during the pilot proof load tests. This conclusion corresponds with the measurements gathered with the extensive instrumentation during the pilot proof load tests, where no onset of nonlinearity was observed. The proposed stop criteria are adequate for the application to field testing. However, no information could be gathered regarding the margin of safety since we don't know the ultimate load.

Table 6 Comparison between the measurements obtained during the proof load tests and the stop criteria for flexure

	$\epsilon_c, \text{max measured}$ [$\mu\epsilon$]	ϵ_{stop} [$\mu\epsilon$]	$w_{max, measured}$ [mm]	w_{stop} [mm]	S	LD	TD
Vlijmen oost	80	869	0	0.15	3.7%	$>P_{max}$	NA
Halvemaans	150	729	0	0.11	-	P_{max}	$>P_{max}$
Zijlweg	240	842	0	0.17	4%	$>P_{max}$	$>P_{max}$
De Beek	887	919	0.12	0.13	18	$>P_{max}$	$>P_{max}$

Table 7 Comparison between the measurements obtained during the proof load tests and the stop criteria for shear

	$\epsilon_c, \text{max measured}$ [$\mu\epsilon$]	ϵ_{CSDT} [$\mu\epsilon$]	$w_{max, measured}$ [mm]	w_{ai} [mm]	S	LD	TD
Vlijmen oost	35	459	0	0.16	7.8%	$>P_{max}$	NA
Zijlweg	224	416	0	0.06	12%	$>P_{max}$	$>P_{max}$
De Beek	225	697	0.11	0.13	10%	$>P_{max}$	$>P_{max}$

5 Discussion and future research

The stop criteria for flexural and shear failure were evaluated. The stop criterion for limiting concrete strain for shear failure (ϵ_{CSDT}) proved to be more adequate in comparison to the limit proposed by the German guideline. Regarding the stop criteria for flexural failure proposed in [9], the results for residual crack width were not consistent and the limit values were smaller than 0.05 mm. The limit for maximum deflection did not reflect accurately the effect of existing cracks on the beams. Thus, these criteria are not suitable.

Table 7 shows the updated proposal for flexural and shear stop criteria. It includes four theoretically derived stop criteria: the limiting concrete strain (ϵ_{stop}) and the maximum crack width (w_{stop}) for flexural failure, as well as the limiting concrete strain (ϵ_{CSDT}) and the maximum crack width (w_{ai}) for flexural shear failure. The addition of ϵ_{CSDT} is an improvement to the previous proposal [7] since it has a theoretical background compared to the stop criterion from the German guideline that uses one limiting strain value. This proposal neglects all crack widths that are smaller than 0.05 mm. The limit for residual crack width w_{res} , was taken from the German guideline (see Table 1) and it is evaluated

after each cycle. For the case of a specimen previously cracked in bending, the crack widths can be taken as the width of a new crack or the increase of an existing crack. For all cases, the reduction of stiffness is limited to 25% and it is determined from the load-deflection diagram. Additionally, the proposal contains qualitative stop criteria: load-deflection diagram and the deformation profiles. The overall structural behavior can be assessed with the load-deflection diagram during and after the test. The deformation profiles can be determined with the deflection in the longitudinal and transversal direction and they provide an insight into the overall structural behavior.

The proposed stop criteria are promising, however, it is still necessary to continue studying the margin of safety with further experiments as well as to explore other parameters. In this paper, the margin of safety is defined as a percentage of the maximum applied load. It still requires the quantification in function of the accuracy of the deployed sensors, as well as the quantification of the uncertainties linked to the model and the theory, which are related to properties of the structure under consideration such as concrete compressive strength, size effect, etc. This topic is still under research, but will require modeling and simulation [27]. Moreover, research is needed to investigate the effects of the transverse redistribution of the load on slabs and the implication on the proposed stop criteria.

Table 7 Updated proposed stop criteria for flexural and shear

Failure mode	Not cracked in bending	Cracked in bending
Flexural	ϵ_{stop} $w_{max} \leq w_{stop}, w_{res} \leq 0.3 w_{max}$	ϵ_{stop} $w_{max} \leq w_{stop}, w_{res} \leq 0.2 w_{max}$
Shear	ϵ_{CSDT} $w_{max} \leq 0.4 w_{ai}$	ϵ_{CSDT} $w_{max} \leq 0.75 w_{ai}$
Flexural and shear	25% stiffness reduction, deformation profiles and load-deflection diagram	

6 Summary and conclusions

A proof load test consists of applying a factored lived load to structure to directly prove that it can carry the load and fulfill the code requirements without any signs of distress. Proof loading involves heavy loads, so it is necessary to monitor the structural responses during the test. Limits are given to the structural responses to avoid any irreversible damage; these limits are denoted as stop criteria. Some existing codes and guidelines provide stop criteria, however, they are limited to flexural failure and are usually related to serviceability requirements or single limit values.

Stop criteria for flexural and shear failure were proposed based on theoretical background. For flexure, the flexural beam theory was used to derive a stop criterion for limiting concrete strain and crack width [7]. For shear, the Critical Shear Displacement Theory was chosen to derive a stop criterion for limiting crack width [17] and limiting concrete strain [16]. The stop criteria include the limit of 25% of the reduction of stiffness and the evaluation of the deformation profiles.

The stop criteria were evaluated. First, the results from the two series of beam experiments and the failure tests on the Ruytenschildt bridge were used to analyze the margin of safety. The flexural tests had a margin of safety between 42 and 65% and for the shear tests the range was 50% to 57%. Thus, the stop criteria showed to have a sufficient margin of safety. Secondly, the stop criteria were compared to the results from the measured structural responses from the pilot proof load tests. The conclusion was that none of the stop criteria were exceeded and thus, the tests did not lead to irreversible damage.

The proposed criteria can be used for proof load testing, however, the number of experiments used to draw these conclusions is still limited, especially for the specimens failing in shear. Further experiments on slabs are needed for further validation in combination with noncontact measuring techniques.

References

- [1] FIB 2012, *Model Code 2010*. International Concrete Federation: Lausanne, Switzerland.
- [2] Lantsoght, E.O.L., C. van der Veen, and D.A. Hordijk. 2016. *Proposed stop criteria for proof load testing of concrete bridges and verification*. in *IALCCE*. Ghent, Belgium.

- [3] Lantsoght, E.O.L., *Verification of stop criteria for proof load tests*, in *Stevin Report*. 2017, TU Delft: Delft.
- [4] Deutscher Ausschuss für Stahlbeton, *DAtStb-Guideline: Load Tests on Concrete Structures (in German) DAfStb-Richtlinie : Belastungsversuche an Betonbauwerken*, D.A.f. Stahlbeton, Editor. 2000: Berlin.
- [5] ACI Committee 437, *Code requirements for Load Testing of Existing Concrete Structures (ACI 437.2M-13) and Commentary*. 2013, American Concrete Institute: Farmington Hills, MI.
- [6] Deutscher Ausschuss für Stahlbeton, *DAfStb-Guideline Load Tests on Concrete Structures (Draft) (in German) DAfStb-Richtlinie Belastungsversuche an Betonbauwerken (Entwurf)*, D.U.B.v. Bestandsbauwerken, Editor. 2019: Berlin.
- [7] Lantsoght, E.O.L., et al., 2019, *Stop Criteria for Flexure for Proof Load Testing of Reinforced Concrete Structures*. *Frontiers in Built Environment*. **5**.
- [8] Frosch, R.J., 1999, *Another Look at Cracking and Crack Control in Reinforced Concrete*. *ACI Structural Journal*. **96**(3).
- [9] Vos, W., 2016, 'Stop criteria for proof loading. The use of stop criteria for a safe use of 'Smart Proof loading'. **Master Thesis**. TU Delft, Master Thesis
- [10] Van Leeuwen, J., 1962, *About the cracking in slabs and beams (in Dutch) Over de scheurvorming in platen en balken*. *Heron* **10**(1): p. 50-62.
- [11] Monnier, T., 1970. *The Moment-curvature Relation of Reinforced Concrete*. Stevin-Laboratory of the Department of Civil Engineering, Delft University of Technology.
- [12] Yang, Y., J. den Uijl, and J. Walraven. 2016, *Critical shear displacement theory: on the way to extending the scope of shear design and assessment for members without shear reinforcement*. *Structural Concrete*. **17**(5): p. 790-798.
- [13] Mörsch, E., 1909. *Concrete-steel Construction: (Der Eisenbetonbau)*. Engineering News Publishing Company.
- [14] Baumann, T. and H. Rüsch. 1970, *Experimental study on dowel action in reinforced concrete beams (in German) Versuche zum Studium der Verdübelungswirkung der Biegezugbewehrung eines Stahlbetonbalkens*. Deutscher Ausschuss für Stahlbeton (DAfStb).
- [15] Walraven, J.C., 1981, *Fundamental Analysis of Aggregate Interlock*. *Journal of Structural Engineering-ASCE*. **107**: p. 2245-2270.
- [16] Benitez, K., E.O.L. Lantsoght, and Y. Yuguang. 2018. *Development of a Stop Criterion for Load Tests based on the Critical Shear Displacement Theory*. in *IALCCE*. Ghent, Belgium.
- [17] Lantsoght, E.O.L., 2017, *Development of a stop criterion for shear based on aggregate interlock*. **Stevin Report**(25.5-17-09): p. 33.
- [18] Rijkswaterstaat, *Guideline for Assessment of Structures, evaluation of the safety of a existing structure for renovation, reused and demoliton (in Dutch) Richtlijnen Beoordeling Kunstwerken, Beoordeling van de constructieve veiligheid van een bestaand kunstwerk bij verbouw, gebruik en afkeur.*, in *RTD 1006:2013*. 2013. p. 117.
- [19] Lantsoght, E.O.L., et al., 2016, *Ruytenschildt Bridge: Field and laboratory testing*. *Engineering Structures*. **128**: p. 111-123.
- [20] Lantsoght, E.O.L., et al., 2017, *Beam Experiments on Acceptance Criteria for Bridge Load Tests*. *ACI Structural Journal*. **114**(4).
- [21] Lantsoght, E., et al., 2017, *Proof load testing of reinforced concrete slab bridges in the Netherlands*. *Structural Concrete*. **18**(4): p. 597-606.
- [22] Fennis, S.A.A.M., et al., 2015, *Assessment of Viaduct Vlijmen Oost by Proof Loading*. **Stevin Report**(25.5-15-10): p. 126.
- [23] Fennis, S.A.A.M. and D.A. Hordijk. 2014, *Proof Load Halvemaans bridge in Alkamar(in Dutch) Proefbelasting Halvemaansbrug Alkmaar* **Stevin Report**(25.5-14-05): p. 72.
- [24] Koekkoek, R.T., E. Lantsoght, and D.A. Hordijk. 2015, *Proof loading of the ASR-affected viaduct Zijlweg in highway A59*. **Stevin report**(25.5-15-08): p. 189.
- [25] Koekkoek, R.T., et al., 2016, *Assessment of Viaduct De Beek by Proof Loading*. **Stevin Report**(25.5-16-01): p. 125.
- [26] Lantsoght, E., et al., 2016, *Collapse test and moment capacity of the Ruytenschildt reinforced concrete slab bridge*. *Structure and Infrastructure Engineering*. **13**(9): p. 1130-1145.
- [27] Schmidt, J.W., et al., 2020, *Challenges Related to Probabilistic Decision Analysis for Bridge Testing and Reclassification*. *Frontiers in Built Environment*. **6**.

Wave-based Indicators of Shear Failure in Reinforced Concrete Members without Shear Reinforcement: A Review

Fengqiao Zhang¹, Yuguang Yang¹, Gabriela Zarate Garnica¹, Max A.N. Hendriks^{1,2}

¹*Faculty of Civil Engineering and Geosciences,
Delft University of Technology,
Stevinweg 1, Delft (2628 CN), the Netherlands*

²*Department of Structural Engineering,
Norwegian University of science and technology (NTNU),
Rich. Birkelandsvei 1A, 7491 Trondheim, Norway*

Abstract

Many existing concrete members without shear reinforcement risk shear failure. As shear failure often leads to collapse of structural members, indicators of shear failure beforehand are needed for safety. According to the rational models of shear failure, some parameters, like crack width or stress, can serve as shear failure indicators. To measure these parameters, wave-based monitoring techniques stand out as they can work remotely and non-destructively. Based on literature, this paper links the measurable parameters from wave-based monitoring techniques with indicators for shear failure, and provides possible wave-based indicators of shear failure. This paper updates the understanding of wave-based measurements to a level of structural failure.

1 Introduction

Existing concrete structures without shear reinforcement may suffer from shear failure, which is brittle and often leads to the collapse of the structure. For safety reason, indicators of shear failure beforehand are needed. Based on the rational shear failure models, some measurable parameters, such as crack opening, stress, strain or force at critical locations, can be used as indicators.

A promising way to measure some of these indicators is to use wave-based techniques, as they can non-destructively detect changes in concrete, such as crack initiating and opening (Maji 1994), presence of existing cracks (Naik T.R. 1991, Zhang, Yang et al. 2018), and stress changes (Zhang, Planes et al. 2016, Kevinly, Zhang et al. 2020). Wave-based techniques can also detect the damages which are not measurable in traditional techniques, like the internal cracks.

This paper aims to identify possible wave-based indicators of the critical shear failures in reinforced concrete members without shear reinforcement. We first review the available shear failure models, including the failure mechanisms and the associated indicators. Then, by reviewing the principles and applications of the wave-based techniques relating to the shear failure indicators, we will suggest possible wave-based indicators. The involved techniques and theories are explained conceptually, with detailed derivation in the references.

2 Shear Failure of Reinforced Concrete Members without Shear Reinforcement

This section reviews the current understanding of shear behaviour of reinforced concrete members without shear reinforcement. We introduce the available shear failure models which were derived considering one or some of the shear transfer actions. In these shear models, measurable indicators of shear failure like crack opening and stress at critical positions were proposed.

2.1 Shear transfer actions

Four types of shear transfer actions along a flexural shear crack are widely accepted since 1970s (ACI-ASCE Committee 426 1973, ACI-ASCE Committee 445 1998). They are: shear stress in uncracked concrete, aggregate interlock at crack faces, residual tensile stress at limited normal opening of the cracks, and dowel action at the longitudinal bars. Considering a free body diagram along a crack cross section, the internal forces and the external forces should reach an equilibrium. The four shear transfer actions are visualized in Fig. 1.

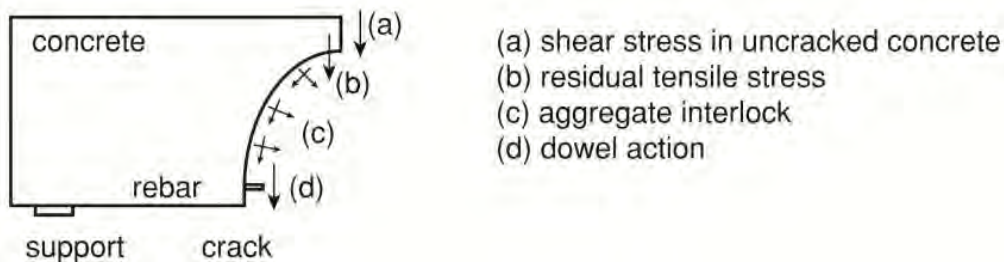


Fig. 1 Free body diagram with four shear transfer actions along a flexural shear crack.

Depending on whether the structure fails upon the flexural shear crack, two different failure modes can be distinguished: flexural shear failure and shear compression failure. The latter failure mode displays a higher shear capacity. But, there is an uncertainty on which shear failure mode will occur (Yang 2014, Yang, Walraven et al. 2017). Therefore, this paper focuses on flexural shear failure, which gives the lower bound of the shear capacity.

2.2 Shear failure models

Considering the fail of aforementioned shear transfer actions, researchers have developed multiple rational models to predict the shear failure and calculate the ultimate shear capacity. This section discusses the following models: tooth model, critical shear crack theory (CSCT), critical shear displacement theory (CSDT), and model by Tue et al..

Tooth model was first proposed by Kani (Kani 1964). In his work, flexural cracks shape the beam into a teeth-like structure (Fig. 2). Each concrete tooth works like a cantilever beam, with one end loaded by the reinforcement in the tensile zone, and the other end fixed at the compression zone. Breaking off of the tooth on the fixed end, which is also the crack tip, results in the shear failure of the beam. Combined with the fail of compression zone, Kani provided a famous Kani's valley, showing the shear capacity under different shear span ratio.

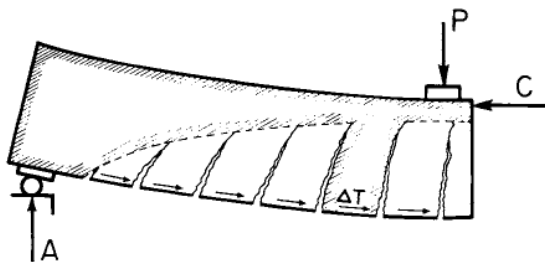


Fig. 2 Illustration of Kani's tooth model (Kani 1964).

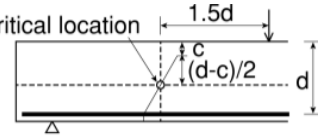
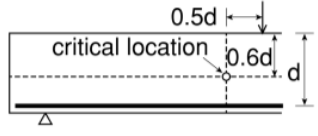
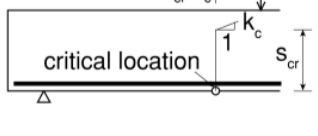
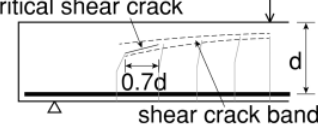
Further improvements were carried out by adding more shear transfer actions into the tooth model (MacGregor and Walters 1967, Fenwick and Pauley 1968). Reineck (Reineck 1991) included the crack friction (aggregate interlock), dowel action and shear in compression zone in the tooth model. In this approach, the teeth inclination is assumed to be 60 degrees. Reineck found that the main contributor of the shear capacity is the crack friction. According to aggregate interlock theory, larger crack width results in less crack friction. Therefore, he defined the critical crack width at a specific location which will lead to shear failure (Table 1).

CSCT was based on the crack location and crack width as they were found influencing the shear capacity (Muttoni and Fernández Ruiz 2008). When the shear crack goes through the compressive strut between the load and support, the shear capacity is reduced. He proposed a new shear transfer mechanism, which is a combination of elbow strut and direct strut. In the direct strut with shear crack, the compression force was transferred by aggregate interlock. Based on this new mechanism, he proposed that the shear capacity is related to the critical crack width/strain at a predefined cross section (Table 1).

CSDT considers dowel cracking as the trigger of shear failure (Yang 2014). Yang combined multiple shear transfer actions including shear in uncracked concrete, aggregate interlock and dowel action. In principle, the shear transferred by aggregate interlock can reach extremely high values with large shear displacements. But, this does not comply with the experiments. Yang found that the opening of dowel crack limits the shear capacity. With wider dowel crack, the aggregate interlock effect is reduced, thus needs further shear displacement, which again widens the dowel crack. This loop results in the collapse of the beam. He assumed a crack profile containing two branches: major branch perpendicular to the reinforcement and secondary branch at crack tip. He back-calculated the critical shear displacement from shear tests database, and proposed an approach of estimating the shear capacity based on the critical shear displacement at a certain location (Table 1).

The former models deal with the shear failure based on displacement like crack width, strain or shear displacement. Model by Tue et al. (Tue, Theiler et al. 2014) solves the problem differently based on fracture mechanics. Tue et al. studied the stress distribution over several cross sections along the beam. Based on this, they defined the concrete tension zone at the flexural crack tips as the shear crack band (Table 1). The critical shear crack develops in the shear crack band, when the principal tensile stress reaches the concrete tensile strength. But, cracking at one cross section doesn't necessarily cause a shear failure. Instead, the critical shear crack has to reach a defined length. Therefore, the failure indicator from this model can be the presence and length of critical shear crack.

Table 1 Summary of the discussed shear failure models.

Models	Description	Critical location	Failure indicator
Reineck's tooth model	Concrete tooth, formed by flexural cracks, breaks at failure. Shear is transferred by crack friction, dowel action and compression zone.		Critical crack width
CSCT	Compression force in the direct strut is carried by aggregate interlock. Shear failure happens when aggregate interlock fails.		Critical crack width/strain
CSDT	Dowel cracking is the trigger of shear failure. Shear is transferred by aggregate interlock, dowel action and compression zone.		Critical shear displacement
Model by Tue et al.	Shear failure happens when the critical shear crack reaches a certain length. Shear is transferred by uncracked and cracked concrete.		Presence and length of the critical shear crack

The aforementioned models disagree on the trigger of shear failure. But, these models are still valuable in understanding the shear failure, even with some limitations or criticisms. We can learn from these models in the following aspects:

- In Reineck's tooth model, CSCT and CSDT, aggregate interlock highly contributes to the shear capacity. Larger crack opening results in less aggregate interlock. Therefore, crack opening is strongly related to the shear capacity. Crack opening at critical location can be an indicator of shear failure.
- From tooth model and model by Tue et al., crack tip opening near the neutral line triggers the shear failure. Therefore, parameters related to crack tip activities can be shear failure indicators.
- Shear failure is considered starting from the crack tip opening, which in turn will result in loss of aggregate interlock and opening of dowel crack. The interaction of these three effects leads to the sudden collapse.

3 Wave-based Monitoring of Shear Failure

In the presented shear failure models for reinforced concrete members without shear reinforcement, crack opening is considered an important parameter in the formula of shear capacity. Based on the aforementioned models, some researchers proposed failure indicators related to the crack opening, like the crack openings in shear zone and flexural zone (Dieteren, Bigaj-van Vliet et al. 2017), crack opening in shear direction (Yang, Zárate Garnica et al. 2018) and the maximum flexural crack opening with the applied shear force (Benitez, Lantsoght et al. 2018). Therefore, displacement measurement techniques have been widely applied to measure the crack opening, including the displacement measurement at fixed locations like LVDT and laser, and full-field displacement measurement like digital image correlation (DIC) (Bergmeister 2003). These techniques measure the displacement directly from the change of relative location.

However, the direct displacement measurements require accessibility to the interesting zone. This challenges their detectability, especially for internal cracks. Wave-based technique is a promising solution as it can detect the damages remotely. The sensors don't need to be next to the inner cracks. Moreover, wave-based technique is very sensitive to changes in concrete, including cracking, the presence of cracks, and the stress changes.

With different working principles, wave-based technique generally can be categorized into two types: passive measurement, where source signal is generated by concrete changes like cracking, and active measurement, where source signal is sent by transducers. This section reviews the working principles and applications of the passive measurement and the active measurement. Based on this, a discussion on possible wave-based indicators of shear failure is carried out.

3.1 Passive measurement

Passive measurement often refers to Acoustic Emission (AE). Sudden changes in concrete, like cracking, will release energy which excites elastic waves. The elastic waves propagate to the AE sensors and are converted into electric signals. By continuously recording and processing the AE signals, AE can detect the damage process during loading (Ohtsu 1996). Researches have shown that AE is also powerful in detecting micro cracks in the early stage (Otsuka and Date 2000, Aggelis 2011, Lantsoght, Zhang et al. 2019).

By counting the received AE signals during loading, one can evaluate the structural damage level in terms of the maximum crack opening (Ohtsu, Uchida et al. 2002). In counting AE signals, AE hit is normally used as a term to indicate that an AE signal has been detected by a sensor (Ohtsu 2010). In a cyclic loading, two parameters related to AE hits were found valuable. One is load ratio, which compares the load at onset of AE hit with the previous load, and the other is calm ratio, which compares the number of AE hits during unloading with the total AE hits during the load cycle. Lower load ratio and higher calm ratio indicate the damage accumulation with larger crack opening.

Besides, the feature of an AE signal can provide more information on cracking. An AE signal can be described by several parameters, including amplitude, energy, rise time, averaged frequency, duration etc. The definition of these parameters can be found in (Ohtsu 2010). Cumulative AE energy was found related to concrete fracture process (Otsuka and Date 2000, Landis and Baillon 2002, Muralidhara, Prasad et al. 2010). Ratio between rise time and amplitude (RA), together with averaged frequency, can classify tensile cracks and friction (Ohtsu 2010). A more advanced classification method is clustering based on waveform. This method calculates the correlation distance between every two signals and groups signals with small distances. The clustering results based on waveform agree with the classification by parameters (Van Steen, Pahlavan et al. 2019). Since waveform analysis takes more computation time, to distinguish tensile cracks from friction, the analysis based on the signal parameters is considered sufficient.

AE monitoring can also locate the AE activities based on the arrival times, which is called AE source localization (Kundu 2013). This technique provides the location of the signal source. With sufficient accuracy (Zhang, Pahlavan et al. 2019), one can find the crack profile from the located AE activities. The accuracy of source localization can be improved by considering variable wave speed distribution (Pahlavan, Paulissen et al. 2014, Shiotani, Osawa et al. 2015, Gollob 2017). With the location information of AE activities, one can not only acquire the global damage condition, but also study the failure locally. An approach proposed by Zhang et al. divided the measuring zone and cumulate the AE hits in each cell (Zhang and Yang 2019). In this way, the local cumulative AE hits during unloading were found related to the local crack opening. They also indicated that this relationship required calibration for different measuring setup, as higher threshold resulted in less AE hits.

3.2 Active measurement

In active measurement, waves are sent into concrete by transducers. By comparing the received signals with the sent ones or the received signals at different loading stages, one can detect the changes in the concrete medium.

One application is to detect the presence of cracks. A widely-applied parameter is the wave speed obtained from the first arrivals, which will be reduced at the presence of cracks (M. Malhotra and Carino 2004). This technique is called Ultrasonic Pulse Velocity (UPV) (Naik T.R. 1991). A recent research found a certain relationship between wave speed and crack width (Du, Yang et al. 2018). By arranging a groups of sensors and performing UPV between every two sensors, multiple ray paths can be generated. Combining UPV results with the tomographic reconstruction techniques (Kak and Slaney 2001) can map the crack distribution in the measuring area. This is called wave speed tomography (Kobayashi, Shiojiri et al. 2006). Combined with AE source localization, further development is AE tomography (Schubert 2004), which uses AE as the source. The benefit of AE tomography is that we can have more ray paths covering the measuring area. As cracks not only reduce wave speed, but also lower the amplitude of the received signals, researchers also developed tomography algorithm based on the wave attenuation (Chai, Momoki et al. 2011).

Active measurement can also detect the stress changes in concrete. Acoustoelastic effect relates the stress change to the wave speed change (Hughes and Kelly 1953). Since the stress change can be very small, to amplify, multiply-scattered waves (coda wave) are used. This technique is called coda wave interferometry (CWI) (Snieder 2006, Stähler, Sens-Schönfelder et al. 2011). Combining CWI with sensitivity kernel for diffuse waves can map the stress changes in the measuring area (Zhang, Planes et al. 2016). A recent research found that CWI can also indicate the presence of cracks, as the correlation between coda waves with and without cracks was poor (Kevinly, Zhang et al. 2020).

3.3 Discussion on possible wave-based indicators of shear failure

Reliable wave-based indicators should have theoretical background of shear failure. Therefore, to propose wave-based indicators, an initial approach could be checking the measurable parameters that can reflect the shear failure mechanisms, especially the trigger of shear failure. Here, the proposed wave-based indicators remain in the conceptual stage. The critical values of these indicators related to the final failure remain to be explored.

From the available shear failure models, we understand that shear failure could be caused by the interaction of three activities: crack tip opening, loss of aggregate interlock and dowel cracking. Therefore, a detection of any above activity could inform us the activation of the interaction, which may lead to shear failure.

In measuring crack tip opening, AE is promising as it is sensitive to even micro cracking. Since cumulative AE energy has been found related to fracturing process, with the estimated location of AE activities, local cumulative AE energy at crack tip could serve as an indicator of shear failure. When local cumulative AE energy reaches a certain level, a local opening of crack tip is expected. Moreover, the length of critical shear crack, which is relevant in model by Tue et al., can be estimated from the localization results. Another possible indicator of crack tip opening is the wave speed change from coda. Wave speed change from coda is found related to stress change in concrete. When the stress level is near or over the tensile strength of concrete, crack tip opening may occur.

The loss of aggregate interlock can be monitored from two respects. Firstly, based on theory of aggregate interlock, friction often occurs between the protruding aggregates. This means AE signals from friction at the crack profile could be an indicator of presence of aggregate interlock. The AE signals from friction could be distinguished using clustering techniques, either based on parameter or waveform. In a loading step, if less AE signals from friction is found along the crack profile than before, possibly the crack surfaces lose aggregate interlock. On the other hand, aggregate interlock is highly influenced by the crack opening. Larger crack opening results in less aggregate interlock. Therefore, parameters that are related to the crack opening, like the local cumulative AE hits during crack closure or the wave speed from the first arrivals, could be indicators of loss of aggregate interlock.

Dowel crack opening can be indicated in a similar way as crack tip opening, by AE using the parameters local cumulative AE energy or wave speed change from coda. Regarding to measuring the shear displacement at dowel cracking, which is proposed in CSDT model, the indicator related to crack width could be used, which is the local cumulative AE hits during crack closure or the wave speed from the first arrivals.

4 Conclusions

The aim of this paper is to find possible wave-based indicators of shear failure for reinforced concrete members without shear reinforcement. This problem has been approached by reviewing the available shear failure models and the capabilities of wave-based monitoring. Several conclusions are made:

- Shear failure is considered starting from the crack tip opening, which in turn will result in loss of aggregate interlock and the opening of a dowel crack. The interaction of these three effects leads to the sudden collapse. Therefore, measures of any of these effects could be candidates for shear failure indicators.
- Crack tip opening can be indicated by local cumulative AE energy, which is related to fracturing process, or wave speed change from coda, which is related to concrete stress change.
- Loss of aggregate interlock can be indicated by AE signals from friction, or the crack width-related parameter, which is the local cumulative AE hits during crack closure or the wave speed from the first arrivals.
- Dowel crack opening can be detected in a similar way as crack tip opening.

As a summary, possible wave-based indicators of shear failure could be: local cumulative AE energy at the crack tip, local cumulative AE hits during crack closure along the crack profile, AE signals from friction along the crack profile, wave speed from the first arrivals, and wave speed from coda. The critical values of these indicators related to the final failure remain to be studied.

References

- [1] ACI-ASCE Committee 426 (1973). "The Shear Strength of Reinforced Concrete Members." *Journal of the Structural Division, ASCE* **99**(6): 1091-1187.
- [2] ACI-ASCE Committee 445 (1998). "Recent Approaches to Shear Design of Structural Concrete." *Journal of Structural Engineering, ASCE* **124**(12): 1375-1417.

- [3] Aggelis, D. G. (2011). "Classification of cracking mode in concrete by acoustic emission parameters." Mechanics Research Communications **38**(3): 153-157.
- [4] Benitez, K., E. O. L. Lantsoght and Y. Yang (2018). Development of a Stop Criterion for Load Tests based on the Critical Shear Displacement Theory. IALCCE. Gent, Belgium.
- [5] Bergmeister, K. (2003). Monitoring and safety evaluation of existing concrete structures: State-of-art Report, fib Fédération internationale du béton.
- [6] Chai, H. K., S. Momoki, Y. Kobayashi, D. G. Aggelis and T. Shiotani (2011). "Tomographic reconstruction for concrete using attenuation of ultrasound." NDT & E International **44**(2): 206-215.
- [7] Dieteren, G., A. Bigaj-van Vliet, Y. Yang and A. Sangers (2017). Development of a Smart Key Performance Indicator for In-Situ Load Tests. fib symposium. Maastricht.
- [8] Du, C., Y. Yang and D. Hordijk (2018). Experimental investigation on crack detection using imbedded smart aggregate. IALCCE 2018. Ghent.
- [9] Fenwick, R. and T. Pauley (1968). "Mechanism of shear resistance of concrete beams." Journal of the Structural Division **94**(10): 2325-2350.
- [10] Gollob, S. (2017). Source localization of acoustic emissions using multi-segment paths based on a heterogeneous velocity model in structural concrete, ETH Zürich.
- [11] Hughes, D. S. and J. L. Kelly (1953). "Second-Order Elastic Deformation of Solids." Physical Review **92**(5): 1145-1149.
- [12] Kak, A. C. and M. Slaney (2001). Principles of Computerized Tomographic Imaging, Society for Industrial and Applied Mathematics.
- [13] Kani, G. N. J. (1964). "The Riddle of Shear Failure and its Solution." ACI Journal Proceedings **61**(4).
- [14] Kevinly, C., F. Zhang, Y. Yang, D. Draganov and C. Weemstra (2020). A Study on Monitoring Multi-scale Concrete Members with Coda-wave Interferometry Using Embedded Transducers. Tenth International Conference on Bridge Maintenance, Safety and Management. Sapporo.
- [15] Kobayashi, Y., H. Shiojiri and T. Shiotani (2006). "Damage identification using seismic travel time tomography on the basis of evolutionary wave velocity distribution model." Proc. Structural Faults and Repair-2006 (Ed. M. Forde), June: 13-15.
- [16] Kundu, T. (2013). "Acoustic source localization." Ultrasonics **54**: 25-38.
- [17] Landis, E. N. and L. Baillon (2002). "Experiments to Relate Acoustic Emission Energy to Fracture Energy of Concrete." Journal of Engineering Mechanics **128**(6): 698-702.
- [18] Lantsoght, E. O. L., F. Zhang, G. I. Zárate Garnica, Y. Yang and R. Braam (2019). Measurement report of prestressed beams from Helperzoom viaduct. Delft University of Technology.
- [19] M. Malhotra, V. and N. Carino (2004). CRC Handbook on Nondestructive Testing of Concrete.
- [20] MacGregor, J. G. and J. R. V. Walters (1967). "Analysis of Inclined Cracking Shear in Slender Reinforced Concrete Beams." ACI Journal Proceedings **64**(10).
- [21] Maji, A. K. A. A. K. (1994). "Acoustic emissions from reinforced concrete." Experimental Mechanics **34**(4): 379-388.
- [22] Muralidhara, S., B. K. R. Prasad, H. Eskandari and B. L. Karihaloo (2010). "Fracture process zone size and true fracture energy of concrete using acoustic emission." Construction and Building Materials **24**(4): 479-486.
- [23] Muttoni, A. and M. Fernández Ruiz (2008) "Shear strength of members without transverse reinforcement as function of critical shear crack width." **105, No 2**, 163-172-163-172.
- [24] Naik T.R., M. V. M. (1991). The ultrasonic pulse velocity method. CRC handbook on nondestructive testing of concrete, CRC Press: 169-188.
- [25] Ohtsu, M. (1996). "The history and development of acoustic emission in concrete engineering." Magazine of Concrete Research **48**(4): 321-330.
- [26] Ohtsu, M. (2010). "Recommendation of RILEM TC 212-ACD: Acoustic emission and related NDE techniques for crack detection and damage evaluation in concrete: Measurement method

- for acoustic emission signals in concrete." Materials and Structures/Materiaux et Constructions **43**(9): 1177-1181.
- [27] Ohtsu, M. (2010). "Recommendation of RILEM TC 212-ACD: Acoustic emission and related NDE techniques for crack detection and damage evaluation in concrete: Test method for classification of active cracks in concrete structures by acoustic emission." Materials and Structures/Materiaux et Constructions **43**(9): 1187-1189.
- [28] Ohtsu, M., M. Uchida, T. Okamoto and S. Yuyama (2002). "Damage assessment of reinforced concrete beams qualified by acoustic emission." ACI Structural Journal **99**(4): 411-417.
- [29] Otsuka, K. and H. Date (2000). "Fracture process zone in concrete tension specimen." Engineering Fracture Mechanics **65**: 111-131.
- [30] Pahlavan, P., J. Paulissen, R. Pijpers, H. Hakkesteegt and R. Jansen (2014). Acoustic Emission on Health Monitoring of Steel Bridges.
- [31] Reineck, K.-H. (1991). "Ultimate shear force of structural concrete members Without Transverse Reinforcement Derived From a Mechanical Model (SP-885)." ACI Structural Journal **88**(5).
- [32] Schubert, F. (2004). Basic principles of acoustic emission tomography.
- [33] Shiotani, T., S. Osawa, S. Momoki and H. Ohtsu (2015). Visualization of Damage in RC Bridge Deck for Bullet Trains with AE Tomography, New York, NY, Springer New York.
- [34] Snieder, R. (2006). "The Theory of Coda Wave Interferometry." pure and applied geophysics **163**(2): 455-473.
- [35] Stähler, S. C., C. Sens-Schönfelder and E. Niederleithinger (2011). "Monitoring stress changes in a concrete bridge with coda wave interferometry." Journal of the Acoustical Society of America **129**(4): 1945-1952.
- [36] Tue, N. V., W. Theiler and N. D. Tung (2014). "Schubverhalten von Biegebauteilen ohne Querkraftbewehrung." Beton- und Stahlbetonbau **109**(10): 666-677.
- [37] Van Steen, C., L. Pahlavan, M. Wevers and E. Verstrynge (2019). "Localisation and characterisation of corrosion damage in reinforced concrete by means of acoustic emission and X-ray computed tomography." Construction and Building Materials **197**: 21-29.
- [38] Yang, Y. (2014). Shear Behaviour of Reinforced Concrete Members without Shear Reinforcement. PhD dissertation, TU Delft.
- [39] Yang, Y., J. Walraven and J. d. Uijl (2017). "Shear Behavior of Reinforced Concrete Beams without Transverse Reinforcement Based on Critical Shear Displacement." Journal of Structural Engineering **143**(1): 04016146.
- [40] Yang, Y., G. I. Zárate Garnica, E. O. L. Lantsoght and D. Hordijk (2018). Calibration of the shear stop criteria based on crack kinematics of reinforced concrete beams without shear reinforcement. fib congress.
- [41] Zhang, F., L. Pahlavan and Y. Yang (2019). "Evaluation of Acoustic Emission Source Localization in Concrete Structures." Structural Health Monitoring.
- [42] Zhang, F. and Y. Yang (2019). Acoustic Emission based Crack Tracking for Existing Concrete Structural Members. 9th International Conference on Acoustic Emission.
- [43] Zhang, F., Y. Yang, K. Hashimoto and T. Shiotani (2018). A comparative study of acoustic emission tomography and digital image correlation measurement on a reinforced concrete beam. IALCCE 2018. Ghent.
- [44] Zhang, Y. X., T. Planes, E. Larose, A. Obermann, C. Rospars and G. Moreau (2016). "Diffuse ultrasound monitoring of stress and damage development on a 15-ton concrete beam." Journal of the Acoustical Society of America **139**(4): 1691-1701.

Assessment of Existing Masonry Structures (The ARES project)

Ivan Hafner¹, Tvrtko Renić¹, Janko Koščak¹, Tomislav Kišiček¹, Mislav Stepinac¹

¹*University of Zagreb Faculty of Civil Engineering
Fra Andrije Kačića-Miošića 26, 10000 Zagreb, Croatia*

Abstract

It is well established that in Europe, masonry is one of the most commonly used materials in construction due to its characteristics and construction simplicity. In addition, the majority of buildings that have any cultural and historical significance in Europe are built in masonry. Seeing that most of these masonry structures were built before the development of seismic regulations, many of them need to be evaluated and, if needed, strengthened. Today, standards and guidelines for the assessment of existing masonry structures do exist but are not very comprehensive and require a lot of engineering subjective judgment to implement. Furthermore, the energy renovation of existing buildings is one of the most pressing matters in the construction sector today, but structural aspects are somewhat ignored and/or disregarded. Since great financial resources are intended for energy renovation throughout Europe, it seems that structural updating and strengthening can and must be an added value for the energy renovation of buildings. This specifically applies to masonry structures, which in most cases need seismic strengthening. The assessment techniques focus mainly on damage identification, damage localization and damage evaluation as well as determination of certain material properties of existing structures. The diagnoses are based on the design procedures of new structures and the planning of interventions often suggests reinforcement. The current practice of the assessment of existing structures might not be considered suitable to facilitate confident decisions about the reliability of structures. The main objective of the ARES project, partially presented in this article, is to study the role of assessment on the reliability analysis of existing structures.

1 Introduction

According to various literature and recent events, it is certain that masonry is one of the most commonly used materials across the world, due to its construction simplicity and characteristics. Despite the fact that the use of masonry as a building material in earthquake-prone regions pointed out its limitations (limited tensile resistance, relevant mass and stiffness), extensive research has been carried out in the last few decades mainly focusing on the material characteristics and structural behaviour of masonry, even under extreme loads such as earthquakes. These efforts enabled engineers to design masonry structures on sound and safe principles, with greater exactitude, economy and confidence. If it is taken into account that most of the buildings with high cultural significance and historical importance are built in masonry, it is quite clear that the assessment and rehabilitation of existing masonry structures must be conducted on a very high level.

The main goal of a seismic design is to protect property and lives in buildings in case of earthquake events. However, a proper seismic design should be developed on the knowledge gathered from existing structures. Past events have showed that seismic loads cause significant damage to masonry buildings due to their large mass and stiffness. Given that a great number of people across the world live and work in masonry buildings this represents a great risk. Furthermore, a huge number of these buildings were built before the development of seismic codes, so no confining or reinforcing elements exist. Based on all of the above, a concise strategy for masonry buildings must be activated.

The seismic behaviour of buildings depends on several important factors such as material properties, the geometry of a structure, stiffness properties and many more. Thus, the issue of seismic vulnerability of underperforming existing masonry structures is very complex [1]. “Seismic vulnerability” can be conventionally defined as a measure of the inadequacy of a given structure to resist to seismic actions [2]. Modern methods for the assessment of seismic vulnerability are represented by design curves which express the physical vulnerability as a function of the intensity of the process and the degree of loss [3]. However, when it comes to masonry, seismic vulnerability is quite difficult to

assess and it requires a number of specialized technical skills [4]. But are these methods in use applicable to the assessment of existing masonry buildings?

This question remains unanswered since extensive research needs to be carried out on the topics of seismic risk and vulnerability assessment. Traditional assessment methods, in most cases, are well-known to allow the assessment of only the actual condition of a given existing structure, once its stability has already been compromised. In this paper, assessment methods of critical properties (structural and material parameters) are presented for masonry structures. A focus is set on the available methods able to provide crucial data and feedback for preventing failure mechanisms and collapses under extreme design loads.

2 The Croatian Résumé

Approximately 75 % of Croatia's building stock is older than 30 years, an age requiring renovation/modification of primary structural components. More than 40 % is older than 50 years, meaning that the service life of these buildings has expired. Finally, in the building sector in Croatia, 40 % of the expenses are assigned to the demolition or rehabilitation of existing structures (Fig. 1 (left)) [5].

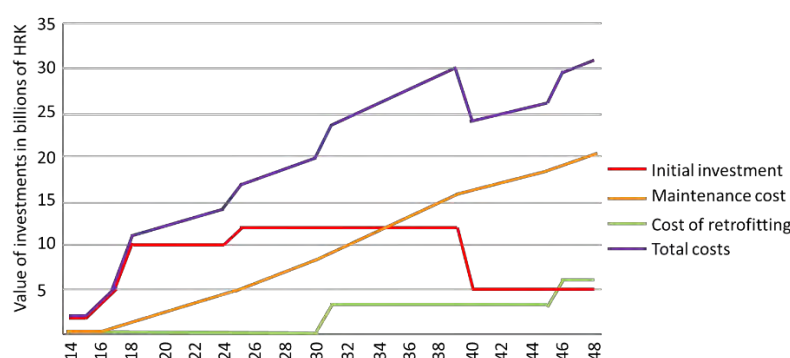


Fig. 1 (left) Investment (HRK) for the renovation of Croatian national building stock [5]; (right) Typical masonry building in Zagreb (photo by I. Hafner).

Most of Croatian buildings constructed in the period before the 1970s, when the seismic codes were introduced to the civil engineering community, were built using traditional construction materials such as masonry and timber (Fig. 1 (right)). Buildings were built as full-brick masonry structures with 30-60 cm thick walls and wooden ceilings. Unfortunately, it is recognized that in Croatia the majority of residential buildings older than 50 years are masonry structures without adequate bonding elements connecting the floors and the walls [6].

3 Maintenance issues of existing masonry structures

Existing structures can be divided into two groups regarding their value. Some buildings have a higher economical value like most of the modern buildings that exist today, and some buildings have a more non-material value like heritage structures (cultural and historical buildings).

Accordingly, the assessment of existing structures can be performed in different steps with a different level of precision. The level of precision depends on the importance of the building assessed and can be achieved by breaking down the assessment into phases. The number of these phases is dependent on a number of factors like the remaining level of doubt, simplicity and/or feasibility of repair etc. taking into account the economic aspects [7].

When it comes to masonry structures per se, a variety of assessment methods do exist, but their frequency and scope, the decision-making process and the necessary interventions are not yet agreed upon. The need for an assessment of an existing structure can come from a number of reasons [7]. Besides that, there may be situations where questions are raised regarding the design assumptions of a building. In the following scenarios a re-assessment of a structure might be necessary [8]: extended service life, change in utilization, required increase in the level of reliability, lack of maintenance and inspection, inadequate serviceability, exposure to extreme loads, availability of new knowledge gathered from negative experience from similar structures and revised design codes etc.

4 Assessment methods

Masonry structures are composite systems made from masonry units that are connected by mortar layers. Both can be made of different materials with different characteristics. Besides the type of the material used, the overall mechanical behaviour can be affected by a number of factors such as geometry of masonry units (length, width, height, volume of holes etc.), the thickness of mortar and the area it covers. For the assessment of masonry structures specifications of compressive strength are often required. Assessing the variability of these properties and the uncertainty in the modelling of the masonry compressive strength is hence a topic of great importance [9].

When it comes to existing structures the problem lies in the uncertainty of the strength classes of the materials used. Therefore, the assessment methods used should aim at identifying these properties with the highest degree of certainty so that the uncertainty regarding the resistance of a structure in whole is reduced to a minimum.

Parameters that are always measured during the assessment of a masonry structure are (a) the compressive strength of masonry units, (b) the compressive strength of masonry mortar, (c) the compressive strength of concrete infill (if any), (d) the strength of reinforcing steel bars (if any), (e) the compressive, shear and flexural strength of masonry, (f) the Modulus of Elasticity (MoE) and the geometry of the masonry structure (size and location of bearing walls, location and size of openings).

For obtaining these parameters several NDT (Non-Destructive Testing) methods are used and summarized in Table 1 and Figure 2.

Table 1 Available Non-Destructive Testing (NDT) assessment methods for existing masonry structures.

NDT Method	Device	What Is Measured?	How Is It Measured?	References
Visual inspection	/	Quality of masonry (mechanical parameters, dimension, shape), mortar and wall connections	Without a device, using a base/set of rules (i.e., Masonry quality index-MQI)	Borri et al. [10]
Measurement of reinforcement location	Ground Penetrating Radar (GPR)	Location (depth) of reinforcement	The device is placed on the measured surface and moved along a linear axis (with a calibration needed), transmitting radio wave signals into a structure and detecting echoes	Agred, Klysz and Balayssac [11]
Measurement of masonry unit hardness	Rebound hammer (Schmidt hammer)	Compressive strength of masonry units, mortars and built masonry	A predefined number of tests is conducted in both horizontal and vertical direction (with a calibration needed)	Breyse et al. [11], Sýkora et al. [12]
Stress wave transmission	Ultrasonic Pulse Velocity test (UPV) test/Resonant frequency test (RF)	Compressive strength of concrete or masonry	UPV-two transducers are placed on two sides of the specimen after which the time of wave travel is measured RF-a piezometric sensor is used with different attachment techniques to obtain resonant frequency	Sajid et al. [12]
Ultrasonic velocity testing	Impact hammer and accelerometer	Characterization of masonry wall homogeneity and variability	On opposite sides of the wall, an impact hammer and an accelerometer are placed. The mechanical impulse is gener-	Mesquita et al. [13]

			ated by the hammer striking the material and the signal is then received by the accelerometer.	
Sonic velocity testing	Impact hammer and accelerometer	Location of heterogeneities, voids or inclusions of other materials in masonry elements	On opposite sides of the wall, an impact hammer and an accelerometer are placed, after which the mechanical impulse is generated by the hammer striking the material and the signal is then received by the accelerometer	Martini et al. [14] Valluzzi et al. [15]
Surface penetrating radar	Ground Penetrating Radar (GPR)	Location (depth) of reinforcement, thickness of elements, position of voids and moisture content	The device is placed on the measured surface and moved along a linear axis (with a calibration needed) transmitting radio wave signals into a structure and detecting echoes	Martini et al. [14] Wai-Lok Lai, Dérobert and Annan [16]
Infrared thermography	Thermography cameras Visual IR thermometers	Defects in the building's envelope, the monitoring of reinforcing steel in concrete, the detection of moisture etc.	The specimen is under thermal stimulation and its surface temperature variation is monitored during the heating or cooling phase (the presence of inhomogeneity in a material causes local temperature variations)	Meola [17]
Borescope and mortar hardness with pendulum rebound hammer	Borescope and pendulum rebound hammer	Borescope-anomalies and internal wall components, such as ties, flashing and drainage cavities Pendulum rebound hammer-mortar type and strength	The borescope is inserted into small holes drilled into mortar joints (with fiber optics and internal light source) The pendulum rebound hammer utilizes a low energy impact and the resulting rebound from the surface of a mortar joint is used to measure surface hardness	Schuller [18]
Flat-jack tests	Flat jacks	Deformability parameters in compression, compressive strength and shear strength parameters	Two cuts are made with a predefined distance between them (horizontal cuts for compression, vertical cuts for shear), after which the jack is inflated with a liquid that transmits hydrostatic pressure	Parivallal et al. [19], Simões et al. [20],
Acoustic emission		The damage evolution in masonry, evaluation of the reliability of reinforcing techniques, analysis of residual capacity of masonry	A group of transducers are set to record signals, then locate the precise area of their origin by measuring the time for the sound to reach different transducers.	Invernizzi et al. [21]



Fig. 2 (left) Ground penetrating radar [14]; (middle) Pendulum rebound hammer [22]; (right) The flat jack test [23]

Supplementary to the assessment methods, a continuous Structural Health Monitoring (SHM) system might be of great use for a better understanding of the actual behaviour of a given structure. Since this way of monitoring a structure is quite useful, it should be seen as a goal to enhance the benefit of SHM by the utilization of applied decision analysis on how to assess the value of SHM even before it is implemented. By using SHM techniques the decision-making basis for the design, operation and life-cycle management can be much improved and can facilitate more cost-efficient and reliable strategies for maintaining and developing the built society [24].

5 The ARES Project

Maintenance of the building stock today is not only an issue that concerns the civil engineering community, but it is also an environmental, social and resource efficiency issue that should concern the general public.

The wide range of assessment methods presented in the previous paragraph shows that a big step forward has been taken in this field in recent years, but this has not yet changed the quality of assessment in regard to the evaluation of the reliability of an entire structure. Since most methods focus on the determination of local properties and damages that do not represent the properties and the capacity of an entire structure it is obvious why these methods are considered insufficient. Advanced methods for the assessment of existing structures make use of updated information but unfortunately that is not quite the case with masonry structures [25]–[27].

At this moment the assessment methods and the design checks of existing structures are not at the same level. Without high quality guidelines it is difficult to approach a problem which consequently results in a false interpretation of collected data and a wrong decision-making process for the rehabilitation of an existing structure. The development of investigation techniques for the updating of material properties will help with the uncertainties associated with the prediction of the structural behaviour of existing structures.

The ARES project, funded by the Croatian Science Foundation, was established with the idea of ironing out the mentioned insufficiencies. The aim is to deliver a basis for the advanced assessment and the design of existing structures, allowing a more economic design and a more accurate analysis of the consequence of failure. To sum it up, the idea is to improve the way assessment is carried out. Standard methods will be compared, and the necessary procedures will be determined to simplify assessment for practical use. Furthermore, it is aspired to develop general guidelines, to review the safety factors in place and to gather great knowledge about the building stock in Croatia in general. With the knowledge gained in this project, Croatian society of engineers will have an opportunity to actively participate in the research and will contribute (via National Standardization Committee) to a production of a new standard.

6 Conclusion

The Croatian and the European building stock consist of many masonry structures that are vulnerable to seismic activities. To reduce this vulnerability, they are strengthened with mostly steel and sometimes non-metallic reinforcement after the assessment is performed. Since sustainability is becoming a prevailing issue, the general aim seems to be shifting from building new structures to the maintenance of existing ones. That is why the assessment of structural behaviour and strengthening techniques are becoming a hot topic in the civil engineering society. However, many questions regarding seismic vulnerability and the assessment of masonry structures remain unanswered even with the tools and techniques that are already at disposal. One of the main issues lies in the fact that most of the historic and a great amount of residential buildings are built with masonry, so both the economic and cultural aspect are at risk. Also, in most cases the access to the interior of a building is not even possible so the array of assessment methods and retrofitting techniques decreases significantly. Furthermore, on a more global scale, energy efficiency is currently being improved in a lot of structures without any seismic or even structural considerations. Some simple solutions may lead to a large improvement in seismic behaviour, such as adding horizontal steel rods to ensure a box-type behaviour of a structure.

Most of the existing rules and standards regulate the design of new structures but the maintenance and if needed repair are not elaborated that well. Some guidelines and documents do exist, but they need to be improved. That is why further research about material properties and their variability, risk assessment and modelling are needed. Currently, there is a huge knowledge gap, especially in the assessment methods and design checks for existing structures, in every aspect of the assessment process.

First of all, it is very important to define which parameters need to be tested and which can be calculated or approximated (i.e. Is it necessary to measure mortar characteristics or are they similar for the Croatian building stock?). The plan of the project is to make case studies on existing masonry structures to form an exact procedure. Secondly, the idea is to find an economic approach for modelling such a series of structures since the current practice is usually either too complex or too simple. This will be achieved by modelling a structure with various input data and afterwards trying to assess the structure before the testing. The values will be compared to the ones provided by tests and models will be calibrated. This procedure will be repeated until a reliable system will be obtained. Thirdly, gaps exist in the way strengthening is ensured (which safety factors can be expected for a specific strengthening technique, masonry and standard practice characteristic of Croatia? How does strengthening influence the parameters for modelling? etc.).

The ARES project tries to address these shortcomings, allowing for a more economic design and a more accurate analysis of the consequences of failure.

Acknowledgement

This work has been fully supported-supported in part by Croatian Science Foundation under the project number UIP-2019-04-3749.

References

- [1] Negro, P. and Mola, E. 2017. "A performance based approach for the seismic assessment and rehabilitation of existing RC buildings," *Bull. Earthq. Eng.*, P. 10.1007/s10518-015-9845-8.
- [2] Barbieri, G. et al. 2013. "Assessing the seismic vulnerability of a historical building," *Eng. Struct.*, 523–535-57, P. 10.1016/j.engstruct.2013.09.045.
- [3] Papathoma-Köhle, M. 2016. "Vulnerability curves vs. Vulnerability indicators: Application of an indicator-based methodology for debris-flow hazards," *Nat. Hazards Earth Syst. Sci.*, P. 10.5194/nhess-16-1771-2016.
- [4] Lourenco, P. and Karanikoloudis, G. 2019. "Seismic behavior and assessment of masonry heritage structures. Needs in engineering judgement and education," *RILEM Tech. Lett.*, P. 10.21809/rilemtechlett.2018.76.
- [5] Republic of Croatia Ministry of Construction and Physical Planning 2014. "Proposal of the Long-Term Strategy for Mobilising Investment in the Renovation of the National Building Stock of the Republic of Croatia," Zagreb.
- [6] Sigmund, Z. et al. 2016. "Decision support model for seismic strengthening technology selection of masonry buildings," *Teh. Vjesn. - Tech. Gaz.*, 791–800-23, P. 10.17559/tv-

- 20151208142529.
- [7] Dietsch, P. and Kreuzinger, H. 2011. "Guideline on the assessment of timber structures: Summary," *Eng. Struct.*, P. 10.1016/j.engstruct.2011.02.027.
 - [8] Steiger, R. and Kohler, J. 2008. "Development of New Swiss Standards for the Reassessment of Existing Load Bearing Structures," in *CIB-W18 Meeting 41*, 2008.
 - [9] Dymiotis, C. and Gutleiderer, B. M. 2002. "Allowing for uncertainties in the modelling of masonry compressive strength," *Constr. Build. Mater.*, 443–452-16, P. 10.1016/S0950-0618(02)00108-3.
 - [10] Borri, A. et al. 2018. "Calibration of a visual method for the analysis of the mechanical properties of historic masonry," *Procedia Struct. Integr.*, 418–427-11, P. 10.1016/j.prostr.2018.11.054.
 - [11] Agred, K. et al. 2018. "Location of reinforcement and moisture assessment in reinforced concrete with a double receiver GPR antenna," *Constr. Build. Mater.*, 1119–1127-188, P. 10.1016/j.conbuildmat.2018.08.190.
 - [12] Sajid, S. H. et al. 2018. "Strength estimation of concrete masonry units using stress-wave methods," *Constr. Build. Mater.*, 518–528-163, P. 10.1016/j.conbuildmat.2017.12.044.
 - [13] Mesquita, E. et al. 2018. "Non-destructive characterization of ancient clay brick walls by indirect ultrasonic measurements," *J. Build. Eng.*, 172–180-19, P. 10.1016/j.jobbe.2018.05.011.
 - [14] Martini, R. et al. 2017. "Advances on the use of non-destructive techniques for mechanical characterization of stone masonry: GPR and sonic tests," *Procedia Struct. Integr.*, 1108–1115-5, P. 10.1016/j.prostr.2017.07.096.
 - [15] Valluzzi, M. R. et al. 2018. "Calibration of sonic pulse velocity tests for detection of variable conditions in masonry walls," *Constr. Build. Mater.*, 272–286-192, P. 10.1016/j.conbuildmat.2018.10.073.
 - [16] Wai-Lok Lai, W. et al. 2018. "A review of Ground Penetrating Radar application in civil engineering: A 30-year journey from Locating and Testing to Imaging and Diagnosis," *NDT E Int.*, 58–78-96, P. 10.1016/j.ndteint.2017.04.002.
 - [17] Meola, C. 2007. "Infrared thermography of masonry structures," *Infrared Phys. Technol.*, 228–233-49, P. 10.1016/j.infrared.2006.06.010.
 - [18] Schuller, M. P. 2003. "Nondestructive testing and damage assessment of masonry structures," *Prog. Struct. Eng. Mater.*, 239–251-5, P. 10.1002/pse.160.
 - [19] Parivallal, S. et al. 2011. "Evaluation of in-situ stress in masonry structures by flat jack technique," *Natl. Semin. Exhib. Non-Destructive Eval.*, 8–13.
 - [20] Simões, A. et al. 2012. "Flat-Jack Tests on Old Masonry Buildings," *15th Int. Conf. Exp. Mech.*, 3056-1.
 - [21] Invernizzi, S. et al. 2018. "Structural monitoring and assessment of an ancient masonry tower," *Eng. Fract. Mech.*, P. 10.1016/j.engfracmech.2018.05.011.
 - [22] Galvão, J. et al. 2018. "Variability of in-situ testing on rendered walls in natural ageing conditions – Rebound hammer and ultrasound techniques," *Constr. Build. Mater.*, 167–181-170, P. 10.1016/j.conbuildmat.2018.02.152.
 - [23] Łatka, D. and Matysek, P. 2017. "The Estimation of Compressive Stress Level in Brick Masonry Using the Flat-jack Method," *Procedia Eng.*, 266–272-193, P. 10.1016/j.proeng.2017.06.213.
 - [24] Stepinac, M. et al. 2018. "Condition Assessment of Timber Structures – Quantifying the Value of Information," in *IABSE SYMPOSIUM NANTES, 2018 Tomorrow's Megastructures International Association for Bridge and Structural Engineering*, 2018.
 - [25] Sýkora, M. et al. 2018. "Assessment of compressive strength of historic masonry using non-destructive and destructive techniques," *Constr. Build. Mater.*, 196–210-193, P. 10.1016/j.conbuildmat.2018.10.180.
 - [26] Vailati, M. et al. 2012. "Probabilistic assessment of masonry building clusters," *Proc. 15th World Conf. Earthq. Eng. - WCEE*, 9.
 - [27] Asteris, P. G. et al. 2019. *Stochastic Vulnerability Assessment of Masonry Structures: Concepts, Modeling and Restoration Aspects*, 9. 2019.

Seismic assessment of a RC frame building designed for gravity loads including joint deformation capacity model

Maria Zucconi¹, Marcello Sabene^{1*}, Stefano Pampanin², Barbara Ferracuti¹

¹ *Department of Engineering,
Niccolò Cusano University,
Via don Carlo Gnocchi 3, 00166, Rome, Italy*

² *Department of Structural and Geotechnical Engineering,
University of Rome "La Sapienza",
Via Eudossiana 18, 00184 Rome, Italy*

Abstract

In seismic Italian regions, the building stock is characterized by a large percentage of RC (Reinforced Concrete) Gravity Load Designed (GLD) frame buildings without seismic provisions and structural details. A significant number of earthquakes that caused great economic losses and casualties have highlighted the crucial role of correctly identifying the local and global frame mechanisms as the actual demand identification within frame sway mechanisms. In this paper, non-linear pushover analyses have been carried out to assess the seismic performance of a GLD case study building, both considering and neglecting the beam-column joints non-linear behavior and deformation capacity. The main goal is to investigate, in both cases, the significant difference in terms of predicted local hierarchy of strength, global system response, and seismic risk classes achieved. The latter classification has been evaluated using the simplified methodology recently introduced by the Italian Ministerial Decree No 58/2017.

1 Introduction

Worldwide seismic events are the unfortunate greatest demonstration and reminder of how existing reinforced concrete (RC) buildings have inadequate structural performance against horizontal actions. Their structural weaknesses are often related to the shear failure of the beam-column joints [1], [2], which were generally designed without stirrups in the panel zone connection and without adequate construction details, according to pre-seismic codes of the time [3]-[6]. Within the Italian building stock, it is estimated that 60% of the existing buildings have been constructed in what, at the time, were considered 'no-seismic areas', based on the obsolete seismic zone classification of the 1930-1940's [7]-[9]. Most of the pre-1970s reinforced concrete structures were not designed with capacity design philosophy, thus leading to a strong-beam and weak-column (soft-storey) mechanism. When further considering the likelihood of a brittle joint failure, the recurrent large number of victims and economic losses should not come – anymore – to a surprise [8], [10], urging for a retrofitting intervention [10]-[13] and, more appropriately, for a renewed proactive approach for the development of a coordinated national plan for seismic risk reduction [14]. In the recent past, experimental and numerical studies have focused on the evaluation of the seismic performances of poorly detailed beam-column joints. The strong seismic vulnerability of RC buildings opens different research topics for the development and validation of capacity models and analytical tools to reliably assess the seismic performance of joints.

In this paper, with the aim of highlighting the effect of joints deformability on the overall structural performance, an existing 2D RC frame has been modeled. Two types of joint modeling approaches are involved: the first one does not consider joint deformability, whereas the second one contains a simplified macro-model for the joint core, which takes into account the joint strength-deformation capacity [4], [6], [14]. The proposed frame has a strong beam-weak column hierarchy and the lack of proper transverse reinforcements in the joint panel leads to a premature shear failure. The first goal of this work is to compare, for the case study building, the differences between a classic modeling approach

that considers the panel zone as infinitely rigid, and a simplified modeling approach that takes into account the rotational capacity of the joint [6], [15]. The main differences in terms of global base shear-displacement curves, considering or neglecting joint deformability, through a non-linear static analysis, have been quantified. The simplified seismic risk class evaluation constitutes a further goal.

2 RC Frame building

An existing pre-1970 non-ductile RC frame building designed for gravity loads only and characterized by the absence of any seismic design criteria has been considered. The building is located in L'Aquila, Italy, on C soil class. This case study respects the construction rules observed for the gravity load design, so it is characterized by the lack of structural seismic details and, overall, by the absence of any Capacity Design (CD) principles, according to the Italian R.D. 2229/1939 and earlier [16]. The plan is rectangular in shape and has two bays (each of length 5 m) in the transverse direction and four (each of length 6 m) in the longitudinal direction. The structure spreads over four levels with an inter-floor height equal to 3 m, as shown in Fig. 1 (Left). The central frame, highlighted in the dashed red box of Fig.1 (Bottom), was used to conduct both non-linear static analysis and the seismic risk class evaluation, as well.

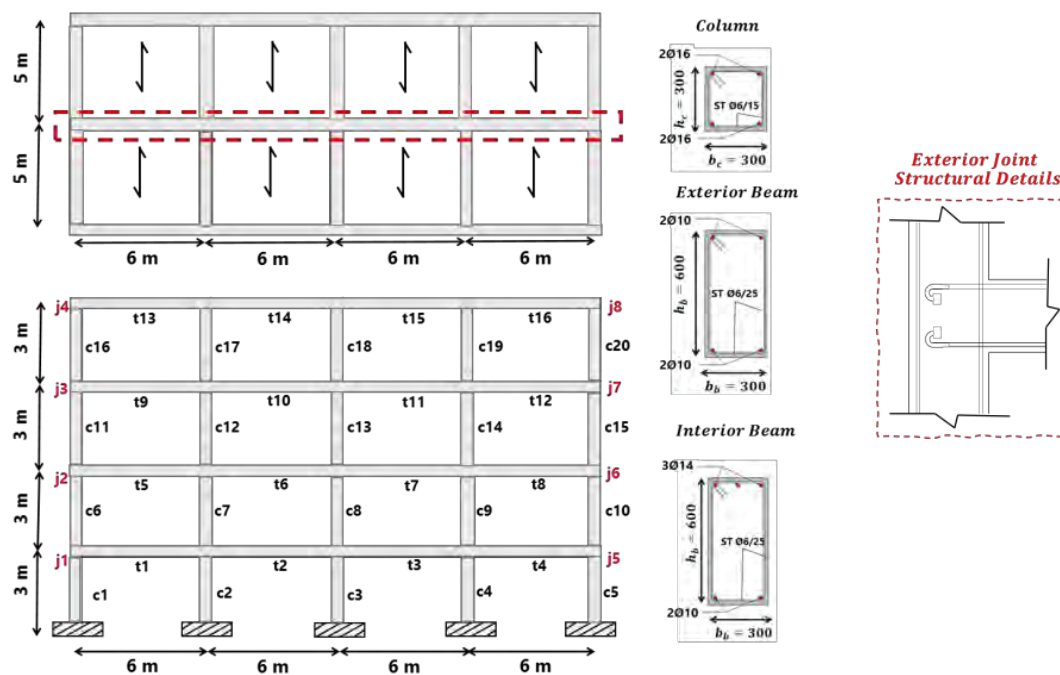


Fig. 1 (Left) Plan view, rectangular shape, bear frame front view, long side. (Middle) Element's cross-sections. (Right) Exterior joints structural details

The columns and beams sections are 300×300 ($b_c \times h_c$) mm² and 300×600 ($b_b \times h_b$) mm², respectively. Columns are reinforced symmetrically with two 16 mm reinforcing bars on the top/bottom section. Beams are reinforced as follows: at the external support with two 10 mm bars below and two 10 mm bars at the top; at the internal support with two 10 mm bars below and three 14 mm bars at the top, see Fig. 1 (Middle). No stirrups are present in the joint's panel zone (concrete core), as typical of most existing buildings in Italian and Mediterranean areas of the period, see Fig. 1 (Right). Regarding the materials choice, for the concrete, the cylindrical strength (f'_c) was chosen equal to 18 MPa and the elastic modulus (E_c) equal to 26243 MPa. Smooth bars of 10, 14, 16, and 6 mm in diameter were used as longitudinal and transverse reinforcement, respectively. The main steel properties were yielding stress (f_y) of about 321.2 MPa, ultimate stress (f_u) of about 463 MPa, and an elastic modulus (E_s) of about 200 GPa. As steel reinforcements, smooth mild steel bars Aq42 were used, according to the construction practice of pre-1970's existing buildings.

3 Global frame modeling including joint deformability

In the numerical model, the structural members are represented by lumped- plasticity beam elements. Once defined the elements geometry, reinforcement details, and material properties, the main goal was to predict the structural performance of the case study RC frame, with inadequate seismic structural details. A Force Based Plastic Hinge (FBPH) element, based on the flexibility formulation, was considered [17]. The FBPH element divides beams or columns into three parts: two hinges at the ends and a linear-elastic region in the middle. The length of each hinge was specified using Priestley formulation [7].

Regarding the joint panels, they are modeled in two ways: i) by rigid links, neglecting their deformability; ii) by rotational springs accounting both their deformability and their non-linear behavior.

For both models, for simplicity, the interior joints were modeled with rigid links neglecting their deformability and non-linear behavior (Fig. 2, Right), as they typically show a lower seismic vulnerability than the exterior ones due to a more reliable diagonal strut shear transfer mechanism even in the absence of specific stirrups.

Instead, the exterior joints were modeled with a simplified macromodel which considers the joint strength-deformation capacity through a rotational spring placed in the core of the joint panel [6], [15], as shown in Fig. 2 (Left). This spring can represent the joint behavior both in the linear and in the non-linear ranges. The linkage between the joint panel and converging elements (beams, columns) is modeled by rigid links. The joint spring moment-rotation characteristics are derived from the principal tensile, p_t , or compression stresses, p_c , versus the shear deformation, γ , relationship, where the principal (tensile or compression) stresses take into account the axial load acting on each joint. It has to be highlighted that, as part of a simplified modeling approach, the axial load for each joint is evaluated considering the gravity loading only while the axial load variation due to the seismic action is not directly modeled. Yet, in the evaluation of the hierarchy of strength of the beam-column joint within a M-N interaction domain [18], the variation of the axial load has to be taken into account.

In this way, the exterior beam-column-joint subsystem comprises of four areas of lumped plasticity, represented by a beam plastic hinge region, two column plastic hinge regions (both at the joint's interface), and a rotational spring in the joint panel when compared to the two areas of the interior one.

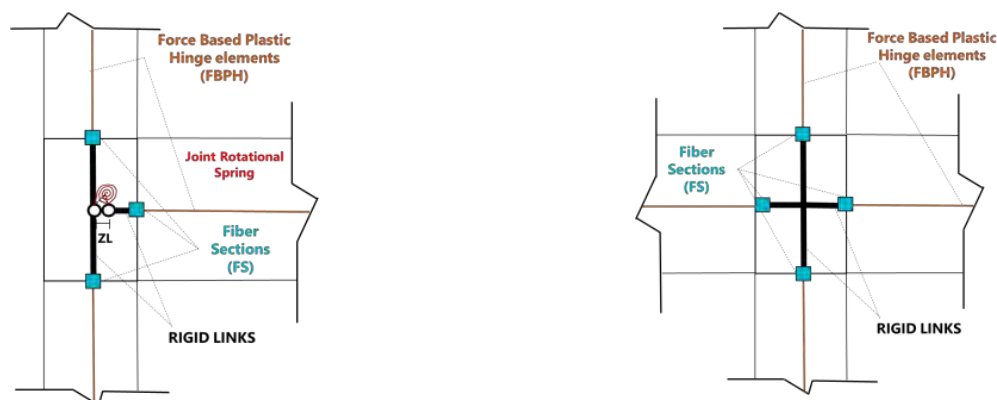


Fig. 2 (Left) External beam-column joint numerical model. (Right) Internal beam-column joint numerical model.

Exterior joint core spring was included through a Zero-Length (ZL) element and an elasto-plastic capacity-curve relationship was assigned to describe its behavior both in linear and non-linear range. Notably, in terms of cyclic behavior, a better hysteresis rule to describe the joint non-linear cyclic behavior should have pinched and stiffness degrading characteristics. However, the scope of the paper is to develop and assess simplified modeling approaches for the daily practice of engineers and such more complex rules are often not – or not yet - available in the library of typically adopted commercial softwares.

In Fig. 3 (Left), the capacity curves for the external joints are reported. They are all elasto-plastic and have the same rotation both at the yielding point and in ultimate conditions, according to NZSEE-2017 Seismic Assessment Guidelines [5,19]. This implies that each joint has a different capacity curve

for the bending Moment capacity M , which closely depends on floor axial load value N . Instead, according to [5,19] the deformation capacity is the same for each joint independently from the axial load. This aspect leads to the elastic sections having different K_0 slopes, moving from the smallest slope at the first floor to the greatest one at the last. The bending moment M , the axial load N , the K_0 slopes, and the joint rotations assumed are all reported in Fig. 3 (Middle) and (Right) tables.

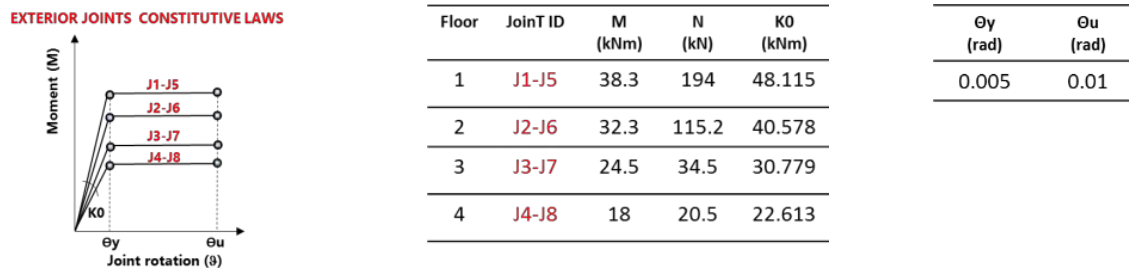


Fig. 3 (Left) External joints constitutive laws. (Middle) Tables with external joints capacity values. (Right) Exterior joints rotation values according to NZSEE2017 guidelines.

4 Failure criteria

Beams and columns deformation capacities, defined in terms of chord rotation θ , are strongly influenced by the lack of adequate seismic details in the longitudinal reinforcement, as well as by the type of bars used, whether they are smooth or/and cold-worked brittle steel. Inadequate development of the overlaps along the beam's length and columns height joined with an inappropriate anchoring within the beam-column joints can govern the element response against the seismic action, drastically limiting its capacity. The previously mentioned limitations on deformation capacity were therefore considered to verify the entire frame against horizontal actions.

According to EC8-Part 3 - Appendix A, deformation capacity and shear capacity checks for the overall frame elements were carried out. The following three failure criteria for beams and columns, according to EC8-Part3, were considered: chord rotation capacity at Light Damage limit state (LD), chord rotation capacity at Life Safety limit state (LS) and shear resistance at Life Safety limit state. Moreover, for the model where the non-linear behavior of exterior joints is included, another failure criterion was added. According to NZSEE-2017 Seismic Assessment Guidelines [17], as reported in section 3 joint ultimate rotation ($\theta_u = 1\%$) was considered as capacity criteria and a joint yielding rotation ($\theta_y = 0.5\%$) was adopted to represent the onset of the significant non-linear stage of the joint behavior.

5 Comparison and discussion of the results

A direct comparison between the numerical results obtained through the pushover analysis on the case study frame performed with the two models is reported in this section with reference to global response curves, damage distribution and interstory drifts reached at the considered limit states. The static pushover analysis was conducted using a force distribution proportional to the first modal shape.

Fig. 4 compares the top drift-base shear curves, which show the global structural response obtained both for the Rigid Joints (RJ) frame and for the Deformable Joints (DJ) frame, modeled considering exterior joint deformation capacity. Worth noting that the DJ frame (green curve) shows for the very early stages a softer behavior with lower initial stiffness. As a result, for the same base shear imposed, the DJ frame (green curve) developed higher top drift than the RJ frame (black curve), until the ultimate conditions for the DJ frame are reached, represented by the red cross on the green curve.

The points highlighted on the two global response curves represent the achievement of a certain limit state, as shown in Fig. 4. For the RJ frame, the chord rotation at LD and LS has been reported as the first and the ultimate damage condition, respectively. For the DJ frame, due to its different plastic hinges activation sequence, yielding and ultimate joint rotations have been considered as the first and the ultimate damage condition because they anticipate the achievement of chord rotation in the columns.

Globally, the RJ frame (black curve) appear to achieve remarkably higher values both in terms of strength and ductility when compared to the DJ frame (green curve). This phenomenon is due to greater plastic resources, which involve beams and columns elements within the RJ frame. However, these

apparent plastic resources derive from having neglected the joints deformation capacity in the RJ model; this leads its capacity curve to end at the first LS chord rotation achievement, represented by the red cross on the black curve. Instead, when considering the joints deformability, the DJ frame globally shows a much less ductile behavior than the RJ frame, so that its plastic resources end at the joint ultimate rotation achievement. This event concentrates the deformation demand in the joint panel region, changing the plastic hinges activation sequence in the DJ frame with respect to the RJ one.

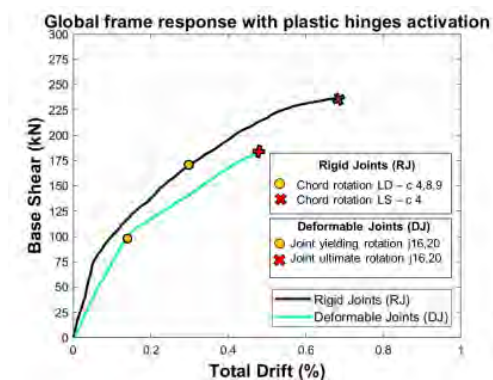


Fig. 4 Global force-displacement curves with failure criteria achievement. (Black) RJ backbone curve. (Green) DJ backbone curve. For elements labels see Fig. 1 (Left).

In Fig. 5 the damage distribution reached at different interstory drifts for both models is shown: flexural plastic hinges activation referred to beams, columns, and external joints are reported. Two different interstory drift values have been considered for the RJ frame, which correspond to the achievement of the chord rotation at LD and LS. In particular, the first cracking condition corresponds to chord rotation at LD limit state that occurs for a top drift value equal to 0.28% in columns c4, c8, and c9. Furthermore, the collapse condition coincides with the achievement of the chord rotation at LS limit state that occurs for column c4 for a top drift value equal to 0.67%. For the DJ frame, two interstory drift values have been considered, which correspond to the activation of yielding and ultimate joint rotation. The first one is reached at a top drift value equal to 0.15%, the second one at a top drift value equal to 0.48%.

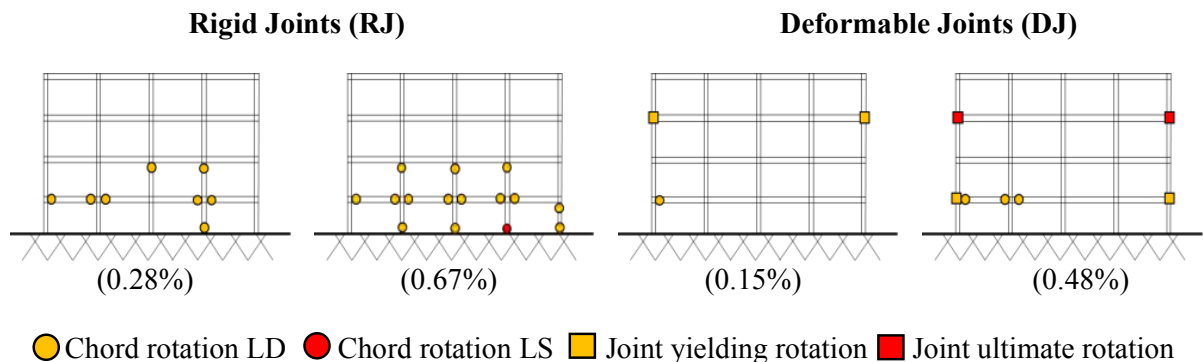


Fig. 5 Comparison of frame model response with and without exterior joint deformability. (Left) Damage distribution RJ frame. (Right) Damage distribution DJ frame.

From the different plastic hinges activation sequence, it is possible to deduce how the RJ frame involves the ductile resources of beams and columns belonging to the first and second floors, while the deformable DJ frame, unlocking the external joints rotation, concentrates the displacement demand in the joint panel regions with high damage at an early stage.

The graphs shown in Fig. 6 are referred to different limit states and they represent the capacitive displacements of the structure, according to the two models with rigid and deformable joints. For the RJ frame, the chord rotation at the reaching of LD and LS limit states is reported. For the DJ frame, due to its different collapse activation sequence, which involves the exterior joints, the yielding and ultimate joint rotation were chosen as failure criteria. As it can be observed in Fig. 6 (Left) in terms of total drift,

the RJ frame reaches higher displacements than the deformable one. This phenomenon, linked to the achievement of greater floor displacements, is closely connected to neglecting the joints deformation capacity. The same results are visible in Fig. 6 (Right) in terms of Interstory Drift Ratio (IDR), the RJ model shows high required deformation at first and second floor, instead in ultimate condition the DJ model shows limited required IDR in columns since the required deformation is concentrated in the joints with total drift of only 0.48%.

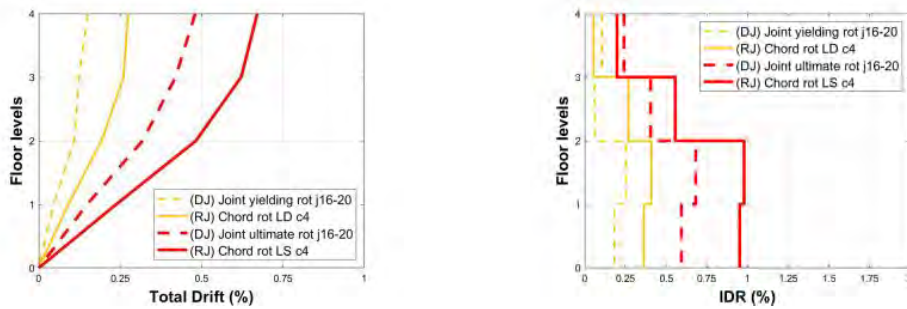


Fig. 6 (Left) Total drift. (Right) Interstory drift ratio. Solid lines are referred to Rigid Joints (RJ) frame, dashed lines are referred to Deformable Joints (DJ) frame.

6 Seismic risk classes

The aim of the present work is to compare the effect of rigid joint modeling with respect to the deformable one in terms of the structural performance and of economic seismic losses. For the loss assessment, different approaches can be adopted depending on the required level of accuracy. In this section, the simplified methodology introduced by the Italian Ministerial Decree No 58/2017 [20], accurately described in [21], was employed. According to this method, in order to assign the seismic risk classes for the two analyzed cases, two indicators are adopted. The first one consists in evaluating the building life Safety Index IS-V (conceptually equivalent to the %NBS in the NZSEE2017 Guidelines), defined as $= PGA_C / PGA_D$, where PGA_C and PGA_D are the capacity and demand peak ground accelerations at Life Safety limit state, respectively. The second one consists in evaluating the Expected Annual Losses (EAL), defined as the integral of the losses curve that, in the simplified methodologies, is discretized and substituted by a sum. More precisely, the losses curve was computed only for few limit states associated with a repair cost evaluated on collected post-seismic damage and consequences in terms of economic losses. The pairs of points (λ_i, RC_i) , where, for the i -th Limit State, $\lambda_i = 1/T_{rci}$ is the average annual frequency of exceedance, T_{rci} is the capacity return period and RC_i is the Repair Cost (defined a priori using the macroseismic data). Then, the EAL index is evaluated using the expression.

$$EAL = \sum_{i=2}^5 [\lambda_i - \lambda_{i-1}] \cdot \frac{[RC_i + RC_{i-1}]}{2} + \lambda(C-LS) \cdot RC(C-LS) \quad (1)$$

where the subscript i in (1) represents the i -th limit state, among those covered. Here C-LS denotes the Collapse Limit State. Moreover, it holds:

$$\frac{T_{rci}}{T_{rDi}} = (Sa(T_1)_{Ci} / Sa(T_1)_{Di}) \quad (2)$$

In (2) the term T_{rDi} is the demand return period for each limit state; $Sa(T_1)_{Ci}$ and $Sa(T_1)_{Di}$ are the spectral accelerations assessed with reference to the period T_1 , which have been used in order to evaluate the demand and the capacity of the structure. Using this simplified approach, the final Seismic Risk Class (SRC) is evaluated as the lower between the class associated to the IS-V index and the one associated to the EAL. In this work, the period T_1 has been evaluated from the modal response analysis, while the building performance, expressed in terms of spectral acceleration $Sa(T_1)_{Ci}$, and the corresponding PGA_C value, related to LD and LS limit states, has been evaluated by means of the N2 method [22]. In Fig. 7 are represented, only for the LS limit state case, the outcomes obtained by exploiting the ADRS spectra representation, showing the demand spectrum and the capacity one, evaluated by N2 method with the bi-linearized pushover curve of the equivalent single degree of freedom system. Subplots on the left are referred to RJ frame, those on the right to the DJ frame. The comparison between the two figures shows that the RJ frame capacity spectrum is greater than the DJ frame.

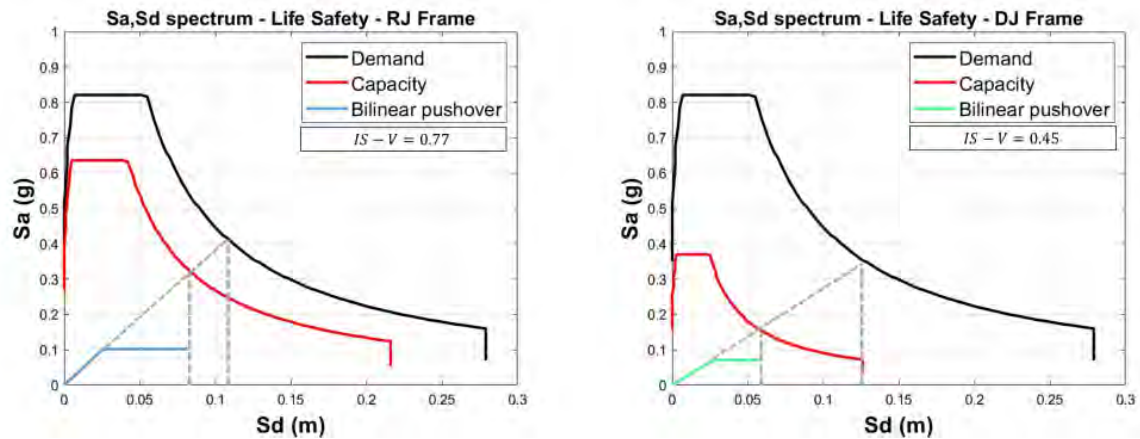


Fig. 7 ADRS spectra. (Left) RJ frame. (Right) DJ frame

The outcomes of the seismic risk analysis are summarized in Table 1. Notice that, neglecting the joints deformation capacity an incorrect estimation of the entire structure SRC is obtained. The RJ frame reaches a IS-V index equal to 0.77 (B class), and an EAL index equal to 1.5% (C class), so that its SRC class is C. On the other hand, the DJ frame reaches a IS-V index equal to 0.45 (C class), and an EAL index equal to 3.8% (E class), so that the final SRC class achieved is E.

Table 1 Safety Index, Expected Annual Losses, and Seismic Risk Class evaluation from results obtained by RJ frame and DJ frame models.

Reference Model	IS-V - class	EAL - class	SRC class
RJ Frame	0.77 - B	1.5% - C	C
DJ Frame	0.45 - C	3.8% - E	E

7 Conclusions

In this paper, a case study of a reinforced concrete building built before the 1970's, according to the Italian R.D. 2229/1939 and earlier, has been analyzed. It showed a high seismic vulnerability, due to its structural deficiencies - e. g. absence of transverse reinforcements in the joint panel, smooth bars, inadequate concrete cover, end-hook anchorage of beam bars. More precisely, the frame structure is characterized by a strong beam-weak column hierarchy, consistently with most gravity load-designed buildings. In the first instance, a pushover analysis was conducted, assuming a force distribution proportional to the first mode, in order to evaluate the structure capacity curves. The frame was used to highlight the importance of properly modeled the non-linear behavior of joints in order to detect a premature failure due to reaching the joint rotation capacity. A simple macro-model for the exterior joint was used for making it suitable also for practitioners. The joint rotation values were adopted by using NZSEE2017 prescriptions for the external joints [19]. The results obtained in terms of capacity curves, floor displacements, and interstory drift, shows how moving from the rigid joints frame to the deformable one, the plastic hinges sequence activation significantly changes. The rigid joints frame seems to own more significant ductile resources with respect to the other one. However, this outcome is attributable to modeling issues relative to the proper evaluation of the joint's capacity. In addition, an overestimation of the global capacity of the rigid joints frame leads to a rough evaluation of the seismic risk class that results lower for the rigid joints frame than for the deformable one. The RJ frame has an IS-V index equal to 77% and an EAL index equal to 1.5%, while the DJ frame has an IS-V index equal to 45% and an EAL index equal to 3.8%. In conclusion, the traditional modeling techniques, where the deformability and the non-linear behaviour of the joint panel zone are neglected, can lead to substantial and unconservative under-estimation of both seismic safety and seismic losses. Furthermore, an incorrect 'diagnosis' can clearly lead to an inadequate 'prognosis' and 'therapy', i.e. retrofit intervention. It should thus be highly recommended to include simple yet reliable modeling approaches for the non-linear behavior of the exterior joint as part of the daily practice of engineers as part of the vulnerability assessment and retrofit strategies definition of existing RC building.

Acknowledgements

The authors wish to acknowledge the financial support received by the Italian Department of Civil Protection (ReLUIS 2019-2021 Grant – Inventory of existing structural and building types- CARTIS).

References

- [1] Masi A., Santarsiero G., Lignola G. P., and Verderame G. M., “Study of the seismic behavior of external RC beam-column joints through experimental tests and numerical simulations”, *Eng. Struct.*, vol. 52, pp. 207–219, 2013.
- [2] Shayanfar J., Bengar H. A., and Parvin A., “Analytical prediction of seismic behavior of RC joints and columns under varying axial load”, *Eng. Struct.* 174 (2018) 792-813.
- [3] Calvi G., Magenes G., and Pampanin S. (2002). “Relevance of beam-column joint damage and collapse in rc frame assessment”. *J. Earthq. Eng.*, 6, 75-100.
- [4] Pampanin S., Calvi G. M., and Moratti M., “Seismic behaviour of R.C. Beam-column joints designed for gravity loads”, *12nd European Conf. on Earthquake Engineering*, 2002, Paper 726.
- [5] Pampanin S., Magenes G., and Carr A., “Modelling of shear hinge mechanism in poorly detailed RC beam-column joints”, *fib Symposium Concrete Structures in Seismic Regions*, 2003, 171.
- [6] De Risi M. T., Ricci P., and Verderame G. M., “Modelling exterior unreinforced beam-column joints in seismic analysis of non-ductile RC frames”, *Earthq. Eng. Struct. Dyn.*, 46, no. 6, pp. 899–923, May 2017.
- [7] Priestley, M. J. N. “Displacement-based seismic assessment of reinforced concrete buildings”, *J. Earthq. Eng.*, 1(1), 1997, 157–192.
- [8] Romano F., Faggella M., Gigliotti R., Zucconi M., and Ferracuti B., “Comparative seismic loss analysis of an existing infilled RC building based on element fragility functions proposals”. *Eng. Struct.* 2018; 177: 707–723.
- [9] Zucconi M., Sabene M., Kioumars M. and Ferracuti B., “Pre-code RC Bare Frame: seismic retrofit with alternative strategies”, *AIP Conference Proceedings* 2293, 240004 (2020);
- [10] Pampanin S., “Alternative Performance-Based Retrofit Strategies and Solutions for Existing RC Buildings”, Chapter 13 (pp. 267-295) in *Seismic Risk Assessment and Retrofitting*, Geotechnical, Geological, and Earthquake Engineering 10 (Editors A. Ilki et al.), 2009.
- [11] Pampanin, S., “Towards the practical implementation of performance-based assessment and retrofit strategies for RC buildings: challenges and solutions”, *SMAR2017- 4th Conf. on Smart Monitoring, Assessment and Rehabilitation of Structures*, Keynote Lecture, Sept. 2017, Zurich.
- [12] Ferracuti B., Savoia M., and Zucconi M., “RC frame structures retrofitted by FRP-wrapping: A model for columns under axial loading and cyclic bending”. *Eng. Struct.* 2020; 207: 110243.
- [13] Romano F., Alam M.S., Zucconi M., Faggella M., Barbosa A.R., and Ferracuti B., “Seismic demand model class uncertainty in seismic loss analysis for a code-designed URM infilled RC frame building”. *Bull. Earthq. Eng.* 2021; 19(1): 429–462.
- [14] Sabene M., Zucconi M., Ferracuti B., and Pampanin S., “Open Issues on Testing and Modeling Existing RC Beam-Column Joints”, *AIP Conference Proceedings* 2293, 240002 (2020).
- [15] O’Reilly G. J., and Sullivan T. J., “Modeling Techniques for the Seismic Assessment of the Existing Italian RC Frame Structures”, *J. Earthq. Eng.*, 2469, 1–35, 2017.
- [16] Regio Decreto, 1939 16 Novembre 1939 –XVIII, n. 2228.
- [17] Scott M. H., and Fenves G.L., “Plastic hinge integration methods for force-based beam-column elements”, *J. Struct. Eng.*, Vol. 132, No. 2, February 1, 2006.
- [18] Pampanin S., Bolognini D., and Pavese A., “Performance-Based Seismic Retrofit Strategy for Existing Reinforced Concrete Frame Systems Using Fiber-Reinforced Polymer Composites”, 2007, *J. Compos. Constr.*, Vol. 11(2), 211-226.
- [19] NZSEE (2017). "New Zealand Society for Earthquake Engineering, Wellington, New Zealand.
- [20] Ministry Decree n.58 28/02/2017 Allegato A: linee guida per la classificazione del rischio sismico delle costruzioni (in Italian). Italian Ministry of Infrastructures and Transport, Italy. [http://www.mit.gov.it/norma tiva/decre to-minis teria le-numer o-58-del-28022 017](http://www.mit.gov.it/norma%20tiva/decreto-ministeriale-n-58-del-28022017)
- [21] Cosenza E, Del Vecchio C, Di Ludovico M, Dolce M, Moroni C, Prota A, and Rendi E. The Italian guidelines for seismic risk classification of constructions: technical principles and validation. *Bulletin of Earthquake Engineering* 2018(July).
- [22] Fajfar P. A nonlinear analysis method for Performance-based Seismic Design. *Earthquake Spectra* 2000; 16(3): 573–592.

Fatigue of concrete structures

Cyclic Shear Response of Reinforced Concrete Dapped-End Beams (RCDEBs) Under Bond Deterioration

Ajibola Ibrahim Quadri¹ and Chikako Fujiyama²

¹Graduate School of Urban Innovation,

²Faculty of Urban Innovation,

Yokohama National University,

79-5 Tokiwadai, Hodogaya-ku, Yokohama 240-8501, Japan

Abstract

The shear response of the reinforced concrete dapped end beams (RCDEBs) undergoing cyclic loading experimentally and moving loading analytically under bond deterioration of the RC composite was examined. PVC hollow pipe was adopted for bond loss at the inaccessible recessed corner to form the RC composite bond loss in experiment. Cyclic loading using a universal testing machine was carried out on the test beams by adopting a minimum confirmed static capacity of 15% with the same percentage increment until failure. By using the interface element considering the bond loss, the numerical assessment was extended to the moving load by the direct path integral scheme. The beam failure depends on the loading point and the position of bond deterioration.

1 Introduction

Over the decades, due to the rise in economic activity and population, many existing reinforced concrete bridges have faced frequent vehicular overloading, and many structural failures have been reported. The long-term fatigue loading results in the deterioration of the bridge structures' service life. Some are also confronted with environmental effects such as the freezing and thawing effect, the occurrence of carbonation by acid rain, and the ingress of chloride ion that affect the existing reinforced concrete structures, resulting in corrosion effects and reducing the structures' durability in general, Fig. 1. As many researchers provided qualitative reports on fatigue damage, some of these structures lack quantitative service life assessment. As such, Adequate design to assess the degree of risk presented and to ensure impregnability of the fatigue damage-prone structural member to collapse during service life.



Fig. 1 Dapped end beam and corbel corrosion: Granada, Spain (left) and M-30, Madrid (right) [1]

This study focuses on the performance response of reinforced concrete dapped end beams (RCDEB) under sustained cyclic loading and bond degradation of its critical section due to bond loss caused by corrosion. (RCDEB) can be used as replacements for precast members of bridge girders. They are recessed at the ends and supported by cantilevers, columns, corbels, or inverted T-beams [2]. RCDEB increases the flexibility of the structural support members laterally, it can also minimize the total height distance of the precast concrete frameworks and there is often a decrease in its self-weight due to a change in the cross-section of the re-entry portion [3]. However, the cross-sections of the RCDEBs used in the construction are weakened at the re-entrant corner near the support due to the discontinuity region (D-region) [4], this disrupts the flow of internal stress in the members and induces a stress concentration at the re-entrant portion of the beam, which can lead to cracking if adequate stiffness is not provided. In addition, the investigation of the RCDEB anchorage zone in the bridge

girder is often difficult due to the presence of recess portions on other structural parts, the retention of water or soiled materials on these sections, which accelerates the deterioration of concrete beam by causing corrosion of the reinforcing bars. In reinforced concrete frameworks, the reinforcing bar lugs create the mechanical benefit of the bond mechanism, so the concrete crack is due to the issue of durability. On the one side, cracks decrease the service life of structures due to the entrance of the corrosion agent to the reinforcement, on the other hand, the guarantee of concrete consistency and the thickness of the cover are the necessary criteria for avoiding steel corrosion in concrete.

It is known from the reassessment of the current literature that numerous assorted works have been carried out on the RCDEB response under static loading conditions [4],[5], but that the experimental and analytical examinations of the RCDEB fatigue behavior are inadequate, as is the effect of the deterioration of the RC composite bond on the RCDEB anchorage region, on the load-bearing capacity and the response. Therefore, this research aims to understand the behavior of these beams in such circumstances through experimental under low fatigue loading and numerical analysis under the moving wheel load.

2 Methodology

The struts-and-Tie inclination method set out in Eurocode 2 [6] was implemented in the detailing of the RCDEB to gain the efficiency of the amount of shear reinforcement required Fig. 2 (left). The concrete stress permeating across the nib is resisted by the tension force in the web reinforcement positioned near the full-deep end of the beam. Additionally, the capacity of the undapped end is often dictated by the diagonal tension crack, which is mainly triggered at the recessed corner and from the full depth corner of the beam. Six dapped end beams (labeled S0-S5) were planned and cast to test the performance of the DEB under bond deterioration. 9 mm diameter deformed bar is designed to withstand the forces emanating from the nib area at a spacing of 150 mm, whereas the 210 mm spacing is used for the stirrups in the middle part of the beam. The 22 mm deformed bar is built for all longitudinal reinforcements, both at the re-entrant corner (nib) and at the maximum bottom depth of the beam as shown in Fig. 3 (left), so that the reinforcements will reach their yield strength before the final failure. The hollow PVC pipe, 140 mm long and 27 mm inner diameter was used to create a deterioration of the bond between the longitudinal reinforcement and the concrete. Silicon gum was infused within the PVC hollow pipe and the longitudinal reinforcement was inserted into the PVC pipe as shown in color red as shown in Fig. 3b. The dimensions of the RCDEB is also presented. S0 is a control beam with no bond loss loaded monotonically at the shear span to the depth ratio ($a_v/d=1$). S1 and S5 have the same bond losses in the nib section, the bond losses in S3 and S4 are included in the flexure region. S5 was also subjected to static loading at the midpoint, while the rest of the beams were assessed experimentally under the low cycle fatigue conditions. S2 and S3 were loaded at $a_v/d=1$, and S1 and S4 were cyclically loaded at the midpoint. The constituents of the concrete mix adopted for the investigation are ordinary Portland cement, fine aggregate, and coarse aggregate with a maximum size of 20 mm, mixed at a ratio of 1:1.6:2.94 by weight of cement. The water-cement ratio (w/c) of 0.43 and the air-entraining water-reducing of 0.5% of cement were used. The results of the load-displacement for S0 and S5 are presented in Fig. 3d.

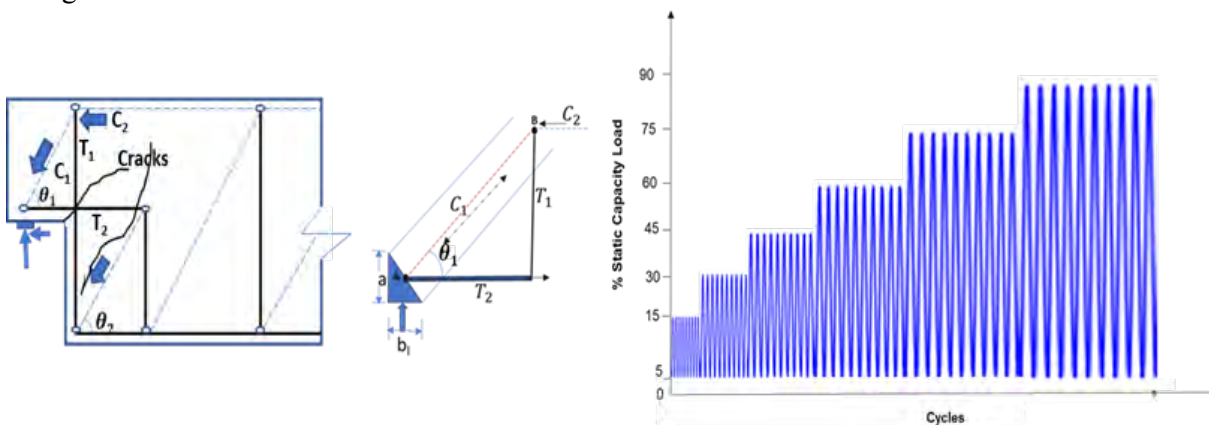


Fig. 2 Struts and Tie approach for DEB (left) and Pattern of Cyclic Amplitude Loading (right)

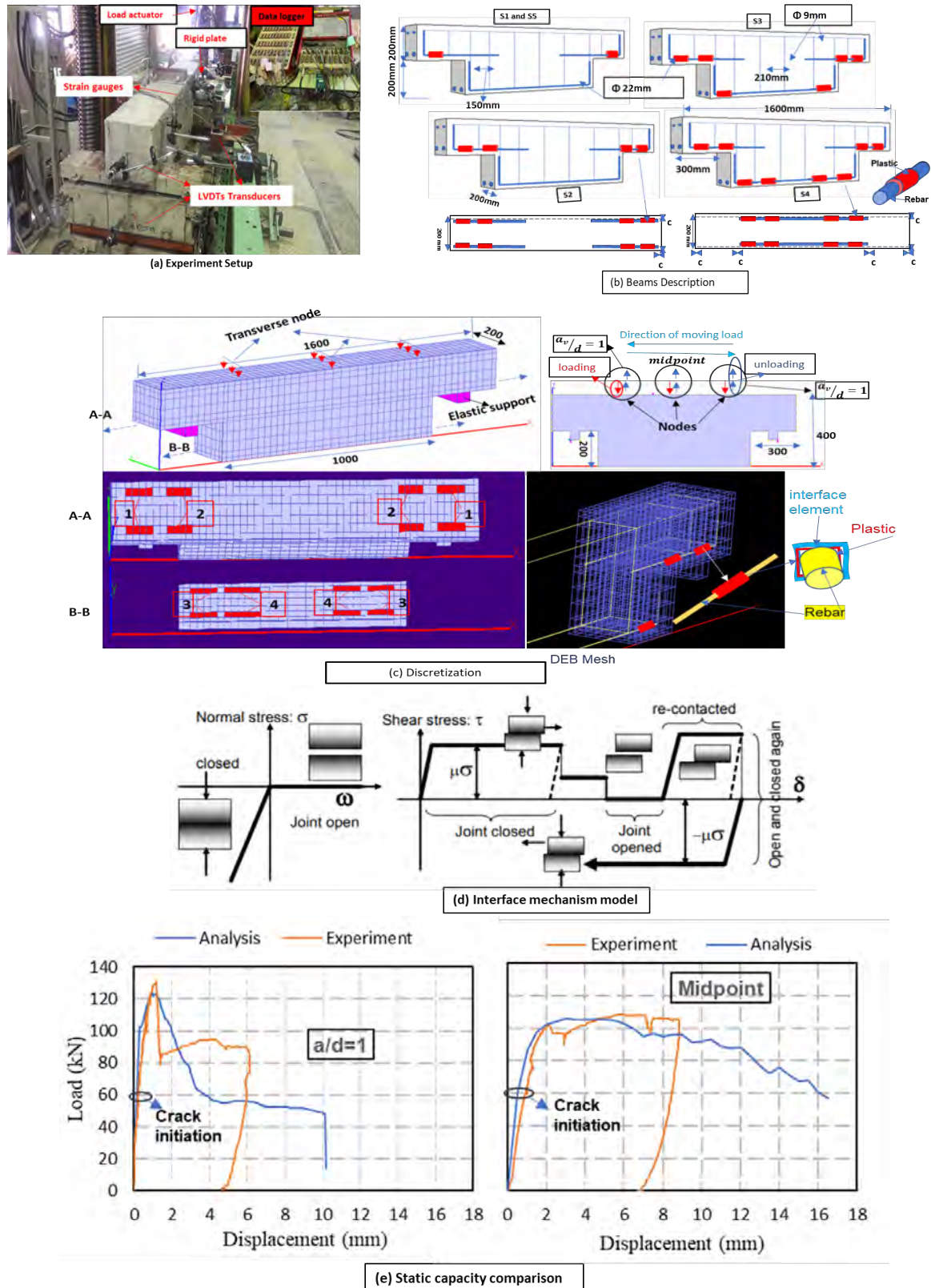


Fig. 3 (a) Experimental setup (b) Beam geometry description (c) FEM discretization (d) interface element model [7] (e) Monotonic loading comparison of analysis and experiment

To obtain as much information as possible, the specimens were instrumented particularly at the dapped section where the bond loss was made. The results were recorded automatically with the help of the data logger. Steel strains were measured using 5 mm electrical resistance strain gauges connected to the hanger reinforcement close to the dapped sections. Concrete strain gauges were also attached to the critical sections of the beam close to the reentrant corner. Three 25 mm capacity linear variable differential transducers (LVDTs) were placed on the beam, Fig. 3a, on the lower part of the loading

point and on the upper side of the supports, to capture the vertical displacement of the beam. The test beams were subjected to three-point bending in a compression machine with a total capacity of 2,000 kN, and in the case of static loading, the load was gradually applied at an amount of 5 kN until failure. The static capacity for evaluating the requirements for the low cycle fatigue loading was adopted from the experimental result after the failure. 105 kN static capacity was adopted. A minimum of 15% static capacity was introduced in the case of cyclic loading, with an increase of 15% loading capacity per 20 cycles until failure. To ensure an adequate contact between the loading system and the test specimen, the minimum load amplitude was maintained at 5 percent static capacity. As shown in Fig. 1 (right), the cyclic amplitude loading was performed in the form of increasing stages.

In the case of the numerical investigation, the test beam configuration was mocked up to resemble the experimental investigation, which is accomplished by the 3-dimension concrete model (COM 3D). Under the multi-fixed crack method, COM3D considers the complete reinforcement model within the concrete material to form the RC mesh. The standard model consists of 4,288 elements and 7,234 nodes, and the elastic supports were simply supported. The complete FEM discretization and the bond loss elements in the modeled beam (color red) for the case of S4 are shown in Fig. 3c. Sections A-A and B-B show the orientation of the bond deterioration with an interface slip model, Fig. 3d, considered in place of the steel and concrete properties under the Mohr-Coulomb's frictional law [7]. Free normal stress is assumed after the separation of the element, frictional coefficient, μ , of 0.8 is adopted on the contact surface of the element with an open-slip mode of the interface assumed to be rigid until the tensile stress normal to the interface surpasses the initial bonding. Hence, separation causes loss of contact and the Mohr-Coulomb's circle friction is activated. After re-contact, the transfer of stress restart. This path-dependency is the frictional contact planes in the analysis. Here, the interaction of softened crack shear and gap opening is considered. In this study, a sudden jump from continuum to perfect separation is assumed for simplicity in the FEM analysis. The bond loss labeled 1 in section A-A was only considered for the case of beams S1 and S5. The bond loss marked 1 and 2 was considered for beam S2, while the bond loss marked 1, 2, and 3 was considered for beam S3. S0 was considered without the bond loss.

The beams were simulated under similar conditions to the experimental investigation. Beams S0 and S5 were subjected to monotonic loading in the transverse direction at shear span to depth ratio ($a_v/d=1$), and at the midpoint respectively on a set of nodes (left side). The load versus displacement response between the experiment and the numerical analysis were compared as presented in Fig. 3d. Numerical examination under the low cycle fatigue is not reported in this study due to the limited space, this has however been considered at the midpoint and $a_v/d=1$ by Quadri and Fujiyama [8]. In this study, the structure of the moving wheel load is discussed. In the RC bridge deck, approximately 2 to 3 order differences in service life reduction have been reported experimentally when fatigue moving wheel was applied [9]. A similar decrease was also recorded when the effect of water coupling was considered under the conditions of cyclic loading [10]. In conducting a numerical analysis under moving load, the direct integral path constitutive model was considered to capture the action of the RCDEB under the influence of bond deterioration. Three nodes in the transverse direction have been picked, loaded, and unloaded consecutively as shown in Fig. 3c, these include; the node corresponding to the shear span to depth ratio equal to 1 on the right and the left sides and the node at the midpoint of the beam. The same time phase applied for the low cycle fatigue in 0.003 seconds was adopted. This is equal to 60 km/h in actual realistic consideration of the moving vehicle. As a result, approximately 3853 steps of 20 iterations are needed to complete 5 million cycles in 45 hours.

3 Discussion of Results

3.1 Experimental Results

For the modification of low cycle fatigue under the experimental approach and high cycle fatigue under the numerical analysis, the monotonic loading distinction between the experimental and the analytical results reported in Fig. 3e was adopted since an agreement in the load-displacement response is established. The damage pattern of beams S1-S4 under the experimental low cycle fatigue loading is presented in Fig. 4a. There was no visible crack when, in the case of S1 and S4 loaded at the midpoint, 15%, and 30% static capacities loading were considered under the cyclic conditions. However, in the first cycle of 45% static capacity load, a hairy crack was initiated on the left side of the re-entrant portion of the beams but disappeared when the beams were unloaded. The crack width extended

gradually throughout the 20 cycles of the 45% static capacity loading. As the load was further cycled to 60% capacity, an inclined crack at the critical section of the beam's full depth with flexural cracks were observed in beam S4 which gradually increase while the previous cracks traverse towards the loading point, crack was also initiated at the other corner of the beam. At 75% static capacity, the beam stiffness degraded with an increase in irrecoverable deformation. The same scenario was also observed in beam S1 however without flexural cracks, and when beam S1 was cycled to 90% capacity, the shear cracks increased drastically. This implies that once a weak zone is formed due to high stress under unloading and reloading conditions, the damage tends to accumulate incessantly. The existence of more bond losses in S4 expedited its early failure, with about 75% of its total capacity which is equal to 60% of the static loading capacity, diagonal and shear cracks were formed. This points to the fact that coupled corrosion and cyclic loading effect can exacerbate the service life of the RCDEBs since more damage is sustained during the bond deterioration of the RC composites.

Crack was initiated at the re-entrant corner at 30% static capacity when cyclic loading was considered at $a_v/d=1$ for the case of beams S2 and S3 in Fig. 4b. when the load was further increased to 45% static capacity, the crack width extended, which caused a diagonal crack on the other side of the re-entrant portion at the 8th cycle, resulting in dowel shear at the re-entrant corner. At 60% capacity, the re-entrant crack propagated diagonally to the loading point, and when the load was further increased to 75%, the crack travelled vertically down from the compression zone to the flexural zone due to aggregate interlocking during the reloading and unloading process.

Variation of strains of the hanger reinforcing bar and the concrete mounted close to the re-entrant corner of the beams were examined and plotted against the time taken to complete the cyclic loading for each beam, Fig. 5(a and b). The beams' displacement against the time taken was also assessed as presented in Fig. 5c, Fig. 5d shows the position of the strain gauges of the hanger bar and concrete. The strain development close to the dominant crack is present here. As the applied load is cycled and unloaded to 5% of the static capacity, the deformation and strain gradually increased. The steel yield strain and concrete tensile strain are attained at about 60% of the static capacity when the diagonal tensile cracks propagated more causing an opening at the re-entrant corner. The applied load at position $a_v/d=1$ is more critical compared to the midpoint since only half of the time is required for the beam failure under the same loading condition. Also, an increase in bond loss contributes a significant effect to the failure as beams under the same loading effect failed at a different interval. the creep effect could also have been a result of the intensity of the machine used.

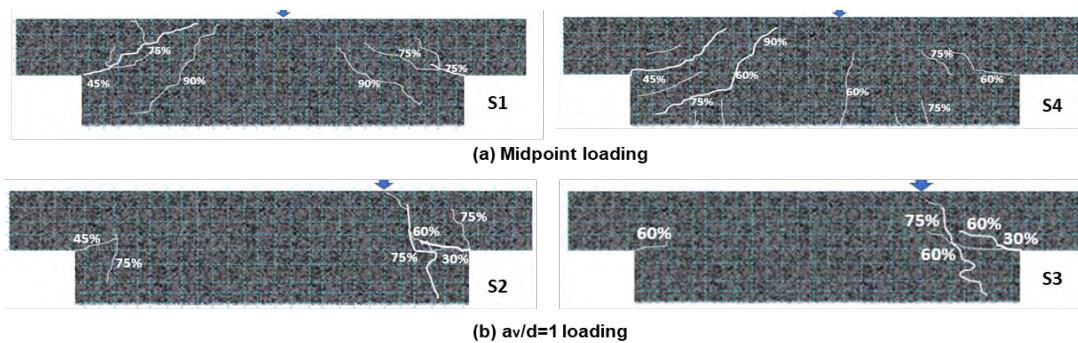


Fig. 4 Failure pattern of RCDEB under cyclic loading (a) at midpoint (b) at $a_v/d=1$

3.2 Numerical Analysis Results of the moving load

Results of the applied moving load on the beams S1, S2, S3, and S4 under the influence of the bond deterioration explained previously are presented. The damage response of the beams under the moving load is shown by the strain distribution in the x-x direction as presented in Fig. 6. This direction was referred to to determine the crack strain propagation. The high cycle fatigue loading and unloading process was applied to the three selected nodes in the transverse direction (see Fig. 3c). This was considered at 15 %, 30 %, 45 %, and 60 % of static capacity. Firstly, the fatigue load was applied at the midpoint under the stepwise loading, then unloaded and reloaded at $a_v/d=1$ on the right, and then at $a_v/d=1$ on the left side. Crack is initiated at the re-entrant portion of all the beams when a minimum constant fatigue load of 15% of the static capacity is considered, however at different cycles as indicated on the displacement to the number of cycles in the logarithmic scale, Fig. 7. As the fatigue load amplitude is increased below the static capacity limit, high stress is produced, resulting in reduced time to failure. The pattern of damage at each stress level depends on the level of bond loss in each beam. At

60% of the static capacity, the beams suddenly fail at about 2 to 3 cycles. As a result, RCDEB is more threatened by the diagonal tension crack at the re-entrant portion as well as the shear crack at the critical section of the beam. The shear failure usually occurs at high stress when the cyclic load is applied at the shear span to the depth ratio (a_v/d) = 1.

The accumulation of fatigue stress in terms of normalized static capacity and the number of cycles to failure (S-N) of the RCDEB examined were assessed. The fatigue requirements for evaluating the beam performance were set as serviceability and ultimate limit states for structural assessment. The beam deflection, using the EN-2 specification and clause given under section (7.4) and the reinforcement yield strain at strain value of 2000μ as the ultimate limit criterion. Figure 8 (left) shows the S-N plot by following the measured deflection limit of 4 mm in terms of serviceability limit, while Figure 8 (right) shows the reinforcement yield criteria. There is a general reduction in fatigue life at an increased bond deterioration, the damage under the S-N diagram accounts for about 50-55% of the fatigue life cycle when the ultimate limit state criterion is considered. Accelerated corrosion of the critical section of the RCDEB could therefore promote early failure and decrease the fatigue life expectancy of the beam.

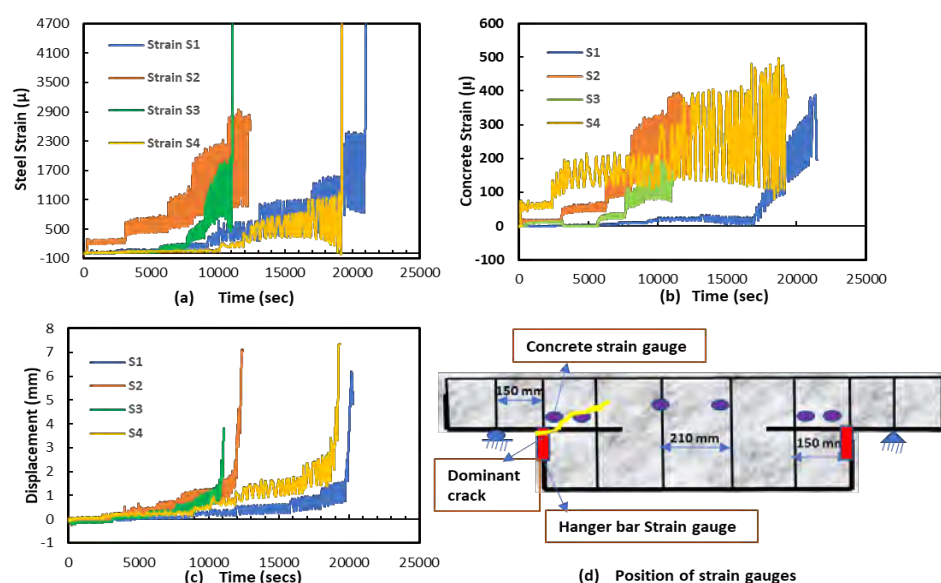
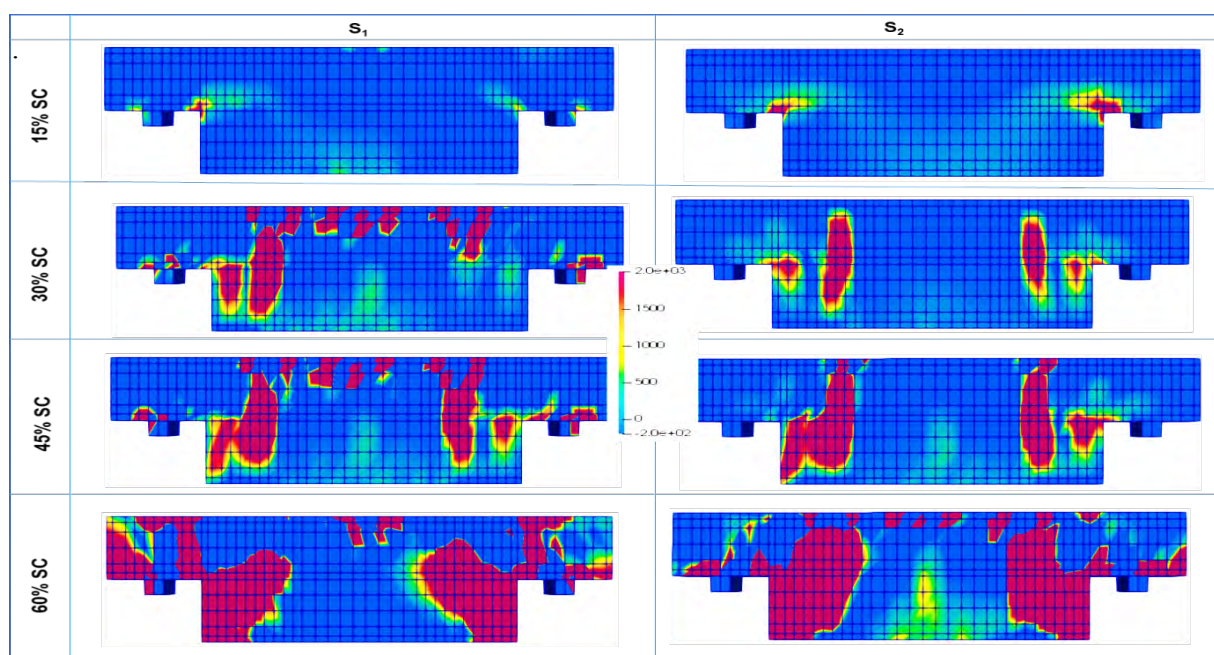


Fig. 5 Beam Response under the cyclic loading. Strain-time of (a) steel (b) concrete, (c) Displacement-time, and (d) position of strain gauges on the test beams



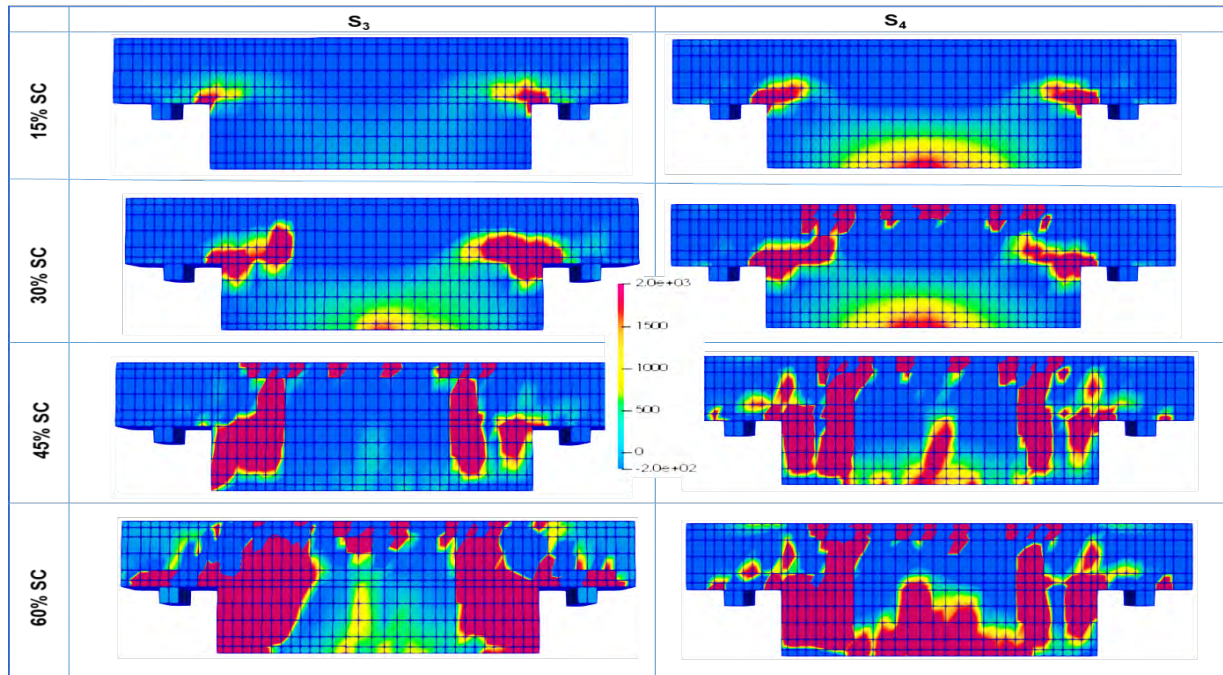


Fig. 6 Strain distribution under fatigue moving load (x-x direction).

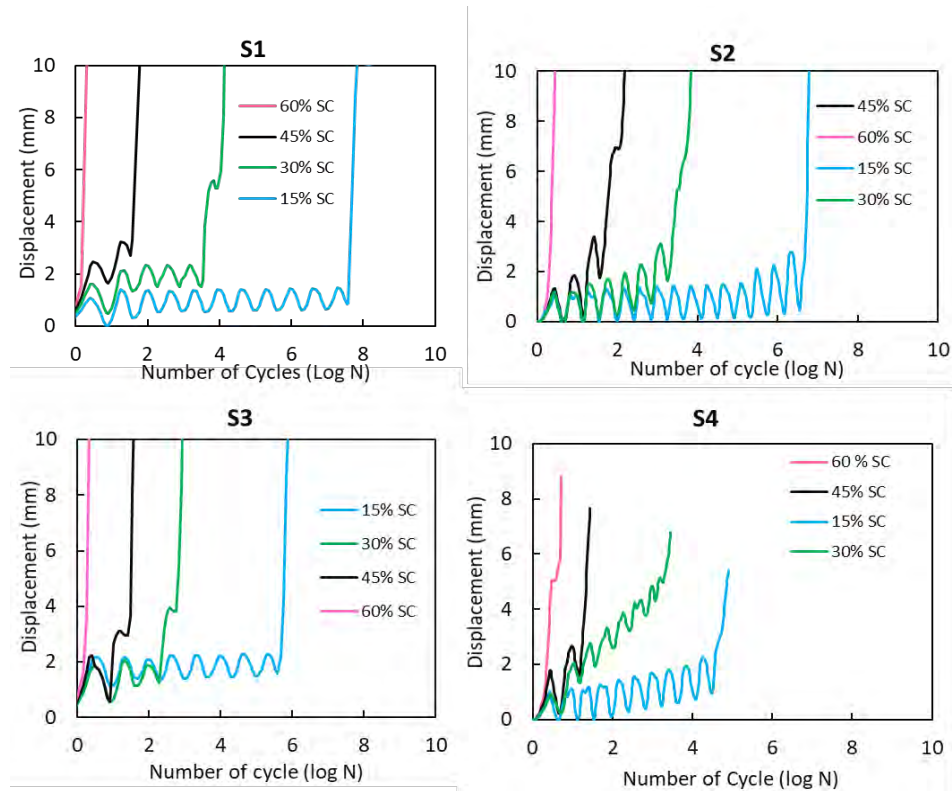


Fig. 7 Displacement versus the number of cycles under the fatigue moving load.

4 Conclusion

The response of reinforced concrete dapped end beams subjected to cyclic loading under the influence of bond deterioration of RC composite at the critical portion has been examined experimentally. Analytical investigation under the moving load by adopting the direct-path integral scheme was conducted to determine the service life degradation on account of the bond loss. The following conclusions are drawn.

1. An increase in the position of the bond loss hastened the damage of the beam with shear and diagonal tension cracks forming the dominant cracks and resulting in damage at the critical section

of the beam. These cracks are mostly resisted by the hanger bars (stirrups) close to the reentrant corners of the beams.

2. The position of the applied load is an additional factor that dictates when the beams fails. Thus, RCDEB is more threatened by the diagonal tension cracks emanating from the recess portion when loaded near this corner. More attention is therefore required area as the dominant damage perpetuates this portion.
3. The number of cycles to failure under the moving load, considered in the numerical analysis, decreased as the amplitude of the fatigue loading increased below the static capacity. This is also confirmed in the S-N diagrams. The fatigue life criterion under the ultimate state presented a relatively reduced service life compared to the serviceability state which partly relies on the level of the bond loss and the moving load magnitude.

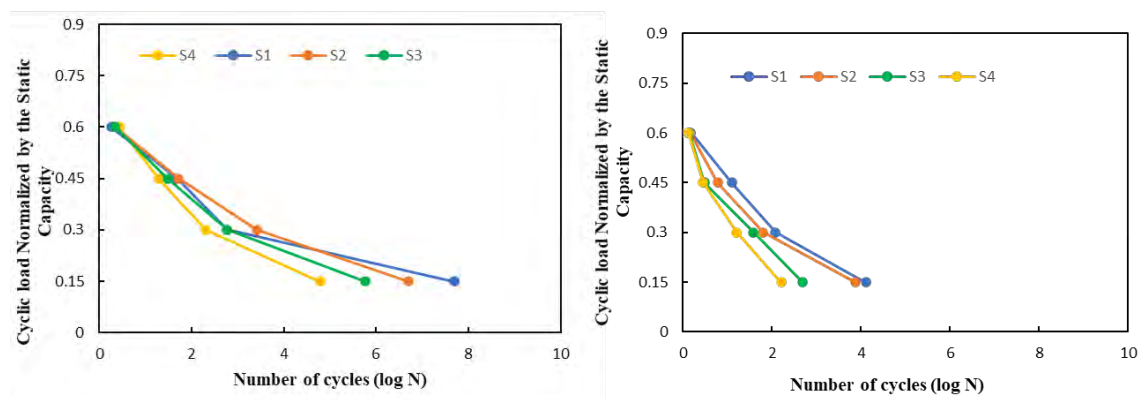


Fig. 8 S-N diagram of the moving load normalized by static capacity; Deflection criterion (left) and yield strength of reinforcement criterion (right).

References

- [1] Dapped end beam and corbel corrosion. "Accessed December 22/2020.". <https://www.prontu-beam.com/articles/2020-12-19-Dapped-end-beams-and-corrosion>.
- [2] Taher S. E.-D. M. F. 2005\ "Strengthening of critically designed girders with dapped ends," *Proceedings of the Institution of Civil Engineers - Structures and Buildings*, vol. 158, no. 2, pp. 141–152.
- [3] Mata-Falcón, Jaime, Luis Pallarés, and Pedro F. Miguel. 2019. "Proposal and Experimental Validation of Simplified Strut-and-Tie Models on Dapped-End Beams." *Engineering Structures* 183: 594–609.
- [4] Mattock A.H and Chan T.C 1979. "Design and Behavior of Dapped-End Beams". *pcij*. 1;24(6):28–45.
- [5] Quadri, Ajibola I., and Fujiyama Chikako. 2021 "Numerical Analysis of RC Gerber Bridge Girder Subjected to Fatigue Loading." in *Bridge Maintenance, Safety, Management, Life-Cycle Sustainability and Innovations* (eds. Yokota, H. & Frangopol, D. M.) 2682–2689. doi:10.1201/9780429279119-366.
- [6] British Standards Institution. Eurocode 2: design of concrete structures: British standard. London: BSI; 2006.
- [7] Fujiyama, C. and Maekawa, K. 2011. "A Computational Simulation for the Damage Mechanism of Steel-Concrete Composite Slabs under High Cycle Fatigue Loads," *ACT*, 9 (2): 193–204.
- [8] Quadri Ajibola I., and Fujiyama Chikako. 2021 "Bond Loss Response of Reinforced Concrete Dapped-End Beam Subjected to Static And Low Cycle Fatigue Loading" *Concrete Engineering Annual Paper of the Japan Concrete Institute (JCI)*. vol.43 no.2 pp439-444.
- [9] Tang XJ, Fujiyama C, Shang F, Maekawa K, An XH. 2014. "Residual Fatigue Life Assessment of Damaged RC Bridge Slabs Based on Site-Inspection for Cracking: A Quantitative Discussion. *Advances in Structural Engineering*". 17(4):481–94.
- [10] Fujiyama C, Kobayashi K, Zhan J, Maekawa K. 2011. "Fatigue Life Simulation of RC Bridge Slab with Initial Defects under Water. *Procedia Engineering*". 14:1897–905.

Influence of silica fume on the deterioration under compressive fatigue loading in high-strength concrete

Tim Scheiden, Nadja Oneschkow

*Institute of Building Materials Science,
Leibniz University Hannover
Appelstraße 9A, 30167 Hannover, Germany*

Abstract

The fatigue behaviour of concrete is strongly dependent on various influencing factors. The influence of different concrete composition on the fatigue behaviour of high-strength concrete has not yet been sufficiently investigated. In addition, most research was concerned with the effect on the number of cycles to failure without including detailed damage indicators, which describe the changes in the micro-structure. In this paper, analyses and results concerning the fatigue behaviour of a high-strength concrete with and without silica fume are presented. Thereby, especially the combined analysis of different damage indicators such as strain and the acoustic emission points to different damage mechanisms caused by the addition of silica fume. However, the fatigue behaviour of the high-strength concrete could be improved by the addition of silica fume.

1 Introduction

In the last several decades, fatigue of concrete research was mainly focused on the numbers of cycles to failure and partially on the development of strains and stiffness, e.g. [1]-[3]. Hence, even today very little knowledge is available concerning the damage processes in concrete microstructure due to fatigue loading. For this reason, the Priority Program SPP 2020 “Cyclic deterioration of High-Performance Concrete in an Experimental-Virtual Lab”, funded by the German Research Foundation, is focused on the evaluation of damage indicators in combination with new methods, such as acoustic emission analysis.

Different results are documented in literature considering the formation and propagation of cracks under fatigue loading. Some investigations found out that fatigue loading leads to the development of cracks in the bond between coarse aggregate and mortar, the interfacial transition zone (ITZ) [4]. Results in [5] indicate that, in addition, already existing microcracks in cement stone develop further and unite, forming macrocracks. Other investigations found that new microcracks mainly occur [6]. Altogether, there might be a dependency on the stress level concerning the formation of cracks [6], [7]. The microstructure of concrete, and therefore the concrete composition, influences the occurrence and development of damage due to fatigue loading [8], [9]. For static loading, an increase in compressive strength due to the addition of silica fume is noticed by Sharaky et al. [10]. They explained this increased strength due to the increased filler effect of silica fume as well as the greater solid volume of C-S-H gel and thus additional reduction of capillary porosity during hydration. However, currently no results are documented in literature, to what extent the addition of silica fume and thus the strengthening of the cement stone and the ITZ have an effect on the ongoing damage mechanism and crack development under pure compressive fatigue loading.

Within a research project of the SPP 2020, the influence of silica fume in high-strength concrete composition on the damage mechanisms under pure compressive cyclic loading is investigated. For this, fatigue tests with two different stress levels were conducted. Different damage indicators like strain, stiffness, dissipated energy and acoustic emission [11], [12] were used for comparative analyses. The results obtained show, that the combination of strain dependent damage indicators and the acoustic emission analysis points to a different and improved fatigue behaviour due to the addition of silica fume.

2 Experimental Programme

2.1 Concrete and specimen

The experimental investigations of the fatigue behaviour under uniaxial compressive loading were conducted on two high-strength concretes whose compositions only differ in the addition of silica fume. Based on the approach of the same paste film thickness [13], silica fume was added to the mixture to improve the binder matrix and the ITZ between the aggregates and the binder matrix. The compositions of the high-strength concrete RH1-B and the concrete with silica fume RH1-B-Si are given in Table 1.

The concrete composition RH1-B is the high-strength reference composition of the SPP 2020. The fatigue tests were conducted on cylindrical specimens with $h/d = 180/60$ mm. The PVC form-works were removed after 7 days and the cylinders were stored in standardized conditions (20 °C / 65 % R.H.) until testing. The test surfaces of the specimens were plane-parallel ground and polished to achieve a more uniform stress distribution under loading.

Table 1 Concrete composition

Concrete	RH1-B	RH1-B-Si
Ordinary Portland Cement (CEM I 52.5 R HS/NA)	500.00 kg/m ³	446.60 kg/m ³
Micro silica	/	44.70 kg/m ³
Quartz sand (0/0.5 mm)	75.00 kg/m ³	75.00 kg/m ³
Sand (0/2 mm)	850.00 kg/m ³	850.00 kg/m ³
Basalt (2/5 mm)	350.00 kg/m ³	350.00 kg/m ³
Basalt (5/8 mm)	570.00 kg/m ³	570.00 kg/m ³
PCE plasticizer	5.00 kg/m ³	4.90 kg/m ³
Stabilizer	2.85 kg/m ³	2.80 kg/m ³
Water	176.00 kg/m ³	172.00 kg/m ³

Before the fatigue tests, the concrete compressive strength and the modulus of elasticity were determined on three test specimens each and the respective mean values were determined (cf. table 2). The average 28 d compressive strength after storage under water $f_{cm,cube}$ is higher for the RH1-B-Si. Thus, there is an increase in the compressive strength due to the addition of silica fume, which was expected (cf. section 1). The modulus of elasticity E_m was determined in accordance to DIN EN 12390-13 [14] on cylindrical specimens with $h/d = 150/300$ mm after 28 days. The reference concrete RH1-B has an 10 % lower modulus of elasticity than that one of the silica concrete RH1-B-Si. In addition and for the purpose of comparison with the stiffness development under fatigue loading, the secant modulus or rather stiffness of the stress-strain curve before the fatigue tests was determined also using cylinders with $h/d = 180/60$ mm (cf. table 2). The average stiffness S_m under monotonically increasing loading is higher for RH1-B-Si. Thus, the addition of silica fume leads to an increase in stiffness of approx. 18 %. These properties confirm the aimed improvement of the microstructure by the addition of silica fume. The reference compressive strengths $f_{cm,ref}$ of the high-strength concretes, which are required to determine the axial test forces based on the stress levels, were determined just before conducting the fatigue tests, using five specimens from the same batch having the same geometry as the specimens used in the fatigue tests. The reference compressive strength is also given in Table 2. All fatigue tests were conducted using specimens with a minimum concrete age of 56 days.

Table 2 Hardened concrete properties of RH1-B and RH1-B-Si

Concrete	RH1-B	RH1-B-Si
$f_{cm,cube}$	113 [MPa]	133 [MPa]
E_m	39,967 [MPa]	44,337 [MPa]
S_m	32,145 [MPa]	37,857 [MPa]
$f_{cm,ref}$	96 [MPa]	123 [MPa]

2.2 Experimental set-up

The fatigue tests were carried out force-controlled using a class 0.5 servo-hydraulic testing machine with a 500-kN actuator (according to ISO 7500-1 [15]). The full amplitude was applied in the first load cycle. The minimum stress level was kept constant with $S_{c,min} = 0.05$ for all test series, while the maximum stress level was either $S_{c,max} = 0.85$ or $S_{c,max} = 0.70$. The test frequency applied was $f_t = 1.0$ Hz. The axial deformations were measured continuously during the tests using three laser distance sensors positioned around the specimen at 0° , 120° , and 240° . In addition, the axial force, the axial stroke of the actuator, and the temperature on the specimen's surface at mid-height and the ambient temperature were measured, all with a sampling rate of 300 Hz. Six sensors were attached to the specimens tested under fatigue to characterize the degradation using acoustic emission. The sensors with a wideband frequency response with the range of 250–1,600 kHz were positioned at 60° from one another, alternating in the upper and lower third of the specimen. In preliminary tests, a threshold of 40 db was defined to separate the useful signal from background noise. This means that all signals with an amplitude smaller than the threshold are not recorded. The experimental set-up is shown in Fig. 1. Also visible in Fig. 1 but not further used for obtaining the results presented in this paper, are additional linear variable differential transformers (LVDT) and strain gauges.

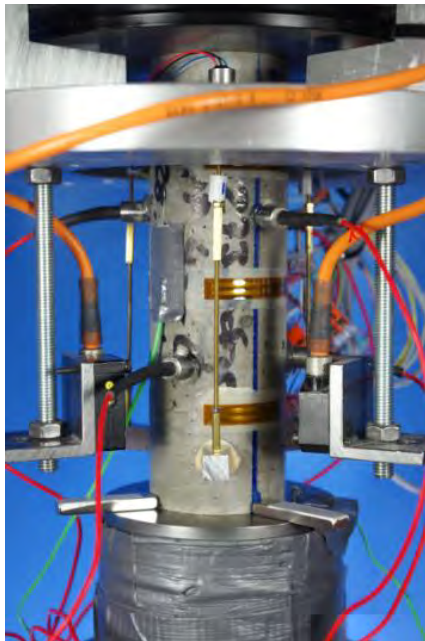


Fig. 1 Experimental set-up [9]

3 Results and Discussion

3.1 Number of cycles to failure

First of all, it must be stated that the maximum temperature increase during the fatigue process was maximal 14 K and, therefore, relatively low. The correlation between the maximum compressive stress level $S_{c,max}$ and the log. numbers of cycles to failure $\log. N_f$ is shown in Fig. 2. The test results are presented for both high-strength concretes as single values on each maximum stress level. Furthermore, the S-N curves for pure compressive fatigue loading of fib Model Code 2010 [16] and Eurocode 2 [17] are shown in Fig. 2.

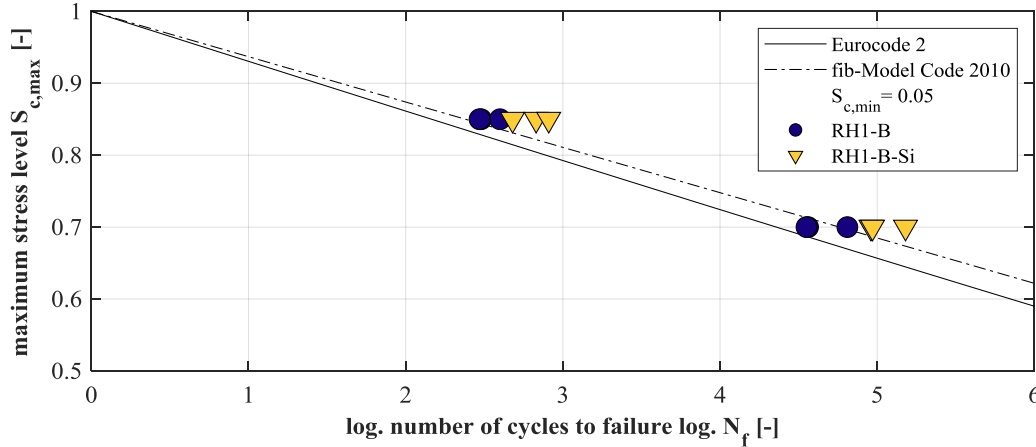


Fig. 2 Number of cycles to failure

It is obvious from Fig. 2 that the scatter of the tests results is relatively low for both concretes compared to other investigations documented in the literature [1], [2], [18]. It also becomes clear that the average number of cycles to failure for the RH1-B-Si is higher than for the RH1-B for both stress levels. The difference in mean values is smaller for $S_{c,max} = 0.85$, but no overlapping of single values for both stress levels exists. Both concrete mixtures meet the requirements of the S-N curves of fib Model Code 2010 [16] and Eurocode 2 [17], being mean curves.

3.2 Damage indicators

Fatigue damage indicators are used to describe the differences in the fatigue behaviour of both concretes. Hereinafter, the following fatigue damage indicators are analysed comparatively for both concrete mixtures, investigating their developments in the fatigue process:

- Strain at maximum stress level ϵ_{max} [‰]
- Strain at minimum stress level ϵ_{min} [‰]
- Overall growth of strain at maximum stress level $\Delta\epsilon_{c,max}^{0-1.0}$ [‰]
- Overall growth of strain at minimum stress level $\Delta\epsilon_{c,min}^{0-1.0}$ [‰]
- Gradient of development of strain at maximum stress in phase II $\text{grad}\epsilon_{c,max}^{II}$ [-]
- Gradient of development of strain at maximum stress in phase II $\text{grad}\epsilon_{c,min}^{II}$ [-]
- Stiffness E_S [MPa]
- Percentile loss of stiffness $\Delta E_S^{0-1.0}$ [%]
- Gradient of development of stiffness in phase II $\text{grad}E_S^{II}$ [-]
- Dissipated energy per cycle E_D [kJ/m³]
- Total dissipated energy $\sum E_D$ [MJ/m³]
- Total number of hits $\sum n_H$ [-]

Thus, a selection of indicators as in [12] were used to ensure comparability to the results published before. The developments of maximum and minimum strain including the last complete cycle before failure. The strain at failure is not included in the developments of strains evaluated due to the high-grade unstable state of microstructure in the load cycle where failure occurs. The stiffness E_S is calculated for each load cycle as the secant modulus between the maximum and minimum peaks in the unloading branch. The dissipated energy per cycle E_D is determined as the area of the hysteresis loop.

The hits from the acoustic emission analysis are characterized as single transient signals and evaluated as the development of cumulated hits.

The developments of the damage indicators are shown in Fig. 3 and Fig. 4 for three specimens of each concrete and for both stress levels.

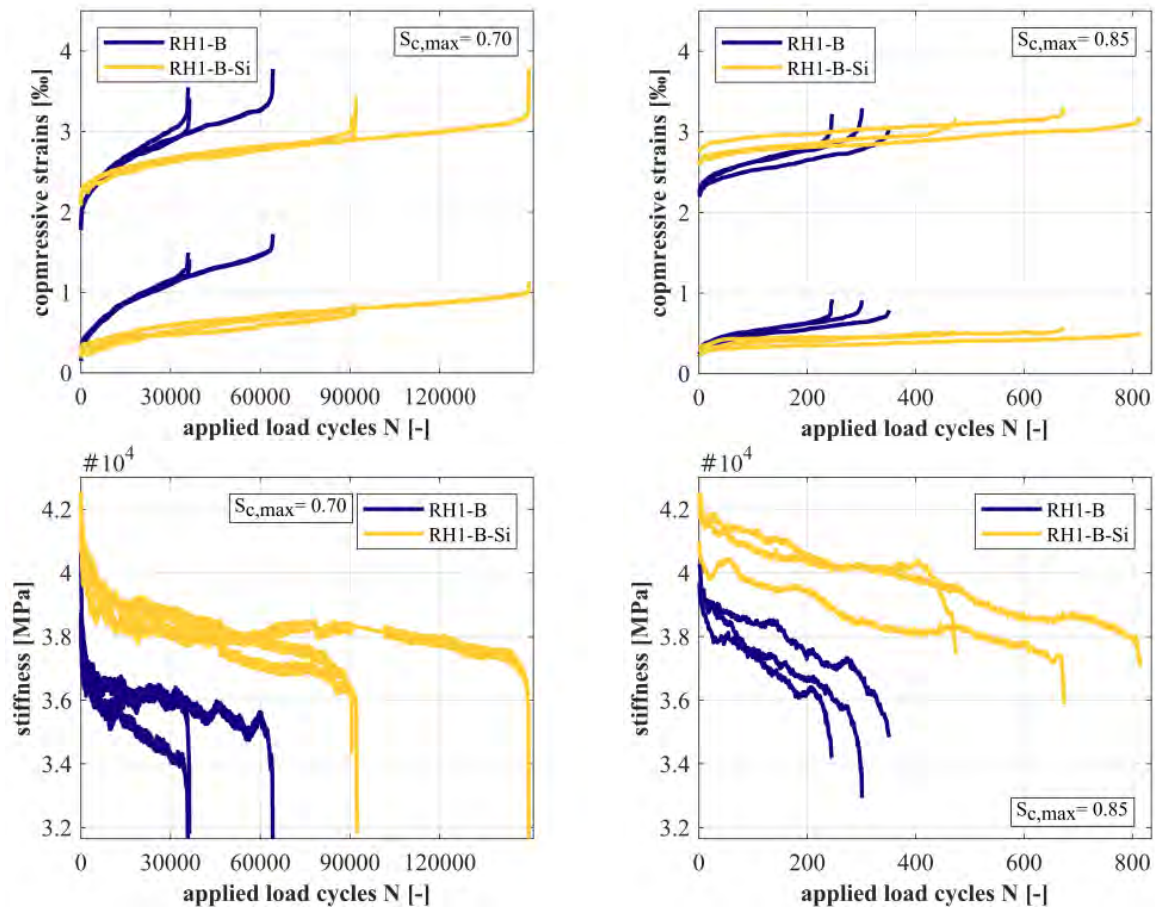


Fig. 3 Developments of compressive strain and stiffness for $S_{c,max} = 0.70$ (left) and $S_{c,max} = 0.85$ (right)

The developments of strain (cf. Fig. 3) show the well-known three-phase shape [1], [18]. It becomes clear that the concrete with silica fume RH1-B-Si has a lower gradient in phase II meaning a lower increase in strain per cycle for both stress levels compared to the concrete without silica fume RH1-B. The gradient $\text{grad}\epsilon_{c,max}^{II}$ in phase II of the RH1-B-Si is 65 % for $S_{c,max} = 0.70$ and 33 % for $S_{c,max} = 0.85$ related to the RH1-B. Also the overoverall growth of strain at maximum and minimum stress level in the fatigue process $\Delta\epsilon_{c,max}^{0-1.0}$ and $\Delta\epsilon_{c,min}^{0-1.0}$ is lower for the concrete with silica fume RH1-B-Si for both stress levels despite the higher number of cycles to failure. The higher initial strain at start of loading for RH1-B-Si, despite of the increased stiffness, can be explained by the ratio between the applied stress level in combination with the ratio of modulus of elasticity.

Regarding the stiffness development, it becomes clear that the RH1-B-Si has a higher initial stiffness E_S under fatigue loading, compared to the RH1-B, due to the addition of silica fume. This is congruent with the results for the monotonically increasing loading (cf. section 2.1). The decrease of stiffness per cycle in phase II ($\text{grad}E_S^{II}$) is almost identical for both concretes for the lower stress level $S_{c,max} = 0.70$. For $S_{c,max} = 0.85$, the gradient of stiffness in phase II $\text{grad}E_S^{II}$ is lower for the concrete with silica fume. However, for RH1-B-Si, the overall percentage stiffness reduction in the fatigue process is determined of approx. $\Delta E_S^{0-1.0} = 23$ % for $S_{c,max} = 0.70$ and $\Delta E_S^{0-1.0} = 12$ % for $S_{c,max} = 0.85$ with respect to the initial stiffness in the first load cycle. For comparison, RH1-B shows stiffness reduction of $\Delta E_S^{0-1.0} = 18$ % for $S_{c,max} = 0.70$ and $\Delta E_S^{0-1.0} = 13$ % for $S_{c,max} = 0.85$ and thus similar or lower values than the RH1-B-Si. Higher overall stiffness reductions despite similar or

lower gradients in phase II for RH1-B-Si can be traced back to the higher numbers of cycles to failure for the concrete with silica.

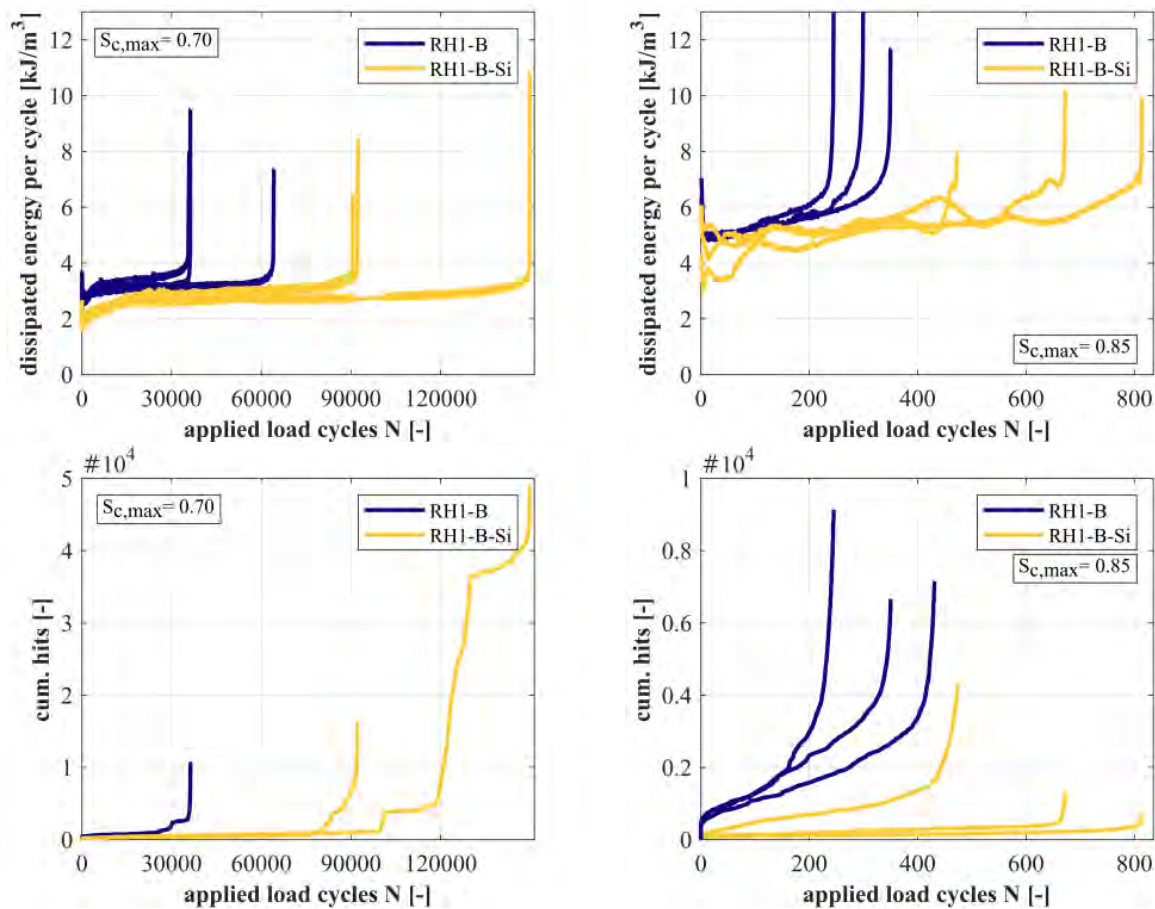


Fig. 4 Developments of dissipated energy and hits for $S_{c,max} = 0.70$ (left) and $S_{c,max} = 0.85$ (right)

The dissipated energy per cycle (cf. Fig. 4) shows at first a rapid decrease and then a short non-linear increase, which is followed by a steady linear increase in phase II. Shortly before failure, the dissipated energy disproportionately increases until failure. Characteristic for the RH1-B-Si is the lower initial dissipated energy and a lower dissipated energy per cycle in phase II. Despite the lower energy dissipation per cycle, the sum of the dissipated energy is higher for RH1-B-Si with approx. $\sum E_D = 258 \text{ MJ/m}^3$ for $S_{c,max} = 0.70$ and $\sum E_D = 3.5 \text{ MJ/m}^3$ for $S_{c,max} = 0.85$. For comparison the RH1-B sums up $\sum E_D = 86 \text{ MJ/m}^3$ for $S_{c,max} = 0.70$ and $\sum E_D = 2.0 \text{ MJ/m}^3$ for $S_{c,max} = 0.85$. The higher sum of the dissipated energy of the RH1-B-Si despite the lower energy dissipation per load cycle can be traced back to the higher number of cycles to failure. As well as for the strain and stiffness indicators, shortly before failure the dissipated energy increases significantly faster than the RH1-B. Furthermore, it is remarkable that while the courses of the dissipated energy for $S_{c,max} = 0.70$ are very continuous for both concretes, the courses of the dissipated energy for the RH1-B-Si oscillates at $S_{c,max} = 0.85$. This means that the area of hysteresis loops increases and decreases again within phase II of the damage process. This behaviour seems to be characteristic for the concrete with silica fume on this stress level and therefore gives a strong indication of a different viscous behaviour under fatigue loading.

For the acoustic emission it should be mentioned that the results for the lower stress level of $S_{c,max} = 0.70$ are based on one specimen for RH1-B and two specimen for RH1-B-Si. The cumulated hits of the acoustic emission show a three-phase shape, like the other strain dependent damage indicators. For the stress level of $S_{c,max} = 0.70$ it is characteristic for both concretes, that from approx. 85 % of the fatigue process, a stepwise course can be identified. Compared to the other strain dependent damage indicators, the third phase of the RH1-B-Si seems to announce itself earlier on the basis of the acoustic emission. This behaviour is not determined for the higher stress level of $S_{c,max} = 0.85$. Here,

for both concretes, the transition from phase II to phase III correlates with those of the strain dependent damage indicators.

The RH1-B-Si emits significantly less detectable hits up the beginning of the stepwise course starts. For each concrete, a characteristic range of cumulated hits at the beginning of the disproportionate increase of hits could be determined, which is independent of the stress level. For RH1-B-Si this is between 300 and 1700 hits and between 3500 and 4000 hits for the concrete RH1-B without silica fume. Thus, there might exist a concrete specific limit range of hits, independent of the stress level, which might mark the transition to an increased damage activity in the microstructure. Due to the locally increased strength and the improved bond between aggregate and hardened cement paste matrix, there are comparatively less relative displacements and correspondingly lower acoustic emissions. In addition, the filler effect, crystallizing effects, and pozzolanic effect of silica fume can reduce the number and size of the initial damaged areas in the bulk of concrete and therefore reduces acoustic emissions [19].

4 Conclusions

Within a research project of the priority program SPP2020, the behaviour of high-strength concretes under compressive fatigue loading is intensively investigated. In this paper, results concerning the influence of silica fume are presented comparatively. The focus is on two high-strength concretes differing in the addition of silica fume. Fatigue tests were conducted using two stress levels of $S_{c,max} = 0.70$ and $S_{c,max} = 0.85$ and a test frequency of $f_t = 1.0$ Hz.

The addition of silica fume leads to increased concrete compressive strength and modulus of elasticity, which was expected (cf. also [8],[19]). For fatigue loading, the addition of silica fume leads to increased numbers of cycles at failure and therefore an improved fatigue behaviour. This becomes more significant with decreasing stress level. During the fatigue loading, the concrete with silica fume shows smaller increase in strain and decrease in stiffness, despite increased numbers of cycles to failure. Furthermore, the dissipated energy per cycle and the cumulated hits are lower up to the transition to phase III compared to the concrete without silica fume. Thereby, it was detected, that the areas of hysteresis loops increase and decrease for $S_{c,max} = 0.85$, which was not expected. The addition of the silica fume resulted in an average of approx. 60 % less detectable hits up to the beginning of the stepwise course. Because no other changes in concrete composition were done, the effects described before can clearly be assigned to the addition of silica fume. Thus, they must be traced back to the advantages of silica fume, such as a filler effect and further pozzolanic reactions which are well known from investigations under static loading [8]. The results presented in this paper give strong indication of a different viscous behaviour under fatigue loading (due to the effect of silica fume in the microstructure). For both concretes, a limit range of hits might exist, independent of the stress level, which is reached at the point where the disproportionate increase of hits starts. Further detailed analyses of the acoustic emission signals are necessary, combining with the results of high-resolution imaging techniques regarding damage occurrence and development in concrete microstructure.

Acknowledgements

This research project was funded by the Deutsche Forschungsgemeinschaft (DFG, German Research Foundation) – 353530889, within the scope of Priority Programme 2020 “Cyclic deterioration of High-Performance Concrete in an experimental virtual lab”. The authors would like to express their gratitude for the financial support.

References

- [1] Holmen, J. O.. 1979. “Fatigue of concrete by constant and variable amplitude loading.”. Trondheim: The Norwegian Institute of Technology, University of Trondheim.
- [2] Petković, G.. 1991. “Properties of concrete related to fatigue damage with emphasis on high strength concrete.” Trondheim: University of Trondheim.
- [3] Wefer, M.. 2010. “Materialverhalten und Bemessungswerte von ultrahochfestem Beton unter einaxialer Ermüdungsbeanspruchung.” (in German). Doctoral dissertation. Report of the Institute of Building Materials Science, 7. Hannover: Leibniz University Hannover.

- [4] Lloyd, JP., Lott JL., Kesler, CE.. 1968. "Fatigue of concrete." Engineering experiment station. Bulletin 499. Vol 66. Illinois: University of Illinois, p. 42.
- [5] Thiele, M. (2016): "Experimentelle Untersuchungen und Analyse der Schädigungsevolution in Beton unter hochzyklischen Ermüdungsbeanspruchungen.", BAM.Dissertationsreihe Band 140, Berlin
- [6] Breitenbücher, R., Ibuk, H., Yüceoglu, S.. 2008. "Beeinflusst die Kornsteifigkeit der Gesteinskörnung im Beton den Degradationsprozess infolge zyklischer Druckbeanspruchung?" Beton- und Stahlbetonbau. 103(5):318–323.
- [7] Lee, MK., Barr, BIG.. 2004. "An overview of the fatigue behaviour of plain and fibre reinforced concrete." Cement & Concrete Composites. 26:299–305.
- [8] Bennet, E.W., Muir, S.E.St.J.. 1967. "Some fatigue tests of high-strength concrete in axial compression." Magazine of Concrete Research, Vol. 19, No. 59, 1967, pp. 113-117.
- [9] Guo, L.-P., Carpinteri, A., Spagnoli, A., Sun, W.. 2010. "Experimental and numerical investigations on fatigue damage propagation and life prediction of high-performande concrete containing reactive mineral admixtures.", Int. Journal of Fatigue 32, 2010, pp. 227-237
- [10] Sharaky, I.A., Megahed, F.A., Seleem, M.H. and Badawy, A.M. 2019. "The influence of silica fume, nano silica and mixing method on the strength and durability of cocnrete." SN Appl. Sci. 1, 575.
- [11] Scheiden,T., Oneschkow, N., Löhnert, S., Patel, R.. 2019. "Fatigue damage of high-strength concrete with basalt aggregate" Proceedings of the fib Symposium 2019: Concrete - innovations in materials, design and structures, Krakow, Poland, 27-29 May, 2019, pp. 1896-1903.
- [12] Scheiden,T., Oneschkow, N.. 2019. "Influence of two coarse aggregates on the damage mechanism in highstrength concrete under compressive fatigue loading." Structural Concret, 20, 4, 2019, pp. 1212–1219. doi: 10.1002/suco.201900029.
- [13] Leusmann, T., Basutkar, G., Lunardelli, M., Lowke, D.. 2019. "Characterizing the 3D mesostructured of high performance concrete by computed tomography" Proceeding RILEM Spring convention and sustainable materials, systems and structures conference 2019
- [14] German Institute for Standardization (Ed.) (2014). DIN EN 12390-13 Testing hardened concrete – Part 13: Determination of secant modulus of elasticity in compression; German version EN 12390-13:2013. Berlin: Beuth Verlag; [in German].
- [15] DIN EN ISO 7500-1:2018-06. Metallic materials –Calibration and verification of static uniaxial testing machines – Part 1: Tension/compression testing machines – Calibration and verification of the force-measuring system, German version of EN ISO 7500-1:2018.
- [16] fib: federation international du Béton (ed.) 2013. fib model code for concrete structures 2010. Berlin: Ernst & Sohn.
- [17] GIS: German Institute for Standardization (ed.) 2011. Eurocode 2: design of concrete structures – Part 1-1: General rules and rules for buildings, German version DIN EN 1992-1-1:2004 + AC:2010. Berlin: Beuth Verlag (in German).
- [18] Oneschkow, N.. 2016. "Fatigue behaviour of high-strength concrete with respect to strain and stiffness." International Journal of Fatigue, Vol. 87, pp. 38-49, doi: 10.1016/j.ijfatigue.2016.01.008.
- [19] Yan, H., Sun, W., Chen, H. 1998. "The effect of silica fume and steel fiber on the dynamic mechanical performance of high-strength concrete." Cement and Concrete Research, Vol. 29, pp.423-426

Influence of the concrete production and specimen preparation techniques on the compressive strength and fatigue resistance of HPC

Marco Basaldella, Nadja Oneschkow, Ludger Lohaus

*Institute of Building Materials Science,
Leibniz University Hannover,
Appelstraße 9A, 30167 Hannover, Germany*

Abstract

The results of tests under monotonically increasing load and cyclic compression load are often analysed employing probabilistic methods. Although there is a considerable scattering in the results, especially in the number of cycles to failure, the cause of these cannot be completely explained. The imperfections of the specimens tested are among the causes of this scattering mentioned in the literature. Based on a round-robin test the influence of HPC production and specimen preparation techniques on the mean values of the compressive strengths, number of cycles to failure and data scattering have been evaluated. The main findings of the study are that the production techniques influence the compressive strength, however, do not affect the mean number of cycles to failure. Moreover, the accurate preparation of the specimens has a positive influence on the compressive strength and the scattering of the results of both compression and cyclic load tests. Due to the use of the reference strength, the mean number of cycles to failure of HPC specimens is not influenced by the preparation techniques.

1 Introduction

Fatigue stress is a frequently repeated stress whose maximum stress level is smaller than the strength of the material under monotonically increasing stress [1]. Typical for fatigue stresses is that they can lead to failure of the material although the strength of the material is not reached. The "fatigue strength" of concrete is generally defined as the maximum stress that can be withstood for a given number of load cycles [2]–[4]. The fatigue verification for concrete plays a decisive role in slender structures of high- and ultra-high performance concrete subject to high vibration loads.

Fatigue tests exhibit a large scattering of results [5] and are influenced by other factors, such as the load frequency [6], environmental conditions [7]–[10] and specimen dimensions [11]. A further influence is the quality of the specimens tested both in terms of the geometry and concrete produced, which are generally assumed to be uniform and homogeneous, respectively.

A typical way to present the results of fatigue tests are the S-N (stress level – number of cycles to failure) curves, in which the ordinate represents the maximum cyclic stress level, while the abscissa describes the number of cycles at failure on a logarithmic scale. It is possible to find the "best fit" line that optimally describes the empirical results and the related confidence intervals employing linear regression techniques. Taking into account the scattering and statistical distribution of the empirical data, S-N-P (stress level – number of cycles to failure – probability of failure) curves are obtained in which the probability of failure is introduced and the reliability of the material can be evaluated [12]–[15]. Thus, the study of the influences on data scattering is an important aspect in establishing material reliability. A large scattering of results was observed in [16] because the nature of each individual specimen used, such as the quality of the load surfaces, had a considerable influence. The inhomogeneous nature of the concrete itself, partially influenced by production techniques [17], is also considered to be part of the cause of the scattering of results.

Although the scattering of empirical fatigue results is examined from a statistical point of view, no research in the literature investigates the influence of specimen production and preparation on the number of cycles to failure. The first occasion in which the influence of HPC specimen production and preparation on the concrete strength and number of cycles to failure can be extensively investigated in the framework of a round-robin test within the Priority Programme SPP 2020 "Cyclic deterioration of High-Performance Concrete in an experimental virtual lab".

2 Experimental programme

2.1 Concrete and specimens

The concrete used in the round-robin test is the reference concrete developed and used within the SPP 2020. This is a HPC with 28-day mean compressive strengths of about 113. The complete composition of the reference concrete is given in Table 1.

Table 1 Concrete composition

Content	HPC
CEM I 52.5 R-HS/NA	500.00 kg/m ³
Microsilica	-
Quartz sand (0/0.5 mm)	-
Fine sand (0/0.5 mm)	75.00 kg/m ³
Sand (0/5 mm)	850.00 kg/m ³
Basalt (2/5 mm)	350.00 kg/m ³
Basalt (5/8 mm)	570.00 kg/m ³
Superplasticizer	5.00 kg/m ³
Stabilizer	2.85 kg/m ³
Water	176.00 kg/m ³
28-d Mean compressive strength (100 mm cube)	~ 113 MPa

The participating laboratories were anonymized by numbering them from 1 to 4. The mixing process of the raw materials was also given to them. They were free to use their own concrete mixers and technique to compact the concrete in the formworks. The formworks (PVC) were the same type for all participants. Three different batch mixers were used, two of them with a vertical axis of rotation and one, at laboratory 2, with a horizontal axis. The used concrete compaction technologies and techniques were similar with slightly different vibration frequencies and different total vibration duration.

The timing for the concrete curing and formwork removal has been set as follows for all laboratories. After filling the formwork and compacting the concrete, the specimens initially remained covered in the formwork for 48 h. Laboratories 1, 2 and 3 removed the formwork by cutting it vertically, while laboratory 4 pushed manually the hardened concrete specimens out of the formworks. The specimens were then stored in the climatic chamber at standard conditions (20 °C/65 % R.H.).

The preparation of the specimens was carried out when the concrete had reached 14 days of curing. Each participating laboratory prepared only half of the specimens produced employing its own techniques. The letter “O” (Own preparation technique) then identifies this group of specimens. Then, the specimens have been sent to the central laboratory of Hannover with a concrete age of at least 35 days in shockproof boxes. They were additionally wrapped in polyethylene film to protect them from drying during transportation. Once they have been delivered, the other half of the specimens of each laboratory were prepared in the laboratory of the Institute of Building Materials Science in Hannover using the technology available there. The letter “R” (Reference preparation technique) thus, identified this group. The procedure for the preparation of the specimens consists generally of sawing a few centimetres off at the upper and lower ends of the specimens to remove areas that could have been disturbed by the production process. The test surfaces of the concrete cylinders were then parallel ground and/or polished individually. The reference preparation technique consisted of accurate sawing and polishing of the test surfaces (SP). The nominal specimen dimensions ready for the test were $d = 60$ mm and $h = 180$ mm. The concrete production in the laboratories was scheduled to obtain a minimal concrete age difference of all the specimens on the day of the test, whose influence on the concrete ageing could be considered irrelevant.

The production and specimen preparation techniques used are summarised in Table 2.

Table 2 Specimen production and preparation techniques

Laboratory	1	2	3	4
Concrete	HPC			
Concrete mixer	Pemat ZK 150 HE	CEM 60 S Elba	UEZ ZM 100	Pemat ZK 150 HE
Max. material (dry) [l]	170	60	200	170
Engine Power [kW]	4	3.3	4	4
Formwork	PVC			
Compacting technique	Shaking table	Shaking table	Shaking table	Shaking table
Vibration frequency [Hz]	50	n.a.	40–80	70–90
Total vibration duration [s]	120	80–120	135	60
Formwork removing system	Form cutting	Form cutting	Form cutting	Spec. push out
“O” specimen preparation	SG	SGP	SG	SG
“R” specimen preparation	SP			

S: Sawing; G: Grinding (one side at a time); P: Polishing

2.2 Main investigations

The main investigations onto the two groups of specimens (O: Own preparation technique; R: reference preparation technique) consist of monotonically increasing and cyclic compression load tests, both carried out in the same servohydraulic testing machine with a 1 MN actuator.

Six specimens from each group were tested under force-controlled conditions at a constant speed of 0.5 MPa/s. The resulting mean compressive strength value was used as the reference strength for the following cyclic load tests on the same specimen group type.

The cyclic load tests were performed on at least six specimens using a sinusoidal cyclic load with a frequency of $f_p = 1$ Hz. Only one cyclic load with a minimum stress level of $S_{c,min} = 0.05$ and maximum stress level of $S_{c,max} = 0.75$ was investigated.

The deformations in both types of tests were measured continuously by three laser distance sensors, which were positioned at 120° from one another. The surface temperature during the cyclic load tests was recorded by means of thermocouples as well as the ambient temperature in the testing chamber. These measurements were used to monitor the tests and will not be used in the analysis in this paper as the focus is on the compressive strength and the number of cycles to failure. An example of the test set-up is shown in Figure 1.

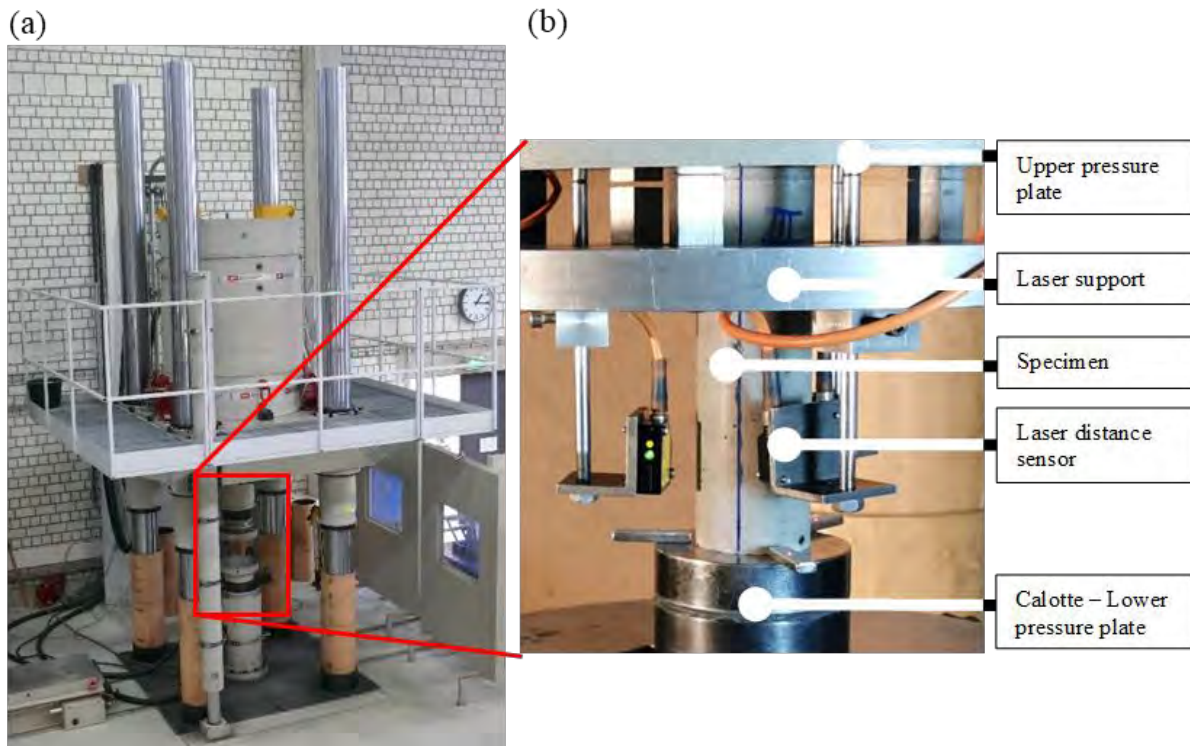


Fig. 1 Servohydraulic testing machine with 1 MN actuator (a) and measurement set-up (b) for the compressive strength and the cyclic load tests.

2.3 Complementary investigations

Before the compression and fatigue tests were carried out, the geometrical characteristics of the cylindrical specimens, resulting from the various preparation techniques used, were measured. In addition to the diameter and height of the specimens, the flatness of the test surfaces and the perpendicularity of the lateral surface of the cylinder to the test surface was also measured according to [18]. The perpendicularity is described as the maximum deviation (v_{\max}) of a point on the cylinder shell from the lateral reference plane and expressed in millimetres.

The surface roughness of both test surfaces, defined according to ISO 25178, has been measured using the 3D laser scanning confocal microscope “VR-5000” by KEYENCE. Additionally, the parameter called “effective area ratio” (EAR) has been defined, with the aim to identify surface edge imperfections, such as edge breaks, that cause a reduction of the contact surface with the loading plates of the test machine. The “EAR” is the ratio between the area excluding edge imperfections, determined by the profilometer, and the flawless area, calculated using the average diameter of the specimen.

3 Compressive strength and number of cycles to failure

A total of 48 specimens were investigated under compressive load and 53 specimens were investigated under compressive cyclic load within the framework of this investigation of HPC.

The results of the compression tests and the cyclic load tests carried out on HPC specimens from laboratories 1 to 4 are shown in Figure 2: The whiskers indicate the standard deviations, while the red and blue dots represent the mean values obtained from the specimen sets “O” and “R”, respectively. Additionally, the standard deviation is also represented on the secondary co-ordinate system on the right vertical axis for the sake of clarity.

Considering the results obtained from the specimens from all the laboratories, an overall mean compressive strength value of 98.7 MPa is obtained, while the overall standard deviation is 11 MPa, which is higher than the standard value between 6 and 8 MPa stated by [19] for the production of HPC. From a graphical point of view, by aggregating the results by groups of laboratories it is possible to identify in Figure 2(a) a trend in the influence of the laboratory productions on the compressive strength of each batch of concrete.

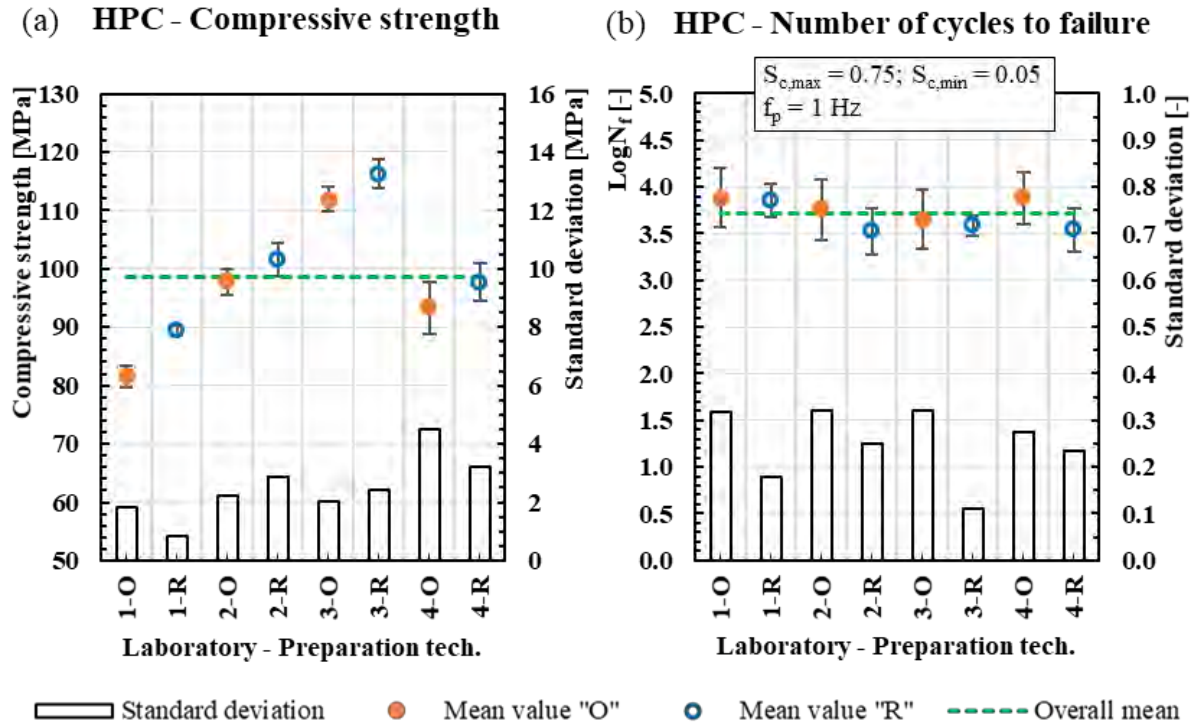


Fig. 2 HPC – (a) Compressive strength, (b) Number of cycles to failure.

In order to analyse only the influence of concrete production techniques, the results obtained from the test specimens prepared with the reference technique were analysed using the principles of analysis of variance. The ANOVA indicates a statistically significant difference between the groups, confirming the influence of the laboratories on the compressive strengths obtained from the “R” specimens.

The compressive mean values obtained from specimen sets “R” tend to be higher than those obtained from specimen sets “O” for all laboratories. This result is also statistically confirmed by the classical t-test. Such a difference is particularly strong in the results obtained from specimens of laboratory 1. A weaker difference can be seen in the results from the specimens of laboratory 4. In this case, the production of concrete in laboratory 4 causes a high scattering of the results, which tends to cover the influences of the specimen preparation techniques.

To summarize, there is a positive influence of the reference technique, i.e. of the preparation by careful sawing and polishing, on the compressive strength.

The resulting overall number of cycles to failure mean is 3.713 on a logarithmic scale with an overall standard deviation of 0.28. It is obvious from Figure 2(b) that the mean values of the different specimen sets do not deviate significantly from the overall mean value and remain within the distance of one standard deviation from it. Hence, from a first analysis, the strong influence of the concrete production on the concrete strength is not to be found in the number of cycles to failure on the logarithmic scale. Furthermore, by applying the classical t-test to the results of “R” and “O” for each laboratory specimen set, the influence of the preparation techniques on the mean number of cycles to failure is not present. A closer look at the standard deviations for each specimen set shows that the standard deviation of the specimens prepared according to the reference technique is generally smaller than that from the set of specimens prepared directly by the laboratories.

3.1 Specimens geometrical characteristics

The geometrical characteristics of all the specimens were assessed as described in section 2.3. No significant differences were recorded regarding the specimen diameter. Only the preparation technique of laboratory 2 provided specimens on average 2 mm higher than the nominal height ($h = 180$ mm). The assessment of the test surface flatness of all specimens gave no evidence of deviations, which means that all the preparation techniques allow the realisation of perfectly flat surfaces, according to the definition of [18].

The results of the measurements of the three most significant geometric parameters, namely, perpendicularity of the lateral surface, roughness and effective area ratio, are shown in Figure 3 for each set of specimens and laboratory.

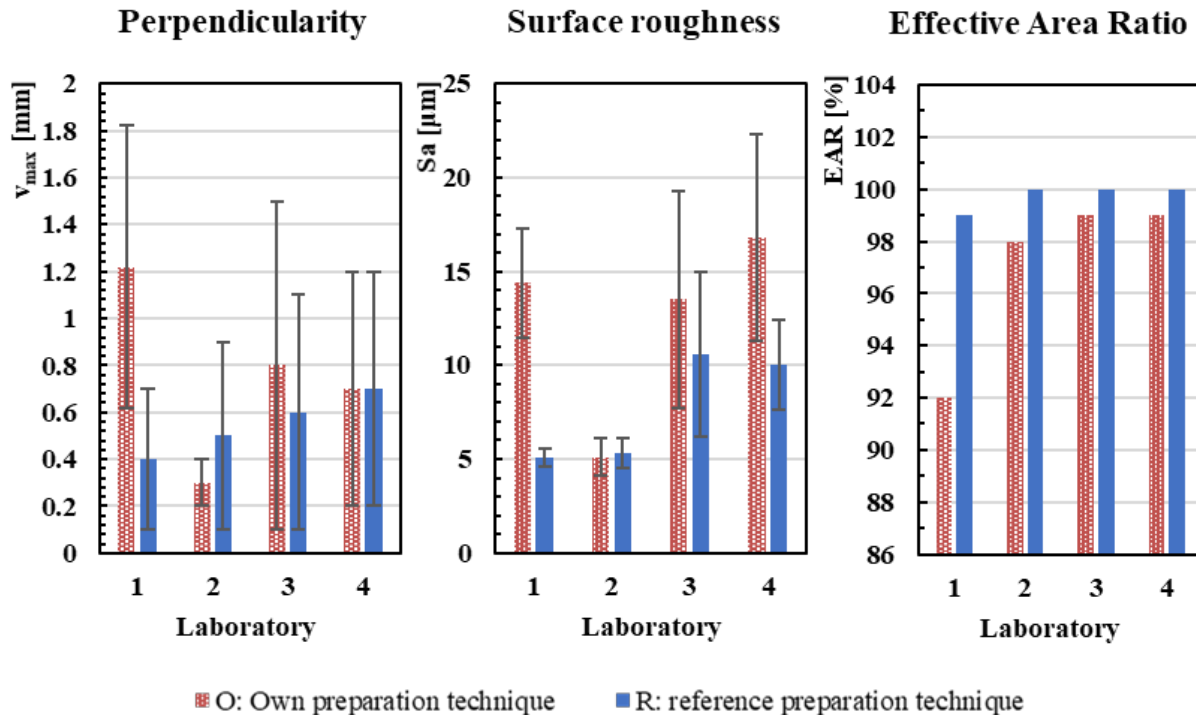


Fig. 3 Geometrical characteristics – (a) Perpendicularity of the specimens, (b) Surface roughness of the test surfaces, (c) Effective Area Ratio (EAR).

The preparation techniques used by laboratories 3 to 4 can obtain perpendicularity values comparable to those obtained from the reference preparation technique. The technique used in laboratory 2 can obtain the most accurate perpendicularity value, while the technique used in laboratory 1 is the less accurate. The grinding and the following polishing technique used in laboratory 2 produce a surface roughness equal to the one obtained by the polishing of the reference technique. The grinding technique used in the remaining laboratories produces a higher surface roughness than that resulting from the reference technique.

The results of the effective area ratio parameter, which aims to identify local imperfections and breaks in the edges of test surfaces, are meaningful. The reference technique generally allows one to obtain specimens with intact edges that do not reduce the contact surface with the pressure plates of the test machine. The techniques used by laboratories 3 and 4 caused slight imperfections that reduced the contact surface by an average of about 1 %. An average reduction of approximately 2 % is recorded for specimens prepared by laboratory 2, while the average reduction recorded for specimens from laboratory 1 is about 8% and, thus, much higher.

The extent of the imperfections found on the specimens prepared by laboratory 1 is given in the example shown in Figure 4. The picture of the test surface of a specimen is on the left-hand side and the 3D image taken by the profilometer is on the right-hand side. The breakage of a part of the edge of the specimen is evident and of considerable size. Besides, there are small imperfections along the entire edge that further reduce the contact surface with the pressure plates of the machine. On the contrary, Figure 5 shows an example of a test surface of a specimen produced by the same laboratory 1 but prepared with the accurate sawing and polishing of the reference technique. This example shows that the edges are undamaged. Consequently, there is no reduction of the contact surface with the load plates of the test machine.

In conclusion, the specimens prepared with the reference technique show accurate and homogeneous geometric characteristics. This has a positive effect on the results of the compression tests and on the scattering of the number of cycles to failure obtained from the cyclic tests as shown in the previous section.

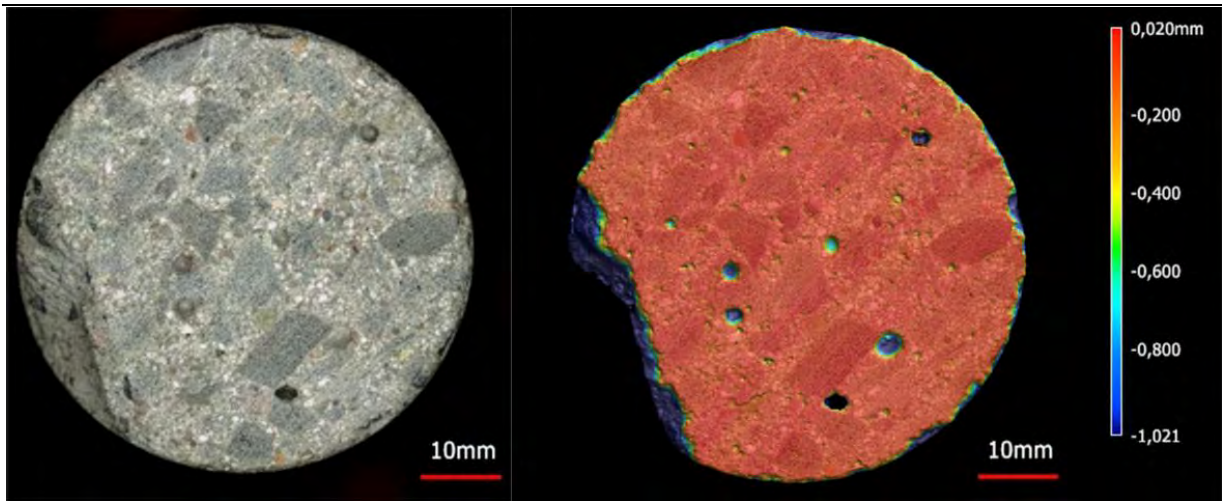


Fig. 4 Example of a HPC specimen from laboratory 1 prepared using their own preparation technique (SG). On the left: test surface. On the right: 3D profilometer.

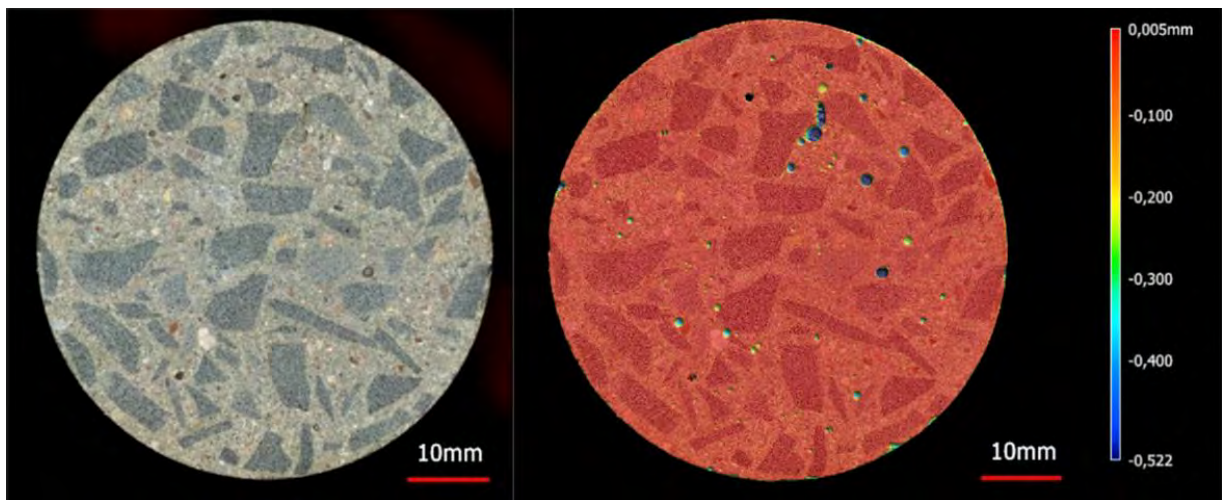


Fig. 5 Example of a HPC specimen from laboratory 1 prepared using the reference preparation technique (SP). On the left: test surface. On the right: 3D profilometer.

4 Conclusions

Tests carried out on concrete specimens for the determination of compressive strength and fatigue strength expressed in number of cycles to failure on logarithmic scale can be influenced by various factors as shown in the literature. The influence of the production and preparation techniques of HPC specimens was extensively investigated in a round-robin test involving four different laboratories. The authors analysed the results of the tests under monotonically increasing load and cyclic compression load in relation to the concrete production techniques and geometrical characteristics of the concrete specimens reaching the following main conclusions:

1. On one hand, the different techniques used to produce the HPC batches influence the compressive strength. On the other hand, the production techniques do not significantly affect the mean number of cycles to failure on a logarithmic scale since the cyclic load tests are performed on specimens using the reference strength obtained from the respective production batch.
2. The preparation by accurate sawing and polishing allows specimens with uniform and accurate geometrical characteristics to be produced. Broken specimens obtained due to poor sawing and improper grinding/polishing resulting in damaged edges have a negative influence on the compressive strength. Moreover, they have a negative influence on the scattering of the tests under monotonically increasing load and cyclic compression load in terms of maximal strength and number of cycles to failure for the HPC specimens tested in this round-robin test. However, the mean number of cycles to failure on a logarithmic scale are not influenced due to the use of the reference strength obtained from specimens of the same set, i.e. with similar characteristics.

Acknowledgements

This research project was supported by the German Research Foundation (DFG) within the scope of Priority Programme 2020 “Cyclic deterioration of High-Performance Concrete in an experimental virtual lab”. The authors would like to express their gratitude for the financial support.

References

- [1] N. Oneschkow, C. von der Haar, J. Hümme, C. Otto, L. Lohaus, and S. Marx, ‘Ermüdung von druckschwellbeanspruchtem Beton - Materialverhalten, Modellbildung, Bemessung’, in *Beton Kalender 2018*, Weinheim, Germany: Wiley-VCH Verlag GmbH & Co. KGaA, 2018, pp. 643–755.
- [2] H. Weigler and W. Freitag, *Dauerschwell- und Betriebsfestigkeit von Konstruktionsleichtbeton*. Bundesminister Fuer Verkehr, 1971.
- [3] D. Klausen, *Festigkeit und Schädigung von Beton bei häufig wiederholter Beanspruchung*, vol. Thesis. Darmstadt: Technische Hochschule Darmstadt, 1978.
- [4] D. Klausen and H. Weigler, ‘Damage to Plain Concrete Under Cyclic Compressive Loading’, *Durability of Building Materials and Components*, pp. 593–602, 1980.
- [5] fib-federation internationale du beton, *fib Model Code for Concrete Structures 2010*. John Wiley & Sons, 2013.
- [6] N. Oneschkow, ‘Fatigue behaviour of high-strength concrete with respect to strain and stiffness’, *Int. J. Fatigue*, vol. 87, pp. 38–49, Jun. 2016.
- [7] K. Waagaard, ‘Fatigue strength of offshore concrete structures, COSMAR report PP2-1 and PP2-2’, 1981.
- [8] F. Aldakheel, C. Tomann, L. Lohaus, and P. Wriggers, ‘Water-induced failure mechanics for concrete’, *Proc. Appl. Math. Mech.*, vol. 19, no. 1, 2019.
- [9] C. Tomann and N. Oneschkow, ‘Influence of moisture content in the microstructure on the fatigue deterioration of high-strength concrete’, *Struct. Concr.*, vol. 20, no. 4, pp. 1204–1211, Aug. 2019.
- [10] N. Oneschkow, J. Hümme, and L. Lohaus, ‘Compressive fatigue behaviour of high-strength concrete in a dry and wet environment’, *Construction and Building Materials*, vol. 262, p. 119700, 2020.
- [11] S. Schneider, J. Hümme, S. Marx, and L. Lohaus, ‘Untersuchungen zum Einfluss der Probekörpergröße auf den Ermüdungswiderstand von hochfestem Beton’, *Beton Stahlbetonbau*, vol. 113, no. 1, pp. 58–67, Jan. 2018.
- [12] J. O. Holmen, *Fatigue of concrete by constant and variable amplitude loading*. Trondheim: Division of Concrete Structures, Norwegian Inst. of Technology, University, 1979.
- [13] N. K. Raju, ‘Prediction of the fatigue life of plain concrete in compression’, *Building Science*, vol. 4, no. 2, pp. 99–102, Sep. 1969.
- [14] B. H. Oh, ‘Fatigue life distributions of concrete for various stress levels’, *ACI Mater. J.*, vol. 88, no. 2, pp. 122–128, 1991.
- [15] Do Minh-Tan, Chaallal Omar, and Aïtcin Pierre-Claude, ‘Fatigue Behavior of High-Performance Concrete’, *J. Mater. Civ. Eng.*, vol. 5, no. 1, pp. 96–111, Feb. 1993.
- [16] S. Urban, R. Wagner, A. Strauss, M. Reiterer, C. Dehlinger, and K. Bergmeister, ‘Monitoring-based Lifetime Assessment of Concrete Structures-Research Project MOSES’, *Beton-und Stahlbetonbau*, vol. 108, no. 9, pp. 630–640, 2013.
- [17] C. F. Ferraris, ‘Concrete Mixing Methods and Concrete Mixers: State of the Art’, *J. Res. Natl. Inst. Stand. Technol.*, vol. 106, no. 2, pp. 391–399, Mar. 2001.
- [18] Deutsches Institut für Normung e. V., ‘DIN EN 12390-1:2012-12, Prüfung von Festbeton - Teil 1: Form, Maße und andere Anforderungen für Probekörper und Formen; Deutsche Fassung EN_12390-1:2012’, Beuth Verlag GmbH: Berlin, Germany, 2012.
- [19] P. Grünbl, H. Weigler, and S. Karl, *Beton: Arten, Herstellung und Eigenschaften*. John Wiley & Sons, 2002.

Long-term strain development of concrete subjected to creep and cyclic loading

Bianca Kern, Nadja Oneschkow, Ludger Lohaus, Michael Haist

*Institute of Building Materials Science,
Leibniz University Hannover,
Appelstraße 9A, 30167 Hannover, Germany*

Abstract

The deformations during the service life of concrete structures are predicted using creep models, assuming a constant loading. However, many structures are not only subject to static creep loads but to cyclic loads as well. The superposition of both load types can lead to significantly increased concrete deformations compared to deformations predicted by existing creep models. This might result in serious damage and safety risks.

Hereinafter, the viscous strain development of a normal-strength concrete due to static creep and cyclic loading under corresponding stress levels are presented. The results show that even for low stress levels of $S_{max} \leq 0.45$, there are differences in the cyclic and creep strain curves. For higher stress levels, the influence is expected to be even more significant. Therefore, an adjustment of current dimensioning models is necessary.

1 Introduction

Measurements and recalculations on existing reinforced and prestressed concrete bridges have shown that long-term deformations of concrete structures can significantly exceed deformations predicted by creep models currently available. *Bažant* [1] and, previously [2]–[5], ascertained that the superposition of static creep loading and cyclic loading causes an increase in long-term deformations of concrete. The underestimation of deformations might lead to serious damage and safety risks. However, neither the magnitude of additional deformation caused by the superimposed cyclic loading nor the long-term development of these additional deformations during the service life are known so far. In this paper, the differences in strain development due to creep or cyclic loading are investigated in a first step to analyse the effect of superposition of creep and cyclic loading.

The total strain due to static creep loading $\varepsilon_{tot,cr}$ consists of an elastic strain ε_{el} and a time-dependent creep strain component $\varepsilon_{v,cr}$ [2], [6]–[7], (see Fig. 1 b)). In the field of cyclic strain analysis, the development of strains at maximum $\varepsilon_{tot,max}$ and minimum peak stress $\varepsilon_{tot,min}$ are usually investigated. Those peak strains also consist of an elastic strain ε_{el} and a time-dependent, viscous strain component ε_v (Fig. 1 d)). In addition, a load cycle-dependent, plastic strain component could be induced by damage [8]–[10].

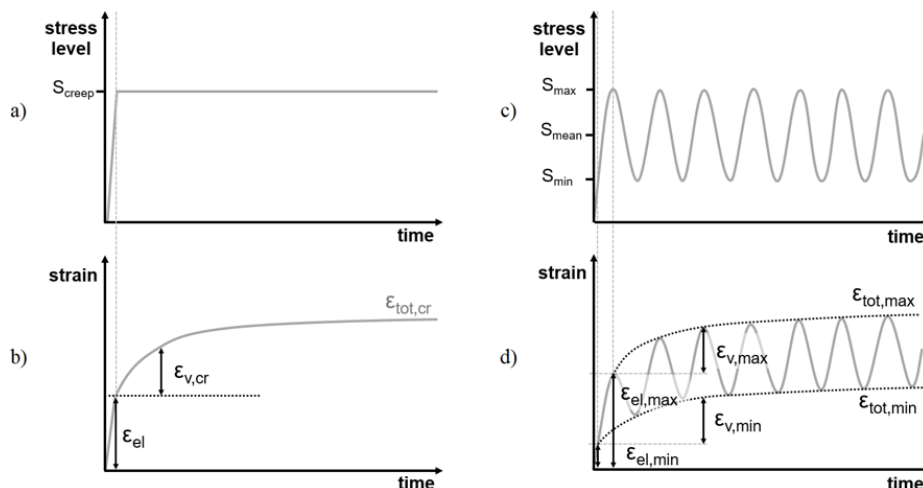


Fig. 1 Schematic presentation of creep and cyclic loading as a function of time (a) and c)) and corresponding strain components (b) and d))

The similarity in shapes of strain curves due to creep and cyclic loading led to the assumption that the strain development due to cyclic loading can be described by the strain development caused by a specific static creep stress level [3], [10], [11]. The *fib* Model Code 2010 [12] provides equation (1), following creep formulations for calculating the total strain due to cyclic loading. The equation given is valid for maximum stresses $|\sigma_{c,max}| < 0.6 f_{ck}$ and mean stresses $(|\sigma_{c,max}| + |\sigma_{c,min}|)/2 < 0.5 f_{ck}$. The first term describes the elastic strain component ε_{el} as a constant strain component resulting from the maximum cyclic stress. The second term describes the time-dependent, viscous strain $\varepsilon_{v,cycl}$ resulting as a function of creep due to the mean cyclic stress, calculated as the mean value from the maximum stress $\sigma_{c,max}$ and the minimum stress $\sigma_{c,min}$.

$$\varepsilon_{cf}(t, t_o) = \underbrace{\frac{\sigma_{c,max}}{E_{ci}(t_o)}}_{\text{elastic strain } \varepsilon_{el}} + \underbrace{\frac{\sigma_{c,max} + \sigma_{c,min}}{2 \cdot E_{ci}} \cdot \varphi(t, t_o)}_{\text{viscous strain } \varepsilon_{v,cycl}} \quad (1)$$

The mean stress level concept of *fib* Model Code 2010 [12] is controversially discussed in the literature. A stress level between the mean and maximum cyclic stress level is often indicated as a creep stress level leading to comparable strain curves [3], [10], [11]. *Whaley and Neville* [2] found that the total cyclic strains at maximum peak stress for cyclic loading with a frequency of 9.75 Hz and maximum stress levels in the range of $S_{max} = 0.15$ to $S_{max} = 0.55$ are even higher than those resulting from static creep stress levels equal to the maximum cyclic stress level. Hereby, the difference between the total cyclic and creep strains increases with increasing stress levels. But *Mehmel and Kern* [3] showed that the total cyclic strains at maximum peak stress of cyclic loading with a frequency of 6.3 Hz and maximum stress levels in the range of $S_{max} = 0.40$ to $S_{max} = 0.60$ are comparable to the total strains at a creep stress level equal to the maximum stress level of cyclic loading.

Whaley and Neville [2] and *von der Haar* [10] defined an equivalent creep stress level as a stress level for which the creep strains are equal to those due to cyclic loading depending on the mean stress level and the relative stress amplitude. It must be stated that *von der Haar* [10] investigated only cyclic strains with maximum stress levels $S_{max} \geq 0.6$, whereby *Whaley and Neville* [2] and *Mehmel and Kern* [3] performed comparative investigations concerning creep and cyclic strains with maximum stress levels $S_{max} < 0.5$.

There is generally no consensus in the literature about if and to which extent the developments of strain due to static creep and cyclic loading are comparable or which principal differences exist. Therefore, the developments of viscous strain are analysed comparatively for static creep and cyclic loading with coordinated stress levels $S_{max} \leq 0.45$ in this paper. Special attention is paid to the comparability of creep and cyclic strains.

2 Concrete composition and specimens

All investigations were carried out on a normal-strength concrete. The samples were cast in two batches with 28-day mean compressive strengths according to DIN EN 12390-3 [13] of $f_{cm,cube} = 35.7$ MPa (batch 1) and $f_{cm,cube} = 37.5$ MPa (batch 3), respectively. The composition of the concrete is given in Table 1.

Table 1 Concrete composition

Component	Unit	Value
Ordinary Portland cement (CEM I 42.5 R)	[kg/m ³]	290
Quartz powder (0/0.25 mm)	[kg/m ³]	40
Sand (0/2 mm)	[kg/m ³]	790
Gravel (2/8 mm)	[kg/m ³]	966
PCE superplasticizer	[kg/m ³]	1.7
Water	[kg/m ³]	202
Water to cement ratio w/c	[-]	0.70

The creep and cyclic tests were conducted on cylindrical specimens with a height $h = 180$ mm and a diameter $d = 60$ mm. PVC formwork was used for the casting. The concrete was filled into the formwork in two equal layers and each layer was mechanically compacted using a vibrating table. All samples were stored at 20 °C and demolded after five to six weeks. After removal from the formwork, the test surfaces of the specimens were plan-parallel ground and polished. The entire sample was sealed with aluminium-coated butyl tape and stored at 20 °C until testing for at least 140 days to ensure an almost complete hydration and avoid additional hardening of the concrete during testing. The storage condition chosen (referred to as V100) ensures a constant pore moisture content of approx. 100 %. The specimens were tested in sealed state to prevent drying shrinkage.

3 Experimental programme

3.1 Experimental set-up

The static creep tests were conducted using a creep testing machine with a maximum load capacity of 45 kN and a load precision of ± 1 kN. The stress was monotonically increased up to the intended creep stress level S_{creep} using a hydraulic load cylinder connected to a high-pressure buffer reservoir and subsequently maintained constant.

A class 0.5 servohydraulic universal testing machine (according to ISO 7500-1 [14]) with a load capacity (compression) of 500 kN was used for the cyclic testing. First, the stress was monotonically increased up to the mean stress level. Subsequently, the load oscillation, as defined by the mean stress level S_{mean} , the amplitude and the frequency f_i , was started.

In both, static creep and cyclic tests, the axial deformations of the specimens were measured continuously throughout the entire test using three linear variable differential transformers (LVDTs) positioned around the specimen's axis at angles of 0°, 120° and 240° (Fig. 3). In addition, the axial force, the axial stroke of the actuator, the ambient temperature and the temperature at the top of the loading plate were measured and recorded. The sampling rate was 1 Hz for creep investigations and 10 Hz for the cyclic investigations.

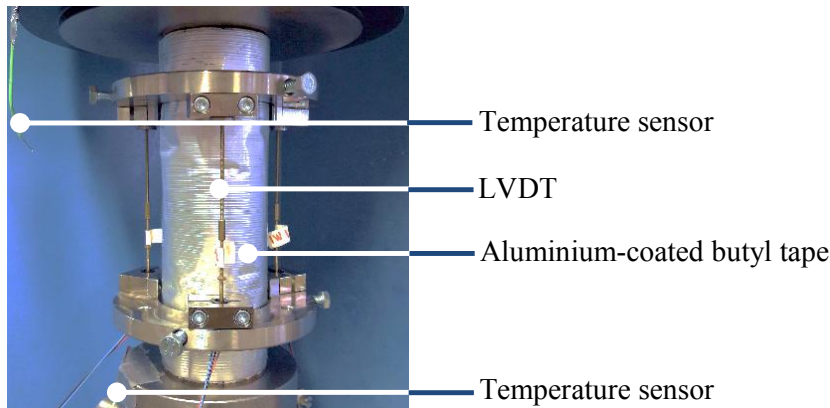


Fig. 3 Experimental set-up

3.2 Test programme

The compressive strength of the concrete was determined force-controlled immediately before testing using three cylindrical specimens of the same batch, with the same dimensions and storage condition (sealed) as those used in the creep and cyclic loading tests. The reference compressive strength $f_{cm,ref}$ was calculated as mean value and used for the determination of the stress levels ($S_i = \sigma_{c,i} / f_{cm,ref}$). The maximum stress level S_{max} , mean stress level S_{mean} and minimum stress level S_{min} or creep stress level S_{creep} were kept constant within each test.

The test programme is given in Table 2. The stress levels are chosen with regard to typical stresses during the service life of concrete structures such as bridges. The maximum stress level S_{max} was varied while the minimum stress level S_{min} and the load frequency f_i of the cyclic tests were the same in all tests. Two accompanying static creep tests with load levels of $S_{creep} = S_{max}$ and $S_{creep} = S_{mean}$, respectively, were carried out for each type of cyclic test (S_{max} , S_{mean} , S_{min}). Each test regime was carried out with three different test durations (3, 6 and 13 days). The number of creep

tests was respectively twice the number of the cyclic tests. This test regime was chosen to enable a sufficient number of repetitions while keeping the total duration of the test programme limited.

Table 2 Stress levels investigated and frequency for cyclic and creep tests

Line	Load type	Cyclic loading				Static creep loading	Test duration	Number of specimens per test duration
		S_{max}	S_{mean}	S_{min}	f_t	S_{creep}		
	[-]	[-]	[-]	[-]	[Hz]	[-]	[d]	[-]
1	Cyclic	0.35	0.20	0.05	0.1	-	3/6/13	1
2	Creep	-	-	-	-	0.35	3/6/13	2
3	Creep	-	-	-	-	0.20	3/6/13	2
4	Cyclic	0.45	0.25	0.05	0.1	-	3/6/13	1
5	Creep	-	-	-	-	0.45	3/6/13	2
6	Creep	-	-	-	-	0.25	3/6/13	2

As mentioned before, the specimens were cast in two batches due to the number of test specimens required. Even though the same composition and the same casting procedures were used, there are slight differences in compressive strength and modulus of elasticity at the age of loading (cf. Tab. 3). As described previously, the reference strength $f_{cm,ref}$ was determined directly before testing using three cylindrical specimens of the same batch, with the same dimensions and storage condition (sealed) as those used in the creep and cyclic loading tests. The modulus of elasticity at the age of loading $E_{ci}(t_0)$ was determined as a secant modulus of the stress-strain curve while the stress was monotonically increased at a rate of approx. 0.5 MPa/s.

Taking into account the batch dependency, the specimens for cyclic tests with $S_{max} = 0.35$ and those for the corresponding creep tests (Tab. 2, line 1-3) were taken from batch 1. For $S_{max} = 0.45$ and the corresponding creep tests (Tab. 2, line 4-6), the specimens were taken from batch 3. The specimens of batch 2 were used for other investigations not presented in this paper.

Table 3 Reference compressive strength and modulus of elasticity of cylindrical specimens (h/d = 180/60 mm) at the age of loading

	Reference compressive strength $f_{cm,ref}$	Modulus of elasticity $E_{ci}(t_0)$
Batch 1	34.9 [MPa]	30,500 [MPa]
Batch 3	42.0 [MPa]	29,400 [MPa]

3.3 Data analysis

The axial deformations were measured using three LVDTs directly on the specimen, as described in section 3.1. The strains measured are averaged for each specimen to determine the total strain ε_{tot} and its development due to static creep or cyclic loading. The viscous strains analysed are the mean viscous curves of those specimens investigated with different test durations (Tab. 2).

In the following, the total strain curve $\varepsilon_{tot,cr}$ for creep loading and the peak curve at maximum stress $\varepsilon_{tot,max}$ for cyclic loading are analysed (Fig. 1 b) and d)). The peak curve at minimum peak stress $\varepsilon_{tot,min}$ for cyclic loading is not analysed hereinafter, as there are no significant differences in the viscous strains due to maximum peak stress $\varepsilon_{v,max}$ and minimum peak stress $\varepsilon_{v,min}$. In accordance with fib Model Code 2010 [12] (see eq. (1)), a distinction was made between the elastic strain ε_{el} emerging immediately at the beginning of loading and the time-dependent viscous strain $\varepsilon_{v,cr}$ or $\varepsilon_{v,max}$. In this paper, the elastic strain component ε_{el} is defined as the strain when the creep stress S_{creep} is reached or, in the case of cyclic loading, the strain when the maximum stress S_{max} is reached in the first load cycle. The time-dependent viscous strain component $\varepsilon_{v,cr}$ or rather $\varepsilon_{v,max}$ is calculated from the total strain $\varepsilon_{tot,cr}$ or rather $\varepsilon_{tot,max}$ by subtracting the elastic strain component.

4 Results and Discussion

The mean curves of the viscous strains at maximum stress level due to cyclic loading $\varepsilon_{v,max}$ (blue) are shown for both maximum stress levels together with the mean viscous strains due to creep loading $\varepsilon_{v,cr}$ at $S_{creep} = S_{mean}$ (red) and $S_{creep} = S_{max}$ (yellow) in Fig. 4 and Fig. 5. Strain developments in fatigue research are usually analysed in relation to the number of load cycles. Therefore, it is important to state here that the analysis of strain developments is done in relation to the loading duration in order to enable the comparison with the static creep strain curves.

From Fig. 4 it can be seen that the viscous maximum strains due to cyclic loading $\varepsilon_{v,max}$ for $S_{max} = 0.35$ exceed the strains due to static creep loading $\varepsilon_{v,cr}$ with $S_{creep} = S_{mean}$. For $S_{max} = 0.45$, the viscous maximum strains due to cyclic loading $\varepsilon_{v,max}$ exceed the strains due to static creep loading $\varepsilon_{v,cr}$ with $S_{creep} = S_{mean}$ even more, as shown in Fig. 5. The viscous strains due to cyclic loading $\varepsilon_{v,max}$ with $S_{max} = 0.35$ (Fig. 4) are less but extremely close to that one caused by static creep loading $\varepsilon_{v,cr}$ at $S_{creep} = S_{max}$. In comparison for $S_{max} = 0.45$, the strains due to cyclic loading $\varepsilon_{v,max}$ are significantly lower than the creep strains $\varepsilon_{v,cr}$ at $S_{creep} = S_{max}$ (Fig. 5). It can be assumed that these differences between the strains due to cyclic $\varepsilon_{v,max}$ and creep loading $\varepsilon_{v,cr}$ for $S_{creep} = S_{max}$ increase further with increasing maximum stress level. The growth of the mean viscous maximum cyclic strains $\varepsilon_{v,max}$ and the mean viscous creep strains $\varepsilon_{v,cr}$ due to $S_{creep} = S_{max}$ is generally most similar at the beginning of loading. As soon as the growth flattens and the curves become more linear, the differences between the cyclic curve and the creep curve for $S_{creep} = S_{max}$ become evident. In this area, the gradients of the cyclic strain curves of both stress levels are smaller than the gradient of the appropriate creep strain curve with $S_{creep} = S_{max}$. Furthermore, the gradients of the cyclic strain curves are closer to the gradients of the creep curves at mean stress level $S_{creep} = S_{mean}$. Whether the gradients due to cyclic loading and creep loading at $S_{creep} = S_{mean}$ will converge for a longer loading duration and correspond at a certain time can be neither confirmed nor disproved by the presented investigations.

The results obtained are in contradiction to the results of *Whaley and Neville* [2], where the cyclic strains for an increasing stress level are increasingly higher than the creep strains for $S_{creep} = S_{max}$. Thus, the results presented here show exactly the opposite influence of cyclic loading. However, these results also disagree with *Mehmel and Kern* [3], who stated that the total strains due to cyclic loading are comparable to those caused by creep loading with $S_{creep} = S_{max}$. Nevertheless, the results obtained agree with *Whaley and Neville* [2] and *Mehmel and Kern* [3] in the fact that the strains due to cyclic loading are closer to the strains due to those caused by creep loading with $S_{creep} = S_{max}$. This contradicts with the current design approach in *fib Model Code 2010* [12] for cyclic strain development, which considers the viscous strains due to creep loading on a mean cyclic stress level (see eq. 1).

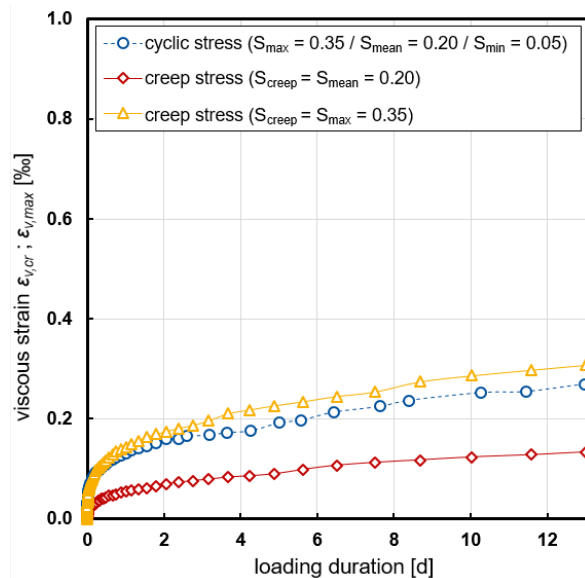


Fig. 4 Development of viscous strains due to cyclic loading and creep loading ($S_{max} = 0.35$)

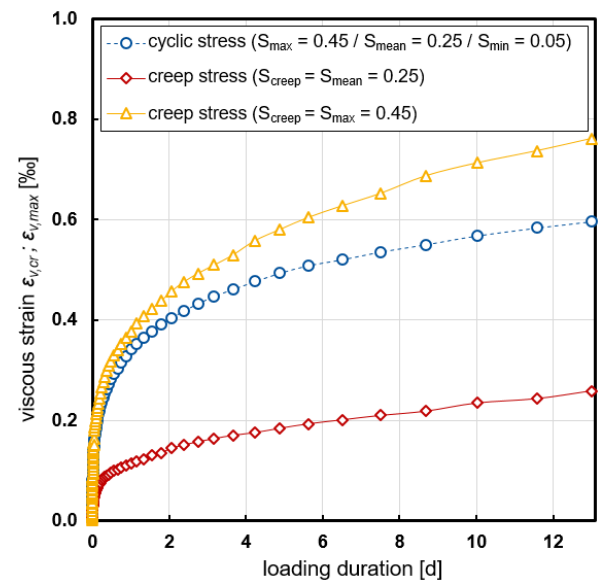


Fig. 5 Development of viscous strains due to cyclic loading and creep loading ($S_{max} = 0.45$)

5 Conclusions and Outlook

The overall objective of the research project is to examine the mutual influence of both types of loading – i.e. static creep and cyclic loading – and to prove and improve the approaches for the description of the strain development. The investigations presented in this paper are focused on the comparison of the developments of strain due to cyclic or static creep loading considering two stress levels. A normal-strength concrete, which has a high constant pore moisture content of approx. 100 %, was investigated.

Cyclic tests with a minimum stress level of $S_{min} = 0.05$ and two different maximum stress levels of $S_{max} = 0.35$ and $S_{max} = 0.45$ and corresponding creep tests were conducted to determine the influence of the load type with respect to the maximum stress level.

The results obtained clearly show that the viscous maximum strains due to cyclic loading are higher than those due to creep loading at $S_{creep} = S_{mean}$ and below the creep strains at $S_{creep} = S_{max}$ within the duration of loading of 13 days investigated. Thus, the approach of *fib* Model Code 2010 [12] for modelling the strain development due to cyclic loading by using the strain caused by creep loading with $S_{creep} = S_{mean}$ is not correct (at least for short durations of loading). Furthermore, the viscous maximum strains due to cyclic loading are closer to the viscous strains due to creep loading with $S_{creep} = S_{max}$. However, the creep strains at $S_{creep} = S_{max}$ exceeds the cyclic strains at the maximum stress level S_{max} . After the initial strong increase in all strain curves, the gradients of the cyclic strains are lower than those of the creep curves for $S_{creep} = S_{max}$ and instead more similar with the one for $S_{creep} = S_{mean}$.

The results obtained generally reveal that the mean stress level concept of the *fib* Model code 2010 [12] is not suitable for the modelling of the development of cyclic strain. A transfer to the usage of the maximum stress level does not seem to be suitable either at this state of investigation, because this approach, would increasingly overestimate the viscous cyclic strains with increasing maximum stress level. This would lead to an uneconomical dimensioning of buildings.

The experimental investigations conducted were limited to a duration of loading up to 13 days. To what extent the conclusions drawn can be transferred to longer loading will be examined in further tests. Furthermore, the influence of other parameters such as the minimum stress level and the test frequency has to be investigated.

Acknowledgements

This research project was funded by the Deutsche Forschungsgemeinschaft (DFG, German Research Foundation) within the collaborative project “Linear and nonlinear cyclic creep at defined moisture conditions” (399508601). The authors would like to express their gratitude for the financial support.

References

- [1] Bažant ZP, Wan-Wendner R, Hubler MH, Yu Q. Pervasive lifetime inadequacy of long-span box girder bridges and lessons for multi-decade creep prediction. Paper presented at the Third International Symposium on Life-Cycle Civil Engineering, Vienna; 2012.
- [2] Whaley CP, Neville AM. Non-elastic deformation of concrete under cyclic compression. *Mag Concr Res* 1973;25(84):145–54; 1973.
- [3] Mehmehl A, Kern E. Versuche über die Festigkeit und die Verformung von Beton bei Druckschwellbeanspruchung [Investigations on the strength and deformation of concrete under compressive fatigue loading]. *Deutscher Ausschuss für Stahlbeton* 144, Berlin; 1962 [in German].
- [4] Alda W. Zum Schwingkriechen von Beton [For cyclic creep of concrete]. Doctoral dissertation. Technical University Braunschweig; 1978 [in German].
- [5] Le Camus B. Recherches sur le comportement du béton et du béton armé soumis à des efforts répétés [Research on the behaviour of concrete and reinforced concrete subjected to repeated stressing]. Circular of the Inst. Technique du Bâtiment et des Travaux Publics, Series F 27, Paris; 1946 [in French].
- [6] Schwabach E. Verformungsverhalten- und Degradationsverhalten von nieder-zyklisch uniaxial druckbeanspruchten Beton [Deformation and degradation behavior of low-cycle uniaxial compression stressed concrete]. Doctoral dissertation. Bauhaus University Weimar; 2005 [in German].
- [7] Müller HS. Zur Vorhersage des Kriechens von Konstruktionsbeton [Prediction of the creep of structural concrete]. Doctoral dissertation. Karlsruhe Institute of Technology; 1986 [in German].
- [8] Oneschkow N. Analyse des Ermüdungsverhaltens von Beton anhand der Dehnungsentwicklung [Analysis of the fatigue behaviour of concrete with respect to the development of strain]. Doctoral dissertation. Report of the Institute of Building Materials Science, 13, Leibniz University Hannover; 2014 [in German].
- [9] Oneschkow N. Fatigue behaviour of high-strength concrete with respect to strain and stiffness. *Int J Fatigue* 2016;87:38–49. doi: 10.1016/j.ijfatigue.2016.01.008.
- [10] Von der Haar C. Ein mechanisch basiertes Dehnungs-modell für ermüdungsbeanspruchten Beton [A mechanically based strain model for fatigue-stressed concrete]. Doctoral dissertation. Leibniz University Hannover; 2016 [in German].
- [11] Thiele M. Experimentelle Untersuchung und Analyse der Schädigungsevolution in Beton unter hochzyklischen Ermüdungsbeanspruchungen [Experimental investigation and analysis of damage evolution in concrete under high cyclic fatigue loading]. Doctoral dissertation. BAM-Dissertationsreihe, Vol. 140. Berlin; 2016 [in German].
- [12] fib – Fédération International du Béton (ed.). *fib model code for concrete structures* 2010. Berlin: Ernst & Sohn; 2013.
- [13] DIN EN 12390-3:2019-10. Testing of hardened concrete –Part 3: Compressive strength of test specimens, German version of EN 12390-3:2019.
- [14] DIN EN ISO 7500-1:2018-06. Metallic materials –Calibration and verification of static uniaxial testing machines – Part 1: Tension/compression testing machines – Calibration and verification of the force-measuring system, German version of EN ISO 7500-1:2018.

Damage indication by electrical resistivity measurement of carbon short fiber reinforced concrete in fatigue testing

Philipp Lauff, Oliver Fischer

Chair of Concrete Structures, Technical University of Munich, Germany
Corresponding author email: philipp.lauff@tum.de

Abstract

The newly developed material carbon short fiber reinforced concrete (CSFRC) was investigated extensively in the last years. This material combines high tensile strength of the carbon fibers with ultra-high compression strength of concrete. The focus lies on orienting the fibers in order to gain the most possible tensile enhancement. This is achieved by admixing the carbon fibers in the wet concrete and extruding the paste throughout a small nozzle guided by a specifically designed concrete 3D-printer.

Due to very high fatigue resistance of carbon fibers, this study is looking at bone shaped tensile specimens under high cyclic fatigue load. In order to observe the process of crack growth and the mechanics of fatigue failure, we combined measuring techniques as digital image correlation and electrical resistivity measurement. Carbon fibers are electrical conductive and they transfer this ability to the compound material and to the specimen. By measuring the voltage drop at several specific points on the specimen's surface, allows to detect material degradation. The amount of electrodes and connection nodes were increased continuously in order to enhance accuracy and to obtain a localization of material degradation. Comparing the results with digital image correlation, both measuring methods show up parallels, meaning changes in strain are also visible in conductivity measurement.

1 Carbon short fiber reinforced concrete (CSFRC)

Extended investigations on the newly developed material carbon short fiber reinforced concrete (CSFRC) have been carried out in the last years [1], [2]. This material combines high tensile strength of carbon fibers with high compression strength of concrete. Thereby, the focus lies on orienting the fibers in order to gain the most possible tensile enhancement.

Looking at statistics, when molding fiber reinforced concrete in a conventional way only very few fibers are oriented in the desired direction of force. In [3] it is pointed out, that only 6% of the fibers are arranged within an angle of 20° . This angle is, however, a very important key fact in order to increase the tensile strength and to use the fibers in a resource-saving manner. The tensile strength reduces by approximately 40% for a fiber-load-angle of 20° and even by 65% for an angle of 30° [4]. Similar coherence are known for carbon fiber reinforced polymer [5]. In CSFRC, 70% of the fibers align within an angle of $\pm 10^\circ$ to 15° of the desired direction as an examination using an X-ray CT [6] shows.

The fiber orientation can be adjusted by considering the mold process. [7] shows very clearly the effect of fiber orientation by investigating steel fiber reinforced concrete with an X-ray radiography. There, a chute was used to fill an oblong mold from one side and let the fresh concrete flow to the far end of the mold. Only because of coherent concrete movement, the admixed steel fibers oriented in flow direction within an angle of 15 to 25° . The very same effect takes place when extruding CSFRC throughout a small nozzle.

The carbon fibers (ZOLTEK PX35) used for the production of CSFRC are 7 μm in diameter and 3 mm in length, thus having a length-diameter-ratio of 428 which is much higher compared to steel fibers with a common ratio of about 50. They are heat pretreated in order to remove the facing, which is optimized for the use in resin systems but disturbs the connection of concrete phases. Also, the fiber surface starts to oxidize and therefore the ability for fiber separation while admixing in concrete is increased. [1] examines different methods for improving fiber-matrix-bonding turning out with the described method as the best for carbon fibers.

Table 1 Concrete mixture for 3D-printed carbon short fiber reinforced concrete.

Component	Name	Amount
Cement	Holcim Sulfo 52.5R	34.6 wt.%
Microsilica	Sika Silicol P	21.5 wt.%
Quartz powder	Sikron Quartz SF500	21.5 wt.%
Quartz sand	Quarzwerke Quarzsand H33	7.6 wt.%
Water	-	11.5 wt.%
Superplasticizer	BASF Master ACE 460	2.5 wt.%
Carbon fiber	Zoltek PX35	1.0 vol.-% (0.8 wt.%)

The concrete mixture can be found in Table 1. The dry components are poured in the mixing machine and homogenized before adding water and superplasticizer. The admixture has to be stirred very well to reduce nozzle choking due to dry agglomerates of cement, silica fume or aggregates. At the end, the dry, pretreated carbon fibers are added and mixing is continued for only a short amount of time to dispense the fibers homogenously during concrete mixing process. Investigations on separated carbon fibers from the admixture show, that long term mixing destroys the fibers and lower tensile and flexural strength are measured [8]. Finally, the admixture is extruded through a nozzle with a diameter of 4 mm using a 3D-printer (Figure 1).

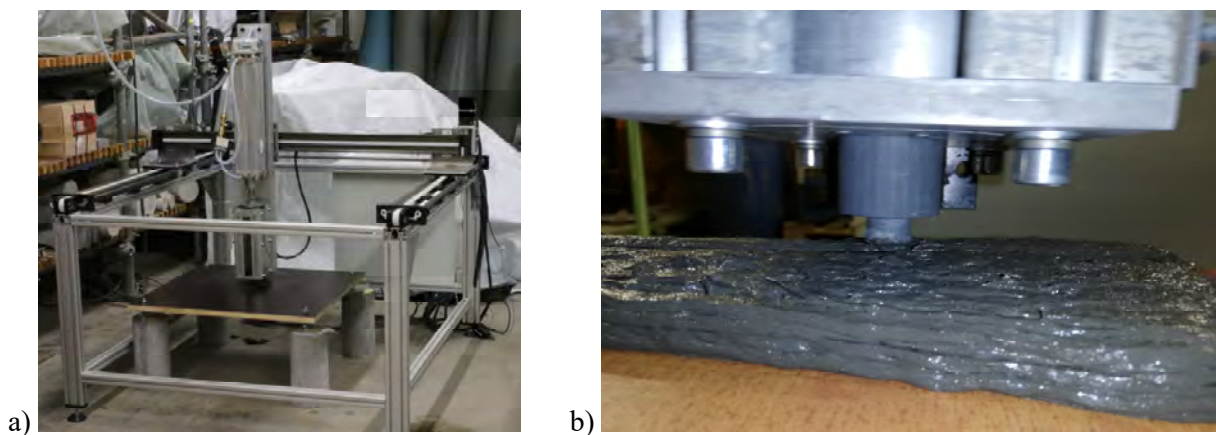


Figure 1 a) 3D concrete printer with working volume of 1.00 x 1.00 x 0.50 m. b) Printing process by extruding carbon short fiber reinforced concrete throughout a 4 mm nozzle.

Preparation of specimen is executed by adding several layers of extruded material while guiding the nozzle in the desired direction. Without the need of a mold, freeform specimens can be produced. Limiting factors are the height and overhanging constructions. Because of high amount of superplasticizer, the wet concrete tends to flow apart after extrusion when exceeding a certain number of layers or buckling problems lead to tilting over of uncured concrete parts. In order to achieve more precise specimen edges and waveless surfaces a mold is pressed onto the specimen's sides after printing process has finished.

With this kind of probe preparation and concrete extrusion, the tensile and flexural strength is improved tremendously. For reaching the best strengthening effect, an orientation in direction of the principle tension stress is preferred. Under static loads a tensile strength of 23.8 N/mm² can be reached utilizing a fiber content of 2 Vol.-%. In flexural tests a 28-day strength of 57.6 (±5.4) N/mm² is reached. By using a higher fiber content the number of nozzle choking increases and specimen production becomes more complex. However, in smaller dimensions the use of fiber contents of 3 and 4 Vol.-% are described to lead to flexural strengths of 119.6 (±7.6) N/mm² [9], which meets the compression strength of this material at the same level. The reason for failure, meaning fiber rupture or fiber pull-out, is unknown to this point but shall be observed in further studies.

2 Electrical conductivity

The use of carbon fibers changes the properties of concrete in such a way that electricity can be conducted. The quite big amount of fibers leads to small distances between themselves and several junction points as well, making current flow through the specimen.

It is well known, that changes in stress and strain influence the electrical resistivity of specimen [10]-[15]. [10] examines the effect of compression on cubes under quasistatic load with repeated load cycles. Their results show very well, that it is possible to show a change in electrical resistivity, although there seems to be no linear relation between strain and change in resistance (Figure 2a). Another study [11] though states that in 3-point-bending tests measuring the change in resistance on compression and tension side shows a linear correlation (Figure 2b).

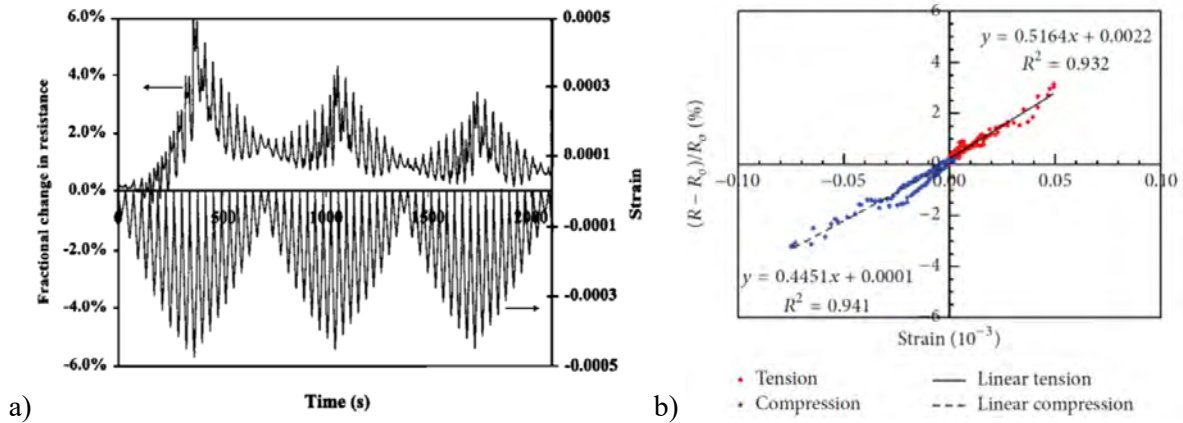


Figure 2 a) Change in resistance measured in compression tests with no linear correlation to strain [10] versus b) linear relationship in a 3-point-bending-test [11].

This study examines the change in electrical resistance under tensional fatigue load. In a first approach, the change of resistivity is measured by supplying a uniform voltage of $U_{out} = 10$ V to a resistor, which is put in series with the probe (Figure 3a). The resistor is used to calculate the current running through the specimen with Ohm's law (1):

$$I = \frac{U_R}{R} \quad (1)$$

The size of the resistor was chosen in the beginning of the tests and set to 10 k Ω due to accuracy reasons. The measured resistance of a specimen varies between from about 100 Ω to 5,000 Ω , conditioned by better and worse connections of the electrodes on the specimen's surface. To connect the electrodes to the specimen's surface, different methods were tested. At first a carbon spray was used leading to a big sized connection of about 40 x 40 mm and higher resistance measurements. Next, a glue filled with milled carbon fibers was used, so the connection area could be reduced to about 5 x 5 mm. However, the measured resistance was still in a range of about 10 k Ω . At last, a silver lacquer reduced the resistance to a range of 1 k Ω . Further investigations showed even better results of about 200 Ω when applying the electrodes to an untreated surface of the specimen in comparison to an area which was sandblasted or cut with a stone saw. It can be assumed that using these surface treatments, the carbon fibers are broken and only small fiber tips are sticking out of the surface, while in an untreated area the carbon fibers lie aligned to the surface making up a bigger connection area.

As the junction itself always implies an unknown resistance, the measurement was extended to the four-terminal sensing [16]. With this method, current is brought into the specimen at two electrodes, while voltage measurement takes place at two other electrodes positioned between the current electrodes (Figure 3b). As the input resistance of the voltmeter is very high (>1 M Ω), current flowing through the voltage measuring electrodes is neglectable and therefore there is quasi no voltage drop at the connections which leads to undisturbed voltage and resistance measurement.

In this study, the four-terminal sensing was extended by combining it with the first approach measurement in order to gain more information about the part of specimen where damage occurs (Figure

3c). By looking at the change in voltage at each electrode, damage increases the partial resistance between two electrodes and the voltage difference rises. This setup can be reduced to the four-point sensing by subtracting U_1 and U_2 . The voltage measurement U_0 is used to calculate the current applied to the outer electrodes.

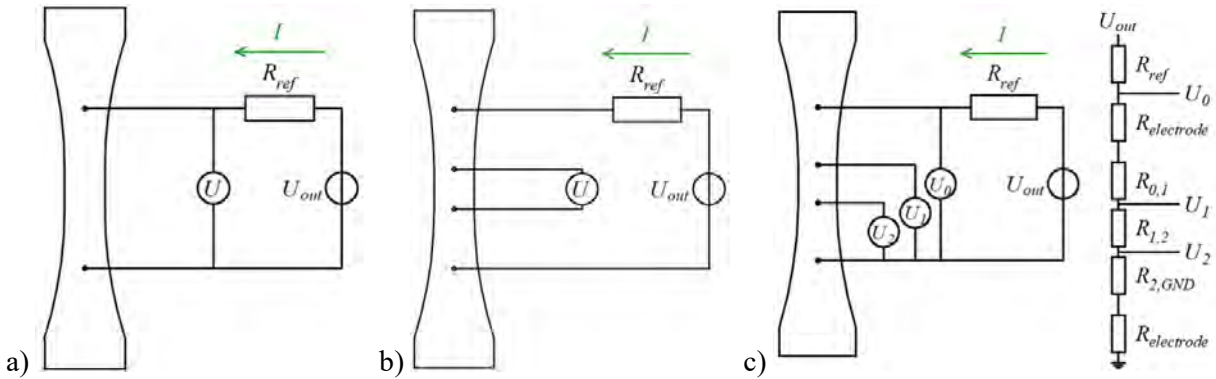


Figure 3 Development of electrical circuit for localized damage indication. a) initial approach for overall resistance measurement, b) four-point sensing in order to get undisturbed resistance measurement due to high electrode connection resistances, c) extended four-point sensing and equivalent circuit used for localized damage detection.

Figure 3c also shows the equivalent circuit for the extended measurement setup. As all components are arranged in series, current is the same at each point within the circuit, meaning that the resistance can be derived from the measured voltage with the following equations:

$$I = \frac{U_{out} - U_0}{R_{ref}} \quad (2)$$

$$R_i = \frac{U_i}{I} = \frac{U_i}{U_{out} - U_0} \cdot R_{ref} \quad (3)$$

$$\Delta R_{i,i+1} = \frac{\Delta U}{I} = \frac{U_i - U_{i+1}}{U_{out} - U_0} \cdot R_{ref} \quad (4)$$

To measure voltages at different electrodes, a *HBM QuantumX MX840B* universal measurement amplifier with 24-bit ADCs and eight channels is used. Looking at the resolution capacity of this device shows the good eligibility of this setup. By setting the amplifier's measuring voltage range from -10 V to 10 V, a resolution of 1.19 μ V per ADC-increment can be achieved. Calculating with (3) the overall resistance R_0 from the measured voltage U_0 (see Figure 3a), an accuracy of $\Delta R = 1.472$ m Ω per ADC-increment for a voltage of 1 V and $\Delta R = 4.768$ m Ω per ADC-increment for a voltage of 5 V. Even for larger measured resistances than the chosen reference resistor R_{ref} this setup works quite well as ΔR is only 1 Ω while the specimen's resistance is about 279.6 k Ω ($U = 9.655$ V).

3 Implementation in fatigue testing

In order to detect damage during load cycles, 16 electrodes were attached to the specimen's surface (Figure 4). The specimen's outer size is 450 x 100 x 50 mm, the cross section of the center part is 50x50 mm. The electrodes are arranged on three edges with a vertical distance of 25 mm to each other. Voltage is supplied via the reference resistor to electrode U_0 according to Figure 3c with additional electrodes. Next to electrical resistivity measurement, several other measuring sensors like LVDTs, strain gauges, temperature sensors and digital image correlation (DIC) are set up for damage detection.

Voltage applied induces an electric field within the specimen leading to a non-constant current density over the cross section of the specimen. The considerations shown above in Figure 3 and equations (3) to (5) cannot be transferred directly to the measurement setup depicted in Figure 4. They work out well for the vertical string U_2 - U_6 where the external voltage is applied, however the other two strings are faulty as the probe is three dimensional and actual current depends on the distance to the input and output electrodes. The size of current density behaves in an onion-shape or like an electric

field with the center axis going from the input electrode U_0 to output electrode GND . The measured voltages in string $U_{2a}-U_{6a}$ are smaller than in string U_2-U_6 , $U_{2b}-U_{6b}$ are smallest. Nevertheless, looking at the measured voltages, the results are qualified very well for damage detection.

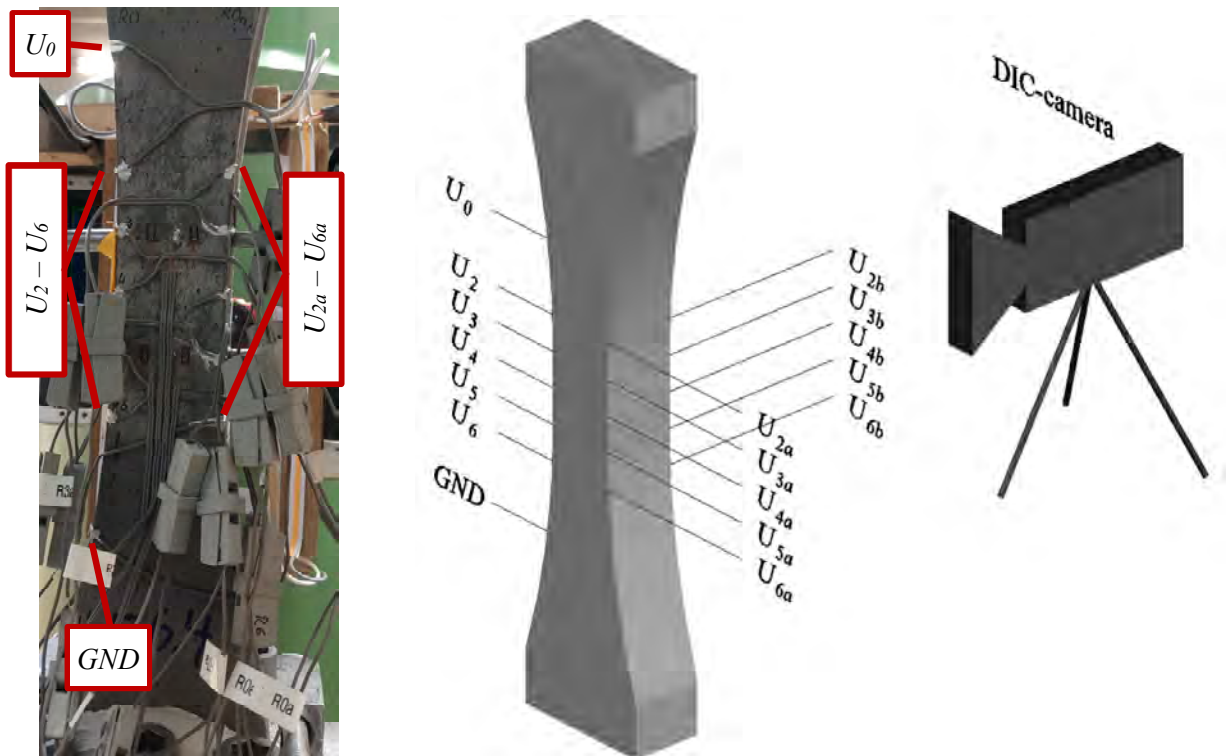


Figure 4 *left*: picture of applied electrodes during fatigue test showing electrodes $U_2 - U_6$ on the left and $U_{2a} - U_{6a}$ on the right. *right*: electrode arrangement and position of DIC-camera. The camera is located on the opposite side compared to the left picture.

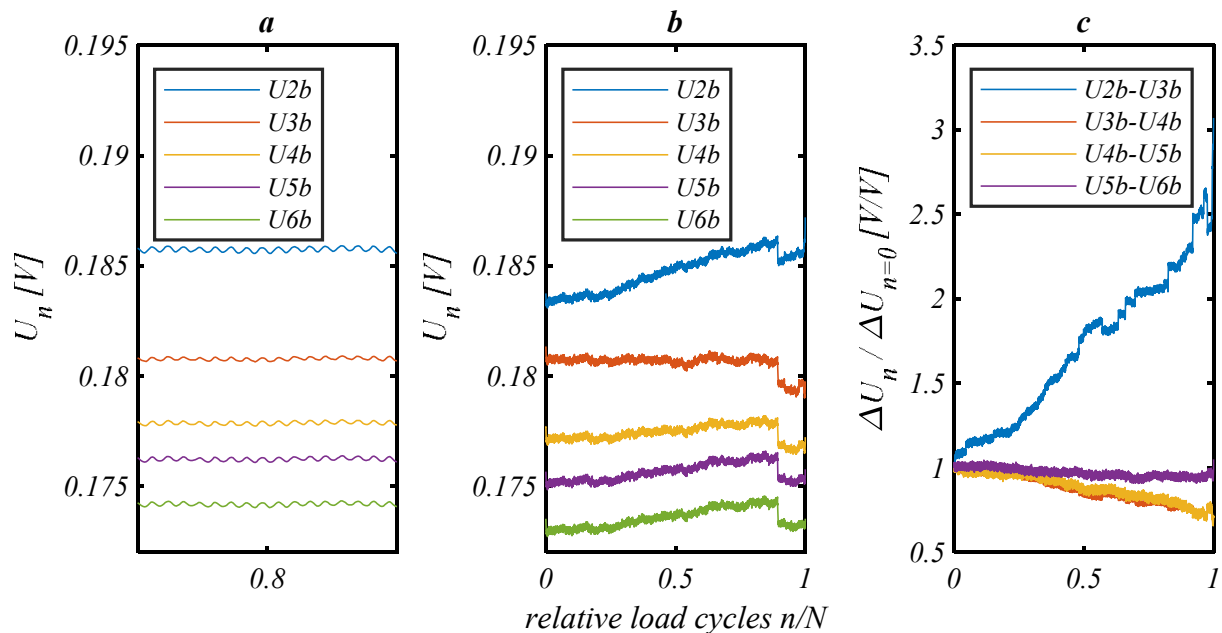


Figure 5 Voltage measurement of string $U_{2b}-U_{6b}$ during fatigue test with a total of $N = 409,063$ cycles. a) Each load cycle can be traced back using the voltage measurement. b) Overall voltage evolution. c) Relative voltage evolution with clearly revealing areas of damage progression.

The executed fatigue tests clearly show similar results compared to literature findings [10]-[15] as each load cycle can be detected (Figure 5a) even in the distant measuring string.

Figure 5b and c show two different evaluations of the same measurement. Figure 5b shows the real measured voltages. The extreme rise of sensor U_{2b} is clearly visible, however smaller changes of the other electrodes are hard to see. The measured voltages are all dependent on the electrode U_0 , where external voltage is applied. The voltage drop at a relative load cycle of 0.90 is visible in all sensors and can be reversed to a voltage drop at electrode U_0 . To cancel this effect out, the change of two adjoined electrodes is examined. To improve apparently furthermore, the change in voltage between two adjacent electrodes is related to their primary voltage drop of the first load cycle as shown in Figure 5c. The formula for this is (5), where i describes the number of electrode and n describes the load cycle.

$$\frac{\Delta U_n}{\Delta U_{n=0}} = \frac{U_{i,n} - U_{i+1,n}}{U_{i,n=0} - U_{i+1,n=0}} \quad (5)$$

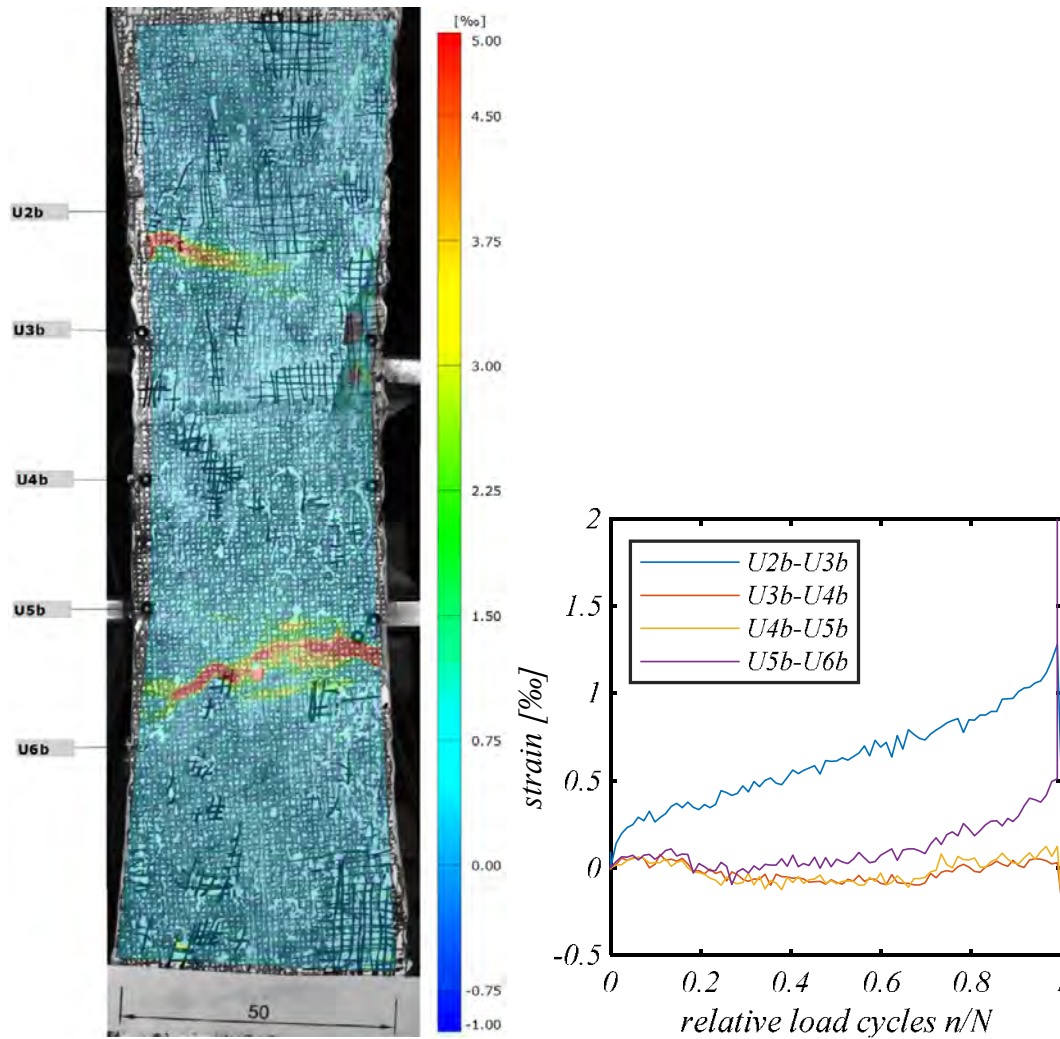


Figure 6 Strain measured with digital image correlation across the specimen's surface. The electrodes U_{2b} - U_{6b} are attached as marked on the specimen's left side, showing very similar results to Figure 5c.

Comparing this result with digital image correlation proves very well the reliability of electrical conductivity measurement. The electrodes were attached to the left side as marked in Figure 6. The image was taken at a relative load cycle of 0.99 shortly before collapse. There are many micro cracks all over the probe's surface visible in a light green color. Two major cracks (though with a very small crack

opening of about 40 μm) arose during fatigue test with high tensional strain marked in red. The crack in the lower area between electrodes U_{5b} and U_{6b} is not totally proceeding to the left edge, while the one in the upper area at electrodes U_{2b} and U_{3b} seems to originate from there. This perception matches the curve progression in Figure 5c. Evaluation U_{3b} - U_{4b} and U_{4b} - U_{5b} behave simultaneously while the other two detect some change in electrical conductivity. As the upper crack is very close to the electrodes, current is forced to find a way around the crack and the voltage difference increases vastly. As the lower crack barely reaches the electrodes on the specimen's left edge, the measurement of sensor U_{5b} - U_{6b} is barely affected. Compared to the plot in Figure 6 the strain evolution matches the resistivity revolution very well.

To improve testing and localization, additional investigations are planned. Connecting electrodes on all four sides of the specimen or with a fine-meshed sensor grit all over the surface can help to detect damage during fatigue testing more accurately. As current is always accompanied by electric and magnetic fields, techniques like EEG (Electroencephalography) [17], [18] or MEG (Magnetoencephalography) [19], which are widely used for medicine purposes as for detecting cerebral activity, could lead to a more detailed observation of the damage process during fatigue testing. These techniques are highly complex and need to be elaborated for this material in further studies.

4 Conclusion

The development of including carbon fibers as a reinforcement in concrete increases its tensile strength significantly. Techniques like fiber pretreatment and fiber orientation help to achieve best strength results and an economic use of materials. These qualities are accompanied by the effect of reducing the concrete's electrical resistivity, which makes it possible to monitor damage progression during fatigue tests. Best electrode linkage has been obtained with conductive silver lacquer. Compared to digital image correlation very similar results to strain measurement were detected, proving the reliability of this technique.

Acknowledgements

The researchers thank the German Research Foundation for funding the priority program SPP2020 of which this research is part of.

References

- [1] Hambach, M. 2016. *Hochfeste multifunktionale Verbundwerkstoffe auf Basis von Portlandzement und Kohlenstoffkurzfasern*. PhD diss., University Augsburg, Germany.
- [2] Fischer, O., Volkmer, D., Lauff, P., Hambach, M., Rutzen, M. 2019. *Zementgebundener kohlenstofffaser-verstärkter Hochleistungswerkstoff (Carbonkurzfaserbeton)*. Stuttgart, Germany: Fraunhofer IRB Verlag. ISBN 978-3-7388-0422-5.
- [3] Lauff, P., Fischer, O., Rutzen, M., Volkmer, D. 2017. *Carbonkurzfaserbeton – Eine neuartige Komposition mit gezielter Faserausrichtung beeindruckt durch signifikante Steigerung der Zugfestigkeit*. Paper presented at the 58. Forschungskolloquium des DAfStb, Kaiserslautern, Germany, September 20-21.
- [4] Rutzen, M., Lauff, P., Niedermeier, R., Fischer, O., Raith, M., Grosse, C. U., Weiss, U., Peter, M. A., Volkmer, D. 2021. *Influence of fiber alignment on pseudoductility and microcracking in a cementitious carbon fiber composite material*. Materials and Structures, Vol. 54. DOI 10.1617/s11527-021-01649-2
- [5] Bergmeister, K. 2003. *Kohlenstofffasern im Konstruktiven Ingenieurbau*. Berlin, Germany: Ernst & Sohn Verlag. ISBN 978-3-433-02847-6.
- [6] Rutzen, M., Lauff, P., Niedermeier, R. et al. 2021. Influence of fiber alignment on pseudoductility and microcracking in a cementitious carbon fiber composite material. Materials and Structures 54, 58. <https://doi.org/10.1617/s11527-021-01649-2>
- [7] Raju, R. A., Lim, S., Kageyama, T., Akiyama, M. 2019. *Visualization of the fibre dispersion in the steel fibre reinforced concrete using x-ray image*. Proceedings of the fib Symposium, Krakow, Poland, Mai 27-29.
- [8] Schneider, M. 2018. *Untersuchung von Pumpverfahren für faserverstärkten Zementleim und Mörtel und deren Einfluss auf die Fasern*. Bachelor's Thesis, Technical University of Munich, Germany.

- [9] Hambach, M., Möller, H., Neumann, T., Volkmer, D. 2016. *Portland cement paste with aligned carbon fibers exhibiting exceptionally high flexural strength (>100 MPa)*. Cement and Concrete Research Vol.89, DOI 10.1016/j.cemconres.2016.08.011
- [10] Chung, D.D.L. 2001. *Electrical Cunduction Behavior of Cement-Matrix Composites*. Journal of Materials Engineering and Performance, Vol. 11(2). DOI 10.1361/105994902770344268
- [11] Yeh, F.-Y., Chang, K.-C., Liao, W.-C. 2015. *Experimental Investigation of Self-Sensing Carbon Fiber Reinforced Cementitious Composite for Strain Measurement of an RC Portal Frame*. International Journal of Distributed Sensor Networks. DOI 10.1155/2015/531069
- [12] Azhari, F., Banthia, N. 2017. *Carbon Fiber-Reinforced Cementitious Composites for Tensile Strain Sensing*. ACI Materials Journal, Vol. 114. DOI 10.14359/51716765
- [13] Chacko, R. M., Banthia, N., Mufti, A. A. 2007. *Carbon-fiber-reinforced cement-based sensors*. Canadian Journal of Civil Engineering, Vol. 34. DOI 10.1139/L06-092
- [14] Xu, J. 2010. *Modeling of conductivity in carbon fiber-reinforced cment-based composite*. Journal of Materials Science, Vol. 45. DOI 10.1007/s10853-010-4396-5
- [15] Noh, H. W., Kim, M. K., Kim, D. J. 2019. *Comparative Performance of Four Electrodes for Measuring the Electromechanical Response of Self-Damage Detecting Concrete under Tensile Load*. Sensors MDPI, Vol. 19. DOI 10.3390/s19173645
- [16] Webster, J. G. 2003. *Electrical Measurement, Signal Processing, and Displays*. Boca Raton, USA: CRC Press. ISBN 0-8493-1733-9
- [17] Zschocke, S., Hansen, H.-C. 2012. *Klinische Elektroenzephalographie*. Springer Verlag. ISBN 978-3-642-19942-4
- [18] Niedermeyer, E., da Silva, F.L. 2004. *Electroencephalography: Basic Principles, Clinical Applications, and Related Fields*. Lippincott Williams & Wilkins.
- [19] Hämäläinen, M., Hari, R., Ilmoniemi, R., et al. 1993. *Magnetoencephalography theory, instrumentation, and applications to noninvasive studies of the working human brain*. Reviews of Modern Physics. Volume 65, Issue 2. 413-497. ISSN 0034-6861. DOI: 10.1103/revmodphys.65.413

Influence of temperature increase in fatigue behaviour of concrete during compressive fatigue loading

Martin Markert, Harald Garrecht

*Materials Testing Institute,
University of Stuttgart,
Pfaffenwaldring 4d, 70569 Stuttgart, Germany*

Abstract

Due to research activities on the topic of concrete mixtures during the last decades, concrete compressive strength has increased significantly. At the same time, the lifespan of concrete structures has continuously extended. Therefore, the fatigue behaviour of high-performance concrete (HPC) becomes more important with in regard of service life design. Previous studies on concrete prove that the number of cycles to failure due to pure compressive cyclic loading mainly depends on frequency and amplitude. By conditioning the humidity of high-performance concrete test specimen, a significant change of the number of cycles to failure can be determined. Other research activities on high-strength concrete point out that concrete heats up significantly during cyclic compressive fatigue loading. According to the literature, surface temperatures of over 100 °C were measured. This heating effect depends mainly on load level, loading frequency and humidity. As studies have shown, the static compressive strength of concrete depends on the temperature. This influence depends mainly on the concrete composition, such as the quantity of cement and the type of aggregate. This paper considered the static compressive strength of concrete at a temperature of up to 105 °C. This effect shows a significant loss of strength at increased temperature. However, as the concrete heats up during the fatigue test and the compressive strength decreases due to temperature, the assumed upper load level of $S_o = \sigma_o / f_{c,cyl}$ increases and the maximum number of load cycles to failure is reduced. Therefore, the temperature increase has a direct influence on the number of cycles during compressive fatigue loading. In a further step, the influence of the loss in compressive strength due to the temperature increase on the actual number of cycles to failure is analysed. Experiments on concrete with different degrees of humidity and different load levels are used as a basis. It can be shown that the temperature increase is a reason for a reduction of the number of cycles to failure.

1 Introduction

The fatigue behaviour of concrete, especially of HPC, is very complex and even after many years of research, the design is still very conservative. Therefore, the fatigue behaviour of high-performance concrete is becoming more important in regard of service life design. Previous studies on normal strength concrete prove that the number of cycles to failure under pure compressive cyclic loading mainly depends on frequency and amplitude. An increase of the loading frequency leads to a higher number of load cycles to failure [1]. In addition to the frequency, the related upper and lower stress level influences the number of cycles to failure [2]. Recent research work shows that the humidity of the specimen also influences the fatigue behaviour of concrete. [3] shows that the fatigue behaviour of concrete under water is worse compared to dried samples. In all these studies, the focus is usually on the number of cycles to failure or the strain curve. Beyond that, [4] has shown that the specimens can heat up to such an extent that water steam condenses on the pressure plate after the failure. It is also known that an increased temperature has an influence on the compressive strength of concrete. As a result of the increase in temperature, the static compressive strength decreases, which was shown in [5]-[7].

This paper will compare the different factors that can affect temperature development. In addition, the number of cycles to failure with concrete of different humidity are shown and connected with the decrease in strength due to the increase in temperature.

2 Temperature development

In the following, the individual influencing factors are named and shown on the basis of the literature how they affect the heating of the concrete during cyclic compressive fatigue loading tests.

2.1 Influencing factors

2.1.1 Frequency and stress level

The influence of frequency on the number of cycles to failure and on the temperature increase can be found in the literature. Among others [4]-[12] have dealt with temperature development at different frequencies. The investigation of the frequency influence was always accompanied by an investigation of the stress level. Thus the frequency influence can be considered independent of the stress level but also the influence of the stress level independent of the frequency. In [4] the Fig.1 shows the comparison of two high-strength grouting mortar at 1 Hz (green) and 10 Hz (blue) as well as at two different stress levels. (Left: Stress level of 0.85 – Right: Stress level of 0.60)

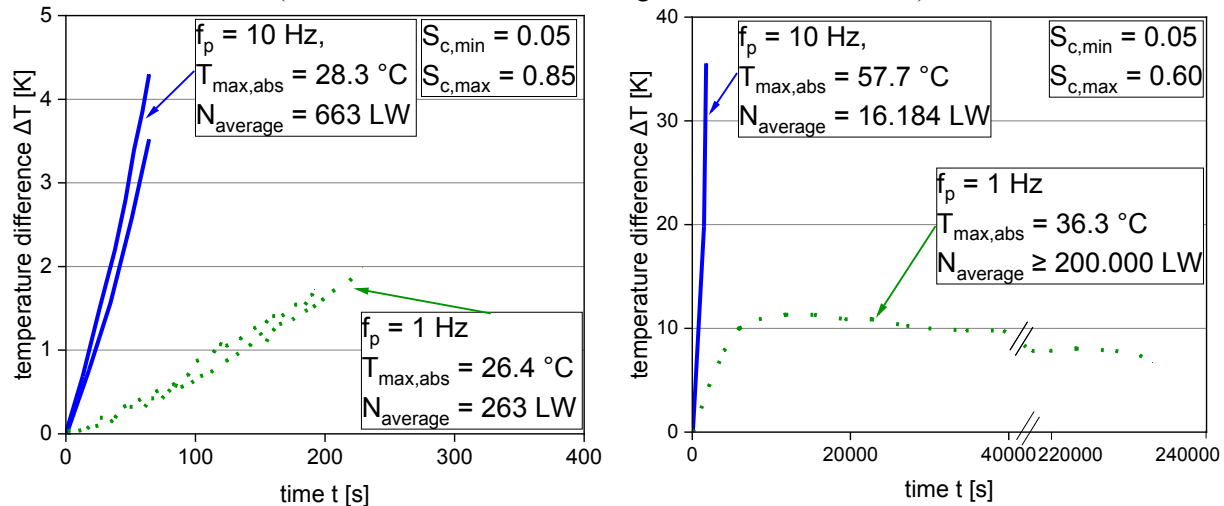


Fig. 1 Specimen's heating depending on the testing frequency and the load level according to [4].

It is noticeable that at a higher stress level the maximum heating is significantly lower than at a lower stress level. This effect has also been determined by [12]. This is due to the different running times until failure.

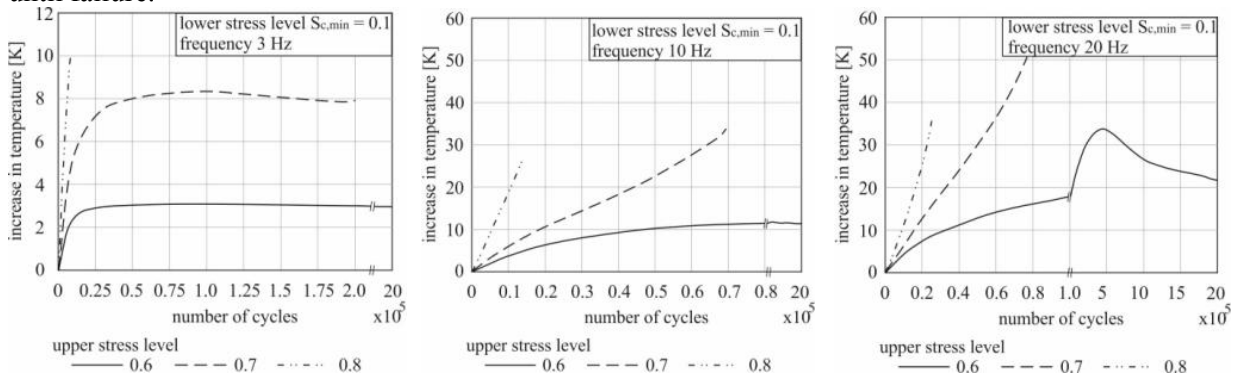


Fig. 2 Temperature development for 3 Hz, 10 Hz and 20 Hz on three load levels [8].

Thus the test specimen with a lower stress level is longer under cyclic compressive loading than a test specimen with a higher stress level. If the diagrams are compared separately, the increase in temperature development is significantly stronger with a higher frequency than with a lower frequency. This effect is investigated in [8] on an UHPC with 3 Hz, 10 Hz and 20 Hz (see Fig 2). In these investigations the frequencies and the stress levels are varied. In contrast to the other investigations, the normalised minimum stress was $S_u = 0.10$. Each individual diagram shows the frequency influence with three different load levels, it is noticeable that in all three diagrams the temperature development decreases significantly with decreasing stress level. In Fig 2 on the right, it can be seen that at 20 Hz a

heating of more than 50 K is achieved. The fact that heating to over 100 °C is possible has been shown by [10] in their studies. A higher strength normal concrete was tested in a resonance testing machine at a frequency of ~ 62 Hz. All these investigations show that the frequency has an influence on the temperature development as well as on the maximum temperature. Furthermore, the influence of the stress level is clearly visible. Thus the temperature rises faster at a high stress level, but a higher maximum temperature is reached at lower stress levels.

2.1.2 Humidity

Concretes with different humidity at different load levels at 10 Hz were compared to evaluate the effect of humidity. [12] tested an HPC with three different storage conditions and the resulting humidities. The concrete humidity varies between 0.1% by weight for the dried test specimen of series D and 5.1% by weight for under water stored test specimen of series UW. The test specimen stored with normative climate conditions (20 °C / 65%) show 4.0% per weight which is very close to the under water storage results. Figure 4 (left) shows the maximum temperature increase values of all tests plotted versus the number of cycles to failure. The run-out tests were not considered. It can be seen that for the dried samples the maximum temperature increase is lower compared to the tests with a concrete humidity of 4.0% and 5.1% respectively (series N and UW) even if the number of cycles to failure is in the same order. It is obvious that the temperature increase rises with increasing number of load cycles for both humid and dried samples because the specimen has more time to heat up. The temperature increase depending on the concrete humidity is exemplary shown for three tests at the stress level of $S_0 = 0.7$ in Fig. 3. For both humid concrete specimens (series N and UW) the temperature increase is much faster compared to the red curve of the dried concrete.

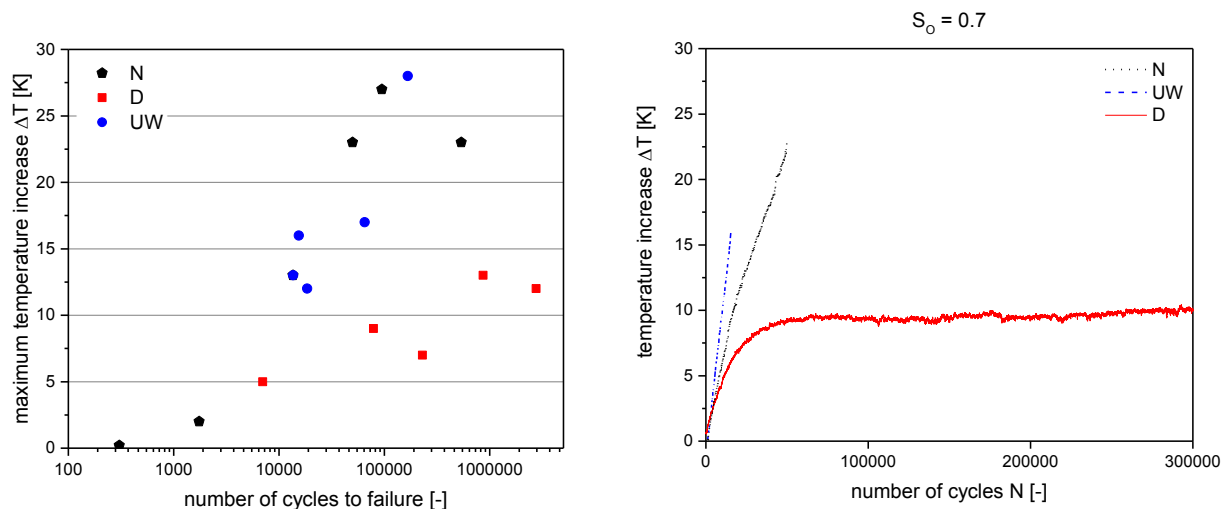


Fig. 3 Maximum temperature increase of the three series (left) and temperature increase of the three series at the load level $S_0 = 0.7$ [12].

2.1.3 Specimen and maximum grain size

Fatigue tests under cyclic compressive fatigue loading are normally performed on cylindrical specimens with an h/d ratio of 3:1. Specimen sizes of 300/100 or 180/60 are often used. If HPC or UHPC concretes are used, cylinders with a diameter of 60 mm are used for reasons of the load to be placed. To determine the influence of the sample size, [3] examined samples with a diameter of 60 or 100 mm. The specimens were stored under water until the test. They were tested unsealed at 1 Hz and at a load level of $S_0 = 0.7$. The results of the investigations (Fig. 4, right) have shown that the specimens with a diameter of 60 mm (black dotted) compared to the specimens with 100 mm (black line) at first have a similar temperature curve, but already after a few hundred load cycles the temperature increase reduces with the smaller diameters. Looking at the maximum temperature increase that has been realized, the samples with a diameter of 100 mm become significantly warmer. Accordingly, the specimen size also has an influence on the temperature curve. The fact that the largest grain has an influence was investigated by [4]. Three high-strength grouting mortar with different maximum grain sizes were tested. Fig. 4 shows in the left diagram the temperature increase over time during the fatigue process. The three grouting concretes were examined at a frequency of 10 Hz and a maximum

stress of 75% and a minimum stress of 5%. Although all three mixtures approximate the same maximum temperature, they differ in their temperature increase. [4] therefore shows that the smaller the largest grain, the stronger the specimen heating at the same loading level. Since the maximum temperature increase for all specimens is between 13 and 16 K, there seems to be a correlation between temperature and lifetime. Besides the variation of the maximum grain size, the size of the test specimen can also be varied.

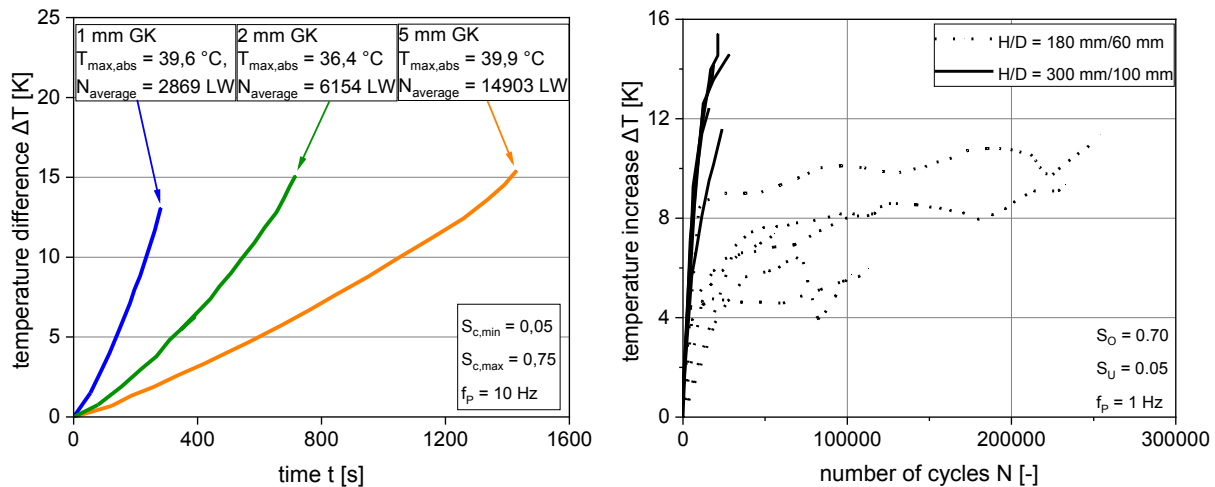


Fig. 4 Heating of the specimens depending on the maximum grain size according to [4] (left) and temperature increase of different specimen sizes according to [3] (right).

3 Experiments

3.1 Material and geometry

For the experimental work, an HPC with a water/cement ratio of 0.35 was used. The mixing of the concrete was done with a conventional single-shaft mixer. For comparability between the different batches, the same amount of concrete was produced at each concreting. The overview of the exact composition of the concrete and the fresh concrete properties is given by [12]. All samples for the compressive strength and for the fatigue tests had a cylindrical shape with 180 mm in height and a diameter of 60 mm (d/h ratio of 1/3).

3.2 Storage conditions and humidity

Two test series with different storage conditions were planned to investigate the influence of the concrete humidity. The test series D with dried test specimen and the test series N with storage conditions of 20°C and 65% relative humidity were conducted. After concreting, all samples were stripped after 24 h and stored under water for 7 days. Subsequently the test specimens were cut to length and the top surfaces were grinded plane-parallel and polished. To minimise the influence of drying on the concrete hardening process the test specimens of series D were stored under the same conditions as series N for the first 56 days. Afterwards they were stored at 105°C for 28 days until the age of at least 70 days. The humidity of the concrete was determined for each test series on two samples by oven drying at 105°C . The age of the samples was the same as in the fatigue tests. Before testing, all specimens were wrapped in a diffusion-tight foil to prevent changes of the concrete humidity during the test. The storage conditions and the humidity of the series are summarised in Table 1.

Table 1 Storage conditions and humidity of the three series

Series	Day 1	Day1-7	Day 8-56	Day 56 - Test	Before testing	Humidity
D (Dry Specimen)	strip the form- work	under- water	20 °C / 65%	105 °C	wrap	0.1%
N (Normative Storage			20 °C / 65%			4.0%

3.3 Test setup fatigue test

The fatigue tests were conducted on a servohydraulic Schenck testing machine with a maximum load capacity of 400 kN. Each test was operated load controlled. The testing machine and the test setup are shown in [12]. To minimise unintended bending of the test specimen due to imperfection of the plane-parallel top and bottom sides of the cylinders, a load transfer plate with a cup and ball bearing was used. During the tests, the number of load cycles, the applied loads, the deformation of the specimen and the temperature development were measured. The deformation was measured by four displacement transducers WA 1 - 4 adapted between the load transfer plates. The strain is calculated from the measured deformations under the assumption of constant strain over the height of the specimen. The positions of the transducers are shown in [12].

3.4 Experimental programme

All tests were carried out with a sinusoidal loading at a constant frequency of 10 Hz. The normalised minimum stress was $S_u = \sigma_u / f_{c,cyl} = 0.05$ and the normalised maximum stress $S_o = \sigma_o / f_{c,cyl}$ varied from $S_o = 0.55$ to $S_o = 0.8$ according to Table 2. Tests with > 2.5 million load cycles were treated as run-outs. The test program of the two series is shown in Table 2.

Table 2 Experimental outline of the three series [12]

Series	Frequenzy [Hz]	S_o	S_u	Sealed/Unseald
D	10	0.8/0.7	0.05	Sealed
N	10	0.8/0.7/0.6/0.55	0.05	Sealed

4 Experimental Results

4.1 Temperature dependent static compressive strength

The static compressive strength was determined for each temperature on at least three test specimens. The cylinders were wrapped with the foil and heated to the respective temperature for 20 hours before the static compressive strength was determined. The static compressive strengths determined in this process in relation to the static compressive strength at 20 °C are plotted versus temperature in Fig. 7. The compressive strength of the series D is shown in red, series N in dashed black. It can be seen that the strength of the dried samples remains the same except at 50 °C. This can be attributed to the variation in compressive strength. In contrast, the compressive strengths of the samples with a humidity of 4.0% (N series) decrease with increasing temperature. The minimum is reached at 90 °C. At this temperature, the reduction due to the increased temperature was 28.6%. The fact that the strengths increase again with higher temperatures can also be seen in the literature [5].

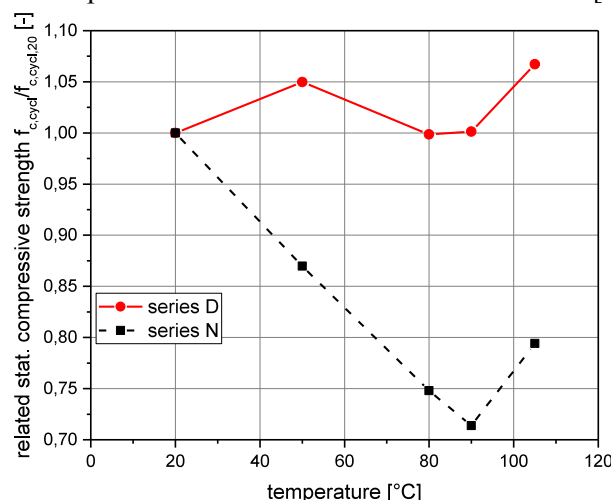


Fig. 5 Reduction of the static compressive strength depending on the concrete temperature.

4.2 Number of cycles to failure

The results of the fatigue tests according to Table 2 are given in Fig. 6. The number of cycles to failure is plotted in log scale versus the normalised maximum stress S_o . Additionally, a linear regression function was determined by using the function $f = m \times \log(N) + b$ for each of the two test series. The use of a bilinear function as suggested in [13] was not possible due to the small amount of high cycle tests with $n > 10^6$ cycles. Because of the few test results up to now the run-out tests were also used for the regression which is normally not the case in evaluation of fatigue test results. In Fig. 6 the run-out tests are marked with an arrow.

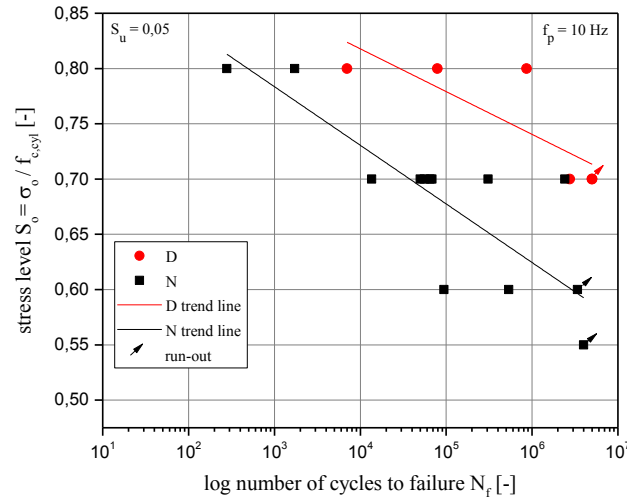


Fig. 6 Normalised stress versus number of cycles to failure

Comparing the tests at the highest stress level $S_o = 0.8$, it is obvious that the test specimen of series N (black) with a concrete humidity of 4% fail significantly earlier than the test specimen with dried concrete (concrete humidity of 0%). On the stress level $S_o = 0.7$ the same effect becomes visible. The humid concrete test specimen (4%) of series N fail up to two powers of ten earlier than the dried concrete specimen. At stress levels of $S_o \leq 0.6$ it was not possible to generate failures with Series N concrete specimens up to $n = 5 \times 10^6$ cycles.

4.3 Temperature increase

If the maximum final temperature on the surface in the middle of the specimen is considered and plotted over the number of cycles to failure, Fig. 7 is obtained. There it can be seen that the concrete reaches a higher final temperature as the number of cycles to failure increases. It can be shown that at the same number of cycles to failure, the samples of the series N reach a higher final temperature than the samples of the series D. The maximum final temperature measured during the tests was 58.9 °C. Accordingly, humidity has an influence on the maximum final temperature.

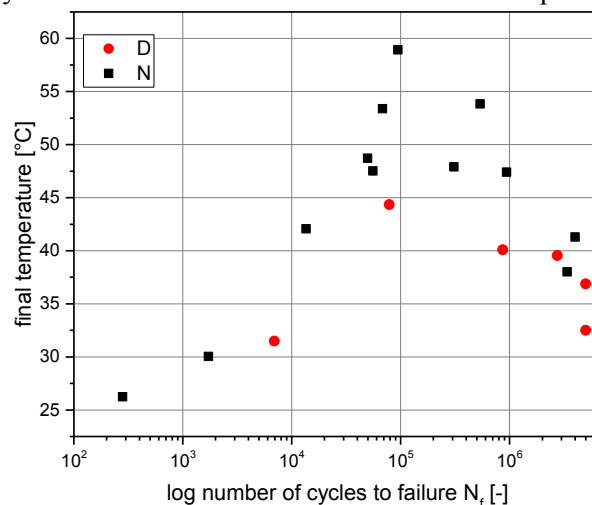


Fig. 7 Final temperature versus number of cycles to failure.

5 Effect of the temperature increase

As shown in chapter 4.3, the temperature of the sample increases during the experiment. The increase in temperature can dry out the sample [14] and pore water pressure can be generated [3]. Another point which should not be ignored is the reduction in static compressive strength due to the temperature increase. This effect can be seen in fig. 5 (chapter 4.1). A reduction in strength during the test has immediate consequences, because before the test begins the static compressive strength is determined and used as the basis for the stress levels with $f_{c,cyl,20^{\circ}C}$. If this value now changes due to an increase in temperature, the static compressive strength of concrete with humidity also changes, as shown in 4.1. This change in compressive strength means that the actual compressive strength no longer corresponds to the value at the beginning of the test. The results are the changes of the stress level and the stress range. This is shown as an example in Table 3 for the high stress level 0.7 with different reductions. If the increase in temperature results in a 15% reduction in compressive strength, the high stress level S_o increases from 0.7 by 17.65% to 0.82. It also behaves equivalently with the low stress level S_u and the stress range. Consequently, the increase in temperature has a significant influence on the stress levels and this has a great influence on the number of cycles to failure.

Table 3 Effect of the reduction in compressive strength on the stress levels

Reduction	S_o	S_u	$S_o - S_u$	Increase
0%	0.70	0.050	0.65	0.00%
10%	0.78	0.056	0.72	11.11%
15%	0.82	0.058	0.76	17.65%
20%	0.88	0.063	0.81	25.00%

6 Conclusions and outlook

Finally, there are many factors that influence the heating of concrete during cyclical compressive fatigue loading tests. In addition to the main influencing factors of frequency, stress level and humidity, there are others such as the maximum grain size. The influence of the heating of the concrete has a direct influence on the compressive fatigue tests. Heating of the concrete results in drying out of the concrete, the build-up of pore water pressures, but also in changes in the static compressive strength. In the investigations it could be shown that a distinction must be made between humid and dried concrete. In dried concrete, no humidity can dry out and no pore water pressure can build up. The dried concrete also shows no significant reduction in static compressive strength in the relevant temperature range. The situation is different for concrete with existing humidity. This concrete heats up more than dried concrete, it can dry out and pore water pressures can build up due to the compact structure of HPC. Furthermore, an important aspect is the effect of the temperature increase on the static compressive strength. Static tests have shown that the reduction can be as much as 28.6% compared to 20 °C. This reduction of the static compressive strength leads to a change in the stress levels and the oscillation width during the test. This effect makes it difficult to compare the tests with each other. Therefore, are further investigations useful and necessary. In further investigations it is planned to test the temperature development at 1 Hz and compare it with earlier experiments at 10 Hz. A further point of investigation is the behaviour of the concrete at a higher environmental temperature. For this purpose, the specimens are to be heated to 80 °C and tested in a climatic chamber to investigate the influence of fatigue under higher temperatures. Furthermore, the same oscillation widths at different levels of upper and lower stress levels have to be investigated in order to calculate the influence of the increase in stress range over time due to the increase in temperature.

Acknowledgements

Financial support was provided by the German Science Foundation (DFG) as part of the framework of the project “Temperature and humidity induced damage processes in concrete due to pure compressive fatigue loading” of the priority program 2020 through grand number GA519/9-1,2. This support is gratefully acknowledged.

References

- [1] Hohberg, R. 2004. “Zum Ermüdungsverhalten von Beton.” PhD diss., Karlsruhe Institute of Technology
- [2] Reinhardt, H.W., Stroeve, P., Uijl, J.A., Kooistra, T.R., Vrencken, J.H.A.M. 1978. “Einfluß von Schwingbreite, Belastungshöhe und Frequenz auf die Schwingfestigkeit von Beton bei niedrigen Bruchlastspielzahlen.” *Betonwerk + Fertigteil-Technik* 9:498-503
- [3] Hümme, J. 2018. “Ermüdungsverhalten von hochfestem Beton unter Wasser.” *Berichte aus dem Institut für Baustoff 18*.
- [4] Elsmeier, K., Hümme, J., Oneschkow, N., Lohaus, L. 2016. “Prüftechnische Einflüsse auf das Ermüdungsverhalten hochfester feinkörniger Vergussbetone.” *Beton- und Stahlbetonbau* 111(4):233-40.
- [5] Blundell, R., Dimond, C., Browne, R. 1976: “The properties of concrete subjected to elevated temperatures.” London: Ciria Underwater Engineering Group.
- [6] Budelmann, H. 1987. “Zum Einfluß erhöhter Temperatur auf Festigkeit und Verformung von Beton mit unterschiedlichen Feuchtegehalten.” PhD diss., Technische Universität Braunschweig.
- [7] Thienel, K.-Ch. 1993. “Festigkeit und Verformung von Beton bei hoher Temperatur und biaxialer Beanspruchung - Versuche und Modellbildung.” PhD diss., Technische Universität Braunschweig
- [8] Deutscher, M., Tran, N.L., Scheerer, S. 2019. “Experimental investigation of load-induced increase of temperature in UHPC.” *Advances in Engineering Materials, Structures and Systems: Innovations, Mechanics and Applications - Proc. of the 7th Int. Conf. on Structural Engineering (SEMC), Mechanics and Computation*, Zingoni, A. (Ed.), 2–4 September 2019, Cape Town (South Africa), London: Taylor & Francis. 1450-55.
- [9] Haar C, von der., Wedel, F., Marx, S. 2016. “Numerical and Experimental Investigations of the Warming of Fatigue Loaded Concrete.” Paper presented at the fib Symposium, Cape Town.
- [10] Grünberg, J., and Oneschkow, N. 2011. “Gründung von Offshore-Windenergieanlagen aus filigranen Betonkonstruktionen unter besonderer Beachtung des Ermüdungsverhaltens von hochfestem Beton.” *Abschlussbericht zum BMU Verbundforschungsprojekt*. Leibniz University Hannover.
- [11] Haar C, von der., Hümme, J., Marx, S., Lohaus, L. 2015. “Untersuchungen zum Ermüdungsverhalten eines höherfesten Normalbetons.” *Beton- und Stahlbetonbau* 110(10):699-709.
- [12] Markert, M., Veit, B., Garrecht, H. 2019. “Temperature and humidity induced damage processes in concrete due to pure compressive fatigue loading.” *Proceedings of the fib Symposium, Krakow, Poland*.
- [13] Fédération internationale du béton. 2013. “fib Model Code for concrete structures 2010.” Ernst & Sohn. Berlin.
- [14] Elsmeier, K. 2019. “Einfluss der Probekörperwärmung auf den Ermüdungswiderstand von hochfestem Vergussbeton.” PhD diss., *Berichte aus dem Institut für Baustoff 19*.

Microcracking of high-performance concrete under cyclic loading and the influence of the aggregate

Niklas Schäfer, Rolf Breitenbücher

*Institute for Building Materials,
Ruhr University Bochum,
Universitätsstraße 150, 44801 Bochum, Germany*

Abstract

The higher demand to create slender constructions makes the use of high-performance building materials indispensable. A consequence of such lightweight constructions is an increasing vulnerability to fatigue loads, caused by time variant loadings, which may ultimately lead to earlier fatigue failure. As a result of the inhomogeneity of the microstructure of concrete, even minor external mechanical stresses can lead to local stress peaks which consequently lead to changes in the microstructure. Under cyclic load, new microcracks are generated but also already existing microcracks propagate. An accumulation of these micro-damages oftentimes leads to premature failure. The design of filigree and slender constructions implies an increased sensitivity to vibrations due to variable external loads. This, however, may cause higher fatigue loads under cyclic stresses, which may further lead to damages or even failure of the concrete components before the bearable maximum static stress is reached. High-performance concretes have a denser matrix in comparison to normal-strength concretes, but the influence of the size and type of the aggregate on fatigue failure or microcracking for this case is still unknown.

In this context, systematic investigations of high-strength concrete, mortar and hardened cement paste subjected to static and cyclic compressive loadings were conducted to understand the influence of the aggregate on microcracking. The strain in longitudinal and transverse directions were continuously recorded by means of strain gauges. Strains in the transverse direction increased faster and thus represented an earlier indicator of fatigue progress than the longitudinal strains. This observation was more pronounced with high-strength mortar than with high-strength concrete.

Furthermore, the material degradation was investigated by means of microscopic analysis of the microcrack development. This analysis shows that both in concrete and in mortar microcracking primarily takes place in the interfacial transition zone (ITZ) and that the crack width changed only marginally during the applied load changes, predominantly newly formed microcracks appeared with increasing degradation. In hardened cement paste, it can be observed that microcracks originate in structural defects and pores such as imperfections. Additionally, it can be concluded that the increasing degradation essentially is caused by the formation of new microcracks. Furthermore, it can be assumed that a drop in stiffness only occurs when the microcrack density is so large that it leads to a connection of the microcracks. For the conducted tests, cylindrical specimens were subjected to a predefined number of load cycles. In order to reduce the time of the experimental investigations, a test setup has been developed which allows the simultaneous testing of three specimens. In this paper, the objective is to analyse the observed behaviour of high-performance concrete, mortar and hardened cement paste under cyclic loading and to identify the main causes for this behaviour on the micro-level.

Keywords: cyclic loading, microcracking, degradation, fatigue, high-strength concrete, SPP 2020

1 Introduction

In the last decades in concrete construction, an increasing demand for higher strength, smaller aggregate fractions and higher flowability has been gaining more attention. Fine-grained concretes are increasingly used in different areas of structural engineering. Examples for this are the load-carrying areas between supporting structures and the foundation structures of wind turbines (onshore and offshore). Therefore, high-strength mortars can be exposed to high cyclic loads of several hundred million load cycles. An increasing optimization of the grain size distribution in high-strength concretes also shows the need for research with regard to the influence of the aggregates on the micro-

cracking behaviour of high-strength concrete structures. Due to the fact that concrete is an inhomogeneous material, even minor external mechanical stresses can lead to high local stresses and consequently to structural degradation of the concrete. This is particularly important for cyclical load effects. Structural degradation in form of microcracking can already be seen with stresses far below of the static strength of the concrete. These microcracks and thus a degradation in the microstructure increase with increasing load cycles and can cause premature failure in the course of these stresses [1].

Microcracks, as they are considered in this paper, can also occasionally accrue in the unloaded state. This usually takes place along the aggregate boundaries and is caused primarily due to thermal and hygric incompatibilities between hardened cement stone and aggregate [2], [3]. Accordingly, the contact zone between the aggregate and the hardened cement stone ("Interfacial Transition Zone" = ITZ) is a weak point in the structure, at least in normal-strength concrete. Depending on the largest aggregate size and the rigidity of the aggregate, such microcracks are usually less than 10 µm wide and their length varies between about 50 µm and 1500 µm [3], [4].

In high-strength concrete there are three phases of damage evolution which finally lead to a fatigue failure. In a first step, a significant number of microcracks are created (phase I). After this a further steady formation of microcracks takes place (phase II) which is significantly slower than during phase I. The formation of a coherent crack network ultimately leads to final failure (phase III) [5].

In normal strength concrete, microcracks usually originate in the contact zone between the aggregate and the hardened cement stone (ITZ) [6]. So far, no clear starting point for the microcracks could be identified in high-strength concretes due to the more homogeneous structure [3]. According to [7], in high-performance concretes predominantly microcracks, which connect aggregates were found, usually at the location of the smallest distance between the aggregates. Accordingly, in addition to the tensile strength of hardened cement paste, the bond between the aggregate and the cement paste is of considerable importance. [3] also showed that the number of microcracks and the area of the microcrack increased the larger the largest aggregate or the greater the aggregate stiffness [8].

Newer investigations on ultra high-performance concrete show a preliminary stage of cracks in the matrix of high-strength concretes on a nanometer scale. It is also shown that after early-stage fatigue, the cement paste already appears much more densely packed with microcracks. In conclusion of these investigations, it can be said that fatigue of ultra high-performance concrete manifests as nanometer-scale crack precursors in the cement paste matrix, beginning in phase I of fatigue [9]. It can also be said that in ultra high-performance concrete the crack initiation and propagation have an exponential growth and the failure is dominated by the ITZ. Reason for this are the stress concentrations around the aggregate which are induced into the ITZ [10].

The investigations on the influence of aggregates on fatigue behaviour and the behaviour of high-performance concrete presented here are part of the Priority Program 2020 "Cyclic deterioration of High-Performance Concrete in an experimental-virtual lab". The aim of this paper is to describe the testing set-up and to present an excerpt of the results.

2 Experimental investigations

Since fatigue tests are always carried out with a load level below the maximum strength, thus the static compressive strength must be determined prior to testing. In this study, cyclic tests were carried out on specimens with three different compositions that were characterized by the stepwise elimination of aggregate. The reference composition was common for a high-strength concrete.

2.1 Materials and composition

The experimental investigations within this paper are conducted on high-strength concrete, mortar and hardened cement paste with compressive strengths of 108 MPa (concrete), 91 MPa (mortar) and 76 MPa (hardened cement paste). The respective compositions are shown in Table 1. For all compositions a Portland cement I 52.5 R was used. Fine quartz sand, mineral sand and basalt with a maximum particle size of 8 mm were used for the compositions with aggregate. A superplasticizer and a stabilizer were added (exception: hardened cement paste). From the reference composition HPC-08 (08 represents the maximum aggregate size of 8 mm) a high-strength mortar (HPC-02) was derived by eliminating all aggregates with a particle size above 2 mm so that there is no basalt aggregate in the composition. Consequently, the hardened cement paste (HPC-00) has no aggregate at all. The w/c

ratio was kept constant at 0.35. Different water absorption of the aggregates were only relevant for fresh concrete properties and were compensated by superplasticizer.

Table 1 Compositions.

Materials	HPC-08	HPC-02	HPC-00
Cement [kg/m ³]	500	646	1460
Quartz sand 0/0.5 [kg/m ³]	75	150	-
Mineral sand 0/2 [kg/m ³]	850	1333	-
Basalt 2/5 [kg/m ³]	350	-	-
Basalt 5/8 [kg/m ³]	570	-	-
Superplasticizer [kg/m ³]	5.0	4.85	-
Stabilizer [kg/m ³]	2.85	2.76	-
Water [kg/m ³]	176	227.4	513.9
w/c [-]	0.35	0.35	0.35

2.2 Experimental method and variations

In force-controlled fatigue tests, the test specimens were subjected to compressive stresses at sinusoidal load functions with varied upper and lower loads. The stress levels were chosen in dependence on common fatigue tests carried out at the Institute for Building Materials of the Ruhr University Bochum. The cyclic loading was completed after up to 1 million cycles respectively at the maximum reachable number of load cycles. The load frequency of the cyclic tests was 5 Hz. A total of 72 specimens were tested as part of the present study.

The following parameters were varied and investigated:

- maximum particle size of the aggregate and no aggregate at all,
- upper load level: 70 % and 45 % of the maximum static compressive strength($f_{c,max}$)
- number of load cycles: 0, 100,000, 1 million

The lower level of 10 % of $f_{c,max}$ was kept constant. For hardened cement paste it was increased to 15 % of $f_{c,max}$ due to test restrictions.

2.3 Experimental setup and investigation

Cyclic compressive tests were carried out on cylindrical specimens with a diameter of 100 mm and a height of 300 mm for HPC-08. For HPC-02 and HPC-00 cylindrical specimens with a diameter of 50 mm and a height of 150 mm were used (Fig. 1). Due to the slenderness of the test specimen the transverse strain in and around the mid side of the specimen is unimpeded. The strain in longitudinal and transverse directions were continuously recorded by means of strain gauges (Fig. 1).

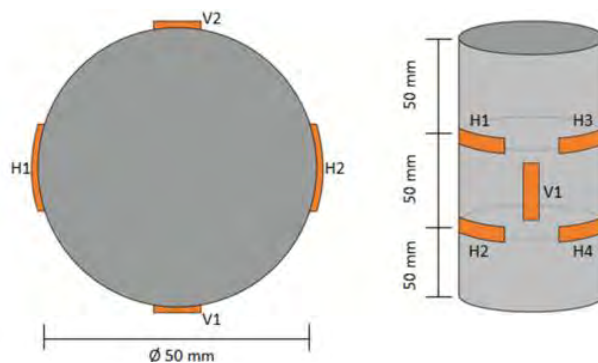


Fig. 1 Schematic test specimen with strain gauges for high-strength mortar and hardened cement paste.

In order to be able to carry out as many cyclical tests as possible and thus ensure the reproducibility of the results, a multiple test setup was designed and built based on the test setups for cyclic bending tests [11] already developed at Ruhr University Bochum. This enables the simultaneous and congruent loading of three test specimens under compressive load. The test setup consists of three rigid steel frames (Fig. 2), each equipped with a hydraulic differential cylinder with a maximum piston force of 1000 kN (force-controlled) and a maximum load frequency of 7 Hz. The load is introduced via spherical balls specifically designed for the multiple test setup with connected pressure plates. The flexible structure of the test frame allows testing of specimens with different heights and diameters. The typical dimensions for specimens in fatigue research are 300/100 mm, 180/60 mm, 150/50 mm, which corresponds to an h/d ratio of 3/1.[12]

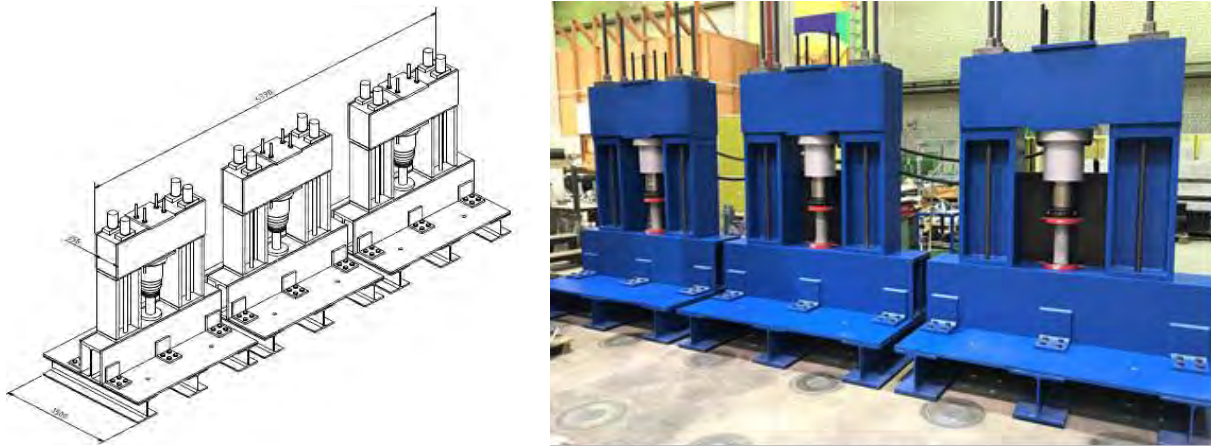


Fig. 2 Multiple test set-up: schematic (left), reality (right) [12].

2.4 Microscopic investigations

After 0, 100,000 and 1 million load cycles, one test specimens of the three tested specimens each series is extracted, from which partial samples for microscopic examinations (amount, length, width and position of the microcracks) are prepared as thick-sections with colored resin (blue). Therefore, two thick-sections were taken out of the test specimen in longitudinal and in transverse direction, see Figure 3. Thick-sections refers to a preparation with a thickness of 100-200 μm . With the thick sections being prepared after the specimens were subjected to a different number of load cycles it is possible to capture the crack evolution over the course of fatigue behaviour.

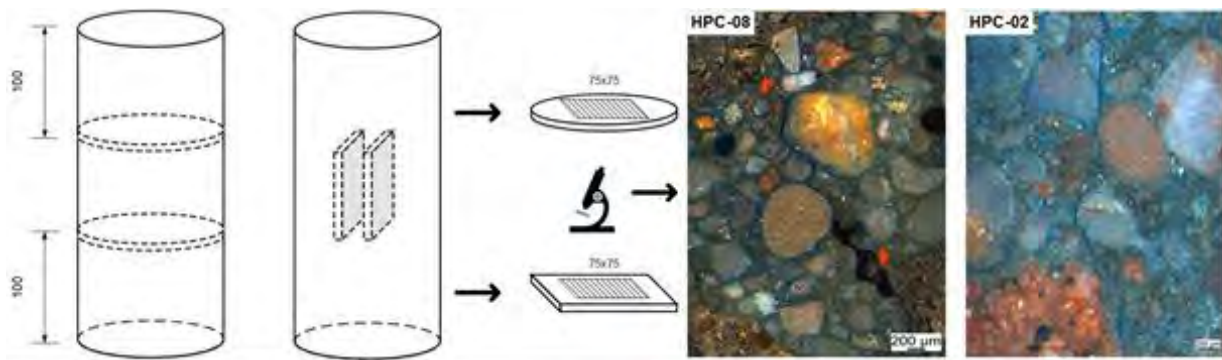


Fig. 3 Schematic representation of microscopic investigations [12].

3 Results

3.1 Longitudinal and transversal strains

Systematic investigations of high-strength concrete, mortar and hardened cement paste subjected to static and cyclic compressive loadings were conducted to understand the influence of the aggregates with special regard to the microcracking. Another aim of the study was to gain knowledge about the starting point of microcracks in comparison to the size of aggregate respectively without aggregate. The comparison of the longitudinal and transverse strain of high-strength concrete, mortar and hardened cement paste is shown in Figure 4 and 5. The strain in longitudinal and transverse directions were continuously recorded by means of strain gauges. Strains in the transverse direction increased faster and thus represented an earlier indicator of fatigue progress than the longitudinal strains. This observation was more pronounced with high-strength mortar than with high-strength concrete. In hardened cement paste it was comparable with high-strength concrete. There is a characteristic relationship between transverse and longitudinal deformation. Until the limit of proportionality was reached, the ratio between transverse and longitudinal strain is almost constant. However, when the stress increased above the limit of proportionality, the transverse strain grow faster compared to the longitudinal strain. That means the ratio between transverse and longitudinal strain increased. For the hardened cement paste a crossing to phase III of the fatigue evolution could not be observed. The longitudinal strains are characterized by an inverse, disproportionate growth of the upper and lower expansions in the beginning of the curves. After this, the upper and lower strains increase almost linearly and parallel to one another (HPC-00).

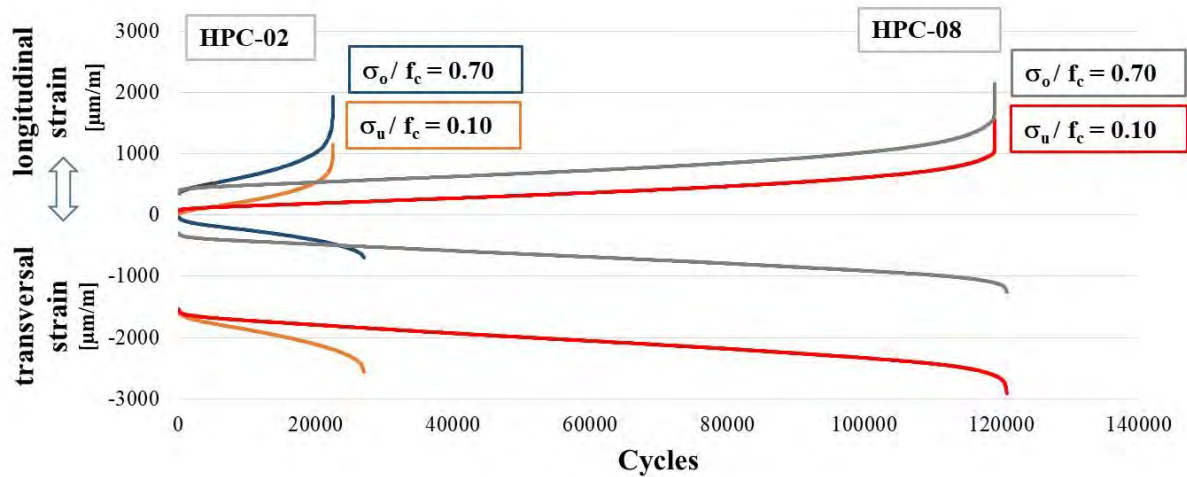


Fig. 4 Transverse and longitudinal strain of HPC-08 and HPC-02.

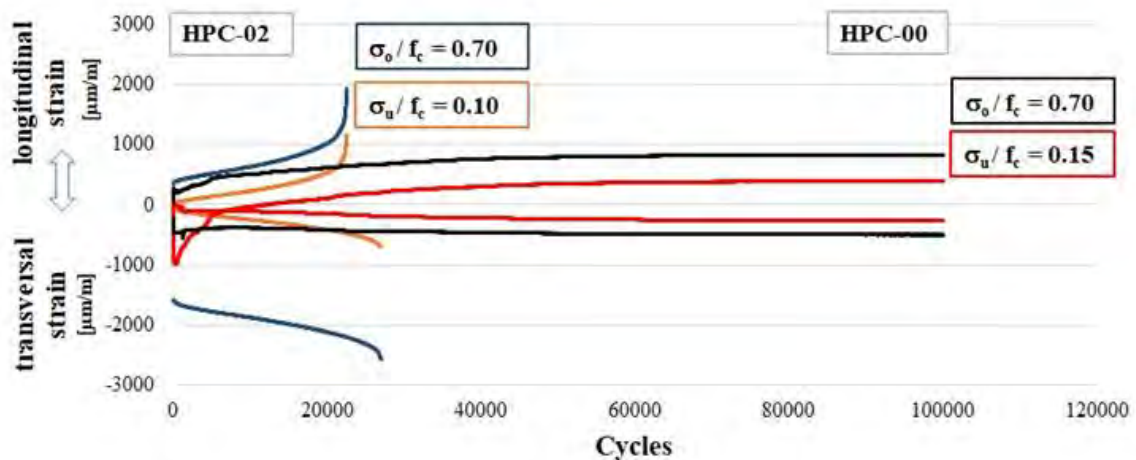


Fig. 5 Transverse and longitudinal strain of HPC-02 and HPC-00.

3.2 Microscopic investigations

To gain knowledge of the microcracking behaviour (amount, length, width and position) as a function of the size and the presence of aggregates, four thick-sections (two vertical and two horizontal, see Fig. 3) were taken from each test specimen after a defined number of load cycles. In this paper only thick sections are considered which were loaded with an upper load of 45 % of $f_{c, \max}$. For HPC-08 predominantly new microcracks formed (Tab. 2) and the microcracks are detected in > 90 % in the ITZ. Just less than 10 % of the microcracks are only in the hardened cement paste. It can be assumed that the decrease in stiffness only occurs when the microcrack density is so large that the microcracks are connected. Furthermore, it can also be concluded from this that the increasing degradation is essentially due to the formation of new microcracks. In HPC-02 the number of microcracks is generally larger and there is also no noticeable increase in the number of microcracks with increasing load cycles (Tab. 3). Cracks were often found in the ITZ and within the aggregate. In HPC-02, around 50-60 % of the microcracks run through the aggregate and around 30 % in the ITZ. For hardened cement paste it can be said that in addition to the clear microcracks, the thick sections also show structural defects or pores that could not be identified as a microcrack. Structural defects can be defined as sections where the cement paste matrix has a smaller density. Microcracks primarily could be found in the areas of structural defects. It could be seen that part of the colored resin had penetrated into the imperfections, but there were no clear microcracks with clear crack edges. It could also be observed that in many cases the hardened cement paste along the crack edge had turned a light grayish, almost whitish or brownish discoloration (Fig. 6). Another starting point for microcracks in HPC-00 was detected in pores (Fig. 7). The evaluation of the vertical thick sections, i.e. the thick sections that were taken in the direction of load, predominantly showed cracks in the vertical direction, i.e. in the direction of the load. This could be observed most clearly with HPC-02 (73 % vertical; 27 % horizontal), followed by HPC-00 (60.3 % vertical; 39.7 % horizontal) and with HPC-08 the divergence was relatively balanced (52.5 % vertical; 47.5 % horizontal).

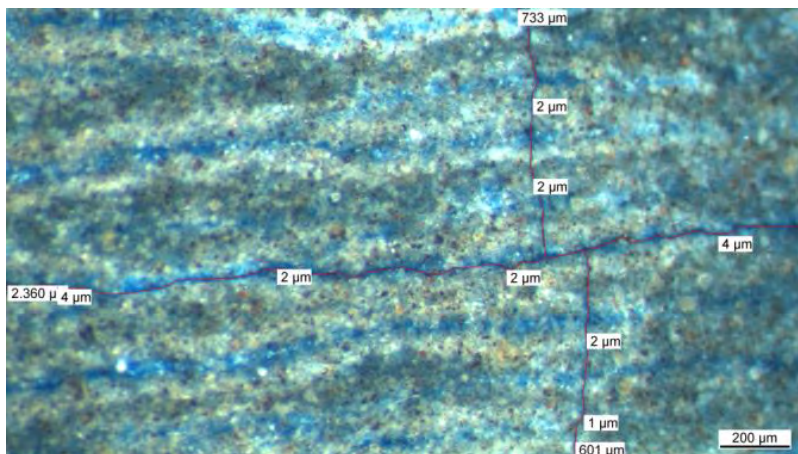


Fig. 6 Example of structural defects as a starting point of microcracks in HPC-00.

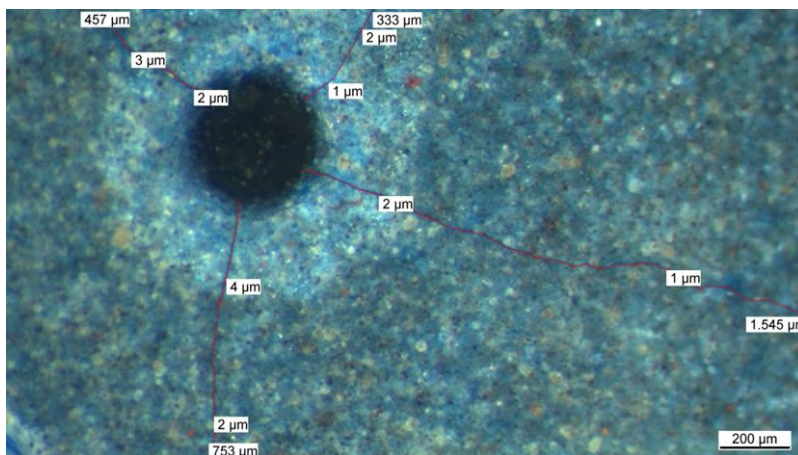


Fig. 7 Example of a pore as a starting point of microcracks in HPC-00.

Table 2 Microscopic analysis of HPC-08.

HPC-08		Reference	$\sigma_{\max} / f_c = 0.45$ $\sigma_{\min} / f_c = 0.10$			
		Cycles				
			vertical ¹		horizontal ²	
		0	100,000	1 Mio.	100,000	1 Mio.
Number of cracks	[-]	143	387	382	382	375
Mean crack width*	[μm]	3,48	6,0	6,0	7,0	6.0
Mean crack length*	[μm]	471	462	550	346	546
Mean crack area*	[μm²]	1960	3250	4275	2750	3235
Total crack area (75x75 mm²)	[μm²]	279,672	1,207,317	1,810,517	1,048,073	1,205,251

Table 3 Microscopic analysis of HPC-02.

HPC-02		Reference	$\sigma_{\max} / f_c = 0.45$ $\sigma_{\min} / f_c = 0.10$			
		Cycles				
			vertical ¹		horizontal ²	
		0	100,000	1 Mio.	100,000	1 Mio.
Number of cracks	[-]	106	78	75	69	68
Mean crack width*	[μm]	5.53	4.0	3.7	4.7	5.2
Mean crack length*	[μm]	565.5	606	568	614	504
Mean crack area*	[μm²]	3470	2460	2350	2800	2550
Total crack area (75x75 mm²)	[μm²]	368,205	189,127	171,518	192,884	171,984

Table 4 Microscopic analysis of HPC-00.

HPC-00		Reference	$\sigma_{\max} / f_c = 0.45$ $\sigma_{\min} / f_c = 0.15$				
		Cycles					
			vertical ¹		horizontal ²		
		0	100,000	1 Mio.	100,000	1 Mio.	
Number of cracks	[-]	173	278	220	374	303	
Mean crack width*	[μm]	3,36	7.39	10,5	7,56	8,29	
Mean crack length*	[μm]	1517	1508	1482	1485	1500	
Mean crack area*	[μm²]	5390	11,745	17,050	11,690	13,030	
Total crack area (75x75 mm²)	[μm²]	933,059	3,228,224	3,744,658	4,357,824	3,940,240	

*individual crack ¹vertical thick-sections (load direction) ²horizontal thick-sections

4 Conclusion

Fatigue tests on high-strength concrete, mortar and hardened cement paste specimens were conducted to investigate the influence of aggregates on the fatigue behaviour. Furthermore, a microscopic analysis on prepared thick sections of the tested specimens was carried out. The described test procedure lead to the following conclusions regarding the specific stress levels and stress amplitude:

- It is shown that the high-strength mortar had an earlier fatigue failure in comparison to the high-strength concrete and hardened cement paste.
- For all compositions, the strains in the transverse direction increased faster and thus represented an earlier indicator of fatigue progress than the longitudinal strains.
- The microscopic crack analysis of the thick sections showed an increased formation of new microcracks during cyclic loading for high-strength concrete. An extension or widening of pre-existing cracks was rarely observed at all compositions.
- The size of the aggregate had no influence on the starting point of the microcracks. Most microcracks start at ITZ between aggregate and hardened cement stone (HPC-08 and HPC-02). In addition, for HPC-02 a larger number of microcracks within or through the aggregate were detected.
- In HPC-00 a starting point for microcracks could be found in structural defects or pores.
- Most (> 60 %) of the microcracks are orientated in vertical (load) direction.

Acknowledgements

The authors are grateful to the German Research Foundation (DFG) for their financial support of this research project. The author is solely responsible for the content.

References

- [1] Ibuk, H. 2008. Ermüdungsverhalten von Beton unter Druckschwellbelastung. PhD thesis, Ruhr-Universität Bochum.
- [2] Hohberg, R. 2004. Zum Ermüdungsverhalten von Beton. PhD thesis, Technische Universität Berlin.
- [3] Kustermann, A. 2005. Einflüsse auf die Bildung von Mikrorissen im Betongefüge. PhD thesis, Universität der Bundeswehr München, Institut für Werkstoffe des Bauwesens.
- [4] Przondziono, R.; Timothy, J.J.; Nguyen, M.; Weise, F.; Breitenbücher, R.; Meschke, G.; Meng, B. 2015. Vorschädigung in Beton infolge zyklischer Beanspruchung und deren Auswirkung auf Transportprozesse auf eine schädigende AKR. *Beton- und Stahlbetonbau*, 110(1), pp. 3-12.
- [5] Thiele, M. 2015. Experimentelle Untersuchung und Analyse der Schädigungsevolution in Beton unter hochzyklischen Ermüdungsbeanspruchungen. PhD thesis, Technische Universität Berlin
- [6] Tasdemir, C. 1995. Microstructural Effects on the brittleness of High Strength Concrete. *Fracture Mechanics of Concrete Structures (Proceedings FRAMCOS-2)*, pp. 125-134.
- [7] Guse, U.; Hilsdorf, H. K. 1998. Dauerhaftigkeit hochfester Betone. *Deutscher Ausschuss für Stahlbeton*, Heft 487, Beuth Verlag Berlin.
- [8] Breitenbücher, R.; Ibuk, H.; Yüceoglu, S. 2008. Beeinflusst die Kornsteifigkeit der Gesteinskörnung im Beton den Degradationsprozess infolge zyklischer Druckbeanspruchung? *Beton- und Stahlbetonbau*, 103(5), pp. 318-323.
- [9] Schaan, G.; Rybczynski, R.; Schmidt-Döhl, F.; Ritter, M. 2020. Fatigue of Concrete Examined on the Nanoscale. *Imaging & Microscopy 2020* (2), pp. 25-27.
- [10] Rybczyński, S.; Dosta, M.; Schaan, G.; Ritter, M.; Schmidt-Döhl, F. 2020. Numerical study on the mechanical behavior of ultrahigh performance concrete using a three- phase discrete element model, *Structural Concrete*, pp. 1-16.
- [11] Przondziono, R.; Schulte-Schrepping, C.; Breitenbücher, R. 2018. Innovativer Mehrfachprüfstand zur zyklischen Beanspruchung großformatiger Betonprobekörper. In: *Beton- und Stahlbetonbau* 01/2018, Vol. 113, pp. 48-57.
- [12] Schäfer, N.; Breitenbücher, R. (2020). Influence of Aggregate on Fatigue Behavior of High-Performance Concrete Under Cyclic Loading. In: *Proceedings of the fib Symposium 2020*, Shanghai, China, pp. 781-787.

Author Index

- Abdul Razak Hashim, 18–26
Al Haffar Noha, 122–129
Al Haj Sleiman Sara, 130–136
Alam Syed Yasir, 130–136
Aldrighetti Gianluca, 98–105
Anthiniac Patrice, 160–167

Basaldella Marco, 243–250
Berto Luisa, 98–105
Boháček Lukáš, 27–36
Bolešová Mária, 76–82
Bonger Addisu Desalegne, 144–151
Bouchaïr Abdelhamid, 52–58
Breitenbücher Rolf, 275–282
Bujnak Jan, 52–58

Cherki El Idrissi Anass, 184–193
Chijiwa Nobuhiro, 83–90
Couavoux Laurie, 52–58

De Almeida Luiz Carlos, 68–75

Fabbri Antonin, 122–129
Ferracuti Barbara, 218–225
Fischer Oliver, 258–265
Fujiyama Chikako, 227–234
Fukaya Takahisa, 144–151

Garrecht Harald, 266–274
Gašpárek Jakub, 152–159
Ghayeb Haider Hamad, 18–26
Grabowska Kalina, 115–121
Grimal Etienne, 184–193
Grondin Frederic, 130–136

Hafner Ivan, 211–217
Haist Michael, 251–257
Hendriks Max A.n., 203–210
Hosoda Akira, 144–151
Húlek Lukáš, 152–159

Ito Youhei, 83–90
Izoret Laurent, 130–136

Katarína Gajdošová, 76–82
Kern Bianca, 251–257
Keršner Zbyněk, 10–17
Kim Hung Mo, 18–26
Kišiček Tomislav, 211–217
Kolmayer Philippe, 184–193
Koniorczyk Marcin, 115–121
Koschemann Marc, 176–183
Kosior-Kazberuk Marta, 37–43
Koščák Ianko, 211–217

Kucharczyková Barbara, 10–17
Kurihara Ryota, 83–90

Lacombe Clement, 160–167
Lantsoght Eva O.l., 195–202
Lauff Philipp, 258–265
Lehký David, 10–17
Leone Marianovella, 169–175
Li Kefei, 107–114
Lipowczan Martin, 10–17
Lohaus Ludger, 243–257
Loukili Ahmed, 130–136

Manzanal Diego, 137–143
Markert Martin, 266–274
Martín Christian Marcelo, 137–143
Masson Benoit, 184–193
Mcgregor Fionn, 122–129
Menon Devdas, 2–9, 91–97
Morenon Pierre, 184–193
Multon Stéphane, 184–193

Noret Christine, 160–167
Novak Drahomir, 45–51
Novak Lukas, 45–51

Oneschkow Nadja, 235–257

P Mary Williams, 91–97
Pampanin Stefano, 218–225
Paulík Peter, 152–159
Piqué Teresa María, 137–143
Prasad A Meher, 2–9
Prasad Anumolu Meher, 91–97

Quadri Ajibola Ibrahim, 227–234

Ramli Sulong N.h., 18–26
Renić Tvrtko, 211–217
Romanazzi Vincenzo, 169–175

Sabene Marcello, 218–225
Saetta Anna, 98–105
Salem Hamed, 144–151
Sanabria Díaz Rafael Andrés, 68–75
Scarponi Nadia Belén, 137–143

Scheiden Tim, 235–242
Schäfer Niklas, 275–282
Sellier Alain, 160–167, 184–193
Shaji Aishwarya, 2–9
Sharma Akanshu, 59–67
Stehle Erik Johannes, 59–67
Stella Alberto, 98–105
Stepinac Mislav, 211–217

Talledo Diego Alejandro, 98–105
Trautwein Leandro Mouta, 68–75

Vidal Thierry, 160–167
Villagrán-Zaccardi Yury A., 137–143
Vo Daniela, 184–193

Wang Zhen, 107–114
Wasilczyk Rafal, 37–43

Yang Yuguang, 203–210

Zarate Garnica Gabriela, 203–210
Zarate Garnica Gabriela I., 195–202
Zhang Fengqiao, 203–210
Zucconi Maria, 218–225

Šimonová Hana, 10–17

Previous *fib* International PhD Symposia

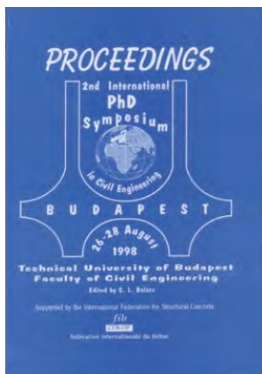


1st *fib* International PhD Symposium in Civil Engineering

May 1996, Technical University of Budapest, Budapest, Hungary

Order info:

Balazs, Gyorgy (Ed.)
Sokszorosította a Muegyetemi Kiado
Risograph technologiaival
Fedelos vezető: Veress Janos
Munkaszám: 96-Mk10
E-mail: fib@eik.bme.hu
ISBN 963 420 504 6



2nd *fib* International PhD Symposium in Civil Engineering

August 1998, Technical University of Budapest, Budapest, Hungary

Order info:

Balazs, Gyorgy (Ed.)
Publishing Company of Technical University of Budapest
Head: Janos Veress
Offset printing No: 98-0134
E-mail: fib@eik.bme.hu
ISBN 963 420 560 7



3rd *fib* International PhD Symposium in Civil Engineering

October 2000, University of Agricultural Sciences Vienna, Austria

Order info:

IKI - Institute for Structural Engineering
BOKU – University of Agricultural Sciences
Peter Jordanstr. 82, A-1190 Vienna, Austria
Phone: +43 1 47654 5250
Fax: +43 1 47654 5292
E-mail: lilo@iki.boku.ac.at
ISSN 1028-5334



4th *fib* International PhD Symposium in Civil Engineering

September 2002, Technische Universität München

Universität der Bundeswehr München, München, Germany

Order info:

Springer-VDI-Verlag GmbH & Co. KG
Düsseldorf, Germany
ISBN 3-935065-09-4



5th *fib* International PhD Symposium in Civil Engineering

June 2004, Delft University of Technology, Delft, The Netherlands

Order info:

W. Sutjiadi
Faculty of Civil Engineering and Geosciences
Delft Univ. of Technology
Stevinweg 1, 2628 CN Delft, The Netherlands
Tel: +31 15 278 4665
Fax: +31 15 278 7313
E-mail: w.sutjiadi@ct.tudelft.nl
ISBN Vol 1: 90 5809 677 7
ISBN Vol 2: 90 5809 678 5



6th *fib* International PhD Symposium in Civil Engineering

August 2006, ETH Zurich, Zurich, Switzerland

Order info:

fib secretariat
Case Postale 88
CH-1015 Lausanne, Switzerland
Phone: + 41 21 693 2747
Fax: + 41 21 693 6245
E-mail: fib@epfl.ch



7th *fib* International PhD Symposium in Civil Engineering

September 2008, University of Stuttgart, Stuttgart, Germany

Order info:

PhD Symposium Secretariat
IWB Universitat Stuttgart
Pfaffenwaldring 4
70569 Stuttgart, Germany
Phone: +49 711 685 63320
Fax: +49 711 685 67681
E-mail: stumpp@iwb.uni-stuttgart.de



8th *fib* International PhD Symposium in Civil Engineering

June 2010, Technical University of Denmark, Kgs. Lyngby, Denmark

Order info:

Technical University of Denmark
Department of Civil Engineering, Brovej, Building 118
DK-2800 Kgs. Lyngby, Denmark
Phone: + 45 45 25 17 00
Fax: + 45 45 88 32 82
E-mail: byg@byg.dtu.dk



9th *fib* International PhD Symposium in Civil Engineering

July 2012, Karlsruhe Institute of Technology (KIT), Karlsruhe, Germany

Order info:

KIT Scientific Publishing
 Strasse am Forum 2
 D-76131 Karlsruhe
 Germany Phone: + 49 721 608 43104
 Fax: + 49 721 608 44886
 E-mail: info@ksp.kit.edu
 Available as download at: <http://www.ksp.kit.edu>



10th *fib* International PhD Symposium in Civil Engineering

July 2014, Université Laval, Quebec, Canada

Order info:

Research Centre on Concrete Infrastructure (CRIB)
 Université Laval
 Quebec (Quebec)
 Canada, G1V 0A6
 Phone: + 418-656-3303
 E-mail: josee.bastien@gci.ulaval.ca
 Available as download at: <https://www.fib-phd.ulaval.ca>

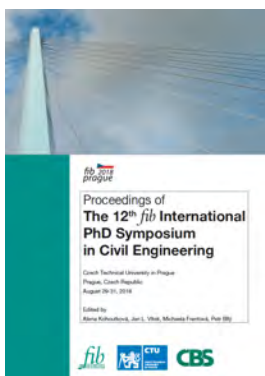


11th *fib* International PhD Symposium in Civil Engineering

August 2016, The University of Tokyo, Japan

Order info:

The University of Tokyo
 7-3-1 Hongo, Bunkyo-ku
 113-8656, Tokyo, Japan
 Phone: + 81-3-5841-6010
 E-mail: fib-phd2016@concrete.t.u-tokyo.ac.jp
 Available as download at:
http://concrete.t.u-tokyo.ac.jp/fib_PhD2016/
 ISBN 978 4 9909148 0 6



12th *fib* International PhD Symposium in Civil Engineering

August 2018, Czech Technical University in Prague, Czech Republic

Order info:

Czech Technical University in Prague
 Jugoslávských partyzánů 1580/3
 160 00 Prague 6 - Dejvice
 Czech Republic
 Available as download at:
www.fib-international.org/publications/fib-proceedings.html
 ISBN 978-80-01-06401-6

Proceedings of the 2021 session of the
13th *fib* International PhD Symposium in Civil Engineering
held in Paris, France,
July 21-22, 2021.

Edited by: Fabrice Gatuingt & Jean-Michel Torrenti

The *fib*, Fédération internationale du béton, is a not-for-profit association formed by 45 national member groups and approximately 1000 corporate and individual members. The *fib*'s mission is to develop at an international level the study of scientific and practical matters capable of advancing the technical, economic, aesthetic and environmental performance of concrete construction.

The *fib* was formed in 1998 by the merger of the Euro-International Committee for Concrete (the CEB) and the International Federation for Pre-stressing (the FIP). These predecessor organizations existed independently since 1953 and 1952, respectively.